Transactions of the ASME®

Transactions of the ASME, Journal of Fluids Engineering (ISSN 0098-2202) is published quarterly (Mar., June, Sept., Dec.) by The American Society of Mechanical Engineers, Three Park Avenue, New York, NY 10016. Periodicals postage paid at New York, NY and additional mailing offices.
POSTMASTER: Send address changes to Transactions of the ASME, Journal of Fluids Engineering, c/o THE AMERICAN SOCIETY OF MECHANICAL ENGINEERS, 22 Law Drive, Box 2300, Fairfield, NJ 07007-2300.
CHANGES OF ADDRESS must be received at Society headquarters seven weeks before they are to be effective. Please send old label and new address.
STATEMENT from By-Laws. The Society shall not be responsible for statements or opinions advanced in papers or ... printed in its publications (B7.1, Par. 3).

INDEXED by Applied Mechanics Reviews and Engineering Information, Inc. Canadian Goods & Services Tax Registration #126148048.

Journal of Fluids Engineering

Published Quarterly by The American Society of Mechanical Engineers

VOLUME 122 • NUMBER 2 • JUNE 2000

This journal is printed on acid-free paper, which exceeds the ANSI Z39.48-1992 specification for permanence of paper and library materials. ♾™
♻ 85% recycled content, including 10% post-consumer fibers.

Journal of Fluids Engineering Volume 122, Number 2 JUNE 2000

TECHNICAL BRIEFS

ANNOUNCEMENTS

Journal of Fluids Engineering

Editorial

As the readers have been informed in the March 2000 volume, Professor Demetri Telionis has recently completed his 10 year tenure as the Technical Editor of *JFE*. I would like to take this opportunity, in the last volume edited by Demetri, to thank him and to highlight the enormous contributions that he has made to the quality and breadth of this journal. I am very pleased, honored and challenged by the tasks of following in his footsteps and living up to his legacy. I am looking forward to continuing and expanding the service that this journal provides to the fluids engineering community.

Under Professor Telionis' leadership, the past 10 years have been characterized by the transition process and progress in electronic publishing. Articles and abstracts are now available on-line. In addition, Professor Telionis established the *JFE* Data Bank in 1993 and progressed to an on-line version with downloadable information from authors. The Data Bank provides authors with the opportunity to present extended databases of their results and make them easily accessible to the readers. The Data Bank now contains substantial information and we hope that it will continue expanding in the coming years.

The last ten years are also characterized by technical innovations designed to meet the needs of readers and authors from both industrial and academic backgrounds. The journal included Industrial Discussions and extended review articles on several topics. Several volumes contained themed topics in specific areas and Technical Forums which featured extensive backgrounds on specific issues, such as competitiveness and unanswered questions in relevant fields.

Under Professor Telionis' guidance, efforts have been continuously made to enhance the quality of papers published in the journal. A policy requiring inclusion of experimental uncertainty in papers containing experimental data has been established. Standards for numerical accuracy have also been adopted. We are committed to maintaining and expanding these standards as new techniques and technologies become available.

Professor Telionis also attracted teams of high quality Associate Editors who are renowned experts in their fields. Their contributions have been a critical component in maintaining the quality of the papers published in the journal. Demetri also made special efforts to attract authors of quality *JFE* conference papers to submit their manuscripts to the journal. I have been present at several authors' breakfasts of FED summer meetings, at 7:30 AM, where he informed the audience about the *Journal* and asked them to submit their papers for publication. Such efforts are an inspiration for us in the future and they have led to a considerable increase in the number and quality of submitted papers.

In addition to his excellent service as an editor, Professor Telionis has consistently maintained a well-funded and internationally visible research program. He has supervised many graduate students, acting both as a teacher and a mentor. His contribution to science is attested to by the large numbers of publications in prestigious journals, mainly in the area of unsteady flow mechanics, a field in which he is a renowned expert. His service includes also consultancies, panel review memberships, invited keynote lectures, session chairmanships at meetings, one patent and two teaching excellence awards. Professor Telionis has also found time to found a company, Aeroprobe Corporation, and write two outstanding textbooks, *Unsteady Viscous Flow*, published by Springer-Verlag in 1981, and *Nonsteady Fluid Dynamics*, published by the ASME in 1990.

Several new Associate Editors will be joining us this year. Their names and brief backgrounds on each one of them are as follows:

1 Professor Juan Lasheras, University of California, San Diego. Originally from Spain, Professor Lasheras received his Ph.D. from Princeton University. He is a well-known expert in multiphase flows and turbulence as well as in experimental fluid mechanics.

2 Bruno Schiavello, Ingersoll Dresser Company. Mr. Schiavello graciously agreed to serve a second continuous term as an Associate Editor, continuing his valued service and generous use of his time. Educated in Italy and Belgium, he is our industrial expert in pumps and pump fluid dynamics.

3 Professor George Karniadakis, Brown University. Educated at MIT, Professor Karniadakis is a well-known expert in all aspects of CFD and numerical techniques. This would be his second (noncontinuous) term as Associate Editor of *JFE*. We hope to use his expertise in re-establishing quality standards for papers containing CFD results.

4 Professor Yoichiro Matsumoto, University of Tokyo. Professor Matsumoto received his Ph.D. from the University of Tokyo. He has vast experience in modeling of multiphase flows and molecular dynamics. He has also been very active in the fluids engineering and multiphase flow communities.

5 Lisa Mondy, Sandia National Laboratory. An alumna of Rice University, Ms. Mondy has decades of experience working in fluids engineering, particularly multiphase flows involving solid particles, flow in porous media, both computationally and experimentally.

6 Professor Yoshinobu Tsujimoto, Osaka University. Educated at Osaka University, Professor Tsujimoto is a renowned leader in the turbomachinery community, particularly in problems related to instabilities in pumps. He has also been very active in organizing symposia world-wide.

7 Dr. James Bridges, NASA Glenn Research Center. Dr. Bridges received his Ph.D. from the University of Houston, and has spent over 10 years working with NASA. He is an expert in all aspects of applied fluid mechanics and acoustics, including measurement techniques. He also has background in hydrodynamics, vortex dynamics and turbulence.

These recently nominated Associate Editors are joining an impressive community of experts that have already served for the past several years, including Professors Peter W. Bearman, Peter Bradshaw, Muhammad R. Hajj, Peter E. Raad, David R. Williams, and Dr. Khairul B. M. Q. Zaman in fluid mechanics, Professor Urmila Ghia in computational fluid mechanics, and Dr. Frederic K. Wasden in multiphase flows. With such a team we hope that the transition of editors will take place with minimal disturbances.

As for the future, our primary objective is to maintain and enhance to the best of our ability the quality and reputation of the journal that would make it attractive both to authors and readers. We will continue introducing special topics and pursue extended review articles of interest to the community. We also plan to introduce an option to publish short articles, which will be termed ''letters,'' that will be reviewed in less than three months and published in six. We would also like to enhance our ties with the Fluids Engineering Division community and increase the contributions of participants in these meetings to the *Journal*. We also plan to revisit our standards for accuracy and uncertainty.

The recent change to a new publisher and the availability of on-line manuscripts are some of the indicators that technical publishing, including *JFE*, is in a period of transition characterized by the increasing role of electronic publishing. We plan to adapt to this new age also during the reviewing process. Manuscripts posted on the Web can become accessible to referees shortly after submission, all through email communication. We plan to make such modes of communication available to authors, Associate Editors and referees very soon. This process will be part of a continuing effort to expedite the reviewing process. We hope that a faster review process would make *JFE* more attractive to authors and to the readers.

Joseph Katz
Technical Editor

Experimental Simulation of Fish-Inspired Unsteady Vortex Dynamics on a Rigid Cylinder

Promode R. Bandyopadhyay
Mechanical Engineer
Fellow ASME

John M. Castano
Mechanical Engineer

William H. Nedderman
Industrial Designer

Naval Undersea Warfare Center,
Newport, RI 02841

Martin J. Donnelly[1]
Mechanical Engineer,
Virginia Polytechnic Institute
and State University,
Blacksburg, VA 24061

The unsteady hydrodynamics of the tail flapping and head oscillation of a fish, and their phased interaction, are considered in a laboratory simulation. Two experiments are described where the motion of a pair of rigid flapping foils in the tail and the swaying of the forebody are simulated on a rigid cylinder. Two modes of tail flapping are considered: waving and clapping. Waving is similar to the motion of the caudal fin of a fish. The clapping motion of wings is a common mechanism for the production of lift and thrust in the insect world, particularly in butterflies and moths. Measurements carried out include dynamic forces and moments on the entire cylinder-control surface model, phase-matched laser Doppler velocimetry maps of vorticity-velocity vectors in the axial and cross-stream planes of the near-wake, as well as dye flow visualization. The mechanism of flapping foil propulsion and maneuvering is much richer than reported before. They can be classified as natural or forced. This work is of the latter type where discrete vortices are forced to form at the trailing edge of flapping foils via salient edge separation. The transverse wake vortices that are shed, follow a path that is wider than that given by the tangents to the flapping foils. The unsteady flap-tip axial vortex decays rapidly. Significant higher order effects appear when Strouhal number (St) of tail flapping foils is above 0.15. Efficiency, defined as the ratio of output power of the flapping foils to the power input to the actuators, reaches a peak below the St range of 0.25–0.35. Understanding of two-dimensional flapping foils and fish reaching their peak efficiency in that range is clarified. Strouhal number of tail flapping does emerge as an important parameter governing the production of net axial force and efficiency, although it is by no means the only one. The importance of another Strouhal number based on body length and its natural frequency is also indicated. The relationship between body length and tail flapping frequency is shown to be present in dolphin swimming data. The implication is that, for aquatic animals, the longitudinal structural modes of the body and the head/tail vortex shedding process are coupled. The phase variation of a simulated and minute head swaying, can modulate axial thrust produced by the tail motion, within a narrow range of ±5 percent. The general conclusion is that, the mechanism of discrete and deterministic vortex shedding from oscillating control surfaces has the property of large amplitude unsteady forcing and an exquisite phase dependence, which makes it inherently amenable to active control for precision maneuvering. [S0098-2202(00)00102-4]

1 Introduction

1.1 Background of This Work. In nature, the inherent actions of swimming and flying have been perfected over millions of years. Such actions have been the inspiration of several fluid engineering inventions. In an underwater habitat where predators and preys coexist, one fondly hopes that there are fluid dynamic mechanisms of maneuvering, propulsion, and stealth in play that might prove useful to technology development. However, transitioning natural actions to engineering can be difficult. The goal of this work is to uncover these mechanisms by simulating these actions in a controlled engineering context.

1.2 Related NUWC Work. In NUWC, the gap in maneuverability between nature, fish in particular, and small underwater engineering vehicles has been quantified (Bandyopadhyay et al. [1]). The morphology of the control surfaces of a fish and its inertial characteristics were first examined to determine the clue to the gap. Twenty-eight species of fish were grouped into three categories, namely, those which are slow but extremely agile (normally from the coral reefs), those which are fast and poor in maneuverability (open water large fish), and an overlapping category which has both speed and maneuverability. It was observed that the maneuverable species have a clearly identifiable fin morphology. From the third category, mackerel and bluefish, which are known to be predatory and abundant in the neighboring Narragansett bay, were further studied although in a captive environment. Mazes were built and their recorded and digitized turning trajectories were examined. The variation of their normal acceleration with turning radius, nondimensionalized by body length, were compared with those of small underwater vehicles. A gap in turning capability can be seen. Compared to the 1950s, in the 1990s, the gap has narrowed significantly, which is largely attributed to developments in control technology. It then is indicated that, further improvement in maneuverability might be possible by integrating modern control approaches to the hydrodynamic mechanisms practiced by the fin morphologies of fish. A practical need for taking a closer look at fish hydrodynamics was thus recognized.

The aforementioned fin scaling for maneuverability was then examined for a dorsal fin on a rigid cylinder. They were found to have a much lower time constant as opposed to maneuvering by affecting a large scale separation over the cylinder as commonly practiced in engineering (Bandyopadhyay et al. [1]). The pectoral fins of a euthynnid were simulated on a rigid cylinder by means of

[1]Current Address: Naval Surface Warfare Center.

Contributed by the Fluids Engineering Division for publication in the JOURNAL OF FLUIDS ENGINEERING. Manuscript received by the Fluids Engineering Division June 29, 1999; revised manuscript received December 8, 1999. Associate Technical Editor: D. P. Telionis.

computational modeling. The incorporation of such a pair of small wing attachments were found to decrease turning radii, angle of attack and even drag, particularly at low speeds (Bandyopadhyay et al. [2]). An experimental investigation showed that such wings dampen the pitching effects of traveling waves. A closed-loop control theory has been developed that makes use of dorsal and caudal fins, described here, in proximity of perturbations like surface waves, to achieve a precision maneuverability in the vertical plane (Bandyopadhyay et al. [3]). The successful incorporation of the dynamics of the control surfaces into a closed-loop control theory has helped demonstrate to some extent the engineering value of fish hydrodynamics. The following summarizes the experience: although difficult, the biologically based mechanisms need to be applied to rigid bodies and not just to flexible bodies; the emphasis should be on precision maneuvering, rather than the production of pure axial propulsion whose technology is well developed; production of all forces, viz., thrust, drag and cross-stream maneuvering forces should be viewed in an integral manner because they have a common production mechanism in fish hydrodynamics. The NUWC work has also led to the exploration of a new area, viz., biologically-inspired maneuvering of small underwater bodies. The studies indicate that the maneuvering and control of man made vehicles like aircraft are based on moments, while those of biologically based engineering vehicles would be force based. In the latter, this makes brisk maneuvering, which has a low time constant, feasible.

1.3 Other Related Work. Propulsive and lifting forces produced by flapping foils were studied by Knoller and Betz from 1909–1912 (see Jones, Dohring, and Platzer [4]). From 1924–1936, Birnbaum, von Kármán, Burgers, and Garrick conducted theoretical studies that proved propulsive efficiency improved with slower flapping. Though there is no verification, it appears that German scientists tested a flapping foil device for torpedo propulsion during the early 1940s (see HSVA Towing Tests [5]). Gopalkrishnan et al. [6], Hall and Hall [7], and Jones et al. [4] have made recent progress. Lighthill [8] and others in their earlier works (Wu [9], Webb [10]), have remained silent on the existence of a discrete vortex shedding mechanism. On the other hand, the elucidation of the role of a discrete shedding process, and its accounting by Strouhal number, has been a significant clarification of the mechanism offered by M. Triantafyllou and his coworkers. Anderson et al. [11] have reported efficiency measurements and computations on oscillating two-dimensional foils. They found that inviscid linear or nonlinear theories, in general, do not apply. Wolfgang et al. [12] have reported drag measurements on a fish-like swimming body. In this work, in addition to the flapping of the tail fin (caudal fin), a traveling wave passes through the body. When the phase speed of the traveling wave is higher than the forward speed, a maximum of 70 percent ''drag reduction'' is achieved compared to that for the towed rigid body. They have suggested that, the traveling wave laminarizes the boundary layer on the body, and in addition, there is a favorable interaction between the vorticity shed by the body and the tail.

1.4 Origin of Discrete Vortex in Flapping Foils. The mechanism of momentum transfer by a flapping foil to the surrounding fluid is not universal and three possibilities are shown in Fig. 1. They belong to basically two groups: natural and forced. An analogy to boundary layer transition can be made where the mechanisms are either the natural amplification of Tollmien-Schlichting (T-S) waves, or the forced transition due to surface roughness which has been termed by Morkovin as a ''bypass'' transition because the natural T-S amplification route is bypassed. In a similar vein, consider the three kinds of wakes that result from a thrust producing flapping foil, shown in Fig. 1. The wakes resulting from the low amplitude oscillations shown in Fig. 1(*a*) and 1(*b*) can be termed ''natural,'' while that due to large amplitude oscillation (Fig. 1(c)) can be termed ''forced.'' In the former, a natural breakdown of the laminar wake is involved and,

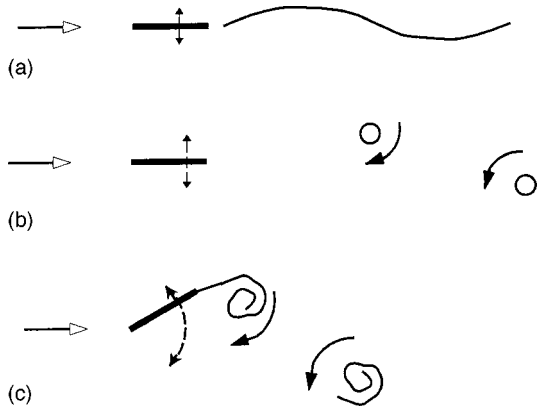

Fig. 1 Manifestations, namely *natural* and *forced*, of momentum transfer from flapping foils. (*a*) Unsteady and continuous distribution of vorticity in wake; (*b*) discretization (or wrapping) of unsteady vorticity layer in wake via a natural instability process; (*c*) forced discretization (or wrapping) of vorticity via salient edge separation at flap trailing edge, ''bypassing'' natural instability process.

as shown by Triantafyllou et al. [13], the vortices distribute themselves spatially in an optimum manner. In such a natural wake breakdown process, thrust efficiency may reach a maximum at a preferred Strouhal number of the wake vortices. However, in the forced case, the vortices are produced due to salient edge separation at the flap trailing edge and not due to any 'natural' breakdown downstream. Therefore, in the forced flapping case, thrust efficiency cannot a priori be expected to depend on flap or wake vortex Strouhal number. It is possible that a natural process describes the wake in a fish, while in many engineering experiments today, the mechanism in fact is not natural, but is forced in character.

1.4.1 Relationship Between Strouhal Number and Efficiency. There is much controversy in the understanding of the mechanisms of biolocomotion. Gray's paradox and the development of compliant walls for drag reduction are examples of that. They stem from appealing speculations but weak data. Another difficulty is a paucity of controlled fluid dynamic experiments with live animals in captivity or in their natural habitat (Fein [14]). The live biolocomotion data tends to have a large scatter due to large uncertainties in the measurements of speed, dynamic scales and efficiency (Fish [15]). There is a general lack of accurate theories to verify the mechanisms, the phenomena being viscous three-dimensional and unsteady in nature. The picture is not entirely gloomy though. The most developed is the case of two dimensional small amplitude oscillating foils where there is a general agreement between inviscid theories and measurements. However, understanding is murky even in case of two-dimensional high amplitude oscillations, and more so in three-dimensional situations. There are yet inexplicable differences between data sets of efficiency and axial force. As the present work shows, the subject of flapping foil propulsion is richer than reported in the literature.

In the present work, Strouhal number St of tail flapping appears as an important variable. (Here, $St = fA/U$, where f is frequency, A is amplitude of oscillation, and U is flow speed.) This could be successfully incorporated into a control theory (Bandyopadhyay et al. [3]). However, efficiency is not the highest in the range $0.25 < St < 0.35$. This calls for a closer examination of claims about the effect of St on efficiency or other factors determining an optimum behavior.

In the oscillating foil literature related to fish propulsion, there is frequent unsubstantiated extrapolation from two-dimensional to three-dimensional cases. The variable for optimization is sometimes not defined, and the St behavior of efficiency and drag re-

duction (compared to a rigid body) is assumed to be analogous. Trainatafyllou and Traintafyllou ([16], p. 4) have claimed that ''a Strouhal number between 0.25 and 0.35 is a hallmark of efficient swimming.'' This statement is too general and inapplicable to both two-dimensional foils or three-dimensional foils attached to rigid bodies, as the present work shows. There is no fish data on the relationship between efficiency (η) and their tail beat Strouhal number. Such a relationship, but for a two-dimensional oscillating foil, is given in Trainatafyllou et al. [13]; however, very little data are available and the peak in St is practically flat. A more extensive data, again for two-dimensional foils is given in Anderson et al. ([11], Fig. 5), where a peak is reached at mostly lower or sometimes even higher values of St, but certainly not in the range $0.25 < St < 0.35$. Even in their two-dimensional work, St versus η does not have a universal relationship indicating that there are yet unknown variables involved in efficient swimming. Wolfgang et al. [12] have reported drag measurements on a swimming three-dimensional scaled model of a bluefin tuna with a flapping tail and a flexible body. A reduced drag is reported compared to the rigid body suggesting a coupling of the body and tail motions. The data base is limited in their paper. Drag reduction is reported to peak at several Strouhal numbers. A number of additional variables, other than St are found to be important. The present conclusion is that, as more data is becoming available on both two- and three-dimensional oscillating foils and on the interacting effects of attached bodies/surfaces, the propulsion mechanism is emerging as richer than reported: the role of St on tail flapping is not as simple as originally thought, and there are other variables that affect efficiency and forces produced; the understanding is not adequate and optimization issues are unclear.

1.5 Unsteadiness in Aquatic Locomotion. A remarkable feature of the flapping foil locomotion of a fish like aquatic animal is the production of large unsteady forces. On the other hand, in man-made propulsive systems, resorting to such unsteady mechanisms is rare. Further differences can be seen by comparing Figs. 2 and 3. These figures are due to the basic model in the present experiment, namely a 76 mm diameter and nominally 1 m long flow aligned cylindrical body, to which a pair of flapping foils are attached at the tail. Figure 2 shows drag levels and indicate the order of thrust for steady state. Figure 3 shows the unsteady axial force signature due to flapping foils. In the former figure, the steady drag levels at 20 cm/s are 1/100*th* of the peak unsteady forces due to a pair of flapping foils attached to a rigid cylinder, shown in the latter figure. The drag values in Fig. 2 are 1/50*th* of the time mean thrust values shown in Fig. 3. Although these biologically based mechanisms give us an impressive level of force, their necessity in an aquatic animal is probably due to the amenability of their origin, viz., an unsteady deterministic vortex shedding, to active control. This makes precision maneuvering, defined as quick acceleration and deceleration, and rapid turning compared to body length, feasible.

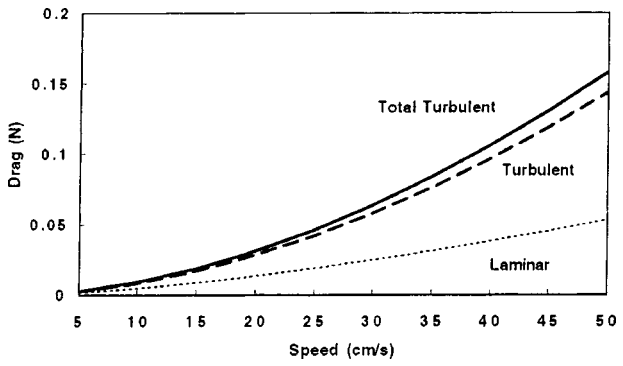

Fig. 2 Estimated steady state drag on the basic cylinder model shown in Fig. 6. Horizontal axis: speed of water (cm/s).

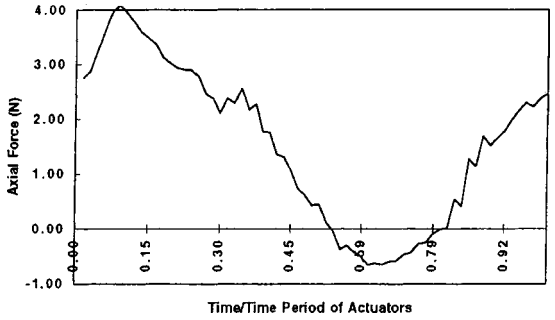

Fig. 3 Ensemble averaged time trace of axial force on the model shown in Fig. 6. Positive axial force indicates thrust.

The unsteady aspect of flapping foil locomotion depicted in Fig. 3 raises an intriguing question, namely, why do fish swim so elegantly, meaning without jerkiness, although that is what one would expect from Fig. 3? In this paper, we have also examined a hypothesis, namely, is the head oscillation of a fish during swimming also a propulsive mechanism that has a phased relationship with the tail flapping, the net result being an uniform axial force leading to the jerk-free motion? Simply put, this paper examines these two unsteady locomotive aspects of a fish, namely, the flapping of its tail and the oscillations of its head, in the context of a rigid body which removes the apparent complication of the effects of a flexible body.

1.6 Interaction of Main Body Length and Flapping Foil Frequency. While the theoretical inviscid-flow efficiency of a two-dimensional flapping foil is 100 percent, the efficiency of a finite span flapping foil attached to a body would be lower, and conceivably significantly lower. (Efficiency, to be defined later, is given by the ratio of output power of the flapping foils to the power input to the actuators.) How a finite body interacts with a finite flapping foil is an important question. Yet, not much is known about this interaction. Efficiency is generally difficult to measure accurately in aquatic animals. However, evidence is presented below showing that the main body length is related to the flapping foil mechanism in a dolphin. This is considered below where dolphin swimming is modeled as a pendulum.

1.6.1 A Pendulum Model of Dolphin Swimming. The tail beat mode of dolphin swimming is considered. It is hypothesized that the tail beat frequency is related to the length of the dolphin and the zeroth order swimming is modeled as a simple pendulum. Available measurements of tail beat frequency are found to be consistent with the model. It is shown that natural frequency varies inversely with the square root of length, while the rate of change of tail beat frequency with speed is universal.

1.6.1.1 Introduction: As mentioned earlier, in a bid to learn from nature and apply to engineering, recently, the gap in maneuvering between fast yet agile species of fish like mackerel and bluefish and small underwater bodies, has been quantified (Bandyopadhyay et al. [1]). The maneuvering ability is expressed as a relationship between normal acceleration, nondimensionalized by $g(c_g)$, and turning radius r/L, where r is turning radius and L is fish or vehicle length. A departure from inverse power relationship is observed at lower values of r/L. However, a more consistent trend is observed when speed U is expressed as body lengths traveled per second (U/L). As considered below, this intriguing appearance of L is observed in dolphin swimming also. No satisfactory explanation is available. Biological data sets tend to have large scatter and mechanistic theories are generally few, but may be worth developing to extract trends hidden in the apparent scatter.

Dolphin swimming has been the source of several drag reduction concepts. Fein [14] and Rohr et al. [17] have pointed out that the belief that dolphins possess any secret to drag reduction is

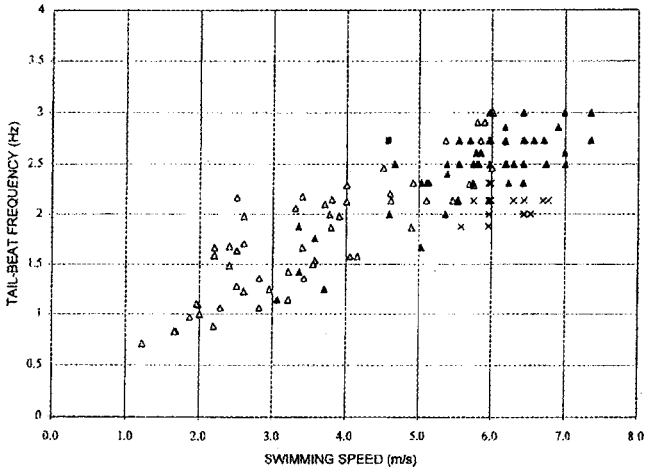

Fig. 4 Measurements of dolphin tail beat frequency, reproduced from Rohr et al. [17]. Legend: Fish [15]: □-*Tursiops Truncatus*; Rohr et al. [17] ▲-*Tursiops Truncatus*, X-*Pseudorca Crassidens*; Lang and Daybell [18]: ■ - *Lagenorhyncus Obliquidens*. This data is modeled in the present work as a family of parallel lines each being for a characteristic dolphin length.

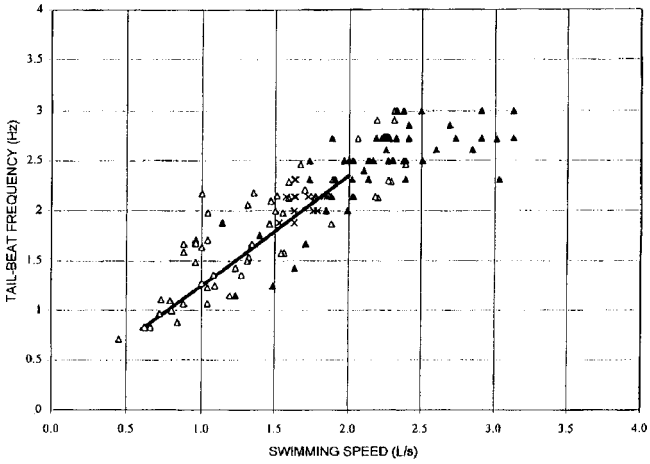

Fig. 5 Reproduced from Rohr et al. [17]. Data in Fig. 4 is replotted expressing swimming speed as body lengths traveled per second. Legend: Fish [15]: □-*Tursiops Truncatus*; Rohr et al. [17]: ▲-*Tursiops Truncatus*, X-*Pseudorca Crassidens*; Lang and Daybell [18]: ■-*Lagenorhyncus Obliquidens*; Kayan and Pyatetskiy [19]: — *Tursips*.

based on their seeming extraordinary speeds, which however, are largely anecdotal. That prompted them to take a fresh look and undertake the measurements of dolphin swimming. However, drag reduction is not the subject of this paper, but the measurements out of that investigation will be used here. They have conducted careful redundant measurements of speed (U), tail beat frequency (f) and amplitude (A). The mean amplitude A/L (0.2 ± 0.08) is independent of speed. However, frequency f varies linearly with speed U. The summary of the f (*versus*) U data is reproduced in Fig. 4. Linear fits to two of the four individual data sets (□ and ▲) are as follows:

$$f = 0.47 + 0.37U[\text{m/s}] (R^2 = 0.72, \text{ Fish } [15]) \ (\square) \qquad (1)$$

$$f = 0.45 + 0.35U[\text{m/s}] (R^2 = 0.67, \text{ Rohr et al. } [17]). (\blacktriangle) \qquad (2)$$

Here, R^2 is the correlation of fit. Note that the extrapolated mean trends do not go through the origin. The f intercept for $U = 0$ can be called the natural frequency f_0. The mean value of f_0 is 0.47 Hz in Fish [15] and 0.45 Hz in Rohr et al. [17], both for *Tursiops Truncatus*. In Fig. 4, observe that the limited *Pseudorca Crassidens* data of Rohr et al. fall below their *Tursiops Truncatus* data and the lone *Lagenorhyncus Obliquidens* data from Lang and Daybell [18] falls above, suggesting that their natural frequencies f_0 are lower and higher than those given in Eqs. (1) and (2), respectively. However, as shown in Fig. 5, when speed U is expressed as body lengths traveled per second, then the mean trend in the captive *Tursiops* data of Kayan and Pyatetskiy [19], given below in Eq. (3), that also describes the data in Fig. 4 well, passes practically through the origin, in other words, $f = 0$, for $U[L/s] = 0$. (The scatter in f data is within ± 0.5 Hz.)

$$f = 0.15 + 1.1U[L/s] \ (\text{Kayan and Pyatetskiy } [19]) \qquad (3)$$

Equation (3) describes the mean trend in the data of Kayan and Pyateskiy [19] and is not a fit to all the data sets in Fig. 4. A somewhat steeper line passing through the origin might well describe the entire data set. Rohr et al. have remarked that the collapse of their *Pseudorca Crassidens* and *Tursiops Truncatus* data in *f versus U* coordinates are ''noticeably poorer'' (Fig. 4). However, observe in Fig. 5 that, when speed is expressed in terms of body lengths traveled per second, then these data sets agree with Eq. (3) rather well. Considering the usual scatter of biological data, the excellent collapse of five data sets in the *f versus* U/L coordinates is probably indicative of the involvement of a zeroth order mechanistic law. We interpret this collapse to mean that natural frequency f_0 is not universal, and only the slope of *f versus U* is. This contains the hint that the variation of f_0 between data sets is somehow accounted for by L. These issues are not clear in Eqs. (1) and (2) because, as argued here, the dolphins in Eqs. (1) and (2) are of nearly the same length (Table 1).

Biologists generally believe that, to allow a comparison, there should be some manner of accounting for the differences in the horse power of individual members of the same specie (adult versus young), or between different species. Length appears to be an easily measurable variable that is a rough measure of the muscle power. However, while the data clearly highlights an important role of length, this justification appears to be vague.

1.6.1.2 The Pendulum Model and Discussion: Now consider the wake vortex pattern due to flapping foils attached to a main body. Phase-matched laser Doppler measurements of vorticity-velocity vectors in the wake presented later, show that, under right conditions, a reverse Karman vortex street is produced and the downstream pointing jet between the neighboring vortex pairs is the source of thrust (Gopalkrishnan et al. [6]). It is instructive to compare this with the recent flow visualization of fluttering and tumbling by Belmonte et al. [20]. They dropped long and short

Table 1 Lengths of dolphins whose tailbeat frequencies are given in Fig. 4 and their modeled natural frequencies

Author	Lang and Daybell [18]	Fish [15]	Rohr et al. [17]	Rohr et al. [17]
Dolphin specie	Lagenorhyncus Obliquidens	Tursiops Truncatus	Tursiops Truncatus	Pseudorca Crassidens
Range of L (cm)	209	251–270	182–283	365
Average L (cm)	209	260	240	365
Natural Frequency f_0 (Hz) Based on Eq. (4)	0.34	0.31	0.32	0.26
Symbol in Figs. 4 and 5	■	□	▲	X

strips of flat steel, plastic and brass in a narrow liquid filled tank. One of two kinds of motion are possible: a predominantly side to side oscillation (fluttering), or an overturning (tumbling). Whether they fluttered or tumbled depended on the value of a Froude number, defined as the ratio of the time it takes for the strip to fall its own length to the time it takes to execute the pendulum-like side to side motion. Longer or lighter strips, which have a low Froude number fluttered, while short and heavier strips, which have a high Froude number tumbled. We observe that the wake pattern during fluttering is identical to the thrust producing reverse Karman vortex street generated by flapping foils mentioned earlier. The close analogy of the wake pattern and the terms in the Froude number, suggest that the dolphin wake could be modeled as a simple pendulum.

The frequency n of a simple pendulum is given by:

$$n = f_0 = 1/(2\pi\sqrt{L/g}) \tag{4}$$

The values of the range of L of the dolphins in Fig. 4, and their averages, are given in Table 1. The values of natural frequencies based on the average lengths are also shown. The apparent scatter in tail beat frequency characteristics between sets of dolphin swimming data are explained. As shown in Table 1, we conclude that natural frequency varies inversely with the square root of length of the dolphin. We tentatively conclude that the rate of variation of tail beat frequency with speed is linear and universal for dolphins.

Two remarks of caution may be made. First, the experimental data base has some gaps. In view of that, what has been presented is an internally consistent model with a minimal number of invocation of higher order effects. The present work may help plan future experiments, because it highlights the importance of varying length and the need for tailbeat frequency data for $U \rightarrow 0$. Second, while the inverse relationship between natural frequency and the square root of length has been shown, a clarification of the appearance of g in the constant of Eq. (4) is needed. The appearance of an Internal Froude number in the maneuvering work of Bandyopadhyay et al. [1], the appearance of g in the present model and the equivalence of longer and lighter strips, and short and heavier strips in the work of Belmonte et al. [20] are intriguing. Perhaps a zero gravity experiment conducting measurements of the tailbeat frequency of fish for $U \rightarrow 0$ in an aquarium and flow visualization plus measurements of perturbed strips will help clarify the mystery.

1.7 Rationale for This Work. The origin of this work lies in the desire to learn about the mechanism of stealth and maneuvering as practiced by fish for potential application in underwater vehicles. The current efficiency of propulsion of such vehicles is very high and therefore, propulsion is not a focus per se. For example, one is interested to learn if the fish wake dies down quickly and what is the mechanism behind it. This has been met to some extent because we have found that the flapping of a tail produces tip vortices which have a tendency to dissipate faster than steady conventional longitudinal vortices. The maneuvering mechanism has been an area of focus. We have been interested in learning about the fundamentals and their difference from engineering practices. For example, one may ask, what allows a fish to turn at a low radius with respect to body length, what makes their response time low and makes their maneuvering so exquisitely precise? This paper forms a part of a series of papers where some of these results have been reported (Bandyopadhyay et al. [1,2,3]). In the present work, we have looked at the production of discrete vortices due to tail flapping and head swaying of a fish, and their interaction. Live animal or even laboratory simulations and qualitative experiments have sometimes been reported, which have led but only to notional descriptions of mechanisms. To conduct precise measurements, the head and tail motions have been simulated on a model and well controlled experiments have been carried out. The main body is cylindrical and is not flexible. This eliminates the added complication of a flexible body and makes the cause and effects studied unambiguous. This has the added advantage that we can study the fish control surfaces in isolation and determine their potential for application to a rigid main body of an engineering vehicle.

The movements of the tail and head of a fish are glaring motions and worth studying in a controlled engineering laboratory experiment. However, there was another motivation for conducting the second experiment. The first experiment showed that efficiency of thrust production is slightly higher in the waving mode of operation of the rigid flapping foils than in the clapping mode.[2] The waving mode produces a cross-stream moment and a small yawing oscillation of the model that mimics fish swimming. This also suggests a possible role of the body length as a relevant scale. The higher efficiency in the waving mode led to the hypothesis that there might be an additional vortex shedding process from the nose that regulates the net thrust produced due to the vortex shedding from the tail flaps.

1.8 Outline of This Work. Two water tunnel experiments have been carried out on two rigid cylindrical models. In the first experiment, the hydrodynamics of tail flapping has been studied. A dual flapping foil device is used because, when the two flaps operate out of phase (called *clapping mode* here), they produce no net cross-stream force and there is no side-to-side head swaying. The latter is a desirable property of underwater vehicles for heading to a target. Dynamic measurements of axial and cross-stream forces and moments have been carried out in a range of flapping frequency, mode and flow speed. Dye flow visualization of vortex shedding from the tail flapping foils has been carried out. Laser Doppler velocimetry measurements in three-dimensional planes have then been carried out of the same tail vortex shedding process and these measurements are matched to the phase of tail flapping. In the second experiment, the head swaying of a fish is simulated by a nose vortex shedding device on the just mentioned model with the dual flapping foil device attached to the tail. Dynamic measurements of the six-Cartesian components of forces and moments acting on the entire model have been carried out. The dynamic balance data have been ensemble averaged. The mean axial force data have been compared with two-dimensional theories and others measurements. The laser Doppler measurements have been analyzed to produce vorticity-cross-stream velocity vector maps, phase-matched to tail flapping, and also circulation distributions. The hydrodynamic mechanisms have been extracted. The experiments are described in Section 2. The results and discussion of the two experiments are given in Sections 3 and 4, respectively. The conclusions are listed in Section 5.

2 Description of Experiments

Two experiments are described in Sections 2.1 and 2.2. The tail flapping foil experiment is described first, which is followed by the experiment on the interacting vortex shedding from the nose and the tail flaps.

2.1 Experiments on A Pair of Flapping Foils Attached to the Tail of a Rigid Cylinder. A schematic diagram of the water tunnel model is shown in Fig. 6. Figure 7 is a photograph of the partially assembled model. The cylinder diameter is 7.62 cm and the length is about 1 m. The two flaps are 7.62 cm×7.62 cm in size. A fixed divider plate of the same size is located between the two flaps. The divider plate serves to reduce the rigid body drag and it also ''trains'' the vortex array allowing accurate phase-averaged wake vortex measurement. The flaps are activated by two magnetic actuators and phase is determined by two differential transducers that measure displacement. The actuators and phase sensors are housed internally. The entire model ''floats,''

[2]A referee has pointed out the following. Animals using clapping motion (such as seals) have fins that collapse when they are pulled apart, which then expand when pushed together. Thus, the possibility remains that a clapping motion with nonrigid fins may also be highly efficient if they are collapsed and extended at appropriate phase.

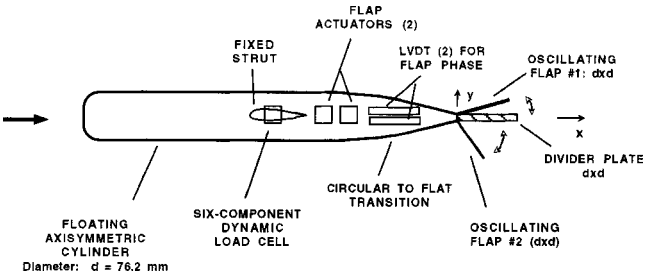

Fig. 6 Schematic diagram of the dual flapping foil device mounted at the end of the tail cone of a rigid cylinder. Axis *z* is along span of flap.

and is mounted on a six-component dynamic balance located under the strut. The strut is fixed and hangs from the tunnel's top wall. The balance (ATI Inc.) measures the strain in a monolithic structure containing three symmetrically placed beams. Temperature compensation and water proofing are provided. A balance with high moment range had to be chosen. The axial force resolution is 0.24 *N*. The vortices shed by the flapping foils are created by salient edge separation and, thus, their effects are independent of any boundary layer tripping. The data presented here are mostly for natural transition on the main cylinder because tripped cases show little effect. The two flaps can be operated in one of two modes, viz., clapping or waving—so named because of the kind of animation they simulate (see Fig. 12). In the clapping mode, the two flaps approach or recede from each other simultaneously, while in the waving mode, the flaps always follow the direction of motion of each other. In other words, in clapping, the phase of the two flaps is opposite to each other, while phase is the same in the waving mode. After the first experiment was completed, we observed that seals and sea lions, which have a streamlined body and are known as wonderful swimmers, also have dual-flapping foils in their tails (Fig. 8).

All measurements were performed for both flapping modes, i.e., waving and clapping. The balance measurements were conducted with a single flap as well as the dual flap. The actions of the maneuvering device and the phase sensors in air and in a water tunnel were video taped (Bandyopadhyay et al. [21]). The robustness of the device was demonstrated by the fact that it worked in the water tunnel nonstop for about five days during which time the phase-matched turbulence measurements were carried out. These measurements were conducted in the water tunnel at Virginia Polytechnic Institute (Zeiger et al. [22]). The cross-section of the test section is large for our purpose: 0.56 m wide and 0.61 m deep. The balance data were collected for flow speeds between 10 and 80 cm/s and flap frequencies of 2.65, 4.237, and 6.2 Hz. These parameters are in the same range as those in several relevant aquatic animals (Bandyopadhyay and Donnelly [23]). The flow visualization was carried out at 5 cm/s and the laser Doppler velocity data were collected at 20 cm/s with a flap frequency of 2.65 Hz. The flap tip travel was commonly 38 mm, that is upto the cylinder edge, which made an angle of 30 degrees about the axis. Data acquisition was carried out in the following manner. First, the balance data were collected. One desk-top computer was used to operate the balance and another was used to read out, process, and store the data. Next, a two-component laser Doppler anemometer was used to make phase-matched turbulence measurements in the wake. The measurements were conducted first in three axial planes downstream of the flaps. Then they were conducted in three cross-stream planes. The data were processed to produce phase-averaged vorticity-velocity vector contours in the axial and cross-stream planes. Finally, distributions of circulation were calculated by two integral methods, i.e., velocity-time integrals and vorticity-areas. The efficiency measurements were carried out in the NUWC water tunnel, which is 30 cm×30 cm in cross-section.

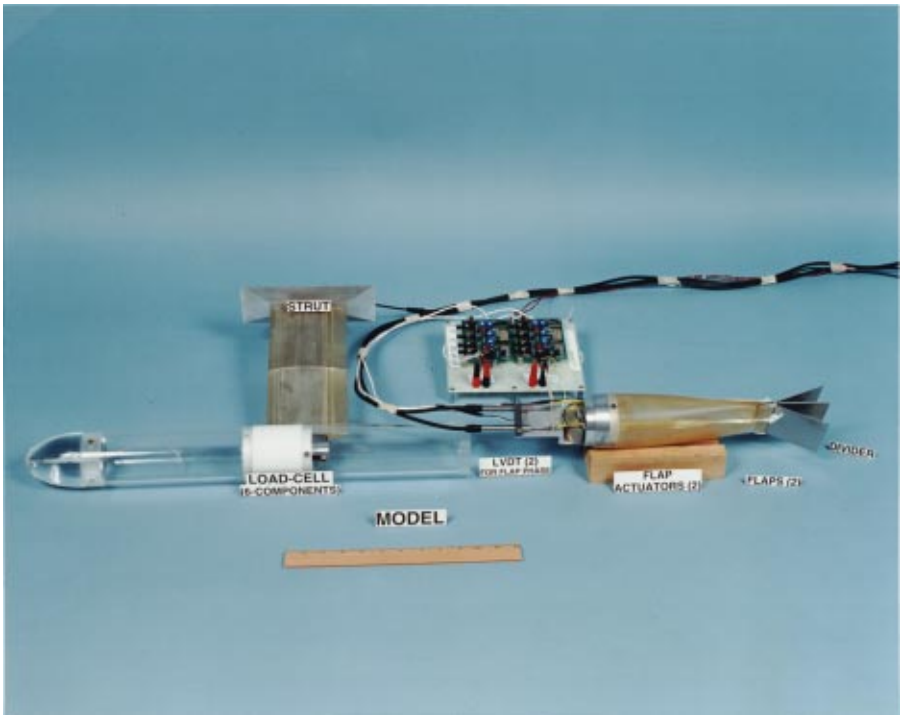

Fig. 7 Photograph of water tunnel model of the dual flapping foil device. Dual flapping foils and divider plate are shown at the right end; to the left of foils lie the actuators, two phase transducers, and actuator control circuits. The six-component load cell is located at the junction of the strut and cylinder.

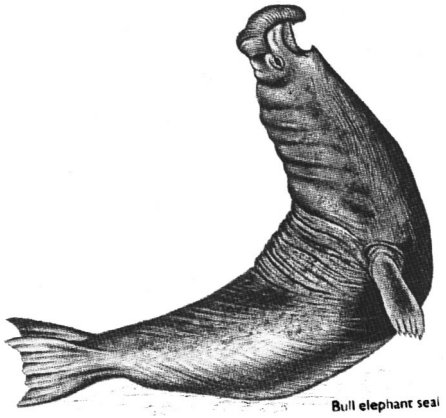

Fig. 8 The caudal fins of seals and sea lions are examples of dual-flapping foils which make them wonderful swimmers

2.2 Experiments on the Interaction of Phased Vortex Seeding From Forebody and Tail Flaps. This model is shown schematically in Fig. 9. Figure 10 is a photograph of the model and the in-house built 3-channel digital phase controller of the actuators. This model is essentially similar to that in the first experiment (Figs. 6 and 7), except for the oscillating nose slider and the phase controller. Two magnetic actuators are used to oscillate the tail flaps and two LVDTs are used to measure their phase as in the first experiment. A third actuator is used to oscillate a 1 mm thin plate near the nose.

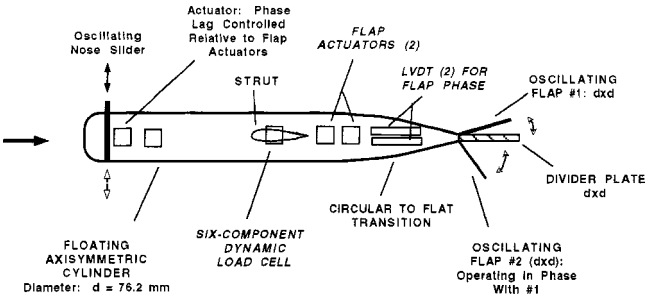

Fig. 9 Schematic of second model. A software operated digital controller is used to select the phase lag of the nose slider actuator relative to the two flap actuators which operate in phase, called waving mode here (as opposed to clapping mode where they operate in anti-phase).

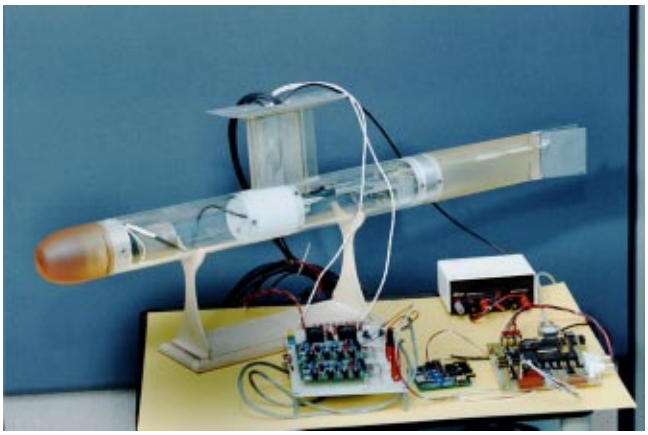

Fig. 10 Photograph of second model and digital controller of actuators

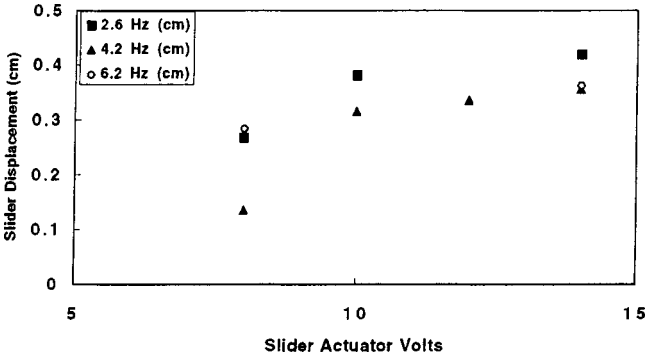

Fig. 11 Variation of nose slider depth with actuator voltage and frequency

The nose slider protrudes out of the cylinder surface alternately at port and starboard sides. Figure 11 shows the distribution of nose slider protrusion from the cylinder surface *versus* actuator voltage. The maximum protrusion is 3–4 mm in the working range of 12 V. This is of the order of the local thickness of the boundary layer which is laminar at a flow speed of 20 cm/s. At a nose slider frequency of 3.65 Hz and speeds of 20–40 cm/s, a nose Strouhal number based on the slider protrusion of 3–4 mm varies between 0.274 and 0.73.

The second set of experiments were carried out at flap frequencies between 2.6 and 6.2 Hz and flow speeds of upto 1.5 m/s. A computer driven controller was built to operate the actuators (Fig. 10). All three actuators were operated at the same frequency. The phase of the nose actuator was digitally shifted with respect to the flaps by means of a software. The tail flap actuators operated in phase (clapping mode). The drag balance was operated by a second computer. A third computer was used to monitor the tunnel characteristics in real time and for acquisition of all data, namely the balance output, flap phase, actuator currents and voltages and their phase, and flow speed. The balance signals were digitized at 250 Hz and the other signals at 8 KHz. The balance trace was ensemble averaged over 5 cycles of flap oscillations and then a three-point averaging was performed to further filter out. The flow speed was measured both by a Pitot tube located in the test section near the tail of the model and also from the pressure drop along the tunnel nozzle. The experiments were carried out in the NUWC Low Speed Water Tunnel. The test section is 30 cm×30 cm in cross-section and the length is 3 m. The tunnel is ''noisy'' at low speed.[3] Close tracking of flow speed with a sensitive Pitot tube mounted in the test section is required for accuracy. This is in view of the fact that the mechanism on hand is exquisitely Strouhal number dependent. A perforated metal plate was placed in the latter experiments downstream of the test section to improve flow steadiness at low speeds.

3 The Swimming Hydrodynamics of a Pair of Flapping Foils Attached to the Tail of a Rigid Body—Results and Discussion

3.1 Flow Visualization. Dye flow visualization was carried out to examine the vortex shedding process at a flow speed of

[3]Turbulence intensity in the tunnel measured with LDV is 0.25–0.5 percent between 20 cm/s and 6 m/s. However, the drive rpm varies about ±2 rpm below 1.5 m/s which causes a 3–5 percent variation in the freestream speed. This behavior is not well reflected in the turbulence intensity data. Installing a perforated plate at the downstream end of the test section minimized this unsteadiness. All unsteadiness can be completely eliminated at low speeds by building a flow apparatus with a drive that is specially engineered to work only in low speeds, rather than cover a large speed range.

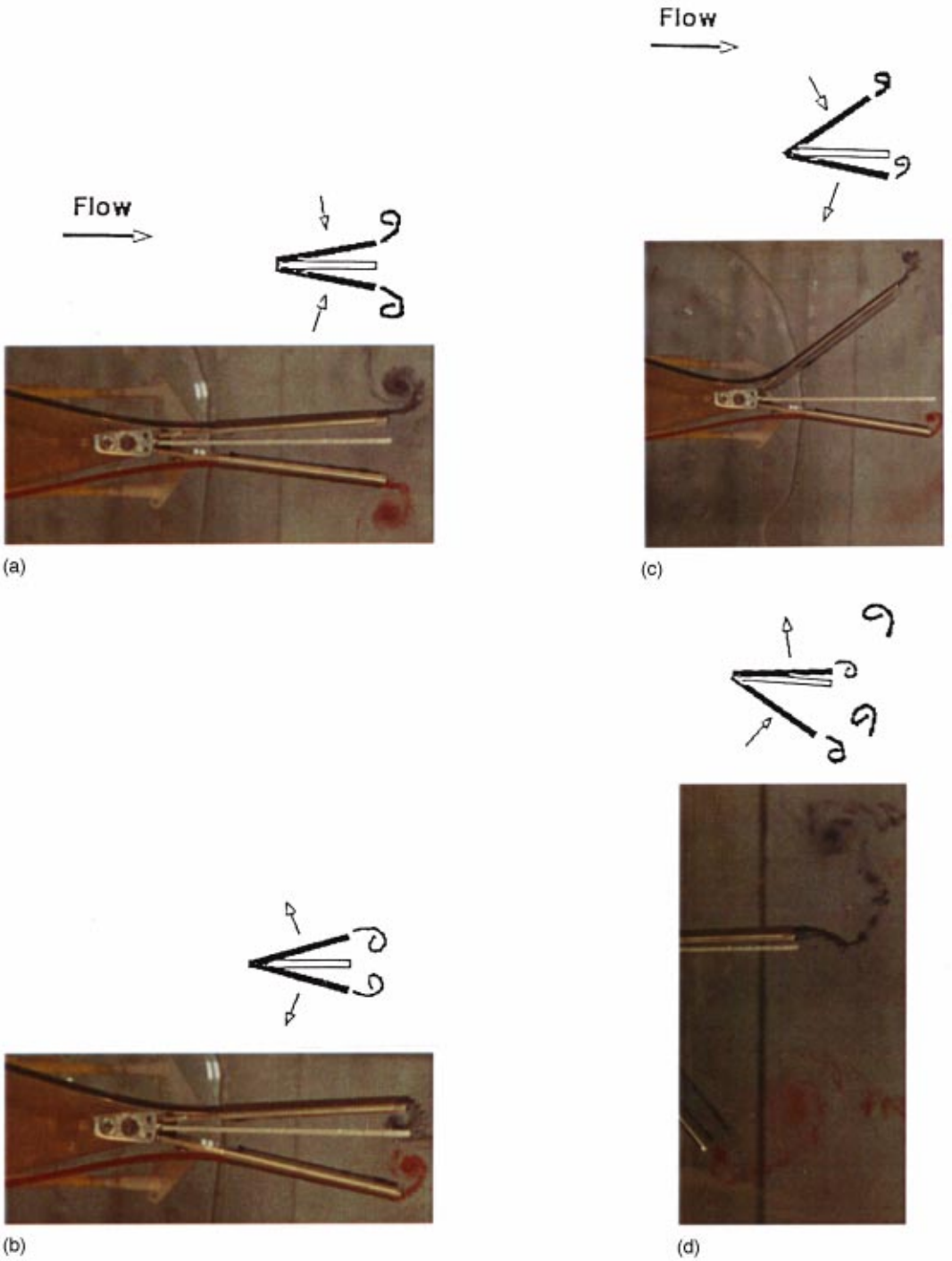

Fig. 12 (***a***) **Flow visualization tests of clapping mode: flaps closing** (**top, graphic depiction; bottom, photograph**) (***b***) **Flow visualization tests of clapping mode: flaps opening** (**top, graphic depiction; bottom, photograph**) (***c***) **Flow visualization tests of waving mode: flaps toward port** (**top, graphic depiction; bottom, photograph**) (***d***) **Flow visualization tests of waving mode: flaps toward starboard** (**top, graphic depiction; bottom, photograph**).

5 cm/s. The vortex is forced to rollup at the flap tip and is shown in Fig. 12 for the two modes of flapping. The complete wake can be seen in the video (Bandyopadhyay et al., [21]). For a flap angle of 30 deg, the outer tip vortices are spread at an angle of 70 deg to the axis, the resulting wake spread angle being 140 deg. This is a very wide wake that produces thrust and maneuvering forces. As shown later, this wake dissipates very quickly.

3.2 Definition of Coefficients. The coefficient of axial force, c_a, is defined as

$$c_a = \frac{F}{1/2\rho U_\infty^2 D^2}, \tag{5}$$

where F is axial force, being positive for thrust, ρ is density of water and U_∞ is freestream velocity. When F is positive, c_a

$=c_t$, the coefficient of thrust, and when F is negative, $c_a=c_d$, the coefficient of drag. The coefficient of yawing moment is defined as

$$c_m=\frac{T}{1/2\rho U_\infty^2 D^3}, \tag{6}$$

where T is yawing moment, D is the length scale of the model and flaps. Time, t, is nondimensionalized as $t^*=tU_\infty/D$. The Reynolds number is defined as

$$\mathrm{Re}=\frac{U_\infty D}{\nu}, \tag{7}$$

where ν is kinematic viscosity of water. In calculating vorticity, velocity and circulation, nondimensionalization is performed using U_∞ for velocity scale, D for length scale, and D/U_∞ for time scale.

The Strouhal number, St, of tail flaps, is defined as

$$\mathrm{St}=\frac{fA}{U_\infty}, \tag{8}$$

where f is flapping frequency and A is maximum crossstream travel of a flap tip.

Efficiency of the flapping foils is defined as

$$\eta=\frac{\text{Output Power}}{\text{Input Power}}=\frac{T\cdot U_\infty}{\eta_a\int 2VIdt}, \tag{9}$$

where T is integrated thrust, η_a is actuator efficiency, V and I are actuator volts and currents, respectively. The factor 2 accounts for two actuators.

3.3 Forces and Moments

3.3.1 Time Signatures. The ensemble-averaged coefficient of axial force (c_a) due to a single flapping foil is shown in Fig. 13(a)–(c). A net thrust is produced only at 4.24 Hz. For the dual-

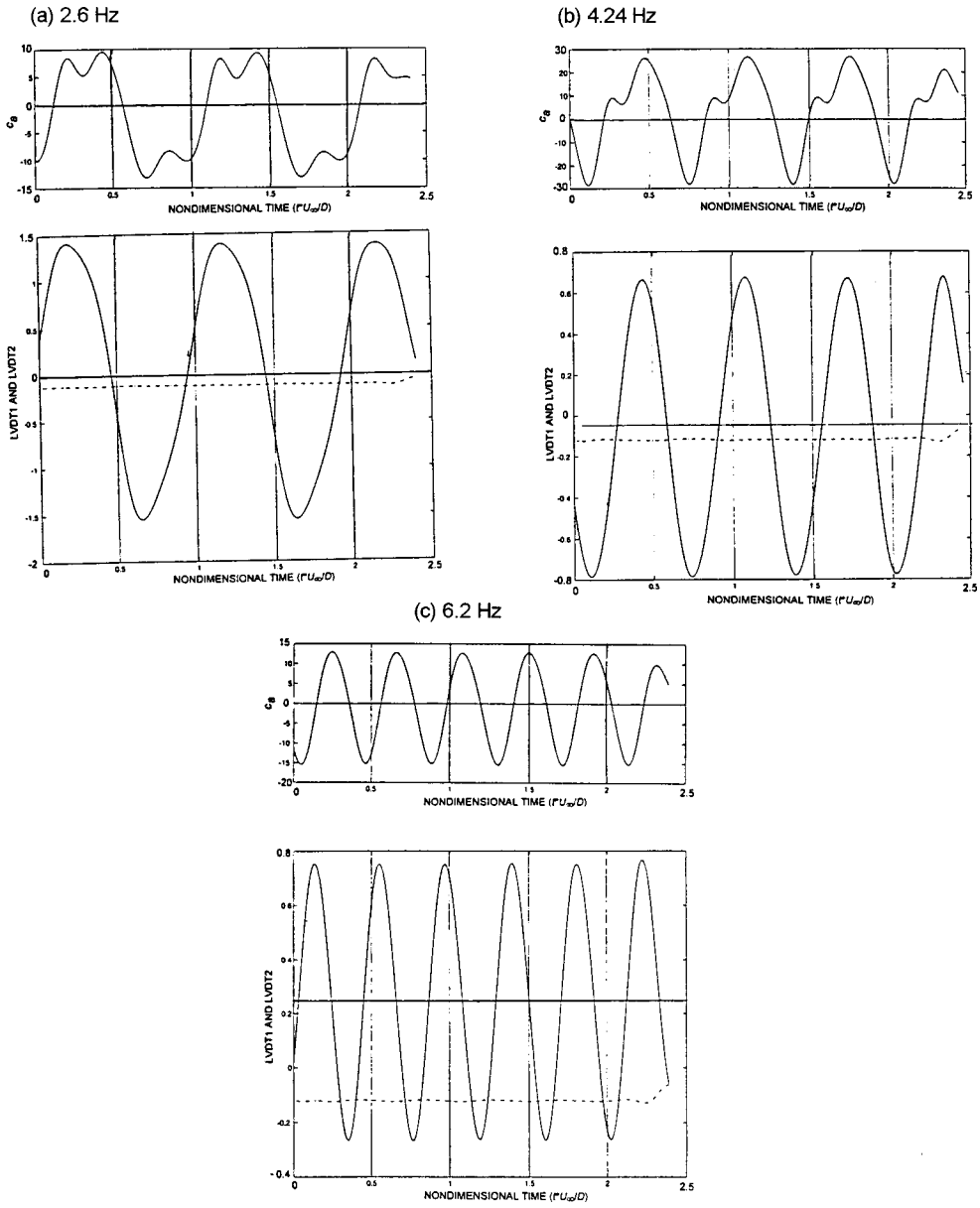

Fig. 13 Ensemble-averaged coefficient of axial force (c_a) due to a single flapping foil; positive values indicate thrust (c_t) and negative values indicate drag (c_d); $U_\infty=20$ cm/s: (a) 2.6 Hz, (b) 4.24 Hz, and (c) 6.2 Hz. LVDT signature indicates flap phase≡highest values: flap fully open; lowest values, flap fully closed.

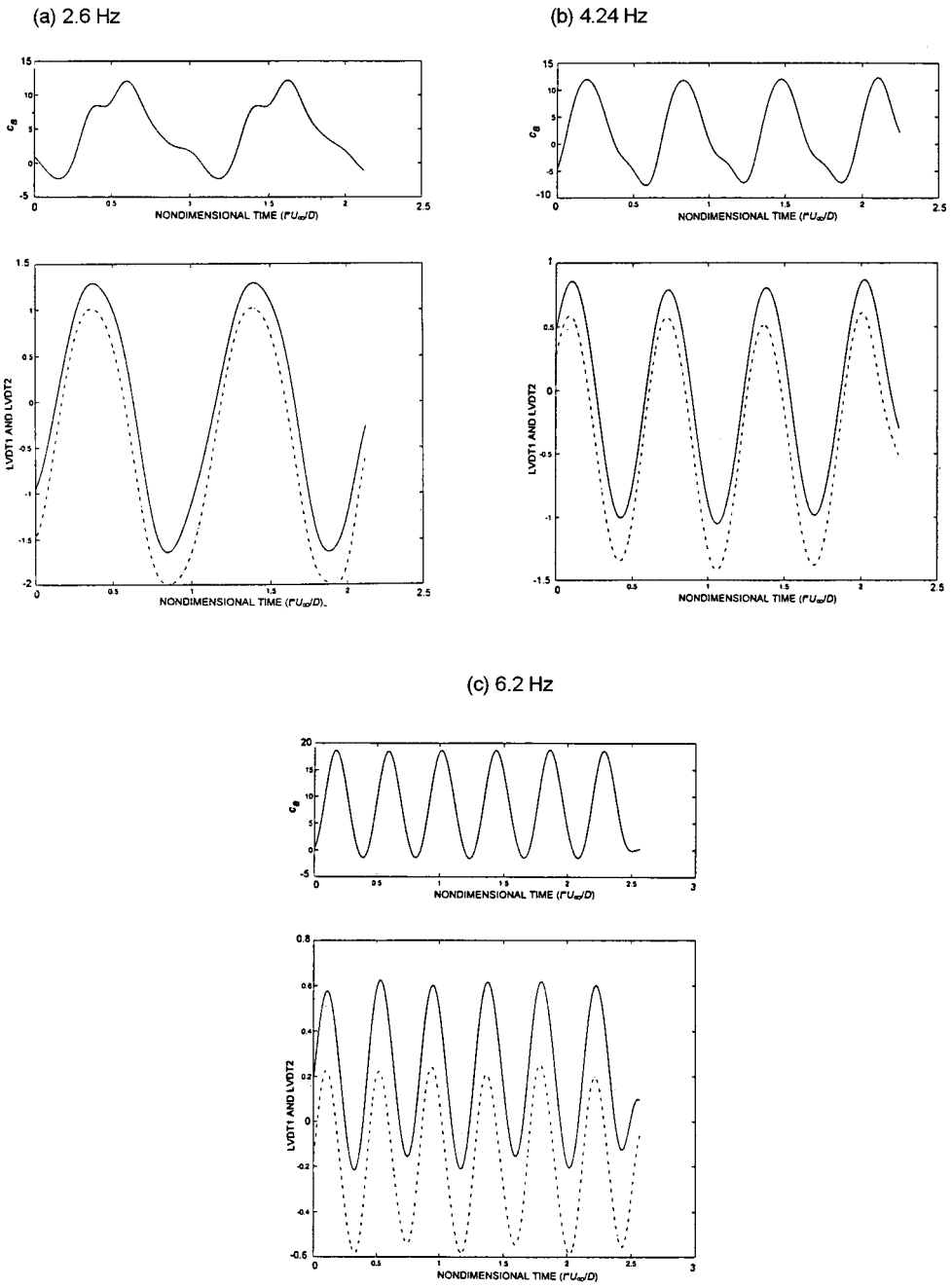

Fig. 14 Ensemble-averaged axial force and flap opening due to dual-flapping foils in clapping mode. High LVDT values≡flap fully open; low LVDT values≡flap fully closed. The flaps are actually in opposite phase. (*a*) 2.6 Hz; (*b*) 4.24 Hz; (*c*) 6.2 Hz.

flapping foil case, the ensemble-averaged time histories of axial force and yawing moment are shown in Figs. 14 and 15, respectively. A thrust is produced at all three frequencies. In Fig. 14, positive values of force indicate thrust and negative values indicate drag. Clearly, the device has produced more thrust than drag. The net values of the moment can be made nonzero and acting toward port or starboard by operating the flaps differentially. The data in Fig. 15 have been used to design control laws for maneuvering (Bandyopadhyay et al. [3]). Observe the 90 deg phase difference between axial force and yawing movement.

Yawing moment is at a maximum or a minimum when the flap is at its extremity and axial force is at a maximum or a minimum when the flap is at the mid-point of its travel.

3.3.2 Thrust Coefficient and Efficiency. The distributions of the coefficient of axial force with Strouhal number are shown in Fig. 16. The dual flapping foil data are compared with the two-dimensional theories of Lighthill [9] and Chopra [24] and the two-dimensional measurements of Triantafyllou et al. [16] and Isshiki and Murakami [25]. Our measurements are also compared with the discrete forced vortex momentum model of Bandyopadhyay [26]. Here, the mass of water affected per unit span of flap, as contained in the discrete vortices formed at the salient edges of the flaps, is taken to be

$$2\nu_\theta \cdot R_\nu, \tag{10}$$

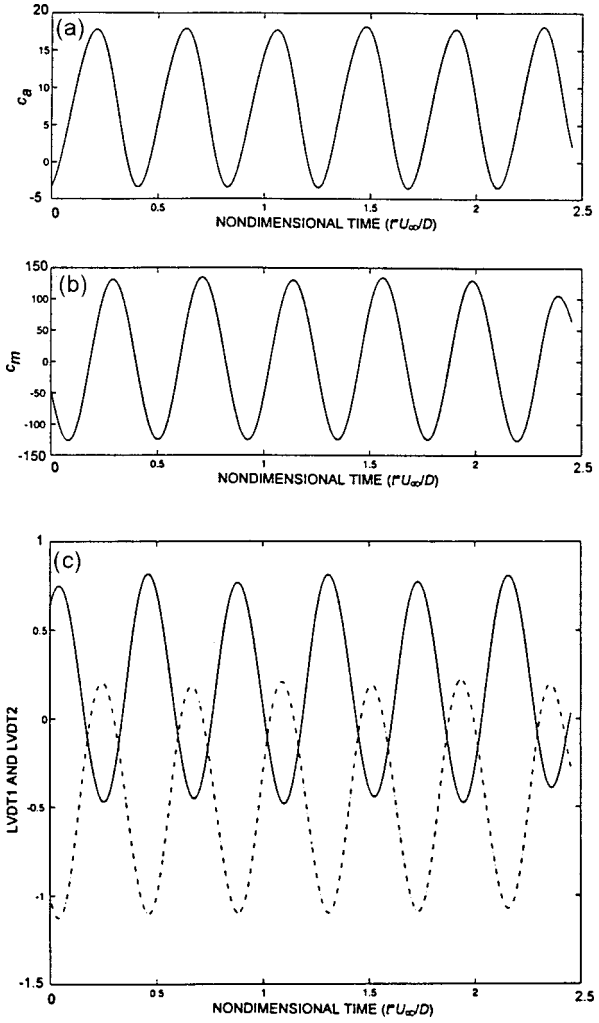

Fig. 15 Ensemble-averaged (*a*) axial force, (*b*) yawing moment, and (*c*) flap phase in waving mode; $U_\infty = 20$ cm/s/s; $f = 6.2$ Hz. The flaps are actually in phase.

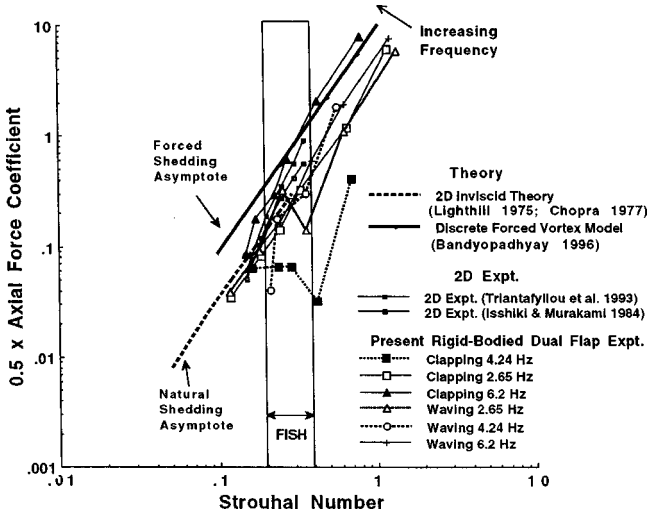

Fig. 16 Comparison of measurements of axial force (thrust) coefficient

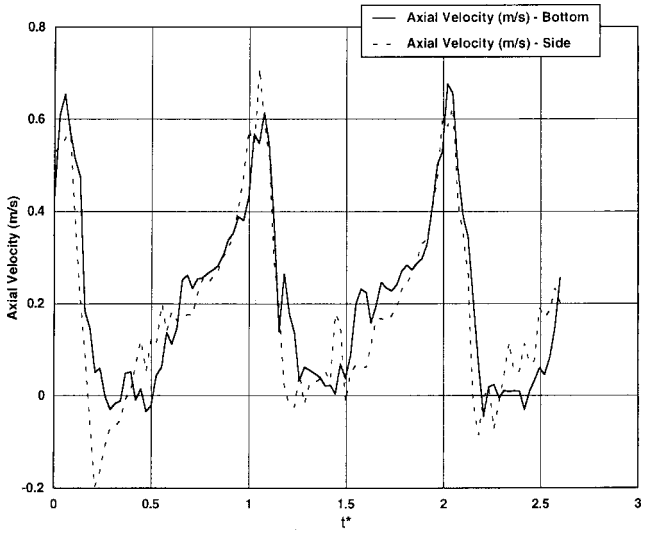

Fig. 17 Phased-average measurements of axial jet speed due to dual-flapping foil. Axial velocities shown are relative to U_∞ of 20 cm/s. Measurements in two different planes are compared.

where $v_\theta = c \cdot \Omega$. Here v_θ is azimuthal speed of the flap, R_ν is vortex radius at the flap tip, c is flap chord$=D$; Ω is rotational speed of flap$=2\pi f$, and the factor 2 accounts for two vortices formed in each cycle of flapping.

From dye flow visualization experiments, R_ν was taken to be 0.173 cm at all values of U_∞ and f. From the phase-matched LDV measurements shown in Fig. 17, the axial jet speed relative to U_∞ was taken to be 60 cm/s at all values of U_∞ and f. Thrust coefficients calculated using these values of mass of water affected and jet speed are also shown in Fig. 16. Several interesting trends are revealed in Fig. 16. First, the discrete forced vortex model thrust is higher than that due to the low amplitude inviscid theory. Second, for St<0.15, all data tend to the inviscid theory line which is reminiscent of the natural manifestation in Fig. 1(*a*). Third, the data fan out from the small amplitude inviscid line for St>0.15 displaying the effects of frequency and mode of flapping. The fact that the data do not collapse for St>0.15, indicates that Strouhal number of flapping does not account for all the dynamics. In fact, at the highest end of St, axial force coefficient increases systematically with frequency. Third, the data tend to the discrete forced vortex model line at higher values of St and frequency of flapping. The behavior for St>0.15 and higher values of f is reminiscent of the forced nature of the wake as introduced in Fig. 1(*c*). The momentum model appears to be the asymptotic limit of thrust that can be produced by the forced flapping foil technique. Fourth, in the St range common among fish (Triantafyllou [13]), some of the dual flapping foil data ($f=4.24$ Hz) exhibit sensitivity to St, which is not yet captured by any theory. The sensitivity of the cylinder model at $f=4.24$ Hz is discussed further later. These results support the classification of flapping foil wakes into two categories, viz., natural and forced. The former is a low St asymptotic behavior, while the latter is a high St high frequency asymptotic behavior. In this light, Fig. 16 can be treated as a stability diagram.

In case of the rigid body and forced shedding, the shed vortices do not propagate tangential to the trailing edge when the flap is at the outer extremity. In the range of 5–20 cm/s, while the flap trailing edge is at 30 deg to the axis, the outboard vortex moves away from the axis at 70 deg. There is also a rapid decay in the vortex circulation (discussed later, Figs. 28 and 29).

The axial force efficiency of the flapping foil device (Eq. (9)) is shown in Fig. 18. The efficiency of the magnetic actuator, η_a, is assumed to be 18 percent as supplied by the manufacturer. The actual η_a is lower and, thus, the actual values of η of the dual

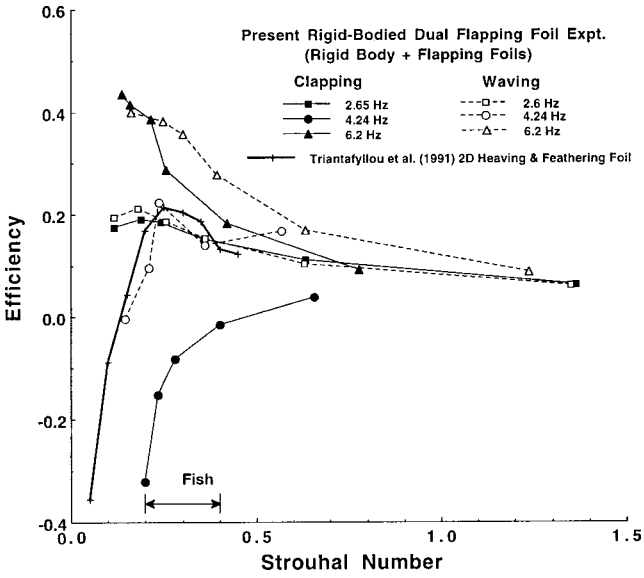

Fig. 18 Measurements of the axial force efficiency of the dual-flapping foils

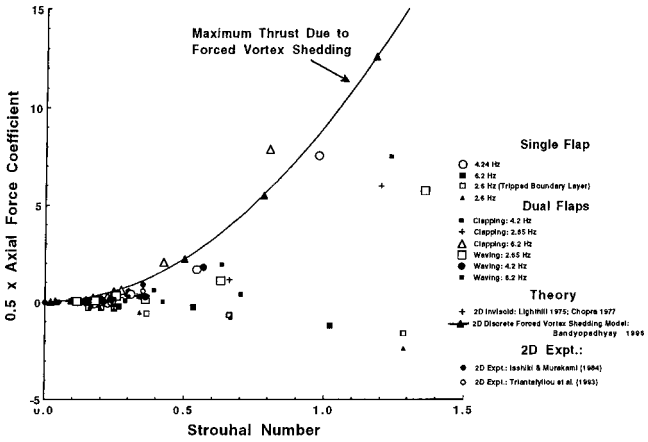

Fig. 20 Summary of all single- and dual-flap axial force coefficients. Solid line: Two-dimensional discrete Vortex Shedding Model of Bandyopadhyay [26]. Both thrust- and drag-producing cases are shown. Note that body drag is included in axial force.

flaps shown are higher. There is a general agreement with Triantafyllou's [13] experiment on a two-dimensional heaving and feathering foil. It is interesting to note that the dual flaps show a tendency to achieve a higher efficiency in the waving mode. Because the nose exhibits a yawing oscillation in the waving mode, it is hypothesized that this sheds vortices which lowers the drag on the rigid body due to boundary layer interaction, or it enhances the thrust (by augmenting jet speed) due to the vortices produced by flapping. This line of thinking led to the second experiment.

The efficiency plots in Fig. 18 include the cylinder drag. The viscous and form drag coefficient of the cylinder is 0.145. When this is taken into account, the efficiency of the flapping foils alone are higher as shown in Fig. 19. At lower values of St, efficiency has a stronger dependence on *f*.

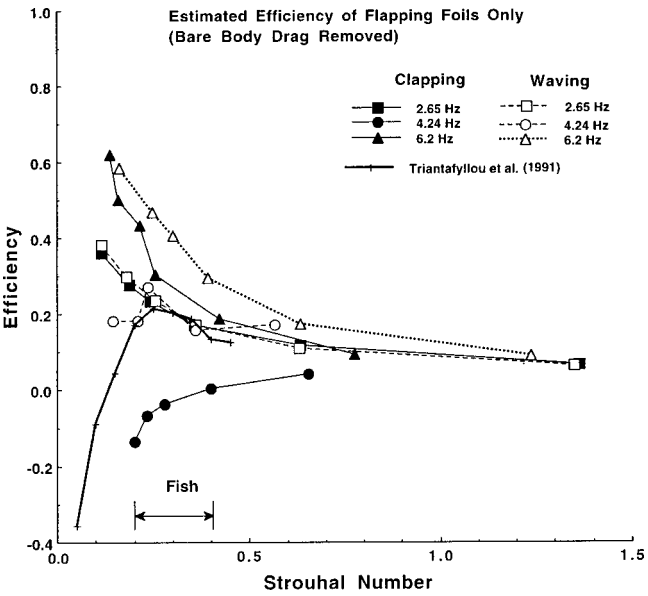

Fig. 19 Estimated efficiency of dual-flapping foils. Estimated values of bare body drag (viscous+form) removed from measurements of total efficiency (rigid body+flapping foils) shown in Fig. 18.

All measurements of axial force coefficient due to single and dual-flapping tails are shown in Fig. 20. Both thrust and drag producing cases are included. The trend displays a sensitivity to *f*. At $f=2.6$ and 6.2 Hz, the single foil does not produce a net thrust. However, it does at $f=4.24$ Hz, where the single and dual flaps in both modes follow a similar trend. Tripping of the cylinder boundary layer has no effect on the thrust produced. The data indicate that thrust produced is governed by St, *f*, and number of flaps. Mode of flapping has a minor effect. According to Triantafyllou (Pvt. Comm. 1997), the ''robotuna'' vortex cores make an angle of 10–15 deg to the forward direction. However, the wake angle is 140 deg in the present case. The wider wake growth in the present case of a rigid cylinder requires a closer examination.

3.3.3 Sensitivity to Strouhal Number and Flapping Frequency: Single Foil Case. Figure 21 shows the time-averaged coefficients of axial force and pitching moment for one single foil attached to the rigid body in the presence of the dividing plate. The coefficients do not depend solely on St, they also depend on *f*. The sign of the axial force and yawing moment change when $f=4.24$ Hz. For the single flap, the higher sensitivity of c_a and c_m to St at $f=4.24$ Hz can be further demonstrated by examining the unsteady behavior. Figures 13 and 14 show that a peculiar aspect of the fish propulsion and maneuvering mechanism is the fact that large unsteady forces are produced to generate a range of time-averaged levels. We believe that this unsteady behavior holds the key to its propulsion and maneuvering mechanism and the long-time-averaged values do not clarify this. The maximum and minimum values within a cycle of the time signatures of c_a and $c_m(y)$ are expressed as

$$y=e^{a}(\mathrm{St})^{n}, \tag{11}$$

where the exponents *a* and *n* are characteristics of *f*. The sensitivity *Q* is then given as

$$Q=ne^{a}(\mathrm{St})^{n-1}. \tag{12}$$

The values of Q_a and Q_m are calculated at St$=0.3$ as shown in Fig. 22. The sensitivity of the unsteady mechanism is highest at $f=4.237$ Hz. The cause of this sensitivity to *f* is not well understood. Triantafyllou and coworkers have not examined moments and have not noticed such dependence on (St, f). We propose that an interaction between the vortex shedding from the cylinder and the flapping foil is causing an instability in the vortex train. Another Strouhal number involving the length of the cylinder, amplitude of its head swaying, and *f* are likely involved. The result is

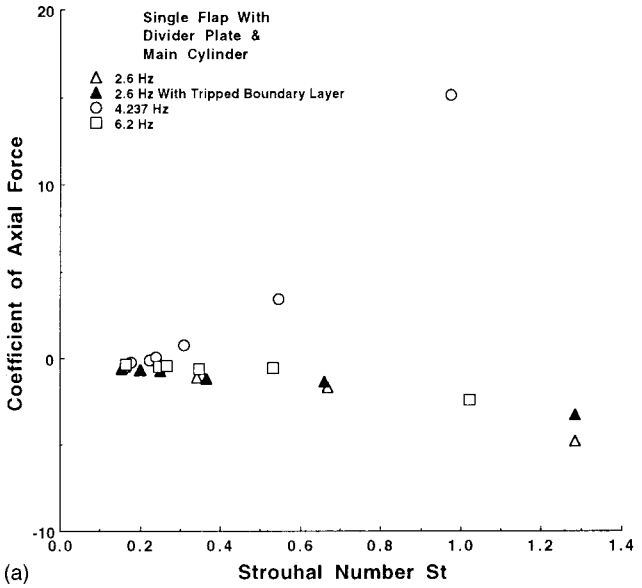

Fig. 21 (*a*) The variation of time-averaged axial force with Strouhal number in the single foil-rigid body cases; (*b*) the variation of time-averaged yawing moment with Strouhal number in the single foil-rigid body case

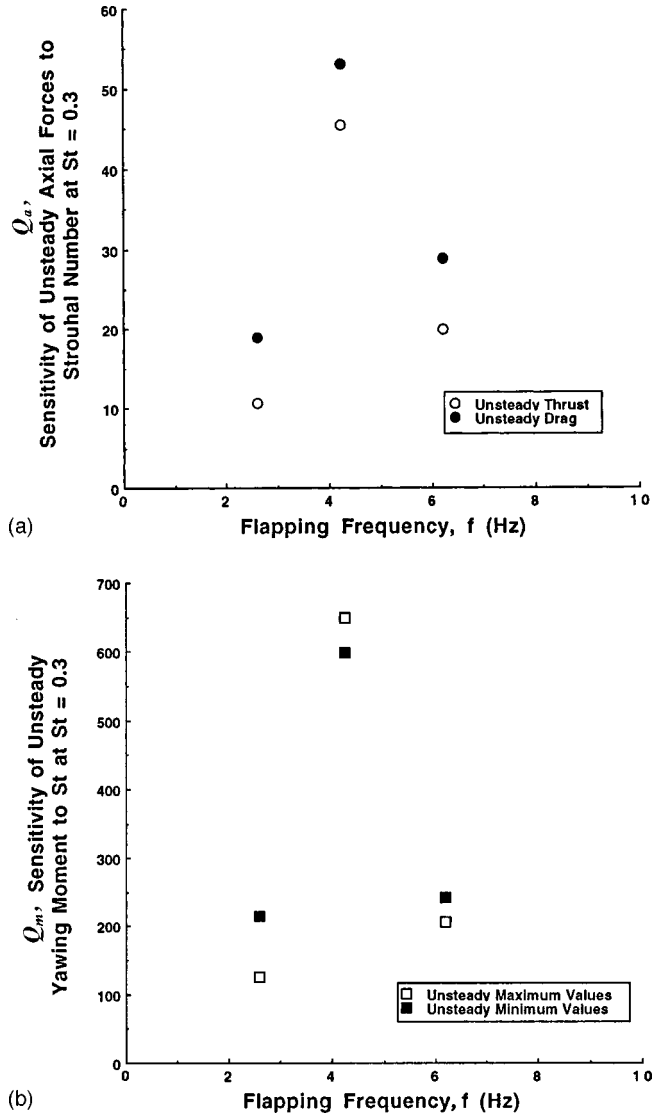

Fig. 22 (*a*) Sensitivity of unsteady axial force in single flapping foils to flapping frequency at St=0.3; (*b*) sensitivity of unsteady yawing moment in single flapping foils to flapping frequency at St=0.3

a catastrophic switch from a regular Karman train to a negative Karman train. Further work is needed to verify this hypothesis.

3.4 Vortex Shedding: Vorticity-Velocity Vector Maps

3.4.1 Vorticity-Velocity Vector Maps. The vorticity-velocity vector measurements of the vortex shedding process from the tail flapping foils, phase matched to its motion, were carried out at a flow speed of 20 cm/s. Their maps in the axial (diametral) midplane ($z=0$) are shown in Figs. 23, 24, and 25 for clapping, waving and clapping modes, respectively (phase is given by $t^*=tU_\infty/D)d=0$. Similarly, the phase-matched vorticity-velocity vector maps in the cross-stream plane at the trailing edge of the flap ($x/D=0.066$) are shown in Figs. 26 and 27 for the waving and clapping modes, respectively. Such maps were used to compute circulation values of the vortices by two methods: by calculating velocity line integrals and vorticity area integrals. The distributions of circulation of the axial vortex generated at the flap tip are shown in Figs. 28 and 29 for $x/D=0.0656$ and 0.5577, respectively. The two methods of circulation calculation, based on vorticity-area and velocity-line integrals, are in reasonable agreement. Note that within a short length after formation ($x/D \cong 0.5$), the absolute value of the minimum circulation has dropped by a factor of 3. Measurement resolution is higher in Fig. 23. This figure captures the radially far-flung vortices. The maps in Figs. 23, 24, and 25 show the jets between vortex pairs which give rise to thrust. The information in Figs. 26 and 27 has been used in Fig. 30 to depict the trajectory of the axial vortex schematically and the effect of the divider on it. The vortex arrays and the mechanism of thrust and yawing moment are depicted schematically in Figs. 33 and 34, for clapping and waving modes, respectively.

Figures 24 and 25 indicate that, in the clapping mode, the two flaps produce arrays of vortices that are mirror images. They produce a net thrust but no net maneuvering cross-stream forces (Fig. 33). On the other hand, in the waving mode, the two arrays of vortices from the two flaps are staggered in the streamwise direction. Due to this fact, the waving mode produces both axial and cross-stream forces (Fig. 34). The vortex shedding process is

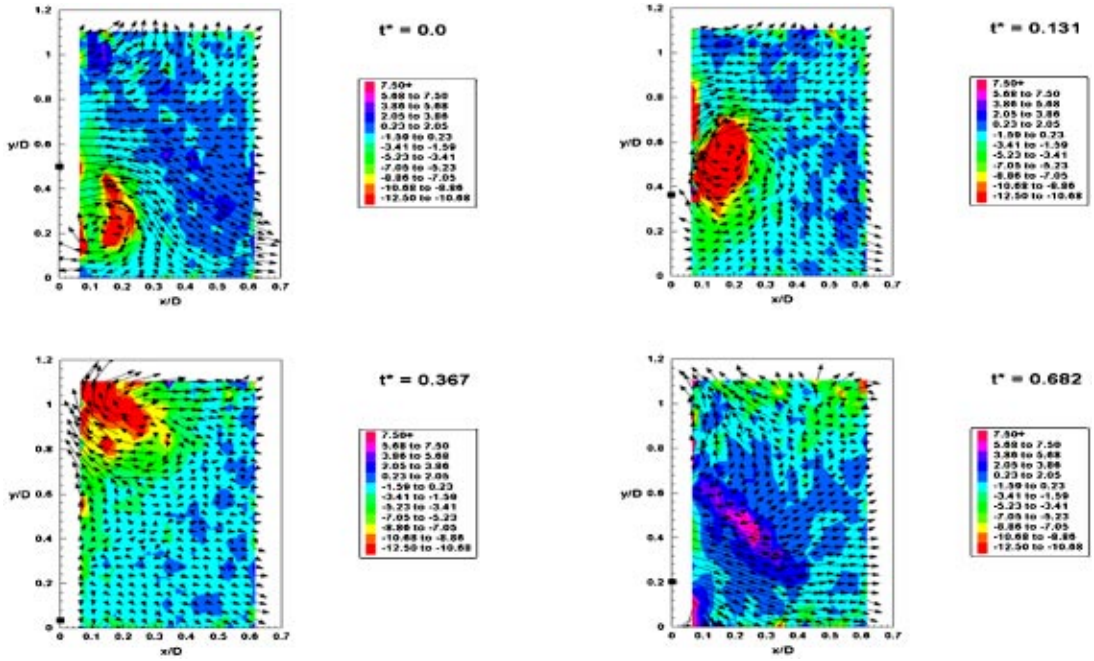

Fig. 23 Vorticity-velocity vector plots in the axial plane for clapping. The velocity perturbations are with respect to freestream velocity. Filled squares on the *y*-axis indicate the location of flap trailing edge in this and succeeding figures. Note that, when the flap is at outboard extremity, the outer-most vortex trajectory is at 70 deg to the x-axis which is much larger than the flap trailing edge angle of 30 deg.

clarified in Figures 31–34. Figure 31 shows a drag-producing wake behind a hydrofoil where the induced flow between a pair ofshed vortices is pointed upstream. When the foil is oscillated, the wave train shown in Fig. 32 is produced when the induced velocity points in the downstream direction, which gives rise to thrust. The clapping mode produces the mirror-image vortex train shown in Fig. 33 and the waving mode produces the staggered vortex train shown in Fig. 34. The cross-stream maps in Figs. 26 and 27 were examined for clues to higher efficiency in the waving mode. The wake is three-dimensional due to the finite nature of the flaps. The figures show that the shed axial vortex lying within the divider propagates inward toward the axis of the model while the outer shed axial vortex shows no such tendency. This is shown schematically in Fig. 30. After it is fully formed, the inner axial vortex turns elliptic and takes an inclined position in the *y*-*z* plane. In the clapping mode, during the outward motion of the flaps, four axial vortices would tend to converge near the model axis increasing vortex-vortex and vortex-wall interactions. The induced drag will likely be more affected in the clapping mode than in the waving mode.

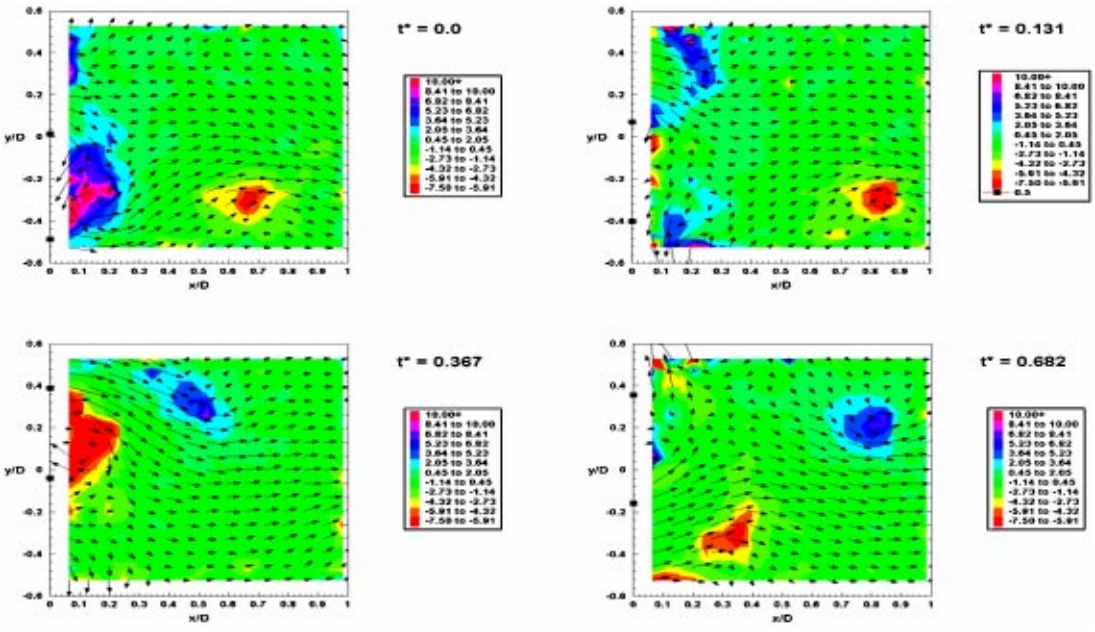

Fig. 24 Vorticity-velocity vector maps in the axial plane in the waving mode.

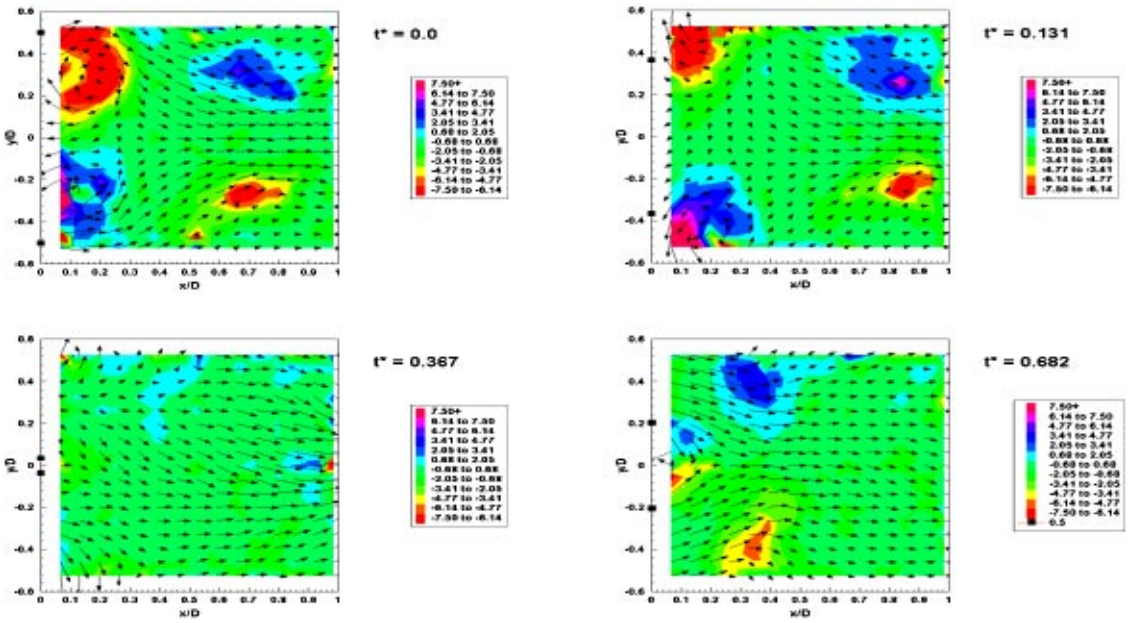

Fig. 25 Vorticity-velocity vector maps in the axial plane in the clapping mode

4 Phased Vortex Seeding From Forebody for Thrust Modulation in a Rigid Cylinder With Flapping Foil Thrusters

4.1 Results. Measurements of axial force are shown in Fig. 35 where the ensemble averaged traces are compared for nose slider on/off cases. The time lag in the on-case is zero with respect to the tail flaps. Mainly the peak levels of thrust, and to a lesser extent the drag values as well, are enhanced by the nose vortex seeding. The time integrated value increases in the on-case, but is only above zero within the uncertainties of measurements. The effect of a lag in nose vortex shedding is shown in Fig. 36. Particularly the thrust peaks are highest at a lag of 300 degrees and lowest at 120 degrees. The difference between the two lags is 180 degrees which shows that an exquisitely phase-dependent mechanism is involved.

These experiments suggested that nose vortex seeding did have a temporal effect on the axial forces. The experiments were repeated at a Strouhal number where the net axial force was clearly a thrust. A perforated plate was installed in the downstream end of the test section to steady the low speed streams. The results are shown in Figs. 37 and 38. Figure 37 shows the temporal effects of a phase lag in nose vortex seeding. The thrust peak is highest at 300 deg and lowest at 120 deg. The effects of phase lag on the time integrated thrust levels are shown in Fig. 38 at three Strouhal numbers St, of tail flapping ($=fA/U$). A sinusoidal effect of lag on net thrust is present. The net thrust is enhanced around 120 deg and reduced at 300 deg. The integrated effect is opposite to the effects on peak values of thrust and drag.

Because the mechanism is exquisitely dependent on Strouhal number St, care had to be taken in tracking the freestream speed. Recall that a perforated plate was installed in the test section to

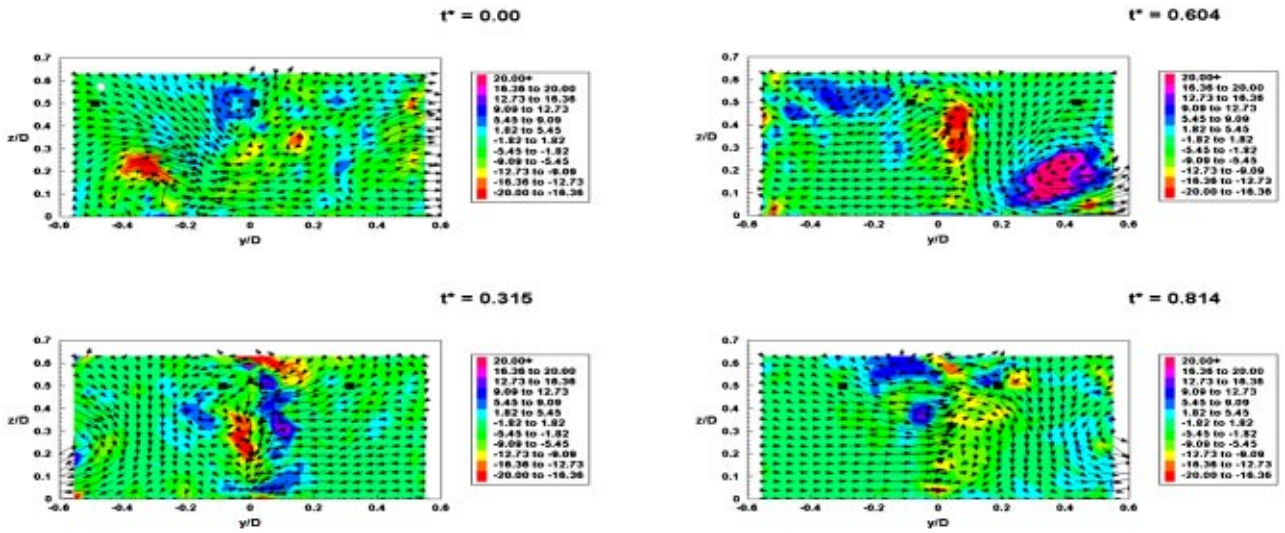

Fig. 26 Vorticity-velocity vector maps in the cross-stream plane in the waving mode; $x/D=0.066$. Filled square markers at $z/D=0.5$ within each frame indicate flap location.

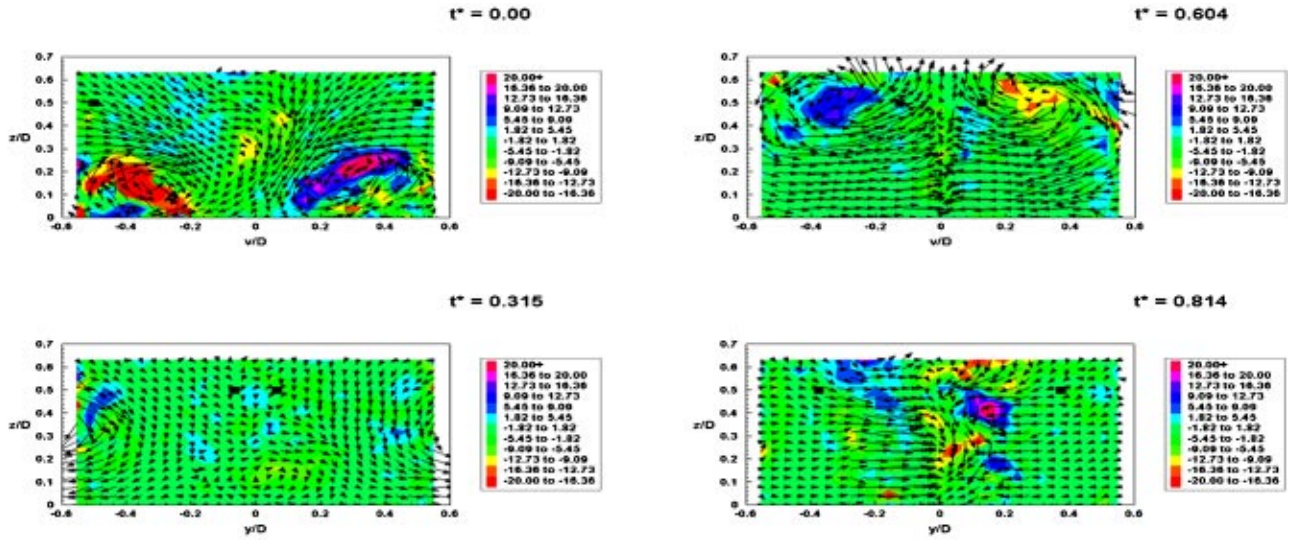

Fig. 27 Vorticity-velocity vector maps in the cross-stream plane in the clapping mode; $x/D=0.066$. Filled square markers at $z/D=0.5$ within each frame indicate flap location.

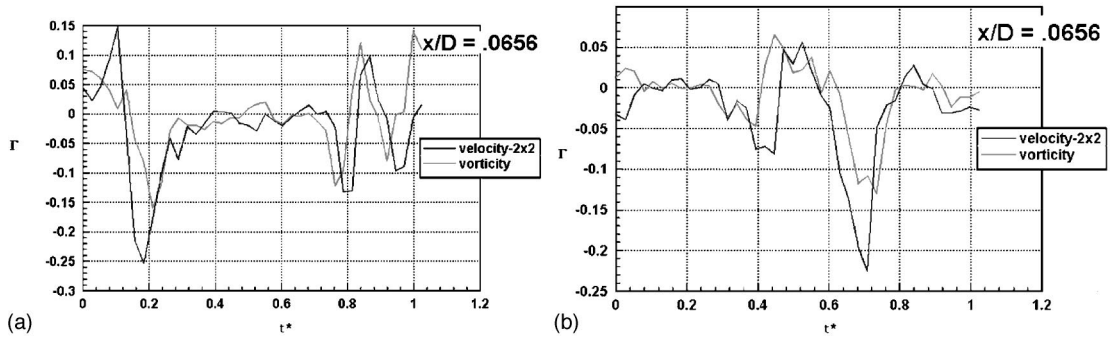

Fig. 28 Vortex circulation versus flap phase; starboard flap $x/D=0.0656$, (*a*) waving and (*b*) clapping

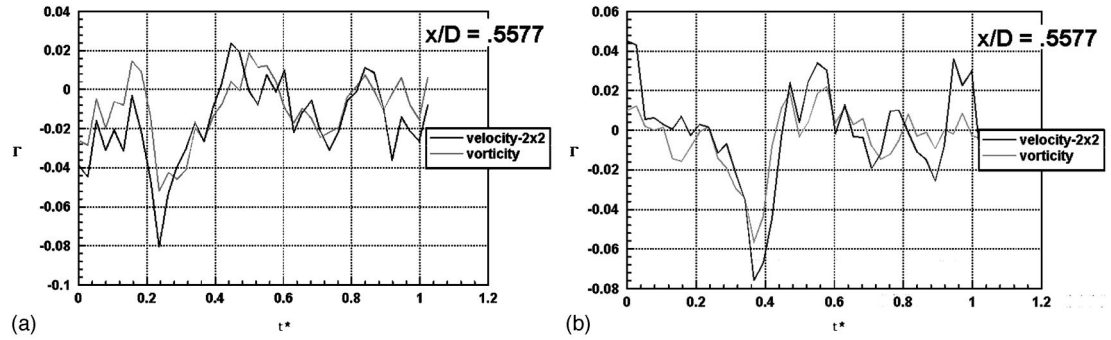

Fig. 29 Circulation distribution at a downstream station ($x/D=0.5577$) compared to that in Fig. 28, (*a*) waving and (*b*) clapping

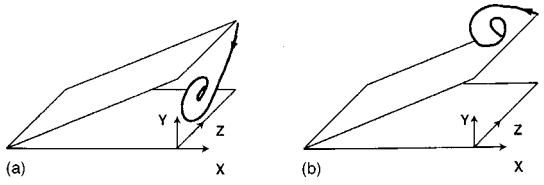

Fig. 30 Schematic diagram showing the inward trajectory of the inner shed axial vortex (*a*) as opposed to the outer shed axial vortex (*b*) in both modes of flap oscillation

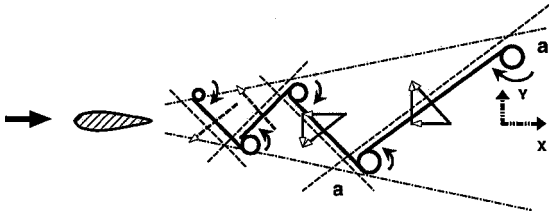

Fig. 31 Schematic of production of drag (momentum deficit) and yaw force due to a Kármán vortex train

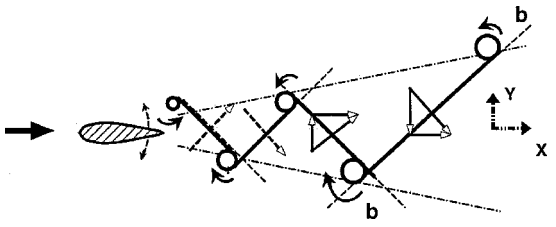

Fig. 32 Schematic of production of thrust (momentum excess) and yaw force due to a negative Kármán vortex train

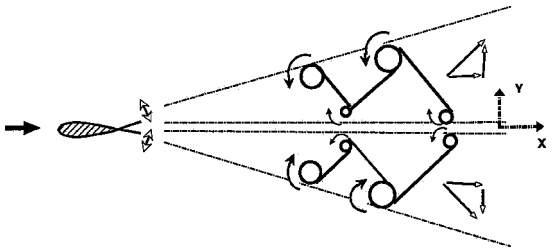

Fig. 33 Schematic of vortex train in clapping mode showing the origin of axial and crossstream force vectors

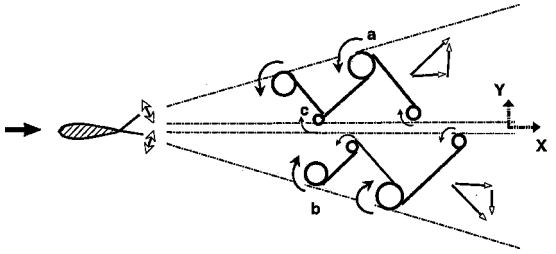

Fig. 34 Schematic of vortex train in waving mode showing the origin of axial and crossstream force vectors

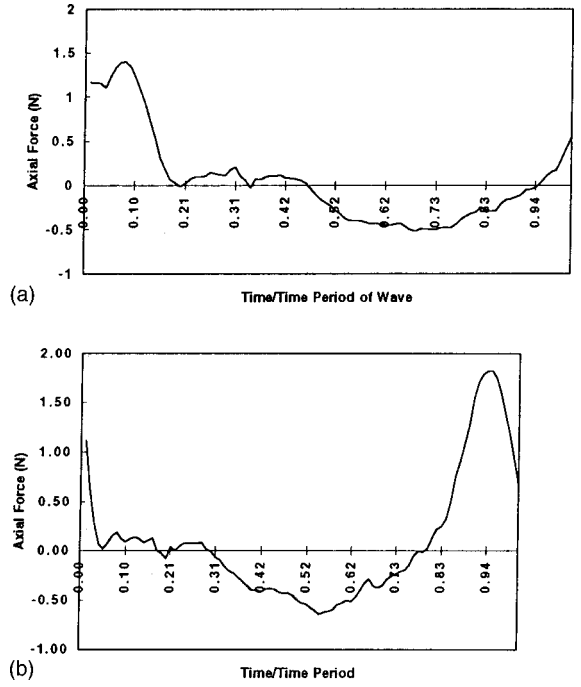

Fig. 35 Ensemble averaged trace of axial force on the model. Tail flap St=0.25–0.35. Nose slider: (*a*) off, (*b*) on.

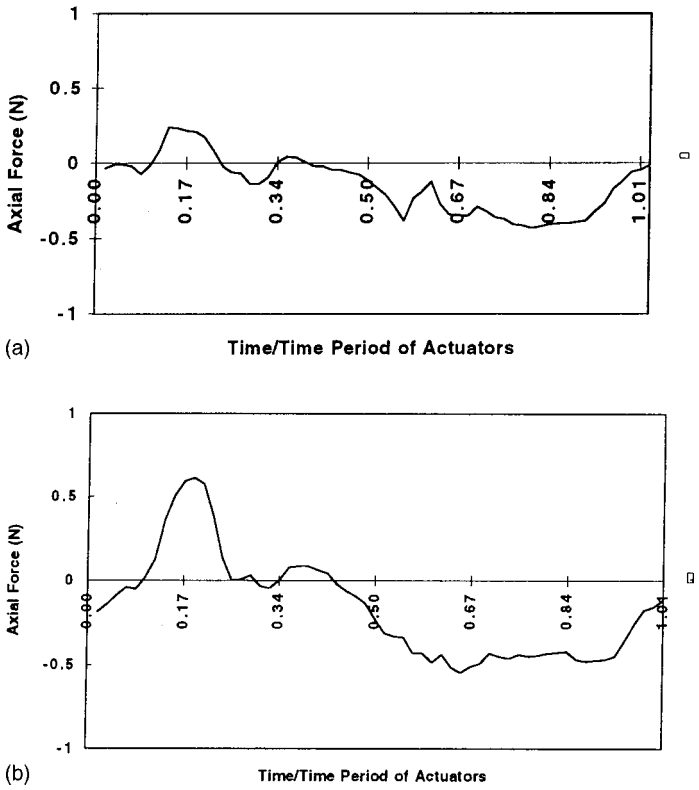

Fig. 36 Effect of phase lag of nose slider on axial force. Tail flap St=0.13. Lag: (*a*) 120 deg, (*b*) 300 deg.

achieve steady freestream speeds. The speeds and Strouhal numbers are 16.2–21.0 cm/s and 0.6–0.46 in Fig. 38(*a*), 27.4–30.5 cm/s and 0.375–0.337 in Fig. 38(*b*), and 36.0–37.8 cm/s and 0.276–0.263 in Fig. 38(*c*), respectively. The speed variation between runs, is within 5 percent at a nominal speed of 40 cm/s, which increased to 20 percent at lower speeds of 20 cm/s. The measurements reported in Fig. 38 are for those runs where the freestream speed remained nearly constant over several successive runs. At that condition, the Pitot readings were at worst, within 5 percent from that obtained from the nozzle pressure drop. The scatter can be reduced by holding the freestream speed more accurately.

Inspite of the scatter in the data, Fig. 38(*a*) indicates that net thrust is slightly enhanced compared to the off case. No attempt has been made to optimize the protrusion of the nose slider for thrust enhancement. This could best be carried out by computational methods.

4.2 Mechanism of Thrust Modulation. Several questions arise: (1) what is the mechanism of thrust modulation? (2) is there any viscous drag reduction over the cylinder involved? (3) how are the presumably tiny nose vortices surviving a distance of 1 m? (4) how relevant are the results to fish locomotion? A hypothesis of flow mechanism given below attempts to provide qualitative answers to these questions.

A starting point would be the question: what is the trajectory of the shed nose vortex? Dye flow visualization and phase-matched laser Doppler measurements of vorticity and velocity vectors of vortex shedding from the flapping foils at the tail reported earlier, is instructive. They indicated that the forced shed vortices from a moving surface do not propagate along the tangent at the trailing edge. In a similar manner, in Fig. 39(*a*) it is hypothesized that the shed vortices from an oscillating surface-normal plate would track at a higher elevation than that from a non-moving obstruction would. This would allow the vortices not to interact with the

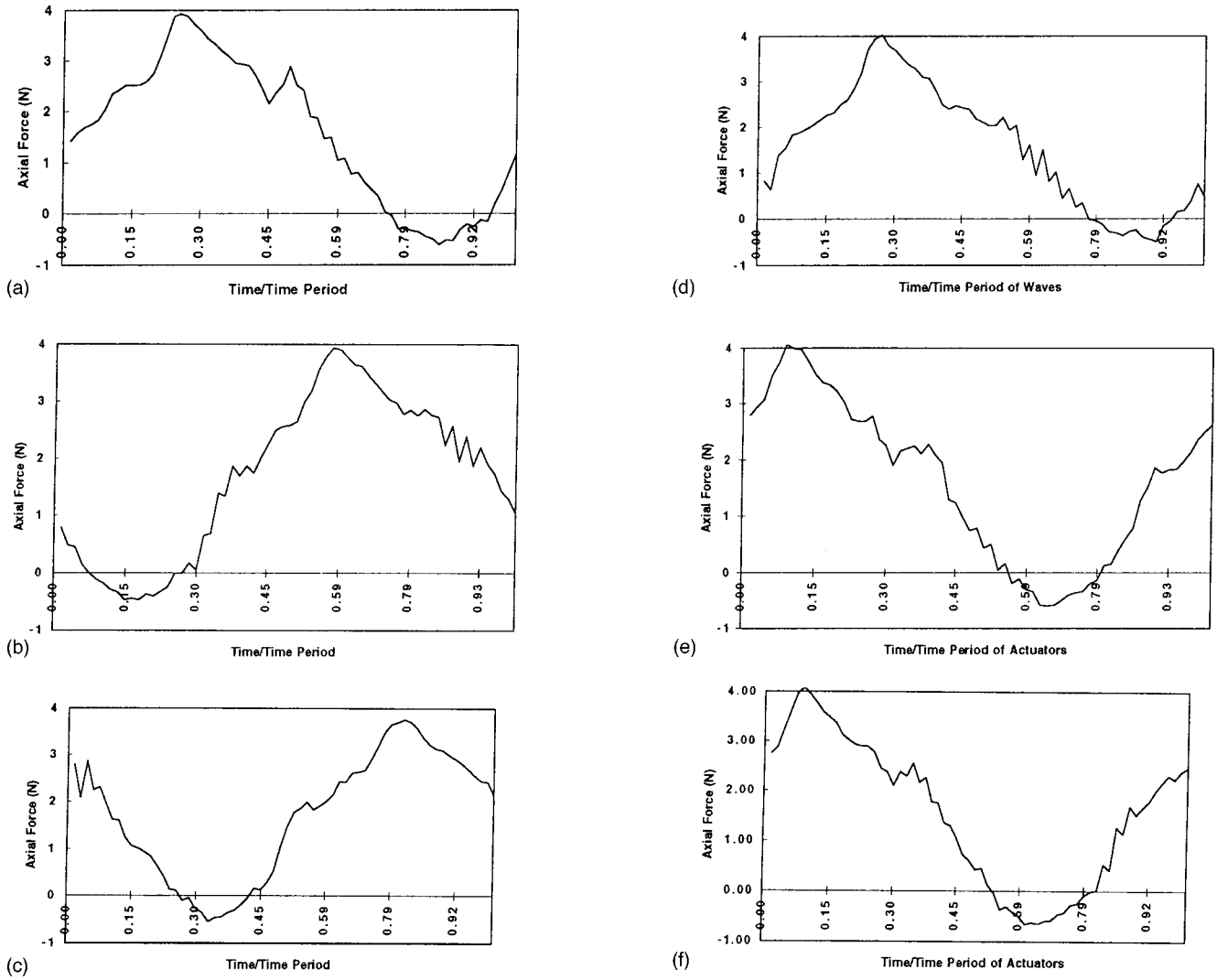

Fig. 37 Ensemble averaged time trace of axial force on the model. (*a*) Nose slider phase lag: 0 deg; (*b*) 60 deg; (*c*) 120 deg; (*d*) 180 deg; (*e*) 240 deg; (*f*) 300 deg.

cylinder boundary layer and to survive longer. As sketched in Fig. 39(*b*), the vortices might undergo a pairing process increasing their spacing and survivability. The seed vortices then interact with those formed by the oscillating flaps. Further pairing could ensue. Negative vortices marked A, B, and C on the port side would have a common induction due to proximity with the positive vortex D and give rise to a downstream vectored jet over the phase 0–180 deg. This would be followed by an agglomerated induction of similar but negative vortices from the starboard side. The net interaction results in the *modulation of the vector of the jets between pairs of vortices* which is the source of the axial force. This mechanism is primarily rotational and inviscid.

The present work suggests that if the head movement of a fish sheds vortices, then the body waving may be a mechanism to ensure the survivability of these vortices in the presence of cross currents so that eventually they become available to modulate the thrust produced by the caudal fins.

5 Conclusions

Two experiments have been carried out in water simulating unsteady fish hydrodynamics on a rigid cylinder. The focus is on the tail oscillation and the swaying of the forebody. The tail oscillation is generated by a pair of flaps which are operated in one of two modes: clapping and waving. They mimic the motion of the pectoral and caudal fins of a fish, respectively. This clapping motion is also found in insects. Detailed dynamic measurements have been carried out of the forces and moments on the entire model, and also of the three-dimensional vorticity-velocity vector field of the vortex shedding process in the near wake. The present work has revealed the presence of several interacting effects and scales. Several questions have been raised and the following conclusions are drawn.

1 The dolphin swimming data shows a relationship between body length and tail flapping frequency which can be modeled as a simple pendulum. The implication is that, for aquatic animals, the longitudinal structural modes of the body and the vortex shedding process from the head and tail are coupled.

2 The generation of vortex trains in the wake due to flapping foils can be termed as natural or forced. The present work falls in the latter category where a salient edge separation at the flap trailing edge is forced. The transverse wake vortices that are shed, follow a path that is wider than that given by the tangents to the flapping foils. The peak value of the circulation of the flap tip axial vortex drops by a factor of three within a distance of only half the flap width.

3 Significant higher order effects appear in axial force coefficients when Strouhal number of tail flapping foils is above 0.15. The axial force coefficient due to flapping foils is bounded be-

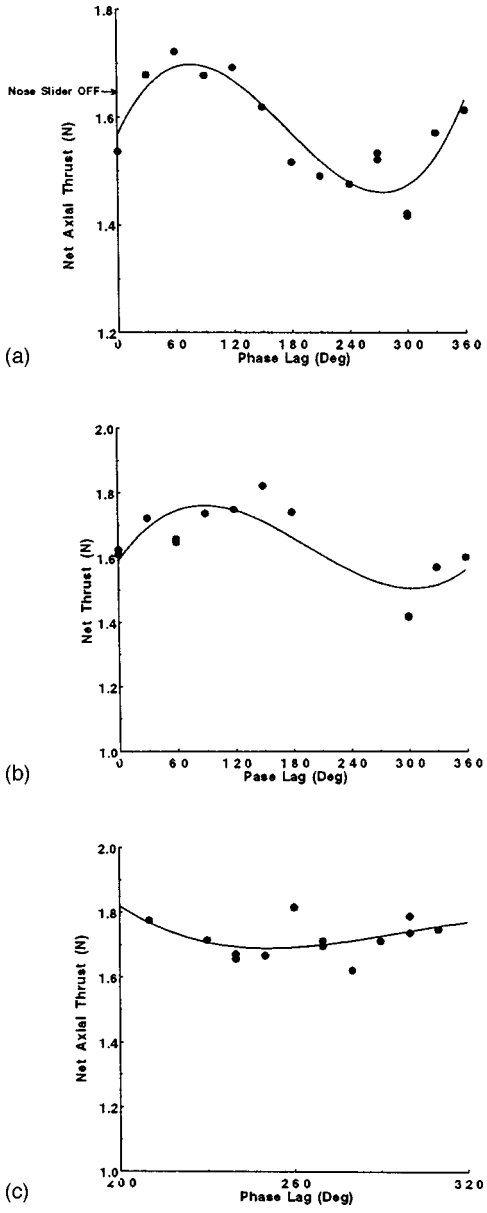

Fig. 38 Variation of time-averaged axial thrust with phase lag of nose slider. Speed, frequency and tail flap St: (*a*) 16.2–21.0 cm/s, 3.77 Hz and 0.6–0.46; (*b*) 27.4–30.5 cm/s; 3.64 Hz and 0.375–0.337; (*c*) 36–38 cm/s; 3.65 Hz and 0.276–0.263.

tween two asymptotes-the natural distribution given by inviscid theories at lower end, and an asymptote given by the characteristics of a forced and discrete shedding process at the higher end. In between, the nature is not universal, but transitional, where details like the mode and frequency of flapping and the number of flaps are influential.

4 Dynamic measurements of axial force and phase-matched measurements of the vorticity-velocity vector maps in the axial and cross-stream planes have confirmed the production of thrust in a rigid body due to flapping foils attached to its tail. The origin of thrust in the establishment of a jet producing vortex structure in the wake is shown via direct measurements. These measurements are a database for the validation of unsteady computational codes.

5 There is a misconception in the literature about Strouhal numbers and efficiency of fish and two dimensional flapping hydrofoils. While this may be true for natural shedding processes, there is no data yet showing that fish attains a sharply peaked highest efficiency in the range $0.25 < St < 0.35$. Several species of

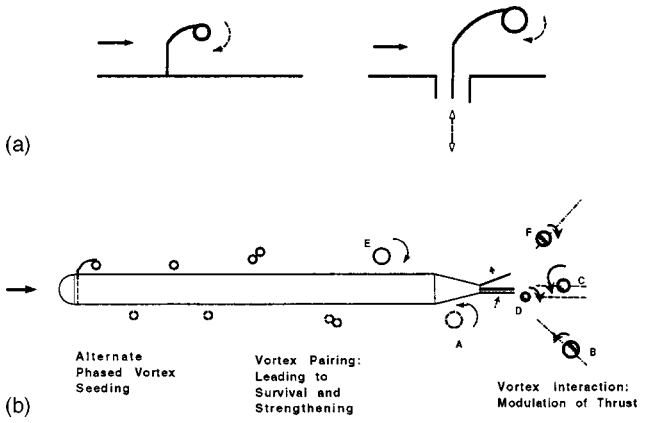

Fig. 39 Schematics of mechanism of vortex interaction: (*a*) effect of unsteadiness of a vorticity source on vortex trajectory and (*b*) mechanism of thrust modulation

fish operate in this range when they swim at their highest speeds. However data about efficiency and a sharp peaking is so far lacking.

6 Efficiency of axial force production reaches a peak below the Strouhal number range of 0.25−0.35. Strouhal number of tail flapping does emerge as an important parameter governing the production of net axial force and efficiency, although it is by no means the only one. Flapping frequency and mode of flapping, namely waving and clapping, are important as well in the forced shedding mechanism. The efficiency of thrust production is slightly higher in the waving mode of oscillation of the dual flapping foils in the tail - *a* mode of motion that mimics the swaying of the forebody of a fish. The importance of induced drag has been traced to the flapping mode and the attendant interaction of the flap-tip axial vortices.

7 The phase variation of a simulated and minute head swaying, can modulate axial thrust produced by the tail motion, within a narrow range of ±5 percent. This precision indicates that the phase relationship of vortex shedding from various discrete vorticity generating surfaces is an effective tool of maneuvering in a fish.

8 The general conclusion is that, the mechanism of discrete deterministic and phased vortex shedding produces large unsteady force vectors, which makes it inherently amenable to active control and suitable for precision maneuvering.

Acknowledgment

This research was funded by the Office of Naval Research and the Naval Undersea Warfare Center Independent Research Program. This support is gratefully acknowledged. The encouragement of and discussions with Mr. James Fein, Dr. Teresa McMullen, Professors Frank Fish and M. Triantafyllou are acknowledged. The authors would also like to acknowledge the assistance of D. Thivierge, J. Dick, M. Zeiger, C. Straney, M. Savoie, and B. Doyle. The first part of this work was presented at the AGARD Workshop on ''High Speed Body Motion in Water,'' held at Kiev, Ukraine, Sept. 1–3, 1997, and the second part was presented at the ''International Symposium on Seawater Drag Reduction,'' held at Newport, RI, July 22–24, 1998.

References

[1] Bandyopadhyay, P. R., Castano, J. M., Rice, J. Q., Philips, R. B., Nedderman, W. H., and Macy, W. K., 1997, ''Low-Speed Maneuvering Hydrodynamics of Fish and Small Underwater Vehicles,'' ASME J. Fluids Eng., **119**, pp. 136–144.

[2] Bandyopadhyay, P. R., Nedderman, W. H., and Dick, J., 1999, ''Biologically-Inspired Bodies Under Surface Waves. Part 1: Load Measurements,'' ASME J. Fluids Eng., **121**, pp. 469–478.

[3] Bandyopadhyay, P. R., Singh, S. N., and Chockalingam, F., 1999, ''Biologically-Inspired Bodies Under Surface Waves. Part 2: Theoretical Control of Maneuvering,'' ASME J. Fluids Eng., **121**, pp. 479–487.
[4] Jones, K. D., Dohring, C. M., and Platzer M. F., 1996, ''Wake Structures Behind Plunging Airfoils: A Comparison of Numerical and Experimental Results,'' Paper No. AIAA 96-0078.
[5] ''HSVA Towing Tests on a G7e Torpedo with SSR-Drive and with Normal Propeller Drive,'' PG/21600, translated by the British from the German, Sept. 1944.
[6] Gopalkrishnan, R., Triantafyllou, M. S., Triantafyllou, G. S., and Barrett, D., 1994, ''Active Vorticity Control in a Shear Flow Using a Flapping Foil,'' J. Fluid Mech., **274**, pp. 1–21.
[7] Hall, K. C., and Hall, S. R., 1996, ''Minimum Induced Power Requirements for Flapping Flight,'' J. Fluid Mech., **323**, pp. 285–315.
[8] Lighthill, M. J., 1975, Mathematical Biofluidynamics, Philadelphia, SIAM.
[9] Wu, T. Y., 1971, ''Hydromechanics of Swimming Propulsion,'' J. Fluid Mech., **46**, pp. 337–355.
[10] Webb, P. W. 1978, ''Hydrodynamics: Nonscombroid Fish,'' *Fish Physiology, Vol. VII*, eds., W. S. Hoar and D. I. Randall, Academic Press, pp. 189–237.
[11] Anderson, J. M., Streitlien, K., Barrett, D. S., and Triantafyllou, M. S., 1998, ''Oscillating Foils of High Propulsive Efficiency,'' J. Fluid Mech., **360**, pp. 41–72.
[12] Wolfgang, M. J., Tolkoff, S. W., Techet, A. H., Barrett, D. S., Triantafyllou, M. S., Yue, D. K. P., Hover, F. S., Grosenbaugh, M. A., and McGillis, W. R., 1998, ''Drag Reduction and Turbulence Control in Swimming Fish-like Bodies,'' *Proc. NUWC Intl. Symposium on Seawater Drag Reduction*, July 22–24, 1998, held in Newport, RI.
[13] Triantafyllou, M. S., Triantafyllou, G. S., and Gopalkrishnan, R., 1991, ''Wake Mechanics for Thrust Generation in Oscillating Foils,'' Phys. Fluids, **3**, No 12, pp. 2835–2837.
[14] Fein, J., 1998, ''Dolphin Drag Reduction: Myth or Magic,'' Proc. Intl. Sympo. Seawater Drag Reduction, NUWC, Newport, RI. pp. 429–434.
[15] Fish, F., 1983, ''Power Output and Propulsive efficiency of Swimming Bottlenose Dolphins (Tursiops Truncatus,'' J. Exp. Biol., **185**, pp. 179–193.
[16] Triantafyllou, M. S., and Triantafyllou, G. S., 1995, ''An Efficient Swimming Machine,'' Sci. Am., **272**, pp. 64–70.
[17] Rohr, J. J., Hendricks, E. W., Quigley, L., Fish, F. E., Gilpatrick, J. W., Scardina-Ludwig, J., 1998, ''Observations of Dolphin Swimming Speed and Strouhal Number,'' Tech. Rept. 1769, US Navy Space and Naval Warfare Systems Center, San Diego, CA.
[18] Lang, T. G. and Daybell, D. A., 1963 ''Porpoise Performance Tests in a Seawater Tank,'' Nav. Ord. Test Sta. Tech. Rept. 3063, pp. 1–50.
[19] Kayan, Y. P., and Pyatetskiy, V. Ye., 1977, ''Kinematics of Bottlenosed Dolphins Swimming as Related to Acceleration Mode,'' Bionika, **11**, pp. 36–41.
[20] Belmonte, A., Elsenberg, H., and Moses, E., 1998, ''From Flutter to Tumble: Inertial Drag and Froude Similarity in Falling Paper,'' Phys. Rev. Lett., **81**, pp. 345–348.
[21] Bandyopadhyay, P. R., Nedderman, W. H., Castano, J. M., and Donnelly, M. J., 1996, '' A Small Maneuvering Device for Energetic Environment,'' NUWC-NPT Video, Naval Undersea Warfare Center Division, Newport, RI.
[22] Zeiger, M., Rediniotis, O. K., Donnelly, M. J., and Telionis D. P., 1995, ''Temporal Evolution of the Flow Field Over a Pitching Tangent-Ogive Cylinder,'' AIAA Paper No. 95-0441.
[23] Bandyopadhyay, P. R., and Donnelly, M. J., 1998, ''The Swimming Hydrodynamics of a Pair of Flapping Foils Attached to a Rigid Body,'' *AGARD-R-827*, 1.1–1.17.
[24] Chopra, M. G., 1977, ''Hydromechanics of Lunate Tail Swim-ming Propulsion,'' J. Fluid Mech., **7**, pp. 46–69.
[25] Isshiki, H., and Murakami, M., 1984, ''A Theory of Wave Devouring Propulsion,'' J. Soc. Naval Architects Jpn., **156**, pp. 102–114.
[26] Bandyopadhyay, P. R., 1996, ''A Simplified Momentum Model of a Maneuvering Device for Small Underwater Vehicles,'' NUWC-NPT Technical Report 10,552, Naval Undersea Warfare Center Division, Newport, RI.

H. Kagemoto
Professor
Department of Environmental Studies,
The University of Tokyo, 7-3-1 Hongo,
Bunkyo-ku, Tokyo 113-0033, Japan

M. J. Wolfgang
Research Engineer

D. K. P. Yue
Professor

M. S. Triantafyllou
Professor

Department of Ocean Engineering,
Massachusetts Institute of Technology,
Cambridge, MA 02139

Force and Power Estimation in Fish-Like Locomotion Using a Vortex-Lattice Method

The forces and power needed for propelling at constant speed an actively swimming flexible fish-like body are calculated. A vortex-lattice method based on a linearized theory is employed and the results are compared against slender body theory predictions, as well as experimental data from an eight-link robotic instrument, the RoboTuna. Qualitative agreement is found between our method and slender body theory; with quantitative agreement over certain parametric ranges and disagreement for other ranges of practical interest. The present linearized vortex lattice calculations predict the power needed for propelling the RoboTuna with less than 20 percent error in most experiments conducted. [S0098-2202(00)01202-5]

1 Introduction

Reported outstanding swimming performance from live fish has sparked considerable attention from many investigators. Lighthill [1,2] applied slender-body theory to model the forces acting on a flexible swimming body, obtaining explicit expressions for the thrust force, power needed and propulsive efficiency. Within slender-body theory the time-averaged thrust force is determined only by the geometrical shape and movement characteristics of the abruptly ending tail. Wu [3] first studied the swimming motion of a two-dimensional plate and obtained closed-form solutions for the thrust force using conformal mapping. He gives a clear explanation of how the features of vorticity shed in the wake provide on average a net jet flow, which is closely associated with the developed thrust: A flow develops consisting of a staggered array of vortices, resembling a Kármán vortex street, but with reverse direction of rotation, compatible with the generation of a jet flow.

Subsequently, Wu [4] and Lighthill [2] studied the swimming of slender fish, obtaining the same results as Lighthill [2] when no vorticity is shed from the main body of the fish. A different result is obtained when body vorticity is shed: The rear part of the fish, defined as the portion after the point of maximum transverse height (i.e., with contracting lateral dimension) is modeled to have sharp ends, hence causing the flow to separate when the body moves transversely to the main flow. The interactions of the upstream shed vorticity with the oscillating lifting surface tail fin can modify the net force and power on the body. As shown similarly by Newman and Wu [5] and Newman [6], the interaction of the tail fin with the impinging flow perturbations from upstream can result in improved performance.

Although the slender-body theory developed by Lighthill [1,2] and Wu [4] gives simple closed-form solutions for the hydrodynamic lateral and thrust forces on a swimming flexible body, there are several approximations and assumptions made. First, it is assumed that the body is slender; however, the aspect ratio of a typical fish body is in the range between 0.2–0.5, with a caudal fin of high aspect ratio, especially for fast fish and cetaceans. This combination of a low-aspect-ratio lifting body with a high-aspect-ratio lifting surface may violate assumptions of slender body theory, and thus there are uncertainties as to the accuracy of the results provided by linear theory for arbitrary fish forms. The linear, ideal flow theory of unsteady foil motions has been studied by several investigators (Wu [4], Lighthill [2], Chopra [7], Chopra and Kambe [8]), providing unique insights into the performance characteristics of a high-aspect-ratio lifting surface as a propulsive device, with nonlinear corrections to the linear theory by Lighthill [2] and Chopra [9]. Katz and Weihs [10,11] showed that adding flexibility to a foil oscillating in pitch and heave may significantly increase the efficiency with marginal reduction in thrust. Works by Bose and Lien [12,13] highlight the thrust production dynamics and efficiencies of fin whale fluke geometries, revealing energy absorption mechanisms in addition to high efficiencies which may be utilized by swimmers. These works form a solid foundation of evidence suggesting that the oscillating lifting surface is an efficient method of producing thrust, resulting in high values of lift coefficient and delayed stall, but they do not consider the interactions of a low-aspect-ratio body producing lifting forces upstream of the tail. Thus, the integral performance of the system is difficult to evaluate analytically.

In order to assess the accuracy of the slender body theory, we employ a vortex-lattice method to predict numerically the thrust forces and propulsive efficiency of the fish-like motions of a low-aspect-ratio lifting body connected to a high-aspect-ratio lifting surface tail. The vortex-lattice method (VLM) has been used widely in the fields of aeronautics and hydrodynamics to predict the lifting forces on bodies of arbitrary planform, such as airplane wings (Katz and Plotkin [14]) or propeller blades (Greeley and Kerwin [15]), without geometric restrictions on the slenderness of the body. Although the viscous resistance of the body is an important quantity to the performance of the fish-like swimming motions, we are primarily interested in thrust development, which is expected to be a largely inviscid mechanism in the absence of significant bluff body flow separation and must balance the viscous resistance for steady straight-line swimming. While the VLM has been used mostly to predict lift forces in some cases it has been applied to the prediction of thrust force as well. Lan [16,17] applied the method to estimate the thrust forces produced by oscillating rigid plates. He showed how to properly evaluate the leading-edge suction force, which often contributes a large portion of the total thrust force. Cheng et al. [18] used a similar method to study the swimming of three-dimensional waving flexible plates. Most recently, Sverdrup [19] completed a comprehensive numerical investigation of the performance of three-dimensional flexible swimming plate motions for varying kinematics using a VLM, identifying regions of outstanding performance for specific ranges of kinematic parametric combinations.

More sophisticated numerical methods have been developed re-

Contributed by the Fluids Engineering Division for publication in the JOURNAL OF FLUIDS ENGINEERING. Manuscript received by the Fluids Engineering Division February 19, 1998; revised manuscript received December 7, 1999. Associate Technical Editor: P. R. Bandyopadhyay.

cently to predict the propulsive performance of fish-like bodies and oscillating foils. Liu [20] developed an inviscid panel method to predict the forces on a three-dimensional oscillating wing with chordwise and spanwise flexibility, but neglected the influence of any upstream body on the total force or inflow into the tail. Wolfgang [21] utilized a similar three-dimensional method to investigate the near-body and wake hydrodynamics of a variety of swimming fish, with multiple fully-nonlinear desingularized wake surfaces, and showed that upstream shedding of vorticity by the fish body by anterior fins is controlled by the oscillating tail to enhance performance and maneuverability (Wolfgang et al. [22]). In both these panel methods, the effects of viscosity are confined to the infinitesimal wake sheet for the large Reynolds numbers considered in the simulated motions, and as a result are an order of magnitude less computationally complex than the fully viscous methods of Liu et al. [23,24] and Carling et al. [25], which are essential at lower Reynolds numbers and bluff body separation is prevalent. Nonetheless, source-dipole panel methods are not well-suited to kinematic and geometric parametric investigation due to the geometric complexity and the heavy computational burden. The VLM allows for geometric modeling simplicity and is computationally rapid. Thus, an accurate VLM lends itself to more complex hydrodynamic challenges such as performance optimization, shown to be sensitive to both kinematic parameter variation (Barrett et al. [26]) and geometric constraints (Kagemoto [27], Kagemoto et al. [28]). Indeed, fish species with common morphological features such as fin placement often swim with similar kinematics (Weihs and Webb [29]; Triantafyllou et al. [30]), suggesting that the performance characteristics of swimming motion are highly dependent on coupled kinematic and geometric constraints. Utilization of a genetic algorithm (Goldberg [31], Barrett [32]) to explore the various parametric spaces can be achieved with a rapid computational scheme for hydrodynamic force prediction.

In this research, we closely follow the methodologies of Lan [16,17] and Cheng et al. [18] and develop a robust vortex lattice code for fish-like geometries for the analysis of thrust forces produced by waving motions which closely emulate motions of a real fish. We compare the power delivered to the fluid calculated by the VLM for the fish geometry with experimental data obtained using a swimming robotic instrument in the shape of a bluefin tuna, the *RoboTuna* (Barrett [33,32], M. S. Triantafyllou and G. S. Triantafyllou [34], M. S. Triantafyllou et al. [35]). Comparisons of the power required to generate useful thrust through largely inviscid mechanisms show good agreement between experiments and computation, validating our choice of simplified computational model to predict swimming performance. While not providing the most general treatment, this linear vortex-lattice method indeed establishes that inviscid mechanisms are principally at work and serves as an excellent tool to conduct more complex performance optimization analyses with minimal computational burden or time.

2 Formulation

We evaluate the hydrodynamic forces on a fish-like object performing rhythmic lateral undulating motions, described by the deviation of the backbone centerline from its position at rest, $H(x,t)$ in a uniform stream U, as shown in Fig. 1. A Cartesian coordinate system (x,y,z) fixed at the mean position of the body is used, in which the x-axis stretches along the body in a longitudinal direction from head to tail, the y-axis points vertically downward and the z-axis points laterally out of the body surface. We assume that the body is performing a waving motion in the lateral direction (z-direction), described as:

$$z = H(x,t) = \mathrm{Re}\{h(x)e^{i\omega t}\} \tag{1}$$

where Re indicates that a real part is taken. We employ an inviscid, linearized theory, which may be useful for capturing the basic features of the flow around a swimming fish-like body. For

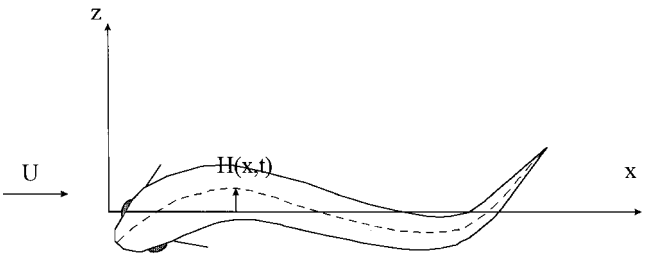

Fig. 1 Definitions

steady-state swimming motions and periodic perturbation quantities of oscillating frequency ω, the velocity potential around the body can be written:

$$\Phi(x,y,z,t) = Ux + \mathrm{Re}\{\phi(x,y,z)e^{i\omega t}\} \tag{2}$$

The kinematic boundary condition that should be satisfied on the body surface is,

$$\frac{D(H(x,t)-z)}{Dt} = \frac{\partial H}{\partial t} + \left(U + \frac{\partial \Phi}{\partial x}\right)\frac{\partial H}{\partial x} - \frac{\partial \Phi}{\partial z} = 0 \tag{3}$$

We assume that the velocity of the lateral motion as well as the perturbation flow velocity are small compared to U so that the quadratic terms can be neglected. Then Eq. (3) is linearized as:

$$i\omega h + U\frac{\partial h}{\partial x} - \frac{\partial \phi}{\partial z} = 0 \tag{4}$$

Further, Eq. (4) is imposed at the mean position of the body surface $(z=0)$ instead of the instantaneous body surface $(z = h(x)e^{i\omega t})$. A Kutta boundary condition on the trailing edge of the body must be prescribed according to Kelvin's theorem:

$$\frac{D\Gamma}{Dt} = 0 \tag{5}$$

which expresses the fact that the total circulation of the body and wake Γ must remain constant. Thus, changes in circulation around the body are reflected by a change in the circulation strength of the wake being shed, which is transported behind the body along the plane $z=0$ at the ambient flow velocity.

3 Application of the Vortex-Lattice Method

Within the vortex-lattice method, the body surface is discretized into small panels, and each panel is described by a vortex ring along its perimeter. Control points are chosen at the geometric center of each panel, and the kinematic boundary condition on each panel is evaluated at its control point. In order to account for the effect of a wake that may be formed behind a trailing edge of the body, the wake is also discretized into panels as shown in Fig. 2. Vortex rings are placed on the wake panels in the same manner as those on the body surface, with control points also at the geometric center of each wake panel. Therefore, unlike Lan [17], the strength of vortices is assumed to be stepwise constant in chordwise direction as well as in spanwise direction. Although in an actual flow the shape of the wake shear layer evolves with time

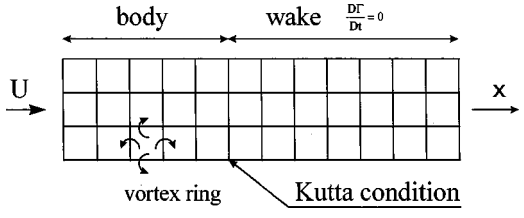

Fig. 2 Discretization into a vortex-lattice

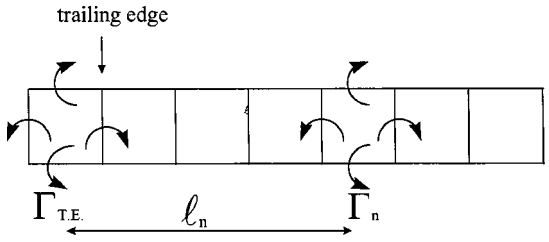

Fig. 3 Relationship of the vortex ring on a trailing edge and that on a wake

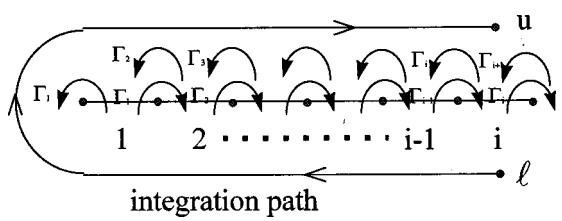

Fig. 5 Evaluation of the potential difference across a body

due to the self-induced and body perturbation velocities, the wake is assumed to be convected with the uniform stream U only in this linearized analysis, and wake panels remain fixed in the mean plane of the body surface $z=0$ where it was shed. The magnitude of the shed vortex rings at a time t are determined so that the body kinematic boundary condition (Eq. (4)) and the Kutta condition (Eq. (5)) are satisfied at a control point on each panel. Then, the pressure difference Δp across the body is written in terms of the velocity potential as:

$$\Delta p = 2\left(\frac{\partial \Delta\Phi}{\partial t} + U\frac{\partial \Delta\Phi}{\partial x}\right) \tag{6}$$

where $\Delta\Phi$ stands for the potential difference across the body.

V_n represents the z-velocity ($\partial\phi/\partial z$) normal to the body at the control point ($x_m, y_m, 0$) of the mth panel on the body induced by the nth vortex ring of unit strength. In this manner, Eq. (4) can be written as follows:

$$\sum_{n=1}^{N_b+N_w} \Gamma_n V_n = \left(i\omega h + U\frac{\partial h}{\partial x}\right)_{(x_m, y_m, 0)} \quad (m=1,2,\ldots,N_b) \tag{7}$$

where $\Gamma_n e^{i\omega t}$ stands for the strength of the nth vortex ring and N_b and N_w represent the number of vortex rings placed on the body surface and on the wake, respectively. The wake is truncated at a sufficient distance away from the trailing edge, determined through convergence tests to evaluate the decay of the far field wake influence on the body with increasing wake length.

Equation (5) requires that the strength Γ_n of a vortex ring around the nth wake panel be related to the strength $\Gamma_{T.E.}$ of the vortex ring at the trailing edge to satisfy Kelvin's theorem in the following manner:

$$\Gamma_n(x,y,0)e^{i\omega t} = \Gamma_{T.E.}(x_{T.E.}, y, 0)e^{i\omega(t-\ell_n/U)}$$
$$(n = N_b+1, N_b+2, \ldots, N_b+N_w) \tag{8}$$

where, as shown in Fig. 3, ℓ_n represents the distance between the centers of the nth vortex ring on the wake and that of the vortex ring at the trailing edge. In addition to Eqs. (7) and (8), we must impose an explicit Kutta condition, requiring the change in the strength of the circulation around the body to be countered by the change in circulation of the wake. Without such a condition, any combination of vortex rings that produce null velocity on the body surface can be added to any particular solution. For a thin trailing-edged body, the Kutta condition requires that the stagnation line coincide with the trailing edge. The Kutta condition for a sharp-trailing-edged tail can be stated in a different but equivalent manner as

$$\Delta p = 2\left(\frac{\partial \Delta\Phi}{\partial t} + U\frac{\partial \Delta\Phi}{\partial x}\right) = 0 \quad \text{at the trailing edge} \tag{9}$$

which requires the pressure jump at the trailing edge point to vanish. This formulation is more convenient in the context of the present vortex-lattice method.

Since the jump in streamwise perturbation velocity across the body $\partial\Delta\Phi/\partial x$ can be written

$$\frac{\partial \Delta\Phi}{\partial x} = \Delta u \tag{10}$$

where Δu represents the difference of the x-velocity across the body. Thus, the following approximation for $\partial\Delta\Phi/\partial x$ may be used, since Δu is approximately equal to the averaged strength of the vortex across the panel:

$$\left.\frac{\partial \Delta\Phi}{\partial x}\right|_{\text{at panel-}i} \sim \frac{1}{2}\{(\Gamma_i - \Gamma_{i+1}) + (\Gamma_{i-1} - \Gamma_i)\}/c_i \tag{11}$$

where c_i represents the chord length of the i-th panel (see Fig. 4). The added mass term in the pressure jump Kutta condition (Eq. 9) $\partial\Delta\Phi/\partial t = i\omega\Delta\phi e^{i\omega t}$ can be evaluated in the following manner (Konstadinopoulos et al. [36]):

$$\Delta\phi = \phi_u - \phi_\ell = \int_\ell^u \tilde{v}\cdot d\tilde{r} \tag{12}$$

where u and ℓ represent the upper and the lower surfaces of the body, respectively. If we denote the velocity potential jump across panel-i as $\Delta\phi_i$, then this potential difference may be evaluated as follows (see Fig. 5):

$$\Delta\phi_i = (\Gamma_{i-1} - \Gamma_i) + (\Gamma_{i-2} - \Gamma_{i-1}) + \cdots + (\Gamma_1 - \Gamma_2) - \Gamma_1 = -\Gamma_i \tag{13}$$

Thus, the unsteady added mass term in the pressure jump Kutta condition may be written,

$$\left.\frac{\partial \Delta\Phi}{\partial t}\right|_{\text{at panel-}i} \sim -i\omega\Gamma_i e^{i\omega t} \tag{14}$$

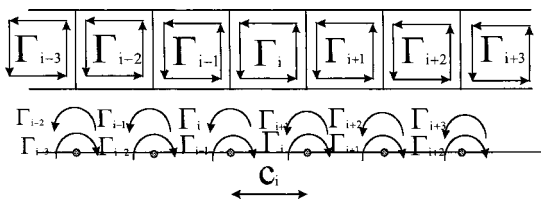

Fig. 4 An array of vortex rings

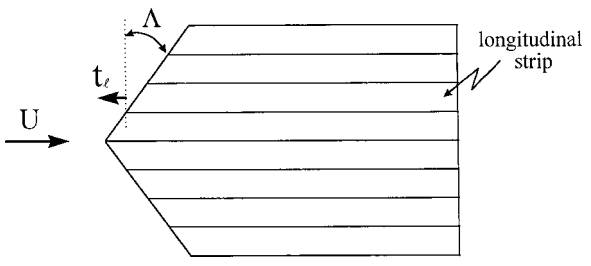

Fig. 6 Definitions of a sectional thrust force and a leading-edge sweep angle

Substituting Eqs. (11) and (14) into Eq. (9), it can be shown that the strengths of the vortex rings located at the trailing edge is determined from the strengths of the vortex rings on the other parts of the body. Since from Eq. (8), the strengths of the vortex rings on the wake can be expressed in terms of the strengths of the vortex rings on the trailing edge, only the strengths of those vortex rings which comprise the body surface not adjacent to the trailing edge are unknown.

4 Evaluation of Forces

Once the strengths Γ_i of each vortex ring on the body surface are determined, in principle the hydrodynamic forces can be evaluated by integrating the pressure jump over the body surface, given by Eq. (6). However, it is known that a large portion of the thrust force comes from the leading-edge suction force (Lighthill [2]; Sverdrup [19]), which is a suction force resulting from the low pressure region caused by the high speed flow over the leading edge. The velocity at the leading edge is known to possess an inverse-square-root singularity, and thus it is difficult to evaluate the force correctly by numerical pressure integration. Lan [16,17] showed how this numerical difficulty can be overcome, and we follow his methodology in the evaluation of the leading-edge suction force.

According to Lan ([17], Eqs. (*B*16) and (*B*17)), the mean sectional leading-edge thrust coefficient c_t for each longitudinal strip can be expressed

$$c_t \equiv \frac{t_\ell}{\frac{1}{2}\rho s U^2} = \frac{1}{2}\pi[\{\mathrm{Re}(C_s e^{i\omega t})\}^2 + \{\mathrm{Im}(C_s e^{i\omega t})\}^2]/(2\cos\Lambda) \tag{15}$$

where t_ℓ is the sectional leading-edge suction force, Λ stands for the leading-edge sweep angle (see Fig. 6), and ρ and s represent the density of the surrounding fluid and the area of the longitudinal strip, respectively. C_s is a parameter that represents the leading-edge singularity and calculated in the vortex-lattice approach from the following equation:

$$\frac{1}{2}N_c C_s H_s = \sum \text{(upwash at leading edge)} - w(x_\ell, y_\ell) \tag{16}$$

where

$$H_s \equiv 2(\tan^2\Lambda + 1)^{1/2} \tag{17}$$

N_c represents the number of panels on the longitudinal strip of the body, and $w(x_\ell, y_\ell)$ represents the lateral velocity at the corresponding point of the leading edge. The total leading-edge suction force T_s is obtained through integration of the sectional leading-edge suction force t_ℓ. The total thrust force (T) is then obtained

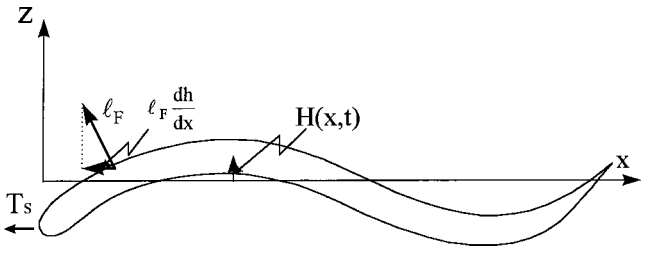

Fig. 7 Contributions of a leading-edge suction force and a lateral force to total thrust force

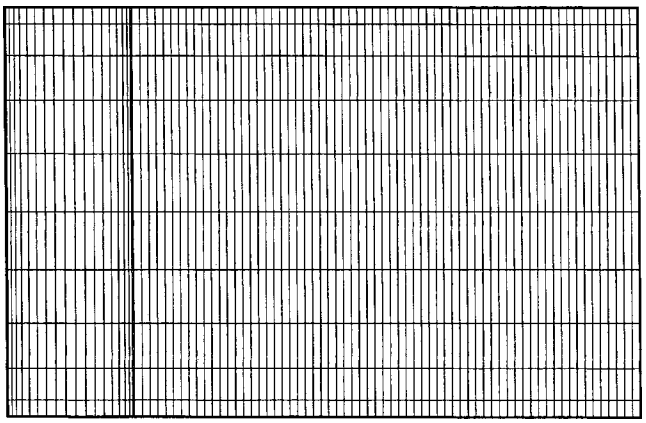

Fig. 8 Example discretization

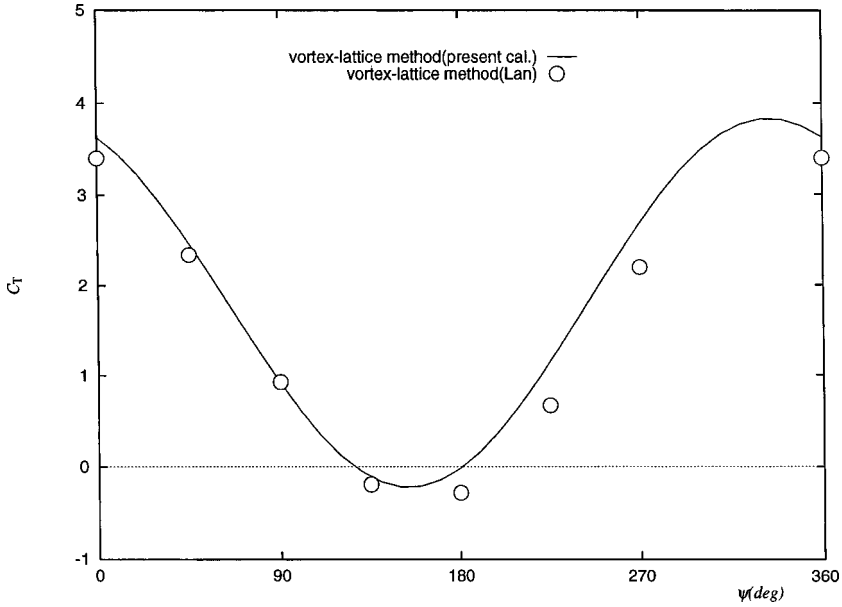

Fig. 9 Thrust force coefficient of a rectangular plate oscillating simultaneously in heave and pitch (A_R=7.0, $\omega L/2U$=0.75, θ=0.8).

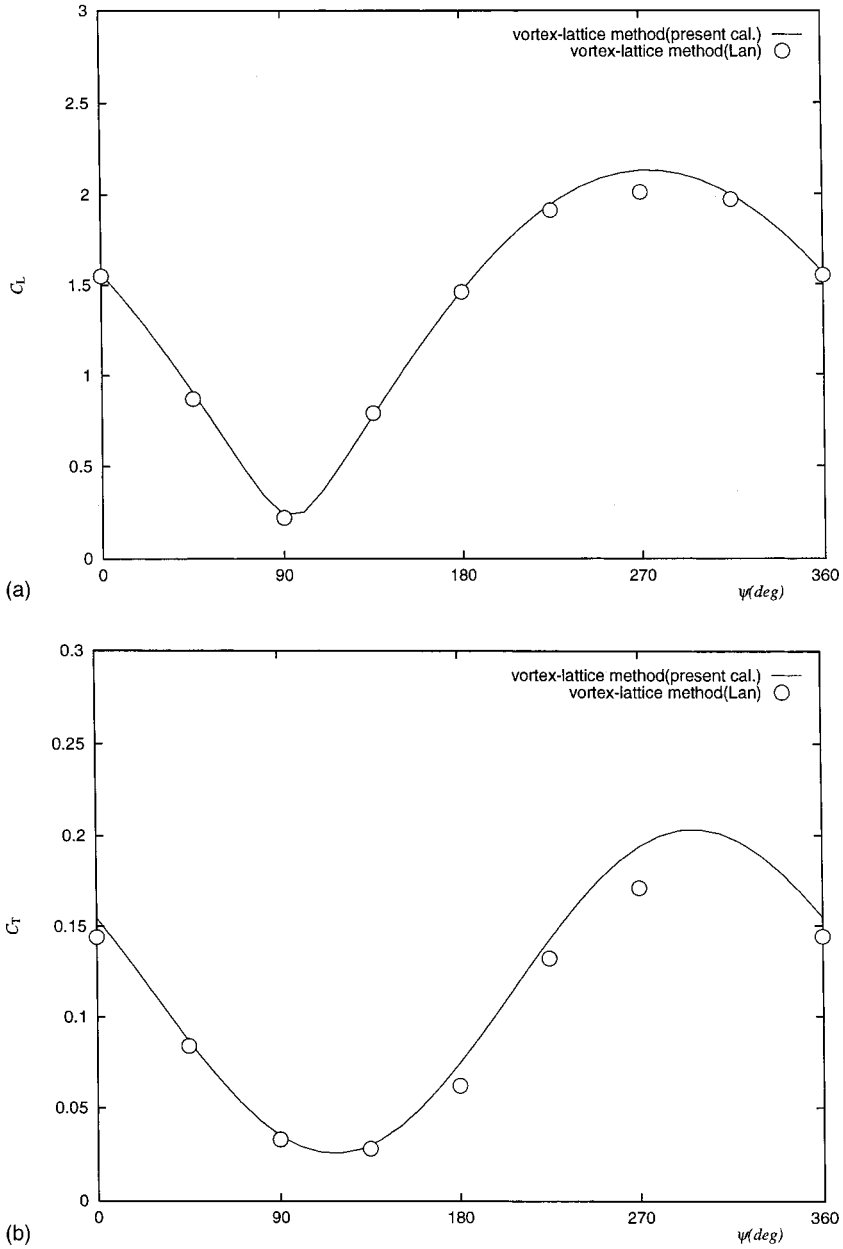

Fig. 10 (*a*) Lateral force coefficient of a rectangular plate oscillating simultaneously in heave and pitch (A_R=7.0, $\omega L/2U$=0.15, θ=0.8) (*b*) Thrust force coefficient of a rectangular plate oscillating simultaneously in heave and pitch (A_R=7.0, $\omega L/2U$=0.15, θ=0.8).

as a summation of the leading-edge suction force (T_S) and the thrust force component of the lateral force (ℓ_F) as shown in Fig. 7.

$$T = T_S + T_L = T_S + \int_0^L \ell_F \frac{dh}{dx}\, dx \tag{18}$$

The lateral force ℓ_F can be evaluated directly from the pressure difference integration over the body surface without numerical difficulty.

5 Results and Discussion

5.1 Comparison With Other Numerical Results. In order to first confirm the validity of the present analysis, comparisons are made with published results. The results obtained by Lan [17] include computations of lateral and thrust forces on oscillating rigid rectangular plates in a uniform flow. Although, as described above, both the present method and that used by Lan are vortex-lattice methodologies, Lan's method differs slightly from the present one in that he discretizes the plate into strips that stretch infinitely along the direction of the uniform stream. In the present approach, however, the plate is discretized in the chordwise direction as well as in spanwise direction. In this way, the vortex strength is allowed to vary stepwise in both the spanwise and chordwise directions within the present analysis, while in Lan's method it varies stepwise in the spanwise direction but varies continuously in the chordwise direction. Lan carried out the analysis of a rectangular plate oscillating simultaneously in heave and in pitch, a motion which can be described analytically

$$H(x,y,t) = \mathrm{Re}\{-h_a e^{i\omega t} + \alpha_a (x - x_a) e^{i(\omega t + \psi)}\} \tag{19}$$

where $H(x,y,t)$ represents the lateral displacement of the plate,

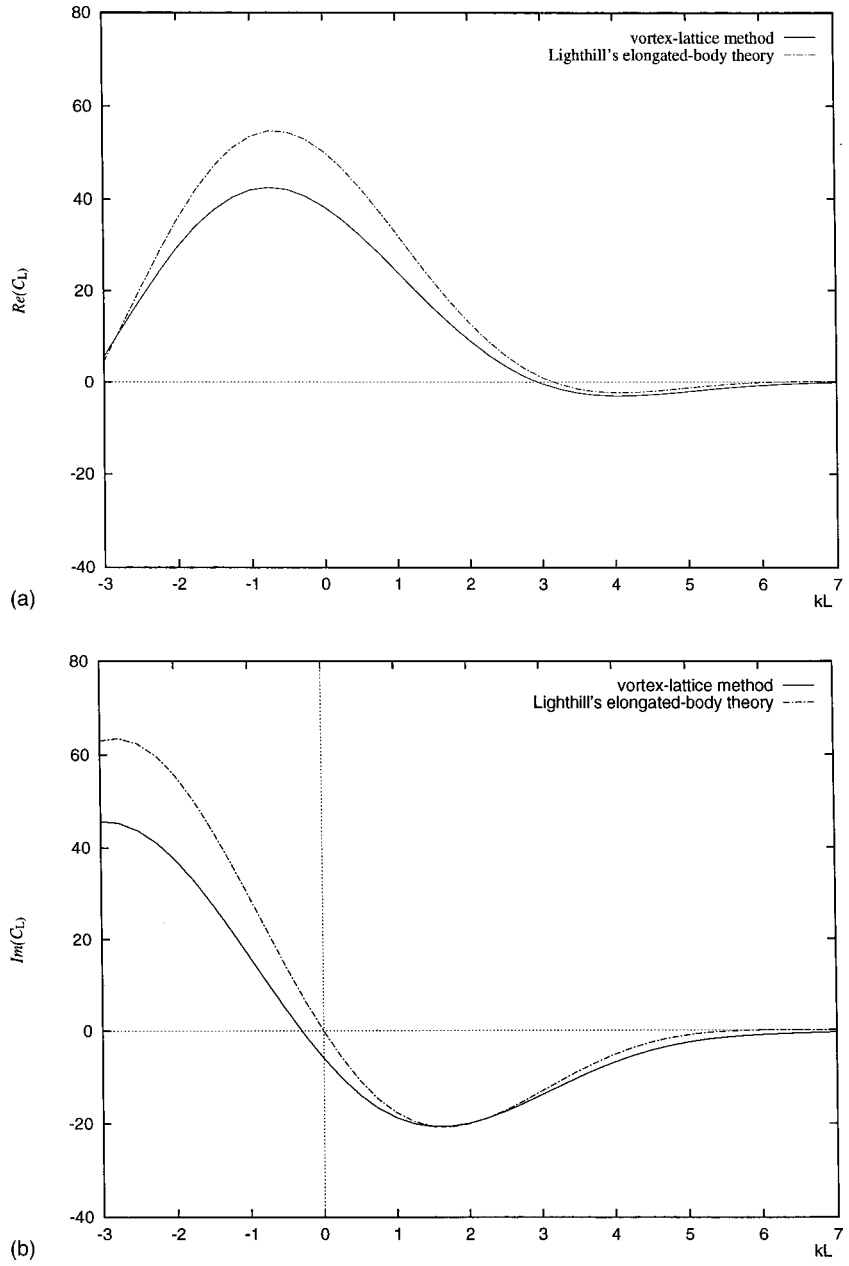

Fig. 11 (*a*) **Lateral force coefficient of a waving rectangular plate (Real part). The waving motion is given by Eq. (20). (A_R=0.5, $\omega L/U$=8.0)** (*b*) **Lateral force coefficient of a waving rectangular plate (Imaginary part). The waving motion is given by Eq. (20). (A_R=0.5, $\omega L/U$=8.0).**

and h_a and α_a represent the amplitudes of the heave and the pitch motion, respectively. The temporal phase angle between the heave motion and the pitch motion of the plate is represented by ψ, and the variation of this phase angle has been shown to strongly affect the performance dynamics of the motions (Lan [17]; Sverdrup [19]; Anderson et al. [37]). The pitch axis is referred to by $x = x_a$, which was chosen along the trailing edge of the plate in this analysis. Figure 8 shows an example of the discretization of the plate and the wake used for the present vortex-lattice calculations. For this analysis, a sufficient number of panels and an appropriate truncation length of the wake were identified through systematic convergence tests. The details of this convergence analysis are given in the Appendix.

Figure 9 shows the thrust force coefficient for reduced frequency $\omega L/2U = 0.75$, and Figs. 10(*a*) and 10(*b*) show the lateral and thrust force coefficients for $\omega L/2U = 0.15$. In the caption of the figure, θ is the feathering parameter, which represents the relative contributions of the pitch and heave motion to the local lateral displacement. The circles in the figures denote the results of Lan [17]. The agreements of the present results with the results of Lan are satisfactory for all the cases presented in Fig. 9 and Figs. 10(*a*) and 10(*b*) when $\psi < 150$ deg, while small but distinct discrepancies are observed for all the cases when $\psi > 180$ deg, likely due to chordwise planform discretization which varies the loading profile and downwash influence, especially for higher loadings realized for these values of the phase angle.

5.2 Comparison With the Slender-Body Theory. We compare the results obtained by the present vortex-lattice calculation with those obtained by the slender-body theory (elongated-

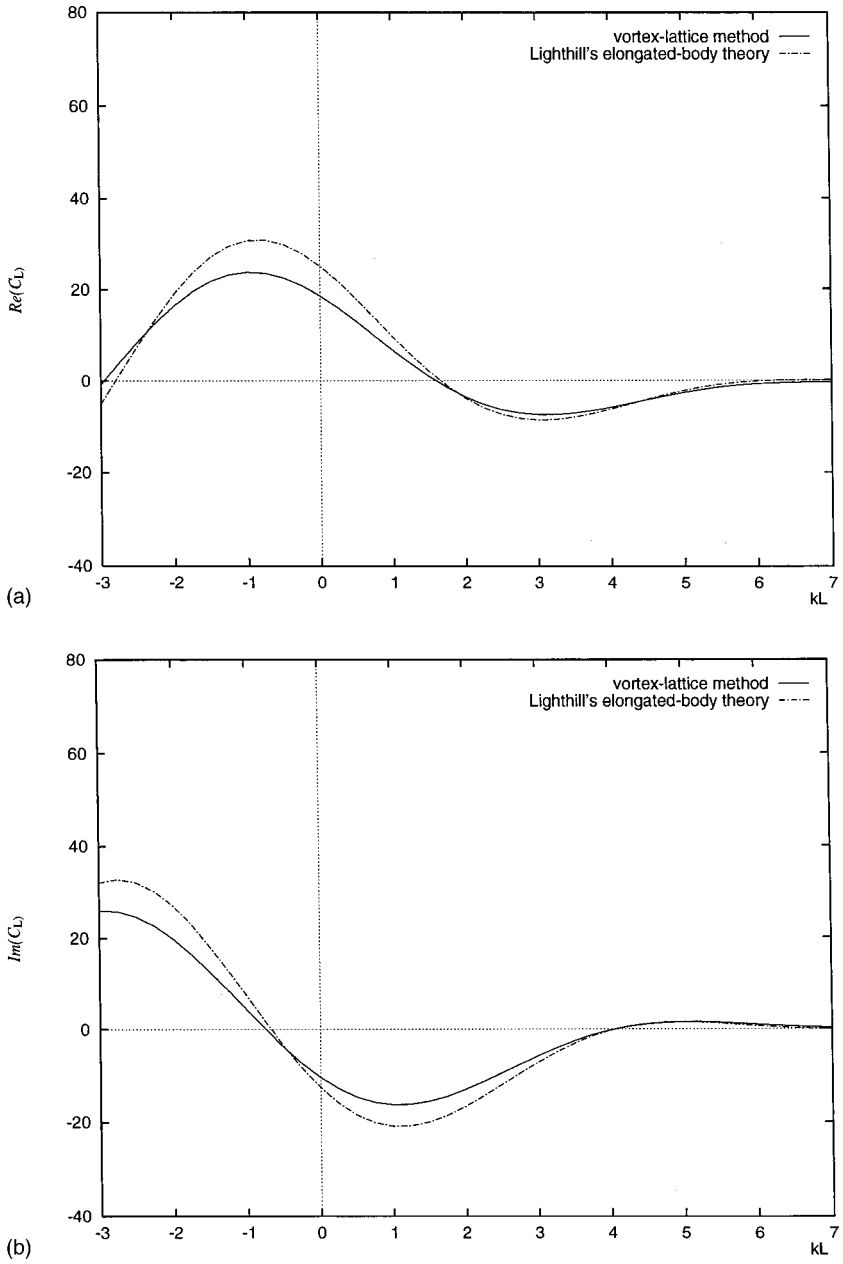

Fig. 12 (*a*) Lateral force coefficient of a waving rectangular plate (Real part). The waving motion is given by Eq. (21). ($A_R=0.5$, $\omega L/U=8.0$) (*b*) Lateral force coefficient of a waving rectangular plate (Imaginary part). The waving motion is given by Eq. (21). ($A_R=0.5$, $\omega L/U=8.0$).

body theory) of Lighthill [1]. Figures 11(*a*) and 11(*b*) compare the magnitudes of the real and imaginary parts, respectively, of the lateral force coefficient C_L for a rectangular plate of aspect ratio $A_R=0.5$ which performs a progressive wave-like backbone undulation motion of constant unit amplitude along the length of the plate L. This motion, for arbitrary wavenumber k, can be written in the form

$$H(x,y,t)=\mathrm{Re}\{e^{i(\omega t-kx)}\} \tag{20}$$

For various values of $kL=2L\pi/\lambda$, where λ is the backbone wavelength, the magnitudes of the force coefficients vary as expected, with comparison between the linear theory and the present VLM revealing similar qualitative and quantitative behavior. For a nonconstant waveform amplitude, the motion is confined to the posterior end of the plate for an origin-centered plate leading edge, and can be described

$$H(x,y,t)=\mathrm{Re}\{x\cdot e^{i(\omega t-kx)}\} \tag{21}$$

Figures 12(*a*) and 12(*b*) compare the results for the magnitudes of the real and imaginary parts of the lateral force coefficient C_L for the waving plate with the linearly-varying amplitude envelope described by Eq. (21). This traveling wave motion is similar that exhibited by the backbone undulation of anguilliform swimmers, in which the motion amplitude increases from head to tail, as observed in the swimming of live fish (Videler [38]). With the motions confined to the afterbody for the results shown in Figs. 12(*a*) and 12(*b*), the total magnitudes of the C_L real and imaginary

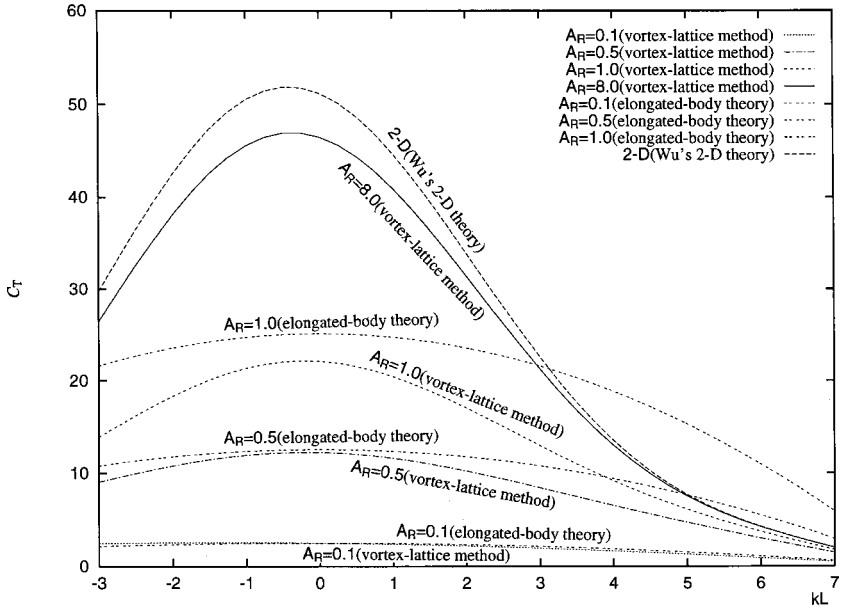

Fig. 13 Comparisons of the vortex-lattice calculations with the slender-body theory and the 2-D theory for a waving plate of various aspect ratios ($\omega L/U = 8.0$)

parts are reduced in comparison to the constant amplitude results of Figs. 11(*a*) and 11(*b*), but the VLM results still compare well with those provided by linear theory. Although some minor quantitative discrepancies exist between the results of the slender-body theory and those obtained by the present vortex-lattice method over a narrow range of wavenumbers, both are accurate in calculating lateral side forces, with differences resulting from the chordwise and spanwise potential variation consequent of the vortex-lattice geometric discretization.

This study is primarily interested in the thrust forces produced by the periodic waving motion of the swimming geometries. Thus, Fig. 13 compares the results of the present vortex-lattice method for waving plates of various aspect ratio with Lighthill's slender-body theory (Lighthill [1]) and Wu's 2-D theory (Wu [3]), when the waving motion is given by Eq. (20). As expected, when the aspect ratio (B/L) is small, the slender-body theory agrees well with the vortex-lattice calculations, whereas, when the aspect ratio is large, the vortex-lattice calculations approach the results given by the 2-D theory of Wu. Therefore, for intermediate aspect ratio plates and geometries, whereas neither slender-body theory will accurately provide performance predictions over a wide range of wavenumbers, the vortex-lattice method is not constrained in its geometric assumptions and can provide reasonable estimates of the thrust produced for both arbitrary as well as complex planform geometries.

As indicated by Lighthill [1], good efficiency is attained when the phase velocity (ω/k) of the waving motion is close to but slightly higher than the swimming velocity (U). In fact, it has been confirmed from observations that live fish swim in this way (Gray [39]), although generally the amount of data is limited. Since the present computation is conducted for $\omega L/U = 8.0$, this means that a good efficiency is attained for values of kL slightly smaller than 8.0, say $kL \sim 7.0$. In this range, however, the vortex-lattice calculations differ slightly from the slender-body theory predictions even when the aspect ratio is small. The slender-body theory overpredicts the thrust required for swimming due to its sectional loading approximation in which the sectional force varies only over the length. The chordwise and spanwise potential variation in the vortex-lattice method, which is more complex than the sectional loading approximations of the slender-body theory, allows for a more accurate pressure jump distribution approximation over the entire planform and, therefore, a more accurate prediction of the useful thrust generated.

5.3 Comparison With Experimental Data From the *RoboTuna*. To further validate the accuracy of the method in predicting the loads on bodies undergoing swimming flexible motions, we compare the results of the vortex lattice calculation with experimental measurements obtained on a laboratory robotic instrument undergoing fish-like swimming motions. The *RoboTuna* is a 1.2 m robot consisting of eight links, covered by a flexible hull with the external shape of a bluefin tuna, capable of performing fish-like swimming motions. The robot was developed in the Ocean Engineering Testing Tank Facility at MIT, and has been described extensively in published literature (Triantafyllou and Triantafyllou [34], Barrett [32], Triantafyllou et al. [35]). Six independently controlled motors provide the actuation through an elaborate assembly of pulleys and strings. Force and motion transducers provide detailed measurements of the forces and motions of each link, hence providing the power needed for oscillation. The robot is supported by an overhead carriage allowing testing at constant speed in a tank with dimension 35 m×2.4 m×1.2 m. The force acting on the overall mechanism is also continuously measured (Fig. 14). This force is the difference between the propulsive thrust and the drag acting on the body; the thrust and drag forces, however, cannot be separated, since actuation is distributed along the length of the mechanism. Detailed calibration and testing results, with extensive error and repeatability analyses, and geometric description of the *RoboTuna* are documented in Barrett et al. [26].

For numerical representation of the *RoboTuna* geometry, a curve-fitting technique is used to determine the profile shape of the body with $\ell = 1.0$, and is given simply by:

$$z(x) = \pm 0.305 \tanh(6x + 1.8) \quad \text{for} \quad -0.3 \leqslant x \leqslant 0.1 \tag{22}$$

$$z(x) = \pm (0.15 - 0.152 \tanh(7x - 3.15)) \quad \text{for} \quad 0.1 \leqslant x \leqslant 0.7 \tag{23}$$

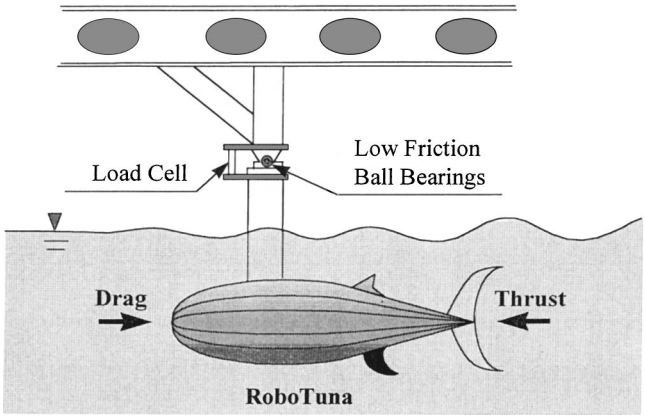

Fig. 14 The experimental setup for *RoboTuna*

The caudal fin leading edge and trailing edge profiles for the semi-span are also determined through a curve-fitting technique, and are given similarly by:

$$x(z)_{LE} = 39.543z^3 - 3.685z^2 + 0.636z \tag{24}$$

$$x(z)_{TE} = -40.74z^3 + 9.666z^2 + 0.07 \tag{25}$$

where $0 \leqslant z \leqslant 0.15$. The leading edge of the tail at midspan intersects the posterior end of the body's contraction region.

The lateral displacement $H(x,t)$ of *RoboTuna* backbone is given in the following form:

when $x \leqslant x_c$

$$H = \mathrm{Re}\left[\left\{a_1\left(\frac{x-x_0}{L}\right) + a_2\left(\frac{x-x_0}{L}\right)^2\right\} e^{i(\omega t - kx)}\right] \tag{26}$$

when $x > x_c$

Table 1 The values of the parameters of *RoboTuna* used in the experiments (St stands for the Strouhal number defined as $2fA_m/U$ where $f=\omega/(2\pi)$ and A_m denotes the amplitude of the tail motion. L_T and α are the maximum chord length of the tail and the maximum angle of attack at the tail, respectively.)

Exp. No.	a_1	a_2	ψ_0(rad)	ψ_α(rad)	$\omega(s^{-1})$	$k(m^{-1})$	$\omega/k(m/s)$	$U(m/s)$	$\omega L_T/U$	St.	$\alpha(deg.)$
Exp.1	-0.00153	0.258	0.410	1.67	4.24	3.85	1.10	0.7	0.42	0.163	3.63
Exp.2	-0.00166	0.178	0.282	1.58	11.6	4.34	2.67	0.7	1.16	0.291	26.4
Exp.3	-0.00294	0.196	0.317	1.71	10.4	6.00	1.73	0.7	1.04	0.303	25.3
Exp.4	-0.00095	0.295	0.662	1.54	9.61	4.72	2.04	0.7	0.96	0.388	12.7
Exp.5	-0.00364	0.270	0.319	1.40	5.28	3.91	1.35	0.7	0.53	0.180	11.2
Exp.6	-0.00376	0.258	0.112	1.40	4.82	4.26	1.13	0.7	0.48	0.168	21.4
Exp.7	-0.00294	0.216	0.117	1.40	5.93	6.00	0.99	0.7	0.59	0.172	21.7
Exp.8	-0.00294	0.201	0.189	1.71	5.96	3.82	1.56	0.7	0.60	0.173	17.7

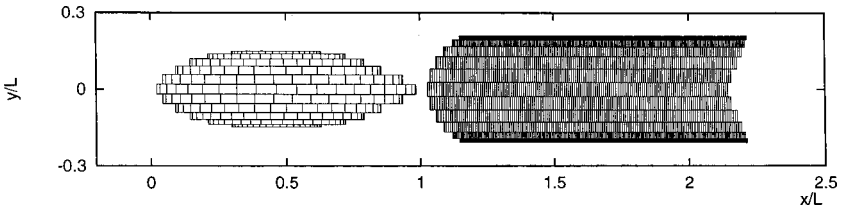

Fig. 15 Discretization of *RoboTuna*

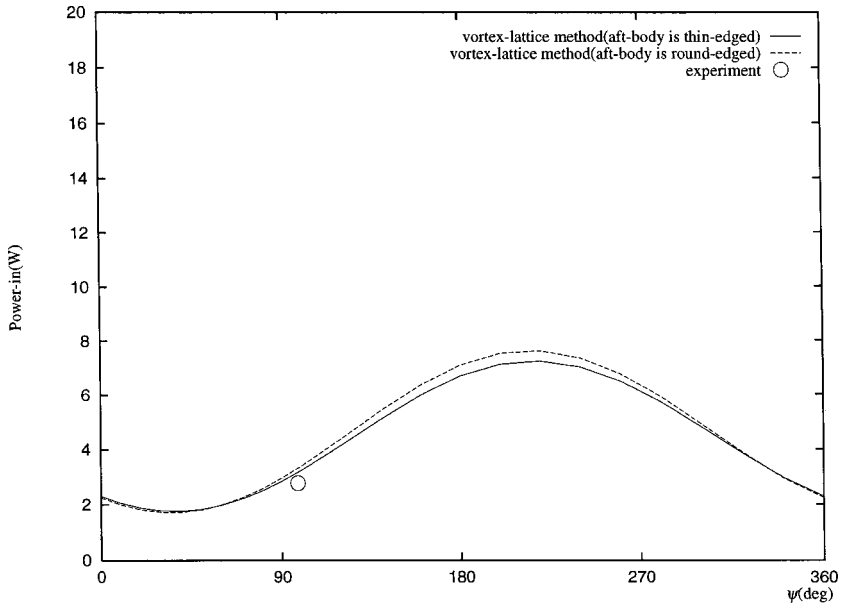

Fig. 16 Comparisons of the results obtained while assuming the trailing edge of the body anterior to a tail-base neck is round-edged and those obtained while assuming it is thin-edged

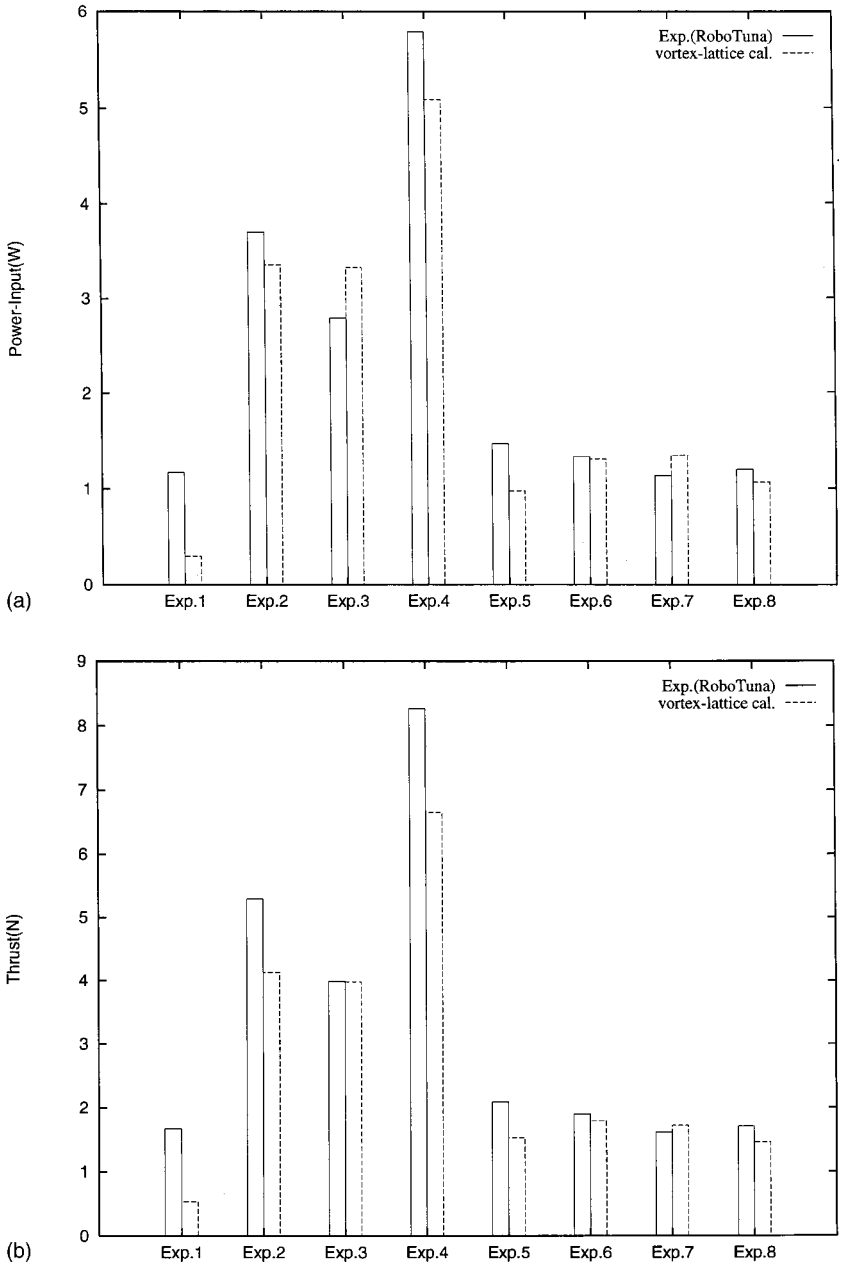

Fig. 17 (*a*) Comparisons of the vortex-lattice estimation of the power-input required for *RoboTuna* locomotion with the corresponding experimental data (*b*) Comparisons of the vortex-lattice estimation of the thrust force produced by *RoboTuna* with the corresponding value obtained from the measured data on power-input while assuming the efficiency is 100 percent

$$H=\mathrm{Re}\left[\left\{a_1\left(\frac{x_c-x_0}{L}\right)+a_2\left(\frac{x_c-x_0}{L}\right)^2\right\}e^{i(\omega t-kx_c)} -(x-x_c)\psi_0 e^{i(\omega t-kx_c+\psi)}\right] \quad (27)$$

where $x=x_c$ corresponds to the x-coordinate of the tail-base neck where the tail fin attaches to the main body, and $x=x_0$ represents the pivot point of the motion and the origin of the backbone wave where the lateral motion is zero. ψ_0 represents the pitch amplitude of the caudal fin or the maximum angle of attack of the tail, and for the linearized analysis in the frequency domain may differ from the experimental tail angle of attack by up to 6 percent. Neither the *RoboTuna* tail nor the numerical representation of the tail have spanwise flexibility, which is the case with live bluefin tuna (Barrett [33]).

Table 1 summarizes the values of parameters of *RoboTuna* varied in the experiments. In the table, the reduced frequency is defined with respect to the tail chord L_T since significant portion of the thrust force is produced by the large amplitude tail motion characteristic of thunniform swimming. All caudal fin dynamics are within ranges which will prevent stall and leading edge separation dynamics (Anderson et al. [37]). Figure 15 shows the discretization of *RoboTuna* and its wake into panels used in the present analysis. The body of *RoboTuna* may be considered as a lifting surface as well as the tail, and thus the main body is represented by a vortex-lattice. Because part of the lift and thrust is

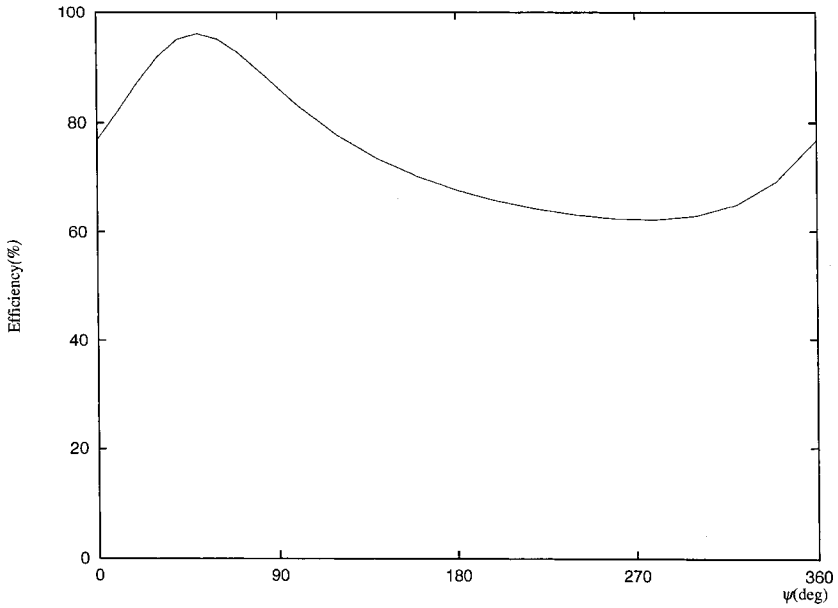

Fig. 18 Example vortex-lattice calculation on the efficiency of *RoboTuna* locomotion

known to develop from the body itself (Wolfgang et al. [40]), it is desirable to shed a wake from the anterior portion of the body before the tail. However, numerical difficulties preclude such a model in the linearized vortex-lattice approach, and a more complex panel method approach (Liu [20]) is required to model interaction dynamics between the tail and tail wakes with upstream generated wakes (Wolfgang [21]). Other concerns about the applicability of a lifting surface theory to *RoboTuna* might include leading-edge helical vortex development, such as those developed on a delta wing, which could cause flow dynamics not easily modeled through linearized vortex-lattice methods. However, such helical vortices are not developed in fish-like bodies undergoing periodic unsteady oscillations of small amplitude. The leading edge of the body anterior to the tail-base neck, as well as that of the caudal fin are round-edged and thick, and leading-edge suction forces are moderate, lending credibility to the inviscid leading-edge flow model with leading-edge suction accountability.

The trailing edge of the caudal fin is thin-edged and thus the Kutta condition is imposed at the edge. However, as for the trailing edge of the body anterior to the tail-base neck, it is not always clear whether these edges can be assumed to be thin-edged or round-edged. Fortunately, as shown in Fig. 16, there is little difference between the required power-input when the edge is assumed to be thin-edged and that obtained when it is assumed to be round-edged. As there exist no sharp-edged surfaces on the anterior portion of the actual *RoboTuna* robotic mechanism which might shed a wake (Barrett [32]) with the exception of small

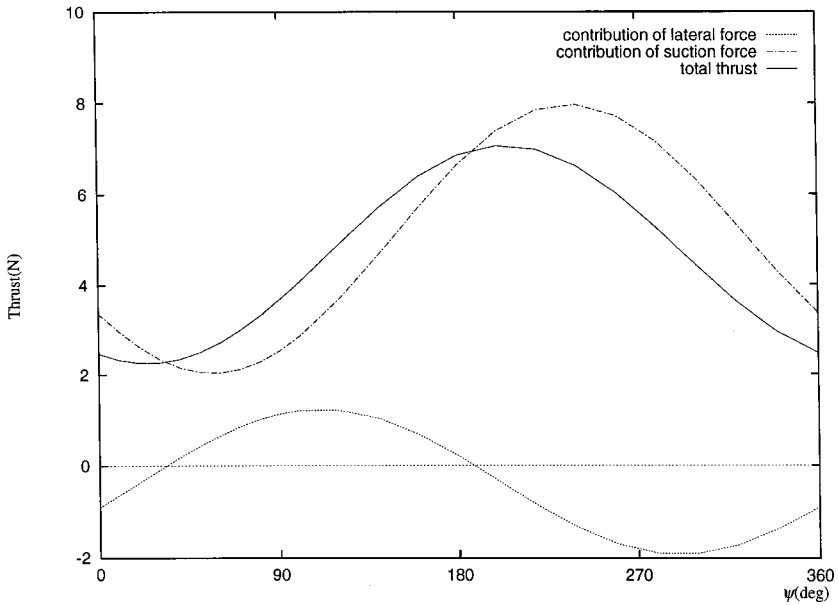

Fig. 19 Contributions of the lateral force and the leading-edge suction force to the total thrust force

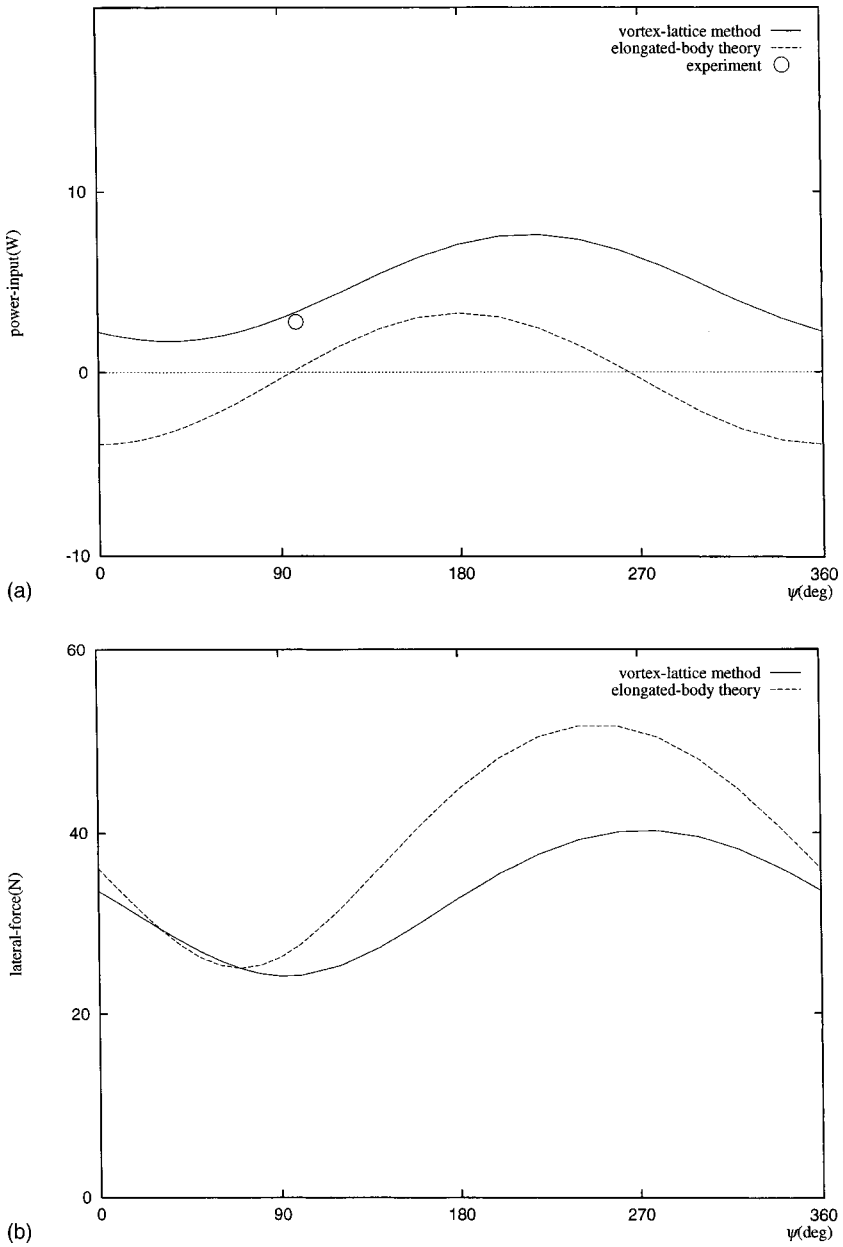

Fig. 20 (*a*) Comparisons of the required power-input for *RoboTuna* estimated by the vortex-lattice calculation and that estimated by the Lighthill's slender-body theory (*b*) Comparisons of the lateral force on *RoboTuna* obtained by the vortex-lattice calculation and that obtained by the Lighthill's slender-body theory.

dorsal and anal fins, all results shown include only a caudal fin sharp trailing edge wake shedding model. Similar wake shedding models are employed by Barrett et al. [26], using higher order numerical methods, showing similar accuracy for caudal wake shedding only.

Figure 17(*a*) compares the power-input required for the realization of the specified motion of *RoboTuna*. Cases are considered where the *RoboTuna* body was self-propelled, i.e., the net force on the supporting mast was zero, thereby balancing the net thrust produced and the net drag. Therefore, thrust produced by the actual robot cannot be measured separately from the drag (Barrett et al. [26]). Since the mechanisms of thrust generation are largely inviscid, prediction of the power required to produce thrust by the *RoboTuna* swimming motions by inviscid VLM formulation should provide reasonable results. As seen in Fig. 17(*a*), the agreement of the vortex-lattice power calculations with the measured power expenditure is quite good and the difference is within less than 20 percent in most cases, except for Experiment 1 where the actual power is underpredicted by the VLM by a significant percentage. Although actual thrust forces cannot be identified from the measured force, the values that are obtained by dividing the measured power-input by the towed velocity U (i.e., assuming 100 percent hydrodynamic efficiency) are compared with the thrust forces computed by the present vortex-lattice approach in Fig. 17(*b*). In all the cases except Exp. 7, the experimental values are larger than the vortex-lattice predictions. This is reasonable, because the experimental values correspond to the thrust forces that would be obtained when the efficiency is 100 percent, that is, when all the power-input is used for the thrust production. For the exceptional case of Exp. 7, any nonideal near-body flow features such as separation which cannot be captured by the VLM may have caused power absorption by the *RoboTuna*, resulting in

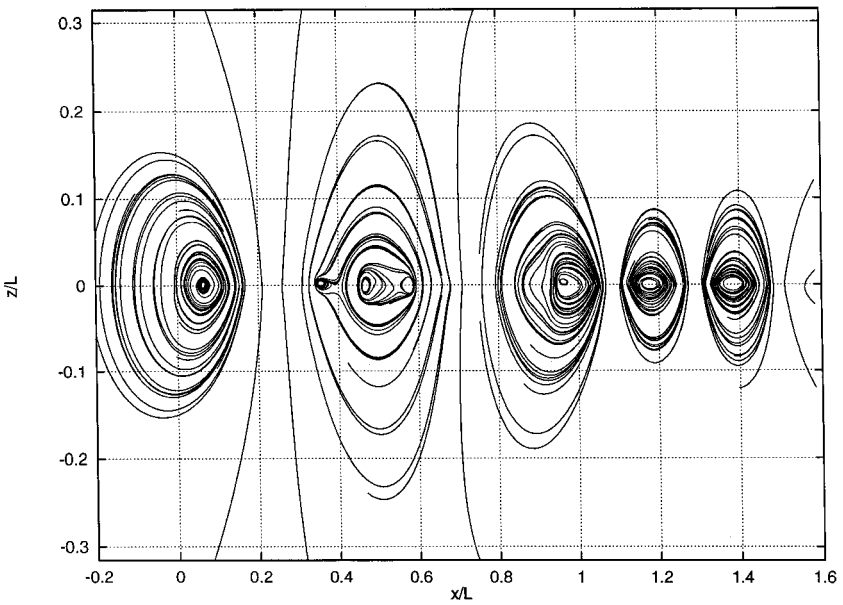

Fig. 21 Example streamlines on the mid-span lateral cross-section of *RoboTuna* when it is swimming. *L* is the length from the head to the tail-base neck (see Fig. 15)

higher computed power than measured. These nonideal flow features, as well as boundary layer development and dynamics, are subjects of continuing experimental research.

To place the computed thrust results in perspective, we compare the predicted thrust with the drag of a similar rigid body. Assuming that most of the viscous wetted surface resistance comes from the main body alone, we find the turbulent drag coefficient from data provided in Hoerner [41] of a streamlined body with length to diameter ratio equal to 5, the approximate scale of the *RoboTuna*. The flow over the *RoboTuna* is tripped turbulent, and for self-propelled experimental motions, the mean thrust produced should cancel the mean body drag. Hoerner shows that for a Reynolds number of Re=829440, the turbulent drag coefficient of the streamlined body is approximately $C_D=0.0085$. For all of the experiments considered, the computed mean thrust coefficient ranges from $C_T=0.0031$ for Exp. 1 to $C_T=0.0461$ for Exp. 4. These differences are to be expected. Barrett et al. [26] showed that the drag of an actively-swimming flexible body can be much lower than the drag on the same body towed rigid, which explains why some values of the thrust coefficient are smaller than the rigid body drag coefficient. In some cases, the thrust coefficient is higher than the drag coefficient, indicating that the efficiency may not always be extremely high. This comparison shows that the values computed by the VLM for thrust are within an acceptable quantitative range, such that the viscous drag on the swimming flexible body may be countered by the thrust produced by the motions, with relatively high efficiency. Since the drag on the actual swimming body cannot be experimentally measured separate from the thrust, we must rely on these estimations to ensure that our numerical predictions are reasonable.

Figure 18 shows an example result of the efficiency as function of ψ, the phase difference between the lateral motion at the tail-base neck and the pitch motion of the caudal fin, obtained by the vortex-lattice calculation for the values of parameters used in Exp. 3 (see Table 1). The efficiency η is defined as the ratio of the actual work used for the propulsion and the work done by the fish:

$$\eta=\frac{T\cdot U}{W} \tag{28}$$

where T and U represent the mean thrust force and swimming speed, respectively, and where W represents the mean work done

Table 2 The lift coefficient of an impulsively-started rectangular foil of aspect ratio *AR*=8 at an angle of attack α=10 deg. Convergence of the numeric scheme is shown for increasing wake length and discretization density.

Wake length	4*L*	6*L*	8*L*	10*L*	4*L*
nx	30	30	30	30	30
ny	10	10	10	10	20
C_L (VLM)	0.752807	0.764775	0.769833	0.772412	0.753166
C_L (Hoerner)	0.79077	0.79077	0.79077	0.79077	0.79077
Error C_L (%)	4.80	3.29	2.65	2.32	4.75

Table 3 The lift coefficient of impulsively-started rectangular foils of varying aspect ratio *AR* at angle of attack α. Lattice discretization parameters nx=30 and ny=10, and wake length is 4*L*.

Aspect ratio (AR)	4	4	8	8
Angle of attack (α)	5°	10°	5°	10°
C_L (VLM)	0.299368	0.601549	0.374251	0.752807
C_L (Hoerner)	0.27739	0.61303	0.37701	0.79077
Error C_L (%)	7.92	1.87	0.73	4.80

Table 4 Values of lattice discretization parameters "nx" (or "nx1" and "nx2") and "ny," and the wake length "wake" employed for the actual computations after individual convergence tests were performed

	nx	ny	wake	
Fig. 9	30	10	4*L*	
Fig. 10	30	10	4*L*	
Fig. 11	30	11	3*L*	
Fig. 12	30	11	3*L*	
	nx1	nx2	ny	wake
Fig. 17	20	10	11	*L*

Table 5 Convergence test for $\omega L/2U=0.75$, $\theta=0.8$, $A_R=7.0$ (corresponds to Fig. 9)

	nx	ny	wake	nx	ny	wake	nx	ny	wake	nx	ny	wake	nx	ny	wake	nx	ny	wake	nx	ny	wake
	10	10	L	20	10	L	20	20	L	30	10	L	30	10	2L	30	10	3L	30	10	4L	30	10	5L
Lateral																								
$\psi=0°$	0.9348948E+1			0.9353263E+1			0.9358126E+1			0.9350203E+1			0.8879462E+1			0.8834608E+1			0.8895810E+1			0.8912325E+1	
$\psi=90°$	0.1995113E+1			0.2028539E+1			0.2029323E+1			0.2045892E+1			0.1934673E+1			0.1940107E+1			0.1955513E+1			0.1955505E+1	
$\psi=180°$	0.6542030E+1			0.6496997E+1			0.6500807E+1			0.6468851E+1			0.6163429E+1			0.6111675E+1			0.6149856E+1			0.6166096E+1	
$\psi=270°$	0.1123478E+2			0.1120621E+2			0.1121234E+2			0.1118420E+2			0.1063435E+2			0.1056592E+2			0.1063635E+2			0.1065955E+2	
Thrust																								
$\psi=0°$	0.3897610E+1			0.3859963E+1			0.3859134E+1			0.3853357E+1			0.3693574E+1			0.3599489E+1			0.3627737E+1			0.3656095E+1	
$\psi=90°$	0.9215707E+0			0.9519553E+0			0.9518731E+0			0.9630717E+0			0.9318084E+0			0.9133157E+0			0.9177839E+0			0.9227695E+0	
$\psi=180°$	0.2789096E+0			0.1057204E+0			0.1056504E+0			0.0465164E+0			-0.0513189E+0			-0.0331915E+0			-0.0161926E+0			-0.0179952E+0	
$\psi=270°$	0.3254953E+1			0.3013734E+1			0.3012917E+1			0.2936808E+1			0.2710454E+1			0.2652989E+1			0.2693767E+1			0.2715337E+1	

by the fish to the ambient fluid. High efficiency is attained when ψ is around 60 deg, trend similarly observed for all the other cases. The efficiency at that value of ψ is always high, exceeding 90 percent. This optimum value of ψ is close to the value of ψ identified by Barrett [32] as optimum by a genetic search algorithm. In his analysis, the optimum value of ψ is identified to be around 90 deg regardless of other kinematic parameters.

Figure 19 shows the contributions of the lateral force and the leading-edge suction force to the total thrust force acting on *RoboTuna*. It can be observed that the leading-edge suction force is far larger than the contribution of the lateral force. Figures 20(*a*) and 20(*b*) compare the required power-input and the lateral force, respectively, obtained by the present vortex-lattice calculations with those obtained by Lighthill's elongated-body theory. Since both the geometry and the lateral motion of *RoboTuna* are not within the range of the slender-body assumption, it is natural that the thrust force predicted by the elongated-body theory deviates from the vortex-lattice calculation or the experimental data. While the trends shown in Figs. 18, 19, and 20 of the dependence of performance on the tail phase angle ψ have been demonstrated by previous works (Lighthill [2], Chopra and Kambe [8], Liu and Bose [42]) for simple wing configurations, the present results reinforce the applicability of the VLM as a tool for predicting the performance of arbitrary geometric profiles, such as coupled low and high aspect ratio lifting surfaces.

Figure 21 reveals instantaneous streamlines on the mid-span lateral cross-section of the *RoboTuna* computed by the present vortex-lattice method. Since the geometry as well as the lateral motion of the *RoboTuna* are symmetrical about the mid-span lateral cross section, the streamlines should be two-dimensional in the cross section. The body extends from $x=0$ to slightly over $x=1$, revealing a sequence of bound circulation regions along the body, in addition to a strong leading-edge circulation and strong wake circulation regions. Although there exist no experimental data that can be compared with the near-body streamlines shown in Fig. 21, these streamlines compare well qualitatively with the streamline patterns observed by Gray [39], p. 448.

6 Conclusions

A vortex-lattice method based on a linearized theory is used to calculate the hydrodynamic lateral and thrust forces on a fish-like body actively swimming at constant speed, while undulating its body harmonically in the lateral direction in the form of a traveling wave. It has been found that slender-body theory predictions agree fairly well with our numerical results for the prediction of the lateral forces, whereas they deviate from the vortex-lattice calculations of the thrust force for certain parametric ranges of practical interest. The present linearized vortex lattice calculations predict the power needed for propelling the *RoboTuna* with less than 20 percent error in most experiments conducted.

Acknowledgments

Financial support of the Office of Naval Research, under contract N00014-96-1-1141 monitored by Dr. P. Purtell, and the Sea Grant Program under grant number NA46RG0434 is gratefully acknowledged.

Nomenclature

A_R = aspect ratio (B/L)
B = breadth of a waving plate
C_L = lateral force coefficient ($=L_F/(\frac{1}{2}\rho U^2 S)$)
C_T = thrust force coefficient ($=T/(\frac{1}{2}\rho U^2 S)$)
$H(x,y,t)$ = lateral displacement of a swimming body ($=h(x,y)e^{i\omega t}$)
k = wavenumber of a waving motion
L = length of a waving plate
L_F = lateral force
ℓ_F = local lateral force
p = hydrodynamic pressure
S = one-sided surface area of a waving plate ($=L\times B$)
T = thrust force
U = swimming speed
Γ_n = strength of the vortex ring on n-th panel
θ = feathering parameter ($\alpha_a U/(h_a\omega)$) (see Eq. (19))
ρ = density of fluid
$\Phi(x,y,z,t)$ = velocity potential ($=\phi(x,y,z)e^{i\omega t}$)
ω = radial frequency of a waving motion
$\omega L/U$ = reduced frequency

Appendix

Convergence Tests for the Vortex-Lattice Calculations

Steady Motion Convergence. The vortex-lattice code was first validated by simulating the impulsively-started motion of a finite-aspect ratio rectangular foil at a small angle of attack to a speed U, in a fluid otherwise at rest. Convergence of the numerical method was confirmed by varying the lattice discretization around the foil, the aspect ratio AR and the truncation length of the wake. The steady lift coefficient is compared with the experimental values illustrated in Fig. 17-5 of Hoerner [43].

Sample convergence results are given in Tables 2 and 3. It can be seen that as the wake length is increased or the lattice density is increased, the continuous representation of the solution is approached, and the error in the steady state lift decreases, as expected. In these tables, ''L'' is the chord length of the foil, and the number of discretizations in the x and y-directions are denoted by ''nx'' and ''ny,'' respectively.

Table 6 Convergence test for $\omega L/U=8.0$, $A_R=0.5$, $H(x,t)=\mathrm{Re}\{x\cdot e^{i(\omega t-kx)}\}$ (corresponds to Figs. 12(*a*) and 12(*b*))

	nx	ny	wake	nx	ny	wake	nx	ny	wake	nx	ny	wake	nx	ny	wake
	15	11	3L	15	21	3L	30	11	3L	35	11	3L	30	11	4L
Lateral															
$k\ell=-3.0$	0.2634239E+2			0.2634283E+2			0.2601318E+2			0.2595741E+2			0.2601474E+2		
$k\ell=0.0$	0.2158105E+2			0.2158157E+2			0.2128870E+2			0.2123793E+2			0.2129003E+2		
$k\ell=3.0$	0.9494887E+1			0.9495051E+1			0.9424167E+1			0.9412274E+1			0.9424553E+1		
$k\ell=6.0$	0.1157688E+1			0.1157630E+1			0.1264383E+1			0.1280557E+1			0.1264103E+1		
Thrust															
$k\ell=-3.0$	0.7023937E+1			0.7024156E+1			0.7172928E+1			0.7193097E+1			0.7173609E+1		
$k\ell=0.0$	0.9778660E+1			0.9778318E+1			0.9649853E+1			0.9627056E+1			0.9650457E+1		
$k\ell=3.0$	0.7972807E+1			0.7972493E+1			0.7641809E+1			0.7595014E+1			0.7642262E+1		
$k\ell=6.0$	0.3623139E+1			0.3622995E+1			0.3201018E+1			0.3151433E+1			0.3201168E+1		

Table 7 Convergence test for *RoboTuna* Exp. 5 (corresponds to Fig. 17(*a*) and 17(*b*))

	nx1	nx2	ny	wake	nx1	nx2	ny	wake	nx1	nx2	ny	wake	nx1	nx2	ny	wake	nx1	nx2	ny	wake
	20	10	11	3L	20	10	15	3L	30	10	11	3L	20	10	11	4L	20	10	11	L
Lateral																				
$\psi = 0°$	0.5707314E+0				0.5699435E+0				0.5645645E+0				0.5707192E+0				0.5707917E+0			
$\psi = 90°$	0.4109352E+0				0.4099165E+0				0.4055916E+0				0.4109346E+0				0.4108995E+0			
$\psi = 180°$	0.5569637E+0				0.5551725E+0				0.5524173E+0				0.5569493E+0				0.5570033E+0			
$\psi = 270°$	0.6834282E+0				0.6819234E+0				0.6777849E+0				0.6834065E+0				0.6835323E+0			
Thrust																				
$\psi = 0°$	0.2466307E+1				0.2444197E+1				0.2471161E+1				0.2466297E+1				0.2466401E+1			
$\psi = 90°$	0.3667643E+1				0.3678068E+1				0.3675168E+1				0.3667662E+1				0.3667309E+1			
$\psi = 180°$	0.6855765E+1				0.6827210E+1				0.6863863E+1				0.6855807E+1				0.6854886E+1			
$\psi = 270°$	0.5654406E+1				0.5593315E+1				0.5659833E+1				0.5654419E+1				0.5653955E+1			

Unsteady Motion Convergence and Consistency. Systematic self-convergence and consistency tests were performed in advance of each computation presented in the paper. The parameters varied in the tests were the number of the discretizations in *x* and *y*-directions, which are denoted by ''nx'' and ''ny,'' respectively, in the following tables. For the *RoboTuna* calculations, ''nx1'' and ''nx2'' replace the use of ''nx'', where ''nx1'' represents the number of discretizations of *RoboTuna* body anterior to the tail in the *x*-direction, and similarly ''nx2'' represents the number of discretizations of *RoboTuna* tail fin in the *x*-direction. Other than these parameters, the truncated length of the wake, which is denoted as ''wake'' in the following tables, was also varied as a parameter in the convergence tests. ''Lateral'' and ''Thrust'' that appear in the following tables stand for the lateral force and the thrust force, respectively. The length of the body is denoted as L. Tables 5–7 correspond to Fig. 9, Fig. 12, and Fig. 17, respectively. The values of ''nx'' (or ''nx1'' and ''nx2''), ''ny'' and ''wake'' used for the actual computations in producing the results shown in the figures are given in Table 4.

References

[1] Lighthill, M. J., 1960, ''Note on the Swimming of Slender Fish,'' J. Fluid Mech., **9**, pp. 305–317.

[2] Lighthill, M. J., 1975, *Mathematical Biofluiddynamics*, Society for Industrial and Applied Mechanics, Philadelphia, PA.

[3] Wu, T. Y., 1961, ''Swimming of a Waving Plate,'' J. Fluid Mech., **10**, pp. 321–344.

[4] Wu, T. Y., 1971, ''Hydromechanics of Swimming Propulsion. Part 3. Swimming and Optimum Movements of Slender Fish with Side Fins,'' J. Fluid Mech., **46**, pp. 545–568.

[5] Newman, J. N., and Wu, T. Y., 1973, ''A Generalized Slender-Body Theory for Fish-Like Forms,'' J. Fluid Mech., **57**, No. 4, pp. 673–693.

[6] Newman, J. N., 1973, ''The Force on a Slender Fish-Like Body,'' J. Fluid Mech., **58**, No. 4, pp. 689–702, .

[7] Chopra, M., 1974, ''Hydromechanics of Lunate-Tail Swimming Propulsion,'' J. Fluid Mech., **64**, pp. 375–391.

[8] Chopra, M., and Kambe, T., 1977, ''Hydromechanics of Lunate-Tail Swimming Propulsion. Part 2.'' J. Fluid Mech., **79**, pp. 49–69.

[9] Chopra, M., 1976, ''Large-Amplitude Lunate-Tail Theory of Fish Locomotion,'' J. Fluid Mech., **74**, pp. 161–182.

[10] Katz, J., and Weihs, D., 1978, ''Hydrodynamic Propulsion by Large Amplitude Oscillation of an Airfoil with Chordwise Flexibility,'' J. Fluid Mech., **88**, No. 3, pp. 485–497.

[11] Katz, J., and Weihs, D., 1979, ''Large Amplitude Unsteady Motion of a Flexible Slender Propulsor,'' J. Fluid Mech., **90**, No. 4, pp. 713–723.

[12] Bose, N., and Lien, J., 1989, ''Propulsion of a Fin Whale (*Balaenoptera Physalus*): Why the Whale is a Fast Swimmer,'' Proc. R. Soc. London, Ser. B, **237**, pp. 175–200.

[13] Bose, N., and Lien, J., 1990, ''Energy Absorption from Ocean Waves: A Free Ride for Cetaceans,'' Proc. R. Soc. London, Ser. B, **240**, pp. 591–605.

[14] Katz, J., and Plotkin, A., 1991, *Low-Speed Aerodynamics: From Wing Theory to Panel Methods*, McGraw-Hill, Series in Aeronautical and Aerospace Engineering, New York, NY.

[15] Greeley, D. S., and Kerwin, J. E., 1982, ''Numerical Methods for Propeller Design and Analysis in Steady Flow,'' Trans. Soc. Naval Arch. Marine Eng., **90**, pp. 415–453.

[16] Lan, C. E., 1974, ''A Quasi-Vortex-Lattice Method in Thin Wing Theory,'' J. Aircraft, **11**, pp. 518–527.

[17] Lan, C. E., 1979, ''The Unsteady Quasi-Vortex-Lattice Method with Applications to Animal Propulsion,'' J. Fluid Mech., **93**, pp. 747–765.

[18] Cheng, J. Y., Zhuang, L. X., and Tong, B. G., 1991, ''Analysis of Swimming Three-Dimensional Waving Plates,'' J. Fluid Mech., **232**, pp. 341–355.

[19] Sverdrup, P., 1997, ''Analysis of Harmonically Flapping Wing in a Steady Stream,'' Sivilingenior thesis, Department of Marine Hydrodynamics, Norwegian University of Science and Technology and the Massachusetts Institute of Technology, Trondheim, Norway.

[20] Liu, P., 1996, ''A Time Domain Panel Method for Oscillating Propulsors with both Chordwise and Spanwise Flexibility,'' Ph.D. thesis, Faculty of Engineering and Applied Science, Memorial University of Newfoundland, St. John's, Newfoundland.

[21] Wolfgang, M. J., 1999, ''Hydrodynamics of Flexible-Body Swimming Motions,'' Ph.D. thesis, Department of Ocean Engineering, Massachusetts Institute of Technology, Cambridge, MA.

[22] Wolfgang, M. J., Yue, D. K. P., and Triantafyllou, M. S., 1999, ''Visualization of Complex Near-Body Transport Processes in Flexible-Body Propulsion,'' J. Flow Visualization, **2**, No. 2, pp. 143–151.

[23] Liu, H., Wassenberg, R., and Kawachi, K., 1997, ''The Three-Dimensional Hydrodynamics of Tadpole Swimming,'' J. Exp. Biol., **200**, pp. 2807–2819.

[24] Liu, H., Ellington, C., Kawachi, K., van den Berg, C., and Willmott, A., 1998, ''A Computational Fluid Dynamic Study of Hawkmoth Hovering,'' J. Exp. Biol., **201**, pp. 461–477.

[25] Carling, J., Williams, T., and Bowtell, G., 1998, ''Self-Propelled Anguilliform Swimming: Simultaneous Solution of the Two-Dimensional Navier-Stokes Equations and Newton's Laws of Motion,'' J. Exp. Biol., **201**, pp. 3143–3166.

[26] Barrett, D. S., Triantafyllou, M. S., Yue, D. K. P., Grosenbaugh, M. A., and Wolfgang, M. J., 1999, ''Drag Reduction in Fish-Like Locomotion,'' J. Fluid Mech., **392**, pp. 183–212.

[27] Kagemoto, H., 1997, ''Design of an Artificial Fish,'' Department of Ocean Engineering Technical Report, Massachusetts Institute of Technology, Cambridge, MA.

[28] Kagemoto, H., Yue, D. K. P., and Triantafyllou, M. S., 1997, ''Optimization of a Fish-Like Swimming Body,'' *50th Annual Meeting of the Division of Fluid Dynamics*, American Physical Society, Nov. 23–25, San Francisco, CA.

[29] Weihs, D., and Webb, P., 1983, ''Optimization of Locomotion,'' Praeger Special Series *Fish Biomechanics*, P. Webb and D. Weihs, eds., Chapter 11, pp. 339–371, Praeger, New York, NY.

[30] Triantafyllou, G. S., Triantafyllou, M. S., and Grosenbaugh, M. A., 1993, ''Optimal Thrust Development in Oscillating Foils with Application to Fish Propulsion,'' J. Fluids Struct., **7**, pp. 205–224.

[31] Goldberg, D., 1989, *Genetic Algorithms in Search, Optimization, and Machine Learning*, Addison-Wesley, Reading, MA.

[32] Barrett, D. S., 1996, ''Forces and Efficiency of a Flexible Hull Vehicle,'' Ph.D. thesis, Department of Ocean Engineering, Massachusetts Institute of Technology, Cambridge, MA.

[33] Barrett, D. S., 1994, ''The Design of a Flexible Hull Undersea Vehicle Propelled by an Oscillating Foil,'' M. S. thesis, Department of Ocean Engineering, Massachusetts Institute of Technology, Cambridge, MA.

[34] Triantafyllou, M. S., and Triantafyllou, G. S., 1995, ''An Efficient Swimming Machine,'' Sci. Am., **272**, No. 3, pp. 64–70.

[35] Triantafyllou, M. S., Barrett, D. S., Yue, D. K. P., Anderson, J. M., Grosenbaugh, M. A., Streitlien, K., and Triantafyllou, G. S., 1996, ''A New Paradigm of Propulsion and Maneuvering for Marine Vehicles,'' Trans. Soc. Naval Arch. Marine Eng., **104**, pp. 81–100.

[36] Konstadinopoulos, P., Mook, D. T., and Nayfeh, A. H., 1981, ''A Numerical Method for General, Unsteady Aerodynamics,'' AIAA paper 81–1877.

[37] Anderson, J. M., Streitlien, K., Barrett, D. S., and Triantafyllou, M. S., 1998, ''Oscillating Foils of High Propulsive Efficiency,'' J. Fluid Mech., **360**, pp. 41–72.

[38] Videler, J., 1993, *Fish Swimming*, Chapman and Hall, London, U.K.

[39] Gray, J., 1968, *Animal Locomotion*, Weidenfeld & Nicolson, London.

[40] Wolfgang, M. J., Anderson, J. M., Grosenbaugh, M. A., Yue, D. K. P., and Triantafyliou, M. S., 1999, ''Near-Body Flow Dynamics in Swimming Fish,'' J. Exp. Biol., **202**, pp. 2303–2327.

[41] Hoerner, S. F., 1965, *Fluid-Dynamic Drag*, Hoerner Fluid Dynamics, Vancouver, WA.

[42] Liu, P., and Bose, N., 1993, ''Propulsive Performance of Three Naturally-Occurring Oscillating Propeller Planforms,'' Ocean Eng., **20**, No. 1, pp. 55–75.

[43] Hoerner, S. F., 1985, *Fluid-Dynamic Lift*, Hoerner Fluid Dynamics, Vancouver, WA.

Limitations of Statistical Design of Experiments Approaches in Engineering Testing

Stelu Deaconu
Graduate Research Assistant

Hugh W. Coleman
Eminent Scholar in Propulsion and Professor,
Fellow ASME

Propulsion Research Center,
Mechanical and Aerospace
Engineering Department,
University of Alabama in Huntsville,
Huntsville, AL 35899

A hypothetical experiment and Monte Carlo simulations were used to examine the effectiveness of statistical design of experiments methods in identifying from the experimental data the correct terms in postulated regression models for a variety of experimental conditions. Two analysis of variance techniques (components of variance and pooled mean square error) combined with F-test statistics were investigated with first-order and second-order regression models. It was concluded that there are experimental conditions for which one or the other of the procedures results in model identification with high confidence, but there are also other conditions in which neither procedure is successful. The ability of the statistical approaches to identify the correct models varies so drastically, depending on experimental conditions, that it seems unlikely that arbitrarily choosing a method and applying it will lead to identification of the effects that are significant with a reasonable degree of confidence. It is concluded that before designing and conducting an experiment, one should use simulations of the proposed experiment with postulated truths in order to determine which statistical design of experiments approach, if any, will identify the correct model from the experimental data with an acceptable degree of confidence. In addition, no significant change in the effectiveness of the methods in identifying the correct model was observed when systematic uncertainties of up to 10 percent in the independent variables and in the response were introduced into the simulations. An explanation is that the systematic errors in the simulation data caused a shift of the whole response surface up or down from the true value, without a significant change in shape. [S0098-2202(00)03102-3]

Introduction

Statistical design of experiments (DE) is a process of experimental planning such that the data obtained are suitable for a statistical analysis. Statistical tests are then applied to the data to determine whether or not possible functional dependencies of the experimental result on process variables are of statistical significance or not. Typically, a regression (using the dependencies found to be significant) is then performed to obtain a mathematical relationship that represents the experimental data. Originally, this type of experimental approach was developed and applied in the field of quality control and process optimization. Many quality control and product development experiments are based on the assumption that the system/process is sensitive to certain input factors but is less sensitive to the interactions of these factors, Hicks [1]. This assumption forms the foundation of the Taguchi philosophy to experimentation, Montgomery [2].

Such an assumption is often not valid in engineering experiments. Engineering experiments (nomenclature here used to refer to experiments in fluid flow, thermal sciences, chemistry, etc as opposed to quality control) often are performed on physical processes in which the result r may depend on the independent variables x_1 and x_2 in ways such as $x_1x_2, x_1x_2^2$, etc. In an experiment in which the forms of such terms are not known a priori, statistical design of experiments approaches can be used to identify the terms (effects) in a proposed regression model that are significant and that therefore should appear in the regression. The experimental data are then used with a least squares analysis (or something similar) to determine the coefficients in the regression equation. In this article, we examine the effectiveness of the statistical DE analysis in identifying the correct terms for first and second-order regression models for a variety of postulated experimental conditions.

Assessment of a regression model can be divided into two complementary parts: (a) determining if the factors identified as significant in the model adequately represent the physical process from which the experimental data are taken, and (b) estimating the uncertainty associated with the predictions of the regression model. This article focuses on the first part of the problem: the adequacy of regression models determined from a statistical DE treatment of the experimental data. A detailed discussion of the methodology for estimating the uncertainty associated with linear regressions has recently been presented (Brown [3], Brown et al. [4]).

In this article we consider several questions: How should DE methods be applied to engineering experiments? What experiments are suitable for such an approach? In addition, how do systematic uncertainties influence the applicability and performance of DE methods? In what follows, some answers to these questions are presented.

Since an objective of this work was to quantify the influences of different experimental conditions on the effectiveness of statistical DE analysis in identifying correct regression models, an experiment to simulate a large variety of possible experimental situations was designed and run. The experiment was performed in a virtual, computer generated environment and is called the hypothetical experiment. A hypothetical experiment could be formally defined as a test run on a statistical procedure. Essentially, this type of experiment is the statistical analysis of data from Monte Carlo type simulations. The behavior of the simulated system (i.e., the correct regression model) is known a priori, thus enabling a comparison with the results of the statistical analysis.

Contributed by the Fluids Engineering Division for publication in the JOURNAL OF FLUIDS ENGINEERING. Manuscript received by the Fluids Engineering Division January 28, 1999; revised manuscript received March 2, 2000. Associate Technical Editor: M. R. Hajj.

Experimental Framework

A relationship of the form (1) is assumed to exist between the system response Φ, the continuous variables x_i, $i=1,2,\ldots,p$, the unobservable variables z_j, $j=1,2,\ldots,q$, and some unknown system parameters θ_k, $k=1,2,\ldots,m$.

$$\Phi=\Phi(x_1,\ldots,z_1,\ldots,\theta_1,\ldots)=\Phi(x,z,\theta) \tag{1}$$

The variables x_i are identified with the controllable factors in the system and the variables z_i are identified with some uncontrollable extraneous factors. The true nature of the unknown relationship Φ cannot be unambiguously determined only from the experimental data. The experimenter could search for a graduating function

$$r=r(x,\theta) \tag{2}$$

that closely approximates Φ in the domain spanned by the experimental data. The relationship, (2), is a regression model.

Assuming that there are N combinations of factor levels, $\xi_j=(x_{1j},x_{2j},\ldots,x_{pj})$, with $j=1,2,\ldots,N$ the matrix **D**, $\mathbf{D}=(\xi_1,\ldots\xi_N)^{\mathrm{T}}$, of N rows and p columns formed with the N factor levels combinations will be called the design matrix or the test matrix of the experiment. Depending on the system, the choice of the design matrix of the experiment differs. Accordingly, the designs are (a) for estimating system parameters and (b) for exploring a response surface, Box and Draper [5]. The end result of both types of design is a relationship between the independent variables (factors) x, and the dependent quantity r, the system response.

The Hypothetical Experiment. In the hypothetical experiment the system is assumed to be affected by two input factors x_1 and x_2. The true relationship of dependence between the factors and system response is known and has the form of (3).

$$r(x_1,x_2)=\sum_i \beta_i\cdot x_1^{a_i}\cdot x_2^{b_i} \tag{3}$$

For convenience the terms in (3) are called effects. It is assumed that a proper randomization of the experimental runs averages out the effect of the uncontrollable variables z_i in (1) that are disregarded in (3). In a real experiment the remaining effect of these variables becomes a model bias and if uniformly distributed across the test matrix of the experiment will be embedded in the model parameters β_i. Methods of treating and reducing the model bias are discussed in more detail in Box and Draper [6].

The hypothetical experiment is designed to identify and test some of the factors that influence the statistical analysis. The result of the test is the model coverage. For a number N of random sets of data generated using the postulated model let $N_s^{\text{favorable}}$ be the number of favorable cases (i.e., the statistical analysis identifies the right model, (3)). The model coverage is then defined by the ratio of the number of favorable cases to the total number of cases, expressed as a percentage

$$\text{percent Model Coverage}=(N_s^{\text{favorable}}/N_s)100 \tag{4}$$

For this study, a typical DE two-factor factorial experiment is considered with the analysis of variance ANOVA/F-test statistics used as the regression model estimator. This choice allows computer automation of the entire Monte Carlo procedure and data analysis. With this type of design, ANOVA distinguishes and quantifies the amount of variability corresponding to each effect in (3). The ANOVA is essentially a method of computing the sums of squares of the factors in the model, and is based on the partition of the total variability in the experimental data into its component parts. The sums of squares decomposition in the ANOVA is completed with the expected mean square E(MS) values for each factor. These values are obtained by dividing the factor sum of squares by the corresponding number of degrees of freedom. The amount of variability in the data unaccounted in the factor sums of squares is the random error. The random error is considered to incorporate the measurement errors as well as the inter-replicate variability, and is for all practical purposes normally distributed (based on the central limit theorem). The normality of the random error is essential in setting up the statistical tests for significance. The ANOVA effects sums of squares are in these conditions distributed as χ^2 (chi-square). Moreover, any ratio of χ^2 distributed sums of squares follows an F distribution. For the two-factor factorial experiments the sum of squares effects are conveniently calculated using the Yates algorithm. For a detailed presentation of the ANOVA/Yates algorithm see Graybill [7], Montgomery [2].

The following six influential experimental conditions were assumed to affect the outcome of the hypothetical experiment and were investigated in this study:

(i) *Type of statistical analysis*. The statistical analysis (ANOVA) is done by setting up the sums of squares associated with each effect in model (3). A continuous type variation is assumed for both x_1 and x_2 as the natural choice in engineering experiments (as opposed to factors taking only some discrete levels in quality control processes). This assumption suggests two ways of setting up the statistical tests for significance (a) components of variance model ANOVA-CV and (b) pooled mean squares error model ANOVA-PMSE. Pooling the error is a procedure derived from the fixed effects analysis, and is an alternative to analyzing data when no replication is available. Generally pooling the error means that sums of squares of effects found insignificant at some prior step are added to the error in the current step. This procedure could result in better chances of finding the true form of the model by increasing the error estimate and its associated degrees of freedom. As a drawback, the errors become (to some extent) biased (or model dependent). A more elaborate discussion on setting up these tests can be found in Graybill [7], Hicks [1], and Montgomery [2].

(ii) *Type of design*. Two types of factorial designs are considered—a 2^2 factorial (two factors at two levels) and a 3^2 factorial (two factors at three levels).

(iii) *F test significance level, α*. Three significance levels, α, of the F test statistics are considered—0.05, 0.025, 0.01. (A significance level of 0.05, for example, means that the probability of rejecting a null hypothesis when it is true is 0.05.)

(iv) *Number of replications*. The experiment considered up to five replicates. The case of no replication was disregarded since it does not provide an unbiased estimate of the error.

(v) *Form of the model and the relative importance of the factors*. For simulation purposes the model, Eq. (3), is written in a dimensionless form. In the process of data generation the importance of the effects is proportional to the coefficients of the effects in the dimensionless model. The relative magnitudes of the coefficients were varied by factors of 10 and 100.

(vi) *Type and magnitude of experimental error*. For numerical simplicity the true model is assumed unbiased or, in other words, of the form (3). The systematic error is the only bias source in the data. A large spectrum of experimental conditions were simulated by assuming both random and systematic errors as (a) percentage of full scale (FSC) and (b) percentage of reading (PRDG) over a range of magnitudes.

For each combination of factor levels in **D**, the computer generates a large number of sets of data. Each set is considered to represent a possible real situation and contains the simulated values of factor levels and the corresponding response of the system. Ideally, an infinite number of data sets would simulate all possible experimental conditions. In the present analysis, ten thousand data sets per combination of factor levels and replication were generated and analyzed. The true values of all variables are known and correspond to some consistently replicated levels of the factors in

the system. This situation is imposed by the necessity of equally spaced factor levels in a factorial design. The simulated data are given by

$$x_1^{\text{sym}} = x_1^{\text{true}} + b_{x1} + e_{x1}$$
$$x_2^{\text{sym}} = x_2^{\text{true}} + b_{x2} + e_{x2}$$
$$r^{\text{sym}} = r(x_1^{\text{sym}}, x_2^{\text{sym}}) + b_r + e_r \quad (5)$$

where b_x is the systematic error in x, x^{sym} is the x simulated value, e_x is the random error in x and x^{true} is the x true value. The b's and e's are drawn from Gaussian parent populations whose 2Φ values correspond to the postulated systematic uncertainties (bias limits) and random uncertainties (precision limits), respectively (Coleman and Steele [8]). The model is fitted to the fixed, equally spaced values of the factors but is predicted from the simulated (error corrupted) data (5). Accordingly (3) is rewritten

$$r(x_1, x_2) = \sum_i \alpha_i \cdot x_1^{a_i} \cdot x_2^{b_i} + \varepsilon(\sigma^2) \quad (6)$$

The new parameters α in (6) are unbiased estimators of the β parameters (3), i.e., $\alpha = E(\beta)$ if and only if $\varepsilon(\sigma^2)$ is a unbiased estimator of the error in the data left after fitting the model $r(x_1, x_2)$, Montgomery and Peck [9].

The hypothetical experiment was designed to explore the influence of the six influential experimental conditions on the statistical analysis model estimation efficiency. The analysis reported here considers (a) first-order models with and without (first order) interaction and (b) simple second-order (quadratic) models. Even for these cases, a method of reducing the number of simulations is required, and therefore it is assumed that the percentage model coverage does not depend on the interactions of any of the six influential experimental conditions. This approach reduces to a classical parametric analysis.

The Simulation

Models. Two types of regression models were investigated in this study. A general form of first-order model and two specific forms of second-order models were used. The first-order model could be further split into (a) a first-order model without the interaction term and (b) a first-order model with interaction. A full first-order model in a dimensionless representation is

$$r^*(w_1, w_2) = 1 + \gamma_1 w_1 + \gamma_2 w_2 + \gamma_3 w_1 w_2 + \varepsilon(\sigma^2) \quad (7)$$

where for a model without interaction $\gamma_3 = 0$. Equation (7) is a general representation of any possible first order model. To see this the input factors in any ''x'' space are transformed to the ''w'' space

$$w_{ij} = (x_{ij} - x_{i\,\text{mean}})/a_i; \quad a_i = (x_{i2} - x_{i1})/2 \ (2^2 \ \text{design}),$$
$$a_i = x_{i2} - x_{i1} \ (3^2 \ \text{design}) \quad (8)$$

with i the index of the input variable x, and j the level of this variable. This centers the design matrix $D(x_1, x_2)$ of the experiment about the origin of the new $(w_1 O w_2)$ space. These transformations have not modified the response of the system. Finally, to obtain the dimensionless expression (7), both sides of the expression are divided by the free (zeroth order) term. With (8) the model (7) may result from either the full first-order model, or from some partial model containing the interaction $(x_1 x_2)$ effect. The inferences drawn are therefore valid for all possible first-order models.

A second-order (or quadratic) model refers to a polynomial model containing one or more terms with second power exponents. There is a large number of possible models containing second order terms, and a complete analysis is not practical. Only two cases involving quadratic terms in the model are considered in this study. One case is the dimensionless simple quadratic model

$$r^*(w_1, w_2) = 1 + \gamma_1 w_1 + \gamma_2 w_2 + \gamma_3 w_1 w_2 + \gamma_3 w_1^2 + \varepsilon(\sigma^2) \quad (9)$$

Transformation of space for second order terms results in an aliasing problem. This is the confounding of the quadratic effects in the model. The aliasing of the effects does not permit later separation of these effects by algebraic manipulations of the model. Accordingly, some simulations were run with the unmodified response (original factor space) of the system

$$r(x_1 x_2) = \alpha_0 + \alpha_1 x_1 x_2 + \alpha_2 x_1^2 x_2 + \varepsilon(\sigma^2) \quad (10)$$

In the dimensionless models (7) and (9) the coefficients γ do not carry units and therefore could be seen as weighting factors for their corresponding effects in the model. Their relative magnitude will therefore determine the relative importance of the effects in the model. It is possible to infer the relative importance of the effects in the model from their ratio of sums of squares in the ANOVA table, Deaconu [10]. In the case of ANOVA run using Yates algorithm (orthogonal contrasts), each effects mean square has one degree of freedom ($\nu_{\gamma i} = \nu_{\gamma j} = 1$) and therefore the ratio of any two γ coefficients in (9) is evaluated by the approximate formula

$$\frac{\gamma_i}{\gamma_j} \cong \sqrt{\frac{MS_{\gamma_i}}{MS_{\gamma_j}}} = \sqrt{\frac{SS_{\gamma_i}/\nu_{\gamma_i}}{SS_{\gamma_j}/\nu_{\gamma_j}}} = \sqrt{\frac{SS_{\gamma_i}}{SS_{\gamma_j}}} \quad (11)$$

where SS_{γ_i} is the sum of squares associated with the effect having γ_i as coefficient. Three levels of magnitude are chosen for these coefficients and they are denoted by L-(relative weight 0.01), M-(relative weight 0.1), and H-(relative weight 1.0). This notation corresponds to low, medium, and high importance levels of the factors in the model.

Results

Details of all facets of this study are presented by Deaconu [10], and only a portion of the results are presented here. The study found that for 2^2 designs $\alpha = 0.05$ was preferable, while for 3^2 designs $\alpha = 0.01$ resulted in a higher percent coverage. It was also found that for the cases considered little was gained by increasing the number of replications above three. The conclusions relative to first-order models were the same for both 2^2 and 3^2 designs.

First-Order Models. Results for first-order models are illustrated in Fig. 1. The particular case shown is for a model with no interaction, but it is typical of all first order cases. The figure shows percent model coverage versus the level of random uncertainty in the result for both the ANOVA CV and ANOVA PMSE approaches. Figure 1(*a*) is for effects levels (w_1, w_2) at (L, M), while Fig. 1(*b*) is for effects levels at (M, M). Not surprisingly, the methods perform better when the effects are of the same magnitude (M, M) and are progressively worse at (L, M) and at (L, H), which is not shown.

The model prediction performance of ANOVA PMSE was found to be better than ANOVA CV performance for all first order cases. Although in a system with continuous variation of factor levels the tests for significance should supposedly be set using the interaction mean square as in the CV approach (Graybill [7]), the tests run with the error mean squares (the PMSE approach) are more effective in identifying the correct model.

Simulations were run with random uncertainties up to 4 percent FSC in the factors (w_1, w_2) in addition to the random uncertainty in the response. No significant changes in model coverage were observed. Additional simulations were also run with both FSC and PRDG type systematic uncertainties of up to 10 percent in the independent variables and in the response, but no significant change in the model prediction was observed. A similar behavior was observed for the second-order models presented in the next section. An explanation is that, in most cases, the systematic errors in the simulation data cause a shift of the whole response surface up or down from the true value, without a significant change in shape. A very large percent of reading systematic un-

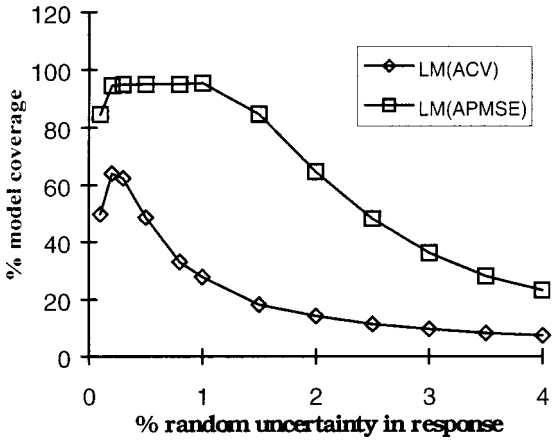

(a) Effects level: x1 - **L**, x2 - **M**

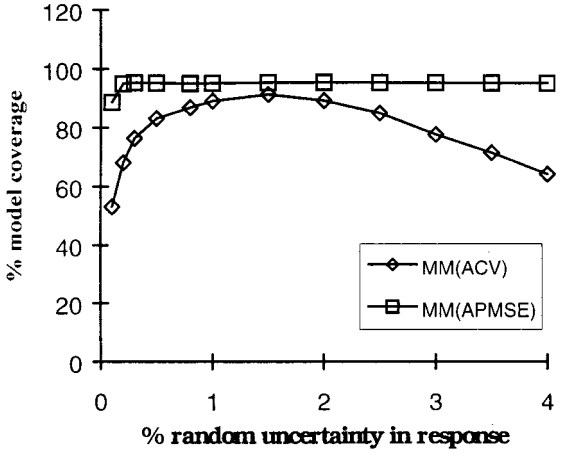

(b) Effects level: x1 - **M**, x2 - **M**

Fig. 1 Coverage using linear model ($\alpha=0.05$, $N_{rep}=3$)

certainty could warp the response surface, but this effect was not observed in the models studied. It should be noted that this insensitivity to the effect of systematic uncertainties in the simulations relates to the ability of ANOVA to identify the statistically significant effects in the proposed regression model. The degree of systematic uncertainties present in the measurements of the response r and the factors x_i certainly affect the uncertainty associated with use of the regression $r=r(x_1,x_2)$, as shown in Brown [3] and Brown et al. [4]. No correlated systematic uncertainty cases were investigated in this study.

For a random uncertainty in the response below about 0.1 to 0.5 percent, a decrease in model coverage was observed in all cases, both for first and second-order models. These results show that even if the error is small, the statistical analysis does not necessarily predict the model better. The construction of the test statistics could explain this type of behavior. As mentioned previously the sum of squares for a random sample follows an approximate χ^2 distribution. This causes the ratio of two sums of squares to be distributed as approximate F. The magnitude of the calculated mean square error plays the lead role in determining the efficiency of the tests. The starting point for this error is the inter-replication variability. When the random error is small, the variability introduced in the data by replication is likely to be small. The constructed F tests have the error in the denominator and therefore the test ratio is likely to be large. This will result in the rejection of the null hypothesis (the assumption of insignificant variability in a factor or set of conditions) when it is true. In other words, the statistical test finds insignificant effects in the model as significant. The resulting model is *overfitted*. On the other hand, as the random error increases, the error estimate becomes large. The constructed test ratios are small. The result is that the null hypothesis is accepted when it is false. In this situation the predicted model does not contain all significant effects and is *underfitted*. Generically these types of model estimation are summarized in Fig. 2.

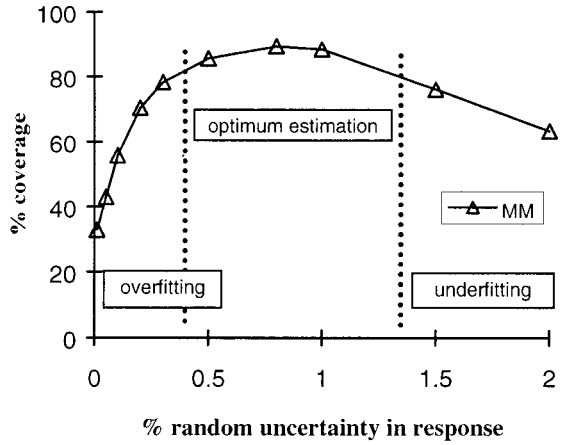

Fig. 2 Generic model estimation as function of random uncertainty

Second-Order Models. Simulations were run with a 3^2 factorial design to investigate the effectiveness of ANOVA CV and ANOVA PMSE in correctly detecting models with quadratic effects. The two models given by Eqs. (9) and (10) were investigated. For the model represented by (9) the relative importance of the factors is denoted by a combination of four letters, e.g., LLLH (w_1-low level, w_2-low level, w_1w_2-low level, and w_1^2-high level). Results for these simulations are presented in Fig. 3. The method used for the simulations in the figure was ANOVA PMSE. The components of variance method were also tested but yielded poorer results in this case.

Closer analysis of the results revealed that the drop in model coverage for the LLLH combination of effects was caused mainly by method inability of finding the linear interaction, w_1w_2, in the model. The quadratic effect in w_1 for this case was found significant in all simulated data sets. In the case of the HHHL effects combination, the method failed to recognize the quadratic effect in

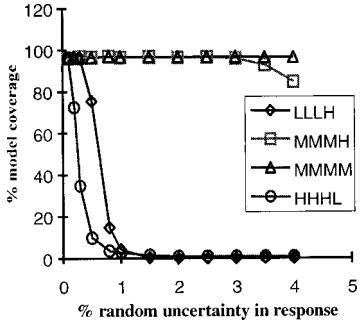

Fig. 3 Coverage using quadratic model (ANOVA PMSE, $N_{rep}=3$, $\alpha=0.01$)

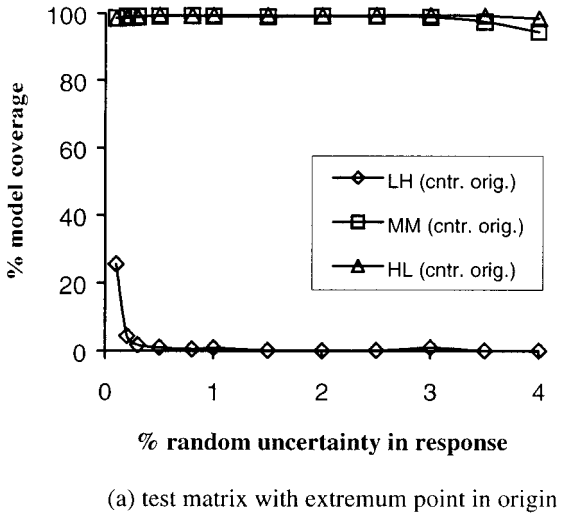

(a) test matrix with extremum point in origin

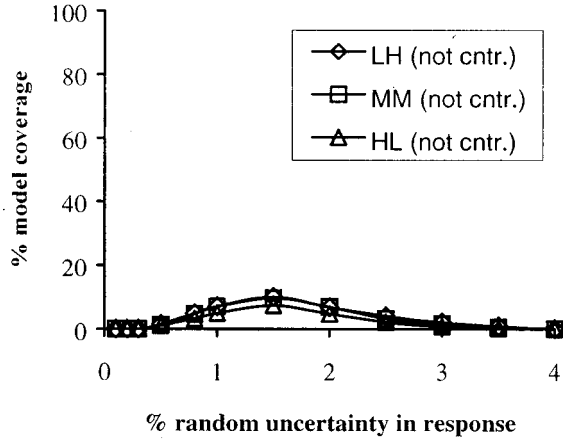

(b) arbitrary test matrix

Fig. 4 Coverage using quadratic model (ANOVA CV, $\alpha=0.05$, $N_{rep}=3$). (*a*) Test matrix with extremum point in origin, (*b*) arbitrary test matrix.

w_1 for a random uncertainty greater than 1.5 to 2 percent (FSC). The model predicted in these conditions was essentially a linear model with interaction.

The simulations run for Eq. (9) are certainly not sufficient to describe method effectiveness for all quadratic models. The response models resulting from engineering experiments are usually mathematical descriptions of physical phenomena. In these cases, it is not uncommon that the optimum approximation of the response contains only some higher-order interactions: w_1w_2, $w_1^2w_2$, $w_1w_2^2$, etc. Based on this, the second quadratic model investigated was that given by Eq. (10)

$$r(x_1,x_2)=\alpha_0+\alpha_1x_1x_2+\alpha_2x_1^2x_2+\varepsilon(\sigma^2) \tag{10}$$

With this model, the simulations were run for random uncertainty in the response of 0.1 percent to 4 percent (FSC and PRDG). The values of the two coefficients α_1 and α_2 were set at different combinations of the three levels: L, M, H. Both ANOVA CV and ANOVA PMSE were used to perform the analysis. ANOVA PMSE showed a complete failure in predicting the correct form of the model. Figure 4 shows the coverage of the model given by ANOVA CV. In this figure, LH denotes a model with x_1x_2 at a low level and $x_1^2x_2$ at a high level. The HL model is the opposite.

Table 1 Experimental conditions for high model coverage

	2^2 design	3^2 design
ANOVA Method	Pooled MSE	Step 1 Run ANOVA CV If Quadratic Interactions Found Then Consider This Model Else Step 2 Run ANOVA PMSE
F Test Significance Level	$\alpha = 0.05$	$\alpha = 0.01$
Number of Replications	2, 3	2, 3
Form of Model and Relative Importance of the Effects	first order balanced effects are best	any (up to quadratic) balanced effects are best
Type and Magnitude of Experimental Uncertainty	FSC, PRDG 1,..., 5% random / systematic	FSC, PRDG 1,..., 5% random / systematic

The standardization of the model in Eq. (9) centered the test matrix of the design about the origin ($w_1=0$, $w_2=0$) of the independent variables space. This point is an extremum point for the quadratic effect in (9). In case of an analysis run on original experimental data, the test matrix of the design is not necessarily centered about such a point. The combined effect of the test matrix departure from the origin and the magnitude of the experimental uncertainty for the model given by Eq. (10) is presented in Fig. 4. The high model coverage shown in Fig. 4(*a*) is explained by the fact that the quadratic effects in the model have a maximum or minimum at the origin, and so the central point in the 3^2 test matrix was located at this extremum. For the same span of the experimental test matrix but with a matrix point not located at the extremum, the model coverage is drastically reduced as shown in Fig. 4(*b*).

The results of these simulations show that if curvature is present in the data (quadratic terms are present in the true regression model), the location of the test matrix plays an important role in the capability of the statistical analysis to determine the significant terms in the model. Two unfavorable situations arise: (a) there is slight curvature in the system but no local extreme point in the space spanned by the test matrix, **D**, and (b) **D** contains an extreme point which is located in between the test points. In the case (a) the quadratic effects are often small compared to first order effects. The statistical tests lose the curvature in the error and retain only a first order model. Box and Draper [6] made an important point related to the case (b)—if the test points of the design miss a possible local maximum or minimum of the system response, then the analysis is unable to find the right form of the model. This situation is described in more detail in the reference mentioned and is closely related to a desirable feature for experimental designs: rotatability.

Conditions for Highest Model Coverage. The results of the simulations performed in this study indicate that the conditions most favorable for obtaining the correct regression model using statistical design of experiments with the ANOVA-F test are those summarized in Table 1.

Summary and Conclusions

In this study, a hypothetical experiment and Monte Carlo simulations were used to examine the effectiveness of statistical design of experiments methods in identifying from the experimental data the correct terms in postulated regression models for a variety of experimental conditions. Two analysis of variance (ANOVA) techniques—components of variance (CV) and pooled mean square error (PMSE)—combined with F-test statistics were inves-

tigated with first-order and second-order regression models. It was concluded that there are experimental conditions for which one or the other of the procedures results in high model coverage (summarized in Table 1), but there are also other conditions in which neither procedure is successful. The ability of the statistical approaches to identify the correct models varies so drastically, depending on experimental conditions, that it seems unlikely that arbitrarily choosing a method and applying it will lead to identification of the effects that are significant with a reasonable degree of confidence. It is concluded that before designing and conducting an experiment, one should use simulations of proposed experiments with postulated truths in order to determine which statistical design of experiments approach, if any, will identify the correct model from the experimental data with an acceptable degree of confidence.

The authors have experienced first hand a proposed test that simulations showed would fail to meet its objective. It had been argued by some that ramjet combustor efficiency scales with mass flow rate divided by diameter (m/D) and by others that it scales with m/D^2. A test program was considered, but a simulation as described in the article showed—with postulated nominal data that contained the anticipated uncertainties—that neither dependence could be discerned at an acceptable confidence level with the statistical techniques.

The model estimation performance of the procedure was found to be very sensitive to the relative importance of the effects in the model, with balanced magnitudes of effects yielding the best model estimates. Data generated by first-order models resulted in a better capability of the statistical analysis. If any second-order (quadratic) interactions are present in the model, the statistical analysis often fails to identify the right model by either overfitting (ANOVA PMSE) or underfitting (ANOVA CV).

No significant change in the effectiveness of the methods in identifying the correct model was observed when systematic uncertainties of up to 10 percent in the independent variables and in the response were introduced into the simulations. An explanation is that the systematic errors in the simulation data caused a shift of the whole response surface up or down from the true value, without a significant change in shape. A very large percent of reading type systematic uncertainty in a first-order model could cause a significant warp in the response surface, as could any type of systematic uncertainty in a second-order model with strong curvature, but no effects on the ability of the statistical methods to identify correct models were observed in this study.

References

[1] Hicks, C. R., 1964, *Fundamental Concepts in the Design of Experiments*, Holt, Rinehart, and Winston, New York.

[2] Montgomery, D. C., 1997, *Design and Analysis of Experiments*, Fourth Edition, Wiley, New York.

[3] Brown, K. K., 1996, ''Assessment of the Experimental Uncertainty Associated with Regressions,'' Ph.D. dissertation, Department of Mechanical and Aerospace Engineering, University of Alabama in Huntsville.

[4] Brown, K. K., Coleman, H. W., and Steele, W. G., 1998, ''A Methodology for Determining the Experimental Uncertainty Associated with Regressions,'' ASME J. Fluids Eng., **120**, No. 3, pp. 445–456.

[5] Box, G. E. P., and Draper, N. R., 1959, ''A Basis for the Selection of a Response Surface Design,'' J. Am. Stat. Assoc., **54**, No. 287, pp. 622–654.

[6] Box, G. E. P., and Draper, N. R., 1963, ''The Choice of a Second Order Rotatable Design,'' Biometrika, **50**, Parts 3 and 4, pp. 335–352.

[7] Graybill, F. A., 1961, *An Introduction to Linear Statistical Models*, McGraw-Hill, New York.

[8] Coleman, H. W., and Steele, W. G., 1999, *Experimentation and Uncertainty Analysis For Engineers*, Second Edition, Wiley, New York.

[9] Montgomery, D. C., and Peck, E. A., 1992, *Introduction to Linear Regression Analysis*, Second Edition, Wiley, New York.

[10] Deaconu, S, 1997, ''Statistical Design of Experiments and the Validation of Regression Models,'' Masters thesis, Department of Mechanical and Aerospace Engineering, University of Alabama in Huntsville.

Friction Factor in U-Type Undulated Pipe Flow

C. O. Popiel
Professor,
Assoc. Mem. ASME
email: popiel@sol.put.poznan.pl

J. Wojtkowiak

Heat and Fluid Flow Research Group,
Poznan University of Technology,
60-965 Poznan, Poland

Measurements of pressure losses in a U-type undulated hydraulically smooth wall pipe, having constant radius curvature, are presented. The effect of the dimensionless curvature radius 2R/d on the Darcy friction factor was investigated in the range of the Reynolds number from about 50 to 10,000 and for the dimensionless pipe curvature radiuses 2R/d=6.62, 7.95, 11.13, 16.03, 22.58, and 27.85. A smooth transition from laminar to turbulent region in the friction factor versus Reynolds number plot, typical for curved pipe flows, was observed. The experimental data were correlated with the relatively simple equation using new Dean number $De_n = Re*(De_n = Re*(d/2R)$: $\ln(f_w*Re/64) = a + b(\ln(De_n))^2$, *which is not valid for larger values of* De_n *and 2R/d, e.g., for* $De_n > 200$ *at 2R/d=22.58, and for* $De_n > 70$ *at 2R/d=27.85. The new Dean number, below which the influence of the pipe curvature in comparison to the straight tube was not seen, is* $De_n \leqslant \sim 3$. [S0098-2202(00)02802-9]

Introduction

The waved pipes are used in a great number of heat transfer equipment because of the more vigorous mixing of fluid provided by the alternating bends. At present, the waved pipes are used, for example, in shell-and-tube heat exchangers for domestic and industrial water heating systems, in floor heating systems, and in plate solar collectors.

We have two kinds of a wavy pipe geometry:

(a) *Sine-wavy pipe*.

(b) *Constant radius curvature wavy pipe* (*Fig. 1)*. This kind of wavy pipe is easier to shape from metal or plastic pipe. We can distinguish two types of this wavy pipe: U-type and S-type wavy pipe. These types of wavy pipe can have the spacer length $l/d = 0$ (undulated pipes) or $l/d > 0$.

Flows in helical coils and in single bends of the pipe of circular cross-section are well recognized (for example: Ward-Smith [1]; Burger and Talbot [2]; Ito [3]). These flows are characterized by a secondary flow imposed on the main flow which has the form of a counter-rotating helical vortex pair (originally described by Dean [4]). At the Dean number De=100 a centrifugal instability near the concave outer wall of the pipe gives the origin of a developing additional pair of vortices called ''Dean vortices'' (Cheng and Yuen [5]). Strong influence of the single bend curvature on the pressure difference between outer and inner pipe walls is observed about two diameters upstream and about three diameters downstream from the bend (Ito [6]). It is expected that the velocity profile distorted by the bend will be observed for much longer downstream distance. Flow in a wavy pipe approaching a consecutive bend is much more complex. Pressure losses of the flow in a wavy pipe are a result of the very complex velocity gradient distribution and friction at the pipe wall and of the dissipation of energy of the vortex pairs produced by each consecutive bend. Very few papers concerning pressure drop in a wavy pipe flow were reported in the available literature. The data published by Shimizu et al. [7] concern the coiled and U-type wavy pipes having relatively small curvatures ($2R/d = 1$, 3, and 6) and they did not fully describe the effect of Reynolds number. Popiel and Van der Merwe [8] investigated the pressure losses for sine-pipe flow.

In our paper, the results of measurements of pressure losses in a U-type undulated pipe flow are presented for a wide range of the bend curvature radius ($2R/d$) and of the Reynolds number.

Contributed by the Fluids Engineering Division for publication in the JOURNAL OF FLUIDS ENGINEERING. Manuscript received by the Fluids Engineering Division June 2, 1999; revised manuscript received February 7, 2000. Associate Technical Editor: M. R. Hajj.

Experimental Setup

Pressure losses in a constant radius-wavy pipe flow were measured using the set-up shown schematically in Fig. 2. A steady flow of water was supplied to the test section from an upstream head tank. The flow rate of water was controlled by a valve located upstream of the entrance section. The entrance section was in the form of the 70 *d* long straight pipe. For the entrance and test sections the 1.6 mm thick transparent plastic pipe having 7.55 mm internal diameter was used. The length of the test section pipe was 1·325.6 *d*. The diameter of the outlet pipe was 20 mm. At low water flow rates the outlet of water was at the same level as the horizontal test pipe. At the higher flow rates (giving pressure losses above $\Delta P = 350$ mm H_2O) the outlet pipe of water was gradually lowered to keep zero pressure head roughly at the middle of the test pipe to avoid the effect of swelling of the plastic pipe.

The constant radius undulated pipe bends were obtained with the 15 mm wide rings cut off from the hard plastic pipes and

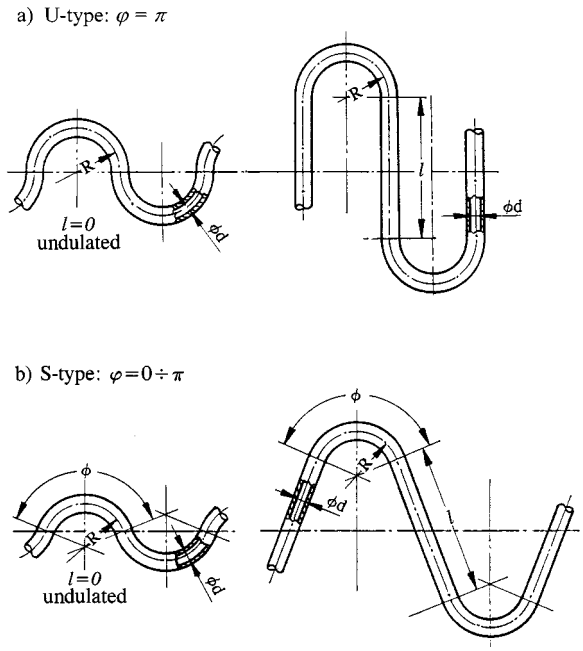

Fig. 1 Wavy pipes of constant radius curvature

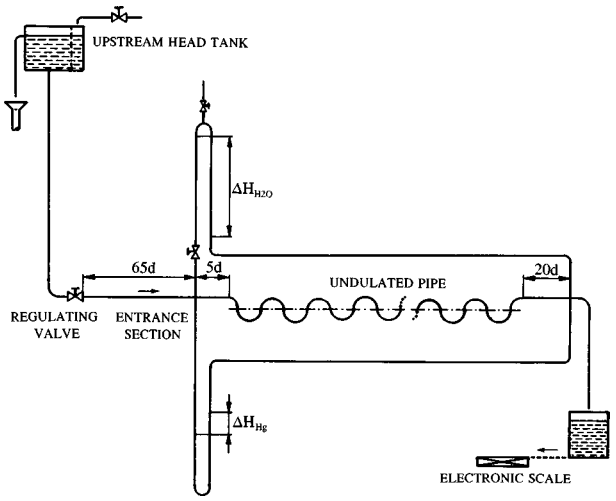

Fig. 2 Experimental rig for pressure-loss measurements

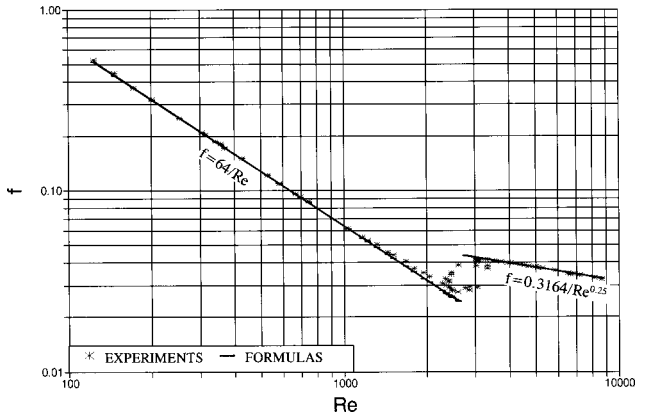

Fig. 3 Friction factor for a straight pipe flow

attached to the thick flat plywood plate. At small curvature radiuses of the undulated pipe some small deformation of the circular cross-section of the pipe was difficult to avoid. One series of experiments for the curvature radius to the pipe radius $2R/d = 6.62$ was performed with the 1 mm thick copper pipe of 3.91 mm in diameter and 333.9 d in length.

Constant pressure and temperature of water at the inlet of the test section assured a constant flow rate during each run when a flow rate, pressure loss, and temperature were recorded. Water mass flow rate was measured with a weight technique using a precise electronic scale of 12 kg in range and 0.1 g in resolution. Pressure losses were measured with 2.4 m high water and 1 m high mercury U-tube manometers. At low pressure losses it was important to keep the temperature of water in U-tube manometer, in both pressure impulse plastic pipes and in the test section, on the same level. To reduce the entry and exit effects the upstream pressure tap was located at the distance above 5 d before the first bend and the downstream pressure tap at about 20 d behind the last bend. At low water flow rates it was important to keep the temperature of water on the same level or slightly higher from the temperature of air in the laboratory, otherwise a significant deposition of the small air bubbles on the pipe surface producing undesirable roughness was observed.

Before the main measurements were started a calibration test was executed with the same straight test section pipe. A very good agreement of the measured pressure losses with the theoretical solution based on the Hagen-Poiseuille law ($f = 64/\mathrm{Re}$) in a laminar region and with the formula of Blassius ($f = 0.3164/\mathrm{Re}^{0.25}$) in turbulent region valid for a hydraulically smooth pipe has been obtained (Fig. 3). A laminar-turbulent transition was observed at the Reynolds number of about Re=2350.

Density and viscosity of water were determined with the following approximating formulas (Popiel and Wojtkowiak [9])

— for density:

$$\rho_s = a + bT + cT^2 + dT^{2.5} + eT^3 \quad [\mathrm{kg/m^3}]$$

where: $a = 999.79684$, $b = 0.068317355$, $c = -0.010740248$, $d = 0.00082140905$, $e = -2.3030988 * 10^{-5}$ — constants, and T — temperature °C,

— for dynamic viscosity:

$$\mu_s = 1/(a + bT + cT^2 + dT^3) \quad [\mathrm{kg/ms}]$$

where: $a = 557.82468$, $b = 19.408782$, $c = 0.1360459$, $d = -3.1160832 * 10^{-4}$, and T — temperature, °C.

The above formulas give density and dynamic viscosity for water along the saturation line in the temperature range from 0°C to 150°C. The density and the dynamic viscosity of water at 1 bar are practically the same as on the saturation line.

The maximum overall uncertainties based on the single sample analysis (e.g., Moffat, [10]) in measurements of the friction factor f were ±4.5 percent at the Re=100, ±2.5 percent at the Re=300 and below ±1.5 percent at the Re≥1000 with 95 percent certainty. These values were dominated by the errors associated with the pressure measurements. The uncertainty in determination of the Re number was ±0.6 percent with 95 percent certainty.

Results and Discussion

Geometrical parameters of the tested pipes are shown in Table 1. The lowest number of bends was 30 and one can assume that the obtained results are valid for the periodically developed flow in the U-type undulated pipe. Total pressure losses for a U-type undulated pipe flow are presented in a form of the Darcy friction factor versus Reynolds number $f_w = f(\mathrm{Re})$ in Fig. 4 where the effect of the dimensionless curvature radius $(2R/d)$ as a parameter is shown. These data do not show an abrupt laminar to turbulent transition. This typical behavior of the friction factor against Reynolds number was also found in the helical pipe flow (e.g., Shah and Joshl [11]) and in the sine-waved pipe (Popiel and Van der Merwe [8]). It is known that curvature of the helical pipe increases the critical Reynolds number. In our case, like in the sine-waved pipe flow, we have more complex mixing and gradual laminar to turbulent transition. It is not precisely clear when and how a laminar counter-rotating vortex flow in waved pipes changes into turbulent flow pattern as the Reynolds number increases. From the smooth laminar-turbulent flow transition, which is shown in Fig. 4 it is concluded that in the elongated transition region the laminar secondary flow and the developing additional Dean vortices are gradually replaced by the turbulent secondary flow.

In Fig. 5, the experimental data are presented in a form of the modified friction factor versus a modified Dean number (after Ito [3]):

$$f_w * (2R/d)^{0.5} = f[\mathrm{De}_m = \mathrm{Re} * (d/2R)^2] \qquad (1)$$

Table 1 Geometrical parameters of the investigated U-type undulated pipes

d [mm]	L/d	$2R/d$	No. of bends
3.91	333.9	6.62	33
7.55	1326.6	7.95	104
7.55	1326.6	11.13	74.5
7.55	1326.6	16.03	51.5
7.55	1326.6	22.58	36.5
7.55	1326.6	27.85	30

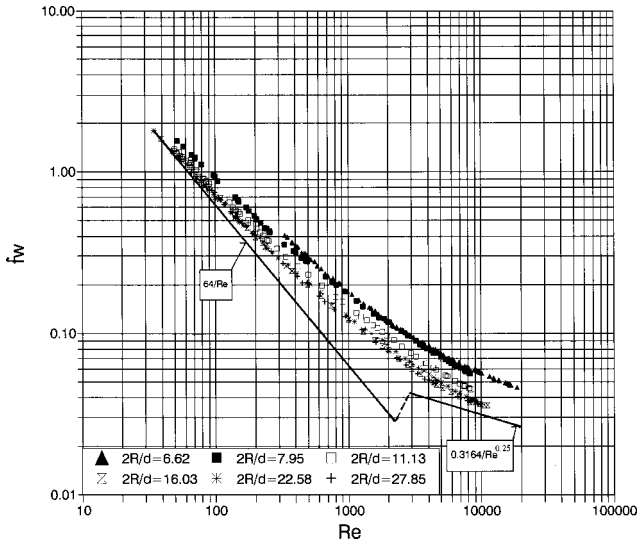

Fig. 4 Friction factor as a function of Reynolds number

At higher values of $De_m = Re*(d/2R)^2$ data for $2R/d = 27.85$ and 22.58 show the beginning of tendency to follow one line, like for a sine-wavy pipe flow (Popiel and Van der Merwe [8]). The friction factor on this line probably is the result of the superimposed effects of the secondary vortex flow and the developed turbulent mixing.

Surprisingly, when the experimental data are presented in a form of the normalized friction factor $f_w*Re/64$ versus a new Dean number $De_n = Re*d/2R$ a main pool of the experimental data fall into one line (Fig. 6), which has been approximated with the following equation

$$\ln(f_w*\mathrm{Re}/64) = a + b(\ln(\mathrm{De}_n))^2 \qquad (2)$$

where: $a = 0.021796$, $b = 0.0413356$ (with FitStdErr=0.219). The above approximation equation was obtained with the last squares error technique of fit using the Table Curve 2D, Automated Curve Fitting Software, Jandel Sci. (1994). The constants a and b were determined for $Re*d/2R > 50$ at $2R/d = 6.62$, and for $Re*d/2R > 25$ at $2R/d = 7.95$ to avoid the effect of the low accuracy experimental data.

A very good agreement of the approximation equation and the experimental data is demonstrated in Fig. 6. However, it should be noticed that the experimental points for larger curvature radiuses show an increasing departure with increasing value of $Re(d/2R)$. For example, this departure is observed for $Re(d/2R) > 200$ at $2R/d = 22.58$, and for $Re(d/2R) > 70$ at $2R/d = 27.85$. The explanation of this situation one can find in Fig. 4, where the corresponding points are getting closer to the straight smooth pipe turbulent flow data. These points are located at some distance above the straight smooth pipe turbulent flow data because of the additional effect of the Dean vortices. At the lower Reynolds numbers a spread of the experimental points is wider because of the lower accuracy of measurements of low pressure losses.

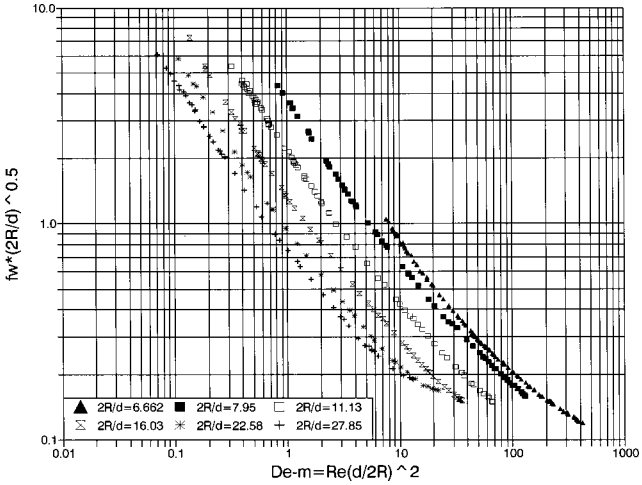

Fig. 5 Modified friction factor as a function of the modified Dean number

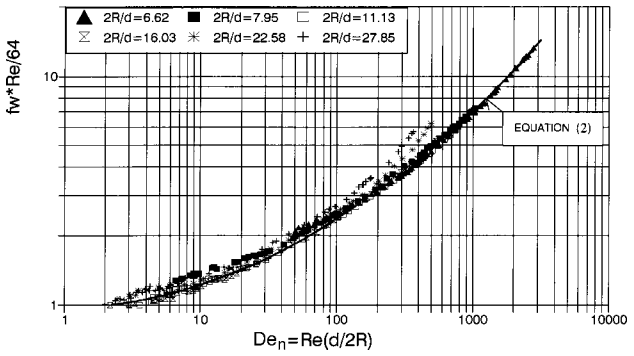

Fig. 6 Normalized friction factor versus new Dean number

From Fig. 6 it is seen that in the laminar region the effect of the pipe curvature on the friction factor vanishes below the new Dean number $De_n < \sim 3$ for all tested geometrical parameters.

Concluding Remarks

The Darcy friction factor versus Reynolds number plot for a U-type undulated pipe flow shows a smooth transition from the laminar to the turbulent regime which is typical for curved pipes. Presumably, as in the sine-waved pipes, in this elongated transition region the effect of the laminar secondary flow and the developing Dean vortices on the pressure losses is gradually replaced by the turbulent secondary flow as the Reynolds number is increased.

In the laminar region the effect of the U-type undulated pipe curvature vanishes below the new Dean number $De_n = Re*d/2R < \sim 3$. Due to the specially chosen dimensionless numbers it was possible to correlate the main part of the experimental data with the relatively simple equation

$$\ln(f_w*\mathrm{Re}/64) = a + b(\ln(\mathrm{De}_n))^2$$

which is not valid for the larger curvature radiuses and higher Dean numbers. For example, it is not valid for $De_n > 200$ at $2R/d = 22.58$, and for $De_n > 70$ at $2R/d = 27.85$. It is interesting to notice that using the original Dean number it was difficult to correlate the experimental data of the friction factor for the U-type undulated pipe flow.

Acknowledgement

This work has been supported by the Polish State Committee for Scientific Research under grant no. 8T10B03914.

Nomenclature

d = diameter of pipe
$\mathrm{De} = \mathrm{Re}(d/2R)^{1/2}$ = Dean number
$\mathrm{De}_m = \mathrm{Re}(d/2R)^2$ = modified Dean number
$\mathrm{De}_n = \mathrm{Re}(d/2R)$ = new Dean number
$f = \Delta P/(0.5*U^2\rho L/d)$ = Darcy friction factor
l = spacer length
L = length of pipe
ΔP = pressure losses

R = radius of the wavy pipe centerline curvature
$\mathrm{Re}=U*d/\nu$ = Reynolds number
U = mean velocity
ρ = density of water
ν = kinematic viscosity of water

References

[1] Ward-Smith, A. J., 1980, *Internal Fluid Flow. The Fluid Dynamics of Flow in Pipes and Ducts. Chapter B: Bends*, Clarendon Press, Oxford, pp. 248–306.
[2] Burger, S. A., Talbot, L., and Yao, L. S., 1983, ''Flow in Curved Pipes,'' Annu. Rev. Fluid Mech., **15**, pp. 461–512.
[3] Ito, H., 1987, ''Flow in Curved Pipes,'' Int. J. JSME, **30**, pp. 543–552.
[4] Dean, W. R., 1927, ''Note on the Motion on Fluid in a Curved Pipe,'' Philos. Mag., **4**, pp. 208–223.
[5] Cheng, K. C., and Yuen, F. P., 1987, ''Flow Visualization Studies on Secondary Flow Patterns in Straight Tubes Downstream of a 180 deg Bend and in Isothermally Heated Horizontal Tubes,'' ASME J. Heat Transfer, **109**, pp. 49–54.
[6] Ito, H., 1960, ''Pressure Losses in Smooth Pipe Bends,'' ASME J. Basic Eng., **82**, pp. 131–143.
[7] Shimizu, Y., Sugino, K., Kuzuhara, S., and Murakami, M., 1982, ''Hydraulic Losses and Flow patterns in Bent Pipes (Comparison of the Results in Wavy Pipes and Quasi-Coiled Ones),'' Bull. JSME, **25**, pp. 24–31.
[8] Popiel, C. O., and Van der Merwe, D. F., 1996, ''Friction Factor in Sine-Pipe Flow,'' ASME J. Fluids Eng., **118**, pp. 341–345.
[9] Popiel, C. O., and Wojtkowiak, J., 1998, ''Simple Formulas for Thermophysical Properties of Liquid Water for Heat Transfer Calculations (from 0°C to 150°C),'' Heat Transfer Eng., An International Quarterly, **19**, pp. 87–101.
[10] Moffat, R. J., 1988, ''Describing the Uncertainties in Experimental Results,'' Exp. Therm. Fluid Sci., **1**, pp. 3–17.
[11] Shah, R. K., and Joshl, S. D., 1987, ''Convective Heat Transfer in Curved Ducts,'' *Handbook of Single-Phase Convective Heat Transfer*, p. 5.8, Wiley.

V. I. Vasiliev[1]
Group Manager,
ABB Uniturbo Ltd.,
13 Ul. Kasatkina,
P.O. Box 16, 129301,
Moscow, Russia

On the Prediction of Axisymmetric Rotating Flows by a One-Equation Turbulence Model

A one-equation model previously tested for parabolic flows and 2-D separated flows was implemented for rotating flows. Flows in rotor-stator disk systems, and in sealed cavities between contrarotating and corotating disks, were calculated and compared with known experimental and numerical data. For buoyancy-driven flow in a rotating cavity, an analytic solution for the turbulent regime was obtained. [S0098-2202(00)01302-X]

Introduction

Flows in rotor-stator disk systems or in rotating cavities are typical examples of the rotating flows which occur in turbomachinery. Therefore, the ability to predict the characteristics of such flows has a significant impact on gas turbine engine design.

Extensive experimental and theoretical studies of rotating flows began in the 1950s, and at that time efforts were concentrated on relatively simple plane disk systems. The results of those studies were summarized in the monograph of Dorfman [1]. More recent research on plane disk systems, including the results of numerical simulations, is described in the monograph of Owen and Rogers [2,3], and also in the review of Owen and Wilson [4]. In the last decade, attention has turned to disk systems with complex geometry, and the numerical simulation of rotating flows has penetrated into design practice (see, for example, the review of Stow and Coupland, [5]). However, the choice of an appropriate turbulence model for numerical calculations is still an open issue.

A satisfactory turbulence model should meet the following requirements: 1) it should provide acceptably accurate predictions of the turbulent stresses and heat fluxes, 2) it should be universal, i.e., allow calculations of different flows without changes of coefficients and source terms, 3) it should be numerically compatible, i.e., should not impose additional restrictions on the algorithm which are not already required for velocity field simulation, and must allow any reasonable boundary conditions.

Low-Reynolds-number k-ε models have been used in several studies of prediction of rotating flows. These models meet the requirement of universality and successfully describe many kinds of rotating flows. On the other hand, they impose significant restrictions on the calculation procedure. For example, the low Reynolds number k-ε models of Launder and Sharma [6] and Morse [7] require very fine grids near the wall ($y^+ < 0.5$) and more than 30 points per boundary layer thickness. Iacovides and Theafonopoulos [8] used an algebraic (mixing length) model near the wall to reduce grid restrictions. For the same reason the high-Reynolds-number k-ε model with wall functions is commonly applied in engineering practice (e.g., Virr et al. [9]). However, the latter approaches, while improving numerical compatibility, do not yield a universal model.

Recently, it was shown, for nonrotating flows, that one-equation models for turbulent viscosity provide a reasonable compromise between the above three requirements. The models of Spalart and Allmaras [10], Secundov [11], and the new version of Secundov's model, $\nu_t 92$ (see Gulyaev et al. [12]) approach universality and have good accuracy and, on the other hand, have very simple numerical realizations. The original Secundov model [11] has been used for different parabolic flow calculations, and took part in the Collaborative Testing of Turbulence Models (Bradshaw et al. [13]), where it showed an accuracy comparable with other models tested. Recently, it has been tested for several kinds of separated flows (Vasiliev et al. [14]). However, these one-equation models have not been applied to rotating flows.

The aim of the present work was to test the one-equation ν_t model (Secundov [11]) for rotating flows. For this purpose several axisymmetric flows were considered:

1 The flow in a sealed rotor-stator rectangular cavity. The results of these calculations were compared with experimental data and calculations by the k-ε model.

2 The flow in a rotor-stator disk system with axial clearance. For this particular case there are no experimental data, but it presents a example of relatively complex geometry and allowed the numerical capabilities of the whole calculation procedure to be checked. Another point is that for cavities with axial clearance and inflow or outflow there are many experimental and calculation data (e.g., Owen and Wilson [4]); at the same time the case without through-flow has not previously been investigated in detail. Therefore, the present numerical study could be useful for engineering estimates.

3 The flow in a sealed rectangular cavity with contra-rotating disks, where the calculations were compared with available experimental data.

4 The flow in a sealed rotating cavity (with corotating disks) driven by buoyancy forces. The agreement with experimental data for this case is rather poor. However, it should be mentioned that this case is the most intractable of all rotating flows and there are several pieces of evidence that it is not axisymmetric. On the other hand, the advantage of a one-equation model for this case is that it has an analytic solution, which is also presented below.

Mathematical Model

Governing Equations. The Reynolds-averaged Navier-Stokes conservation equations for axisymmetric incompressible flows can be written in generalized coordinates as

$$\frac{\partial}{\partial \xi}\left[\frac{y}{J}((A-A_v)\xi_x+(B-B_v)\xi_y)\right] + \frac{\partial}{\partial \eta}\left[\frac{y}{J}((A-A_v)\eta_x+(B-B_v)\eta_y)\right]=\frac{1}{J}S \quad (1)$$

where x,y are axial and radial coordinates, ξ, η are generalized coordinates, and $J=\partial(\xi,\eta)/\partial(x,y)$ is the Jacobian of the coordinate mapping.

The fluxes are given by

[1]Present address: ABB-Alstom Power, GTDBF, 5401 Baden, Switzerland.

Contributed by the Fluids Engineering Division for publication in the JOURNAL OF FLUIDS ENGINEERING. Manuscript received by the Fluids Engineering Division November 24, 1998; revised manuscript received February 9, 2000. Associate Technical Editor: P. Bradshaw.

$$A=\begin{pmatrix}\rho_0 u\\ \rho_0 u^2+p\\ \rho_0 uv\\ \rho_0 uw\end{pmatrix},\quad B=\begin{pmatrix}\rho_0 v\\ \rho_0 uv\\ \rho_0 v^2+p\\ \rho_0 vw\end{pmatrix},$$

$$A_v=\begin{pmatrix}0\\ \tau_{xx}\\ \tau_{xy}\\ \tau_{x\phi}\end{pmatrix},\quad B_v=y\begin{pmatrix}0\\ \tau_{xy}\\ \tau_{yy}\\ \tau_{y\phi}\end{pmatrix}, \tag{2}$$

where u,v,w are axial, radial, and swirl velocity components, p the pressure and ρ_0 the density, which is assumed constant. The viscous stresses τ are assumed proportional to the strain rates:

$$\tau_{xx}=2\nu_{\text{eff}}\left(\frac{\partial u}{\partial x}\right),\quad \tau_{yy}=2\nu_{\text{eff}}\left(\frac{\partial v}{\partial y}\right),\quad \tau_{xy}=\nu_{\text{eff}}\left(\frac{\partial u}{\partial y}+\frac{\partial v}{\partial x}\right),$$

$$\tau_{x\phi}=\nu_{\text{eff}}\left(\frac{\partial w}{\partial x}\right),\quad \tau_{y\phi}=\nu_{\text{eff}}\left(\frac{\partial w}{\partial y}-\frac{w}{y}\right),\quad \tau_{\phi\phi}=2\nu_{\text{eff}}\left(\frac{v}{y}\right)$$

where $\nu_{\text{eff}}=\nu_t+\nu$, ν_t is the turbulent (eddy) viscosity, and ν is the molecular viscosity which is assumed constant.

In the present work, both isothermal and buoyancy-driven rotating flows were considered. In the latter case, the temperature variations were assumed small and the Boussinesq approximation was used. Thus, in a rotating reference frame the source term in (1) is written as

$$S=\begin{pmatrix}0\\ 0\\ p+\rho_0 w^2-\tau_{\phi\phi}+2\rho_0\Omega yw-\rho_0\Omega^2 y^2\theta\\ -\rho_0 vw+\tau_{y\phi}-2\rho_0\Omega yv\end{pmatrix} \tag{3}$$

where Ω is the speed of rotation, $\theta=\beta\Delta T$, where β is the volume expansion coefficient and $\Delta T=T-T_0$; T is the local temperature and T_0 is a reference temperature. In a rotating reference frame p is the deviation of the pressure from its hydrostatic value, i.e., the real pressure is $P=p+\rho_0 y^2\Omega^2/2$. The isothermal flows were calculated in an absolute reference frame, and in these cases the speed of rotation in (3) was set to zero.

The temperature and turbulent viscosity satisfy transport equations, which in generalized coordinates can be written as:

$$\frac{\partial}{\partial\xi}\frac{y}{J}(\rho Uf-Q_\xi)+\frac{\partial}{\partial\eta}\frac{y}{J}(\rho Vf-Q_\eta)-\text{Source}=0 \tag{4}$$

$$Q_\xi=\rho\left(\frac{\nu_1}{\sigma_t}+\frac{\nu}{\sigma}\right)\left[(\nabla\xi\cdot\nabla\xi)\frac{\partial f}{\partial\xi}+(\nabla\xi\cdot\nabla\eta)\frac{\partial f}{\partial\eta}\right],$$

$$Q_\eta=\rho\left(\frac{\nu_t}{\sigma_t}+\frac{\nu}{\sigma}\right)\left[(\nabla\eta\cdot\nabla\xi)\frac{\partial f}{\partial\xi}+(\nabla\eta\cdot\nabla\eta)\frac{\partial f}{\partial\eta}\right]$$

where f stands for θ or ν_t.

The source term and coefficients for the energy equation in Boussinesq-approximation form are given by:
Source$=0.0$, $\sigma_t=\text{Pr}_t=0.9$, $\sigma=\text{Pr}$, where Pr and Pr_t are molecular and turbulent Prandtl numbers respectively.

The source terms and coefficients for Secundov's model are given by:

$$\text{Source}=\rho\nu_t y(0.2\alpha\Gamma-(3\nu_t+50\nu)/D^2)$$

$$\Gamma=(\tau^2_{xx}+2\gamma^2_{xy}+\tau^2_{yy}+2\tau^2_{x\phi}+2\tau^2_{y\phi}+\tau^2_{\phi\phi})/(2\mu^2_{\text{eff}})$$

$$\alpha=\frac{(\nu_t/8\nu)^2+1.4(\rho\nu_t+8\nu)+0.2}{(\nu_t/8\nu)^2-1.4(\nu_t+8\nu)+1.0},$$

$$\sigma_t=0.5,\quad \sigma=1.0,$$

and D is distance to nearest wall.

In numerical calculations the equation for swirl velocity was integrated separately from the meridional flow equations, and for this purpose it was written in the form (4), where f stands for w.

Details of Numerical Procedure. The above equations were solved numerically using the method described by Vasiliev et al. [14]. For incompressible flows this method implements the artificial-compressibility approach and allows the use of high order schemes developed for compressible flows. For rotating flows the artificial-compressibility coefficient was set equal to $(\Omega R)^2$, where R is the radius of the cavity.

For channels flows (Vasiliev et al. [14]) the system of algebraic equations corresponding to the Navier-Stokes equations was solved by a line-relaxation block-tridiagonal algorithm, and the scalar equations by a point Gauss-Seidel method. For rotating flows the block-tridiagonal and tridiagonal ADI (alternating direction implicit) methods were implemented for the Navier-Stokes and scalar equations, respectively, and this increased the rate of convergence.

The calculation method accepts block-structured grids and allows treatment of complex geometries (one example of a relatively complex geometry is given in the present paper).

Results of Calculations

Sealed Rotor-Stator Cavity. The cavity configuration and the calculation grid are shown in Fig. 1(a). The grid nodes are condensed near the solid walls. In Fig. 1 a cavity with inner and outer shrouds is shown, but if the flow domain includes the axis of symmetry (i.e., $r=0$), then there is no condensation of nodes near lower boundary.

The isothermal flow in a sealed rotor-stator cavity of rectangular cross section is characterized by three parameters: r/R, $G=s/R$, and $\text{Re}=\Omega R^2/\nu$. In the present work, the following cases were considered: 1) $r/R=0$, $G=0.155$, $\text{Re}=8\times10^5$, 2) $r/R=0.1$, $G=0.0685$, $\text{Re}=6.9\times10^5$, and 3) $r/R=0$, $G=0.1$, Re in the range from 10^5 to 4×10^6. For the first case the calculated results are compared with experimental data from the monograph of Dorfman [1], for the second one with measurements and calculations by k-ε models (taken from the review of Owen and Wilson [4]). The third case demonstrates the prediction of transition, in comparison with the k-ε model of Morse [7].

The boundary conditions for these cases are the following: (*a*) no-slip boundary conditions on the walls, i.e., $u=v=0$, $\partial p/\partial n=0$, $\nu_t=0$, where n is distance normal to the wall, $w=0$ for

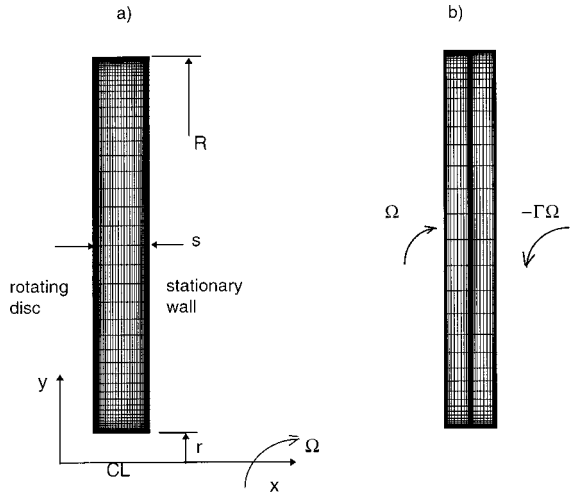

Fig. 1 Scheme of disk cavity and calculation grid: (*a*) rotor-stator system, (*b*) contra-rotating disks

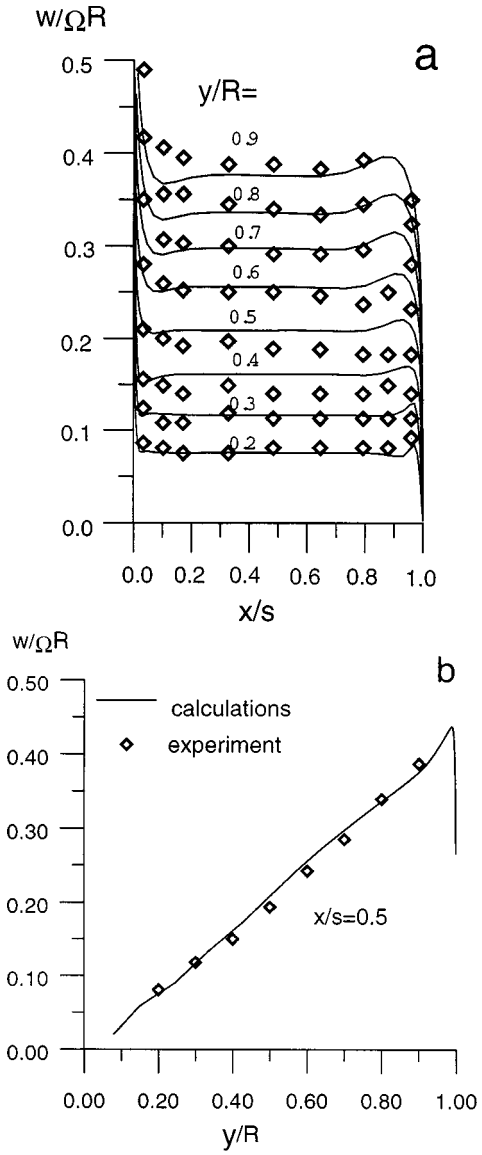

Fig. 2 Swirl velocity distributions: (*a*) axial profiles, (*b*) radial distribution at the mid plane (rotor-stator system, $G=0.155$, $r=0$, $Re=8\times10^5$)

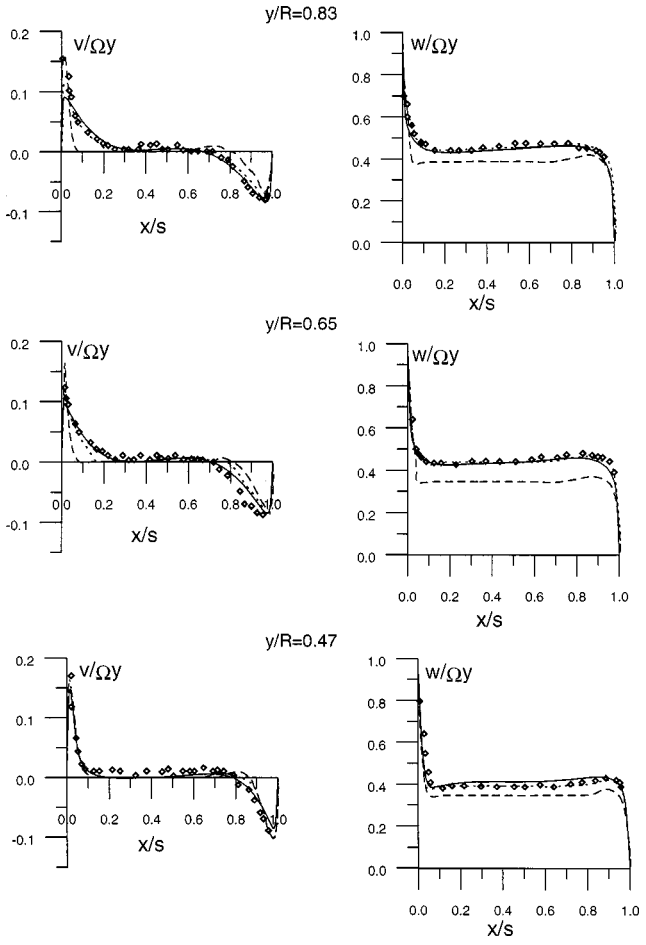

Fig. 3 Velocity distributions in rotor-stator cavity ($G=0.0685$, $r/R=0.1$, $Re=6.9\times10^5$) ◇ experiment — — — Launder-Sharma model, ··· Morse model, —— one-equation model (present calculations)

stationary walls, $w=\Omega y$ for rotating ones; (*b*) symmetry conditions on the axis (for cases 1 and 3), i.e., $v=w=0$, $\partial u/\partial n=\partial p/\partial n=0$, $\partial \nu_t/\partial n=0$.

In Case 1 three grids, with different numbers of nodes ($15\times15,30\times30,60\times60$) but with the same law of node distribution, were used. The results became grid-independent at the finest mesh: however, even the mid-size mesh (30×30) resulted in reasonable accuracy, acceptable for engineering estimates. The comparison of swirl velocity distributions with the available experimental data (Dorfman [1]) is presented in Fig. 2. In general, the agreement is quite reasonable; moreover, in the core region it is good, but there is some discrepancy in the disk boundary layer near the shroud.

In Case 2 the agreement with experimental data is also good. Comparisons of calculated and measured swirl and radial velocity profiles are shown in Fig. 3. Calculations by other turbulence models are also shown in Fig. 3. In the case considered, the one-equation model gives better agreement than the Launder and Sharma k-ε model, and nearly the same accuracy as the Morse k-ε model. However, the last-named has been specially adapted for rotating flows, while we used the one-equation model without modification for rotation effects. Another point is that k-ε models requires $y^+<0.5$ in the first cell, but the one-equation model accepts $y^+\geqslant1.5$ (60×60 grid), and even $y^+=3$ with the coarser grid (30×30), which still ensures reasonable accuracy. Thus, the one-equation model is much less restricted in the near-wall region.

In Case 3, calculations were performed for a range of Reynolds number, to investigate the ability of the one-equation model to

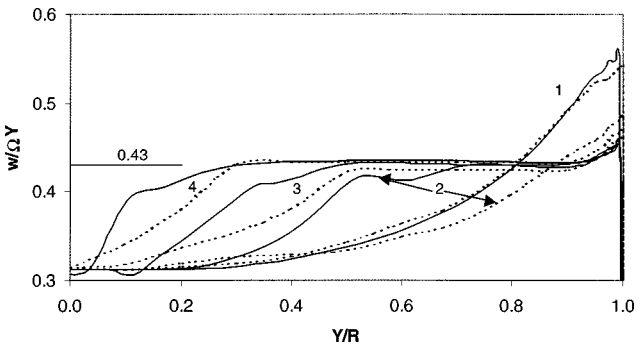

Fig. 4 Effect of Re on radial variation of swirl velocity in rotor-stator cavity ($G=0.1$, $r/R=0$, $x/s=0.5$): 1, $Re=10^5$; 2, $Re=4\times10^5$; 3, $Re=10^6$; 4, $Re=4\times10^6$, ··· Morse model, —— one-equation model (present calculations)

Table 1

	r/R	G	Re	C_M numerical calculations	C_M experimental correlation
Case 1	0	0.155	8×10^5	2.81×10^{-3}	2.79×10^{-3}
Case 2	0.1	0.0685	6.9×10^5	2.61×10^{-3}	2.65×10^{-3}
Case 3	0	0.1	10^5	4.68×10^{-3}	4.65×10^{-3}
Case 3	0	0.1	4×10^5	2.94×10^{-3}	3.07×10^{-3}
Case 3	0	0.1	10^6	2.53×10^{-3}	2.56×10^{-3}
Case 3	0	0.1	4×10^6	1.90×10^{-3}	1.94×10^{-3}

predict transition in rotating flows. The results of the calculations are compared with Morse's predictions, taken from the monograph of Owen and Rogers [2]. The comparison of swirl velocity distribution in the core region (i.e., at $x/s=0.5$) is shown in Fig. 4. For the low Reynolds number (10^5) both models predict laminar flow. For the high Reynolds numbers (10^6,4×10^6) both models predict transition, which takes place not far from the axis. The one-equation and Morse models agree well in the turbulent region, and give a similar onset of transition. However, inside the transition region there is a significant discrepancy. The one-equation ν_t model gives very ''steep'' transition (i.e., the transitional region is short), while the Morse model gives more ''smooth'' transition. This behavior of the ν_t model has been previously observed in nonrotating flows (e.g., Kazarin et al. [15]). An analogous steep transition occurs when the Reynolds number is varied, and it explains the big differences in the predictions for intermediate Reynolds number (4×10^5). For this regime the one-equation model predicts a rather high level of turbulence, but the Morse model predicts even lower swirl than for laminar case.

It should be mentioned that using semi-empirical models (either one-, or two-equation types) one can hardly expect very reliable results *inside* the transition region, and the more important feature is the ability of the model to predict correctly the onset of transition, and to switch automatically from one regime to another. The ν_t model used here has this ability, in spite of its simplicity.

The calculated moment coefficients can be compared with the empirical correlations of Daily and Nece [16]. In the cases considered, the boundary layers on the rotating and stationary walls do not interact with each other, and the appropriate empirical correlations have the forms:

$C_M=1.85G^{1/10}\,\mathrm{Re}^{-0.5}$ (laminar flow, here valid only for case 3, at $\mathrm{Re}=10^5$),

$C_M=0.051G^{1/10}\,\mathrm{Re}^{-0.2}$ (turbulent flow).

A comparison of calculated and empirical values is presented in the Table 1. The discrepancy for most cases does not exceed 2 percent, reaching 4 percent for Case 3 at $\mathrm{Re}=4\ 10^5$, which is still good agreement.

Rotor-Stator Disk System With Axial Clearance. The influence of axial clearance on the cavity without through-flow was studied for a geometry typical of an uncooled power turbine, where the flow in the cavity has a large effect on the heat transfer and on the thermal state of the rotor. The geometry of the cavity, with the computational grid, is shown in Fig. 5. The whole calculation domain consists of two subdomains, and the total number of cells equals 65×58.

The boundary conditions on the walls and axis are the same as for the sealed cavity (i.e., no-slip and symmetry conditions). The most consistent approach for determining the parameters in the clearance is the simultaneous calculation of the cavity flow and the external stream. However, the external flow in a real turbine is 3D and could not be computed in this work. Therefore, for the 2-D case considered a simplified approach was adopted, i.e., the pressure and swirl velocity in the clearance were prescribed, but the swirl was varied over a wide range which covers the possible

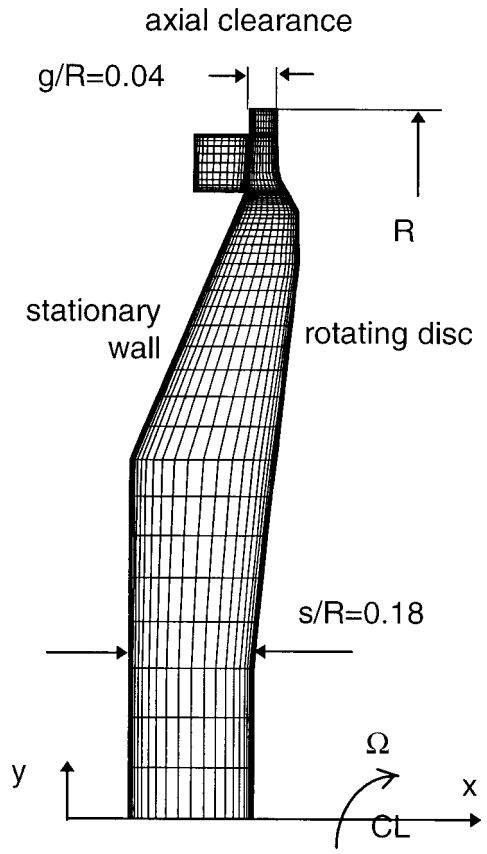

Fig. 5 Computational grid for cavity with axial clearance

swirl deviations in the 3-D case. The radial gradients of other quantities in the clearance were assumed zero (i.e., $\partial f/\partial y=0$).

The distributions of swirl velocity in the clearance are presented in Fig. 6. It was assumed that the external flow would influence the level of core swirl (We) rather than the shape of the profile. In the case of nonswirled external flow (i.e., $We=0$) the radial gradient of w was set to zero.

The calculations were performed at $\mathrm{Re}=4.5\times10^6$, for a closed cavity and a cavity with axial clearance. The calculated maps of streamlines for various levels of swirl in the clearance are presented in Fig. 7.

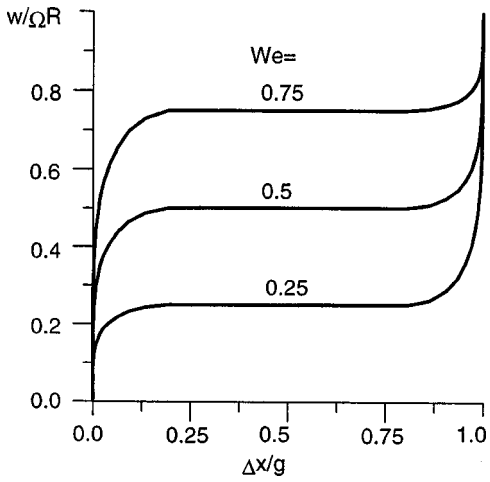

Fig. 6 Prescribed swirl velocity at the axial clearance

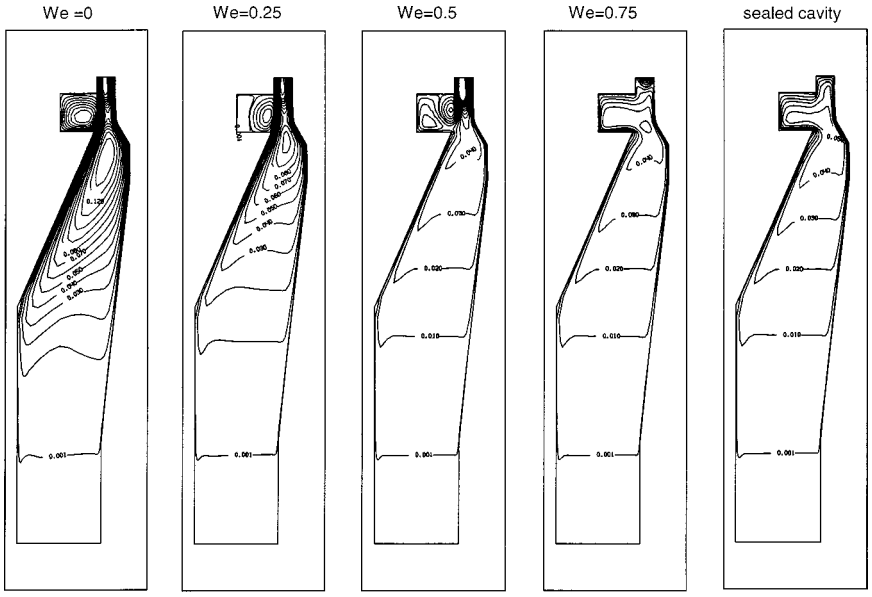

Fig. 7 Streamline maps for different swirl in the clearance (the values of stream-function are normalized by $0.01\Omega R^2$)

In the sealed cavity one large vortex occupies the meridional section. The swirl velocity in the core is about 40 percent of the disk speed at the same radius.

In the cavity with axial clearance the flow structure depends strongly on the external stream characteristics. If the external stream is nonswirling the swirling core in the cavity vanishes and the swirl velocity rapidly decreases at a small distance from the disk surface. A complex structure with three vortices is formed at the meridional section. In the case of a swirling external stream the influence of clearance decreases with increase of *We*, and at $We=0.75$ the swirling core is practically the same as in the sealed cavity. For the latter case the meridional flow structure changes only near the clearance, where a small additional recirculation zone appears.

The moment coefficient as a function of external swirl intensity is shown in Fig. 8. For nonswirling external flow the value of C_M increases to a level typical of the free disk, and for highly-swirled external flow it became even lower than in a sealed cavity ($C_M = 2.07\times10^{-3}$ for sealed cavity).

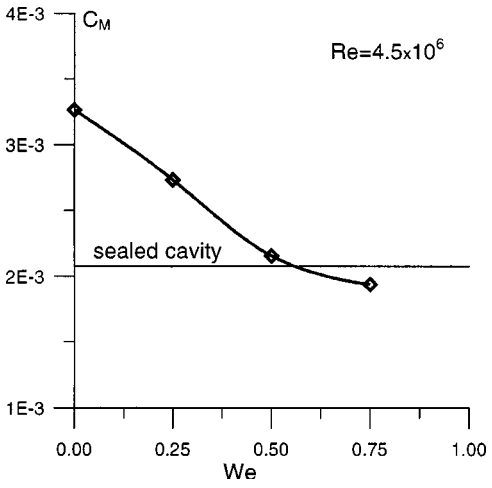

Fig. 8 Influence of the external flfow on the momentum friction

Sealed Cavity Between Contra-Rotating Disks. The flow in a cavity between contrarotating disk is characterized by r/R, G, $\mathrm{Re}=\Omega R^2/\nu$, and by an additional parameter Γ, the ratio of disk speeds (here we considered Γ as positive, but in all cases the disks rotate in opposite direction). In the present work, calculations were performed for one cavity ($G=0.12$), two values of Reynolds number (10^5,1.25×10^6), and disk speed ratios in the range from zero to unity.

The calculation grid is shown in Fig. 1(*b*). To ensure grid-independent solutions the 60×60 grid was used.

The results of the calculations (swirl and radial velocity components) are shown for low Reynolds number in Fig. 9, and for high Reynolds number in Fig. 10. The calculated results are compared with the measurements of Kilic, Gan and Owen (for low Reynolds number Kilic et al. [17], for high Reynolds number Kilic et al. [18]).

For the low Reynolds number (10^5), laminar calculations ($\nu_t \equiv 0$) were performed as well as calculations using the one-equation model. At a disk speed ratio $\Gamma=0$ (i.e., in the limit of a rotor-stator cavity) both calculations give the same results, which means that the one-equation model predicts laminar flow. These results are in good agreement with measurements. An increase of Γ leads to the appearance of turbulence, and the experimental data deviates from laminar solution. The one-equation model qualitatively describes this effect. Moreover, the calculated swirl velocity distributions are in rather good agreement with measurements, and significantly different from laminar data. The radial velocity distributions also agree with measurements in the core region, but there is a significant discrepancy near the wall.

At the high Reynolds number (1.25×10^6), where according to measurements the flow is fully turbulent, the agreement between calculations and experiment is good (see Fig. 10). The model correctly predicts the change of velocity profiles due to variation of disk-speed ratio.

Thus, the one-equation model works well for fully turbulent flows but overpredicts to some extent the turbulence at transitional values of the Reynolds number. The latter is connected with steep transition, as mentioned above.

It is interesting to note that the Launder-Sharma k-ε model

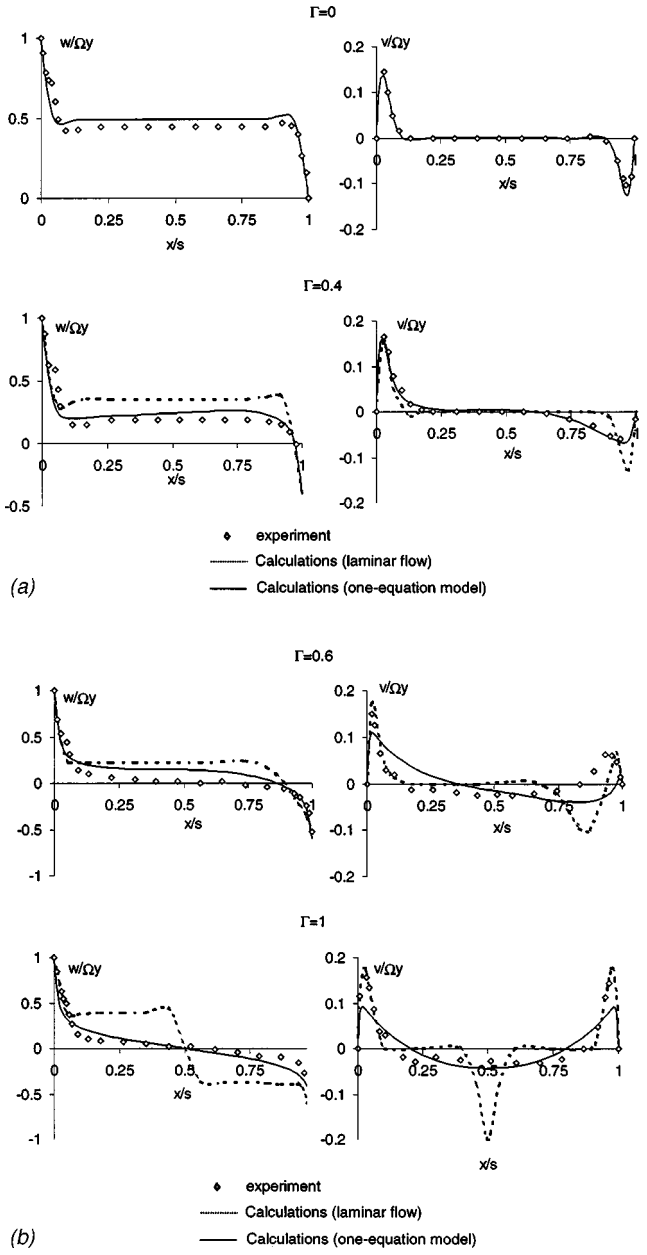

Fig. 9 (*a*) **Velocity distributions between contra-rotating disks (*G*=0.12, Re=10^5, *y*/*R*=0.85, Γ=0;0.4).** (*b*) **Velocity distributions between contra-rotating disks (*G*=0.12, Re=10^5, *y*/*R*=0.85, Γ=0.6;1.0).**

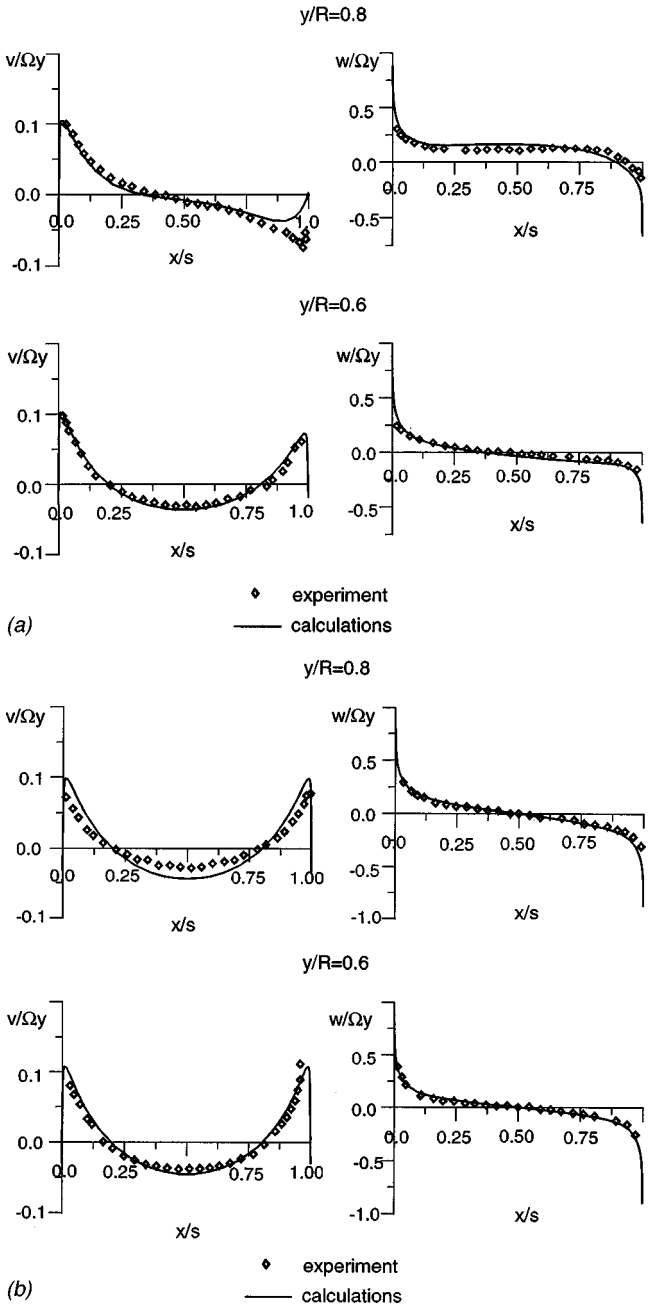

Fig. 10 (*a*) **Velocity distributions between contra-rotating disks (*G*=0.12, Γ=0.6, Re=1.25×10^6)** (*b*) **Velocity distributions between contra-rotating disks (*G*=0.12, Γ=1.0, Re=1.25×10^6)**

underpredicts transition, and at $\Gamma=0.4$ and $\Gamma=0.6$ gives even worse results than the one-equation model (see Kilic, Gan and Owen [17])

Buoyancy-Driven Flow in Rotating Cavity. The buoyancy-driven flow in a sealed cavity is the most intractable of all rotating flows. There is evidence to suggest that this flow is usually three-dimensional and unsteady, but there are no direct data confirming this for the fully- turbulent regime (Owen and Rogers [3]). At the same time there are indirect data which might be associated with turbulent flows. For instance, Schukin and Olimpiev [19], measuring total heat fluxes in rotating cavity at high Reynolds number, observed a change in the heat transfer law, which could be identified in spite of significant data scatter. In the present work the flow for the same conditions was studied numerically, and computations were compared with Schukin and Olimpiev's measurements.

These measurements were performed in a cavity of rectangular cross-section ($G=0.12$, $r/R=0.097$) filled with water. Disk surfaces were maintained at constant temperatures, and shrouds were adiabatic. The data associated with turbulent flow correspond to Reynolds number $\mathrm{Re}>10^7$. Measurements are available up to $\mathrm{Re}=7\times10^7$. The mean temperature (i.e., (Thot+Tcold)/2) was varied in the range 30°C to 60°C, and the normalized temperature difference ($\theta_m=\beta$(Thot−Tcold)) in the range 0.002 to 0.008. The Prandtl number, based on mean temperature, varies from 3 up to 6: therefore the Rayleigh number ($\mathrm{Ra}=\mathrm{Re}^2\,\mathrm{Pr}\,\theta_m$) for the regimes considered was high, $5.3\times10^{12}<\mathrm{Ra}<6.3\times10^{13}$.

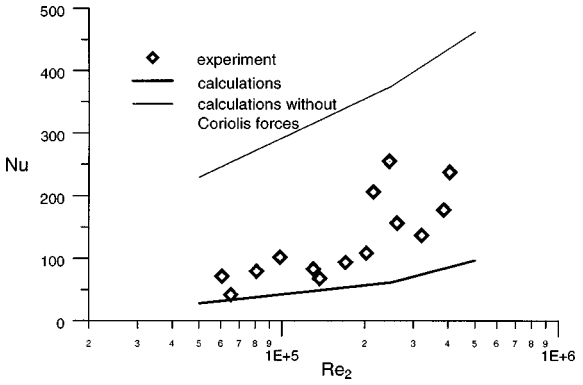

Fig. 11 Comparison of calculated and measured Nusselt number in rotating cavity

The measured Nusselt number is plotted in Fig. 11. Here $\mathrm{Nu}=\mathrm{Rq}/(\mathrm{Thot}-\mathrm{Tcold}))/\lambda$, where q is surface-averaged heat flux, λ is thermal conductivity, and $\mathrm{Re}_2=\mathrm{Re}\,\theta_m$. The measured heat fluxes were correlated by Re_2, because the analysis of the governing equations shows that at high Reynolds number the Coriolis forces are dominant (see also the analytic solution below) and the flow should be controlled by this parameter, rather then by the Rayleigh (or Grashof) number. Therefore, this flow should be significantly different from natural convection. The data in Fig. 11 reveal significant scatter, which is approximately the same as for Schukin and Olimpiev's correlation based on Rayleigh number.

The calculations were performed in the same range of Re_2 as the experiment ($5\times10^4<\mathrm{Re}_2<5\times10^5$). The calculation grid is shown in Fig. 1(*a*). Similarly to the other cases considered, the grid with 60×60 cells ensured a grid-independent solution. The boundary conditions for pressure-velocity fields were the same as for other cases (i.e., no-slip conditions). Normalized temperatures on the disk surfaces were constant ($\theta=0$ on hot wall, $\theta=-\theta_m=-\beta(\mathrm{Thot}-\mathrm{Tcold})$ on cold wall), and the shrouds were assumed adiabatic ($\partial\theta/\partial n=0$). The Prandtl number was fixed in the calculations, $\mathrm{Pr}=3$. However, the influence of Pr variations was evaluated and this influence was much lower than the discrepancy between calculations and measurements.

The calculated Nusselt number is shown in Fig. 11 by the thick solid line. The calculations significantly underestimated the heat fluxes. At the same time, when the Coriolis forces were switched off (i.e., only buoyancy forces were taken into account) the calculations drastically overpredicted the measurements (thin solid line in Fig. 11). The 2-D temperature fields, calculated with and without Coriolis forces, are presented in Fig. 12. This comparison shows that Coriolis forces suppress the recirculation, and therefore reduce the production term in the turbulence model. However, this observation is valid for the 2-D case only. The real flow would be three-dimensional, which is at least a partial explanation of the difference between calculations and experiment. To check this statement, additional 3-D calculations are necessary and could be performed in future.

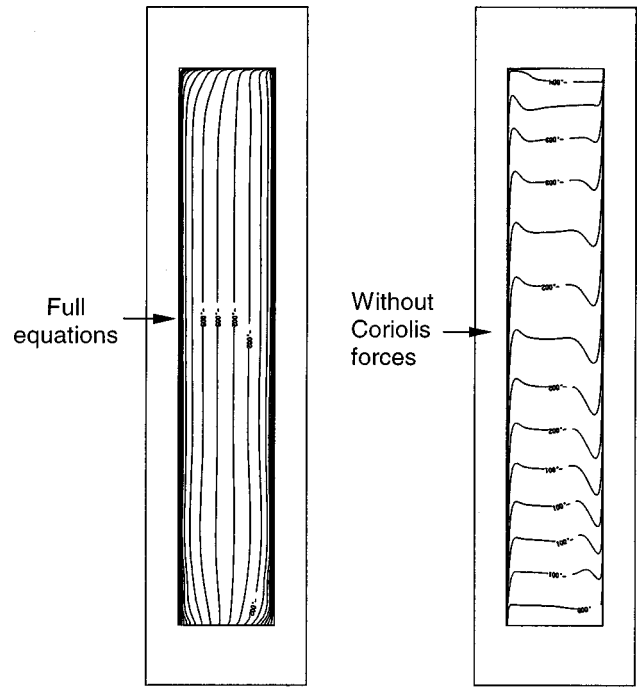

Fig. 12 Influence of Coriolis forces on the temperature distribution in rotating cavity (θ contours at $G=0.12$, $\mathrm{Re}=5\times10^7$, $\theta_m=0.005$)

Analytic Solution for Rotating Cavity

The advantage of the one-equation ν_t model for these cases is that it has an analytic solution. To obtain the analytic solution the following assumptions were made: 1) the Reynolds number is considered to be large ($\mathrm{Re}\to\infty$); 2) the temperatures of the disks are constant; 3) the temperature variations are small ($\theta_m\to0$); 4) the gap between disks is also small, ($G\to0$), i.e., the influence of the boundary layers on the shrouds is assumed negligible for the main part of the flow, 5) $G\,\mathrm{Re}\to\infty$ (this condition ensures that the thickness of the boundary layers is much smaller than the gap), 6) $\mathrm{Re}\,\theta_m\to\infty$ (this condition ensures that the flow is turbulent).

Using assumptions 1) to 5) Homsy and Hudson [20] provided the solution for the laminar case. The one-equation model with the additional assumption 6) has an analytic solution for the turbulent regime.

Under these conditions the flow far from the shrouds can be divided into a rotating core and two wall boundary layers, characterized by thickness δ. The velocity field in the core region is defined as

$$v=0,\ u=u_\infty,\ -2\Omega w=-\frac{1}{\rho_0}\frac{dp}{dy}-\Omega^2 y\theta$$

where the values of swirl and axial velocities estimated as: $w=O(\theta_m)$, and $u_\infty=O(\theta_m\,\mathrm{Re}^{-1/2})$.

The analysis of the ν_t equation shows that under the above assumptions the turbulent viscosity inside the boundary layers is negligible in comparison with laminar viscosity ($\nu_t\sim\nu(\delta/R)^\alpha$, $\alpha=7.6$). Therefore, the velocity field in the boundary layers satisfies the usual linear Ekman-layer equations

$$-2\Omega w=-\frac{1}{\rho_0}\frac{dp}{dy}-\Omega^2 y\theta+\nu\frac{\partial^2 v}{\partial\eta^2},$$

$$2\Omega v=\nu\frac{\partial^2 w}{\partial\eta^2},\ \frac{\partial u}{\partial\eta}+\frac{1}{y}\frac{\partial yv}{\partial y}=0,$$

where $\eta=x$ for the hot side, $\eta=x-s$ for the cold side, $p=p(y)$, and boundary conditions should be prescribed as follows:

$$\eta=0:\ v=w=0\ \ u=0;$$

$$\eta/\delta\to\infty:\ v\to0,\ (2\Omega w-\Omega^2 y\theta)\to(2\Omega w-\Omega^2 y\theta)_\infty$$

Taking into account the linear temperature distribution ($\partial^2\theta/\partial\eta^2=0$) in the boundary layers, one can obtain explicit expressions for the velocity and pressure fields which include two unknown constants: u_∞, and p_∞. These parameters can be found using two matching conditions for axial velocity (i.e., $u_{\mathrm{hot}}(\eta\to\infty)=u_\infty=u_{\mathrm{cold}}(\eta\to\infty)$).

Thus, the composite solution for pressure and velocity fields is given by:

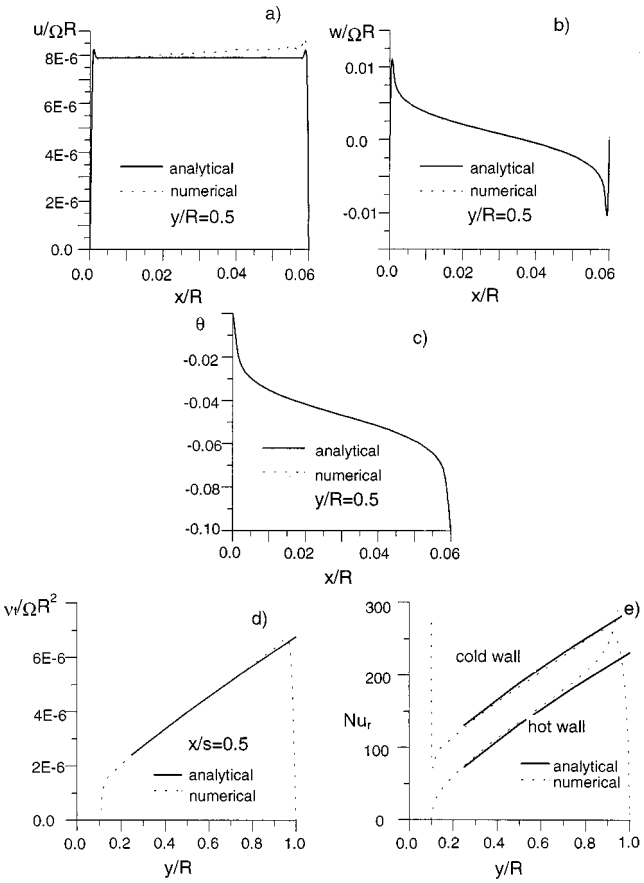

Fig. 13 Comparison of analytical and numerical solutions for rotating cavity ($G=0.06$, $\mathrm{Re}=10^7$, $\theta_m=0.1$)

$$p = p_\infty + \frac{\rho_0 \omega^2 y^2 \theta_0}{4}$$

$$u = u_\infty [1 - e^{-x/\delta}(\cos(x/\delta) + \sin(x/\delta)) - e^{-(s-x)/\delta}(\sin((s-x)/\delta) + \cos((s-x)/\delta))]$$

$$v = \frac{\omega y \theta_0}{4}(-e^{-x/\delta}\sin(x/\delta) + e^{-(s-x)/\delta}\sin((s-x)/\delta)) \quad (5)$$

$$w = \omega y\left(\frac{\theta_0}{4} + \frac{\theta}{2}\right) + \frac{\omega y \theta_0}{4}(-e^{-x/\delta}\cos(x/\delta) + e^{-(s-x)/\delta}\cos((s-x)/\delta))$$

where $\delta = (\nu/\Omega)^{1/2}$.

This solution for the velocity field inside the boundary layer is the same as in the laminar case, and the difference concerns only the swirl velocity in the rotating core.

In the rotating core, ν_t and θ satisfy a system of ordinary differential equations, with the radial coordinate y as a parameter within Γ:

$$u\frac{\partial \theta}{\partial x} = \frac{\partial}{\partial x}\left(\left(\frac{\nu_t}{Pr_t} + \frac{\nu}{Pr}\right)\frac{\partial \theta}{\partial x}\right) \quad (6)$$

$$u\frac{\partial \nu_t}{\partial x} = \left(\frac{\partial}{\partial x}(2\nu_1 + \nu)\frac{\partial}{\partial x}\nu_t\right) + \nu_t\left(0.2\alpha\Gamma - \frac{3\nu_t + 50\nu}{D^2}\right) = 0 \quad (7)$$

$$\Gamma = -\frac{\omega y}{2}\left(\frac{\partial \theta}{\partial x}\right), \quad \alpha = \frac{(\nu_t/8\nu)^2 + 1.4(\nu_t + 8\nu) + 0.2}{(\nu_t/8\nu)^2 - 1.4(\nu_t/8\nu) + 1.0}$$

According to the one-equation model, turbulence is generated in the rotating core due to presence of swirl velocity, which dominates here. On the other hand, using the relationship (5) the swirl velocity in the production term can be replaced by θ. These equations are to be matched to the solution in the boundary layers, so the boundary conditions can be prescribed as follows:

$$x = 0: \quad \nu_t = \theta = 0, \quad x = s: \nu_t = 0, \quad \theta = -\theta_m \quad (8)$$

The analysis also showed that the axial velocity in the convection term could be replaced by the constant core value (u_∞) without loss of accuracy.

The boundary-value problem (6)–(8) was solved numerically, using the procedure described by Vasiliev [21].

The analytic solution is compared with numerical data in Fig. 13. The comparison was made for a cavity with $G=0.06$, $r/R=0.097$, at $\mathrm{Re}=10^7$, $\theta_m=0.1$. The axial profiles of axial and swirl velocities and normalized temperature at the middle radius are shown in Fig. 13(*a,b,c*), respectively. In Fig. 13(*d*) the radial distribution of turbulent viscosity at $x/s=0.5$ is presented, and in Fig. 13(*e*) the distributions of Nusselt number along the hot and cold walls are plotted. The local Nusselt number was defined as $\mathrm{Nu}_r = \mathrm{Rq}/(\mathrm{Thot}-\mathrm{Tcold}))/\lambda$, where q is local heat flux.

This comparison shows that far from the shrouds the two solutions are in very good agreement. For the case considered, the influence of the shrouds extends from the lower shroud up to $y/R \approx 0.3$, and from the upper shroud down to $y/R \approx 0.7$.

Conclusions

1 A one-equation turbulence model was applied to calculations of turbulent rotating flows. It was shown that for sealed rotor-stator cavities of rectangular cross-section the results of the calculations are in rather good agreement with known experimental data. In the cases considered, the one-equation ν_t model gives an accuracy compatible with Morse's k-ε model.

2 The flow in a cavity with axial clearance, but without through-flow, was also studied. The influence of the external stream was simulated by the variation of swirl velocity in the clearance. The reduction in moment coefficient due to the increase of external swirl was evaluated.

3 The results of calculations for contrarotating disks are in good agreement with experiment for fully-turbulent flows (high Reynolds number) and in reasonable agreement for transitional flows (lower Reynolds number).

4 The heat fluxes in buoyancy-driven rotating flows are underestimated; this could be explained by possible 3-D structure of the real flow, which was not taken into account in the present calculations.

5 The one-equation model has an analytic solution for buoyancy driven turbulent rotating flow in sealed cavity.

Acknowledgment

The author would like to acknowledge Prof. A. N. Secundov (CIAM, Moscow) for helpful discussions.

Nomenclature

A,B,S = vector columns
C_f = skin friction coefficient
C_M = moment coefficient
D = minimal distance to the wall (in turbulence model equation)
f = scalar parameter
G = cavity gap ratio
g = clearance width
J = Jacobian
Nu = Nusselt number
n = distance normal to the wall.
p = pressure
Q = fluxes in scalar equations

q = heat flux
R,r = radii
Ra = Rayleigh number
$\mathrm{Re}=\Omega R^2/\nu$ = Reynolds number
s = cavity gap
T = temperature
u,v,w = axial, radial, and swirl velocities
We = core swirl
x,y = axial and radial coordinates
β = volume expansion coefficient
δ = boundary layer thickness
Γ = disk speed ratio
λ = thermal conductivity
ν_{eff} = effective viscosity
ν = laminar viscosity
ν_t = turbulent viscosity
ξ,η = generalized coordinates
$\theta=\beta\Delta T$ = normalized temperature
ρ_0 = density, assumed constant
σ_t,σ = coefficients in scalar equations
τ = viscous stresses
Ψ = stream function
Ω = angular speed of rotation

References

[1] Dorfman, L. A., 1963, *Hydrodynamic Resistance and the Heat Loss of Rotating Solids*, Oliver and Boyd, Edinburgh.

[2] Owen, J. M., and Rogers, R. H., 1989, Flow and Heat Transfer in Rotating-Disc Systems, Vol. 1: Rotor-Stator Systems, Research Studies Press Ltd., Taunton, England, and Wiley, New York.

[3] Owen, J. M., and Rogers, R. H., 1995, ''Flow and Heat Transfer in Rotating Disc Systems, Vol. 2: Rotating Cavities,'' Research Studies Press Ltd., Taunton, England, and Wiley, New York.

[4] Owen, J. M., and Wilson, M., 1995, ''Heat Transfer and Cooling in Gas Turbines, Rotating Cavities and Disc Heat Transfer,'' Von Karman Institute for Fluid Dynamics, Lecture Series 1995-05.

[5] Stow, P., and Coupland, J., 1993, ''Turbulence Modelling for Turbomachinery Flows,'' 2nd International Symposium on Engineering Turbulence Modelling and Measurements, Florence, 31 May–2 June, p. 30.

[6] Launder, B. E. and Sharma, B. I., 1974, ''Application of the Energy Dissipation Model of Turbulence to Flow Near Spinning Disc,'' Lett. Heat Mass Transfer, **1**, pp. 131–138.

[7] Morse, A. P., 1991, ''Application of a Low Reynolds Number k-ε Turbulence Model to High Speed Rotating Cavity Flows,'' ASME J. Turbomach., **113**, pp. 98–105.

[8] Iacovides, H. and Theofanopoulos, I. P., 1991, ''Turbulence Modelling of Axisymmetric Flow inside Rotating Cavities,'' Int. J. Heat Fluid Flow, **12**, pp. 2–11.

[9] Virr, G. P., Chew, J. W., and Coupland, J., 1993, ''Application of Computational Fluid Dynamics to Turbine Disc Cavities,'' ASME-paper 93-GT-89.

[10] Spalart, P. R., and Allmaras, S. R., 1992, ''A One-Equation Turbulence Models for Aerodynamic Flows,'' AIAA paper 92-0439.

[11] Secundov, A. N., 1971, ''Application of a Differential Equation for Turbulent Viscosity to the Analysis of Plane Non-Self-Similar Flows,'' Fluid Dyn., No. 5, pp. 528–840.

[12] Gulyaev, A. N., Kozlov, V. Ye., and Secundov, A. N., 1993, ''A Universal One-Equation Model for Turbulent Viscosity,'' Fluid Dyn., No. 4, pp. 485–494.

[13] Bradshaw, P., Launder, B., and Lumley, J., 1991, ''Collaborative Testing of Turbulence Models,'' AIAA paper 91-0215.

[14] Vasiliev, V. I., Volkov, D. V., Zaitsev, S. A., and Lyubimov, D. A., 1997, ''Numerical Simulation of Channel Flows by One-Equation Turbulence Model,'' ASME J. Fluids Eng., **119**, pp. 885–892.

[15] Kazarin, F. V., Secundov A. N., Vasiliev I. V., Zaitsev, S. A., 1997, ''On the Bypass Transition Prediction by One-Equation Turbulence Model,'' 2nd International Symposium on Turbulence, Heat and Mass Transfer. Delft, Niezerland, June.

[16] Daily, J. W. and Nece, R. E., 1960, ''Chamber Dimension Effects on Induced Flow and Frictional Resistance of Enclosed Rotating Disks,'' ASME J. Basic Eng., **82**, pp. 217–232.

[17] Kilic, M., Gan, X., Owen, J. M., 1994, ''Transitional Flow Between Contra-rotating Disks,'' J. Fluid Mech., **281**, pp. 119–135.

[18] Kilic, M., Gan, X., and Owen, J. M., 1996, ''Turbulent Flow Between Two Disks Contrarotating at Different Speeds,'' ASME J. Turbomach., **118**, pp. 408–413.

[19] Schukin, V. K. and Olimpiev, V. V., 1976, ''Experimental Investigation of Heat Transfer in Closed Rotating Cavity,'' Ingenerno-Phyzichesky Zurnal, **30**, No. 4, pp. 613–618.

[20] Homsy, G. M. and Hudson, J. L., 1969, ''Centrifugally Driven Thermal Convection in Rotating Cylinder,'' J. Fluid Mech., **35**, pp. 33–52.

[21] Vasiliev, V. I., 1994, ''Computation of Separated Duct Flows Using the Boundary-Layer Equations,'' AIAA J., **32**, No. 6, pp. 1191–1199.

Modeling of Flow Transition Using an Intermittency Transport Equation

Y. B. Suzen
Postdoctoral Research Associate

P. G. Huang
Associate Professor

Department of Mechanical Engineering,
521 CRMS Building,
University of Kentucky,
Lexington, KY 40506-0108

A new transport equation for intermittency factor is proposed to model transitional flows. The intermittent behavior of the transitional flows is incorporated into the computations by modifying the eddy viscosity, μ_t, obtainable from a turbulence model, with the intermittency factor, γ: $\mu_t^* = \gamma\mu_t$. In this paper, Menter's SST model is employed to compute μ_t and other turbulent quantities. The proposed intermittency transport equation can be considered as a blending of two models—Steelant and Dick and Cho and Chung. The former was proposed for near-wall flows and was designed to reproduce the streamwise variation of the intermittency factor in the transition zone following Dhawan and Narasimha correlation and the latter was proposed for free shear flows and a realistic cross-stream variation of the intermittency profile was reproduced. The new model was used to predict the T3 series experiments assembled by Savill including flows with different freestream turbulence intensities and two pressure-gradient cases. For all test cases good agreements between the computed results and the experimental data were observed. [S0098-2202(00)02302-6]

1 Introduction

To a large extent, flows in low-pressure turbine applications are transitional, and the behavior of the flow transition is strongly affected by the freestream turbulence level and pressure gradients in the turbine blade passage. In order to predict the losses and heat transfer one must be able to predict accurately the boundary-layer development and its interactions with flow transition and separation.

Although a lot of work has been reported on improving the accuracy of the CFD tools in engineering predictions, specially in the turbulence modeling areas, CFD prediction of transitional flows still remains an almost untouched territory, as compared with other areas of CFD developments. A common way to simulate laminar to turbulent transition in computations is to switch on the turbulence model (or turbulent eddy viscosity) at an experimentally predetermined transition location. This method is ad hoc and ignores the transition physics and the importance of the transitional zone completely. Especially for flows where the transitional region covers a large portion of the flowfield, as observed in many low-pressure turbine experiments, this practice can lead to severe errors in the solution.

Another method of predicting transitional flows is to make use of the low-Reynolds-number turbulence models. The use of current low-Reynolds-number turbulence models for the prediction of bypass transition induced by freestream turbulence was investigated by Savill [1,2] and Westin and Henkes [3]. They tested a large variety of turbulence models and compared models' performances in predicting a few of T3-series transition flow experiments. They showed that no model could predict both transition location and length for a range of flow conditions and concluded that the existing models were inadequate to predict flow transition.

An alternative to this approach is to use the concept of intermittency to blend the flow from the laminar to the turbulent regions. This approach, although highly empirical, has shown some successes in predicting transition behavior. Dhawan and Narasimha [4] correlated the experimental data and proposed a generalized intermittency distribution function across flow transition. The correlation was later improved by Gostelow et al. [5] for flows with pressure gradients subject to a range of freestream turbulence intensities.

Solomon et al. [6], following the work of Chen and Thyson [7], developed an improved method to predict transitional flows involving changes in pressure gradients. In this model, the effects of changing streamwise pressure gradient on the breakdown physics and spot spreading rates were taken into account. This is accomplished by varying the spot spreading angle and propagation parameter through the transition zone according to the local pressure gradient parameter.

Steelant and Dick [8] proposed a transport equation for intermittency, in which the source term of the equation was developed such that the γ distribution of Dhawan and Narasimha [4] across the transition region could be reproduced. Steelant and Dick used their model, coupled with two sets of conditioned Navier-Stokes equations, to predict transitional flows with zero, favorable, and adverse pressure gradients. However, since their technique involved the solution of two sets of strongly coupled equations, the method is not compatible with existing CFD codes, in which only one set of Navier-Stokes equations is involved. Moreover, the model was designed to provide a realistic streamwise γ behavior but with no consideration of the variation of γ in the crossstream direction.

Cho and Chung [9] developed a $k-\epsilon-\gamma$ turbulence model for free shear flows. Their turbulence model explicitly incorporated the intermittency effect into the conventional $k-\epsilon$ model equations by introducing an additional transport equation for γ. They applied this model to compute a plane jet, a round jet, a plane far wake, and a plane mixing layer with good agreements. Although this method was not designed to reproduce flow transition it provided a realistic profile of γ in the crossstream direction.

In the current paper, a new transport equation for intermittency factor is proposed. The main motivation in the development of the new model is to combine the best features of the existing transition models in the proposed model. The model not only can reproduce the intermittency distribution of Dhawan and Narasimha in the streamwise direction but also is able to provide a realistic variation of γ in the crossstream direction. Our aim is to design a model that will predict flow transition under the influences of freestream turbulence and pressure gradients.

A review of a number of transition models is given in Section

Contributed by the Fluids Engineering Division for publication in the JOURNAL OF FLUIDS ENGINEERING. Manuscript received by the Fluids Engineering Division April 29, 1999; revised manuscript received February 8, 2000. Associated Technical Editor: P. Bradshaw.

2. In Section 3, the new model, combining the best features of the models discussed in Section 2, is proposed. Section 4 discusses the numerical issues regarding the implementation of the current method in the existing CFD codes, including our choice of the correlations to predict the onset of the transition under the influences of freestream turbulence and pressure gradients. Section 5 shows the comparisons of the new transition model against T3 series experiments of Savill [1,2] and the predictions of k–ϵ model of Launder and Sharma [10], k–ω model of Wilcox [11], and SST of Menter [12]. Concluding remarks are provided in Section 6.

2 Transition Models

2.1 Dhawan and Narasimha. Dhawan and Narasimha [4] correlated a range of experimental data and provided the following expression for streamwise intermittency distribution

$$\gamma=\begin{cases}1-\exp[-(x-x_t)^2 n\sigma/U] & (x\geqslant x_t)\\ 0 & (x<x_t)\end{cases} \tag{1}$$

where U is the freestream velocity at onset of transition; x_t is the point of transition onset; n is the spot formation rate and σ is the spot propagation parameter.

There are two ways to express Eq. (1) in dimensionless form: one way, as given by Narasimha [13], is to express Eq. (1) in terms of a nondimensional breakdown parameter, $N=n\sigma\theta_t^3/\nu$, where θ_t is the momentum-thickness at the onset point of transition, $x=x_t$, and ν is the kinematic viscosity; and the other way is in terms of dimensionless spot formation rate, $\hat{n}=n\nu^2/U^3$, as used by Mayle [14]. Hence, the first part of Eq. (1) can be written either as

$$\gamma=1-\exp\left[-\left(\frac{x-x_t}{\theta_t}\right)^2\frac{N}{\mathrm{Re}_{\theta_t}}\right] \tag{2}$$

or

$$\gamma=1-\exp\left[-\left(\frac{x-x_t}{\theta_t}\right)^2\hat{n}\sigma\,\mathrm{Re}_{\theta_t}^2\right] \tag{3}$$

Gostelow et al. [5] conducted measurements of boundary layer transition for six different turbulence levels and a wide range of pressure gradients and correlated the nondimensional breakdown parameter N as

$$N=\begin{cases}0.86\times10^{-3}\exp[2.134\lambda_\theta\ln(\mathrm{Tu})-59.23\lambda_\theta-0.564\ln(\mathrm{Tu})] & \lambda_\theta\leqslant 0\\ 0.86\times10^{-3}\exp[-0.564\ln(\mathrm{Tu})] & \lambda_\theta>0\end{cases} \tag{4}$$

where the pressure gradient parameter, $\lambda_\theta\equiv(\theta^2/\nu)(dU/dx)$, and the freestream turbulence intensity, Tu, were evaluated at the onset point of transition.

In contrast, for zero-pressure-gradient flows, Mayle [14] correlated the spot production rate using intermittency measurements as

$$\hat{n}\sigma=1.25\times10^{-11}\,\mathrm{Tu}^{7/4} \tag{5}$$

The constant in Eq. (5) may vary slightly depending on the choice of the data; Mayle also reported a value of 1.5×10^{-11} in the same paper. When subject to pressure gradients, Mayle [14] normalized $\hat{n}\sigma$ by its value at zero-pressure-gradient, $(\hat{n}\sigma)_{\mathrm{ZPG}}$, and showed a plot of $\hat{n}\sigma/(\hat{n}\sigma)_{\mathrm{ZPG}}$ versus the acceleration parameter, $K=(\nu/U^2)(dU/dx)$ over a wide range of freestream intensity, Tu. Steelant and Dick [8] proposed the following correlation to fit Mayle's data

$$\frac{\hat{n}\sigma}{(\hat{n}\sigma)_{\mathrm{ZPG}}}=\begin{cases}(474\ \mathrm{Tu}^{-2.9})^{1-\exp(2\times10^6 K)}, & K<0\\ 10^{-3227K^{0.5985}}, & K>0\end{cases} \tag{6}$$

where K and Tu were evaluated at transition onset.

A comparison of Eqs. (2) and (3) indicates that

$$N=\hat{n}\sigma\,\mathrm{Re}_{\theta_t}^3 \tag{7}$$

If both Gostelow et al. [5] and Mayle [14] used the same data to correlate their dimensionless quantities, N and $\hat{n}\sigma$, respectively, an equation for the Reynolds number at the onset of transition can be identified. For example, for a zero-pressure-gradient case, Gostelow et al.'s [5] correlation, Eq. (4), gives

$$N=0.86\times10^{-3}\ \mathrm{Tu}^{-0.564} \tag{8}$$

Substituting Eqs. (8) and (5) into Eq. (7), yields

$$\mathrm{Re}_{\theta_t}=410\ \mathrm{Tu}^{-0.771} \tag{9}$$

Since Eq. (9) is different from Mayle's correlation (Mayle [14])

$$\mathrm{Re}_{\theta_t}=400\ \mathrm{Tu}^{-0.625} \tag{10}$$

nor does it resemble the well-known Abu-Ghannam and Shaw correlation for zero-pressure-gradient flows (Abu-Ghannam and Shaw [15])

$$\mathrm{Re}_{\theta_t}=163+\exp(6.91-\mathrm{Tu}) \tag{11}$$

the two correlations, Eqs. (5) and (8), are not identical. We concluded that the choice of the transition correlations using either N or $\hat{n}\sigma$ must be tested in company with a proper choice of the correlations for the onset of transition.

2.2 Steelant and Dick. Steelant and Dick [8] developed a transport model for intermittency to be used in conjunction with conditioned Navier-Stokes equations. They derived a model equation starting from the intermittency distribution of Dhawan and Narasimha [4]. Differentiating Eq. (1) along the streamline direction, s, they arrived at the following transport equation

$$\frac{\partial\rho\gamma}{\partial\tau}+\frac{\partial\rho u\gamma}{\partial x}+\frac{\partial\rho v\gamma}{\partial y}=(1-\gamma)\rho\sqrt{u^2+v^2}\beta(s) \tag{12}$$

with

$$\beta(s)=2\,f(s)f'(s) \tag{13}$$

The function $\beta(s)$ represents the $(n\sigma/U)(x-x_t)$ term in Eq. (1). The function $f(s)$ was formulated to account for distributed-breakdown and was given as

$$f(s)=\frac{as'^4+bs'^3+cs'^2+ds'+e}{gs'^3+h} \tag{14}$$

where the coefficients were

$$a=\sqrt{\frac{n\sigma}{U}}\quad b=-0.4906\quad c=0.204\left(\frac{n\sigma}{U}\right)^{-0.5}$$

$$d=0.0\quad e=0.04444\left(\frac{n\sigma}{U}\right)^{-1.5}\quad g=1.0\quad h=10e$$

Equations (5) and (6) were used to evaluate the value of $n\sigma$. In the above equations, U is the freestream velocity at the transition location and the streamline coordinate, s, is defined as

$$s = \int \frac{u\,dx + v\,dy}{\sqrt{u^2+v^2}} \tag{15}$$

and $s' = s - s_t$, where s_t is the transition location.

Steelant and Dick [8] tested their model in conjunction with two proposed sets of conditioned averaged Navier-Stokes equations for zero, adverse, and favorable pressure gradient flows and their results showed that the model performed well for all cases. While the intermittency transport equation reproduces the streamwise intermittency distribution of Dhawan and Narasimha, it assumes a uniform γ distribution in the cross-stream direction. This is inconsistent with the experimental observations of Klebanoff [16], Sohn and Reshotko [17], and Gostelow and Walker [18]. The results of these experiments indicate that γ should decay to zero outside the boundary layer. Klebanoff [18] proposed the following empirical formula for the variation of intermittency in the crossstream direction

$$\gamma(y) = \frac{1}{2}[1 - \mathrm{erf}(\zeta)] \tag{16}$$

with

$$\zeta = 5\left[\frac{1}{8}\left(\frac{y}{\delta^*}\right) - 0.78\right] \tag{17}$$

where δ^* is the displacement thickness. A typical variation of the intermittency-factor profiles through the transition zone for the flat plate experiment is shown in Fig. 1 (Sohn and Reshotko [17]). It is observed that the γ profiles display a peak near the wall and decay to zero near the edge of the boundary layer. The variation of the γ distribution in the crossstream direction is what we intend to mimic with our new intermittency model.

2.3 Cho and Chung. Cho and Chung [9] developed a $k-\epsilon-\gamma$ turbulence model for free shear flows. In their model the intermittency effect was incorporated into the conventional $k-\epsilon$ turbulence model equations explicitly by introducing a transport equation for the intermittency factor γ. The eddy viscosity was expressed in terms of k, ϵ, and γ: $\nu_t^* = \gamma c_\mu k^2/\epsilon$. Their intermittency equation was given as

$$u_j \frac{\partial \gamma}{\partial x_j} = D_\gamma + S_\gamma \tag{18}$$

The diffusion term, D_γ, was represented by

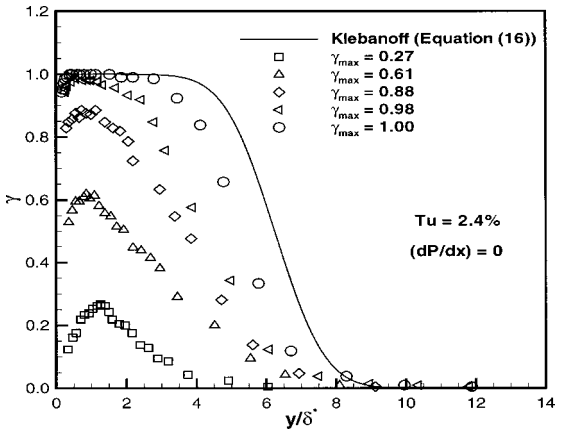

Fig. 1 Variation of γ profiles through transition (Sohn and Reshotko [17])

$$D_\gamma = \frac{\partial}{\partial x_j}\left[(1-\gamma)\frac{\nu_t}{\sigma_g}\frac{\partial \gamma}{\partial x_j}\right] \tag{19}$$

and the source term, S_γ, was

$$S_\gamma = C_{g1}\gamma(1-\gamma)\frac{P_{k,s}+P_{k,n}}{k} + C_{g2}\frac{k^2}{\epsilon}\frac{\partial \gamma}{\partial x_j}\frac{\partial \gamma}{\partial x_j} - C_{g3}\gamma(1-\gamma)\frac{\epsilon}{k}\Gamma \tag{20}$$

where

$$P_{k,s} = -\overline{u_i u_j}\frac{\partial u_i}{\partial x_j} \quad (i \neq j) \tag{21}$$

$$P_{k,n} = -\overline{u_i u_j}\frac{\partial u_i}{\partial x_j} \quad (i = j) \tag{22}$$

and

$$\Gamma = \frac{k^{5/2}}{\epsilon^2}\frac{u_i}{(u_k u_k)^{1/2}}\frac{\partial u_i}{\partial x_j}\frac{\partial \gamma}{\partial x_j}. \tag{23}$$

The modeling constants were

$$\sigma_g = 1.0 \quad C_{g1} = 1.6 \quad C_{g2} = 0.15 \quad C_{g3} = 0.16$$

Cho and Chung [9] tested their model for a plane jet, a round jet, a plane far wake, and a plane mixing layer and showed improved model performance. Although the model did indeed produce a very realistic γ profile for turbulent free shear flows, it was not designed to predict flow transition to turbulence.

3 New Transport Model for the Intermittency

A new transport equation for intermittency is proposed. The main objective of the new model is to reproduce the intermittency distribution of Dhawan and Narasimha in the streamwise direction and at the same time to provide a realistic variation of the intermittency in the cross-stream direction. In order to accomplish this, a transport model for intermittency, blending Steelant and Dick's and Cho and Chung's models, is proposed.

The production term for the new model is a mix of the generation terms of Steelant and Dick and of Cho and Chung. The first term, T_0, is from Steelant and Dick, aiming to reproduce the intermittency distribution of Dhawan and Narasimha. The formula for T_0 is given by

$$T_0 = C_0 \rho \sqrt{u_k u_k}\beta(s) \tag{24}$$

where

$$\beta(s) = 2\,f(s)f'(s) \tag{25}$$

The distributed-breakdown function $f(s)$ used in the new model has the same form as Steelant and Dick's model

$$f(s) = \frac{as'^4 + bs'^3 + cs'^2 + ds' + e}{gs'^3 + h} \tag{26}$$

where the coefficients are

$$a = 50\sqrt{\frac{n\sigma}{U}} \quad b = -0.4906 \quad c = 0.204\left(\frac{n\sigma}{U}\right)^{-0.5}$$

$$d = 0.0 \quad e = 0.04444\left(\frac{n\sigma}{U}\right)^{-1.5} \quad h = 10e \quad g = 50 \tag{27}$$

These coefficients are the same as those used in Steelant and Dick's model except for coefficients a and g. Steelant and Dick's coefficients were calibrated with conditioned Navier-Stokes equations and when used with the current approach they gave rise to excessively long regions of distributed breakdown and hence had a tendency to delay the onset of flow transition (Suzen and Huang [19]). Since the current approach does not use the conditioned Navier-Stokes equations, the adjustment of a and g coefficients is needed to have a shorter distance for the distributed breakdown

and hence to enable a faster response of the mean flow solutions to the intermittent effects (Suzen and Huang [19]).

Two major production terms from Cho and Chung's model are T_1 and T_2. These two terms are combined in the form (T_1-T_2) in the current model. The term T_1 mimics the production of turbulent kinetic energy, P_k, and is given by

$$T_1=C_1\gamma\frac{P_k}{k}=\frac{C_1\gamma}{k}\tau_{ij}\frac{\partial u_i}{\partial x_j} \tag{28}$$

with the shear stresses defined as

$$\tau_{ij}=\mu_t\left[\frac{\partial u_i}{\partial x_j}+\frac{\partial u_j}{\partial x_i}-\frac{2}{3}\frac{\partial u_k}{\partial x_k}\delta_{ij}\right]-\frac{2}{3}\rho k\delta_{ij} \tag{29}$$

The term T_2 represents the production resulting from the interaction between the mean velocity and the intermittency field and is given by

$$T_2=C_2\gamma\rho\frac{k^{3/2}}{\epsilon}\frac{u_i}{(u_ku_k)^{1/2}}\frac{\partial u_i}{\partial x_j}\frac{\partial\gamma}{\partial x_j} \tag{30}$$

The production terms T_0 and (T_1-T_2) are blended by using a function F to facilitate a gradual switching from Steelant and Dick's T_0 to Cho and Chung's (T_1-T_2) inside the transition region

$$P_\gamma=(1-F)T_0+F(T_1-T_2) \tag{31}$$

A nondimensional parameter, $k/S\nu$, is chosen to correlate the blending function F, where k is the turbulent kinetic energy and S is the magnitude of the strain rate. This parameter increases rapidly with distance away from the wall inside the transition region. Using the solution obtained by Dhawan and Narasimha's model coupled with artificial crossstream profiles provided by Klebanoff's formula, Eq. (16), one may divide the transition zone into two regions by arbitrarily selecting a diagonal cut between the point at the edge of the boundary layer located at the beginning of transition ($\gamma=0$) to the point at the wall located at the end of transition region ($\gamma=1$). The relation between γ and $(k/S\nu)$ along this diagonal line is then approximated by the following correlation

$$k/S\nu=200(1-\gamma^{0.1})^{0.3} \tag{32}$$

This line corresponds to the border between the Steelant and Dick and the Cho and Chung models: i.e., below this line, T_0 is active and above this line (T_1-T_2) is active. In order to facilitate a gradual switching from T_0 to (T_1-T_2), the following blending function is proposed

$$F=\tanh^4\left[\frac{k/S\nu}{200(1-\gamma^{0.1})^{0.3}}\right] \tag{33}$$

As can be seen from Eq. (33), when $k/S\nu\gg200(1-\gamma^{0.1})^{0.3}$ (a position above the cutoff line), $F=1$ and the model switches to Cho and Chung's model; when $k/S\nu\ll200(1-\gamma^{0.1})^{0.3}$ (a position below the cutoff line), $F=0$ and the model becomes Steelant and Dick's model. In the fully-developed turbulent-flow region, the model switches to the Cho and Chung's model except for the very thin region close the wall.

In Fig. 2, the proposed correlation for the cutoff line, Eq. (32), is compared with data extracted along the cutoff line, defined by drawing a straight line between the point at the edge of the boundary layer located at the beginning of transition to the point at the wall located at the end of transition region, of the T3A solution obtained using the proposed transition model. As can be seen from the figure, the definition of the cutoff line proposed in Eq. (32) is satisfactory.

An additional diffusion-related production term is introduced by Cho and Chung as

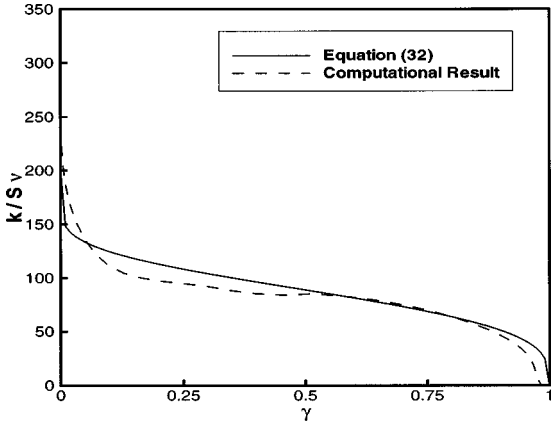

Fig. 2 Blending parameter

$$T_3=C_3\rho\frac{k^2}{\epsilon}\frac{\partial\gamma}{\partial x_j}\frac{\partial\gamma}{\partial x_j} \tag{34}$$

This term is kept active over the entire flowfield, that is, no blending is applied to this term.

Diffusion of γ is represented by the following expression

$$D_\gamma=\frac{\partial}{\partial x_j}\left\{[(1-\gamma)\gamma\sigma_{\gamma_l}\mu+(1-\gamma)\sigma_{\gamma_t}\mu_t]\frac{\partial\gamma}{\partial x_j}\right\} \tag{35}$$

The final form of the model is

$$\frac{\partial\rho\gamma}{\partial t}+\frac{\partial\rho u_j\gamma}{\partial x_j}=(1-\gamma)[(1-F)T_0+F(T_1-T_2)]+T_3+D_\gamma \tag{36}$$

or

$$\begin{aligned}\frac{\partial\rho\gamma}{\partial t}+\frac{\partial\rho u_j\gamma}{\partial x_j}=(1-\gamma)\Bigg[&(1-F)C_0\rho\sqrt{u_ku_k}\beta(s)\\&+F\left(\frac{C_1\gamma}{k}\tau_{ij}\frac{\partial u_i}{\partial x_j}-C_2\gamma\rho\frac{k^{3/2}}{\epsilon}\frac{u_i}{(u_ku_k)^{1/2}}\frac{\partial u_i}{\partial x_j}\frac{\partial\gamma}{\partial x_j}\right)\Bigg]\\&+C_3\rho\frac{k^2}{\epsilon}\frac{\partial\gamma}{\partial x_j}\frac{\partial\gamma}{\partial x_j}+\frac{\partial}{\partial x_j}\Bigg(((1-\gamma)\gamma\sigma_{\gamma_l}\mu\\&+(1-\gamma)\sigma_{\gamma_t}\mu_t)\frac{\partial\gamma}{\partial x_j}\Bigg)\end{aligned} \tag{37}$$

where the modeling constants are,

$$\sigma_{\gamma_l}=\sigma_{\gamma_t}=1.0\quad C_0=1.0\quad C_1=1.6\quad C_2=0.16\quad C_3=0.15$$

Initially γ is set to zero throughout the flowfield. On solid wall boundaries the value of γ is kept as zero; at the freestream, a zero gradient of γ is assumed and on outflow boundaries γ is extrapolated from inside the domain to the outer boundaries.

4 Implementation of the Transition Model

The intermittency concept can be incorporated into the computations either by using the conditioned-average Navier-Stokes equations (Steelant and Dick [8]; Libby [20]) or simply by multiplying the eddy viscosity obtained from a turbulence model, μ_t, by the intermittency factor, γ (Simon and Stephens [21]). The major difficulty of the former method is the requirement to solve two sets of highly coupled conditioned Navier-Stokes equations. This method is computationally expensive and is not compatible with existing CFD approaches. For these reasons the latter approach is recommended in the current paper. Simon and Stephens [21] showed that by combining the two sets of conditioned Navier-Stokes equations and by making the assumption that the

Reynolds stresses in the nonturbulent part are negligible, the intermittency can be incorporated into the computations by using the eddy viscosity, μ_t^*, which is obtained by multiplying the eddy viscosity from a turbulence model, μ_t, with the intermittency factor, γ. That is, $\mu_t^* (=\gamma\mu_t)$ is used in the mean flow equations.

To allow the intermittency factor, γ, to have a full control of the transitional behavior, the turbulence model selected to solve for μ_t must enable the solution of μ_t to display fully turbulent features before the transition location. Menter's SST model (Menter [12]) has found to produce fully turbulent flow in the leading edge of the boundary layer. It is therefore recommended to be used as a baseline model to compute μ_t and other turbulent quantities in the calculations. Menter's SST model is provided in the Appendix.

The value of $n\sigma$ used in evaluating the constants given by (27) is provided by Mayle's correlation (Mayle [14]);

$$\hat{n}\sigma = 1.8\times 10^{-11}\ \mathrm{Tu}^{7/4} \tag{38}$$

where the freestream turbulence intensity, Tu, is evaluated at onset point of transition. It should be noted that a value of 1.8×10^{-11} is used in the current work to give a slightly better fit of Mayle's data. When the flows are subject to pressure gradients, the correlation of Steelant and Dick, Eq. (6), is used.

The current intermittency approach was applied in conjunction with the correlation of Suzen et al. [22] for the onset of transition;

$$\mathrm{Re}_{\theta_t} = (120 + 150\ \mathrm{Tu}^{-2/3})\coth[4(0.3 - K_t\times 10^5)] \tag{39}$$

where K_t is the minimum value of the acceleration parameter in the downstream deceleration region and Tu is the freestream turbulence intensity at onset point of transition. This correlation was found to provide a slightly better approximation than the correlation of Abu-Ghannam and Shaw [15] in favorable pressure gradients, as discussed by Suzen et al. [22].

The computations were performed with a boundary layer code which solved the mean flow, turbulence model, and intermittency equations using the second order finite volume method. In the computations, 175 grid points, expanding from the wall to the freestream, were used in the crossstream direction for all cases. The y^+ values for the first point away from the wall were kept between 0.1 and 0.15 for all cases. The solutions were obtained by using 1000 streamwise steps for all cases. This corresponds to maximum dimensionless streamwise step sizes, Δx^+, of 49, 68, 47, and 37 for cases T3A, T3B, T3C1, and T3C2, respectively. These step sizes and crossstream grid points were found satisfactory by performing a careful grid-independency check, in which the step sizes and grid spacing were both decreased by half; no effect on the solutions was found.

At the inflow, a top-hat velocity profile is prescribed. Inlet turbulent kinetic energy is fixed according to the freestream turbulence levels and the energy dissipation rate is adjusted according to the decay of the freestream turbulence, as will be illustrated in the next section.

5 Results and Discussion

The new transition model was used to predict the experimental test cases assembled by Savill [1,2]: T3A, T3B, T3C1, and T3C2. These experiments were specially selected to test the ability of turbulence models to predict the effects of freestream turbulence on the development and subsequent transition of a laminar boundary layer under zero and varying pressure gradient conditions. Cases T3A and T3B are zero-pressure-gradient flows and cases T3C1 and T3C2 are with continuous change in pressure gradient representing an aft-loaded turbine blade. Comparisons were performed for these cases with the new transition model against conventional turbulence models including the $k-\epsilon$ model of Launder and Sharma [10], $k-\omega$ model of Wilcox [11], and SST of Menter [12].

In all computations, the inlet conditions were prescribed to match the experimental decay of turbulence. In each case, the inlet turbulent kinetic energy was fixed by the experimental freestream turbulence level and the matching of the freestream turbulence decay provided an estimated value for the dissipation rate of turbulent kinetic energy, ϵ, (or the value of μ_t/μ) at the inlet.

In all cases, the onset of transition was specified according to the correlation of Suzen et al. [22], Eq. (39). For T3A, T3B, T3C1, and T3C2, the correlation gave the transition locations as $\mathrm{Re}_{\theta_t}=257$, 204, 194, and 297, respectively, while the experimental data showed $\mathrm{Re}_{\theta_t}=272$, 182, 211, and 378, respectively. The determination of the experimental onset of transition is rather arbitrary. In our calculations, we deliberately used the correlation to predict the onset of transition in order to reduce the dependency on experimental inputs.

T3A experiment of Savill [1] corresponds to a zero-pressure-gradient flow over a flat plate at $\mathrm{Re}=3.6\times 10^5$ per meter. The freestream turbulence intensity at the leading edge of the flat plate is 3.35 percent. The decay of freestream turbulence intensity was matched with the experimental data by specifying $\mu_t/\mu=7.6$ for SST model and Launder-Sharma $k-\epsilon$ model, and 8.5 for Wilcox $k-\omega$ model at the inlet, as shown in Fig. 3.

The predicted skin-friction coefficients were compared with the experimental data in Fig. 4. Menter's SST model and the $k-\omega$ model of Wilcox gave immediate transition to turbulence at the leading edge of the flat plate showing almost no laminar zone. The $k-\epsilon$ model of Launder-Sharma performed better in predicting the

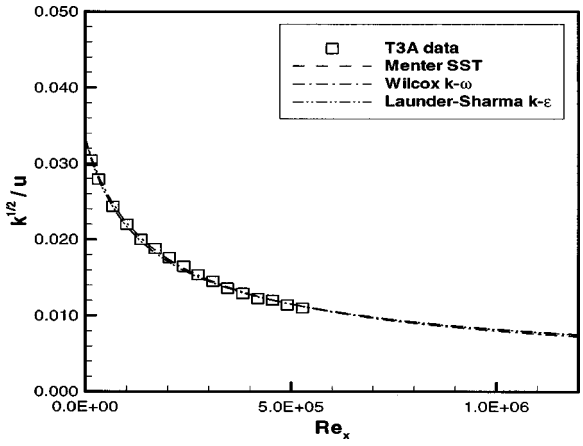

Fig. 3 Comparison of freestream turbulence intensity for T3A case

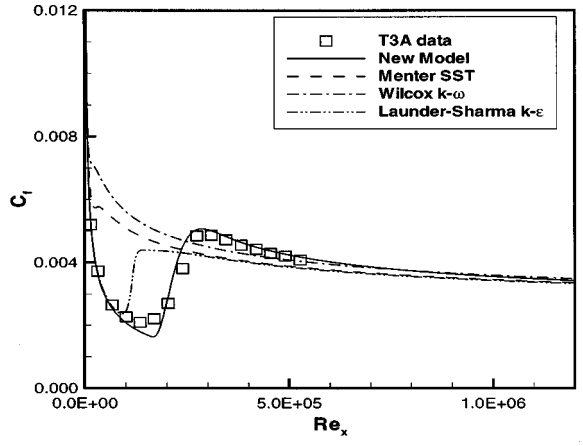

Fig. 4 Comparison of skin-friction coefficient for T3A case

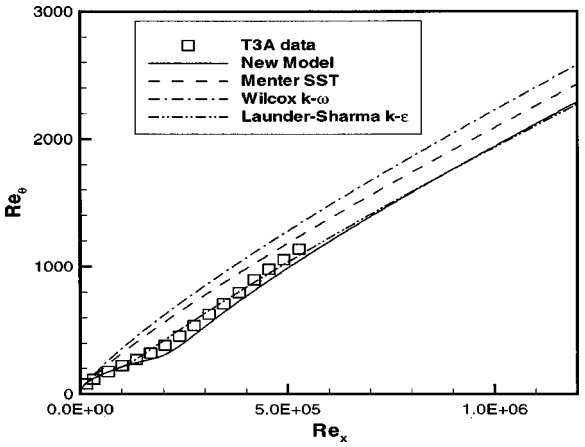

Fig. 5 Comparison of Reynolds number based on momentum-thickness for T3A case

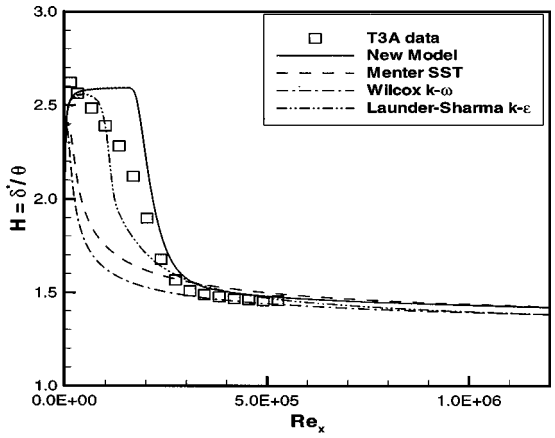

Fig. 6 Comparison of shape factor for T3A case

onset of transition but the transition to full turbulence was abrupt when compared to experimental data. In contrast, the current transition model predicted the length of the transition region well and also correctly displayed an overshoot of skin-friction coefficient, C_f, at the end of transition region.

The comparison of the Reynolds number based on momentum-thickness, Re_θ, for T3A case was shown in Fig. 5. As can be seen from this figure, the results obtained from the new model were in good agreement with the experimental data.

The predicted shape factor variations were compared with the experimental data in Fig. 6. It must be noted that the experimental data showed a premature decline of shape factor from the laminar value of 2.6 (before the onset of transition, $\mathrm{Re}_\theta \approx 270$). On the other hand, the computation with the new model showed a pure laminar flow characteristic before the transition onset point and therefore maintained a shape factor of 2.6 inside the laminar region. It should be noted that the predicted shape-factor profile obtained by the Launder-Sharma $k-\epsilon$ model appeared to match the experimental data better than that of the the current model. This is purely coincidence since these results merely reflect the

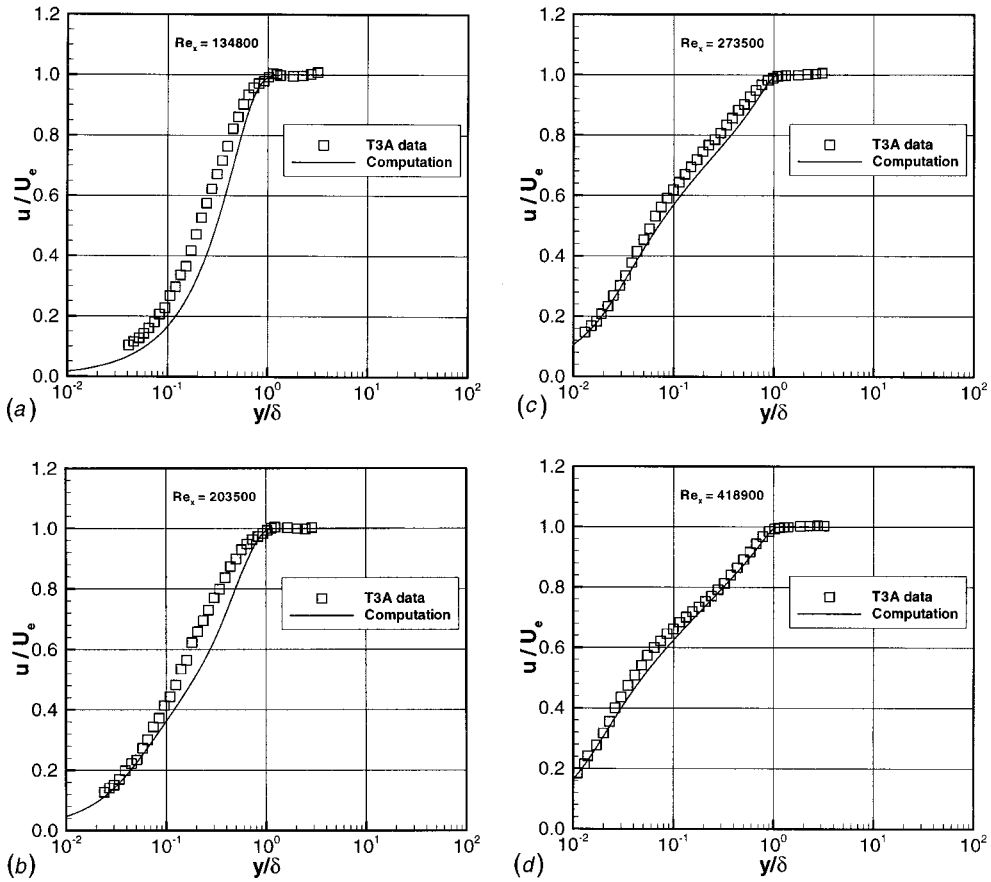

Fig. 7 Mean streamwise velocity profiles for T3A case (*a*) Re_x=134800 (*b*) Re_x=203500 (*c*) Re_x =273500 (*d*) Re_x=418900

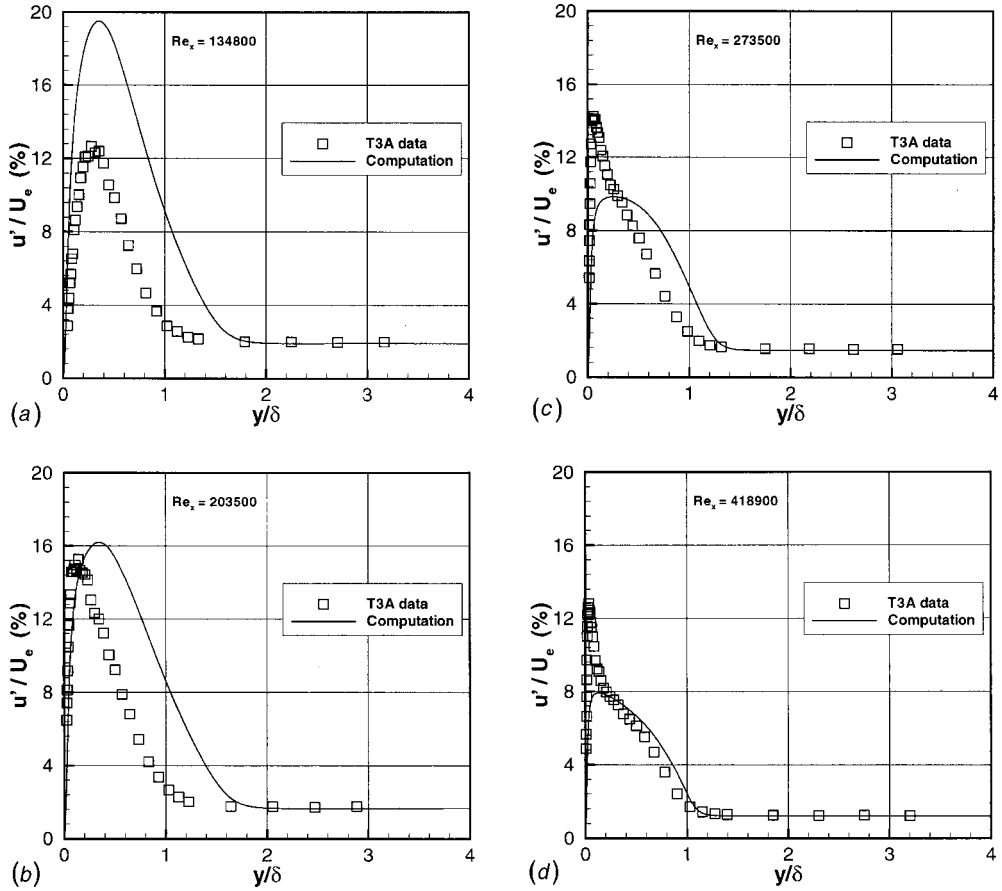

Fig. 8 Fluctuating streamwise velocity component profiles for T3A case (*a*) Re_x=134800 (*b*) Re_x=203500 (*c*) Re_x=273500 (*d*) Re_x=418900

fact that the $k-\epsilon$ model predicted an early flow transition as can be seen from Figure 4. A similar discrepancy in the comparison of the shape factor profiles was also observed by Steelant and Dick [8].

The streamwise mean velocity profiles computed with the new model were compared to the experimental data in Figs. 7(*a*)–7(*d*) at four different locations in the transition region. As can be seen from the comparisons, the computed results agreed well with the experimental data. The profiles of streamwise velocity fluctuation, u', at the same locations were also given in Figs. 8(*a*)–8(*d*). The profiles near the beginning of transition were overpredicted but the agreement improved for stations further downstream.

One of the major features of the current model is its ability to reproduce realistic cross-stream intermittency profiles. The predicted intermittency profiles at various streamwise stations inside the transition zone were shown in Fig. 9. The profiles exhibited a peak between $y/\delta^*=1$ and $y/\delta^*=2$ then dropped off toward zero near the edge of the boundary layer, around $y/\delta^*=8$. These

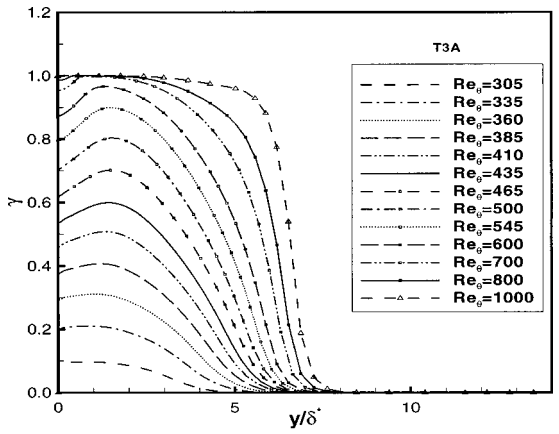

Fig. 9 Intermittency factor profiles for T3A case

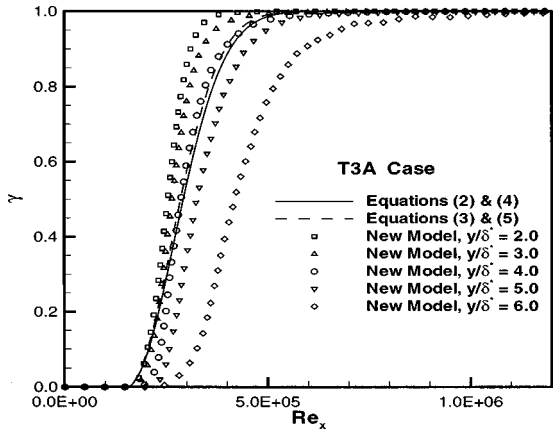

Fig. 10 Streamwise intermittency factor distribution for T3A case

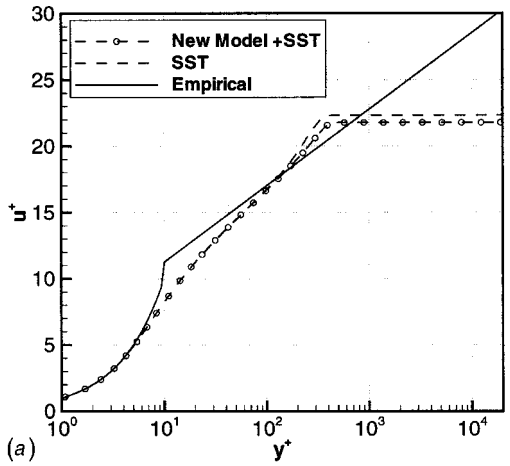

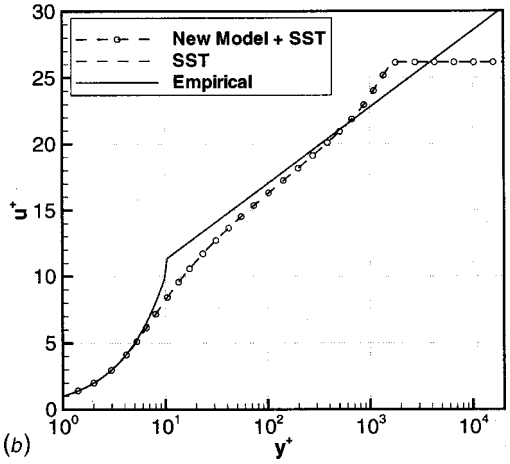

Fig. 11 Comparison of velocity profiles at two stations (*a*) comparison of velicity profiles at Re_θ=1000 (*b*) comparison of velocity profiles at Re_θ=5000

features were consistent with the trends observed in experimental data of Sohn and Reshotko [17], shown in Fig. 1, and those of Gostelow and Walker [5].

The streamwise evolution of intermittency factor for T3A case was shown in Fig. 10. In this figure, γ variations obtained by the new model at five y/δ^* locations were displayed along with the γ profiles represented by Eqs. (2) and (3). In Eq. (2), the nondimensional breakdown parameter, N, was calculated from the correlation of Gostelow et al. [5], Eq. (4), and the spot production rate $\hat{n}\sigma$ in Eq. (3) was obtained from the correlation of Mayle [14], Eq. (5). Since the new model was designed to produce crossstream γ variations as shown in Fig. 9, the streamwise variation of γ would be different depending on the crossstream location chosen to monitor the change of the γ value in the streamwise direc-

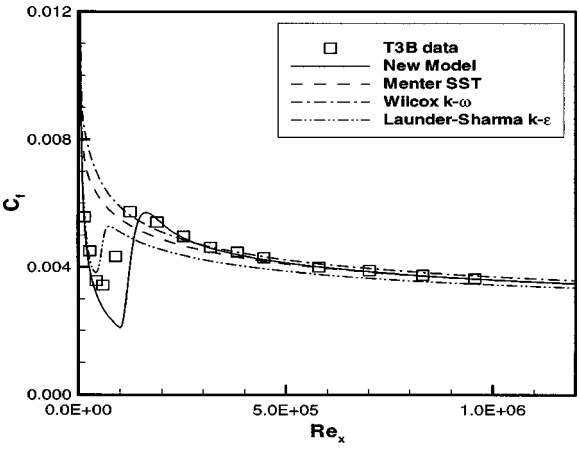

Fig. 13 Comparison of skin-friction coefficient for T3B case

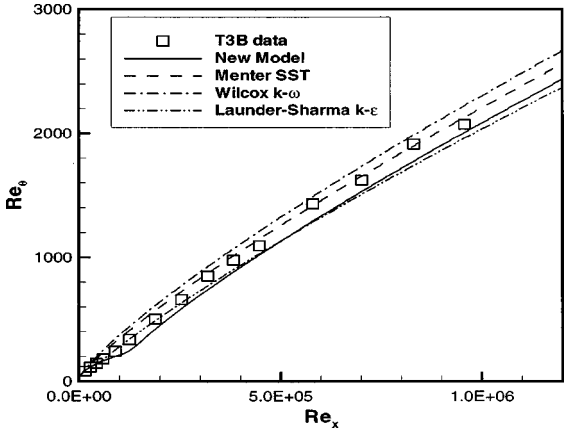

Fig. 14 Comparison of Reynolds number based on momentum-thickness for T3B case

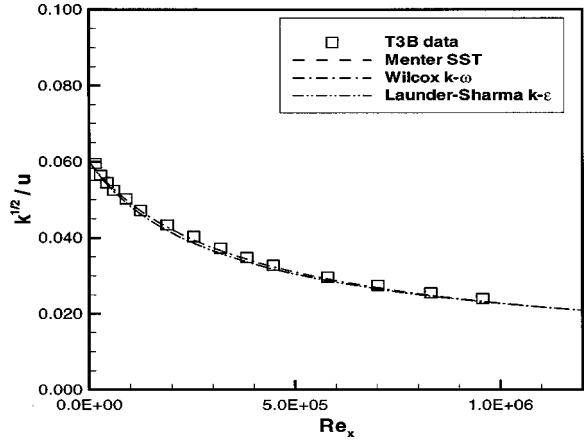

Fig. 12 Comparison of freestream turbulence intensity for T3B case

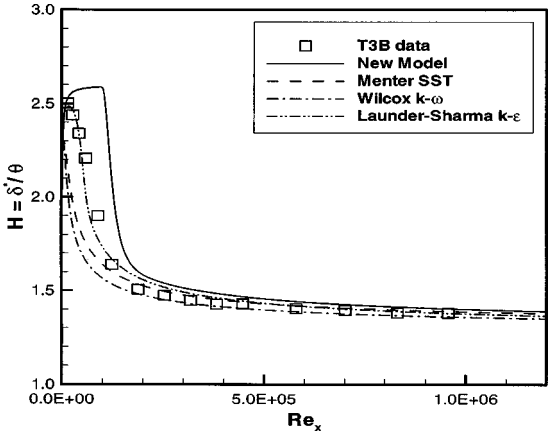

Fig. 15 Comparison of shape factor for T3B case

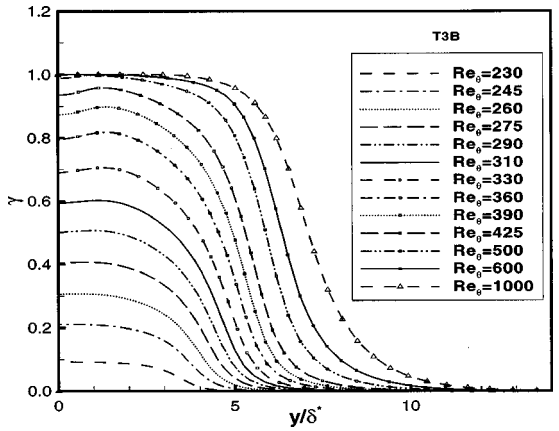

Fig. 16 Intermittency factor profiles for T3B case

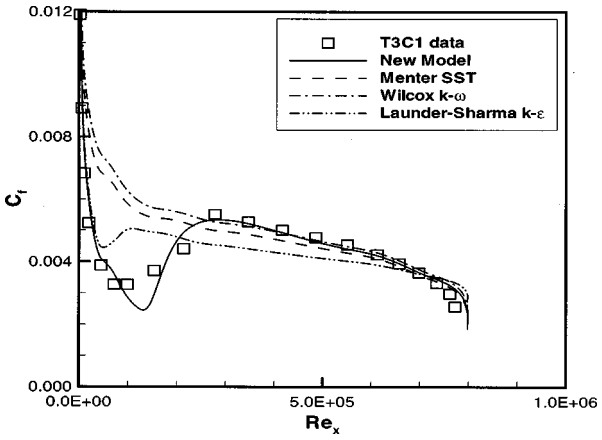

Fig. 19 Comparison of skin-friction coefficient for T3C1 case

tion. Therefore, it was not possible to represent the current γ distributions by a single curve and to make a one-to-one comparison with the correlations. In Fig. 10, the streamwise evolution of γ computed by the new model at the cross-stream locations of $y/\delta^* = 2$, 3, 4, 5, and 6 were compared with the distributions of Eq. (2) and (3). The figure showed that the intermittency distributions of the new model fall into a narrow region around the distributions of the Eqs. (2) and (3).

The current intermittency model does not affect the ability of the turbulence models in the fully developed region, as can be demonstrated in Fig. 11. In Figures 11(*a*) and 11(*b*), the velocity profiles obtained using the current intermittency model (in conjunction with the SST turbulence model) were compared with those predicted by the SST model without the intermittency modification for Re_θ=1000 and 5000, respectively. For Re_θ=1000, the velocity profiles differed slightly near the freestream, indicating the C_f value predicted by the current model was slightly larger.

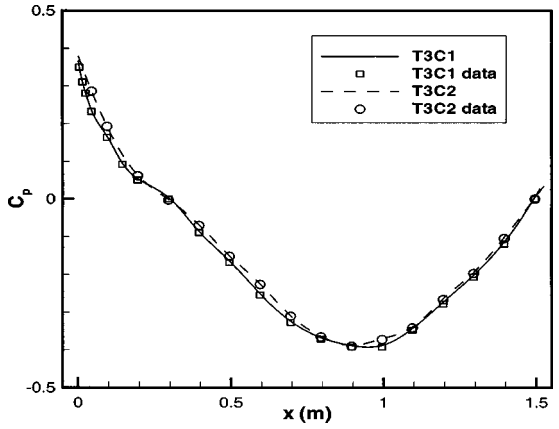

Fig. 17 Pressure coefficient distributions for T3C1 and T3C2 cases

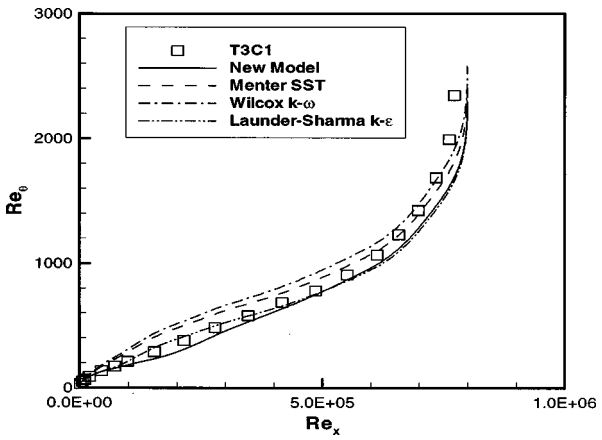

Fig. 20 Comparison of Reynolds number based on momentum-thickness for T3C1 case

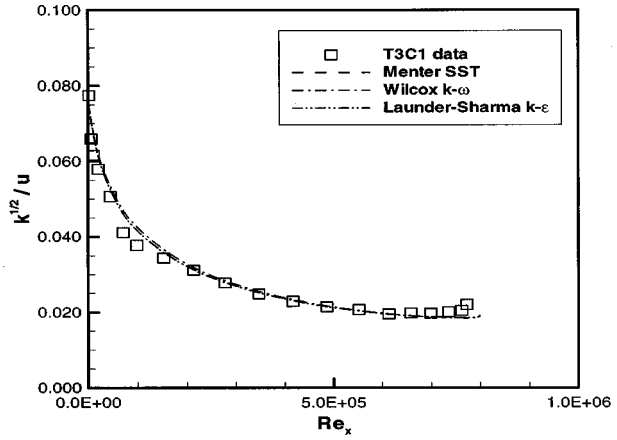

Fig. 18 Comparison of freestream turbulence intensity for T3C1 case

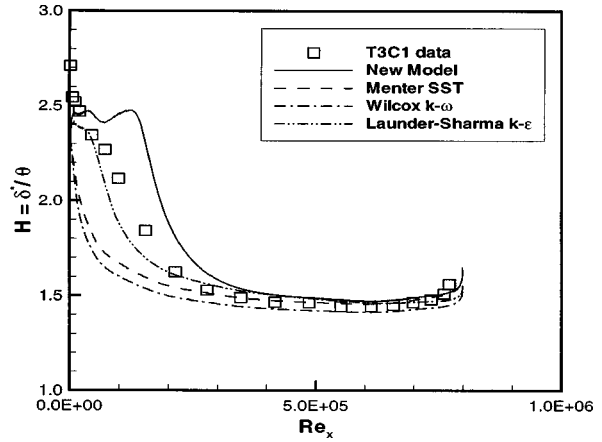

Fig. 21 Comparison of shape factor for T3C1 case

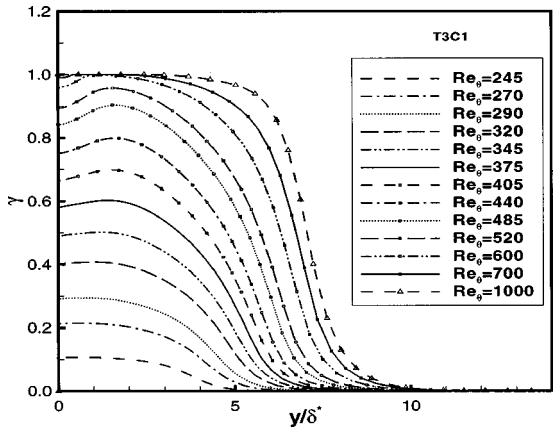

Fig. 22 Intermittency factor profiles for T3C1 case

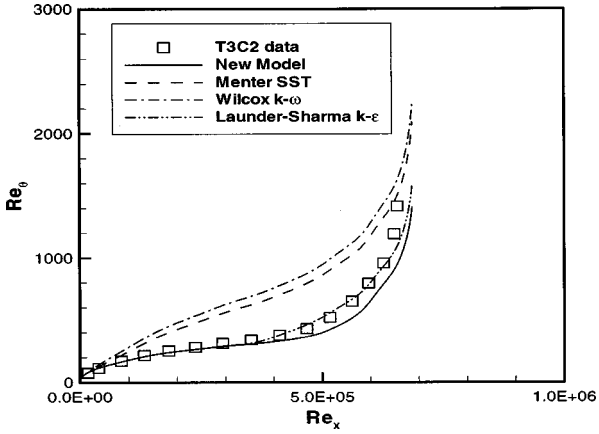

Fig. 25 Comparison of Reynolds number based on momentum-thickness for T3C2 case

This larger value of the skin friction was associated with the overshoot of the skin friction near the end of the transition region, as shown in Fig. 4. Further downstream, at $Re_\theta=5000$ the velocity profile obtained from the new model was essentially the same as the one obtained by using the SST model alone, as shown in Fig. 11(*b*). These results clearly show that the new intermittency model does not affect ''good'' solution behavior of the turbulence model in the fully developed turbulent region.

The second test case is the T3B case of Savill [2]. T3B case is also a zero-pressure-gradient flow with a freestream turbulence intensity of 6 percent at the leading edge of the flat plate. The freestream Reynolds number is 6.3×10^5 per meter. In order to match the experimental decay of free stream turbulence intensity, as shown in Fig. 12, μ_t/μ is specified as 60 for SST model and for Launder-Sharma model, and 67.1 for Wilcox $k-\omega$ model at the inlet.

Figure 13 shows a comparison of the skin-friction coefficients. Menter's SST model and the $k-\omega$ model of Wilcox showed immediate transition to turbulence at the leading edge. The $k-\epsilon$

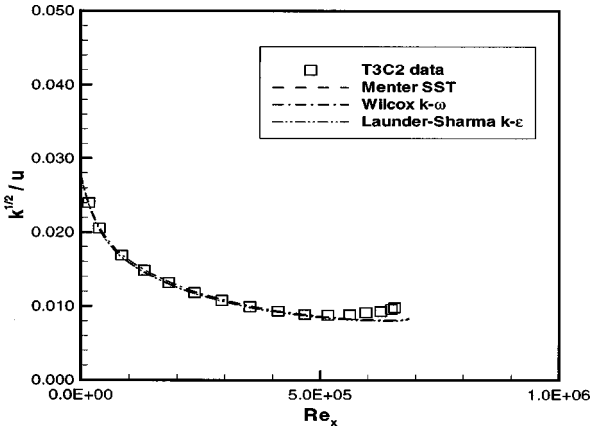

Fig. 23 Comparison of freestream turbulence intensity for T3C2 case

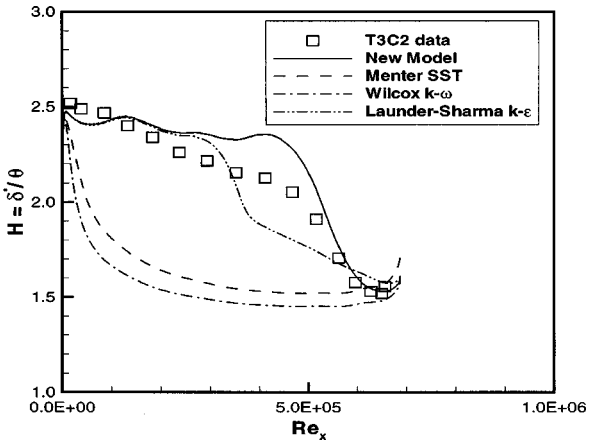

Fig. 26 Comparison of shape factor for T3C2 case

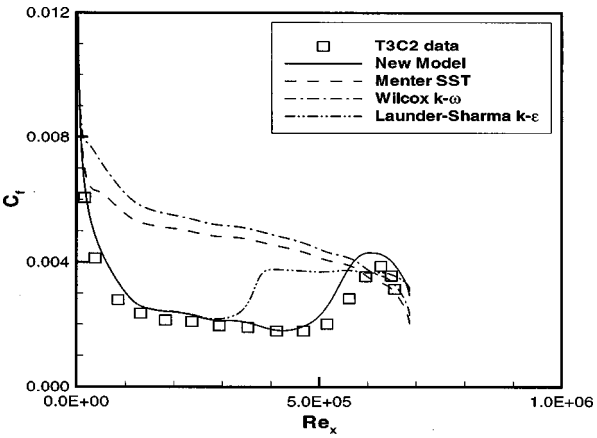

Fig. 24 Comparison of skin-friction coefficient for T3C2 case

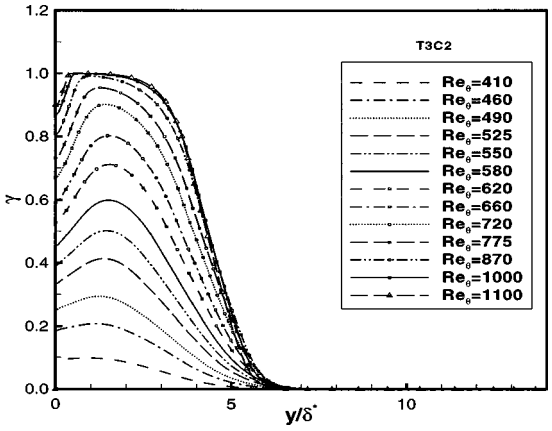

Fig. 27 Intermittency factor profiles for T3C2 case

model of Launder-Sharma also predicted a slightly early flow transition to turbulence. In contrast, the new model resulted in a slight delay of flow transition.

In Fig. 14, the momentum-thickness Reynolds numbers were compared to the experimental data. As can be seen from the results, all models compared well with the experimental data.

In Fig. 15, the predicted shape factor profiles were compared to the experimental data. Again the experimental data showed a rapid decline of shape factor before the onset point of transition and therefore the data matched the results of Launder-Sharma model quite well. On the other hand, the current model showed a delay of the flow transition and the computed results displayed a laminar flow behavior before the transition onset point.

The γ profiles from the new model at various streamwise stations through the transition zone were shown in Fig. 16. The profiles displayed the same characteristics as the T3A case, but due to high freestream turbulence intensity, the results showed that the peaks in the profiles were less pronounced for this case and the spread of the intermittency appeared to be wider across the transition region.

T3C1 and T3C2 experiments of Savill [1] were variable pressure gradient flows representing actual turbine characteristics. Both cases had similar pressure variations, as shown in Fig. 17, but with different Reynolds numbers and free stream turbulence intensities. In Fig. 17, the symbols were the experimental data points and the lines were the curve fitting to the data points. These C_p profiles were input in the boundary layer code to perform the calculations.

T3C1 case had an inlet Reynolds number of 4.1×10^5 per meter. Turbulence intensity at the leading edge of the plate was 7.78 percent and a value of $\mu_t/\mu = 30$ for SST and Launder-Sharma models, and 33.6 for Wilcox $k-\omega$ model was used at the inlet in order to match the decay of free stream turbulence intensity, as shown in Fig. 18.

A comparison of skin-friction was shown in Fig. 19 for the T3C1 case. Again, SST model and $k-\omega$ model of Wilcox showed no flow transition and remained a fully turbulent flow for the entire flow region. Launder-Sharma model predicted a too early flow transition compared to the experimental data. In contrast, the new transition model showed a fairly good comparison of the overall transition behavior.

The predicted Re_θ distributions along the flat plate were compared to experimental data in Fig. 20 for the T3C1 case. In general, the new transition model reproduced the development of the boundary layer slightly better than the conventional turbulence models.

The predicted shape factor profiles were compared to the experimental data in Fig. 21. Once again, the same discrepancy between the computed results and the experimental data observed in previous cases was also observed for this case: the experimental data showed a premature drop of shape factor while the current model maintained a laminar profile up to the onset of the transition point.

The intermittency factor profiles from the new model at various streamwise stations through the transition zone were shown in Fig. 22 for the T3C1 case. The characteristics of the profiles were similar to the T3B cases with mild peaks showing around $y/\delta^* = 1.6$ and the profiles decaying to zero around $y/\delta^* = 10$, near the edge of the boundary layer.

T3C2 case had an inlet Reynolds number of 3.5×10^5 per meter and a free stream turbulence intensity of 2.8 percent at the leading. The decay of freestream turbulence intensity was matched with the experimental data by specifying $\mu_t/\mu = 5$ for SST model and Launder-Sharma $k-\epsilon$ model, 5.6 for Wilcox $k-\omega$ model at the inlet, as shown in Fig. 23.

The predicted skin-friction coefficient distributions were compared with experimental data in Fig. 24. As in the previous cases, SST and Wilcox $k-\omega$ models showed flow transition at the leading edge without displaying any laminar behavior and Launder-Sharma model predicted too early transition onset and an abrupt transition to turbulence. On the other hand, the current transition model showed a fairly good agreement with the data.

The Reynolds number based on momentum-thickness along the flat plate was compared to experimental data in Fig. 25. Overall, both Launder-Sharma model and the current model reproduces the development of boundary layer fairly well.

Figure 26 showed the comparison of the shape factor distributions for T3C2 case. Once again, the data showed a gradual decrease of shape factor even inside the laminar region while the current model displayed a drop of shape factor only after the onset of the flow transition. This behavior seems to be consistent with what was observed in the other cases.

The intermittency factor γ profiles at various stations through the transition zone were shown in Fig. 27 for the T3C2 case. It should be noted that T3C2 had a lower freestream turbulence intensity than T3C1. As a results, the profiles showed more pronounced peaks between $y/\delta^* = 1$ and $y/\delta^* = 2$ and the spread of the intermittency was less wider across the transition zone. These features were similar to the comparison of the zero-pressure-gradient cases, T3A and T3B.

6 Concluding Remarks

A new transport equation for intermittency is developed for modeling transitional flows including influences of free stream turbulence and pressure gradients. The model can be considered as a mix of two existing models, aiming to reproduce the intermittency distribution of Dhawan and Narasimha [4] in the streamwise direction and to result in a realistic variation of intermittency in the crossstream direction.

The new model was tested against both zero-pressure-gradient and variable pressure gradient flows with different freestream turbulence intensities. The new model was used in conjunction with Menter's SST model to predict the T3A, T3B, T3C1, and T3C2 experiments assembled by Savill [1,2]. Comparisons of C_f distributions, the development of the boundary layer, and intermittency profiles were made for all cases. The new model showed a good transition behavior for all cases.

Acknowledgments

This work is supported by NASA Glenn Research Center under grant NCC3-590. The project is part of the Low Pressure Turbine Flow Physics program of NASA-Glenn. The contract monitor is Dr. David Ashpis. The authors would like to thank Prof. Peter Bradshaw of Stanford University for his review and his comments.

Nomenclature

C_p = pressure coefficient
C_f = skin friction coefficient
c_μ = turbulence model constant
K = acceleration parameter, $(\nu/U^2)(dU/ds)$
k = turbulent kinetic energy
N = non-dimensional spot breakdown rate parameter, $n\sigma\theta_t^3/\nu$
n = spot generation rate
$\hat{n}$ = dimensionless spot formation rate
P_k = production of turbulent kinetic energy
Re = Reynolds number per meter, U_{in}/ν
Re_{θ_t} = $\theta_t U_e/\nu$
s = streamline coordinate, $s = \int u\,dx + v\,dy/\sqrt{u^2+v^2}$
s' = $s - s_t$
Tu = turbulence intensity (in percent), u'/U_e
U = freestream velocity at the point of transition
U_e = local freestream velocity
U_{in} = inlet velocity
u = streamwise velocity component

u^+ = u/u_τ
u' = fluctuating streamwise velocity component
u_τ = friction velocity
v = transverse velocity component
y_n = normal distance to wall
y^+ = $y_n u_\tau/\nu$
Δx^+ = $\Delta x u_\tau/\nu$
δ = boundary layer thickness, $u/U_e=0.99$
δ^* = displacement thickness
γ = intermittency factor
θ = momentum thickness
λ_θ = pressure gradient parameter, $(\theta^2/\nu)(dU/ds)$
μ = molecular viscosity
μ_t = eddy viscosity
ν = μ/ρ
ν_t = μ_t/ρ
ρ = density
σ = spot propagation parameter

Subscripts

e = freestream
i,j,k = indices
t = onset of transition

Appendix: Menter's SST Model

Menter's SST model (Menter [12]) is based on a mix of two-equation $k-\omega$ and $k-\epsilon$ turbulence models using a blending function F_1. The model can be written as

k-equation;

$$\frac{\partial \rho k}{\partial t}+\frac{\partial \rho u_j k}{\partial x_j}=P_k-0.09\rho\omega k+\frac{\partial}{\partial x_j}\left((\mu+\sigma_k\mu_t)\frac{\partial k}{\partial x_j}\right) \quad (A1)$$

ω-equation;

$$\frac{\partial \rho \omega}{\partial t}+\frac{\partial \rho u_j \omega}{\partial x_j}=\frac{c}{\nu_t}P_k-\beta\rho\omega^2+\frac{\partial}{\partial x_j}\left((\mu+\sigma_\omega\mu_t)\frac{\partial \omega}{\partial x_j}\right)+2\rho(1-F_1)\sigma_{\omega 2}\frac{1}{\omega}\frac{\partial k}{\partial x_j}\frac{\partial \omega}{\partial x_j} \quad (A2)$$

The constants, c, β, σ_k, and σ_ω, are given by the following general expression

$$\phi=F_1\phi_1+(1-F_1)\phi_2 \quad (A3)$$

where ϕ represents any one of these constants; ϕ_1 represents any constant in the $k-\omega$ model; ϕ_2 represents the corresponding constant in the $k-\epsilon$ model. These constants are defined as

Set 1 ($k-\omega$):

$$\sigma_{k1}=0.85 \quad \sigma_{\omega 1}=0.5 \quad \beta_1=0.075 \quad c_1=0.553 \quad (A4)$$

Set 2 ($k-\epsilon$):

$$\sigma_{k2}=1.0 \quad \sigma_{\omega 2}=0.856 \quad \beta_2=0.0828 \quad c_2=0.44 \quad (A5)$$

The production term is given as;

$$P_k=\tau_{ij}\frac{\partial u_i}{\partial x_j} \quad (A6)$$

where

$$\tau_{ij}=\mu_t\left[\frac{\partial u_i}{\partial x_j}+\frac{\partial u_j}{\partial x_i}-\frac{2}{3}\frac{\partial u_k}{\partial x_k}\delta_{ij}\right]-\frac{2}{3}\rho k\delta_{ij} \quad (A7)$$

The blending function F_1 is defined as;

$$F_1=\tanh(\arg_1^4) \quad (A8)$$

with

$$\arg_1=\min\left\{\max\left[\frac{\sqrt{k}}{0.09\omega d};\frac{500\nu}{d^2\omega}\right];\frac{4\rho\sigma_{\omega 2}k}{CD_{k\omega}d^2}\right\} \quad (A9)$$

where d is the distance to the closest wall and $CD_{k\omega}$ is the positive portion of the cross-diffusion term in Eq. (A2).

$$CD_{k\omega}=\max\left[2\rho\sigma_{\omega 2}\frac{1}{\omega}\frac{\partial k}{\partial x_j}\frac{\partial \omega}{\partial x_j};10^{-20}\right] \quad (A10)$$

The kinematic eddy viscosity is defined as;

$$\nu_t=\frac{a_1 k}{\max(a_1\omega;\Omega F_2)} \quad (A11)$$

where Ω is the magnitude of vorticity and $a_1=0.31$. The function F_2 is given by;

$$F_2=\tanh(\arg_2^2) \quad (A12)$$

with

$$\arg_2=\max\left[\frac{2\sqrt{k}}{0.09\omega d};\frac{500\nu}{d^2\omega}\right] \quad (A13)$$

References

[1] Savill, A. M., 1993, ''Some Recent Progress in The Turbulence Modeling of By-Pass Transition,'' *Near-Wall Turbulent Flows*, R. M. C. So, C. G. Speziale and B. E. Launder, eds., Elsevier Science, pp. 829–848.
[2] Savill, A. M., 1993, ''Further Progress in The Turbulence Modeling of By-Pass Transition,'' *Engineering Turbulence Modeling and Experiments 2*, W. Rodi and F. Martelli, eds., Elsevier Science, pp. 583–592.
[3] Westin, K. J. A., and Henkes, R. A. W. M., 1997, ''Application of Turbulence Models to Bypass Transition,'' ASME J. Fluids Eng., **119**, pp. 859–866.
[4] Dhawan, S., and Narasimha, R., 1958, ''Some Properties of Boundary Layer During the Transition from Laminar to Turbulent Flow Motion,'' J. Fluid Mech., **3**, pp. 418–436.
[5] Gostelow, J. P., Blunden, A. R., and Walker, G. J., 1994, ''Effects of Free-Stream Turbulence and Adverse Pressure Gradients on Boundary Layer Transition,'' ASME J. Turbomach., **116**, pp. 392–404.
[6] Solomon, W. J., Walker, G. J., and Gostelow, J. P., 1995, ''Transition Length Prediction for Flows with Rapidly Changing Pressure Gradients,'' ASME Paper ASME-95-GT-241, International Gas Turbine and Aeroengine Congress & Exposition, Houston, Texas, June 5–8.
[7] Chen, K. K., and Thyson, N. A., 1971, ''Extension of Emmons' Spot Theory to Flows on Blunt Bodies,'' AIAA J., **9**, No. 5, pp. 821–825.
[8] Steelant, J., and Dick, E., 1996, ''Modelling of Bypass Transition with Conditioned Navier-Stokes Equations Coupled to an Intermittency Transport Equation,'' Int. J. Numer. Methods Fluids, **23**, pp. 193–220.
[9] Cho, J. R., and Chung, M. K., 1992, ''A $k-\epsilon-\gamma$ Equation Turbulence Model,'' J. Fluid Mech., **237**, pp. 301–322.
[10] Launder, B. E., and Sharma, B. I., 1974, ''Application of the Energy Dissipation Model of Turbulence to the Calculation of Flow Near a Spinning Disc,'' Lett. Heat Mass Transfer, **1**, pp. 131–138.
[11] Wilcox, D. C., 1988, ''Reassessment of the Scale-Determining Equation for Advanced Turbulence Models,'' AIAA J., **26**, No. 11, pp. 1299–1310.
[12] Menter, F. R., 1994, ''Two-Equation Eddy-Viscosity Turbulence Models for Engineering Applications,'' AIAA J., **32**, No. 8, August, pp. 1598–1605.
[13] Narasimha, R., 1985, ''The Laminar-Turbulent Transition Zone in the Boundary Layer,'' Prog. Aerosp. Sci., **22**, pp. 29–80.
[14] Mayle, R. E., 1991, ''The Role of Laminar-Turbulent Transition in Gas Turbine Engines,'' ASME J. Turbomach., **113**, pp. 509–537.
[15] Abu-Ghannam, B. J., and Shaw, R., 1980, ''Natural Transition of Boundary Layers—The Effects of Turbulence, Pressure Gradient, and Flow History,'' J. Mech. Eng. Sci. **22**, No. 5, pp. 213–228.
[16] Klebanoff, P. S., 1955, ''Characteristics of Turbulence in a Boundary Layer with Zero Pressure Gradient,'' NACA Report No. 1247.
[17] Sohn, Ki-Hyeon and Reshotko, Eli, 1991, ''Experimental Study of Boundary Layer Transition With Elevated Freestream Turbulence on a Heated Flat Plate,'' NASA CR-187068.
[18] Gostelow, J. P., and Walker, G. J., 1991, ''Similarity Behavior in Transitional Boundary Layers Over a Range of Adverse Pressure Gradients and Turbulence Levels,'' ASME J. Turbomach., **113**, pp. 617–625.
[19] Suzen, Y. B., and Huang, P. G., 2000, ''An Intermittency Transport Equation for Modeling Flow Transition,'' AIAA Paper AIAA-2000-0287, 38th Aerospace Sciences Meeting and Exhibit, Reno, NV, January 10–13.
[20] Libby, P. A., 1975, ''On the Prediction of Intermittent Turbulent Flows,'' J. Fluid Mech., **68**, Part 2, pp. 273–295.
[21] Simon, F. F., and Stephens, C. A., 1991, ''Modeling of the Heat Transfer in Bypass Transitional Boundary-Layer Flows,'' NASA Technical Paper 3170.
[22] Suzen, Y. B., Xiong, G., and Huang, P. G., 2000, ''Predictions of Transitional Flows in a Low-Pressure Turbine Using an Intermittency Transport Equation,'' AIAA Paper AIAA-2000-2654, Fluids 2000 Conference, Denver, Colorado, June 19–22.

Carl D. Meinhart
Assistant Professor,
Department of Mechanical
& Environmental Engineering,
University of California,
Santa Barbara, CA 93106
e-mail: meinhart@engineering.vcsb.edu

Steve T. Wereley
Assistant Professor,
Mechanical Engineering,
Purdue University,
1288 Mechanical Engineering Building,
West Lafayette, IN 47909-1288

Juan G. Santiago
Assistant Professor,
Department of Mechanical Engineering,
Stanford University,
Stanford, CA 94305-3030

A PIV Algorithm for Estimating Time-Averaged Velocity Fields

A PIV algorithm is presented for estimating time-averaged or phase-averaged velocity fields. The algorithm can be applied to situations where signal strength is not sufficient for standard cross correlation techniques, such as a low number of particle images in an interrogation spot, or poor image quality. The algorithm can also be used to increase the spatial resolution of measurements by allowing smaller interrogation spots than those required for standard cross correlation techniques. The quality of the velocity measurements can be dramatically increased by averaging a series of instantaneous correlation functions, before determining the location of the signal peak, as opposed to the commonly used technique of estimating instantaneous velocity fields first and then averaging the velocity fields. The algorithm is applied to a 30 μm$\times$300 μm microchannel flow.
[S0098-2202(00)00602-7]

1 Introduction

There has been a significant amount of work over the past 15 years developing theory for particle image velocimetry, including Adrian and Yao [1], Adrian [2,3], Keane and Adrian [4,5], and Westerweel [6]. A large fraction of this effort has been focused on determining optimal conditions for measuring instantaneous velocity information, and understanding the performance of the instrument under a variety of operating conditions. One key advantage of the PIV technique over other conventional techniques such as LDV or hotwire anemometry is the ability to obtain instantaneous full-field velocity information. This instantaneous flow-field information is important for probing the structure of turbulent flow fields (Westerweel, et al. [7], Meinhart and Adrian [8]).

Recently, micro-PIV techniques have been developed to measure flows in microfluidic devices with spatial resolutions on the order of several microns (Santiago et al. [9] and Meinhart et al. [10]). At the microscale, it is difficult to form a light sheet that is only a few microns thick, and even more difficult to align such a light sheet with the objective plane of the recording optics. Therefore, in micro-PIV experiments, the entire test section volume is illuminated with a cone of light emanating from the recording lens, instead of a commonly used light sheet. This limits the number density of particles that can be used to trace the flow. If the particle density is too high, then background noise from out-of-focus particles will dominate the image and reduce the visibility of in-focus particles. If the particle density is too low, then standard cross correlation techniques will fail to provide an adequate signal, causing the measurements to be noisy and sometimes unreliable.

Since many of the low Reynolds number flows in microfluidic devices are laminar and either steady or periodic, it is not necessary to determine instantaneous velocity information. For many of these flows, it is sufficient to measure only the time-averaged or phase-averaged velocity field. In principle, these flow fields can be measured using high-resolution pointwise techniques such as the dual beam laser Doppler anemometer (LDA) system developed by Tieu, Machenzie and Li [11]. This LDA system uses low *f-number* optics to focus the probe volume down to approximately 5 μm$\times$10 μm. The micron-resolution LDA technique has advantages over the micro-PIV technique in that one does not have to deal with out of focus particle images, and that one can obtain large numbers of velocity measurements in real time. Micro PIV has advantages over micro LDA in that it does not require alignment of laser beams inside a microfluidic device, and it does require sweeping the probe volume throughout the measurement domain. In addition, micro PIV takes advantage of the high signal to noise levels offered by fluorescence imaging.

In this paper, we present a PIV algorithm that directly estimates time-averaged or phase-averaged velocity fields. The algorithm can provide reliable measurements in low signal-to-noise conditions where standard cross correlation techniques fail. The PIV algorithm is demonstrated by measuring flow in a 30 μm $\times$300 μm microchannel flow.

2 Decomposition of the Correlation Function

The auto correlation function of a single-frame double-exposure particle image field, $I(\mathbf{X})$, is defined as

$$R(\mathbf{s}) = \int \int I(\mathbf{X}) I(\mathbf{X}+\mathbf{s}) d^2\mathbf{X}, \tag{1}$$

where $\mathbf{X}$ is the spatial coordinate in the image plane and $\mathbf{s}$ is the spatial coordinate in the correlation plane.

$R(\mathbf{s})$ can be decomposed into the following components

$$R(\mathbf{s}) = R_C(\mathbf{s}) + R_P(\mathbf{s}) + R_F(\mathbf{s}) + R_{D^-}(\mathbf{s}) + R_{D^+}(\mathbf{s}), \tag{2}$$

where R_C is the convolution of mean image intensity, R_P is the pedestal component resulting from each particle image correlating with itself, and R_F is the fluctuating component resulting from the correlation between fluctuating image intensity with mean image intensity (Adrian [2]). The positive and negative displacement components are R_{D^+} and R_{D^-}, respectively.

The signal used to measure displacement is contained only in the R_{D^+} component. Consequently, contributions from all other components of the correlation function may bias the measurements, add random noise to the measurements, or even cause erroneous measurements. Therefore, it is desirable to reduce or eliminate all the other components. If both exposures of a double-pulse particle image field are recorded separately as a double-frame image field, then the particle images can be interrogated using cross correlation (Keane and Adrian [5]). In the case of

Contributed by the Fluids Engineering Division for publication in the JOURNAL OF FLUIDS ENGINEERING. Manuscript received by the Fluids Engineering Division May 17, 1999; revised manuscript received February 2, 2000. Associate Technical Editor: S. Banerjee.

double-frame cross correlation, the R_P and R_{D^-} components do not exist. Further improvements in signal quality can be obtained by image processing. By subtracting the mean image intensity at each interrogation spot before correlation, the R_C and $R_F(s)$ components are set identically to zero, leaving only the positive displacement component, R_{D^+}, in the correlation function.

While the R_{D^+} component is commonly considered the signal component, it contains both noise and signal information. In order to make accurate measurements, the signal-to-noise ratio in the R_{D^+} component must be sufficiently high. This paper presents a method in which the signal-to-noise ratio can be increased when one is interested in measuring average displacement fields.

3 Methods of Estimating Average Velocity Fields

Average velocity fields can be obtained by first measuring instantaneous velocities and then averaging them in either space or time. Here we present an alternative method for measuring average velocity fields directly from the correlation function.

Estimation of velocity-vector fields using PIV involves three primary steps:

1 Particle Image Acquisition
2 Particle Image Correlation
3 Correlation Peak Detection

In order to obtain an average velocity measurement, one must apply an averaging operation. The averaging operator is a linear operator, and can be applied after step (1), step (2), or step (3), to produce a nonbiased estimate of average velocity. The particle-image correlation and peak detection operations are both nonlinear, and the order in which the averaging operator is applied can dramatically change the quality of the resulting signal.

In this section, we examine the three different methods for calculating average velocities based upon the order in which the averaging operator is applied. Here we assume that two single exposure images, *Image A* and *Image B*, are separated by a known time delay, Δt, and represent the image acquisition of a single realization. Furthermore, a sequence of two image pairs is acquired at N different realizations of a statistically stationary process. We wish to average over the N realizations to estimate the average velocity.

3.1 Average Velocity Method. In this method, the estimate of the average velocity is determined by (1) correlating *Image A* and *Image B*, (2) detecting the peak from the instantaneous correlation functions, and (3) averaging over the instantaneous velocity measurements. Figure 1(*a*) graphically depicts this process. The primary advantage of this method is that one can obtain instantaneous velocity measurements, which may be of physical importance. However, if one is primarily interested in the average velocity field, this method may not be optimal.

The nonlinear operation of peak detection is susceptible to producing erroneous measurements when the signal to noise is low in the instantaneous correlation. In practice, the vector fields must be validated by identifying and removing erroneous velocity measurements (Meinhart et al. [12], Westerweel [13]). Without vector validation, all the instantaneous measurements must be reliable in order to obtain a reliable average velocity measurement. For situations where the particle image density is low, there may not be adequate signal to obtain valid measurements from the instantaneous correlation functions. In these situations, the alternative methods described below may be employed.

3.2 Average Image Method. In this method, the averaging operation is applied directly on image fields A and B, and then correlated to obtain $R_{\overline{AB}}$. This process is depicted graphically in Fig. 1(*b*). In the situation where particle image number density is low, averaging the image fields together can increase the average number of particles per interrogation spot. However, excessive

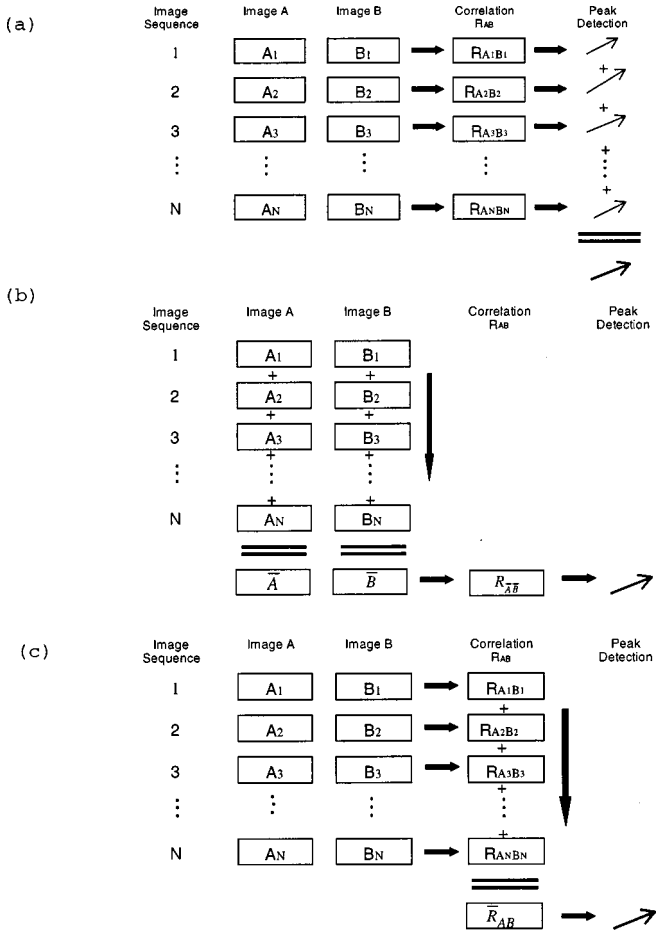

Fig. 1 Diagrams depicting the different ways in which the average velocity can be estimated: (*a*) average velocity method, (*b*) average image method, (*c*) average correlation method

averaging of the image fields can create too many particle images in the interrogation spot and reduce the visibility of individual particle images.

The 2-D spatial correlation function of the average of A and B image fields is defined as

$$R_{\overline{AB}}(\mathbf{s}) = \int \int \overline{A}(\mathbf{X})\overline{B}(\mathbf{X}+\mathbf{s})d^2\mathbf{X}, \tag{3}$$

where $\overline{A} = 1/N\Sigma_{i=1}^{N} A_i$ is the average operator, averaging over N realizations of the flow field. Expanding the integrand of (3) yields

$$R_{\overline{AB}}(s) = \int \int \begin{bmatrix} A_1B_1+A_1B_2+A_1B_3+\cdots+A_1B_N+ \\ A_2B_1+A_2B_2+A_2B_3+\cdots+A_2B_N+ \\ A_3B_1+A_3B_2+A_3B_3+\cdots+A_3B_N+ \\ \cdot \quad\quad \cdot \quad\quad \cdot \\ \cdot \quad\quad \cdot \quad\quad \cdot \\ \cdot \quad\quad \cdot \quad\quad \cdot \\ A_NB_1+A_NB_2+A_NB_3+\cdots+A_NB_N \end{bmatrix} d^2\mathbf{X}. \tag{4}$$

Following the discussion in the previous section, if A and B represent paired single-exposure image fields separated by a known time interval, Δt, which are cross correlated, and if the mean image intensity is subtracted before correlation, then all $N \times N$ terms in (4) are contained in the R_{D^+} component of R.

Only the N diagonal terms in (4) contribute to signal. The $N(N-1)$ off diagonal terms represent random particle correlation

across different realizations, which produce noise in the correlation function that can reduce the accuracy of the measurement and cause erroneous measurements. Since the off diagonal terms are random and uniformly distributed throughout the correlation plane, they may or may not contaminate the signal peak. The number of noise terms increases as N^2, while the number of signal terms increases as N.

In demanding situations when particle-number density is low, or when small interrogation regions are chosen to produce high spatial resolution, it may be impossible to obtain an adequate signal from instantaneous cross correlation analysis. Clearly, averaging the particle-image fields over several realizations and then correlating can increase the signal-to-noise ratio. However, if the number of realizations used in the average is beyond an optimal number, the signal-to-noise ratio can be reduced by further increases in N. Loss of signal occurs because the number of nondiagonal (noise) terms increases faster than the diagonal (signal) terms. The optimal number of realizations depends upon many factors including, interrogation spot size, particle-image number density, and particle-image quality.

3.3 Average Correlation Method. A third method for estimating average displacement fields is to calculate instantaneous correlation functions, average the correlation function, and then determine the location of the signal peak location. The *Average Correlation Method*, is shown graphically in Fig. 1(*c*). The average of instantaneous correlation functions over N realizations can be written as

$$\overline{R}_{AB}(s)=\overline{\int\int A(\mathbf{X})B(\mathbf{X}+\mathbf{s})d^2\mathbf{X}}=\int\int \overline{A(\mathbf{X})B(\mathbf{X}+\mathbf{s})}d^2\mathbf{X}. \tag{5}$$

Figure 2 shows several instantaneous correlation functions, and an average correlation function calculated by averaging 20 instantaneous correlation functions. The instantaneous correlation functions are characteristic of micro-PIV data and were obtained from an actual micro-PIV experiment. The instantaneous correlation functions contain significant amounts of noise that can lead to inaccurate or unreliable measurements. This noise is substantially less in the average correlation function.

Since the operations of averaging and integration commute, the average operator can be taken inside of the integral so that

$$\overline{R}_{AB}(\mathbf{s})=\int\int [A_1B_1+A_2B_2+A_3B_3+\cdots+A_NB_N]d^2\mathbf{X}. \tag{6}$$

From (6), the average correlation function contains only the diagonal (i.e., signal) terms of (4). Therefore, this type of average produces a much higher signal-to-noise ratio than the alternative methods that have been discussed previously. The number of signal terms increases linearly with the number of realizations, N. Unlike the average image method, there is no penalty for including large numbers of realizations in the average. Since the average operator is applied to the correlation function before peak detection, the probability of erroneous measurements is greatly reduced.

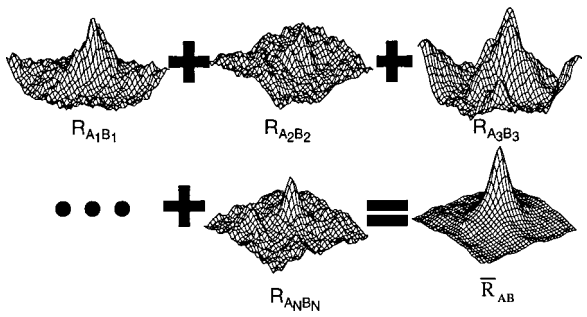

Fig. 2 Instantaneous cross correlation functions that are averaged together to produce an average correlation function. The average correlation function has a much higher signal-to-noise ratio than the instantaneous correlation functions.

4 Application to Microchannel Flow

The three different averaging algorithms were applied to a series of particle image fields taken of steady Stokes' water flow through a $30\,\mu\text{m}\times 300\,\mu\text{m}$ glass microchannel. Details of the same experiment but for a different flow rate are discussed by Meinhart et al. [10]. The out of plane measurement resolution is related to the depth of field of the microscope optics, and is estimated to be approximately 1.8 μm. Based on the discussion of Santiago et al. [9], the error due to Brownian motion for a single particle is estimated to be less than 3 percent full-scale error. The interrogation spot size was 16×64 pixels and 24×72 pixels, for window 1 and window 2, respectively. The relative offset between the windows was adjusted adaptively to approximate the particle image displacement at each measurement location. The interrogation windows were chosen to be small and have a high aspect ratio to achieve high spatial resolution in the wall-normal direction.

The signal-to-noise ratio from standard correlation techniques was relatively low, because there was an average of only 2.5 particle images located in each 16×64 pixel interrogation window. The signal-to-noise ratio could be improved by increasing the size of the correlation windows, but with reduced spatial resolution. Alternatively, the particle concentration in the flow field could be increased, but that would increase the number of out of focus particles, and produce more background image noise.

Figure 3(*a*) shows an instantaneous velocity-vector field, calculated using a standard cross correlation technique without any type of vector validation or smoothing applied to the field. The velocity measurements contained in the row closest to the wall are not considered to be accurate, because part of their interrogation region lies outside the flow domain. The velocity measurements are noisy, and approximately 20 percent appear to be erroneous. An average over 20 instantaneous velocity fields is shown in Fig. 3(*b*). Averaging reduces small random noise in the instantaneous fields. However, the large errors associated with the erroneous measurements are not averaged out quickly. The application of vector validation algorithms can usually eliminate errors due to erroneous measurements producing accurate velocity measurements, however a priori knowledge of the flow field is required.

The same series of double-frame particle image fields were correlated, the correlation functions were averaged, and then the locations of the signal peaks in the correlation plane were determined, following the *average correlation method* depicted in Fig. 1(*c*). The resulting velocity-vector field is shown in Fig. 3(*c*). No vector validation or smoothing has been applied to this field. The field contains only 0.5–1 percent erroneous measurements and has less noise than the vector fields shown in Figs. 3(*a*) and 3(*b*).

The relative performance of the three averaging algorithms was quantitatively compared by varying the number of realizations used in the average, from one to twenty. The fraction of valid measurements for each average was determined by identifying the number of velocity measurements in which the streamwise component of velocity deviated by more than 10 percent from the known solution at each point. For this comparison, the known solution was the velocity vector field estimated by applying the average correlation technique to 20 realizations, and then smoothing the flow field.

Figure 4 shows the fraction of valid measurements for each of the three algorithms as a function of the number of realizations used in the average. The average correlation method better than performs the other two methods, and produces less than 0.5–1 percent erroneous measurements after averaging eight realizations. The average image method produces about 95 percent reliable velocity measurements, and reaches a maximum at four averages. Further increases in the number of realizations used to

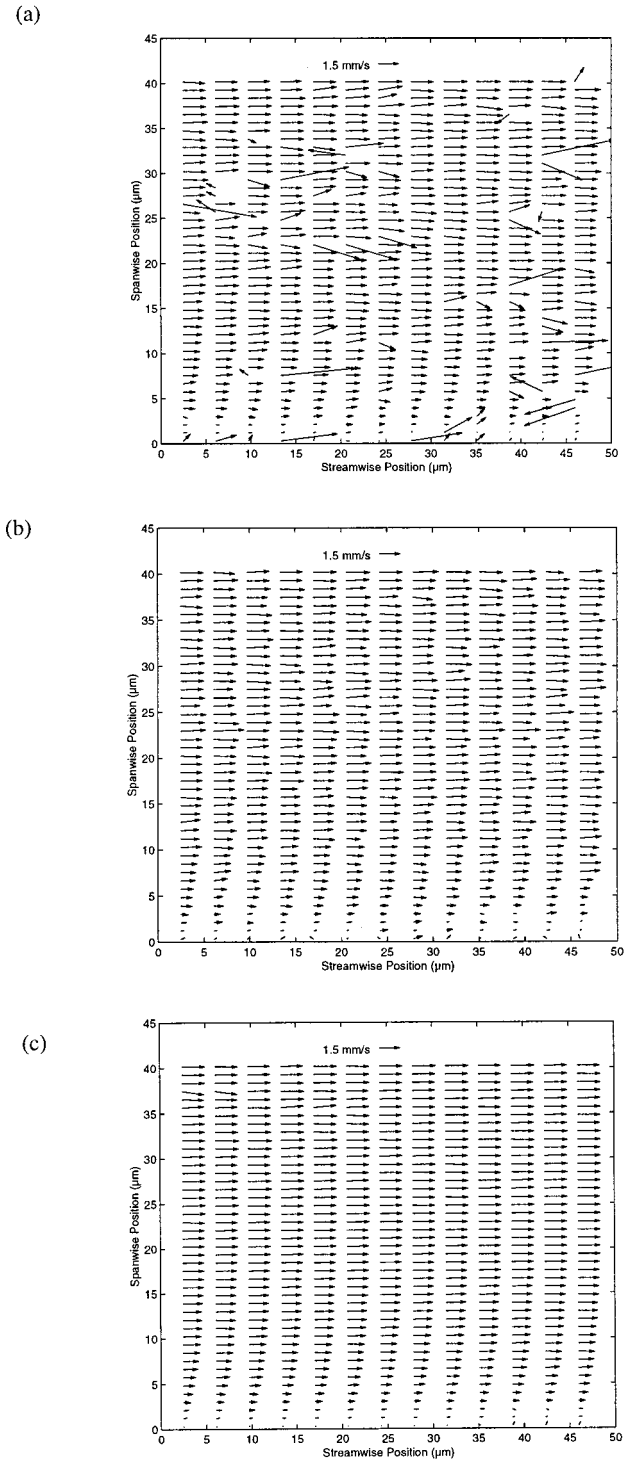

Fig. 3 Velocity vector fields showing the results from the different methods of calculation: (*a*) instantaneous velocity field, (*b*) time average of twenty instantaneous velocity fields, (*c*) velocity field calculated from time-averaged correlation functions

average the images decreases the signal to noise of the average particle-image field, and produces noise in the correlation plane due to random correlation between nonpaired particle images. The average velocity method reaches a maximum of 88 percent reliable measurements using two velocity averages. Further increases in the number of averages decreases the number of reliable measurements, due to an increase in the probability of an encountering an erroneous measurement.

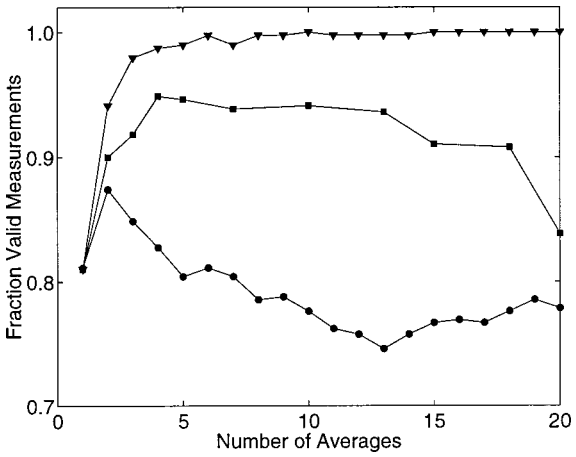

Fig. 4 Comparison of the performance of the three averaging techniques: average velocity ●, average image ■, and average correlation ▼

Conclusions

Three PIV algorithms are compared for estimated time-averaged velocity fields. The process of obtaining PIV measurements involves three primary steps: (1) particle image acquisition, (2) particle image correlation, and (3) correlation peak detection. In order to obtain average velocity fields, an averaging operator must be applied to the data. When signal strength is sufficient, the average can be applied after steps 1, 2, or 3. However, in demanding situations when signal strength is weak, the order in which the average operator is applied is important. The correlation and peak detection operators are nonlinear and do not commute with the average operator. Optimal signal strength can be achieved by first calculating instantaneous correlation functions, and then averaging the correlation functions before locating the signal peak.

The theoretical observations were confirmed by applying the three different algorithms to experimental particle image data from a 30 μm$\times$300 μm microchannel flow. The results showed that, by averaging instantaneous correlation functions before signal peak detection, high quality velocity data can be obtained with less than 0.5–1 percent erroneous measurements, even when only an average of 2.5 particle images were contained in a single interrogation spot.

Acknowledgments

This research is supported by AFOSR/DARPA F49620-97-1-0515, DARPA F33615-98-1-2853, and JPL/NASA 961270.

References

[1] Adrian, R. J., and Yao, C. S., 1985, ''Pulsed laser technique application to liquid and gaseous flows and the scattering power of seed materials,'' Appl. Opt., **24**, No. 1, pp. 44–52.
[2] Adrian, R. J., 1988, ''Double Exposure, Multiple-field particle image velocimetry for turbulent probability density,'' Opt. Lasers Eng., **9**, pp. 211–228.
[3] Adrian, R. J., 1991, ''Particle-imaging techniques for experimental fluid mechanics,'' Annu. Rev. Fluid Mech., **23**, pp. 261–304.
[4] Keane, R. D., and Adrian, R. J., 1991, ''Optimization of particle image velocimeters. II. Multiple pulsed systems,'' Meas. Sci. Technol., **2**, No. 10, Oct., pp. 963–974.
[5] Keane, R. D., and Adrian, R. J., 1992, ''Theory of cross-correlation analysis of PIV images,'' Appl. Sci. Res., **49**, pp. 191–215.
[6] Westerweel, J., 1997, ''Fundamentals of digital particle image velocimetry,'' Meas. Sci. Technol., **8**, pp. 1379–1392.
[7] Westerweel, J., Draad, A. A., van der Hoeven, J. G. Th., and van Oord, J., 1996, ''Measurement of fully developed turbulent pipe flow with digital PIV,'' Exp. Fluids, **20**, pp. 165–177.
[8] Meinhart, C. D., and Adrian, R. J., 1995, ''On the existence of uniform momentum zones in a turbulent boundary layer,'' Phys. Fluids, **7**, No. 4, pp. 694–696.
[9] Santiago, J. G., Wereley, S. T., Meinhart, C. D., Beebe, D. J., and Adrian, R.

J., 1998, ''A micro particle image velocimetry system,'' Exp. Fluids, **25**, No. 4, pp. 316–319.
[10] Meinhart, C. D., Wereley, S. T., and Santiago, J. G., ''PIV measurements of a microchannel flow,'' Exp. Fluids, **27**, pp. 414–419.
[11] Tieu, A. K., Mackenzie, M. R., and Li, E. B., 1995, ''Measurements in microscopic flow with a solid-state LDA,'' Exp. Fluids, **19**, pp. 293–294.
[12] Meinhart, C. D., Barnhart, D. H., and Adrian, R. J., 1994, ''Interrogation and validation of three-dimensional vector fields,'' *Developments in Laser Techniques and Applications to Fluid Mechanics*, R. J. Adrian et al., eds., Springer-Verlag, Berlin, pp. 379–391.
[13] Westerweel, J., 1993, ''Efficient detection of spurious vectors in particle image velocimetry data,'' Exp. Fluids, **16**, pp. 236–247.

Flow Structure in the Wake of a Rotationally Oscillating Cylinder

F. M. Mahfouz
Research Associate

H. M. Badr
Professor

Mechanical Engineering Department,
King Fahd University of Petroleum & Minerals,
Dhahran 31261, Saudi Arabia

The characteristics of the flow in the wake of a circular cylinder performing rotational oscillation about its own axis and placed horizontally in a cross-stream is investigated. The governing equations based on stream function-vorticity formulation are solved numerically to determine the flow field structure. The parameters dominating flow structure are Reynolds number, Re, amplitude of oscillation, Θ_A and frequency ratio $F_R = S/S_0$ where S is the forcing frequency and S_0 is the natural frequency of vortex shedding. The ranges considered for these parameters are $40 \leq Re \leq 200$, $0 \leq \Theta_A \leq \pi$ and $0 \leq F_R \leq 2$. The lock-on phenomenon has been predicted and its effect on the flow hydrodynamics has been determined. The lock-on phenomenon is found to occur within a band of frequency encompassing the natural frequency. This band, however, becomes wider as the amplitude of oscillation increases. The obtained results show that the flow pattern in the near wake has a strong dependence on the oscillation parameters but not the far wake.
[S0098-2202(00)01102-0]

1 Introduction

Flow behavior around a horizontal circular cylinder placed in a cross-stream constitutes a classical problem. However, the flow separation from bluff bodies and the wake structure are important topics from the standpoint of fundamental research as well as in technological applications. It was found experimentally that alternating vortices are shed periodically from the cylinder surface at a certain natural shedding frequency when Re>40. This periodic shedding process induces oscillating lift and drag forces and creates unsteady flow behavior close to the cylinder surface.

If a cylinder oscillates, either in response to the naturally induced oscillating lift force or due to external oscillations, it can cause changes in the flow pattern in the wake region. In the case of a cylinder performing transverse or in-line oscillations, when the oscillation frequency is near the natural shedding frequency (for transverse oscillation) or twice the natural shedding frequency (for in-line oscillation), vortices start shedding at the same forcing frequency. This is called the lock-on phenomenon and is reported in the works of Tanida et al. [1], Bishop and Hassan [2], Hurlbut et al. [3], and Griffin and Ramberg [4].

Among the few studies published on rotational oscillation in a cross-stream, only two authors reported the lock-on phenomenon. Okajima et al. [5] was the first to report these phenomena when he investigated the problem numerically in the range of Re from 40 to 80 and experimentally in the range from 80 to 6100. However, his study did not include the detailed effect of such phenomenon on the wake flow since only one value of velocity amplitude was considered. Tokumaru et al. [6] captured the lock-on phenomenon when studying, through flow visualization at Re=15000, the possibility of rotary oscillation control of a cylinder wake. A number of other investigators studied the same problem but did not report the lock-on phenomenon. This is mainly because they either used the boundary-layer assumption like Hori [7] or used a range of frequency far enough from the natural shedding frequency as in the work by Taneda [8]. Flow over a rotationally oscillating cylinder was also investigated by Wu et al. [9] at frequencies equal or near the natural shedding frequency. The study has shown that a resonant flow state was achieved with lift and drag components reached their maximum. Although the forced frequencies considered were close to the natural frequency, the results which must have fell in the lock-on regime did not draw the authors' attention. Apart from the lock-on phenomenon, Tokumaru et al. [10] investigated the lift variation when a cylinder executes rotary oscillation with net rate of rotation, whereas, Filler et al. [11] investigated the frequency response of the shear layers separating from a cylinder performing rotational oscillations with small amplitudes.

Recently, Lu and Sato [12] and Chou [13] have reported the lock-on phenomenon in their numerical investigation of the problem. In their work, Lu and Sato considered Reynolds numbers of 200, 1000, and 3000, while Chou reported his results mainly at Re=500 and 1000. Lu and Sato used a wide range of frequency ratio Fr=0.5, 1, 2, 3, and 4 with no emphasis on the variation of Fr in the neighborhood of Fr=1 in order to give more details about the lock-on range. The same approach was considered in the work by Chou but only at Re=1000. The main objective of this work is to study the flow structure in the wake as well as the hydrodynamics associated with a circular cylinder performing rotational oscillation in a cross-stream.

2 Problem Statement and the Governing Equations

The physical model considered is shown in Fig. 1. A circular cylinder of radius c is placed horizontally in an unbounded, uniform cross-stream with approaching velocity V. The cylinder surface acquires a harmonic rotational oscillation about its axis of the form

$$\Theta = -\Theta_A \cos(2\pi f \tau) \tag{1}$$

where Θ is the angular displacement, τ is the time, Θ_A, and f are the angular displacement amplitude and frequency, respectively. The governing equations in stream function-vorticity form can be written as

$$\frac{\partial \zeta'}{\partial \tau} + u_r' \frac{\partial \zeta'}{\partial r'} + \frac{u_\theta'}{r'} \frac{\partial \zeta'}{\partial \theta} = \nu \nabla^2 \zeta' \tag{2}$$

$$\zeta' = -\nabla^2 \psi' \tag{3}$$

The boundary conditions to be satisfied are the no-slip and impermeability on the cylinder surface and the free-stream conditions far away from it. These conditions can be expressed as

$$\psi' = \frac{\partial \psi'}{\partial \theta} = 0, \quad \frac{\partial \psi'}{\partial r'} = -u_w \quad \text{at } r' = c$$

and

Contributed by the Fluids Engineering Division for publication in the JOURNAL OF FLUIDS ENGINEERING. Manuscript received by the Fluids Engineering Division June 15, 1998; revised manuscript received November 15, 1999. Associate Technical Editor: P. W. Bearman.

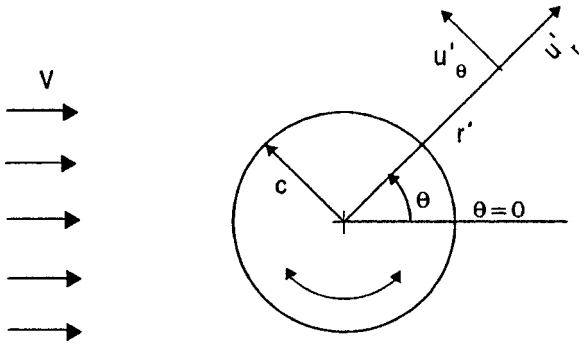

Fig. 1 The physical model and coordinate system

$$\frac{\partial \psi'}{\partial \theta} = r' V \cos(\theta), \quad \frac{\partial \psi'}{\partial r'} = -V \sin(\theta), \quad \zeta' \to 0 \ \text{ as } \ r' \to \infty \tag{4}$$

The solution methodology does not impose any explicit boundary condition for the vorticity at the cylinder surface that is normally computed from the known stream function distribution near the wall using Eq. (3). However, this procedure becomes less accurate when large velocity gradients exist near the wall. This problem has been overcome throughout this study by introducing an integral condition to estimate accurately the surface vorticity, following the work by Badr and Dennis [14]. The above governing equations are normalized by introducing the following dimensionless quantities:

$$r = \frac{r'}{c}, \quad U_r = \frac{u_r'}{V}, \quad U_\theta = \frac{u_\theta'}{V}, \quad t = \tau \frac{V}{c}, \quad \psi = \frac{\psi'}{cV},$$

and

$$\zeta = -\zeta' \frac{c}{V}$$

Using the above variables, Eqs. (2)–(3) can now be written as

$$\frac{\partial \zeta}{\partial \tau} + U_r \frac{\partial \zeta}{\partial r} + \frac{U_\theta}{r} \frac{\partial \zeta}{\partial \theta} = \frac{2}{\mathrm{Re}^2} \nabla^2 \zeta \tag{5}$$

$$\zeta = \nabla^2 \psi \tag{6}$$

where $U_r = 1/r\ \partial\psi/\partial\theta$, $U_\theta = -\partial\psi/\partial r$ and $\mathrm{Re} = 2cV/\nu$ is the Reynolds number.

The dimensionless velocity of the cylinder surface can now be expressed as

$$U_w = \alpha \sin(\pi S t) \tag{7}$$

where α represents the velocity amplitude of oscillation and S is the dimensionless forcing frequency given by $S = 2fc/V$.

In order to have high accuracy near the surface at which large velocity gradients exist and at the same time cover a large computational domain, the modified polar coordinates (ξ,θ) are used, where $\xi = \ell n r$. The equations in the new coordinates can be written as

$$e^{2\xi} \frac{\partial \zeta}{\partial t} = \frac{2}{\mathrm{Re}} \left(\frac{\partial^2 \zeta}{\partial \xi^2} + \frac{\partial^2 \zeta}{\partial \theta^2} \right) - \frac{\partial \psi}{\partial \theta} \frac{\partial \zeta}{\partial \xi} + \frac{\partial \psi}{\partial \xi} \frac{\partial \zeta}{\partial \theta} \tag{8}$$

$$e^{2\xi} \zeta = \frac{\partial^2 \psi}{\partial \xi^2} + \frac{\partial^2 \psi}{\partial \theta^2} \tag{9}$$

The boundary conditions can now be expressed as

$$\psi = \frac{\partial \psi}{\partial \theta} = 0, \quad \frac{\partial \psi}{\partial \xi} = -\alpha \sin(\pi S t) \quad \text{at } \ \xi = 0$$

and

$$\frac{\partial \psi}{\partial \theta} \to e^{-\xi} \cos\theta, \quad \frac{\partial \psi}{\partial \xi} \to -e^{-\xi} \sin\theta, \quad \zeta \to 0 \ \text{ as } \ \xi \to \infty \tag{10}$$

3 The Method of Solution

The method of solution is based on integrating the time dependent governing equations of motion and energy to obtain the time-dependent velocity field. Using the series truncation method and following the works of Collins and Dennis [15] and Badr and Dennis [14], the dimensionless stream function ψ, vorticity ζ and temperature ϕ are approximated using Fourier series expansions as follows:

$$\psi(\xi,\theta,t) = \frac{1}{2} F_o(\xi,t) + \sum_{n=1}^{N} \left[f_n(\xi,t) \sin(n\theta) + F_n(\xi,t) \cos(n\theta) \right] \tag{11a}$$

$$\zeta(\xi,\theta,t) = \frac{1}{2} G_o(\xi,t) + \sum_{n=1}^{N} \left[g_n(\xi,t) \sin(n\theta) + G_n(\xi,t) \cos(n\theta) \right] \tag{11b}$$

where F_o, f_n, F_n, G_o, g_n and G_n are Fourier coefficients and all are functions of ξ and t.

Substitution of Eq. (11) in Eqs. (8)–(9) and using simple mathematical analysis results in the following set of differential equations:

$$\frac{\partial^2 F_o}{\partial \xi^2} = e^{2\xi} G_o \tag{12a}$$

$$\frac{\partial^2 f_n}{\partial \xi^2} - n^2 f_n = e^{2\xi} g_n \tag{12b}$$

$$\frac{\partial^2 F_n}{\partial \xi^2} - n^2 F_n = e^{2\xi} G_n \tag{12c}$$

$$e^{2\xi} \frac{\partial G_o}{\partial t} = \frac{2}{\mathrm{Re}} \frac{\partial^2 G_o}{\partial \xi^2} + S_o \tag{13a}$$

$$e^{2\xi} \frac{\partial g_n}{\partial t} = \frac{2}{\mathrm{Re}} \left(\frac{\partial^2 g_n}{\partial \xi^2} - n^2 g_n \right) + n F_n \frac{\partial G_o}{\partial \xi} - n G_n \frac{\partial F_o}{\partial \xi} + S_{n1} \tag{13b}$$

$$e^{2\xi} \frac{\partial G_n}{\partial t} = \frac{2}{\mathrm{Re}} \left(\frac{\partial^2 G_n}{\partial \xi^2} - n^2 G_n \right) + n f_n \frac{\partial G_o}{\partial \xi} - n g_n \frac{\partial F_o}{\partial \xi} + S_{n2} \tag{13c}$$

where S_o, S_{n1}, and S_{n2} are all easily identifiable functions of ξ and t. Equations (12*a*)–(12*c*) define a set of $(2N+1)$ ordinary differential equations and Eqs. (13*a*)–(13*c*) define another set of $(2N+1)$ partial differential equations, where N is the order of truncation in the Fourier series. All these equations have to be solved at every time step. The boundary conditions for all functions present in Eqs. (12*a*)–(13*c*) are obtained from Eq. (10) and can be expressed as

$$F_0 = F_n = f_n = \partial F_n/\partial\xi = \partial f_n/\partial\xi = 0,$$

$$\partial F_o/\partial\xi = -2\alpha \sin(\pi S t) \quad \text{at } \ \xi = 0,$$

$$e^{-\xi} F_0 \to 0, \quad e^{-\xi} \partial F_o/\partial\xi \to 0, \quad F_n \to 0, \quad f_n \to \delta_{1,n}$$

and

$$e^{-\xi} \partial F_n/\partial\xi \to 0, \quad e^{-\xi} \partial f_n/\partial\xi \to \delta_{1,n}$$

and

$$G_o, G_n, g_n \to 0 \quad \text{as } \ \xi \to \infty \tag{14}$$

Integrating both sides of Eq. (12*a*) with respect to ξ from $\xi = 0$ to $\xi = \infty$ and using the boundary conditions in Eq. (14) give the following integral condition:

$$\int_0^\infty e^{2\xi} G_o d\xi = 2\alpha \sin(\pi St) \tag{15a}$$

Similarly, integrating both sides of Eqs. (12*b*) and (12*c*) subjected to the boundary conditions given in Eq. (14) results in

$$\int_0^\infty e^{(2-n)\xi} g_n d\xi = 2\delta_{1,n} \tag{15b}$$

$$\int_0^\infty e^{(2-n)\xi} G_n d\xi = 0 \tag{15c}$$

where

$$\delta_{1,n} = \begin{cases} 1 & \text{when } n=1 \\ 0 & \text{when } n\neq 1 \end{cases}$$

The above integral conditions are used to calculate the values of the functions G_o, g_n, and G_n which are needed to determine the surface vorticity. The first condition (Eq. (15*a*)) is essential to ensure the periodicity of the pressure on the cylinder surface.

In order to advance the solution of ψ, ζ, and ϕ in time, the initial condition at time $t=0$ must be known. The flow field structure at small times following the impulsive fluid motion is characterized by very thin boundary-layer region close to the cylinder surface bounded by a potential flow elsewhere. The use of potential flow solution as initial solution, as was frequently adopted by many researchers, will definitely lead to inaccurate results following the start of fluid motion. However, the effect of such inaccuracy on the large time results is not known. The proper scaling for such a case is the use boundary-layer coordinates. Let us now introduce boundary-layer coordinates (z,t) defined as:

$$\xi = \lambda z, \quad \text{where } \lambda = 2\sqrt{2t/\mathrm{Re}},$$

and also introduce ψ^* and ζ^* defined as $\psi^* = \psi/\lambda$, and $\zeta^* = \lambda\zeta$.

The corresponding Fourier functions become

$$F_0^* = F_0/\lambda, \quad f_n^* = f_n/\lambda, \quad F_n^* = F_n/\lambda, \quad G_0^* = G_0\lambda,$$
$$g_n^* = g_n\lambda \quad \text{and} \quad G_n^* = G_n\lambda \tag{16}$$

The use of ψ^* and ζ^* is appropriate to the flow field structure at small time in which the viscous flow region is limited to a very thin layer. In that layer, the surface vorticity ζ reaches high values while the stream function ψ is small. Using Eq. (16), the governing equations and the boundary and integral conditions Eqs. (14)–(15) can now be transformed to the new coordinate system and then solved to give an accurate solution at times following the start of motion. The initial solution at $t=0^+$ is obtained by closely following Collins and Dennis [15] and Badr and Dennis [14], and is found to be

$$\psi^*(z,\theta,0) = -[z(1-\mathrm{erf}(z)+\pi^{-1/2}(1-e^{-z^2})]\sin(\theta) \tag{17}$$

$$\zeta^*(z,\theta,0) = 4\sin(\theta)\pi^{-1/2}e^{-z^2} \tag{18}$$

The differential Eqs. (12)–(13) and the boundary and integral conditions (Eqs. (14) and (15)) are different from those obtained by Collins and Dennis [15] and Badr and Dennis [14]. However, the numerical technique is almost the same and will not be repeated here.

In order to examine the pressure distribution on the cylinder surface, let us introduce the dimensionless pressure, p^* such that $p_\theta^* = 2(P_\theta - P_\pi)/\rho V^2$. Now, by applying the angular component of Navier-Stokes equations on the cylinder surface, one gets

$$\frac{\partial P_\theta^*}{\partial\theta} = -2\frac{\partial U_w}{\partial t} - \frac{4}{\mathrm{Re}}\left(\frac{\partial\zeta}{\partial\xi}\right)_{\xi=0} \tag{19}$$

Integrating the above expression w.r.t. θ starting from $\theta=\pi$ to any angle θ on the cylinder surface, the pressure distribution is found to be

$$P_\theta^* = (\pi-\theta)\left[\frac{2}{\mathrm{Re}}\frac{\partial G_0}{\partial\xi}\bigg|_{\xi=0} + 2\frac{\partial U_w}{\partial t}\right] - \frac{4}{\mathrm{Re}}\left[\sum_{n=1}^{N}\frac{\sin n\theta}{n}\frac{\partial G_n}{\partial\xi}\bigg|_{\xi=0} - \frac{\cos n\theta - \cos n\pi}{n}\frac{\partial g_n}{\partial\xi}\bigg|_{\xi=0}\right] \tag{20}$$

The periodicity of surface pressure requires that

$$\frac{2}{\mathrm{Re}}\frac{\partial G_0}{\partial\xi}\bigg|_{\xi=0} + 2\frac{\partial U_w}{\partial t} = 0 \tag{21}$$

Closely following the line of reasoning of Badr and Dennis [14] for the problem of steady rotating cylinder in uniform stream, it can be shown that the condition given in Eq. (21) is implicitly satisfied by the integral condition given in Eq. (15*a*). For steady rotating cylinder, the needed condition for the periodicity of pressure as deduced by Badr and Dennis [14] was $G_0'(0,t)=0$, which represents a special case of Eq. (21) when $U_w=\text{const}$.

The number of points in the ξ direction used in this work is 120 with a grid size $\Delta\xi=0.1$. This sets the outer boundary of the computational domain at a distance of approximately 10,000 times the diameter of the cylinder. Such distance is large enough to ensure that the conditions at ∞ are appropriately satisfied. However, this grid size is reduced to 0.05 for high Reynolds number cases. This matches closely the flow field characteristics since as Re increases the boundary layer becomes thinner and the velocity gradient near the wall becomes steeper. The time steps used are very small at the start of motion $\Delta t = 10^{-3}$ and gradually increase to 0.05 at large time. The numerical solution starts with two terms only in the Fourier series and one more term is added when the last term exceeds 10^{-4}. The maximum number of terms depends on the Reynolds number, forcing frequency and amplitude of oscillation. That number reached a maximum of 40 in all cases considered in this work.

The lift and drag coefficients are defined by $C_L = L/\rho V^2 c$, $C_D = D/\rho V^2 c$, where L, D are the lift and drag forces exerted on a unit length of the cylinder. These two forces are mainly due to pressure and viscous forces acting on the surface. In terms of the Fourier coefficients, C_L and C_D can be expressed as:

$$C_L = -\frac{2\pi}{\mathrm{Re}}\left\{G_1(0,t) - \left(\frac{\partial G_1}{\partial\xi}\right)_{\xi=0}\right\} \tag{22}$$

$$C_D = \frac{2\pi}{\mathrm{Re}}\left\{g_1(0,t) - \left(\frac{\partial g_1}{\partial\xi}\right)_{\xi=0}\right\} \tag{23}$$

The time-averaged drag coefficient is obtained from

$$\overline{C_D} = \frac{1}{t_2-t_1}\int_1^{t_2} C_D dt \tag{24}$$

where the time period between t_1 and t_2 is taken after reaching the quasi-steady state and covering more than one cycle.

In order to verify the accuracy of the method of solution and the computational scheme, the problem of initial flows over fixed and rotating cylinders starting their motion impulsively from rest are first considered. The present prediction of the initial streamline pattern for flow over a fixed cylinder at Re=3000 and $t=3$ is shown in Fig. 2. The pattern compares very well with the corresponding experimental and theoretical patterns obtained by Ta Phuoc Loc and Bouard [16]. A pair of secondary vortices generated near the cylinder surface at such moderate Reynolds number is accurately predicted. Figure 3 shows a good agreement between the velocity distribution along line ($\theta=0$) predicted by Ta Phuoc Loc [17] and the corresponding distribution predicted by the present method for the special case of Re=550. On the other hand, the present predictions for the initial flow development over a rotating cylinder are compared with that obtained experimentally by Coutanceau and Menard [18]. The comparison is carried

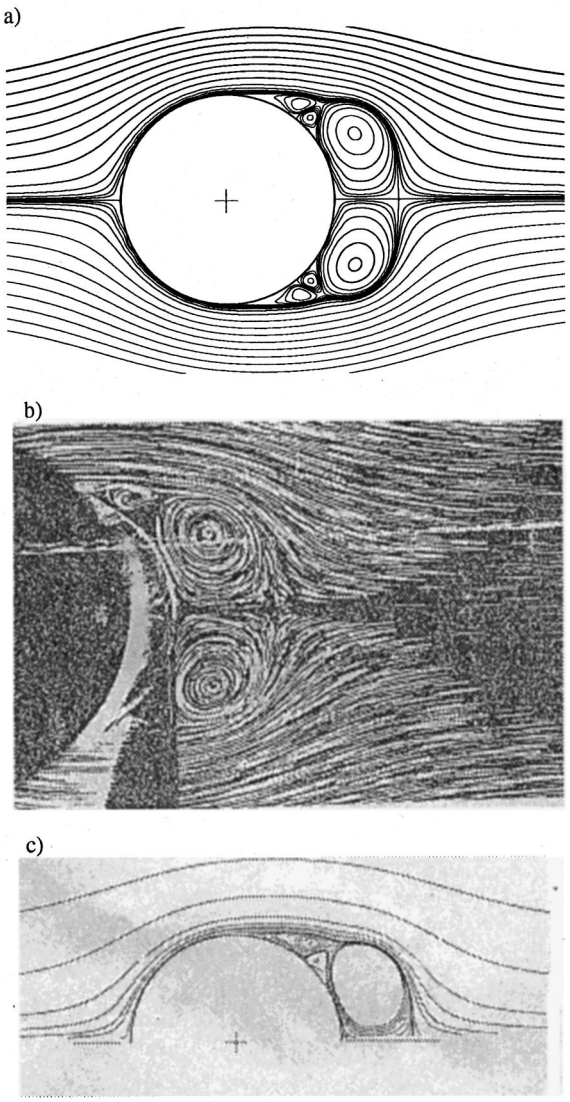

Fig. 2 The streamline pattern for impulsively started over a fixed cylinder for the case of Re=3000 at $t=3$ and comparison with previous results; (*a*) present study, (*b*) experimental, and (*c*) theoretical results obtained by Ta Phuoc Loc and Bouard [16].

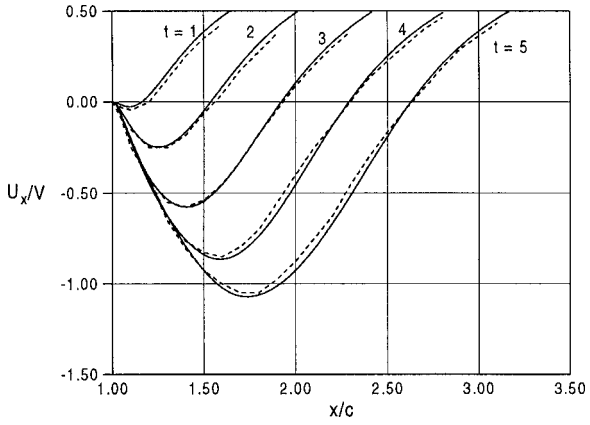

Fig. 3 The time development of the *x*-component of velocity along $\theta=0$ at Re=550; —— present results; – – – numerical results of Ta Phuoc Loc [17].

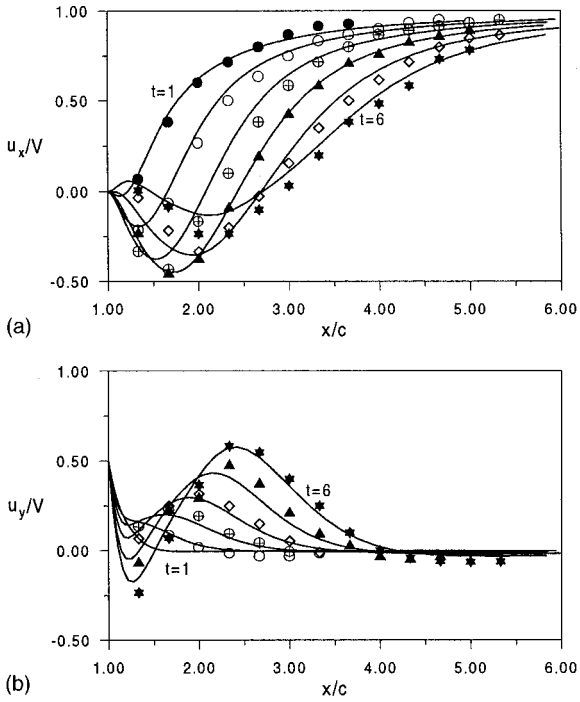

Fig. 4 Time development of velocity components along $\theta=0$ and comparison with experimental results of Coutanceau and Menard [18] at Re=200 and $\alpha=1/2$. Experimental values: ● $t=1$; ○ $t=2$; ⊕ $t=3$; △ $t=4$; ◇ $t=5$; ★ $t=6$; Theoretical curves (*a*) *x*-component, (*b*) *y*-component.

Table 1 Comparison between the natural Strouhal number obtained from the present study and that reported by Roshko [21] and Williamson [26].

Re	Present	Exp. Roshko (1954)	Exp. Williamson (1989)
80	0.156	0.155	0.153
100	0.16	0.165	0.164
200	0.18	0.18-0.2	0.183

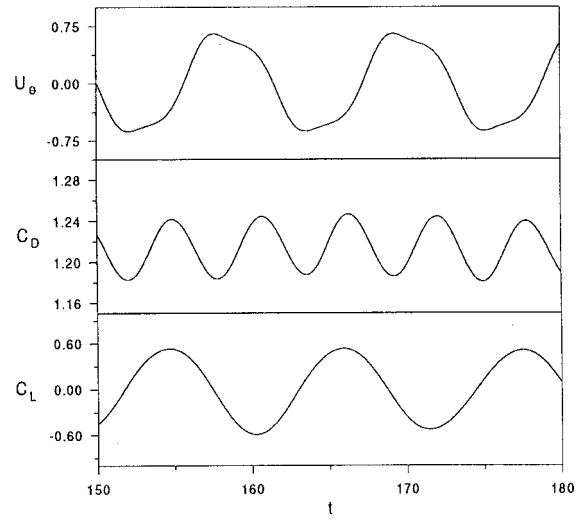

Fig. 5 The time variation of tangential velocity component, drag coefficient and lift coefficient for the case of a fixed cylinder at Re=200.

out for one speed ratio (α=0.5) at Re=200. The velocity components along the line (θ=0) compare quantitatively well with the experimental ones as shown in Fig. 4.

4 Results and Discussion

As a precursor to the case of oscillating cylinder, the process of vortex shedding from a stationary cylinder is examined at the three Reynolds numbers (Re=80, 100, and 200). This range is selected based on Williamson's experimental investigation [19] in which the upper limit of Reynolds number required to keep the flow field laminar and two-dimensional is Re=200. In the numerical scheme, the vortex shedding process is triggered by rotationally oscillating the cylinder only for one complete cycle (at t =40) and fixing it afterwards. The Karman vortex street is developed with vortices being shed alternately from the upper and lower surfaces of the cylinder. The frequency of vortex shedding is computed from either the periodic variation of the velocity at any point in the wake or the time variation of the induced oscillating lift force following Sarpkaya [20]. The dimensionless frequency of vortex shedding is generally expressed as the natural Strouhal number, $S_o = f_o d/V$, where f_o is the vortex shedding frequency. The Fourier analysis for the lift record or the velocity record gives almost the same value for Strouhal number. The predicted values of Strouhal number together with the experimental values reported by Roshko [21] and Williamson [19] are displayed in Table 1.

Figure 5 shows the time variation of the tangential component of velocity in the wake as well as the lift and drag coefficients for the case of Re=200. While both velocity and lift coefficient are found to oscillate at the same vortex shedding frequency, the drag

Table 2 The average drag coefficient obtained from the present study and comparison with previous results for the case of a fixed cylinder.

Re	$\overline{CD}$			
	Present study	Schlichting (7th edition)	Henderson (1995)	Chin-Hsiang et al. (1997)
80	1.56	1.85	1.38	1.33
100	1.55	1.75	1.36	1.32
200	1.21	1.50	1.33	1.31

Data from Ref. [27] Chin-Hsiang et al. (1997).

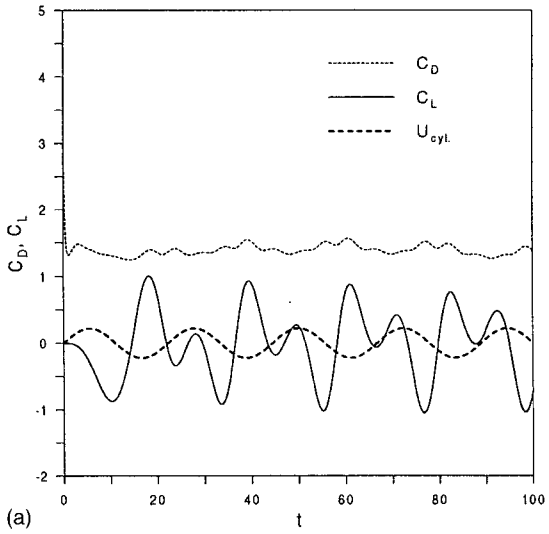

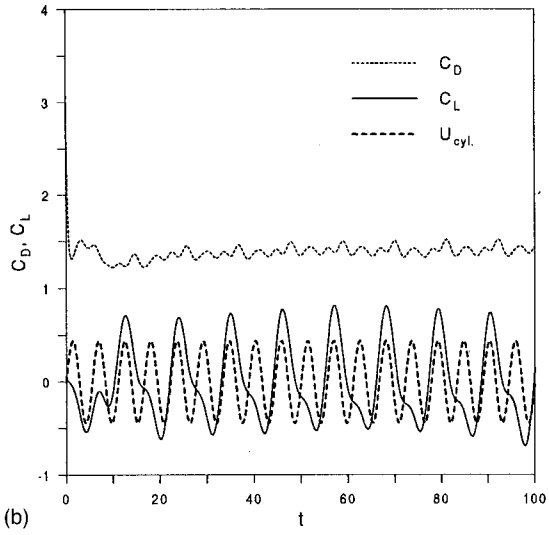

Fig. 6 (*a*) The time variation of lift and drag coefficients for a non-lock-on regime at Re=200, $\Theta_A=\pi/4$ and $F_R=0.5$. (*b*) The time variation of lift and drag coefficients for a non-lock-on regime at Re=200, $\Theta_A=\pi/8$ and $F_R=2$.

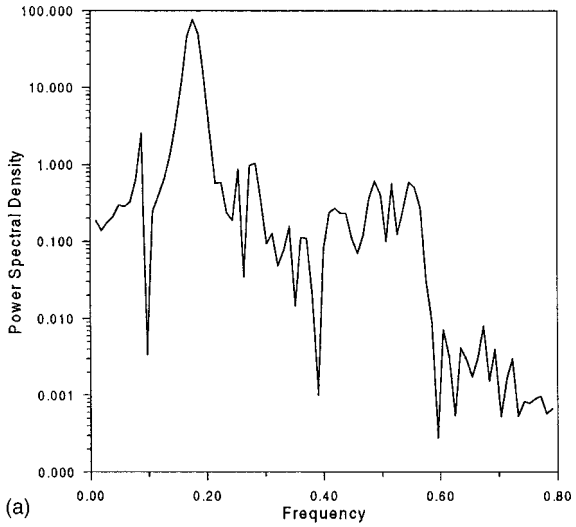

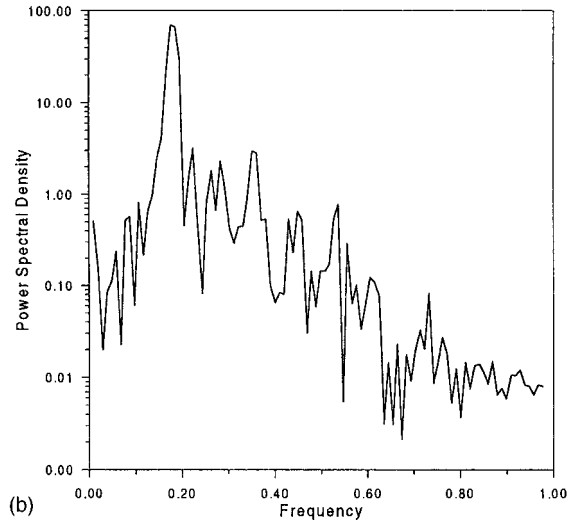

Fig. 7 Fourier analysis of the far wake for two non-lock-on regimes at Re=200 and (*a*) $\Theta_A=\pi/4$, $F_R=1/2$, (*b*) $\Theta_A=\pi/8$, $F_R=2$

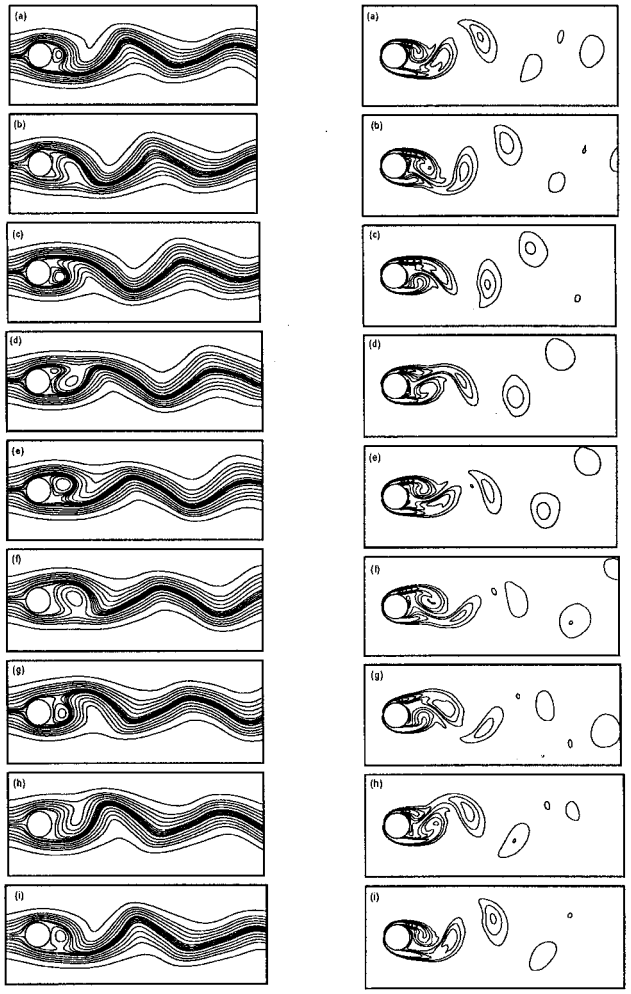

Fig. 8 Streamline patterns (left) equi-vorticity patterns (right) for one complete cycle in case of Re=200, $\Theta_A=\pi/4$ and $F_R=1/2$ at times (*a*) $t=40$, (*b*) $t=42.75$, (*c*) $t=45.5$, (*d*) $t=48.25$, (*e*) $t=51$, (*f*) $t=53.75$, (*g*) $t=56.5$, (*h*) $t=59.25$, (*i*) $t=62$

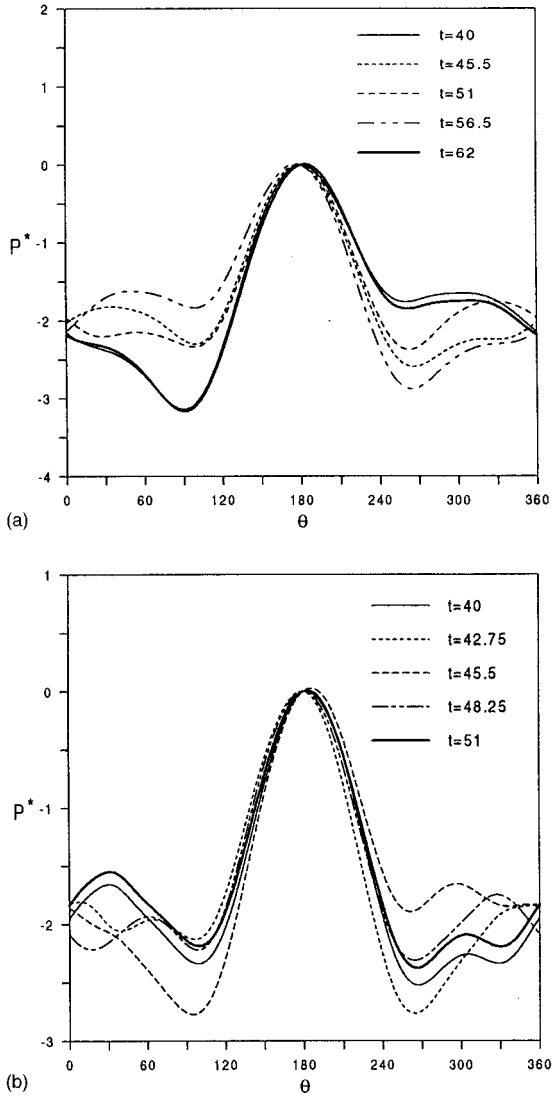

Fig. 9 The time variation of surface pressure distribution for an non lock-on regime during (*a*) one complete cycle in case of Re=200, $\Theta_A=\pi/4$ and $F_R=1/2$, (*b*) two complete cycle in case of Re=200, $\Theta_A=\pi/8$ and $F_R=2$

coefficient oscillates at twice that frequency. The values of the time-averaged drag coefficient at different Reynolds number are compared with previous works displayed in Table 2 which shows a good agreement.

Flow Regimes of the Rotationally Oscillating Cylinder. The flow structure near a cylinder performing rotational oscillation while placed in a cross-stream is dominated by Reynolds number and amplitude and frequency of oscillations. This study covers the range of Reynolds number up to 200, oscillation amplitude up to π and dimensionless oscillation frequency up to $2S_0$. Based on frequency analysis of vortex shedding, and similar to the previous studies reported by Bishop and Hassan [2] and Tanida et al. [1] on cylinders performing transverse oscillations in a cross-stream, the present preliminary results have shown two distinct regimes. The first is called the non-lock-on regime and is characterized by periodic shedding of vortices at the natural frequency, f_0, irrespective of the forced oscillation frequency. This regime occurs when the cylinder frequency, f, is away from f_0. However, when the oscillation frequency approaches f_0, another regime, called the lock-on regime, occurs. In such regime, the vortices are shed at the same frequency of forced oscillations as reported in the works by Lu and Sato [12] and by Chou [13]. The lock-on regime is found to occur within a band of frequency bracketing the natural frequency. This frequency band is termed as the range of synchronization or the lock-on frequency range.

Since the flow field characteristics near the cylinder may differ from that far away, both near and far wakes are examined. The near wake response is analyzed from the lift record whereas the far wake response is computed from analyzing the time variation of the tangential velocity component at a point downstream in the wake ($r=10$, $\theta=0$).

The Non-Lock-On Regime. Figures 6(*a,b*) show the time variations of drag and lift coefficients for the case of Re=200 when forcing frequency was either below the natural frequency (Fig. 6(*a*)) or above the natural frequency (Fig. 6(*b*)). The amplitudes of lift and drag coefficients are not constants but rather change with nearly periodic beating wave forms. Such wave forms were also found in the works by Bishop and Hassan [2] and Tanida et al. [1] in the case of transverse oscillation and attributed to the combined effect of natural and forced oscillations. Figures 6(*a*) and 6(*b*) show the same frequency of C_L as that of the natural vortex shedding frequency although the forcing frequencies in the two cases are quite different. The Fourier analysis

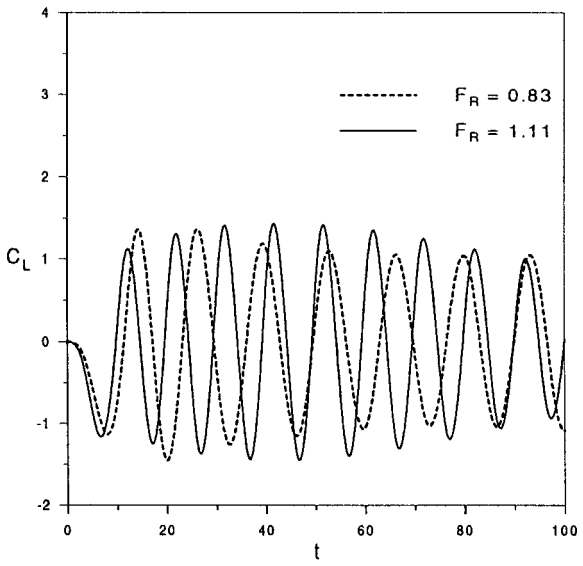

Fig. 10 The time variation of the lift coefficient for a lock-on regime in case of Re=200, $\Theta_A=\pi/4$ and $F_R=0.83$ and 1.11

of the far wake for the two cases is shown in Figs. 7(*a*,*b*). The figures clearly indicate that the far wake response is dominated by the natural frequency.

Typical streamline and equi-vorticity plots for the non-lock-on regime are shown in Fig. 8 for the case of Re=200, $\Theta_A=\pi/4$ and $F_R=0.5$. These plots are prepared at equal intervals through one complete cycle of oscillation. The streamline contours show the details of the flow field structure and its time variation during one cycle. Two opposite vortices are alternately shed from the upper and lower surfaces of the cylinder per half cycle resulting in vortex shedding frequency equal to the natural one. Unlike the case of a fixed cylinder in which the shedding vortices are all equal in size, the vortices generated in the present case are of two different sizes shedding alternately from the upper and lower sides as shown in Fig. 8. This explains the shape of the beating wave form of the lift force plotted in Fig. 6(*a*). A higher peak corresponds to the big vortex detachment and a smaller one corresponds to the small vortex. However, one can see from Fig. 8 that the far wake vortex street is similar to the familiar Karman street developed from a stationary cylinder.

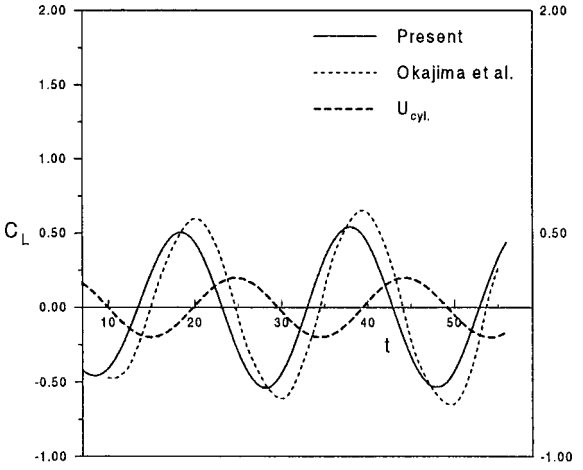

Fig. 11 The time variation of the lift coefficient for the case of Re=40, $S=0.1$ and $\alpha=0.2$ and comparison with the numerical results of Okajima et al. [5].

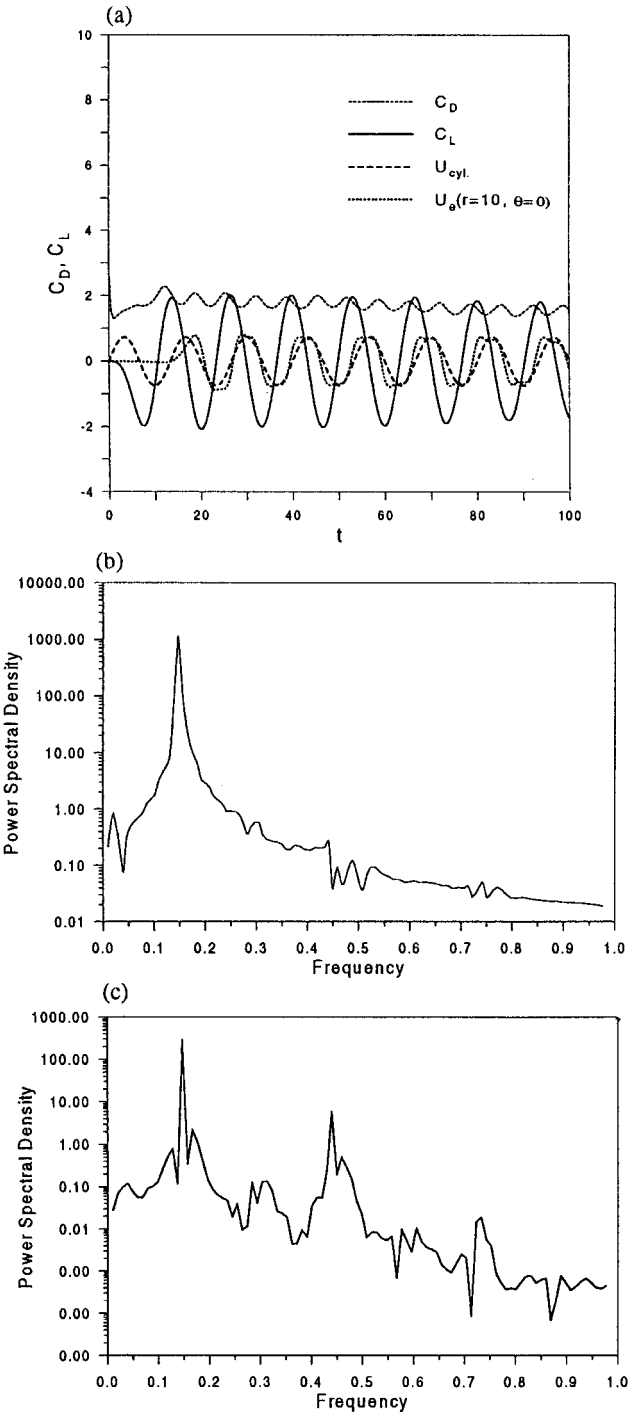

Fig. 12 (*a*) The time variation of lift and drag coefficients and angular velocity in the far wake at Re=200, $\Theta_A=\pi/2$ and $F_R=0.83$ and the corresponding Fourier analysis of (*b*) the near wake and (*c*) the far wake.

Figures 9(*a*,*b*) show the distribution of surface pressure at equal time intervals in the two aforementioned cases. It can be seen that the changes in the surface pressure distribution are small on the upstream side of the cylinder surface while remarkable on the downstream side as a result of vortex shedding. The interesting phenomenon depicted in Fig. 9 is that the pressure distribution in the case of $F_R=2$ attains its nearly periodic behavior at the natural shedding frequency unlike that in the case of $F_R=0.5$ where the nearly periodic behavior is attained at the cylinder frequency. Accordingly, in non-lock-on regimes, the vortices are shed at the

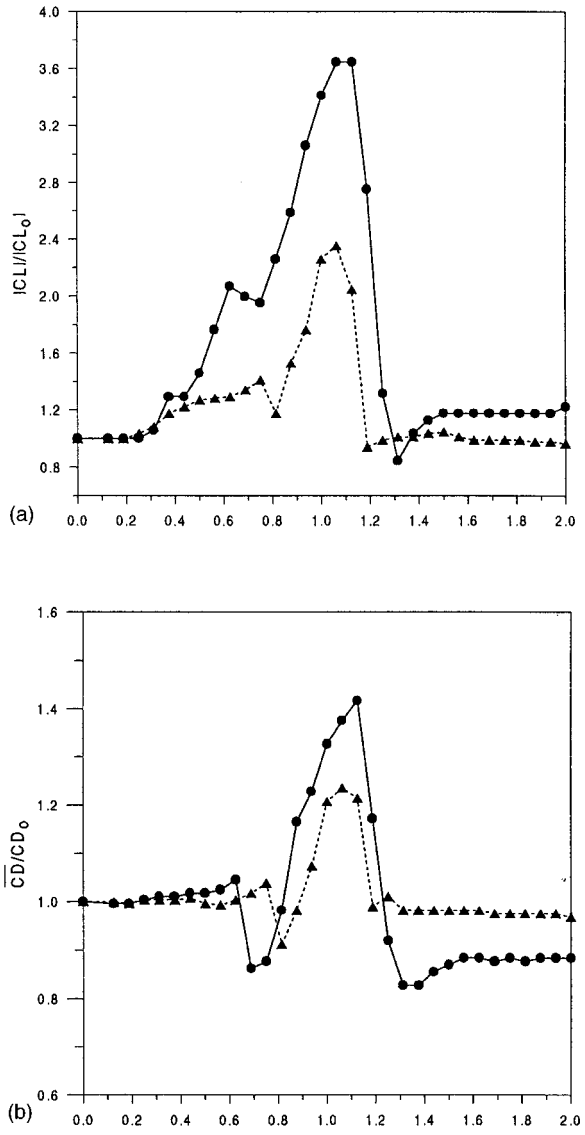

Fig. 13 The effect of frequency ratio on the time-averaged lift and drag coefficients at Re=100, $\Theta_A=\pi/8$ and $\pi/4$; (*a*) lift coefficient and (*b*) drag coefficient. – – – $\Theta_A=\pi/8$; —— $\Theta_A=\pi/4$.

natural frequency whereas the near wake flow field attains its nearly periodic behavior at the lowest frequency (the lowest of the imposed and natural frequencies). On the other hand, the far wake always oscillates at the natural shedding frequency.

The Lock-On Regime. As the forcing frequency approaches f_0, the interaction between the natural and forced shedding mechanisms becomes stronger and the frequency of vortex shedding shifts to synchronize with the imposed rotational frequency. This behavior occurs over a span of frequency bracketing the natural frequency. Figure 10 shows the lift record for a synchronized regime at Re=200 and $\Theta_A=\pi/4$. A quick comparison between the oscillating lift coefficients for the two regimes given in Figs. 6(*a*) and 10 shows a wave form composed of two frequencies (f and f_0) in the first case while only the imposed frequency, f, in the second. Figure 11 shows a comparison between the obtained lift record for a lock-on regime at Re=40, $\alpha=0.2$ and $S=0.1$ and the numerical results reported by Okajima [5]. Although the two records have the same frequency, there is a small difference in amplitudes as well as a phase shift that may be attributed to the different imposed initial conditions. However, the present average value for the lift coefficient amplitude (≈ 0.51) compares very well with experimental value reported by the same authors (≈ 0.47). Figure 12 shows typical examples for records of the lift and drag forces at Re=200, $\Theta_A=\pi/2$ at frequencies within the lock-on range along with time traces of the tangential velocity component in the far wake. It can be observed that the lift force oscillates at the same forced frequency whereas the drag fluctuates at twice the cylinder frequency. The figure also shows that the tangential velocity component in the far wake oscillates at the same cylinder frequency. Fourier analysis of the near wake (Fig. 12(*b*)) and the far wake (Fig. 12(*c*)) for the case of Re=200, $\Theta_A=\pi/2$ and $F_R=0.83$ ($S=0.15$) shows clearly the domination of forcing frequency.

Figures 13(*a*,*b*) show the effect of frequency ratio on the amplitudes of lift and drag coefficients for the two amplitudes $\Theta_A=\pi/8$ and $\Theta_A=\pi/4$ at Re=100. The lock-on range for the case $\Theta_A=\pi/8$ is $0.83<F_R<1.2$ while at $\Theta_A=\pi/4$ the range becomes $0.75<F_R<1.3$. The figure clearly shows that the lift and drag amplitudes increase significantly in the lock-on range and with the maximum occurring near the middle of that range. The same phenomenon was reported in the works of Bishop et al. [2] and Tanida [8]. Shown in Fig. 14 is the present results for the average amplitude of the lift coefficient for the case of Re=80, $\alpha=0.2$ at different frequencies along with both experimental and numerical results reported in Okajima [5]. The figure shows that the obtained C_L amplitude reaches its maximum close to the natural Strouhal number and decreases away from it. The present results roughly fit the experimental data of Okajima [5] with a slight frequency shift of about 0.02.

The streamlines and equi-vorticity lines are plotted for two typical lock-on regimes with the same Reynolds number and amplitude (Re=200, $\Theta_A=\pi/2$) but with two different frequency ratios ($F_R=0.83$ and 1.11) as shown in Figs. 15 and 16. The time period between any two successive plots is one quarter of a cycle. It is clear that the higher rate of vortex shedding occurs at the higher frequency. The longitudinal spacing of the wake wavelength shown in streamlines contours for both cases confirms that the wake wavelength varies inversely with F_R. This agrees well with the results reported by Sarpkaya [20] for the special case of transverse oscillation. The mechanism of diffusion of angular momentum by viscous forces is clearly shown in the equi-vorticity

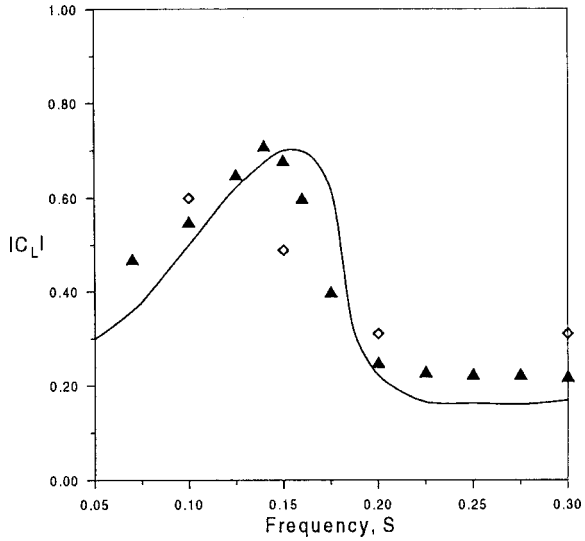

Fig. 14 Effect of frequency on average amplitude of lift coefficient and comparison with previous studies for the case of Re=80 and α=0.2. Π present study; —— experimental and ◇ numerical results of Okajima et al. [5].

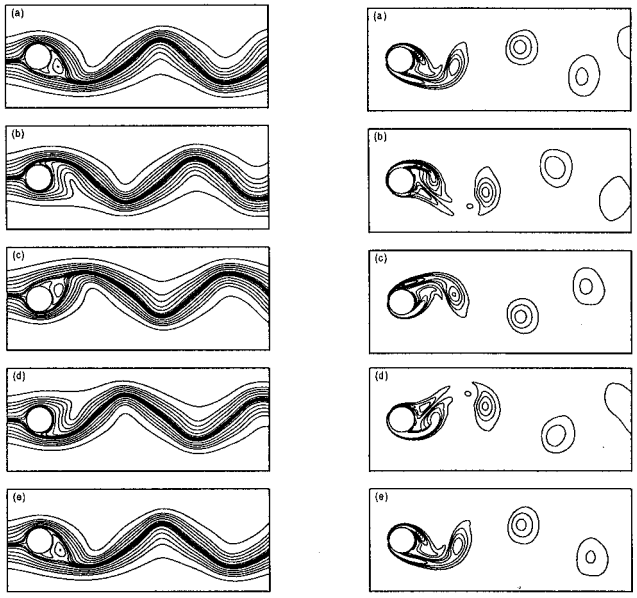

Fig. 15 Streamline patterns (left) and equi-vorticity patterns (right) for one complete cycle in case of Re=200, $\Theta_A=\pi/2$ and $F_R=0.83$ at times (*a*) $t=t_o$. (*b*) $t=t_o+1/4T_p$, (*c*) $t=t_o+1/2T_p$, (*d*) $t=t_o+3/4T_p$ (*e*) $t=t_o+T_p$ where T_p is the time period of cylinder oscillation.

contour plots. The vorticity diffusion mechanism shown in Fig. 16 is similar to the one reported by Lu and Sato [12] for the case of Re=200, Fr=1.0 and $\alpha=2$. Moreover, the periodicity of the flow field is clearly shown in the streamline plots since the start of the cycle is very much the same as the end of it.

The Transition Regime and Lock-On Range. The transition between lock-on and non-lock-on regimes occurs at a certain rotational frequency and is characterized by an intermittent wake flow that switches back and forth between the two regimes. Figure

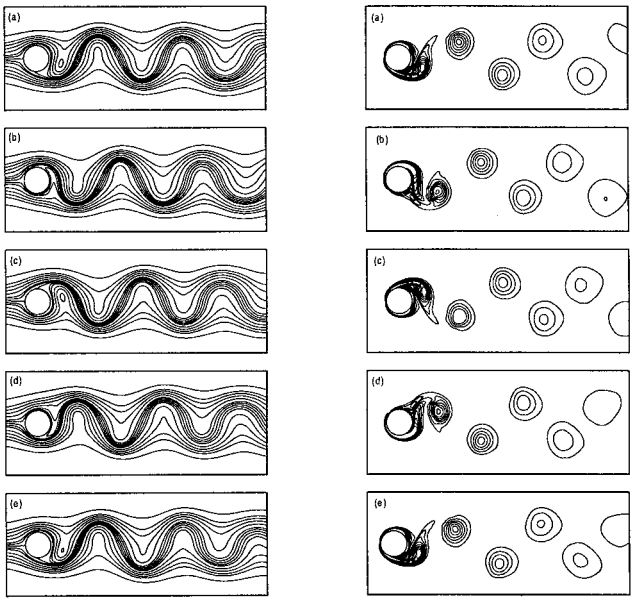

Fig. 16 Streamline patterns (left) and equi-vorticity patterns (right) for one complete cycle of cylinder oscillation in case of Re=200, $\Theta_A=\pi/2$ and $F_R=1.11$ at times (*a*) $t=t_o$. (*b*) $t=t_o+1/4T_p$, (*c*) $t=t_o+1/2T_p$, (*d*) $t=t_o+3/4T_p$, (*e*) $t=t_o+T_p$.

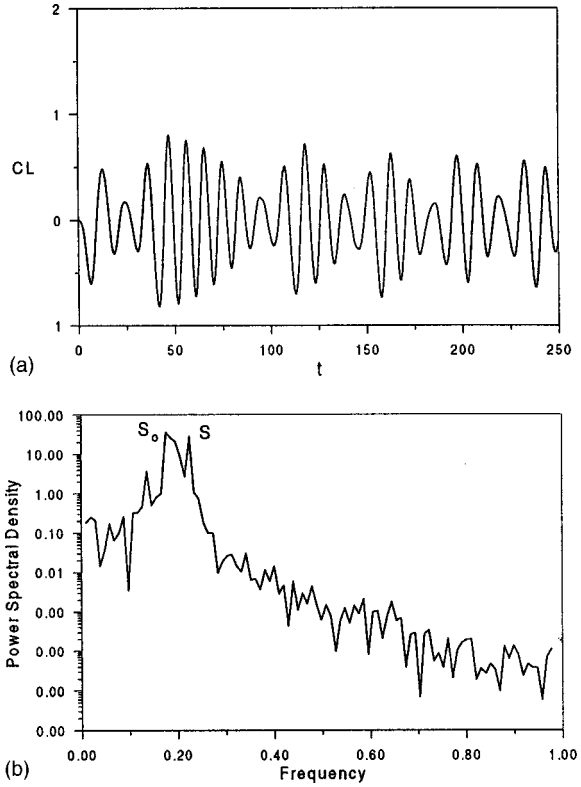

Fig. 17 The time variation of the lift coefficient and corresponding Fourier analysis for the case of Re=200, $\Theta_A=\pi/8$ and $F_R=1.25$: (*a*) lift coefficient, (*b*) Fourier analysis.

17 shows the time variation of the lift coefficient as well as the corresponding Fourier analysis for a typical case representing the transition regime. Figure 17(*a*) shows a change of frequency approximately every two cycles with the larger amplitudes occurring at the forcing frequency and the smaller ones at the natural frequency. The Fourier analysis of C_L (Fig. 17(*b*)) confirms the existence of the two frequencies (S and S_0). Vortex shedding at alternating frequencies at the boundary in between lock-on and

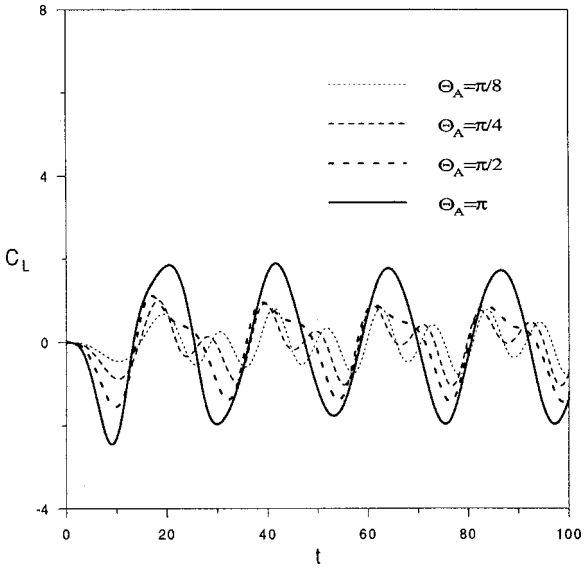

Fig. 18 Effect of oscillation amplitude on the time variation of lift coefficient at Re=200 and $F_R=0.5$

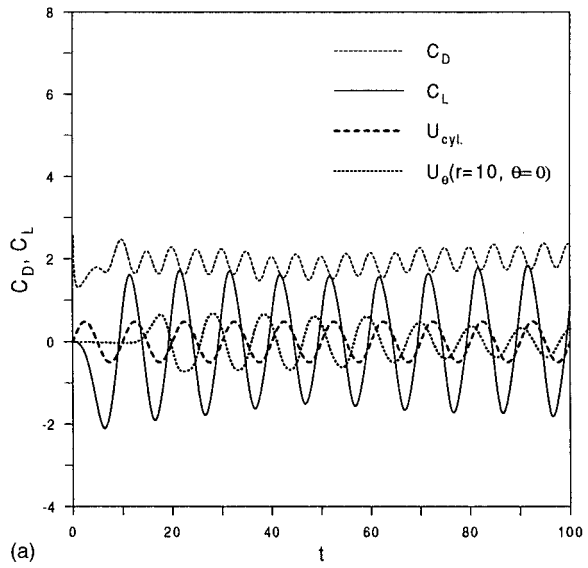

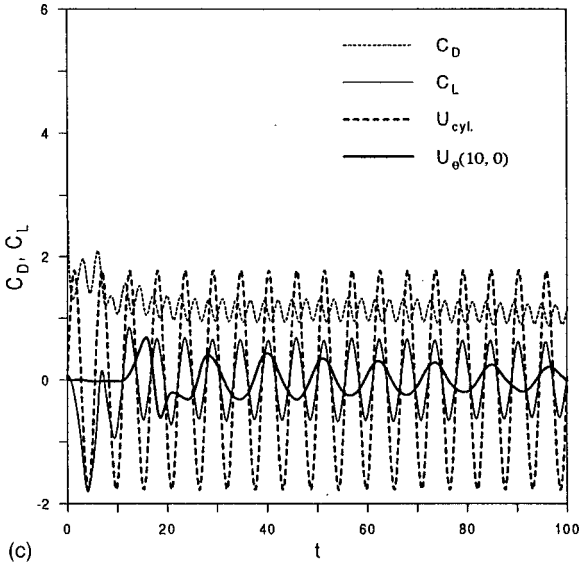

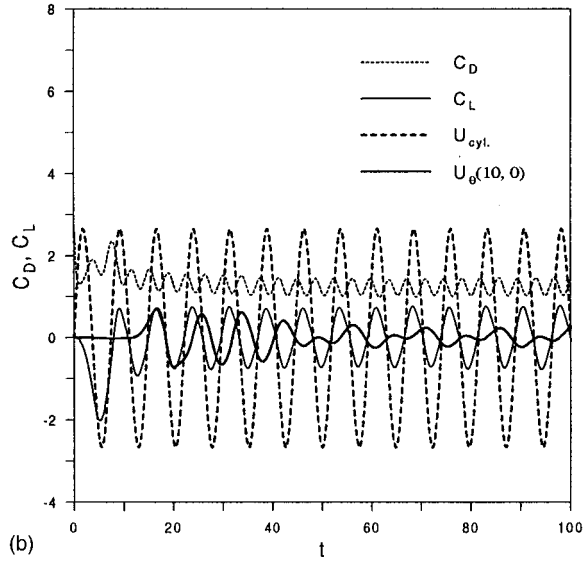

Fig. 19 The time variation of lift and drag coefficients and angular velocity in the far wake ($r=10$, $\theta=0$) at Re=200, $\Theta_A=\pi/2$ and (*a*) $F_R=1.11$, (*b*) $F_R=1.5$, and (*c*) $F_R=2$

non-lock-on regimes was observed experimentally by Stansby [22] and numerically by Karniadakis [23]. The far wake analysis of the same case indicates the same two intermittent frequencies (S and S_0) as before.

The effect of amplitude on the lock-on frequency range has shown to be very significant. The larger the amplitude of oscillation the wider the lock-on frequency range. As the amplitude decreases, the lock-on frequency range becomes narrower until it reaches zero at a threshold amplitude Θ_{A1}. Below this threshold value the lock-on regimes occur only at $F_R=1$. In this study, the numerical experiments have shown that for all amplitudes less than $\pi/40$, the vortices shed at the natural frequency regardless of the forcing frequency, however, the exact threshold value is not known. The existence of such threshold value was also reported in the experimental findings of Koopman [24] for the special case of transverse oscillation. However, this threshold amplitude was not found in the works by Stansby [22] and Meneghini and Bearman [25] in the case of transverse oscillation.

In order to clarify the role of amplitude on the flow regime in the wake, the lift record is examined at Re=200, $F_R=0.5$ and for four different amplitudes ($\Theta_A=\pi/8$, $\pi/4$, $\pi/2$ and π). The two amplitudes $\Theta_A=\pi/8$ and $\Theta_A=\pi/4$ result in non-lock-on regime, with the lift coefficient fluctuating at almost the natural frequency in a beating wave form as shown in Fig. 18. The non-lock-on regime continues to prevail as the amplitude increases to $\Theta_A=\pi/2$ but with clear sign of transition (based on Fourier analysis) to a lock-on regime, which does occur at $\Theta_A=\pi$. The threshold amplitude at this frequency ratio lies between $\Theta_A=\pi/2$ and π. However, no attempt has been made to determine the exact value. Another interesting phenomenon is captured at amplitudes greater than Θ_{A2} (where, in this case, Θ_{A2} lies between $\pi/4$ and $\pi/2$). At such amplitudes, when the frequency is greater than the upper boundary for a lock-on regime, the near wake synchronizes with the cylinder oscillation while the far wake response approaches the non-lock-on regime as the imposed frequency increases. This gradual ''breakup'' in the far wake structure with the increase of forcing frequency was observed experimentally by Tokumaru [6]. To clarify this phenomenon, both the near and far wakes are examined at Re=200, $\Theta_A=\pi/2$ and for three different frequency ratios ($F_R=1.11$, 1.5 and 2). The lift records for these cases are shown in Figs. 19(*a*)–(*c*). Plotted in the same figures is the cylinder surface velocity and traces of the tangential velocity component in the far wake. Figure 19(*a*) clearly shows that both near and far wake regions oscillate at the imposed frequency indicating a periodic lock-on regime. As the frequency increases to $F_R=1.5$ (see Fig. 19*b*), the near wake is only synchronized while the far

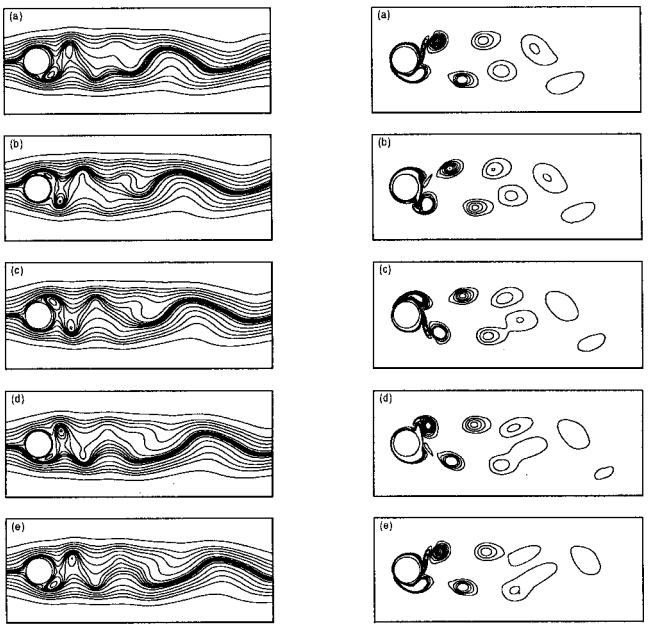

Fig. 20 Streamline patterns (left) and equi-vorticity patterns (right) for one complete cycle of cylinder oscillation in case of Re=200, $\Theta_A=\pi/2$ and $F_R=1.11$ at times (*a*) $t=t_o$. (*b*) $t=t_o+1/4T_p$, (*c*) $t=t_o+1/2T_p$, (*d*) $t=t_o+3/4T_p$, (*e*) $t=t_o+T_p$.

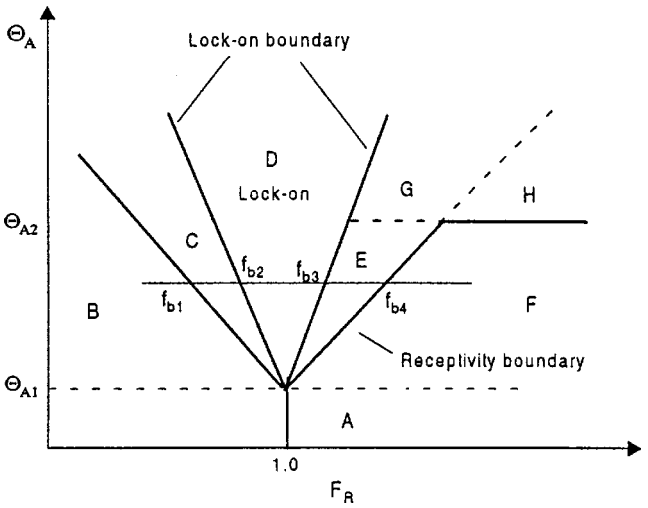

Fig. 21 Frequency selection diagram

wake showing transition between lock-on and non-lock-on regimes. Further increase of frequency to $F_R=2$ (Fig. 19*c*), the near wake response continues to be synchronized whereas the far wake response switches completely to non-lock-on regime where the natural frequency dominates.

The flow field for this last case (Re=200, $\Theta_A=\pi/2$ and $F_R=2$) is plotted at equal time steps during a complete cycle as shown in Fig. 20. The streamline plots show that vortices are shedding alternately at the forcing frequency in the near wake region. These vortices, however, coalesce and evolve into a structure with a lower frequency in the far wake region. The equi-vorticity patterns for the same case show vortices separated by a larger distance in the far wake in comparison with the near wake. The coalescence of vortices is clearly shown in Figs. 20(*b*,*c*,*d*)

In order to summarize all the obtained wake modes, a qualitative frequency-selection diagram is sketched in the frequency-amplitude plane as shown in Fig. 21. Similar diagrams were plotted by Karniadaki and Triantayllou [23] and by Lu and Sato [12]. For amplitudes less than Θ_{A1}, the non lock-on regime prevails (except at $F_R=1$) regardless of the forcing frequency (region A). In the range $\Theta_{A1}<\Theta_A<\Theta_{A2}$, one can distinguish four limiting frequencies, namely, f_{b1}, f_{b2}, f_{b3} and f_{b4}. These frequencies mark the transition between different regimes. The lower and upper boundaries of the lock-on regime (region D) are given by f_{b2}, and f_{b3}, respectively. The two transition regimes (regions C and E) occur at the outskirts of the lock-on region D and identified by the frequency ranges f_{b2} to f_{b1} and f_{b3} to f_{b4}. Forcing frequencies less than f_{b1} or greater than f_{b4}, result in non lock-on regimes (regions B and F). When the amplitude is greater than Θ_{A2} and the forcing frequency greater than f_{b3}, the near wake is locked-on whereas the far wake either has a transition regime (region G) or non lock-on regime (region H).

5 Conclusions

The unsteady flow-characteristics in the wake of a cylinder performing rotational oscillation about its own axis while placed in a steady uniform stream is investigated. The governing equations of motion are solved numerically in the range of Reynolds number up to Re=200, amplitude of oscillation up to $\Theta_A=\pi$ and frequency ratios up to $F_R=2$. The lock-on phenomenon has been predicted and its effect on the hydrodynamics as well as the flow structure in the wake region has been determined. The results show that the lock-on phenomenon occurs within a band of frequency that encompasses the natural frequency. This band becomes wider as the amplitude of oscillation increases. The lift and drag coefficients show an increase within the lock-on frequency range that becomes more significant near the natural frequency. The possible wake characteristics are summarized and presented in the frequency-selection diagram.

Acknowledgments

The authors wish to acknowledge the support received from King Fahd University of Petroleum & Minerals during this study. They also wish to thank the referees for their constructive criticism of the paper and for their valuable comments that were very instrumental in improving the manuscript.

References

[1] Tanida, Y., Okajima, A., and Watanabe, Y., 1973, ''Stability of the circular cylinder oscillating in uniform flow or in a wake,'' J. Fluid Mech., **61**, No. 4, pp. 769–784.
[2] Bishop, R. E. D., and Hassan, A. Y., 1964, ''The lift and drag forces on a circular cylinder oscillating in a flowing fluid,'' Proc. R. Soc. London, Ser. A, **227**, pp. 51–75.
[3] Hurlbut, S. E., Spaulding, M. L., and White, F. M., 1982, ''Numerical Solution for laminar two dimensional flow about a cylinder oscillating in a uniform stream,'' ASME J. Fluids Eng., **104**, pp. 214–222.
[4] Griffin, O. M., and Ramberg, S. E., 1976, ''Vortex shedding from a cylinder vibrating in line with an incipient uniform flow,'' J. Fluid Mech., **75**, pp. 257–271.
[5] Okajima, A., Takata, H., and Asanuma, T., 1975, ''Viscous flow around a rotationally oscillating circular cylinder,'' Inst. Space Aero. Sci. Rep. 532, University of Tokyo.
[6] Tokumaru, P. T., and Dimotakis, P. E., 1991, ''Rotary oscillation control of cylinder wake,'' J. Fluid Mech., **224**, pp. 77–90.
[7] Hori, Ei-ichi, 1962, ''Boundary layer on a circular cylinder in rotational oscillation,'' Bull. JSME, **5**, No. 17.
[8] Taneda, S., 1978, ''Visual Observation of the flow past a circular cylinder performing a rotary oscillation,'' J. Phys. Soc. Jpn., **45**, No. 3.
[9] Wu, J. M., Mo, J. D., and Vakili, A. D., 1989, ''On the wake of a circular cylinder with rotational oscillations,'' AIAA-89-1024.
[10] Tokumaru, P. T., and Dimotakis, P. E., 1993, ''The lift of a cylinder executing rotary motions in a uniform flow,'' J. Fluid Mech., **255**, pp. 1–10.
[11] Filler, J. R., Marston, P. L., and Mih, W. C., 1991, ''Response of the shear layers separating from a circular cylinder to small-amplitude rotational oscillation,'' J. Fluid Mech., **231**, pp. 481–499.
[12] Lu, X., and Sato, J., 1996, ''A numerical study of flow past rotationally oscillating circular cylinder,'' J. Fluids Struct., **10**, pp. 829–849.
[13] Chou, M. H., 1997, ''Synchronization of vortex shedding from a cylinder

under rotary oscillation,'' Comput. Fluids, **26**, No. 8, pp. 755–774.
[14] Badr, H. M., and Dennis, S. C. R., 1985, ''Time-dependent viscous flow past an impulsively started rotating and translating circular cylinder,'' J. Fluid Mech., **158**, p. 447.
[15] Collins, W. M., and Dennis, S. C. R., 1973, ''Flow past an impulsively started circular cylinder,'' J. Fluid Mech., **60**, p. 105.
[16] Ta Phuoc, Loc, and Bouard, R., 1985, ''Numerical solution of the early stage of the unsteady viscous flow around a circular cylinder: A comparison with experimental visualization and measurements,'' J. Fluid Mech., **180**, pp. 93–117.
[17] Ta Phuoc, Loc, 1980, ''Numerical analysis of unsteady secondary vortices generated by an impulsively started circular cylinder,'' J. Fluid Mech., **100**, Part 1, pp. 111–128.
[18] Coutanceau, M., and Menard, C., 1985, ''Influence of rotation on the near-wake development behind an impulsively started circular cylinder,'' J. Fluid Mech., **158**, pp. 399–446.
[19] Williamson, C. H. K., 1991, ''2-D and 3-D Aspects of the wake of a cylinder, and their relation to wake computations,'' Lectures of Applied Mathematics, **9**, Am. Math. Soc., pp. 719–751.
[20] Sarpkaya, T., 1979, ''Vortex-induced oscillations,'' ASME J. Appl. Mech., **46**, 241.
[21] Roshko, A., 1954, ''On the development of turbulent wakes from vortex streets,'' NACA Report, 1191.
[22] Stansby, P. K., 1976, ''The locking-on vortex shedding due to cross-stream vibration of circular cylinder in uniform and shear flows,'' J. Fluid Mech., **74**, pp. 641–665.
[23] Karniadakis, G., and Triantayllou, S. G., 1989, ''Frequency selection and asymptotic states in laminar wakes,'' J. Fluid Mech., **199**, pp. 441–469.
[24] Koopman, G. H., 1967, ''The vortex wakes of vibrating cylinders at low Reynolds numbers,'' J. Fluid Mech., **28**, pp. 501–512.
[25] Meneghini, J. R., and Bearman, P. W., 1995, ''Numerical simulation of high amplitude oscillatory flow about a circular cylinder,'' J. Fluids Struct., **9**, pp. 435–455.
[26] Williamson, C. H. K., 1989, ''Oblique and parallel modes of vortex shedding in the wake of a circular cylinder at low Reynolds numbers,'' J. Fluid Mech., **206**, pp. 579–627.
[27] Chin-Hsiang, C., Jing-Lia, H., and Win, A., 1997, ''Numerical prediction of lock-on effect on convective heat transfer from a transversely oscillating circular cylinder,'' Int. J. Heat Mass Transf., **40**, No. 8, pp. 1825–1834.

Characteristics of Shallow Turbulent Near Wakes at Low Reynolds Numbers

Ram Balachandar
Associate Professor

Shyam Ramachandran
Graduate Student

Mark F. Tachie
Graduate Student

Department of Mechanical Engineering,
University of Saskatchewan,
57 Campus Drive,
Saskatoon, Canada S7N 5A9

The present study deals with the noninvasive measurement of both velocity and concentration in the near region of shallow turbulent wakes using a laser-Doppler anemometer and a video-imaging technique. A 40 mm wide flat plate placed normal to the flow is used as the wake generator. The flow depths considered in the present study are small compared to the width of the channel and the generated wakes are categorized as shallow. Tests were conducted at two depths of flow ($h=20$ and 40 mm) and the boundary layer thickness of the approaching flow is comparable to the depth. The Reynolds number of the flow based on the approaching freestream boundary layer momentum thickness varies from 180 to 400, while, the Reynolds number based on the test body width was maintained nearly constant ($\approx$4000). Measurements were carried out at three axial stations (2.5, 5, and 10 plate widths) downstream of the bluff body. At each axial station, the velocity measurements were carried at distances of h/4, h/2, and 3h/4 from the channel bottom and spanning the cross section of the wake. Appropriate length and velocity scales are identified to characterize the wake. The axial variation of the shallow wake half-width based on both the lateral velocity profile and the lateral concentration profile is also obtained. A shear parameter is introduced to analyze the relative effects of transverse shear and bed friction. [S0098-2202(00)01802-2]

Introduction

Many of the previous studies on bluff body wakes (for e.g., Bisset et al. [1], Browne et al. [2], Kiya and Matsumura [3], Matsumura and Antonia [4], and Townsend [5]) were conducted in test sections of large depths compared to the width of the body (i.e., at large aspect ratio). Several of these studies have been confined to the far wake where the flow is dynamically similar and approximately self-preserving. A few studies have also been carried out in the near wake (Antonia [6] and Cantwell and Coles [7]), and in the intermediate wake (Fage [8], Freymuth [9], Hayakawa and Hussain [10], and Matsumura and Antonia [4]). Recently, Norberg [11] has carried out laser-Doppler velocity measurements in the near region of circular cylinder wakes. In the context of the present study, all the above-mentioned research could be classified as deep wakes (Balachandar et al. [12]).

A shallow flow is defined as the situation where the horizontal length scale of a typical eddy is significantly larger than the vertical scale (e.g., depth of flow). For example, the tanker *Argo Merchant* stranded on the Nantucket shoals produced turbulent eddies in the wake region which have a size of about 2000 ft, while the depth of flow at the same location is only about 50 ft (Van Dyke [13]). Other examples of shallow flow include the wake formed downwind of the mountain in the island of Madeira (Burger and Wille [14]) and the flow past islands in river systems (Ingram and Chu [15]). In shallow flows, bed friction effects become very important and are quantified in terms of a friction length scale, which is usually defined as the ratio of the depth of flow (h) to the skin friction coefficient (C_f). Obviously, the bed friction effects are expected to be minimized in deep flows. For example, the wake region of a bluff body is quite distinct in a deep flow with the formation of well-known Karman vortex street, while in a corresponding shallow flow, the wake is stabilized due to friction effects and the vortex street is annihilated (Balachandar et al. [12]).

Contributed by the Fluids Engineering Division for publication in the JOURNAL OF FLUIDS ENGINEERING. Manuscript received by the Fluids Engineering Division March 12, 1999; revised manuscript received January 21, 2000. Associate Technical Editor: D. R. Williams.

In view of the practical applications, there has been renewed interest in the characteristics of turbulent, shallow open channel wakes (Balachandar et al. [16,12], Chen and Jirka [17], Ingram and Chu [15], Lloyd and Stansby [18], and Wolanski et al. [19]). For example, Ingram and Chu [15] and Wolanski et al. [19] studied the characteristics of flow around islands. Since effluent discharge into shallow waters is often encountered in engineering practice, Balachandar et al. [12] studied the mixing characteristics of a nonreacting pollutant in the island wakes. Other examples of wakes generated in shallow flows include flow past bridge piers and other types of hydraulic structures.

Chu et al. [20] theoretically studied the stability of shear flows in shallow open channel flows. They proposed a bed friction parameter as a relative measure of stabilizing effect of bed friction and destabilizing effect of transverse shear. Based on an order of magnitude argument, Ingram and Chu [15] proposed a wake stability parameter $S=C_f d/h$. Here, d denotes the width or diameter of a bluff body. This definition of S has been used in many subsequent shallow flow bluff body studies (see for example, Lloyd and Stansby [18], Tachie [21], and Balachandar et al. [12]) with no real critical scrutiny. From experimental investigations of shallow flows behind circular cylinders and flat plates, Chen and Jirka [17] proposed critical values of S (denoted as S_c) to signify the onset of particular flow conditions. More specifically, it was suggested that for $S_c \leqslant S_{c1}$ ($\approx$0.20), eddy shedding in the manner of a Karman vortex street is observed, while, for $S_c \geqslant S_{c2}$ ($\approx$0.50), the transverse shear is stabilized and the wake is characterized by a steady wake bubble. For $S_{c1} \leqslant S_c \leqslant S_{c2}$, the wake undergoes transition from vortex shedding to unsteady bubble type flow with instabilities. In a recent study, Lloyd and Stansby [18] made extensive experimental and numerical investigations in shallow wakes behind conical model islands with gentle slopes. They obtained critical stability parameters that were in good agreement with those obtained by Chen and Jirka [17].

A detailed theoretical and experimental investigation of shallow wakes behind flat plates in an open channel flume was made recently by Balachandar et al. [12]. Some useful remarks on the wake stability parameter ($S_c=C_f d/h$) was presented therein. The range of velocities and the depths ($10 \leqslant h$ (mm) $\leqslant 80$) of flow con-

sidered in Balachandar et al. [12] and Lloyd and Stansby [18] studies are similar. However, the size of the wake generators used by Lloyd and Stansby [18] are about 8 to 30 times larger than that used by Balachandar et al. [12]. From careful visual observations and concentration measurements, it was found by Balachandar et al. [12] that for $S_c \leqslant 0.008$, distinct and continuous Karman vortices were noted. For $S_c \approx 0.009-0.018$, weak and intermittent Karman vortices were observed, while the Karman vortex street was completely annihilated when $S_c \geqslant 0.021$. In fact, for a given velocity and plate width, no significant difference between the nature of the Karman vortex street and the development (or spread) of the wake was observed for $h \geqslant 30$ mm. Based on these observations, shallow wakes were reclassified into shallow-shallow wakes and deep-shallow wakes. Given the significant difference in the reported values of the critical wake stability parameter, an alternate measure using the wake velocity data may be more appropriate.

In the study reported by Balachandar et al. [12], only an intermittent Karman vortex street was observed at a flow depth of 20 mm in the wakes generated by a 20 mm and a 40 mm wide flat plate. In the present study, the approaching stream was sufficiently tripped upstream in order that a fully developed turbulent boundary layer is established. As will be discussed later, it is interesting to note that a continuous and distinct Karman vortex street was noted in the present study at $h = 20$ mm. In the earlier study, though no velocity measurements were made in the approaching flow, it can be estimated that the boundary layer was not fully turbulent. If this is true, one might attribute the differences in the shallow wake characteristics to the nature of boundary layer of the approaching stream.

Detailed velocity measurements were recently conducted in deep-shallow wakes generated on smooth and rough beds by Tachie and Balachandar [22] at relatively larger $\mathrm{Re}_\theta = U_e\theta/\nu$. Here, θ is the momentum thickness of the approaching flow and ν is the fluid kinematic viscosity. The flows were tripped and the boundary layer of the approaching stream was fully turbulent. From detailed boundary layer measurements, the skin friction coefficient C_f was determined. The critical wake stability parameter proposed in earlier studies was found to be unsuitable.

Existing literature suggests that detailed information of the velocity field in both the approaching freestream and downstream of the wake generator would be very useful in interpreting the characteristics of shallow turbulent wakes. Such data would also be helpful in defining more representative parameters to characterize the stabilizing effects in the wake region. The characteristics of the velocity field will also aid in interpreting the scalar field data. Currently, velocity measurements are scarce, especially in low Reynolds number, shallow turbulent wakes. In many laboratory-modeling studies, a low Re_θ is dictated by the need to work at low Froude numbers (subcritical flow). The present study is a continuation of earlier research work in shallow wakes. The study is carried out to obtain the velocity and scalar distributions in the near-wake region of a bluff body in a noninvasive fashion. To the knowledge of the authors, this is the first nonintrusive velocity-scalar data set in low Reynolds number shallow turbulent wakes ($\mathrm{Re}_\theta < 400$).

Experimental Setup and Procedure

The present experiments were conducted in a rectangular cross section open channel flume. The flume was 0.6 m deep, 0.8 m wide, and 10 m long. A contraction and several stilling arrangements used to reduce any large-scale turbulence in the flow preceded the straight section of the channel. The sidewalls of the flume were made of transparent tempered glass to facilitate measurement of velocity using a laser-Doppler anemometer. The test body was located 4 m downstream of the contraction. At low velocities, the boundary layer in the test section region is expected to be in a state of transition from laminar to turbulent. Consequently, tripping of the boundary layer was required to achieve a fully developed turbulent regime. The trip was made up of sand particles (median diameter: 1.0 mm) and glued on to the bottom of the channel as a 25 mm strip spanning the entire width of the flume. The trip was located 1.75 m upstream of the bluff body. Two tests were carried out at flow depths $h = 20$ and 40 mm. In each test, measurements were carried out at three axial stations (2.5, 5, and 10 plate widths) downstream of the bluff body. At each axial station, the velocity measurements were obtained at distances of $h/4$, $h/2$, and $3h/4$ from the channel bed and spanning the entire cross section of the wake (Fig. 1). The velocity measurements were carried out using a single-component fiber-optic probe laser-Doppler anemometer (Dantec Inc.). Detailed descriptions of the laser-Doppler anemometer system and the signal processor used in the present study are available elsewhere and avoided here for brevity (Ramachandran [23]). The lateral concentration distribution was also obtained at the three axial stations using a nonintrusive image analysis technique. The method of measurement is similar to that reported in Balachandar et al. [24,12]. Preliminary experiments similar to that reported earlier (Balachandar and Ramachandran [25]) were carried out to ensure that a fully developed turbulent boundary layer did occur in the test section at the lower values of Re_θ. The mean velocity in the boundary layer flow approaching the flat plate is denoted as U_s and the freestream velocity outside the boundary layer is denoted as U_e (Fig. 1). In the present study, the value of U_e was of the order of 0.1 m/s. The longitudinal mean velocity in the wake at any measurement location is denoted as u. Prior to conducting concentration and velocity measurements in the wake, detailed velocity measurements were made in the approaching boundary layer to estimate the skin friction coefficient. A summary of important test parameters is given in Table 1.

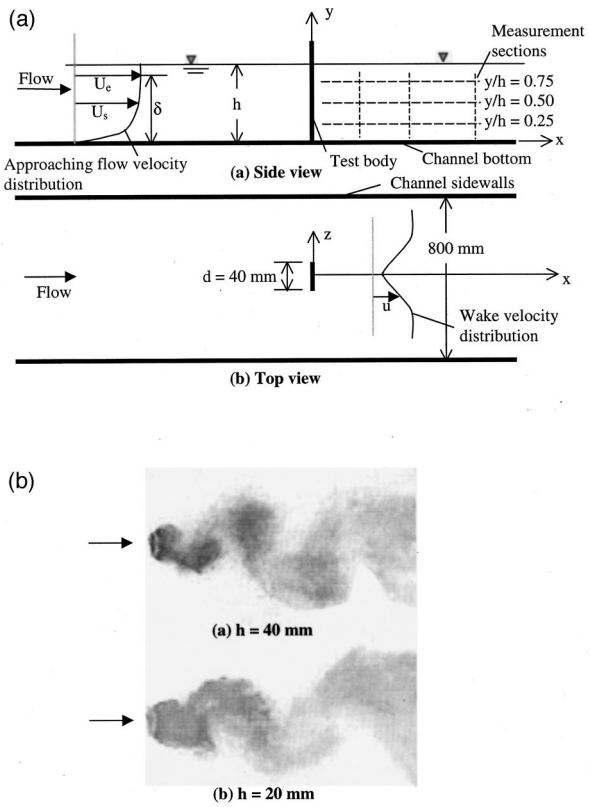

Fig. 1 (*a*) Schematic of the test body and coordinate system; (*b*) photographs of the flow field

Table 1 Summary of test conditions

Test	d (mm)	h (mm)	U_e (m/s)	Re ($U_e d/\nu$)	Re_θ ($U_e\theta/\nu$)	δ/h (%)	C_f ($\times 10^3$)	St
A	40	40	0.10	3988	385	83	6.1	0.15
B	40	20	0.095	3962	188	82	7.5	0.11

Results and Discussion

Visual Observations. Visual observations indicate that a distinct and continuous vortex street was formed in all the test conditions considered in the present study. The vortex patterns are quite well defined in the near wake region. However, for the 20 mm depth, the wake at times resembled the unsteady bubble type flow reported by Chen and Jirka [17]. Figure 1(*b*) shows typical photographs of the near wake region ($x/d<10$). On visually following the vortices in the wake region, one noticed that at the 20 mm depth of flow, the vortex structures started to loose their organized appearance at about 10–15 plate widths from the bluff body. In the case of the 40 mm depth of flow, the organization weakened at a larger distance from the plate (>20 plate diameters). It would appear that the transverse instabilities tend to grow weaker downstream.

Attempts were made to visually determine the dimensionless frequency of vortex shedding (St). The frequency of vortex shedding (f) for each test condition was determined by noting the time for 50 vortices to pass through an axial location ($x/d\approx 5.0$). The values of St ($=fd/U_e$) reported in Table 1 are average values obtained from five such realizations. The value of St=0.15 obtained at $h=40$ mm is in excellent agreement with those found at similar test conditions by Tachie [21] and also by Tachie and Balachandar [22] from spectra analysis of velocity data. The value of St=0.11 observed at $h=20$ mm is low when compared to conventional values for St for sharp-edged flat plates.

Longitudinal Mean Velocity. Figure 2 shows the variation of the mean wake velocity defect at the two depths of flow at three axial stations ($2.5\leqslant x/d\leqslant 10$). At each axial station, measurements were obtained across the wake at $y=0.25$ h, 0.50 h, and 0.75 h from the channel bottom. In Fig. 2, U_s refers to the mean velocity in the approaching boundary layer at the corresponding y/h. The wake half-width (δ_v) is used as the normalizing length scale. Here, δ_v is defined as the location where the velocity defect becomes equal to one half the maximum defect. The data at a given x/d indicate a near collapse of the wake velocity defect profiles irrespective of the measurement location y/h and depth of flow. The data acquired at $y/h=0.25$ for the $h=40$ mm test were lost due to a computer error; however, as the data acquired for various values of y/h collapse onto a single curve, there was no need to reacquire the data at $y/h=0.25$.

At all axial locations considered in the present study, the velocity defect profiles show a single peak. In the recent smooth and rough wall wake velocity measurements made in the same test facility by Tachie and Balachandar [22], well-defined double peaks were observed for $x/d\leqslant 2.5$. It should also be remarked, that the range of velocity considered in the earlier study is about 3–4 times higher than the values considered herein. Furthermore, the maximum velocity defect $(U_s-u)/U_s$, in Tachie and Balachandar [22] is about 1.36 in comparison with the values of 0.8–0.9 obtained in the present study. One important difference between the present profiles and that reported earlier in two-dimensional wakes is the choice of U_s as the velocity scale instead of the freestream velocity U_e.

In Fig. 3, the variation of the wake velocity defect in the present study is compared with some earlier deep wake data. For the deep flows, as indicated in the figure, $U_s=U_e$. To avoid clutter in the data, only the results of the test at $h=40$ mm is shown. To account for the shape of the test body and the relative differences in

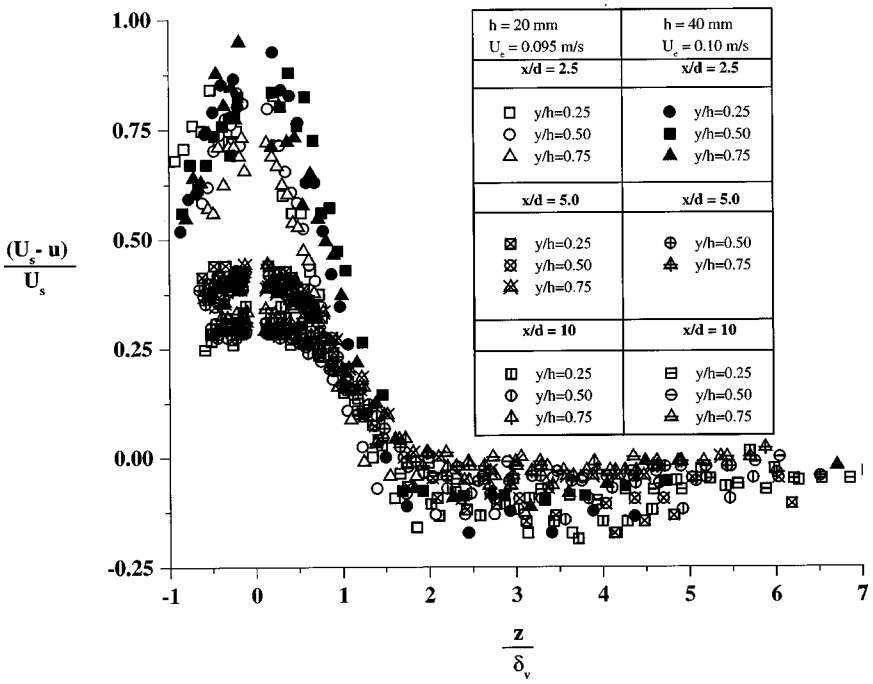

Fig. 2 Variation of mean velocity defect at three axial stations (uncertainty in u: ±0.75 percent, uncertainty in z/δ_v: ±4 percent)

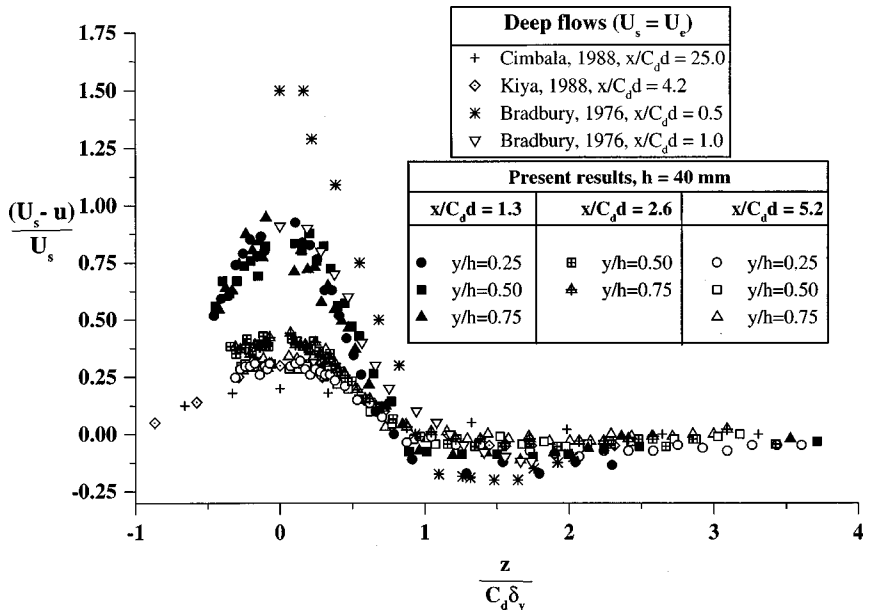

Fig. 3 Mean velocity distribution across the wake (deep and shallow flows) (uncertainty in u: ±0.75 percent, uncertainty in $z/C_d\delta_v$: ± 4 percent)

the axial station location, the normalized distance from the test body is defined as $x/C_d d$ and the lateral distance across the wake is normalized by $C_d\delta_v$. Here, C_d is drag coefficient of the test body. At corresponding values of $x/C_d d$, the present shallow wake results show good agreement with previous deep wake data and serves to validate the procedures used in the present study. Furthermore, the data also indicate that $C_d\delta_v$, is the proper length scale to compare the characteristics of bluff bodies of different shapes.

Attempts were made to choose proper scaling variables to study if the wake mean velocity distributions could be deemed to be self-similar. Many different length and velocity scales were adopted, but there was little success in trying to collapse the velocity profiles at various axial stations and at various distances from the wall (Ramachandran [23]). Figure 4 shows the mean velocity distribution using the most useful set of velocity and length normalizing states that could be identified. Here, the normalized velocity is defined as $U^* = (u - U_{\min})/(U_{\max} - U_{\min})$, where, $U_{\max}$ and $U_{\min}$ are the maximum and minimum velocities

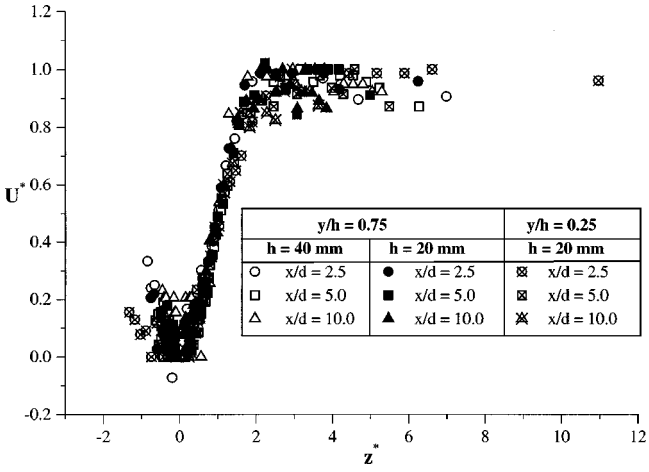

Fig. 4 Normalized mean velocity profiles at three axial locations (uncertainty in u: ±0.75 percent, uncertainty in z: ±4 percent)

at any axial location across the wake cross section. This scaling is similar to that used in plane mixing layer studies (for e.g., see White [26]). The normalizing length scale adopted in Fig. 4 is $z_{0.5}$ and is defined as the lateral location where $U^* = 0.5$ as one moves from the wake axis toward the outer edge of the wake. In Fig. 4, the results for $h = 20$ and 40 mm at $y = 0.75$ h are shown. For comparison, the data at $y = 0.25$ h for the 20 mm test is also shown in Fig. 4. The data for $h = 20$ mm tests, especially at $y/h = 0.25$, contribute to the scatter seen in the vicinity of $z^* \approx 0$ and $z^* > 2$. For the most part, the collapse of data at all axial locations onto one curve is fair. This type of scaling suggests a sense of self-similarity in mean velocity profiles. It should be recalled that in deep wakes, using conventional defect scaling, self-similarity is reported not to be attained until several diameters downstream of the bluff body (≈50 d).

The Shear Layer Parameter. In a shallow wake, the formation and subsequent evolution of the vortex street depends on the relative magnitude of the transverse shear and bed friction. The transverse shear tends to destabilize the flow while the bed friction has a stabilizing effect on the development of the wake. If the bed friction effect becomes relatively strong, the lateral extent or spread will be limited. Moreover, as noted from the visual observations, when one is located relatively farther from the wake generator, the wake tends to become stabilized. As has been pointed out earlier, the wake stability parameter $S = C_f d/h$ is not quite appropriate to characterize the relative effects of transverse and bed friction. In the present study, a transverse shear parameter (β) is defined as:

$$\beta = \left(\frac{U_{\max} - U_{\min}}{U_s} \right) \frac{d}{z_{0.5}}$$

Figure 5 shows the variation of β with $C_f x/d$. The corresponding values of β for wakes generated on smooth and rough walls (Tachie and Balachandar [22]) are also shown for comparison. The results indicate a fair degree of collapse onto a single curve for all the smooth wall data. The C_f values in the present experiments are higher than the corresponding smooth wall values noted in the previous study, and, in fact are comparable to the previous rough wall data. It should also be noted that while both sets of experiments (previous and present) were conducted in the same

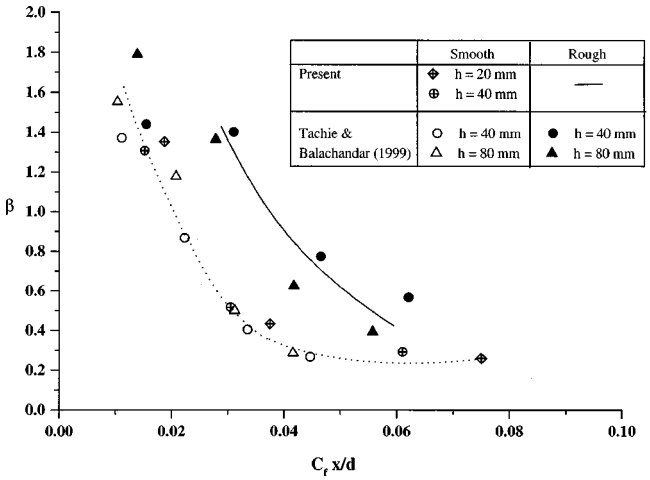

Fig. 5 Variation of β parameter with the normalized axial distance (uncertainty in β: ±4 percent, x/d: ±3 percent)

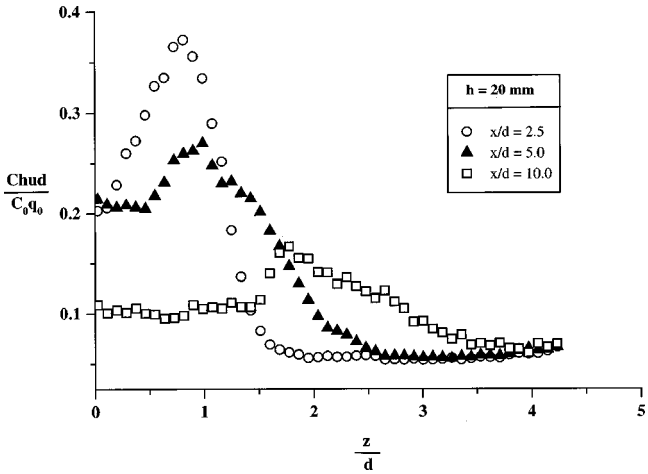

Fig. 6 Normalized concentration distribution across the wake (uncertainty in $Chud/C_0q_0$: ±8 percent, z/d: ±3 percent)

test facility and with the same wake generator, the Reynolds numbers in the present study are lower than that considered in the previous investigation. Figure 5 indicates that the transverse shear parameter β decreases with increasing distance from the bluff body and increasing bed friction. If β is high, a Karman type vortex street is expected to be present in the near wake region even if bed friction effects are high, while, in the far wake, the vortex street is expected to be annihilated as β tends to a low value. The slope of β versus $C_f x/d$ curve is an indication of the relative measure of the transverse shear to the skin friction coefficient and hence, a measure of the stability of the wake. At lower values of $C_f x/d$, the curve through the smooth data indicates a larger gradient when compared to the rough wall wake data. This indicates that wakes on rough walls have a greater tendency to become stable and tend to lose the presence of an organized vortex street earlier in the wake region. Farther from the plate, the gradient is small indicating that bed-friction effects will become more prevalent. The present smooth wall results indicate that β tends to an asymptotic value of about 0.2 beyond which the well-organized structures begin to disappear. For a rough wall, with the limited data available, one cannot conclude the existence of an asymptotic value. However, the trend of the data does indicate that there is a distinct possibility for β to approach the smooth wall data. Overall, one can conclude that the stabilizing effect of skin friction on the transverse shear is more complicated than would appear at first sight, and a wake stability parameter defined similar to that defined in earlier studies is not useful. The use of Fig. 5 would be to some extent more appropriate to characterize the effects of bed friction and transverse shear on the development of shallow turbulent wakes.

Mean Concentration. Figure 6 shows the variation of the normalized mean concentration ($Chud/C_0q_0$) at three axial stations in the near wake region for $h=20$ mm. Here, C is the value of the local mean concentration, C_0 is the initial concentration of dye, q_0 is the dye injection rate, and u is the mean velocity at the measurement location. The mean concentration C at each data point in these figures is an average value obtained from 100 images at a time interval of one-third of a second. The time period considered herein corresponds to a total of 18 vortices (for $h=20$ mm) and 24 vortices (for $h=40$ mm) being shed from the wake generator. For similar test conditions (Balachandar et al. [12]), 50 images obtained in a time interval of one-third of a second were shown to be adequate in providing statistical convergence in the mean concentration data. In developing Fig. 6, it should be remarked that a fit for the velocity data (Fig. 2) was used as both the concentration and velocity data were not available at the same lateral location.

The present concentration profiles show characteristic double peaks reminiscent of scalar data in the near and intermediate turbulent wake (see for example, Balachandar et al. [16,12]). It should be remarked that the concentration data was acquired on both the sides of the wake axis and a lack of symmetry was noticed. This may be attributed to the paths the vortices traverse once they are shed. The value of the concentration within a vortical structure is expected to be highest in the core. Thus, the locations of the vortex centers (relative to the wake axis) would influence the presence (or absence) of true symmetry. In earlier studies, detailed investigation of the trajectories of shed vortices from scalar measurements (Tachie [21], Balachandar et al. [12]) indicate that the location of the vortex centers are irregularly distributed and could lie very close to the wake centerline (and in some cases, on the wake axis). Cantwell and Coles [7] and Hayakawa and Hussain [10] also reported similar vortex core trajectories.

With increasing x/d, it can be inferred from Fig. 6 that the peak of the concentration profile decreases and the wake spreads outwards. Continuity considerations require that the area under each of the curves in Fig. 6 be the same. Variations in the mass balance (up to 20 percent) have been noted over the axial locations considered herein, partly due to the limitations in the concentration measurement technique. It should be noted that the video imaging technique used in the present study provides the depth-averaged concentration in each of the 100 images used to compute C and not the true instantaneous concentration. However, previous studies have noticed a lack of mass balance of up to 60 percent (Tachie [21]) using the approaching stream velocity as the velocity scale.

The Wake Half-Width. In order to study the effects of bed friction and transverse shear on the turbulent entrainment process, the spread of the wakes was determined at various axial locations from both concentration and velocity measurements. Sufficient evidence, both old (for example, LaRue and Libby [27,28]) and new (Balachandar et al. [16,12], Tachie [21]), suggests that the half-width determined from scalar measurements (δ_s) is relatively larger than corresponding values (δ_v) obtained from velocity measurements. In the near wake, it has been found that $\delta_s/\delta_v = 1.5 \sim 2.5$. Typical values reported in the far wake is in the range $\delta_s/\delta_v = 1.3-1.6$. Figure 7 shows the variation of δ_s and δ_v with downstream distance. The half-widths are normalized by d/C_f while the axial distance is normalized by the friction length

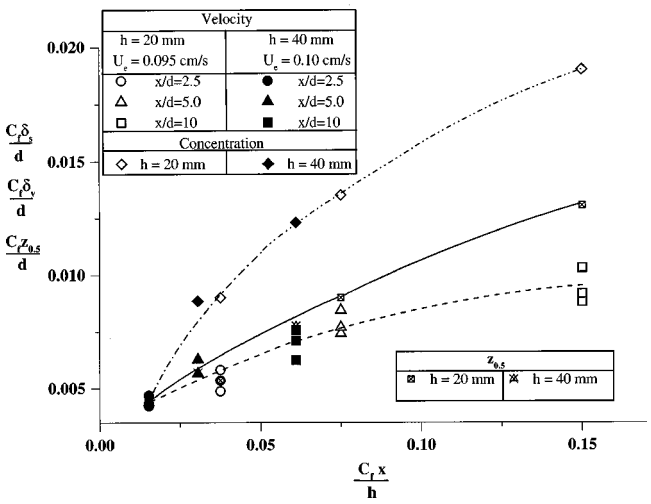

Fig. 7 Axial variation of the wake half-width (uncertainty in $C_f\delta/d$ or $C_f z_{0.5}/d$: ±4 percent, uncertainty in $C_f x/h$: ± 3 percent)

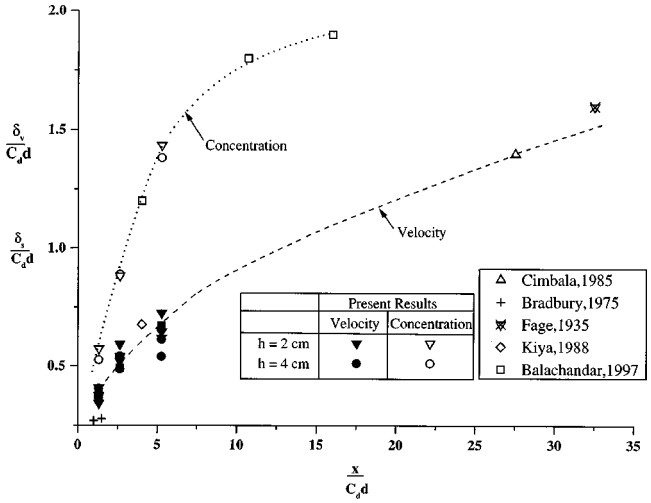

Fig. 8 Variation of the wake half-width with axial distance for deep and shallow flows (uncertainty in $\delta_s/C_d d$: ±4 percent, $x/C_d d$: ±3 percent)

scale h/C_f. The present scalar data shows a higher rate of increase in the wake half-width when compared with the velocity data. Typically, in the near wake region, $\delta_s/\delta_f \approx 2.0$. This is consistent with earlier evidence. Also shown in Fig. 7 is the variation of $z_{0.5}$ (determined from the U^* profile) with axial location. At any axial location, $z_{0.5}$ is about 24–30 percent higher than δ_v. This increase is comparable to the values of 22 to 30 percent reported by Tachie and Balachandar [22].

In Fig. 8, the half-widths obtained from the present dataset are compared with some previous scalar and velocity data. In order to account for the shape of the wake generator used in each experiment, the wake momentum thickness ($=C_d d$) is adopted as the characteristic length scale for both δ and x. Agreement between the two sets of data (i.e., present and previous) is generally good.

Uncertainty Estimates

The uncertainty estimates indicated in the figure captions are obtained at odds of 20:1. To estimate the uncertainty in C/C_0, five known concentrations covering the expected range of measurements were chosen. For each concentration, a set of thirty repeated measurements was carried out and the maximum deviation from the mean determined. The uncertainty estimates in the velocity measurements varied slightly with distance from the wall. For example, at a distance of 10 mm from the channel bottom, thirty replicate tests were carried out in the approaching flow. Using the standard deviation of these measurements and the *t*-value for 29 degrees of freedom, the uncertainty in the mean velocity was estimated to be ±0.75 percent.

Summary and Conclusions

Experiments were carried out to study the characteristics of low Reynolds number, shallow turbulent wakes. The approaching flow boundary layer thickness was comparable to the depth of flow and bed friction effects were large. Both velocity and concentration data were obtained at three axial stations across the wake. At a given axial station, the approaching velocity of flow was found to be the proper normalizing velocity scale to nondimensionalize the velocity defect. The wake velocity defect data collapse fairly onto a single curve and are independent of the measurement location y/h and depth of flow. The U^* versus z^* velocity profiles indicate a sense of similarity in the near wake. The proposed β versus $C_f x/d$ relationship provides a representative wake stability parameter to characterize the relative effects of transverse shear and bed friction. An asymptotic value of $\beta=0.2$ was noticed beyond which the organized vortices begin to disappear. The wake half-width data based on the concentration profiles show a higher spread compared with the velocity data.

References

[1] Bisset, D. K., Antonia, R. A., and Browne, L. W. B., 1990, ''Spatial Organization of Large Structures in the Turbulent Far Wake of a Cylinder,'' J. Fluid Mech., **218**, pp. 439–461.

[2] Browne, L. W., Antonia, R. A., and Shah, D. A., 1989, ''On the Origin of the Organized Motion in the Turbulent Far-Wake of a Cylinder,'' Exp. Fluids, **7**, pp. 475–480.

[3] Kiya, M. and Matsumara, M., 1988, ''Incoherent Turbulence Structure in the Near Wake of a Normal Plate,'' J. Fluid Mech., **190**, pp. 343–356.

[4] Matsumara, M. and Antonia, R. A., 1993, ''Momentum and Heat Transport in the Turbulent Intermediate Wake of a Circular Cylinder,'' J. Fluid Mech., **250**, pp. 651–668.

[5] Townsend, A. A., 1949, ''The Fully Developed Turbulent Wake of a Circular Cylinder,'' Aust. J. Sci. Res., **2A**, pp. 451–468.

[6] Antonia, R. A., 1991, ''Organization in a Turbulent Near Wake,'' Fluid Dyn. Res., **7**, pp. 139–149.

[7] Cantwell, B. and Coles, D., 1983, ''An Experimental Study of Entrainment and Transport in the Turbulent Near Wake of a Circular Cylinder,'' J. Fluid Mech., **136**, pp. 321–374.

[8] Fage, A. and Falkner, V. M., 1935, ''Note on Experiments on the Temperature and Velocity in the Wake of a Heated Cylindrical Obstacle,'' Proc. R. Soc. London Ser. A, **135A**, pp. 702–705.

[9] Freymuth, P. and Uberoi, M. S., 1971, ''Structure of Temperature Fluctuations in the Turbulent Wake Behind a Heated Cylinder,'' Phys. Fluids, **14**, pp. 2574–2579.

[10] Hayakawa, M. and Hussain, F., 1989, ''Three Dimensionality of Organized Structures in a Plane Turbulent Wake,'' J. Fluid Mech., **206**, pp. 375–404.

[11] Norberg, C., 1998, ''LDV-Measurements in the Near Wake of a Circular Cylinder,'' FEDSM98-5202, American Society of Mechanical Engineers Annual Conference, pp. 1–12.

[12] Balachandar, R., Tachie, M. F., and Chu, V. H., 1999, ''Concentration Profiles in Shallow Turbulent Wakes,'' ASME J. Fluids Eng., **121**, No. 1, pp. 34–43.

[13] Van Dyke, M., 1982, *An Album of Fluid Motion*, Parabolic Press, p. 176.

[14] Burger, E. and Wille, R., 1972, ''Periodic Flow Phenomena,'' Annu. Rev. Fluid Mech., **4**, pp. 313–340.

[15] Ingram, G. R., and Chu, V. H., 1987, ''Flow Around Islands in Rupert Bay: An Investigation of the Bottom Friction Effect,'' J. Geophys. Res., **92**, No. C13, pp. 14.521–14.533.

[16] Balachandar, R., Chu, V. H., and Zhang, J., 1997, ''Experimental Study of Turbulent Concentration Flow Field in the Wake of a Bluff Body,'' ASME J. Fluids Eng., **119**, pp. 263–270.

[17] Chen, D. and Jirka, G. H., 1995, ''Experimental Study of Plane Turbulent Wakes in a Shallow Water Layer,'' Fluid Dyn. Res., **16**, pp. 11–41.

[18] Lloyd, P. M. and Stansby, P. K., 1997, ''Shallow Water Flow Around Model Conical Islands of Small Side Slope,'' J. Hydraulic Eng., **123**, No. 12, pp. 1057–1067.

[19] Wolanski, E., Imberger, J., and Heron, M. L., 1984, ''Island Wakes in Shallow Coastal Water,'' J. Geophys. Res., **89**, No. C6, pp. 10553–10569.

[20] Chu, V. H., Wu, J.-H., and Kahyat, R. E., 1991, ''Stability of Transverse Shear Flows in Shallow Open Channels,'' J. Hydraulic Eng., **117**, pp. 1–19.

[21] Tachie, M. F., 1997, ''Scalar Transport in Intermediate Two-Dimensional Turbulent Wakes,'' M. Sc. thesis, University of Saskatchewan.

[22] Tachie, M. F. and Balachandar, R., 2000, ''Shallow Wakes Generated on Smooth and Rough Surfaces,'' to appear in Experiments in Fluids.
[23] Ramachandran, S. S., 1999, ''Bed Friction Effects in Low Reynolds Number Shallow Wakes,'' M.Sc. thesis, Department of Mechanical Engineering, University of Saskatchewan, Canada.
[24] Balachandar, R., Tachie, M. F., and Ramachandran, S., 1998, ''Application of Video Image Processing to Measure Dye Transport in Turbulent Wakes,'' FEDSM-98, ASME Fluids Engineering Division, Washington, DC, June 1998.
[25] Balachandar, R. and Ramachandran, S., 1999, ''Turbulent Boundary Layers in Low Reynolds Number Shallow Open Channel Flows,'' ASME J. Fluids Eng., **121**, No. 3, pp. 684–689.
[26] White, F., 1991, *Viscous Fluid Flow*, 2nd edition, McGraw-Hill, New York.
[27] LaRue, J. C. and Libby, P. A., 1974, ''Temperature and Intermittency in the Turbulent Wake of a Heated Cylinder,'' Phys. Fluids, **17**, No. 5, pp. 873–878.
[28] LaRue, J. C. and Libby, P. A., 1974, ''Temperature Fluctuations in the Plane Turbulent Wake,'' Phys. Fluids, **17**, No. 11, pp. 1956–1967.

Jorge D'Elía
Graduate Researcher,
e-mail: jdelia@intec.unl.edu.ar

Mario A. Storti
Senior Researcher,
e-mail: mstorti@intec.unl.edu.ar

Sergio R. Idelsohn
Professor,
e-mail: rngtm@acride.edu.ar

Centro Internacional de Métodos Computacionales en Ingeniería (CIMEC), INTEC (UNL-CONICET). Güemes 3450, 3000-Santa Fe, Argentina

A Panel-Fourier Method for Free-Surface Flows

A panel-Fourier method for ship-wave flow problems is considered here. It is based on a three-dimensional potential flow model with a linearized free surface condition, and it is implemented by means of a low order panel method coupled to a Fourier-series. The wave-resistance is computed by pressure integration over the static wet hull and the wave-pattern is obtained by a post-processing procedure. The strategy avoids the use of numerical viscosity, in contrast with the Dawson-like methods, widely used in naval-panel codes, therefore a second centered scheme can be used for the discrete operator on the free surface. Numerical results including the wave-pattern for a ferry along fifteen ship-lengths are presented. [S0098-2202(00)01402-4]

1 Introduction

Panel methods are classical and widely accepted in the industry for calculating potential flows, e.g., Morino and Kuo, [1], Katz and Plotkin [2]. In some problems a two-dimensional approach is sufficient, for instance, flows past multicomponent airfoils, infinite cascade and ground effects, e.g., Mokry [3], Storti et al. [4] while in others a three-dimensional approach is necessary. Earlier panel methods were of nonlifting type, which have served as a basis for their lifting successors. Since most subsequent panel developments carried out by aircraft-oriented investigators for whom the lift and the wake are all-important, principal attention was focused on the means of handling them (e.g., Morino [5]). Marine problems, like the flow around propellers, can be also treated by the same methods (e.g., Kinnas and Hsin [6]). However, many of them are truly nonlifting, such as the case of surface ships (e.g., Dawson [7]) and, then, in these problems, where the nonlifting case has received a most extensive development and industrial use. More recently, ship-wake and wave-pattern far downstream are also of interest due to satellite remote sensing. In general, the hydrodynamic problem retains many of the complexities associated with aircraft case such as the need to predict the flow around multiple bodies, for instance, the fuselage/wing interaction can be seen as equivalent to hull/keel interaction. Other approaches are also possible as multigrid Euler schemes with artificial compressibility (e.g., Farmer et al. [8]). In the surface ship case, when a body moves near the free surface of a fluid, a pattern of trailing gravity waves is formed. The energy spent in building this pattern comes from the work done by the body against the *wave resistance*. As a first approximation, the wave resistance can be computed using a potential model, while for the viscous drag it can be assumed that the position of the surface is held fixed at the reference hydrostatic position, i.e., a plane. This is, basically, the *Froude hypotheses*. With this assumption the interaction produced between the boundary layer (which tends to produce a larger body) and the wave pattern is neglected. Even if a potential model is assumed for the liquid, the problem is nonlinear due to the free surface boundary condition.

This work focuses in the computation of the flow field and wave resistance for a body in steady motion on deep water by means of a potential model for the fluid and a linearized free surface boundary condition. This is the basis for most ship design codes in industry. The governing equations are the Laplace equation with slip boundary conditions on the hull and channel walls, inlet/outlet conditions at the corresponding planes and the free surface boundary conditions. At this stage, the mathematical model results in a nonlinear one due to both kinematic and dynamic boundary conditions on the free surface (e.g., see Stoker, [9]). The first of them is related to the unknown position of the free surface, while the second one is related to the nonlinear expression of the Bernoulli equation. A classical strategy in hydrodynamic theory is to make use of asymptotic expansion (e.g., see van Dyke, [10]). In this case, the flow equations are parameterized with respect to an expansion parameter, for example, the Froude number or some of the draft/length and beam/length relations. Then, a *basic* flow is solved which is obtained by taking some limit process on the parameterized equations, so a simpler flow problem is obtained. Finally, a *perturbed* flow is solved, where the perturbation is assumed small enough to remain valid the asymptotic procedure, and usually it is sufficient to stop this procedure at this point. A number of linearizations assuming expansion in the aforementioned parameters can be found in ship hydrodynamic, see e.g., Newman [11]. But the most useful are those related to the slow ship (small Froude number), where the (composed) free surface boundary condition of the perturbed flow amounts to a Neumann boundary condition with a source term proportional to the streamlined second derivative of the basic potential flow. However, without radiation boundary conditions the hydrodynamic problem as stated so far is not well posed, since it is invariant under longitudinal coordinate inversion ($x \rightarrow -x$), and, therefore, unable to capture the characteristic trailing waves propagating downstream. To correct this deficiency, it can be either add a dissipative numerical mechanism or impose some kind of *absorbing* boundary condition. The addition of a third-order derivative to the free surface boundary conditions results equivalent to add a dissipative mechanism and captures the correct sense of propagation for the wave pattern. This is equivalent to the use of a noncentered discretization scheme for the second order operator and falls among the well known *upwind* techniques, e.g., see Baumann et al. [12] or Nigro et al. [13]. The amount of added viscosity is related to the length of the mesh downstream of the body. If the viscosity parameter is too low, the trailing waves arriving at the downstream boundary, are reflected in the upstream direction and pollute the solution. On the other hand, if it is too high, the trailing waves are damped, and incorrect values of the wave-resistance are obtained. Extending the mesh in the down-

Contributed by the Fluids Engineering Division for publication in the JOURNAL OF FLUIDS ENGINEERING. Manuscript received by the Fluids Engineering Division May 27, 1998; revised manuscript received November 30, 1999. Associate Technical Editor: P. Bandyopadhyay.

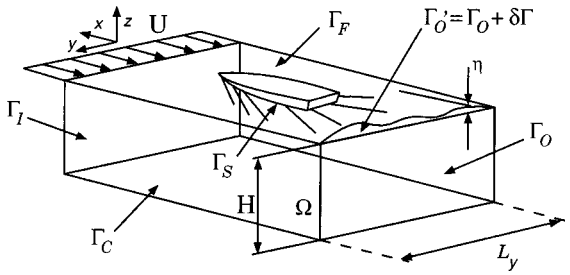

Fig. 1 Geometrical description of the ship wave-resistance problem

stream direction allows the use of a lower viscosity parameter, since the waves are damped over a longer distance, but increases the computational cost (core memory). Numerical experience shows that this third-order streamline viscosity term is too dissipative and the meshes should be extended downstream too much. Dawson proposed a method, where a fourth order derivative (in a velocity formulation) is used instead, with a very particular finite difference discretization. It is astonishing that standard discretization of the same operator does not work and neither do higher order operators (say to the seventh order). As a result, most of today's industrial hydrodynamic codes are still using some kind of variant of the Dawson scheme. However, this very particular viscosity term is hard to extend to general boundary fitted meshes, let alone unstructured computational methods like finite elements. Due to this cause most codes are based on a highly structured panel formulation. Another possibility is to use an *absorbing* boundary condition in the downstream boundary. If such a numerical device were found, then there would be no need to add a numerical viscosity term since the trailing waves are not reflected upstream, and a standard second order centered scheme can be used for the free-surface boundary term. Absorbing boundary conditions have been throughly studied for other wave phenomena like the Helmholtz equation, as the DtN (Givoli and Keller [14]) or the DNL (Bonet et al. [15]). For the ship-wave resistance problem the absorbing boundary conditions are seldom used due to inherent difficulties in its development. Recently, Storti et al. [16–18] have proposed a method with a finite element approach, while Broeze and Romate [19] developed an absorbing boundary condition with a panel method in the context of a temporal evolution of the free surface.

The general objective of this work is the development of a numerical method for the ship-wave flow potential problem with centered schemes in contrast to the Dawson-like methods. This is done by a panel method coupled with a finite Fourier series and discrete nonlocal absorbing boundary conditions. On the one hand, periodic boundary conditions on the beam direction are assumed and, then, the asymptotic wave-potential is represented by a superposition of monochromatic-waves. On the other hand, it is assumed that the mesh is structured both at the upstream and downstream sides with a finite number of strips in the beam direction. Then, additional boundary equations are introduced which are based on the flow kinematics at the upstream and downstream boundaries taking into account the right sense of the wave pattern, so that a second *centered* scheme can still be used for the discrete free surface operator.

2 Formulation of Potential Flow

The flow around a ship moving at a constant speed in a channel of uniform section is considered. It is supposed, for simplicity, that the channel section is a rectangle of depth H and width L_y, as shown in Fig. 1. The fluid occupies the region Ω which is bounded by: the channel walls and bottom Γ_C, the inlet/outlet boundaries $\Gamma_{I/O}$, the wetted surface of the ship Γ_S and the free surface Γ_F. The x-axis is parallel to the upstream nonperturbed velocity $\mathbf{u}_\infty$ and the z-axis positive upwards. The velocity field $\mathbf{u}$ is given by $\mathbf{u}=\nabla\Phi$, where Φ is the total potential, which satisfies the Laplace equation in the flow domain Ω. It is split as $\Phi=\mathbf{u}_\infty^T\mathbf{x}+\phi$ where $\mathbf{x}=(x,y,z)$ is the position vector and ϕ is the perturbation potential. The position of the free surface Γ_F is given by the single valued function $z=\zeta(x,y)$, where ζ is the elevation of the free surface with respect to the reference plane $z=0$ which is the hydrostatic equilibrium plane.

2.1 Kinematic Boundary Condition. The kinematic boundary condition is the slip condition $\partial_n\Phi=0$ at the wetted body surface, channel walls, bottom and free surface. Alternatively, Dirichlet boundary conditions at the bottom can be considered, e.g., see Storti et al. [16]. The unit normal to the free surface $z=\zeta(x,y)$ is expressed as $\mathbf{n}=(n_x,n_y,n_z)=(-\zeta_{,x},-\zeta_{,y},\mathbf{1})$.

2.2 Dynamic Boundary Condition. An additional condition must be added to the Laplace equation and the kinematic boundary conditions, since the position ζ of the free surface is not known beforehand. This is done by means of the Bernoulli equation

$$\frac{p}{\rho}+\frac{1}{2}|\nabla\phi|^2+g\zeta=C \quad \text{in } \Omega; \tag{1}$$

which relates the pressure p, the velocity $\nabla\Phi$ and the height ζ. The vapor pressure and the surface tension of the water are disregarded, therefore the mechanical equilibrium on the air/water interface requires that the pressure p be equal on both sides of them, and equal to the atmospheric pressure p_{atm} which is also assumed to be constant. Then, at infinity upstream, $C=p_{\text{atm}}/\rho+u_\infty^2/2$ and, without loss of generality, $p_{\text{atm}}=0$ is adopted.

2.3 Radiation Boundary Conditions. Roughly speaking, the radiation boundary conditions should allow the energy to flow, in the form of radiating waves propagate downstream and exit cleanly at Γ_O. In contrast, no waves are allowed to propagate upstream to Γ_I so that the boundary condition imposes that the potential should approach the undisturbed one on this boundary. Note that, the different treatment in Γ_I and Γ_O is the unique element that determines the symmetry breaking $x\to -x$, and ensures a physically correct wave pattern.

2.4 Governing Equations. The governing equations for the solution $\{\Phi,\zeta\}$ of this model are:

$$\begin{cases} \Delta\Phi=0 & \text{in } \Omega; \\ \partial_n\Phi=0 & \text{at } \Gamma_S+\Gamma_C; \\ \zeta=(u_\infty^2-|\nabla\Phi|^2)/(2g) & \text{at } \Gamma_F; \\ -\zeta_{,x}\Phi_{,x}-\zeta_{,y}\Phi_{,y}+\Phi_{,z}=0 & \text{at } \Gamma_F; \\ |\nabla\Phi|<\infty & \text{at } \Gamma_{I,O}. \end{cases} \tag{2}$$

3 Slow Ship Expansion

Asymptotic expansions for this flow problem, usually, consider some of the following parameters: the draft relation $\lambda_H=H/L$, the beam relation $\lambda_B=B/L$ or the Froude number $\text{Fr}=U/\sqrt{gL}$, which conduce to the known linearizations of: the *slender* ship when $\lambda_{H,B}\ll 1$, the *thin* ship when $\lambda_B\ll 1$, the *slow* ship when $\text{Fr}\ll 1$ and, of course, some combinations of them. The only case considered here is the slow ship on deep water, where its basic flow is obtained by taking the limit $g\to\infty$ and, then, the free surface $\zeta(x,y)$ shrinks to the hydrostatic equilibrium plane $z=0$, as it immediately follows from inspection of the dynamic boundary condition. That is, the wave-pattern behind the ship is missing, and is also equivalent to a *double body* flow obtained by mirroring the flow regime with respect to the plane $z=0$. After solving the basic flow, the gravity acceleration is restarted to its original value. If the wave heights are small enough, then they would be seen as a perturbation of the basic flow (e.g., see Reference [11]), whose

mathematical treatment, at a first stage, leads to a linearization of the governing equations following some kind of approach on the free surface. Next, a linearized expansion of the dynamic and kinematic boundary conditions over the free surface for the slow ship is considered. The *k*-solution of a perturbation procedure is $\{\phi_k,\zeta_k\}$, potential and elevation, respectively. Here $k=0$ corresponds to the *basic* flow problem and $k=1$ is the *perturbed* flow. In order to obtain the pair solution $\{\phi_1,\zeta_1\}$ an asymptotic expansion is made, $\{\phi_1,\zeta_1\}=\{\phi_0+\psi\varepsilon,\zeta_0+\eta\varepsilon\}$, at first order in ε, with $\varepsilon=\mathrm{Fr}$ and $0<\varepsilon\ll 1$ for the slow ship, where $\{\psi,\eta\}$ is the (incremental) wave-pair solution composed by the wave-potential ψ and the wave-height η. Both potentials $\phi_{0,1}$ are harmonic, $\Delta\phi_{0,1}=0$, in their respective domains $\Omega^{0,1}$, and it will be also assumed that the elevations $\zeta_{0,1}$ are single valued and small enough, so the resulting pair of incremental solutions $\{\varepsilon\psi,\varepsilon\eta\}=\{\phi_1-\phi_0,\zeta_1-\zeta_0\}$ are also small enough when $\varepsilon\ll 1$. The linearized dynamic and kinematic boundary conditions can be expressed in terms of the wave-pair solution $\{\psi,\eta\}$ and they are derived in the Appendix.

4 Linearized Wave-Potential

The linearized perturbed system for the incremental wave-pair solution $\{\psi,\eta\}$ can be written as:

$$\begin{cases} \Delta\psi=0 & \text{in } \Omega; \quad (3a)\\ \partial_n\psi=0 & \text{at } \Gamma_S+\Gamma_C; \quad (3b)\\ g\eta=-\mathbf{U}_0^T\nabla\psi-r_0 & \text{at } z=0; \quad (3c)\\ \partial_n\psi=\nabla^T(\mathbf{U}_0\eta) & \text{at } z=0; \quad (3d)\\ |\nabla\psi|<\infty & \text{at } \Gamma_{I,0}. \quad (3e) \end{cases}$$

where $\mathbf{U}_0=\mathbf{u}_\infty+\nabla\phi_0$ is the velocity field over the hydrostatic plane $z=0$ and r_0 is the residue of the dynamic boundary condition of the basic flow. Replacing (3*c*) in (3*d*)

$$\partial_n\psi=-\frac{1}{g}\nabla^T\mathbf{U}_0\mathbf{U}_0^T\nabla\psi-\frac{1}{g}\nabla^T\mathbf{U}_0 r_0. \quad (4)$$

The residue r_0 is found writing the Bernoulli equation (with $\rho=1$) for the basic flow

$$\frac{1}{2}U_0^2+g\zeta^0=\frac{1}{2}u_\infty^2+r_0; \quad (5)$$

where $\mathbf{\Phi}_0=\mathbf{u}_\infty^T\mathbf{x}+\phi_0$ is the total potential of the basic flow, but, in this case, the free surface coincides with the hydrostatic plane $\zeta^0=z=0$, and from this $r_0=(U_0^2-u_\infty^2)/2$, where $U_0^2=|\nabla\mathbf{\Phi}_0|^2$. Then

$$\partial_n\psi=-\frac{1}{g}\nabla^T\mathbf{U}_0\mathbf{U}_0^T\nabla\psi-\frac{1}{2g}\nabla^T\mathbf{U}_0(U_0^2-u_\infty^2) \quad (6)$$

is a nonhomogeneous Neumann boundary condition (at $z=0$) for the wave-perturbation potential ψ, and it can be seen as a *transpiration* flow $\sigma'\equiv\partial_n\psi$ that is injected to simulate the displacement of the free surface from the hydrostatic plane $z=0$. Therefore

$$\begin{cases} \sigma'=D\psi+f;\\ D=-1/g\nabla^T\mathbf{U}_0\mathbf{U}_0^T\nabla;\\ f=-1/(2g)\nabla^T\mathbf{U}_0(U_0^2-u_\infty^2). \end{cases} \quad (7)$$

5 Panel Formulation

The panel solution is carried out in two steps. First, the basic flow problem is solved and, then, the perturbed one. For both steps the same panel mesh is employed, where the free surface portion coincides with the hydrostatic equilibrium portion over the plane $z=0$. The zero-order panel mesh is a polyhedric one with flat faces, $\Gamma_n=\Gamma_p\cup\Gamma_b$, being Γ_p the mesh with n_p panels over a finite portion of the free surface Γ_F and Γ_b the mesh with n_b panels over the wetted body surface. The total number of panels is $n=n_p+n_b$ where, usually, $n_p\gg n_b$. The panel numeration should be correlative for an easy block-matrix treatment, starting with the free surface Γ_p. A low order panel formulation for both flow cases is employed, with collocation at the centroids of the panels, to set up a linear system of algebraic equations, where the system matrix is square of dimension $N=n$ for the basic flow, and $N=n+2n_y$ for the perturbed one, with $n_y\ll n$.

5.1 Panel Method for the Basic Flow. The system of equations for the basic flow problem is written as $\mathbf{A}\boldsymbol{\mu}^0=\mathbf{b}^0$, where $\mathbf{A}$ is the (bipolar) matrix system, and $\boldsymbol{\mu}^0$ and $\mathbf{b}^0$ are the basic potential and source vectors, respectively, evaluated at the centroids of the *n*-panels. The source vector $\mathbf{b}^0=\mathbf{C}\boldsymbol{\sigma}^0$ is the product of the monopolar influence matrix $\mathbf{C}$ and the flow vector $\boldsymbol{\sigma}^0$ obtained by means of the *slip* boundary condition on the solid walls, $\sigma^0(\mathbf{x}_j)=-\mathbf{U}_0^T(\mathbf{x}_j)\mathbf{n}(\mathbf{x}_j)$, where $\mathbf{n}(\mathbf{x}_j)$ is the *j*-unit panel normal oriented to the wetted side. The bipolar and monopolar matrices $\mathbf{A}$ and $\mathbf{C}$ are given by the surface integrals

$$A_{ij}=\frac{1}{4\pi}\int_\Gamma d\Gamma_j\frac{\mathbf{r}_{ij}^T\mathbf{n}_j}{r_{ij}^3} \text{ and } C_{ij}=\frac{1}{4\pi}\int_\Gamma d\Gamma_j\frac{1}{|\mathbf{r}_{ij}|}, \quad (8)$$

where $\mathbf{r}_{ij}=|\mathbf{x}_i-\mathbf{x}_j|$ is the distance between the centroid $\mathbf{x}_i$ and the integration point $\mathbf{x}_j$ over the *j*-panel surface, and $\mathbf{x}=(x,y,z)$. These discrete integrals are evaluated in closed form following a rotational strategy, e.g., see Medina and Liggett [20], D'Elía [21], or D'Elia et al. [22–24]. The matrix system is split in a plane-body block fashion

$$\begin{bmatrix}\mathbf{A}_{pp} & \mathbf{A}_{pb}\\ \mathbf{A}_{bp} & \mathbf{A}_{bb}\end{bmatrix}\begin{bmatrix}\boldsymbol{\mu}_p^0\\ \boldsymbol{\mu}_b^0\end{bmatrix}=\begin{bmatrix}\mathbf{C}_{pp} & \mathbf{C}_{pb}\\ \mathbf{C}_{bp} & \mathbf{C}_{bb}\end{bmatrix}\begin{bmatrix}\boldsymbol{\sigma}_p^0\\ \boldsymbol{\sigma}_b^0\end{bmatrix}. \quad (9)$$

5.2 Panel Method for the Perturbed Flow. For the perturbed flow problem all the surfaces remain fixed and the same panel mesh is employed. A lineal system similar to the previous one is written. The Neumann boundary condition is split in two components: a null part over the body $\boldsymbol{\sigma}_b=\mathbf{0}$ and

$$\boldsymbol{\sigma}_p=\mathbf{D}_{pp}\boldsymbol{\mu}_p+\mathbf{f}; \quad (10)$$

over the free surface, where $\mathbf{D}_{pp}=\mathrm{diag}(D_i)$, with $D_i=D(\mathbf{x}_i)$, is the free-surface matrix and $f_i=f(\mathbf{x}_i)$ is the forcing vector. Replacing $\boldsymbol{\sigma}_p$ and $\boldsymbol{\sigma}_b$ and rearranging

$$\begin{bmatrix}(\mathbf{A}_{pp}-\mathbf{C}_{pp}\mathbf{D}_{pp}) & \mathbf{A}_{pb}\\ (\mathbf{A}_{bp}-\mathbf{C}_{bp}\mathbf{D}_{pp}) & \mathbf{A}_{bb}\end{bmatrix}\begin{bmatrix}\boldsymbol{\mu}_p\\ \boldsymbol{\mu}_b\end{bmatrix}=\begin{bmatrix}\mathbf{C}_{pp}\mathbf{f}\\ \mathbf{C}_{bp}\mathbf{f}\end{bmatrix}; \quad (11)$$

and it remains to introduce the radiation boundary conditions upstream and downstream since, otherwise, the hydrodynamic problem is not well posed.

5.3 Free Surface Matrix. A discrete version for the scalar operator $\nabla^T\mathbf{U}_0\mathbf{U}_0^T\nabla$ can be obtained with several approaches, for example finite/differences or mesh-less methods. But in any case it will have a compact stencil and the free surface matrix will be quite sparse. Then, the computational cost of evaluating the matrix right product $\mathbf{CD}$ with the (dense) monopolar influence matrix $\mathbf{C}$, will not be expensive if the operations are conveniently rearranged. The artificial viscosity schemes, such as upwind or Dawson-like methods, are usually introduced in the free surface matrix $\mathbf{D}_{pp}$, while for the proposed method a second order *centered* scheme can still be used for the discrete operator. For instance if $\mathbf{U}_0=(U,0,0)\approx\mathrm{cnst}$ over a structured mesh (x_i,y_j) on the free surface, with $n_x\times n_y$ nodes and mesh steps h_x,h_y, then, it can be estimated that $(\mathbf{D}_{pp}\boldsymbol{\mu})_{p,q}\approx-U^2/g\,\partial_{xx}\mu|_{p,q}$, where $p=i+1/2$, $q=j+1/2$, since the potentials are evaluated at the panel centroids, and

$$\partial_{xx}\mu|_{p,q}\approx h_x^{-2}(\mu_{p-1,q}-2\mu_{p,q}+\mu_{p+1,q}). \quad (12)$$

6 Panel-Fourier Method

6.1 Finite Fourier Series. First, a two-dimensional flow is considered, from left to right with non-perturbed velocity U, around a ship-like body of characteristic length L situated at the origin, totally or partially submerged in the flow. The governing equations for the wave-potential $\hat{\mu}(x,z)$ (see e.g., Stoker [9]) and

$$\begin{cases} \nabla^2\hat{\mu} & \text{on } -\infty<z\leqslant 0; \\ \hat{\mu}_{,z}+(U^2/g)\hat{\mu}_{,xx}=0 & \text{at } z=0; \\ \hat{\mu} \text{ and } \partial_z\hat{\mu} \text{ bounded} & \text{for all } y,z. \end{cases} \tag{13}$$

Its asymptotic solution downstream and far enough from the body, are written as a linear combination of sines and cosines in the propagating direction x affected with a decreasing exponential in the draft direction z

$$\hat{\mu}(x,z)=Ae^{Kz}\sin(Kx)+Be^{Kz}\cos(Kx) \tag{14}$$

for $x>x_w$ and $z\leqslant 0$, where x_w is an abscissa far enough from the body, i.e., $0<L<x_w<\infty$, A,B are two arbitrary amplitude constants which are determined from the boundary conditions, and $K=g/U^2$ is the wave number related to the wavelength $\lambda=2\pi K^{-1}=2\pi(U^2/g)$. For the three-dimensional case an equivalent asymptotic solution is developed. This is done by imposing periodic boundary conditions in the beam direction, and is equivalent to an infinite cascade of ship-like bodies with transversal disposition to the mean stream. Then, a finite Fourier series is introduced in the strip $-L_y/2\leqslant y\leqslant L_y/2$ on a structured panel mesh with n_y transversal strips, which allow the asymptotic wave-potential to be $\tilde{\mu}(x,y,z)$ and its x-derivative $\tilde{\sigma}(x,y,z)=\partial_x\tilde{\mu}$ as

$$\tilde{\mu}=\sum_{q=0}^{m-1} e_q[A_q\sin(k_{xq}x)+B_q\cos(k_{xq}x)]\cos(k_{yq}y) + \sum_{q=1}^{m} e_q[C_q\sin(k_{xq}x)+D_q\cos(k_{xq}x)]\sin(k_{yq}y); \tag{15}$$

$$\tilde{\sigma}=\sum_{q=0}^{m-1} f_q[A_q\cos(k_{xq}x)-B_q\sin(k_{xq}x)]\cos(k_{yq}y) + \sum_{q=1}^{m} f_q[C_q\cos(k_{xq}x)-D_q\sin(k_{xq}x)]\sin(k_{yq}y) \tag{16}$$

where $m=n_y/2\geqslant 1$ is assumed, $e_q=e^{k_{zq}z}$, $f_q=k_{xq}e^{k_{zq}z}$, and A_q,B_q,C_q,D_q are the amplitude constants of the Fourier modes, k_{xq},k_{yq} are the Cartesian plane wave-numbers on the hydrostatic equilibrium plane and k_{zq} is the draft attenuation of each mode. It can be shown that this finite Fourier series evaluated at the centroid ordinates y_i satisfies the orthogonal conditions. Now, a relation between k_{xq}, k_{yq} and k_{zq} is needed.

6.2 Dispersion Relation. With the geometrical assumptions made above, the asymptotic wave-perturbation potential $\tilde{\mu}(x,y,z)$ has been represented as the linear superposition of traveling plane-waves $\mu_q(x,y,z)$ on the planes $z=\text{cnst}$, with exponential attenuation in the draft direction $z\leqslant 0$, that is,

$$\tilde{\mu}=\sum_{q=0}^{n_y/2} E_q\tilde{\mu}_q \quad \text{with} \quad \tilde{\mu}_q=e^{ik_{xq}x+ik_{yq}y+k_{zq}z} \tag{17}$$

with E_q being complex constants. By superposition each traveling wave must satisfy the Laplace equation in the domain Ω and the linearized free boundary condition at $z=0$

$$\begin{cases} \partial_{xx}\tilde{\mu}_q+\partial_{yy}\tilde{\mu}_q+\partial_{zz}\tilde{\mu}_q=0 & \text{on } \Omega; \\ \partial_{xx}\tilde{\mu}_q+K\partial_z\hat{\mu}_q=0 & \text{at } z=0. \end{cases} \tag{18}$$

From Eq. (18), the following discrete relations are found

$$\begin{cases} k_{yq}=2\pi q/Ly \\ k_{xq}=\sqrt{K^2/2+1/2\sqrt{K^4+4K^2k_{yq}^2}} \\ k_{zq}=k_{xq}^2/K \end{cases} \tag{19}$$

for $q=0,2,\ldots,n_y/2$. They can be seen as a sort of *dispersion* relation (since the x-coordinate can be regarded as time-like) between the Cartesian wave-numbers k_{xq},k_{yq} and the draft atenuation k_{zq} for each n_y-Fourier mode.

6.3 Absorbing Boundary Conditions. A finite portion of the basic free surface (plane $z=0$) is discretized by a structured mesh in $n_p=n_x\times n_y$ panels, where n_x,n_y are the panel numbers in the length and beam direction, respectively, with a panel numeration $l=(i-1)n_y+j$, for $1\leqslant i\leqslant n_x$ and $1\leqslant j\leqslant n_y$. Next, a vertical wall is introduced at $x=x_w$ far enough downstream from the body, with $0<L<x_w<\infty$, also discretized with a structured panel mesh in $n_w=n_y\times n_z$ panels, where n_z is the number of panels in the draft direction. On the other hand, the mesh *on* the body surface has n_b panels and can be *nonstructured*. The total number of panels is $n=n_p+n_b+n_w$ and the matrix system for the perturbed flow problem is

$$\begin{bmatrix} \hat{\mathbf{A}}_{pp} & \mathbf{A}_{pb} & \mathbf{A}_{pw} \\ \hat{\mathbf{A}}_{bp} & \mathbf{A}_{bb} & \mathbf{A}_{bw} \\ \mathbf{A}_{wp} & \mathbf{A}_{wb} & \mathbf{A}_{ww} \end{bmatrix} \begin{bmatrix} \boldsymbol{\mu}_p \\ \boldsymbol{\mu}_b \\ \boldsymbol{\mu}_w \end{bmatrix} = \begin{bmatrix} \mathbf{C}_{pp} & \mathbf{C}_{pw} \\ \mathbf{C}_{bp} & \mathbf{C}_{bw} \\ \mathbf{C}_{wp} & \mathbf{C}_{ww} \end{bmatrix} \begin{bmatrix} \mathbf{f} \\ \boldsymbol{\sigma}_w \end{bmatrix} \tag{20}$$

where

$$\begin{cases} \hat{\mathbf{A}}_{pp}=\mathbf{A}_{pp}-\mathbf{C}_{pp}\mathbf{D}_{pp}; \\ \hat{\mathbf{A}}_{bp}=\mathbf{A}_{bp}-\mathbf{C}_{bp}\mathbf{D}_{pp}; \end{cases} \tag{21}$$

and Eq. (10) was introduced. Neither $\boldsymbol{\mu}_w$ nor $\boldsymbol{\sigma}_w$ are known and, then, the system is under-specified. Next, a relation between them will be found through the absorbing boundary conditions. First, the n_y-Fourier modes on the vertical wall are introduced

$$\boldsymbol{\sigma}_j=\tilde{\boldsymbol{\sigma}}_j \quad \text{and} \quad \boldsymbol{\mu}_j=\tilde{\boldsymbol{\mu}}_j \tag{22}$$

for $j-n_p-n_b=1,2,\ldots,n_w$. As they already satisfy the governing equations, the last row of Eq. (20) is relaxed. The remaining set of equations in full length form are

$$\sum_{j=1}^{j_1}\hat{a}_{ij}\mu_j+\sum_{j=j_1+1}^{j_2}a_{ij}\mu_j+\sum_{j=j_2+1}^{n}a_{ij}\mu_j=b_j; \tag{23}$$

for $i=1,2,\ldots,(n_p+n_b)$, where $j_1=n_p$, $j_2=n_p+n_p$ and

$$b_j=\sum_{j=1}^{j_2}c_{ij}f_j+\sum_{j=j_2+1}^{n}c_{ij}\sigma_j. \tag{24}$$

Replacing from Eqs. (15), (16), and (20)

$$\sum_{j=1}^{j_1}\hat{a}_{ij}\mu_j+\sum_{j=j_1+1}^{j_2}a_{ij}\mu_j+\sum_{j=j_2+1}^{n}T_j=\sum_{j=1}^{j_1}c_{ij}f_j; \tag{25}$$

with

$$T_j=\sum_{q=1}^{n_y/2}(\alpha_{ijq}A_q+\beta_{ijq}B_q+\gamma_{ijq}C_q+\delta_{ijq}D_q). \tag{26}$$

There are $(n_p+n_b+2n_y)$ unknowns, but there are only (n_p+n_b) collocation equations, then $2n_y$ additional equations must be added for the Fourier amplitudes. Second, $2n_y$ kinematic boundary conditions are introduced upstream and downstream. At upstream, a *null* x-slope on each panel strip is imposed

$$-\mu_i+\mu_{n_y+i}=0 \quad \text{for } i=1,2,\ldots,n_y \tag{27}$$

while at downstream, compatability is imposed between the wave-potential and its asymptotic expansion on each panel strip, at the intersection between the free surface and the vertical wall

$$-\frac{1}{2}\mu_{i-n_y}+\frac{3}{2}\mu_i-\sum_{j=j_2+1}^{n} T_j^*=0; \tag{28}$$

with

$$T_j^*=\sum_{q=1}^{n_y/2}(a_{qi}^*A_q+\beta_{qi}^*B_q+\gamma_{qi}^*C_q+\delta_{qi}^*D_q); \tag{29}$$

for $i-n_p+n_y=1,2,\ldots,n_y$, where the coefficients α_{qi}^*, β_{qi}^*, γ_{qi}^* and δ_{qi}^* are extrapolations of α_{ijq}, β_{ijq}, γ_{ijq} and δ_{ijq} to $(x_w,y_i,0)$, and an extrapolation scheme on the two last panel layers is used, since the potentials are evaluated at the panel centroids. In this way, the algebraic problem is closed, since there are $N=n+2n_y$ equations and unknowns. There are *n active* panels, as rows and unknowns of the matrix equation and $2n_y$ nonlocal absorbing equations, where usually $n_y \ll n$.

7 Asymmetry of Dawson Methods

In order to understand how symmetry is broken in the Dawson-like methods, some properties of the related finite-difference operators should be taken in account. A very comprehensive analysis is shown by Letcher [25]. In these methods the free surface flow is considered to be a small perturbation of the double-body flow, which satisfies a zero normal velocity boundary condition on the hydrostatic equilibrium plane $z=0$. A linear free-surface boundary condition is derived and applied at $z=0$. The flow is then modeled with Rankine source panels placed over both the hydrostatic wetted body surface and a limited portion of the plane $z=0$. On each body panel, the usual Neumann boundary condition is applied and over each free surface panel, a Dawson-like boundary condition supplies one linear equation in the source densities. A key element is the use of upstream finite difference operators to approximate derivatives occurring in the free-surface boundary condition. By means of two-dimensional tests with a variety of difference operators, Dawson found that: (i) centered operators produce solutions exhibiting waves both upstream and downstream; (ii) operators using upstream points succeeded in suppressing upstream waves; (iii) the damping of the downstream wave depend strongly on the choice of the difference operator and on the Froude number; and (iv) a very particular upstream four-point operator (in a velocity formulation) gives near zero damping over a range of moderate speeds. The Dawson boundary condition for the perturbed flow discards all quadratic terms and can be written as

$$2UU_{,x}\tilde{u}+U^2\tilde{u}_{,x}+g\tilde{w}=-2U^2U_{,x} \quad \text{on } z=0 \tag{30}$$

where U is the x-component of the double-body velocity, $\tilde{u}=u-U$, $\tilde{w}=w-W$ are the perturbations on the velocity, with (u,w) as the components of the total (perturbed) velocity. As is noticed by Letcher, the Dawson scheme is an *irrational* approximation in the van Dyke *sense*, since it is not exact in any known limit and does not possess any small parameter allowing terms to be asymptotically ordered, so there is little rational basis to decide which terms to include and which to discard, aside from empirical demonstrations. In case that the double-body velocity U on $z=0$ is constant, e.g. if there is no body or the body is far away, then (30) reduces to the fully linearized free-surface boundary condition

$$\tilde{u}_{,x}+K\tilde{w}=0 \quad \text{on } z=0 \tag{31}$$

with $K=g/U_\infty^2$, and this is invariant under the longitudinal coordinate inversion symmetry $x\rightarrow -x$. In order to break it, the standard Rayleigh procedure is to introduce an *artificial* viscosity ν as

$$\tilde{u}_x+K\tilde{w}+\nu\tilde{u}=0 \quad \text{on } z=0. \tag{32}$$

This artificial viscosity is a small constant (with dimensions of the reciprocal of a length), which eventually approaches zero, and has the effect of moving a pole slightly off the integration path during evaluation of integrals that arise with an equivalent analysis by means of the Green functions and complex variable theory. This artifice is widely regarded as a reliable way to satisfy the radiation boundary conditions. The difference operator for numerical differentiation may be derived from the Taylor series. For data uniformly spaced, the Taylor series about x gives

$$f(x+nh)=\sum_{k=0}^{\infty}\frac{1}{k!}(nh)^k f^{(k)}(x); \tag{33}$$

a difference operator for the first derivative has the form of the weighed sum of several ordinates

$$\frac{df}{dx}\approx h^{-1}\sum_{n=-\infty}^{+\infty} p_n f(x+nh); \tag{34}$$

substituting (33) and reversing the order of the summations

$$\frac{df}{dx}\approx\sum_{k=0}^{+\infty} e_k h^{k-1} f^{(k)}(x); \tag{35}$$

where

$$e_k=\frac{1}{k!}\sum_n p_n n^k \tag{36}$$

is the coefficient of the kth derivative in (35). For a first-derivative operator it is suitable to make $e_0=0$ and $e_1=1$, by suitable choice of the w_n (e.g., see [25] for more details). Thus, the effect of using one of the difference formulas in place of the exact derivative in (32), is to introduce an infinite series of new terms involving various higher derivatives of u

$$\tilde{u}_{,x}+\sum_{k=2}^{+\infty} e_k h^{k-1}(\partial_x)^k\tilde{u}+K\tilde{w}+\nu\tilde{u}=0. \tag{37}$$

If the solution far downstream is assumed in the form

$$\begin{cases}\tilde{u}\sim e^{\tilde{K}z}\sin(\tilde{K}x);\\ \tilde{w}\sim e^{\tilde{K}z}\cos(\tilde{K}x);\end{cases} \tag{38}$$

then (37) conduces to

$$K=\tilde{K}(1-e_3\beta^2+e_5\beta^4-e_7\beta^6+..); \tag{39a}$$

$$\nu=\tilde{K}(e_2\beta^1-e_4\beta^3+e_6\beta^5-..) \tag{39b}$$

where $\beta=\tilde{K}h$. The parameter Kh is 2π over the number of surface panels per wavelength, so (39*a*) shows that if the e_k are small and Kh is not too large, then, the perturbed wavenumber $\tilde{K}$ would be equal to K within $O(K^2h^2)$. The strong effect of the odd terms in the error is thus a small modification of the wavelength. On the other hand, (39*b*) shows that the even terms act exactly like a (speed-dependent) artificial viscosity ν needed to exactly offset the damping effects of the error terms. As Letcher remarks, the Dawson-like methods usually break down at higher Froude number (lower Kh) because the strong decline in the magnitude of νh allows upstream waves, but the breakdown has nothing to do with the question of whether these methods are low-speed theories owing to its basis in a double-body linearization. It is the upstream differencing that fails, not the double-body linearization.

8 Asymmetry of the Wave Expansion

The same procedure can be used for the asymptotic wave expansion. For simplicity, a velocity formulation is used and the linearized free surface boundary condition (32) is rewritten as

$$u_{q,x}+Kw_q+\nu u_q=0 \quad \text{on } z=0. \tag{40}$$

where $u_q=\tilde{\mu}_{,x}$ and $w_q=\tilde{\mu}_{,z}$ are the perturbed (modal) velocities. At far downstream, the wave expansion (38) is assumed and (39) is again obtained. The centered three-point difference operator using the points at $n=-1,0,+1$ has the weights $(p_0,p_1,p_2)=$

$(-1/2,0,1/2)$, its odd terms e_{2k+1} are all nulls, but not its even terms e_{2k}. Then, from (39), both perturbed and unperturbed wavenumber are equals, $\tilde{K}=K$, while the (speed-dependent) artificial viscosity ν remains. In other words, the proposed wave expansion (indirectly) satisfy the absorbing boundary conditions and, with a centered difference free-surface operator, no error is introduced in the wavenumber K.

9 Numerical Examples

9.1 Wigley Hull. The hull shape for the model 1805 A, e.g., see Dawson [7], is given by $\eta^{\pm}=\pm(1-\xi^2)(1-0.6\xi^2)(1-\zeta^2)$, with $\xi=2x/L$, $\eta=2y/B$ and $\zeta=z/H$, where H,B,L are the length, beam and draft of the model, respectively. The prismatic coefficient is defined as $C_p=\Omega/(LS)$ and the wave-resistance coefficient employed is the Circular Froude Coefficient $C_w=F_x/F_0$, with $F_0=(\pi/250)\rho U_\infty^2\Omega^{2/3}$, where Ω is the volume and S the area of the midship section. For this model $\Omega=(88/225)LBH$, $S=(2/3)BH$ and $C_p=44/75\approx 0.587$, respectively. The panel mesh employed, see Fig. 2, covers the free surface of the basic flow with 60×20 quadrilaterals, the wetted hull with about 1800 triangles and a vertical wall with 20×40 quadrilaterals, there are 20 panel strips, 40-Fourier modes and 3000 total unknowns. Fig. 3 shows the wave resistance coefficient plot obtained with the proposed method, compared with Shearer results (from Wehausen [26]), where: (i) the computed curve tends to be less in mean value than the experimental curves; (ii) the humps and the hollows in the computed curve are especially marked in comparison with the experimental one and (iii) the humps and the hollows occur

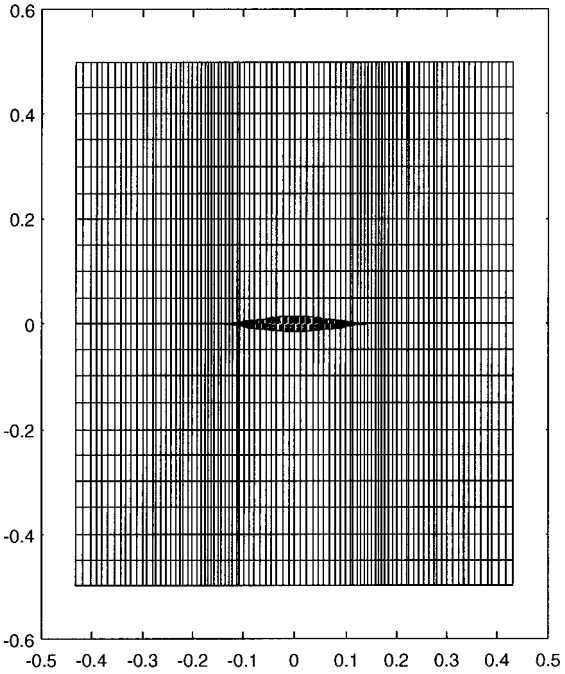

Fig. 2 A structured panel mesh over the free surface, around a Wigley model (*xy*-view)

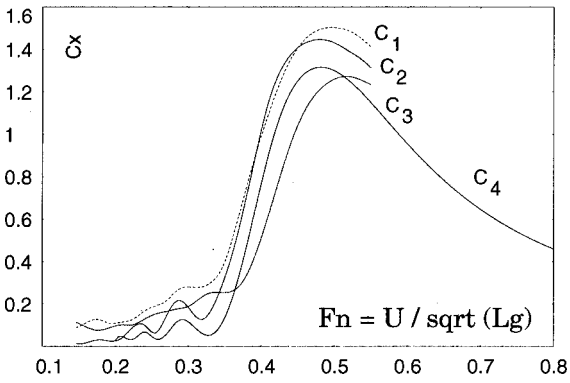

Fig. 3 Wave resistance coefficient for the Wigley model 2891: C_1: residuary for model free to trim, C_2: residuary for model fixed, C_3: calculated Michell resistance (from Wehausen [26], Fig. 20, p. 182); C_4: Panel-Fourier computation.

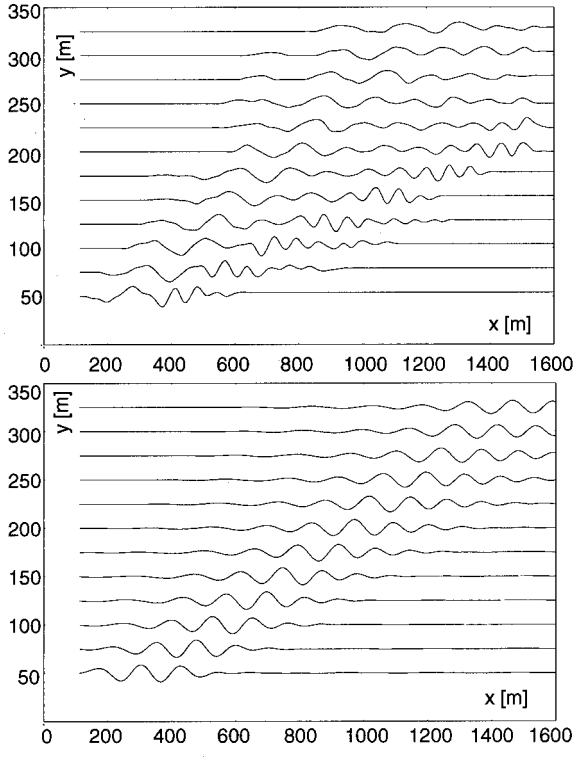

Fig. 4 Wave profiles at 40 knots ferry speed (magnification factor=10), top: from sensor measurements each 25 m on planes parallel to the gallery one, bottom: from a Panel-Fourier computation.

Table 1 Scatter table of the significant wave height H_z as a function of the zero crossing period T_z, at 10 knots, for 10 selected measured waves at each distance. Threshold level $t=0.05$.

Y_{50}	T_z	2.70	2.40	1.80	1.90	3.08	2.70	2.55	3.05	3.08	3.15
	H_z	0.08	0.11	0.06	0.06	0.06	0.14	0.14	0.06	0.06	0.05
Y_{75}	T_z	2.60	2.40	1.92	2.22	3.15	2.88	2.53	2.60	3.10	2.97
	H_z	0.10	0.11	0.05	0.07	0.06	0.07	0.11	0.17	0.12	0.10
Y_{100}	T_z	2.60	2.50	2.28	2.25	2.15	2.33	2.80	2.50	2.63	2.58
	H_z	0.09	0.10	0.06	0.06	0.05	0.07	0.08	0.14	0.11	0.08
Y_{125}	T_z	2.60	2.53	2.50	2.53	2.22	2.55	2.95	2.80	2.72	2.75
	H_z	0.05	0.08	0.10	0.07	0.06	0.07	0.07	0.14	0.14	0.13
Y_{150}	T_z	2.60	2.47	2.42	2.47	2.75	2.58	3.13			
	H_z	0.07	0.07	0.06	0.11	0.10	0.10	0.05			
Y_{175}	T_z	2.70	2.70	2.53	2.42	2.65	3.08	2.40	2.72	2.30	3.25
	H_z	0.05	0.08	0.08	0.07	0.06	0.08	0.13	0.07	0.07	0.06
Y_{200}	T_z	2.42	2.58	2.63	2.40	2.95	2.45	2.53	2.90	2.35	3.22
	H_z	0.05	0.08	0.09	0.06	0.05	0.11	0.15	0.08	0.07	0.07
Y_{225}	T_z	2.63	2.63	2.60	2.53	2.80	2.70	2.53	2.35	2.92	
	H_z	0.07	0.08	0.07	0.07	0.07	0.09	0.12	0.06	0.08	
Y_{250}	T_z	2.63	2.67	2.45	2.45	2.65	2.80	2.53	2.35	2.47	2.95
	H_z	0.07	0.09	0.07	0.08	0.10	0.09	0.11	0.08	0.07	0.07
Y_{275}	T_z	2.60	2.58	2.53	2.42	2.70	2.85	2.55	2.80	3.00	3.28
	H_z	0.07	0.07	0.06	0.07	0.09	0.09	0.09	0.07	0.06	0.05
Y_{300}	T_z	2.72	2.85	2.65	2.53	2.50	2.55	2.85	2.70	2.30	
	H_z	0.06	0.07	0.07	0.05	0.09	0.11	0.09	0.08	0.06	
Y_{325}	T_z	2.70	2.65	2.55	2.50	2.42	2.60	2.88	2.67	2.92	
	H_z	0.05	0.06	0.05	0.06	0.08	0.09	0.09	0.08	0.05	

Table 2 Scatter table of the significant wave height H_z as a function of the zero crossing period T_z, at 40 knots, for 10 selected measured waves at each distance. Threshold level $t = 0.20$.

Y_{50}	T_z	7.70	3.47	3.00	3.72	6.78	11.93	10.93			
	H_z	1.67	1.41	0.71	0.44	0.24	0.22	0.24			
Y_{75}	T_z	8.52	5.38	3.80	3.53	2.97	3.00	8.45	10.32		
	H_z	1.12	0.96	1.51	0.77	0.35	0.32	0.27	0.23		
Y_{100}	T_z	9.48	8.93	4.53	3.38	3.80	4.15	2.75	2.58	3.15	10.00
	H_z	1.02	0.76	0.99	1.32	0.84	0.45	0.27	0.21	0.21	0.20
Y_{125}	T_z	10.07	7.82	5.05	4.78	3.60	3.35	3.92	3.60	2.90	
	H_z	0.69	0.97	0.84	0.93	1.45	0.91	0.32	0.44	0.31	
Y_{150}	T_z	8.55	5.22	6.38	4.03	3.58	3.50	3.50	3.72	3.47	
	H_z	1.03	0.41	0.58	0.84	1.24	1.16	0.45	0.20	0.38	
Y_{175}	T_z	9.13	6.43	6.13	4.80	4.47	3.53	3.35	3.70		
	H_z	0.90	0.58	0.46	0.41	0.78	1.09	1.10	0.70		
Y_{200}	T_z	7.65	5.40	6.53	4.35	4.15	3.85	3.35			
	H_z	0.79	0.38	0.43	0.37	0.84	1.03	1.11			
Y_{225}	T_z	10.98	8.57	5.20	6.97	4.43	5.50	3.67			
	H_z	0.60	0.86	0.43	0.60	0.23	0.54	0.47			
Y_{250}	T_z	8.98	8.60	5.93	6.25	4.78					
	H_z	0.88	0.51	0.47	0.34	0.29					
Y_{275}	T_z	9.25	7.78	5.60	8.80						
	H_z	0.83	0.70	0.29	0.49						
Y_{300}	T_z	10.05	8.30	5.82	6.50						
	H_z	0.59	0.76	0.38	0.47						
Y_{325}	T_z	10.23	8.50	7.05	5.90						
	H_z	0.45	0.82	0.50	0.41						

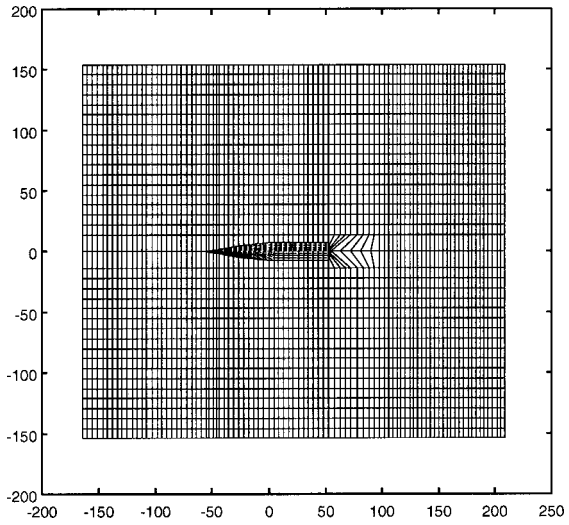

Fig. 5 Structured panel mesh on the free surface, around a ferry (*xy*-view)

rather earlier in the computed curve than in the experimental data. Note that the whole set of secondary maxima is clearly captured, extending to Froude numbers as low as 0.2. On the other extreme, Froude numbers as high as 0.8 are computed without problems, while standard methods like those derived from Dawson suffer from some reflections specially at high Froude numbers.

9.2 Transport Ferry. Tests of the wave-height profile, at 40 equivalent knots, have been performed for a model of transport ferry, in scale (1:25) made of glass fiber and ballasted in order to reproduce the displacement, mean draft and trim corresponding to the real ship. The main model dimensions are: displacement with appendices=1.11 kN, length between perpendiculars=4.4 m, beam of trace=0.588 m, and draft mean=0.095 m. The vessel channel is 150×30×5 m and possesses a planar motion carriage for the dragging and controlling of the model. The water depth in the tests was 5 m equivalent to 125 m at real scale, therefore it can be considered to correspond to deep water. The model was dragged from its center of mass following rectilinear trajectories in such a way that it allows vertical and dynamic trim motions. The measurements were done by means of three resistive sensors to elevation of the free surface, located at fixed points of the central zone of the channel, as to avoid reflections on the walls, and over a same transversal line to the channel, separated at a distance of 2 m between them, equivalent to 50 m at full scale. Four passages at 2, 3, 8, and 9 m between the gallery plane and the nearest sensor were done. In this form the wake was measured between 50 and 325 m with intervals of 25 m at real scale, in planes parallel to the gallery plane of the ship. The wake-profiles

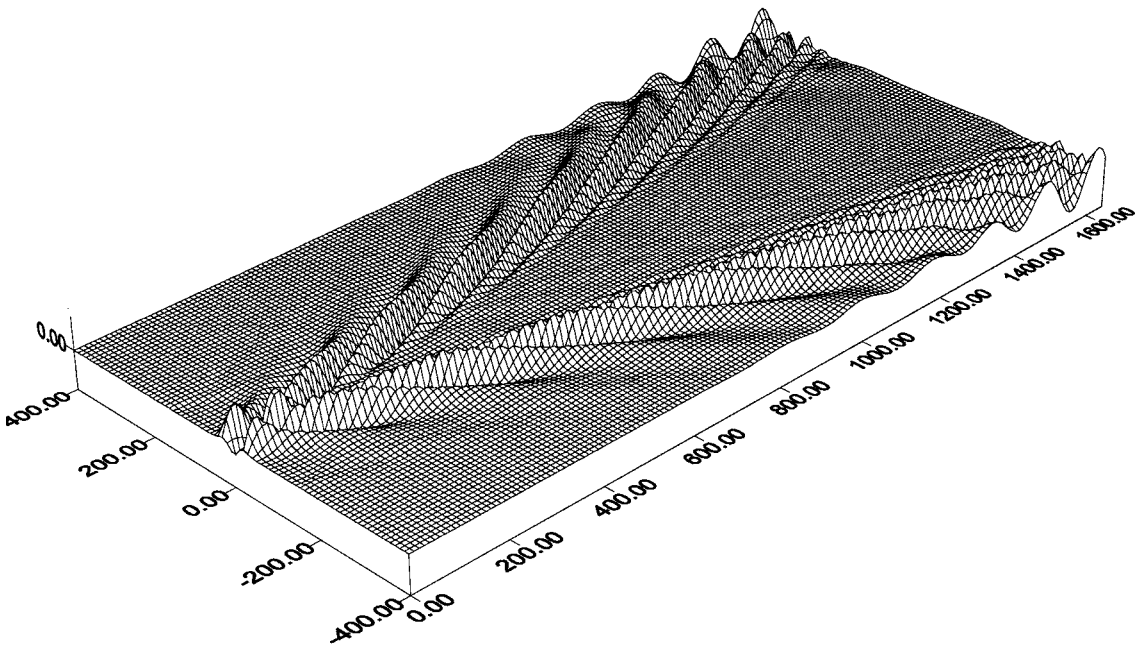

Fig. 6 Perspective view of the wave-pattern for a ferry at 40 knots along 15 ship-lengths, computed with the Fourier series

measured are shown at the top of Fig. 4. Ten measures were selected from the greater zero-crossing waves at each distance, where the measured waves that were smaller than a threshold were discarded in order to reduce interference effects, surface irregularities and noise. The threshold level was varied for each velocity due to the different magnitude of the wake height. The plots of the significant wave height as a function of the zero crossing period (scatter diagrams) are shown in Tables 1 and 2. In the calibration of the wave-resistive sensors, the display constant was of 0.731 mm/point and the sensor constant resulting was -15 V/m. Each sensor generates a proper wave which is a function of the velocity and kind of the measured wave, but in any case was greater than 2 mm. In these tests, the proper wave was measured in vacuum ($<$0.5 mm) and, then, was subtracted to the measured senial. The panel mesh, see Fig. 5, covers: the free surface of the basic flow with 90×36 quadrilaterals, the wetted hull with 438 triangles and a vertical wall with 36×18 quadrilaterals, resulting 3678 active panels, $n_y=36$ panel strips, 72 Fourier modes and 3750 total unknowns. Once a numerical solution over the computational free surface is obtained, the wave-pattern behind the vertical wall may be computed by means of a post-processing computation with the finite Fourier representation of the asymptotic wave-potential coupled to the dispersive relation. The initial data is the wave-potential and its x derivative at the panel strip behind the ship. At the bottom of Fig. 4 the numerical wave-height profiles of the wake are shown, which are found with the post-processing procedure at the same planes as the measured ones, with a reasonable comparison between measured and computed wave-heights profiles, except, of course, near to the transom-stern due to vorticity effects. It is also noted that it can go back as far as 15 lengths in the downstream direction and 3 lengths in the beam one, with a negligible computational effort as compared with a direct strategy of trying to cover this surface with panels. Finally, in Fig. 6 a perspective view of the computed wake is shown.

10 Conclusions

The ship-like flow problem has been considered by means of a three-dimensional potential model and a linearized free-surface boundary condition. This problem has been numerically solved by a panel method coupled with a finite Fourier series. In contrast with the Dawson-like methods, a second centered difference scheme has been used for the free-surface discrete operator. Centered schemes reduce the numerical viscosity in the discretization in such a way that, no error is introduced in the wavenumber while the (speed-dependent) artificial viscosity remains. The wave-resistance has been computed by a pressure integration over the static wetted hull, and the wave-heights in the downstream free surface behind the artificial boundary, have been obtained as a post-processing procedure, therefore, it can go fairly far behind the ship with a lower computational cost than a direct strategy of covering the free surface with panels. This procedure enables to consider significantly smaller meshes for the free surface, and the computation can be done over a broad interval of the Froude number. The overall approach is limited by the restrictions of the potential flow model and the use of a structured free surface mesh. Future modeling efforts would be focused on this area as well as on coupling the hydrodynamic model with a boundary layer solver for a viscous/inviscid interaction.

Acknowledgment

This work was supported by *Consejo Nacional de Investigaciones Científicas y Técnicas* (CONICET, Argentina) and *Banco Interamericano de Desarrollo* through grant BID 802/OC-AR PID 26. The work was partially performed with *Free Software Foundation/GNU-Project* resources. The experimental data was provided by *Centro Internacional de Métodos Numéricos en Ingeniería* (CIMNE, Barcelona) and *Canal de Experiencias Hidrodinámicas de El Pardo* (CEHIPAR, Madrid). The authors thank the referees for their constructive suggestions and careful reading.

Appendix: Linearized Boundary Conditions

A linearized dynamic boundary condition is developed first. At the 0,1-stages (basic and perturbed flows), the potentials are $\mathbf{\Phi}_{0,1}=\mathbf{u}_\infty^T\mathbf{x}+\phi_{0,1}$. Their gradient modules are

$$U_{0,1}^2=u_\infty^2+2\mathbf{u}_\infty^T\mathbf{u}_{0,1}+u_{0,1}^2; \tag{41}$$

where $\mathbf{U}_{0,1}=\nabla\mathbf{\Phi}^{0,1}$ and $\mathbf{u}_{0,1}=\nabla\phi^{0,1}$. Then

$$\Delta U^2=2\mathbf{u}_\infty^T\Delta\mathbf{u}+\Delta u^2; \tag{42}$$

where $\Delta U^2=U_1^2-U_0^2$, $\Delta\mathbf{u}=\mathbf{u}_1-\mathbf{u}_2$ and $\Delta u^2=u_1^2-u_0^2$. Expanding ϕ_1 and η_1 at first order in ε

$$\begin{cases}\varepsilon\psi=\phi_1-\phi_0; & (43a)\\ \varepsilon\eta=\zeta^1-\zeta^0. & (43b)\end{cases}$$

Then $\mathbf{u}_1=\mathbf{u}_0+\varepsilon\nabla\psi$ and

$$\Delta u^2=2\varepsilon\mathbf{u}_0^T\nabla\psi+\varepsilon^2|\nabla\psi|^2. \tag{44}$$

Introducing (44) in (42)

$$\Delta U^2=2\varepsilon\mathbf{U}_0^T\nabla\psi+O(\varepsilon^2). \tag{45}$$

The Bernoulli equations at the 0,1-stages are

$$\frac{1}{2}U^{0,1}+g\zeta^{0,1}=\frac{1}{2}u_\infty^2+r^{0,1}\quad\text{at}\quad\Gamma^{0,1}; \tag{46}$$

where $r^{0,1}$ are the 0,1-residuals since in an asymptotic iterative process it is assumed that the dynamic condition is not fully verified. The difference is

$$\frac{1}{2}\Delta U^2+g\Delta\zeta=\Delta r\quad\text{at}\quad\Gamma^{0,1} \tag{47}$$

where $\Delta\zeta=\zeta_1-\zeta_0$ and $\Delta r=r_1-r_0$. Introducing (43*b*) and (45)

$$\varepsilon(\mathbf{U}_0^T\nabla\psi+g\eta)+O(\varepsilon^2)=\Delta r \tag{48}$$

since $\mathbf{U}_0$ is evaluated at Γ^0 and $\nabla\phi^{0,1}$ are evaluated at $\Gamma^{0,1}$, it should be known the location of the two boundaries $\Gamma^{0,1}$, but a simplified procedure can be introduced by means of a transfer calculus (e.g., Reference [10]). For if we only consider known boundaries, all flow variables are transferred to Γ_0, then $\phi_1(\mathbf{x}')\approx\phi_1(\mathbf{x})$ and $\psi^1(x')\approx\psi^1(\mathbf{x})$ plus terms $O(\varepsilon)$, i.e., a simple boundary displacement. All terms in Eq. (48) are evaluated at Γ^0 and Eq. (3.3) is obtained.

Next, a linearized kinematic boundary condition is obtained. The basic free surface Γ^0 is the plane $z=0$, whereas the perturbed one Γ^1 can be written as $z=\varepsilon\eta(x,y)$, and will be near it for ε small enough. Over the plane $z=0$ the unit normal $\mathbf{n}(\mathbf{x})=(0,0,1)$ is constant, and over the perturbed one $\mathbf{n}(\mathbf{x}')=(-\varepsilon\eta_{,x},-\varepsilon\eta_{,y},1)$, at first order on ε. Its change can be written as

$$\delta\mathbf{n}(x)=\mathbf{n}(\mathbf{x}')-\mathbf{n}(\mathbf{x})=(-\varepsilon\eta_{,x},-\varepsilon\eta_{,y},0) \tag{49}$$

where $\mathbf{x}'\in\Gamma^1$ and $\mathbf{x}\in\Gamma^0$. The transfer of the gradient is considered by

$$\nabla\phi_1(\mathbf{x}')=\nabla\phi_1(x)+\nabla\nabla^T\phi_1(\mathbf{x})\mathbf{n}(\mathbf{x})\eta\varepsilon. \tag{50}$$

Introducing (43) and since $\nabla\nabla^T\phi^{0,1}$ are assumed symmetric, resulting

$$\nabla^T\phi_1(\mathbf{x}')=\nabla^T\phi_0(\mathbf{x})+\nabla^T\psi(\mathbf{x})\varepsilon+\mathbf{n}^T(\mathbf{x})\nabla\nabla^T\phi_0(\mathbf{x})\eta\varepsilon+O(\varepsilon^2). \tag{51}$$

The perturbed kinematic boundary condition and unit normal are

$$\begin{cases}\nabla^T\phi_1(\mathbf{x}')\mathbf{n}(\mathbf{x}')=0 & (52a)\\ \mathbf{n}(\mathbf{x}')=\mathbf{n}(\mathbf{x})+\delta\mathbf{n}(\mathbf{x}). & (52b)\end{cases}$$

Introducing (51) and (52b) into (52a)

$$\nabla^T\phi_1\mathbf{n}=\nabla^T\phi_0\mathbf{n}+\nabla^T\psi\mathbf{n}\varepsilon+\nabla^T\phi_0\delta\mathbf{n}+\mathbf{n}^T(\nabla\nabla^T\phi_0)\mathbf{n}\eta\varepsilon+O(\varepsilon^2). \tag{53}$$

where the left and right side are evaluated at $\mathbf{x}'$ and $\mathbf{x}$, respectively. The boundary velocity in the basic flow is contained by the plane $z=0$ and then $\nabla^T\phi_0\mathbf{n}=0$. Now

$$\nabla^T\phi_0\delta\mathbf{n}=-\varepsilon\eta_{,x}\phi_{0,x}-\varepsilon\eta_{,y}\phi_{0,y}+O(\varepsilon^2). \tag{54}$$

For the last term, it can be written $\mathbf{n}^T(\nabla\nabla^T\phi_0\mathbf{n})=\mathbf{n}^T\mathbf{t}$, where

$$t_i=\frac{\partial^2\phi_0}{\partial x_i\partial x_j}n_j=\frac{\partial}{\partial x_i}\left(\frac{\partial\phi_0}{\partial x_j}n_j\right) \tag{55}$$

for $i,j=1,2,3$, employing Einstein summation convention over repeated indices and it has been taken into account that $\mathbf{n}(\mathbf{x})=(0,0,1)$ is a constant vector. This is reduced to

$$\frac{\partial}{\partial x_i}\left(\frac{\partial\phi_0}{\partial x_j}n_j\right)=\left[\frac{\partial}{\partial x}\frac{\partial\phi_0}{\partial z},\frac{\partial}{\partial y}\frac{\partial\phi_0}{\partial z},\frac{\partial}{\partial z}\frac{\partial\phi_0}{\partial z}\right]. \tag{56}$$

The z-component of the velocity field $u_{0z}=\partial_z\phi_0$ over all the plane $z=0$ is null, then $\partial_x(u_{0z})=\partial_y(u_{0z})=0$ at $z=0$ and

$$\frac{\partial}{\partial x_i}\left(\frac{\partial\phi_0}{\partial x_j}n_j\right)=\left[0,0,\frac{\partial^2\phi_0}{\partial z^2}\right]\quad\text{at}\quad z=0 \tag{57}$$

collecting these partial results

$$\epsilon\left(\frac{\partial\psi}{\partial n}+\eta\frac{\partial^2\phi_0}{\partial z^2}-\frac{\partial\eta}{\partial x}\frac{\partial\phi_0}{\partial x}-\frac{\partial\eta}{\partial y}\frac{\partial\phi_0}{\partial y}\right)+O(\epsilon^2)=0 \tag{58}$$

since ϕ_0 is harmonical in Ω^0, then $\phi_{0,zz}=-\phi_{0,xx}-\phi_{0,yy}$ and, at first order,

$$-\frac{\partial\psi}{\partial n}+\frac{\partial}{\partial x}\left(\eta\frac{\partial\phi_0}{\partial x}\right)+\frac{\partial}{\partial y}\left(\eta\frac{\partial\phi_0}{\partial y}\right)=0\quad\text{at}\quad z=0. \tag{59}$$

References

[1] Morino, L., and Kuo, C. C., 1974 ''Subsonic Potential Aerodynamics for Complex Configurations: A General Theory,'' AIAA J. **12**, pp. 191–197.

[2] Katz, J., and Plotkin A., 1991, *Low-Speed Aerodynamics, From Wing Theory to Panel Methods*, Mcgraw-Hill.

[3] Mokry, M., 1990, ''Complex Variable Boundary Element Method for External Potential Flows,'' *28th Aerospace Sciences Meeting*, January 8–11, Reno, Nevada.

[4] Storti, M., D'Elía, J., and Idelsohn, S., 1995, ''CVBEM formulation for multiple profiles and cascades,'' Appl. Mech. Rev., **48**, No. 11, Part 2. pp. 203–210.

[5] Morino, L., ed., 1985, *Computational Methods in Potential Aerodynamics*, Springer-Verlag.

[6] Kinnas, S. A., and Hsin, C. Y., 1992, ''Boundary Element Method for the Analysis of the Unsteady Flow Around Extreme Propeller Geometries,'' AIAA J., **30**, pp. 688–696.

[7] Dawson, C. W., 1977, ''A Practical Computer Method for Solving Ship-Wave Problems'' *2nd Int. Conf. on Numerical Ships Hydrodynamics*, Berkeley, CA, pp 30–38.

[8] Farmer, J., Martinelli, L., and Jameson, A., 1994, ''Fast Multigrid Method for Solving Incompressible Hydrodynamic Problems with Free Surfaces,'' AIAA J., **32**, No. 6, June, pp. 1175–1182.

[9] Stoker, J. J., 1957, *Water Waves*, Interscience, New York.

[10] van Dyke, M., 1975, *Perturbation Methods on Fluid Mechanics*, Parabolic Press, Stanford.

[11] Newman, J. N., 1978, ''The Theory of Ship Motions,'' Appl. Mech. **18**, pp. 221–283.

[12] Baumann, C., Storti, M., and Idelsohn, S., 1992, ''A Petrov-Galerkin technique for the solution of transonic and supersonic flows,'' Comput. Methods Appl. Mech. Eng., **95**, pp. 49–70.

[13] Nigro, N., Storti, M., and Idelsohn, S., 1995, ''Fluid flows around turbomachinery using an explicit pseudotemporal Euler FEM code,'' J. Commun. Numer. Methods Eng., **11**, pp. 199–211.

[14] Givoli, D., 1991, ''Non-reflecting Boundary Conditions,'' J. Comput. Phys., **94**, pp. 1–29.

[15] Bonet, R., Nigro, N., Storti, M., and Idelsohn, S., 1998, ''A Discrete Non-Local (DNL) Outgoing Boundary Condition for Diffraction of Surface Waves,'' Commun. Numer. Methods Eng., **14**, pp. 849–861.

[16] Storti, M., D'Elía, X., and Idelsohn, S., 1998, ''Algebraic Discrete Non-Local (DNL) Absorbing Boundary Condition for the Ship Wave Resistance Problem,'' J. Comput. Phys., **146**, No. 2, pp. 570–602.

[17] Storti, M., D'Elía, J., and Idelsohn, S., 1998, ''Computing Ship Wave Resistance from Wave Amplitude with the DNL Absorbing Boundary Condition,'' Commun. Numer. Methods Eng., **14**, pp. 997–1012.

[18] Storti, M. , D'Elía, J., Bonet, R., Nigro, N., and Idelsohn, S., 2000 ''The DNL Absorbing Boundary Condition. Applications to Wave Problems,'' Comput. Meth. Appl. Mech. Eng. **182**, (3-4), pp. 483–498.

[19] Broeze, J., and Romate, J. E., 1992, ''Absorbing Boundary Conditions for Free Surface Wave Simulations with a Panel Method,'' J. Comput. Phys., **99**, pp. 146–158.

[20] Medina, D. E., and Liggett, J. A., 1988, ''Three-Dimensional Boundary Element Computation of Potential Flow in Fractured Rock,'' Int. J. Numer. Methods Eng., **26**, pp. 2319–2330.

[21] D'Elía J., 1997, ''Numerical Methods for the Ship Wave-Resistance Problem,'' Ph.D. thesis, Univ. Nacional del Litoral, Santa Fe, Argentina.

[22] D'Elía, J., Storti, M., and Idelsohn, S., 2000 ''Iterative solution of panel discretizations for potential flows. The modal/multipolar preconditioning,'' Int. J. Numer. Methods Fluids, **32**, No. 1, pp. 1–27.

[23] D'Elía, J., Storti, M., and Idelsohn, S., 2000 ''Smoothed Surface Gradients for Panel Methods,'' Adv. Eng. Soft. **31**, No. 5, pp. 327–334.

[24] D'Elía, J., Storti, M., and Idelsohn, S., 2000, ''A Closed Form for Low Order Panel Methods,'' Adv. Eng. Software **31**, No. 5, 335–341.

[25] Letcher, J. S., 1993, ''Properties of finite-difference operators for the steady-wave problem,'' J. Ship Res., **37**, No. 1, Mar., pp. 1–7.

[26] Wehausen, J. V., 1973, ''The Wave Resistance of Ships,'' Adv. Appl. Mech., **13**, pp. 93–245.

Toward Improved Rotor-Only Axial Fans—Part I: A Numerically Efficient Aerodynamic Model for Arbitrary Vortex Flow

D. N. Sørensen
Research Scientist

J. N. Sørensen
Associate Professor

Department of Energy Engineering,
Technical University of Denmark,
DK2800 Lyngby, Denmark

A numerically efficient mathematical model for the aerodynamics of rotor-only axial fans has been developed. The model is based on a blade-element principle whereby the rotor is divided into a number of annular streamtubes. For each of these streamtubes relations for velocity, pressure, and radial position are derived from the incompressible conservation laws for mass, tangential momentum, and energy. The resulting system of equations is nonlinear and, due to mass conservation and pressure equilibrium far downstream of the rotor, strongly coupled. The equations are solved using the Newton-Raphson method, and solutions converged to machine accuracy are found at small computing costs. Calculations are found to agree well with published measurements.
[S0098-2202(00)01502-9]

1 Introduction

Ducted axial fans have for many years been employed to drive the flow in ventilation systems. They range from simple propeller-type fans to constructions with two or more stages comprising impellers and stationary vane rows.

Today, a large variety of different techniques for designing and analysing axial turbomachines exists. These range from simple empirical relations to full three-dimensional Euler/Navier-Stokes algorithms using finite-difference or finite-element methods to discretize the equations. Comprehensive surveys of the various methods can be found in the text books of Cumpsty [1], Lakshminarayana [2], or in Üçer et al. [3]. For baseline designs, the streamline curvature (SC) technique (Novak [4]) is probably the most popular industrial method. Compared to full three-dimensional methods this technique is quick and inexpensive to run on a computer. The SC technique consists of solving the radial equilibrium equation along with the continuity equation in a meridional plane using streamline coordinates. This is done in an iterative manner in which the position of the streamlines is updated after each meridional computation. The azimuthal velocity distribution is obtained either from the blade geometry using correlations or from blade-to-blade calculations.

In the present study, the aerodynamic model will be combined with an optimization algorithm, involving a large number of calculations of possible configurations. Thus, efficiency of the aerodynamic model is of primary importance. Although the SC method is efficient compared to a finite-difference code, we still consider it to be too slow for optimization purposes and instead, we have developed a model based on the blade-element principle in which the governing equations only need to be solved at one axial station, with blade forces determined from tabulated cascade-airfoil characteristics. In contrast to this, even the simplest SC method demands the solution of around 20 axial stations within an iterative loop of 5–10 cycles, making the developed approach at least 100–200 times faster.

The blade-element principle has previously been used successfully for the design of low pressure axial fans. For free vortex type fans, where no radial flow exists, an efficient design method is presented in the textbook by Wallis [5]. However, as a design method, analysis of a given fan configuration, using the free vortex method, can only be expected to succeed if the fan actually fulfills the free vortex requirements. For the arbitrary vortex type fan, where axial velocity and pressure are allowed to vary with spanwise distance from the rotational axis, Wallis also describes an analysis method for approximately linear radial distributions of axial and tangential velocity components. Recently, Downie et al. [6] described a mathematical model for calculating the arbitrary vortex flow of a rotor-only fan without restrictions on the velocity distributions.

In the present work, a simple and computationally efficient, yet reliable, analysis model for low-pressure axial fans of the arbitrary vortex type has been developed. The basic formulation of the model is similar to the one of Downie et al. [6], but the method proposed ensures global continuity to be satisfied at inlet, rotor as well as outlet planes. Furthermore, circulation is preserved downstream of the rotor. The model is suitable for numerical design optimization and computational efficiency was considered of primary importance. The governing equations are solved using the Newton-Raphson method, ensuring quadratic convergence at low computing costs. In the present paper, the governing equations and a description of the numerical solution procedure are presented. Comparing calculations with measurements from Kahane [7], overall fan efficiency and pressure rise are well predicted as are local properties, velocity, and pressure. The implementation of the Newton-Raphson method is found to be extremely efficient, enabling performance curve calculations, converged to machine accuracy, in a fraction of a second on a pentium personal computer.

2 Method

Considering axisymmetric flow, the annulus between the hub and the tip of the rotor is divided into a number of streamtubes in which flow can enter and leave through the end surfaces only. Each streamtube is defined as a control volume in which the continuity equation, the tangential momentum equation and a relation for axial forces, based on energy conservation along a streamline, is derived. Far downstream of the rotor, fully developed parallel flow exists and the spanwise pressure gradient is in balance with tangential velocity across the streamtubes. Downstream of the rotor, no tangential forces exist and the circulation is preserved. For each streamtube, the forces acting on the rotor are determined

Contributed by the Fluids Engineering Division for publication in the JOURNAL OF FLUIDS ENGINEERING. Manuscript received by the Fluids Engineering Division October 21, 1997; revised manuscript received January 21, 2000. Associate Technical Editor: B. Schiavello.

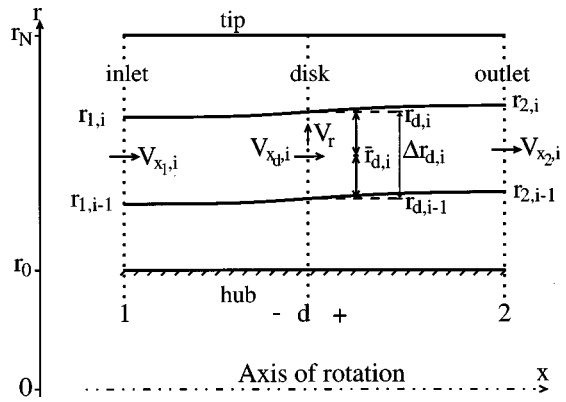

Fig. 1 The computational domain with indices for the *i*th control volume

iteratively from measured airfoil data. Besides the equations for each streamtube, integral conditions ensure global continuity at the rotor and outlet planes.

The model is expressed in cylindrical coordinates, (x,θ,r), with the velocity field denoted as (V_x, V_θ, V_r). In Fig. 1, the coordinate system and the indices, used in the following analysis, are defined. The local axial and tangential velocity components are located at the center of the control volume, whereas the pressure is situated at the radial positions. Directions of the velocity components are shown in Figs. 1 and 2. In the following, $\overline{r}$ and $\overline{p}$ denote radius and pressure in the center of the control volume, respectively.

In the following, all variables are to be taken at the *i*th control volume unless otherwise explicitly stated. The *i*-index is omitted for clarity.

2.1 Kinematic Relations. Inspired by the actuator disk approach, discussed by Horlock [8], the following kinematic relations may be assumed.

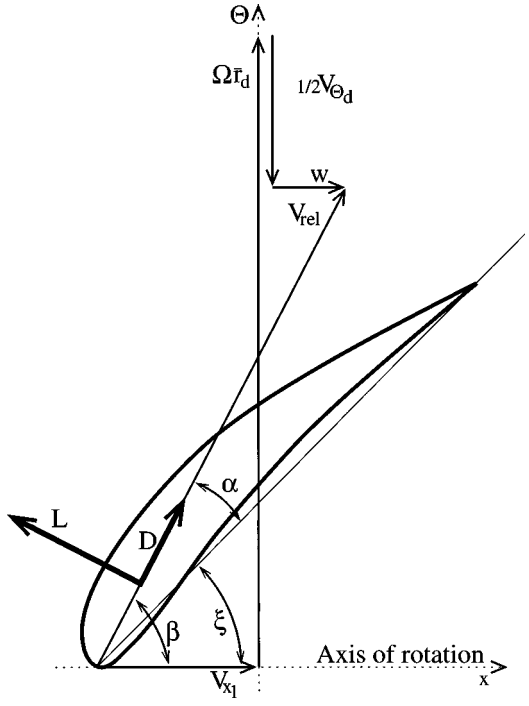

Fig. 2 Coordinate system showing the rotating blade element and the velocities experienced by the blade element. Cut in the (x-θ) plane (constant r).

Axial Velocity. In each control volume the axial velocity varies continuously from far upstream to far downstream of the rotor disk. In the actuator disk theory it is assumed that the axial velocity at the rotor disk is the mean of the values far downstream and far upstream. Thus, introducing the axially induced velocity, $w = w(r)$, at the rotor disk, it follows that the velocity is $V_{x_d} = V_{x_1} + w$ at the rotor disk and $V_{x_2} = V_{x_1} + 2w$ far downstream, respectively. This approach is normally taken for nonducted propellers, but for ducted propellers it does not automatically satisfy global continuity. In the present case, the fan analysis model may be combined with similar modules for stators or pipe bends, and it is of utmost importance that the flow rate leaving the fan unit corresponds to the incoming flow rate. We ensure this by adding a constant level, w_0, to the outflow velocity. Thus, $V_{x_2} = V_{x_1} + 2w + w_0$, where the magnitude of w_0 depends strongly on the skewness of the axial velocity profile experienced at the rotor disk. If the induced velocity, *w*, is zero for all radial positions, which will be the case for fans of the free vortex flow type, w_0 will be zero.

Far from the design-point, the flow in some of the streamtubes may become choked, indicating that $V_{x_2} < 0$. Since this means that flow enters the control volume at both ends, an inconsistency appears, and the model is invalid.

Tangential Velocity. Upstream of the rotor no rotation is present and, since no tangential forces act on the fluid downstream of the rotor, the change in circulation of the fluid occurs in the rotor disk only. The actuator disk theory states that the tangential velocity in the rotor disk is half that occurring immediately downstream of the rotor disk, V_{θ_d}. Downstream of the rotor disk the circulation is preserved, resulting in the following identity for the tangential velocity component from the rotor to far downstream

$$V_{\theta_d} \cdot \overline{r}_d = V_{\theta_2} \cdot \overline{r}_2 . \tag{1}$$

Radial Velocity. At a given radial distance from the centerline, the radial velocity, V_r, varies continuously as a function of axial distance from the rotor disk. Far upstream and far downstream the flow is assumed to be fully developed with no radial flow.

Pressure. Downstream of the rotor, the pressure is divided in a constant level, p_0, and a distribution, p_2, which depends on the radial position. Thus $p(r) = p_0 + p_2(r)$, where p_2 equals zero at the hub radius.

2.2 Governing Equations

Conservation of Mass. The flow is assumed incompressible and considering a control volume consisting of an annular streamtube, mass only enters through the control surface at the inlet and leaves at the outlet, far upstream and far downstream of the rotor disk, respectively. Imposing continuity from the rotor disk to the outlet, results in

$$(r_{d,i}^2 - r_{d,i-1}^2) V_{x_d} = (r_{2,i}^2 - r_{2,i-1}^2) V_{x_2} . \tag{2}$$

Relation for Axial Force. Upstream and downstream of the rotor, ignoring viscous dissipation due to mixing, the Bernoulli equation is valid along a streamline contained in the annular control volume. Since the axial velocity is continuous across the rotor, no change in axial momentum occurs from immediately upstream to immediately downstream of the rotor. This means that the pressure change across the rotor equals the axial force per unit area acting on the rotor. Combining the two Bernoulli equations with the pressure-force relation across the rotor yields the relation of axial forces for a streamtube,

$$p_0 + \overline{p}_2 - \overline{p}_1 + \tfrac{1}{2}\rho (V_{x_2}^2 - V_{x_1}^2 + V_{\theta_2}^2 - V_{\theta_d}^2) = f_x . \tag{3}$$

Pressure Equilibrium Far Downstream. Far downstream of the rotor disk, the flow is assumed parallel and no radial flow exists. Therefore, the radial pressure gradient balances the centrifugal force as

$$\left.\frac{dp}{dr}\right|_2 = \rho \frac{V_{\theta_2}^2}{r_2}.$$

Evaluating the term dp using a finite-difference across the ith control volume yields

$$\frac{p_{2,i} - p_{2,i-1}}{r_{2,i} - r_{2,i-1}} = \rho \frac{V_{\theta_2,i}^2}{\frac{1}{2}(r_{2,i} + r_{2,i-1})}. \tag{4}$$

Conservation of Tangential Momentum. Across the rotor disk the tangential velocity increases from zero immediately before the rotor to V_{θ_d} immediately after the rotor. Denoting the tangential force per unit area, acting on the fluid from the fan rotor, by f_θ, the tangential momentum equation reads

$$f_\theta = \rho V_{\theta_d} V_{x_d}, \tag{5}$$

Global Continuity at the Rotor Disk. Summation of the flow rate through all of the N control volumes in the rotor disk must add up to the flow rate, Q, given at the inlet. Thus

$$\sum_{i=1,N} \pi(r_{d,i}^2 - r_{d,i-1}^2) V_{x_d,i} = Q. \tag{6}$$

Global Continuity Far Downstream. Far downstream of the rotor disk, the flow rate must again correspond to the inlet flow rate. Thus,

$$\sum_{i=1,N} \pi(r_{2,i}^2 - r_{2,i-1}^2) V_{x_2,i} = Q. \tag{7}$$

Equation for Average Lift. The expression for secondary drag, Eq. (15), involves an average value of the lift coefficient. To ensure quadratic convergence in the Newton-Raphson method, discussed in Section 3, a variable, $\overline{C_L}$, is introduced for the area-averaged lift value. Thus

$$\overline{C_L} = \frac{1}{r_t^2 - r_h^2} \sum_{i=1,N} (r_{d,i}^2 - r_{d,i-1}^2) C_{L_i}. \tag{8}$$

2.3 Forces From the Rotor. In Fig. 2, a single blade element at $\overline{r_i}$ is shown. Denoting the angular velocity of the rotor by Ω, the relative speed, V_{rel}, experienced by the rotating blade, and the angle β, between the rotational axis and V_{rel}, are defined by

$$V_{\text{rel}}^2 = \left(\Omega \overline{r_d} - \frac{1}{2} V_{\theta_d}\right)^2 + V_{x_d}^2,$$
$$\tan\beta = \frac{\Omega \overline{r_d} - \frac{1}{2} V_{\theta_d}}{V_{x_d}}. \tag{9}$$

The above implies that the forces experienced by the blade element are determined by the relative speed, V_{rel}, and the local angle of attack, $\alpha = \beta - \xi$. Here ξ is the geometrical stagger angle relative to the axis of rotation.

The lift and drag forces on a single airfoil blade element are defined as

$$L = \tfrac{1}{2}\rho V_{\text{rel}}^2 c (r_{d,i} - r_{d,i-1}) C_L,$$
$$D = \tfrac{1}{2}\rho V_{\text{rel}}^2 c (r_{d,i} - r_{d,i-1})(C_D + C_{D_s} + C_{D_{\text{tip}}}), \tag{10}$$

where C_L and C_D are airfoil-specific data. C_{D_s} and $C_{D_{\text{tip}}}$ loss contributions due to secondary drag and tip clearance, respectively (see discussion in Section 4). The chord length is denoted by c and the number of blades as B. Distributing the force from all blades evenly on the area of the control volume annulus, the local forces per unit area in the axial and tangential direction, respectively, are

$$f_x = \frac{B(L \sin\beta - D \cos\beta)}{\pi(r_{d,i}^2 - r_{d,i-1}^2)},$$
$$f_\theta = \frac{B(L \cos\beta + D \sin\beta)}{\pi(r_{d,i}^2 - r_{d,i-1}^2)}. \tag{11}$$

3 Numerical Solution Procedure

For each control volume, the radial position far downstream of the rotor disk, r_2, the axially induced velocity, w, the pressure far downstream of the rotor disk, p_2, and the tangential velocity immediately downstream of the rotor, V_{θ_d}, are chosen as the variables in the model. Furthermore, three global variables are chosen, namely the pressure level at the hub, p_0, the induced velocity level, w_0, and the average lift value $\overline{C_L}$. Since both hub and tip radii are fixed, only N-1 unknown values of r_2 exist whereas there are N unknowns of w, p_2, and V_{θ_d}.

To rewrite the governing equations using the above variables, $V_{x_2} = V_{x_1} + 2w + w_0$ is introduced into Eqs. (2), (3), and (7). Furthermore, $V_{x_d} = V_{x_1} + w$ is inserted into Eqs. (2), (5), and (6). Finally, $V_{\theta_2} = V_{\theta_d} \cdot \overline{r_d}/\overline{r_2}$ is introduced into Eqs. (3) and (4). After the above, the discretized form of Eqs. (2)–(8) may be written, using compact notation, as

$$E_i(r_{2,i-1}, r_{2,i}, w_i, w_0) = 0$$
$$F_i(r_{2,i-1}, p_{2,i-1}, r_{2,i}, w_i, p_{2,i}, V_{\theta_d,i}, p_0, w_0, \overline{C_L}) = 0$$
$$G_i(r_{2,i-1}, p_{2,i-1}, r_{2,i}, p_{2,i}, V_{\theta_d,i}) = 0$$
$$H_i(w_i, V_{\theta_d,i}, \overline{C_L}) = 0 \tag{12}$$
$$I_1(w_i) = 0$$
$$I_2(r_{2,i}, w_i, w_0) = 0$$
$$I_3(w_i, V_{\theta_d,i}, \overline{C_L}) = 0,$$

where $i = 1,N$ except for the continuity equation (E_i), where the Nth equation is replaced by the boundary condition that $r_N = r_t$. A detailed description of the equations is provided in Sørensen [9].

The discretized governing system of Eqs. (12) is strongly coupled and nonlinear. Solving the equations by the Newton-Raphson method is computationally efficient, robust, and exhibits quadratic convergence. The Jacobian matrix turns out to be sparse and the linear system of equations, occurring in each iteration of the Newton-Raphson method, can be efficiently solved.

The standard formulation of the Newton-Raphson method for solution of a nonlinear system of equations is

$$\mathbf{J_F}(\mathbf{y}^k)\Delta\mathbf{y}^k = -\mathbf{F}(\mathbf{y}^k)$$
$$\mathbf{y}^{k+1} = \mathbf{y}^k + \Delta\mathbf{y}^k, \quad k = 1,2,\ldots, \tag{13}$$

where $\mathbf{y}^k$ contains the solution vector at the kth iteration and the Eqs. (12) are contained in $\mathbf{F}$. In the present case, the problem is described by $4N+3$ variables and thus the Jacobian matrix, $\mathbf{J_F}$, is a $[4N+3]\times[4N+3]$ matrix. The order chosen for the equations in $\mathbf{F}$ and their corresponding variables in $\mathbf{y}$ is

Table 1 Investigation of the influence of the number of blade elements, N, used in the solution of the aerodynamic model. Using the values for $N=891$ as reference, the deviation in efficiency is given as well as the deviation in outlet axial velocity at $r_h/r_t=0.9$. The calculations are for the validation case described in section 4, at the design flow rate of $Q=4.45\ m^3/s$.

N $[-]$	$\eta_{891}-\eta$ $[-]$	$V_{x_2}-V_{x_2,891}$ $[m/s]$
11	$1.9\cdot10^{-5}$	$6.3\cdot10^{-5}$
33	$1.8\cdot10^{-6}$	$7.9\cdot10^{-6}$
99	$6.0\cdot10^{-8}$	$3.6\cdot10^{-7}$
297	$1.9\cdot10^{-8}$	$1.2\cdot10^{-7}$

$$\mathbf{F}=\begin{pmatrix} E_1 \\ F_1 \\ G_1 \\ H_1 \\ \vdots \\ E_N \\ F_N \\ G_N \\ H_N \\ I_1 \\ I_2 \\ I_3 \end{pmatrix} \quad \text{and} \quad \mathbf{y}=\begin{pmatrix} r_{2,1} \\ w_1 \\ p_{2,1} \\ V_{\theta_d,1} \\ \vdots \\ r_{2,N} \\ w_N \\ p_{2,N} \\ V_{\theta_d,N} \\ p_0 \\ w_0 \\ \overline{C_L} \end{pmatrix}. \tag{14}$$

Besides the nonzero elements in the last three columns corresponding to the global variables, the equations corresponding to E_i, F_i, G_i, and H_i in the Jacobian matrix have nonzero elements close to the diagonal only, due to the ordering used in Eq. (14). The explicit differentiation of the equations in **F** with respect to the elements in **y** is omitted in this paper, but the calculations are trivial.

The factorization of the Jacobian matrix, Eq. (13), is performed by Gaussian elimination of the nonzero elements only. The sparseness of the Jacobian matrix results in a computational effort of the factorization being proportional to N (as opposed to the factorization of a full matrix which is proportional to N^3). Since the number of iterations in the Newton-Raphson method is independent of N, the computational effort for the fan analysis is thus found to be proportional to N.

The central difference approximation is used to evaluated the gradients in the governing equations and thus the numerical scheme is second order accurate. To determine the required number of blade elements, N, necessary to resolve the flow, calculations were performed for varying values of N. The integrated property efficiency and the local property V_{x_2} were determined and compared to a reference case with $N=891$. Table 1 shows the deviation between the reference case and computations with $N=11$, 33, 99, 297, respectively. Based on the comparisons, it is found that $N=33$ suffice to resolve the flow accurately.

The Newton-Raphson method uses approximately six iterations to obtain a solution converged to machine accuracy and a performance calculation with e.g., 20 different flow rates takes about 0.2 seconds on a pentium PC. The combination of highly converged solutions and low calculation time makes the model suitable for numerical design optimization.

The Newton-Raphson method may diverge if the initial guess is chosen far from the solution. It was found that converging solutions were usually obtained if $p_{2,i}=p_{1,i}$, $w_i=0$, $V_{\theta_d,i}=0$, $r_{2,i}=r_{d,i}$, $p_0=0$, $w_0=0$ and $\overline{C_L}=0$ for the first point calculated on the performance curve. For succeeding points, the previous solution was used as an initial guess.

4 Results and Discussion

In the work by Kahane [7], investigations were performed to determine whether three-dimensional flow may be utilized in axial fans with the purpose of increasing the pressure rise capabilities. A simplified design method for arbitrary vortex flow fans was proposed. Two rotors were constructed and the predictions of the design method were compared with experiments. Rotating a single tube, containing a yaw head as well as a static and a total pressure tube, along a radial axis enabled determination of spanwise distributions of flow angle, pressures, and velocities. The downstream measurement station was located 1.4 chord lengths behind the blade trailing edges. The method proposed by Kahane [7] is a design method and as such, he only compares calculations with measurements at the design flow rate.

The second rotor investigated by Kahane [7] was designed for solid body rotation at the design flow rate. It was found that the rotor could be constructed as a straight blade at a stagger angle of $\xi=48.2$ degrees with uniform chord and airfoil section along the span. The NACA 65-(12)10 airfoil was chosen for the blading. The tip radius was 0.267 m and the hub-to-tip ratio was 0.69. The rotor consisted of 24 blades and the solidity was 1.22 at the hub and 0.84 at the tip of the blades. The tip clearance height was about 0.4 mm, corresponding to approximately 0.5 percent of the blade height.

To compare measurements and calculations, the definitions of rotor static and total pressure rise from Kahane [7] are used. The input power required to run the fan, P is calculated from L and D. The integrated properties are mass-weighted and the dimensionless parameters from Kahane [7] have been transformed by a density of $\rho=1.21\ kg/m^3$ and a fan angular velocity of 3000 rpm. The design flow rate is $Q=4.45\ m^3/s$.

Only limited information regarding the experimental accuracy is provided in Kahane [7]. However, the tube containing the yaw head and the pressure tubes could be positioned radially to within 0.03 mm and the angle to within 0.1 deg. Readings were taken only when the rotational speed was within ±10 rpm of the specified test value of 3000 rpm.

4.1 Airfoil Data and Losses. The airfoil data used in the following calculations are extracted from Emery et al. [10]. This work reported extensive measurements of the NACA65 airfoil family, performed in a cascade wind tunnel for a range of solidities and stagger angles. Due to limitations in the investigated inflow angles, extrapolations were necessary for a few of the blade element sections, especially at the very low and very high flow rates.

The drag experienced by the individual blade elements is usually defined as a combination of the profile drag, determined from the measured airfoil data, and a secondary drag contribution, C_{D_s}. In the present work, an expression from Wallis [11] is used for the secondary drag

$$C_{D_s}=a\overline{C_L^2}+bc/(\sigma[r_t-r_h]), \tag{15}$$

where a and b are empirical constants, c the blade element chord, σ the solidity, r_h and r_t the hub and tip radii, respectively, and $\overline{C_L}$ the average lift value. The values for a and b have been determined from measurements on a large number of fan configurations. The recommended value for a is 0.018 and for b the recommended value is 0.02. However, for well designed blades, Wallis [11] proposes $b=0$, which has been used in the present calculations.

Further losses stem from the tip clearance leakage. Denoting the tip clearance height by t, these losses are modeled using an expression from Lakshminarayana and Horlock [12]

$$C_{D_{\text{tip}}}=0.7\overline{C_L^2}\cdot t/(r_t-r_h). \tag{16}$$

Finally, losses exist in the downstream expansion from annulus area to full duct area. This loss is modeled by an expression from

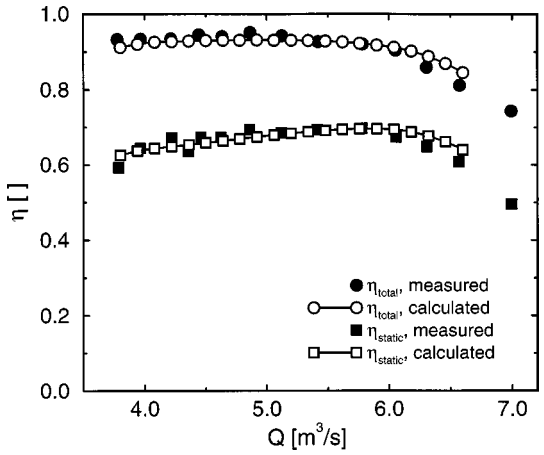

Fig. 3 Measured and calculated efficiency at various flow rates. η_{total} and η_{static} are based on the total and static pressure rise across the fan, respectively.

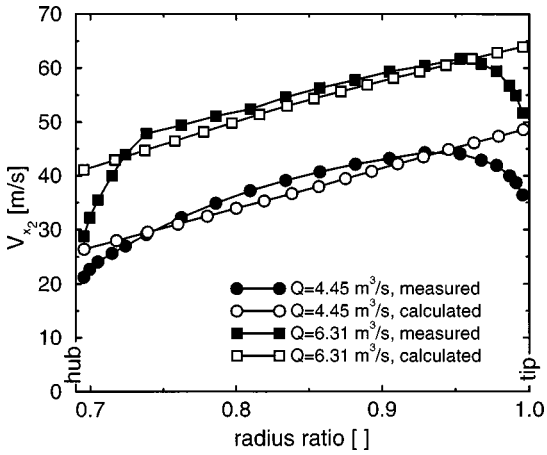

Fig. 5 Spanwise distribution of axial velocity far downstream of the rotor at two flow rates

Wallis [11]. The pressure loss across the diffuser is estimated as a fraction of the axial flow dynamic pressure change across the diffuser. Thus, introducing a diffuser pressure loss, Δp_D, and a diffuser efficiency, η_D, the diffuser loss may be expressed by

$$\Delta p_D = (1-\eta_D)1/2\rho\overline{V}_{x_1}^2\left(1-\left(\frac{A_1}{A_2}\right)^2\right), \tag{17}$$

where the areas A_1 and A_2 are the annulus area and the full duct area, respectively. The diffuser efficiency depends on the fairing of the diffuser. For well designed fairings, Wallis [11] suggests values between 0.8 and 0.9.

In the investigations of Kahane [7], the tip clearance is only 0.5 percent of the blade height and thus the influence is very small. The measurements are performed in the annulus, near the rotor, and thus the downstream diffuser losses are not included in the present calculations.

4.2 Comparison With Measurements. Although the rotor in the experiments of Kahane [7] was designed for a flow rate of $Q=4.45\,\mathrm{m}^3/\mathrm{s}$, measurements were conducted at other flow rates as well. This enables comparisons at off-design conditions and in the present work, we investigate fan performance at flow rates between 3.8 and 6.6 m^3/s.

Predicted and measured efficiencies based on static and total pressure, respectively, are shown in Fig. 3. The agreement is very good except at flow rates above 6 m^3/s, where the discrepancies are believed to be due to the necessary extrapolations of the airfoil data. The static and total pressure rises are depicted in Fig. 4. Again, the agreement is found to be good.

To further validate the model, local flow properties are compared with the measurements. The tangential velocity component is nondimensionalized with the inflow mean velocity, the static pressure with the inflow mean dynamic pressure and the radius with the tip radius.

In Fig. 5, the spanwise distribution of axial velocity at two flow rates is depicted. At the high flow rate, the agreement is very good except at the inner and outer part of the annulus, where the boundary layers influence the flow. At the low flow rate, the agreement is still reasonably good, although the boundary layers have a larger influence on the entire flow field.

In Fig. 6, the tangential velocity is depicted at the same two flow rates. Again the calculations compare reasonably well with the measurements. However, a systematic deviation is seen with smaller calculated tangential velocities at the hub and higher calculated values at the tip. No explanation for this can be given. However, it may be noted that the same deviation was found, at the design flow rate of $Q=4.45\,\mathrm{m}^3/\mathrm{s}$, in the original work by Kahane [7].

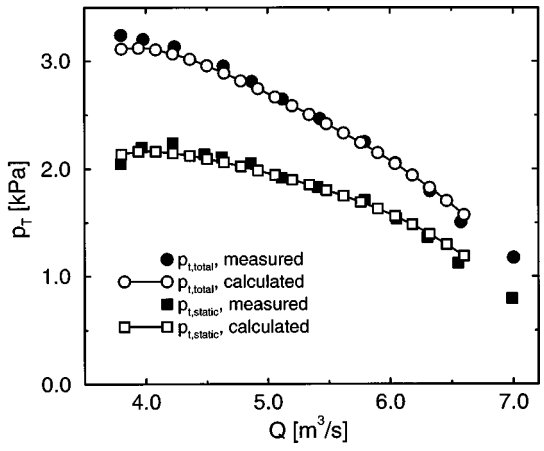

Fig. 4 Measured and calculated pressure rise at various flow rates. $p_{t,\mathrm{total}}$ and $p_{t,\mathrm{static}}$ denotes the total and static pressure rise, respectively.

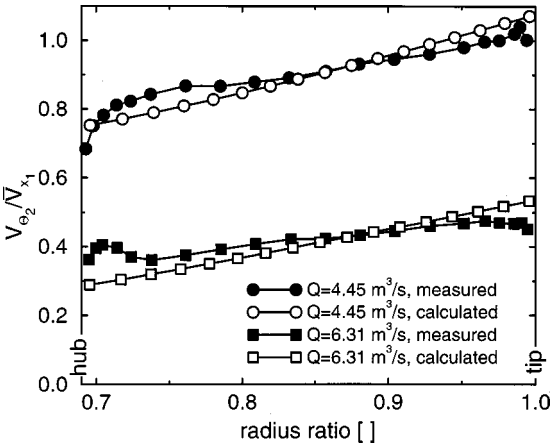

Fig. 6 Spanwise distribution of tangential velocity far downstream of the rotor at two flow rates

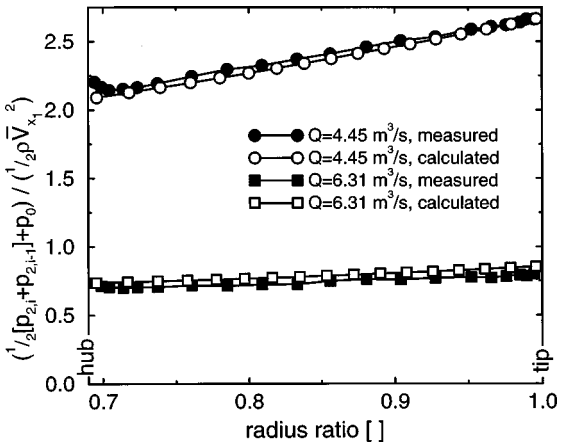

Fig. 7 Spanwise distribution of static pressure far downstream of the rotor at two flow rates

Finally, in Fig. 7, the spanwise distribution of static pressure is depicted. Again the comparisons are good.

5 Conclusion

A numerically efficient model for the aerodynamics of rotor-only axial fans was developed. Compared to previous blade-element based models for arbitrary vortex flow fans, the assurance of global continuity everywhere, as well as preservation of the circulation downstream of the rotor, is new. Furthermore, employing the Newton-Raphson method for the numerical solution of the nonlinear governing equations, results in highly converged solutions at low computing costs.

Comparison with measurements was good for integrated properties, efficiency, and total pressure rise. For local properties, discrepancies at the hub and tip regions of the blade were found, due mainly to the inviscid nature of the model. At the center of the blade, calculations compared well with measurements.

The accurate prediction of efficiency and total pressure rise combined with low computing costs and solutions converged to machine accuracy, makes the model suitable for numerical design optimization of ducted axial fans.

Acknowledgments

The work was partly supported by the Danish Energy Agency under contract no. 1253/96-0002.

Nomenclature

a, b = secondary drag coefficients
B = number of blades
c = chord length
C_D = profile drag coefficient
C_{D_s} = secondary drag coefficient
$C_{D_{\text{tip}}}$ = tip clearance drag coefficient
C_L = lift coefficient
$\overline{C_L}$ = average lift coefficient
D = drag force
E_i, F_i, G_i, H_i = discretized governing equations for each control volume
f_x = axial volume force
f_θ = tangential volume force
$\mathbf{F}$ = RHS vector in the Newton-Raphson iteration
I_1, I_2, I_3 = discretized global governing equations
$\mathbf{J_F}$ = Jacobian matrix
L = lift force
N = number of annular control volumes
p = static pressure
p_0 = static pressure at hub
p_T = integrated fan pressure rise
Δp_D = downstream diffuser loss
P = mechanical shaft power
Q = flow rate
r_h, r_t = rotor hub and tip radii
s = interblade spacing, $s = 2\pi r/B$
t = tip clearance height
V_{rel} = velocity relative to the blade element
V_x, V_r, V_θ = velocity components in cylindrical coordinates
w = axially induced velocity
w_0 = constant level of the axially induced velocity
x, r, θ = cylindrical coordinates axes
$\mathbf{y}$ = solution vector in the Newton-Raphson iteration
$\mathbf{\Delta y}$ = update of solution vector in the Newton-Raphson iteration
α = angle of attack relative to the blade element
β = angle between rotational axis and V_{rel}
η = fan efficiency, $\eta = Q \cdot p_T / P$
η_D = downstream diffuser efficiency
Ω = angular velocity of rotor
ρ = density of fluid
σ = solidity, $\sigma = c/s$
ξ = blade element stagger angle
$(\cdot)_1$ = plane far upstream of the rotor disk
$(\cdot)_d$ = plane at the rotor disk
$(\cdot)_2$ = plane far downstream of the rotor disk
$(\cdot)_i$ = denotes control volume no. i
$(\cdot)^k$ = variable at iteration no. k
$\overline{(\cdot)}$ = value at the center of control volume

References

[1] Cumpsty, N. C., 1989, *Compressor Aerodynamics*, Longman Scientific & Technical.
[2] Lakshminarayana, B., 1995, *Fluid Dynamics and Heat Transfer of Turbomachinery*, Wiley, New York.
[3] Üçer, A. S., Stow, P., and Hirsch, C., 1985. ''*Thermodynamics and Fluid Mechanics of Turbo-Machinery,*'' *Proceedings, Izmir 1984* 1-2, Nijhoff.
[4] Novak, R. A., 1967, ''Streamline Curvature Computing Procedures for Fluid-Flow Problems,'' ASME J. Eng. Power, **89**, pp. 478–490.
[5] Wallis, R. A., 1961, *Axial Flow Fans. Design and Practice*, George Newnes Limited, London. .
[6] Downie, R. J., Thompson, M. C., and Wallis, R. A., 1993, ''An Engineering Approach to Blade Designs for Low to Medium Pressure Rise Rotor-Only Axial Fans,'' Exp. Therm. Fluid Sci., **6**, pp. 376–401.
[7] Kahane, A., 1948, ''Investigation of Axial-Flow Fan and Compressor Rotors Designed for Three-Dimensional Flow,'' Tech. Note 1652, NACA, Langley Memorial Aeronautical Laboratory, Langley Field, Va.
[8] Horlock, J. H., 1978, *Actuator Disk Theory. Discontinuities in Thermo-Fluid Dynamics*, McGraw-Hill, New York.
[9] Sørensen, D. N., 1998, ''Aerodynamic Modelling and Optimization of Axial Fans,'' Thesis ET-PHD 9801, Department of Energy Engineering, Technical University of Denmark, DK2800 Lyngby.
[10] Emery, J. C., Herrig, L. J., Erwin, J. R., and Felix, A. R., 1958, ''Systematic Two-Dimensional Cascade Tests of NACA 65-series Compressor Blades at Low Speeds,'' Report TR-1368, NACA, Langley Aeronautical Laboratory, Langley Field, Va.
[11] Wallis, R. A., 1993, *Axial Flow Fans and Ducts*, Krieger Publishing, Malabar, FL
[12] Lakshminarayana, B., and Horlock, J. H., 1967, ''Leakage and Secondary Flow in Compressor Cascades,'' Report R & M 3483, British Aeronautical Research Council.

D. N. Sørensen
Research Scientist,
Department of Energy Engineering,
Technical University of Denmark,
DK2800 Lyngby, Denmark

M. C. Thompson
Research Scientist,
Department of Mechanical Engineering,
Monash University,
Clayton, Vic. 3168, Australia

J. N. Sørensen
Associate Professor,
Department of Energy Engineering,
Technical University of Denmark,
DK2800 Lyngby, Denmark

Toward Improved Rotor-Only Axial Fans—Part II: Design Optimization for Maximum Efficiency

Numerical design optimization of the aerodynamic performance of axial fans is carried out, maximizing the efficiency in a design interval of flow rates. Tip radius, number of blades, and angular velocity of the rotor are fixed, whereas the hub radius and spanwise distributions of chord length, stagger angle, and camber angle are varied to find the optimum rotor geometry. Constraints ensure a pressure rise above a specified target and an angle of attack on the blades below stall. The optimization scheme is used to investigate the dependence of maximum efficiency on the width of the design interval and on the hub radius. [S0098-2202(00)01602-3]

1 Introduction

Fan engineers are frequently faced with the problem of designing high-efficiency fans at a given flow rate and for a given pressure duty. Design techniques are typically based on engineering experience, and may involve much trial and error before an acceptable design is found. Calculating the specific rotational speed and diameter, discussed by e.g., Wright [1], may aid the designer in determining reasonable values for the rotational speed and diameter of the rotor, based on desired flow rate and pressure rise. Integrating the concept of free vortex flow design (Wallis [2]) in the process reduces the need to build and evaluate new designs. However, the restrictions of the spanwise distributions of velocity and pressure in the free vortex flow design imply that analysis of the fan at off-design duties has only limited validity.

In the work by Wallis [3], an inlet guide vane-rotor-stator installation was investigated. The system considered was of the free vortex flow type and several important parameters, e.g., lift-to-drag ratio, were fixed at reasonable values. This resulted in explicit expressions for efficiency and total pressure rise as a function of tip speed ratio, hub-to-tip ratio, and downstream losses. Parametrical studies of efficiency and pressure rise as a function of the three variables were then carried out.

Recently, Dugao et al. [4] considered numerical design optimization of a rotor-stator configuration for mining ventilation. Employing a free vortex flow design method, considerable improvement in efficiency was gained as compared to an existing installation. Furthermore, as an additional advantage, it was found that the noise emission from the fan installation was reduced.

The above investigations concerned fan performance for a fixed flow rate and pressure rise, i.e., at a predefined design point. Operating the fan under other conditions was not considered and it is therefore possible that it may behave poorly away from the design point. In practice, fans often operate far from the design point and often with low efficiency (Bolton [5]).

Employing an arbitrary vortex flow model (Sørensen and Sørensen [6]) for fan analysis enables the designer to investigate a fan operating under various conditions. Furthermore, a wide range of design alternatives may be tested numerically with equal validity. However, the increased degree of freedom of the arbitrary vortex flow model implies a trial and error process before an acceptable design is found. This in turn limits the number of design variations that may be investigated as well as the complexity of the geometric requirements and operating conditions for the fan.

Design optimization techniques may be used to automate the fan design process. Here, searching algorithms maximize the efficiency while enforcing constraints on geometry, operating conditions and operating limits. Design parameters are automatically varied by the optimization algorithm and the corresponding changes in efficiency and constraints are used to determine an optimal design. Combining an optimization algorithm with the arbitrary vortex flow model enables the fan designer to investigate a large range of design alternatives in an efficient manner. Furthermore, parametrical studies of optimum designs for various operating conditions and geometrical requirements are easily carried out. Many fan configurations are compared in the optimization algorithm and a computationally efficient implementation of the arbitrary vortex flow model is required. In Sørensen and Sørensen [6], a Newton-Raphson method was used to solve the equations of the model, and solutions converged to machine accuracy are found at small computing costs. Furthermore, results agree well with measurements and this model is therefore used in the present work.

The efficiency of a rotor-only fan is considered over a design interval of flow rates rather than at a design point. This enables the design of a fan that operates well under various conditions. The fan duty and size are determined from the specific application of the fan. In the present case, the basis used for the optimizations is the fan from Kahane [7], which was also used for validating the aerodynamic model in Sørensen and Sørensen [6].

In Section 2, a description of the mathematical optimization problem, as applied to fan efficiency maximization, is given. Furthermore, some special implementation details of the optimization algorithm are discussed. In Section 3, optimizations are carried out to clarify the dependence of the efficiency on the width of the design interval and on the hub radius of the rotor.

2 Method

The standard constrained optimization problem can be formally stated as

$$\begin{aligned} &\text{Maximize } F(\Phi_n) && n=1,2,\ldots,\text{NDV} \\ &\text{subject to } g_j(\Phi_n)\geq 0 && j=1,2,\ldots,\text{NCON}, \end{aligned}$$

Contributed by the Fluids Engineering Division for publication in the JOURNAL OF FLUIDS ENGINEERING. Manuscript received by the Fluids Engineering Division October 21, 1997; revised manuscript received January 21, 2000. Associate Technical Editor: B. Schiavello.

where NDV denotes the number of design variables and NCON the number of constraints.

The objective function, F, describes the fitness of the possible designs and, in the present case, reflects the requirements of the manufacturer to produce a high-efficiency fan. The design variables, denoted by Φ_n, define the possible configurations, which can be altered by the optimization algorithm so as to find the maximum of F. Finally, g_j denotes the constraints which describe geometrical restrictions of the designs as well as desired operating conditions and limits of the fan.

In Section 2.1, the definition of the objective function in terms of maximum efficiency is described. The design variables governing the optimization problem are defined in Section 2.2. The constraints, imposing practical restrictions to blade geometry and operating conditions, are discussed in Section 2.3. Finally, in Section 2.4 a brief description of the implementation of the optimization algorithm is provided.

2.1 The Objective Function. Defining a design interval of flow rates and denoting the center of the design interval by Q_c and width by ΔQ, respectively, the primary goal of the optimization is to maximize the mean value, $\overline{\eta}$, of the aerodynamic fan efficiency in the design interval, $Q \in [Q_c - 1/2\Delta Q; Q_c + 1/2\Delta Q]$ [m^3/s].

The mean value is defined by

$$\overline{\eta} = \frac{1}{\Delta Q} \int_{Q_c - 1/2\Delta Q}^{Q_c + 1/2\Delta Q} \eta(Q) dQ, \tag{1}$$

where the efficiency of the fan at a given flow rate, $\eta = \eta(Q)$, is calculated using the model described in Sørensen and Sørensen [6]. In the present work, $\eta(Q)$ is defined as

$$\eta = Q \cdot (p_T - \Delta p_D)/P, \tag{2}$$

where Q is the flow rate, $p_T = p_T(Q)$ is the total pressure rise across the fan rotor, $\Delta p_D = \Delta p_D(Q)$ is the loss in the downstream diffuser, and $P = P(Q)$ is the power input to the fluid. Besides the loss in the downstream diffuser, empirical correlations are used for the loss due to the tip clearance height and for the secondary drag losses. The above empirical loss correlations are further described in Sørensen and Sørensen [6]. Losses in seals, bearings, etc. are excluded from the optimization.

The total pressure rise, p_T, across the rotor is determined as a spanwise integration of the total pressure rise across each streamtube. Similarly, the input power is determined by an integration of the lift and drag contributions. For the rotor-only configuration considered here, the dynamic pressure contained in the tangential velocity cannot be regained and is not included in the calculation of p_T. In the following, the result from the optimization, i.e., the optimum (maximum) value of $\overline{\eta}$, is denoted $\overline{\eta}_{\max}$.

To evaluate the integral in Eq. (1), the design interval is divided into N_d equally spaced flow rate evaluation-points and the efficiency, η, is calculated at each of these points. The mean value, $\overline{\eta}$, is then calculated using an accurate numerical integration method of order $O(1/N_d^4)$ from Press et al. [8]. The integral is constructed by fitting cubic polynomials through successive groups of four points.

2.2 Design Variables. The chosen design variables, which define the various possible fan configurations, are the hub radius of the rotor, r_h, and the spanwise distributions of chord-length, $c(r)$, stagger-angle, $\xi(r)$, from the rotational axis and camber angle, $\theta(r)$, of the airfoils (Fig. 1). Although tip radius and angular velocity of the rotor are key design parameters, they are excluded in the present study. The rationale behind this is to show that, even though the optimized fans have the same dimensionless characteristica in terms of e.g., specific speed, differences in performance can be achieved, depending on the allowed variations in geometry and on the imposed limits on operating conditions.

The spanwise distributions of chord, stagger, and camber are defined using single segment Bézier curves. The radial positions of the vertices in the Bézier polygon are fixed and distributed evenly from hub to tip, whereas the lateral movement of the vertices defines the spanwise distribution of chord, stagger and camber. Thus, the number of design variables describing either of the spanwise distributions corresponds to the number of vertices in the Bézier polygon. An investigation of the required number of vertices in the Bézier polygon is carried out in Section 3.1.

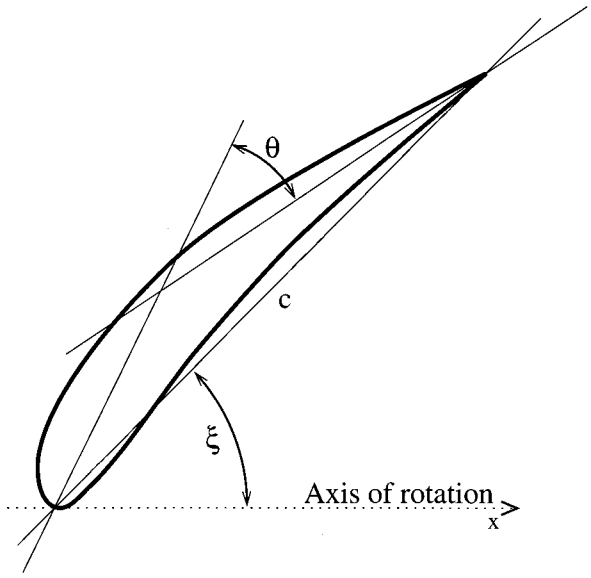

Fig. 1 Definition of the spanwise variables chord (c), stagger (ξ), and camber (θ), used in the optimization

The NACA65 airfoil family is used for the blades and measured airfoil cascade data are obtained from Emery et al. [9]. Only data for camber angles of 12 and 18 degrees were extracted, since these were measured using the broadest range of geometrical variations. The optimization algorithm requires differential functions and it was necessary to smooth the data. This was performed by creating explicit expressions for the lift and drag coefficients as a function of angle of attack, stagger angle, solidity, and camber angle. To find the functional expression which approximated the measurements best, using a least square measure, an unconstrained optimization problem was defined and solved numerically. To evaluate the quality of the functional expressions, the test case from Kahane [7], used in Sørensen and Sørensen [6] was recalculated using the functional expressions and it was found that the efficiency deviated less than 0.6 percent from the original calculations, for all of the investigated flow rates.

2.3 Constraints. Requirements from the manufacturer determine the specifications of the fan and thereby also the constraints. These may be due either to some geometrical restrictions or to some desired property of the fan as discussed below. In the present case, we consider a situation in which the fan used for validation in Sørensen and Sørensen [6] is to be improved, using the following specifications:

- The tip radius of the fan is fixed at $r_t = 0.27$ m.
- $B = 24$ blades is used for the rotor.
- The angular velocity is fixed at $\Omega = 3000$ rpm.
- The center of the design interval is defined as $Q_c = 6.0$ m^3/s.

This value is chosen since the rotor providing the basis for the optimizations exhibits maximum efficiency at this flow rate when the definition of efficiency in Eq. (2) is used (Kahane [7]).

- The total pressure rise, as defined in Section 2.1, should be at least 1800 Pa. for all flow rates.
- The tip clearance height is taken to be constant, $t = 1$ mm and

the efficiency of the diffuser is taken to be $\eta_D = 0.9$ or $\eta_D = 0.95$. The coefficients for the secondary drag contribution are defined as $a = 0.018$ and $b = 0.02$.

For the spanwise distributions of chord, stagger, and camber, differentiable constraints are ensured by calculating the constraints from the parameterized Bézier curves rather than from the discrete points governing the streamtube centers. In the present work, the following constraints are imposed:

Hub Radius, r_h. Due to manufacturing requirements, r_h should be larger than 100 mm. Furthermore, the annulus between hub and tip is chosen to be larger than 30 mm. Thus $r_h - 0.1 > 0$ and $r_t - r_h - 0.03 > 0$. Here, r_t designates the tip radius of the rotor. These constraints are never active for the optimum designs.

Chord Distribution, c. Although not based on geometrical or structural considerations, the measured airfoil data are restricted to solidities between 0.5 and 1.5. To avoid extrapolations of the data, the chord is constrained to solidities between 0.52 and 1.48. Here, the solidity is defined as $\sigma = c/s$, where $s = 2\pi r/B$.

Stagger Distribution, ξ. No natural restrictions apply to the stagger angle and it is bounded between 2 and 88 degrees to aid the optimization algorithm in narrowing the possible values. Thus $[\xi(r) - 2]_{\min} > 0$ and $[88 - \xi(r)]_{\max} > 0$. These constraints are never active for the optimum designs.

Camber Distribution, θ. The measured airfoil data are restricted to camber angles between 12 and 18 degrees. To avoid extrapolations of the data, the camber angle is constrained to values between 12.1 and 17.9 degrees.

Total Pressure Rise, p_T. The designed fan must be able to produce at least the required total pressure rise for all flow rates in the design interval. In the present work, $p_T = 1800$ Pa. was chosen as the minimum pressure rise. Thus $[p_T(Q) - 1800]_{\min} > 0$.

Axial Velocity in Outlet. As discussed in Sørensen and Sørensen [6], the analysis model is unreliable if very small outlet velocities are found. A constraint is imposed, ensuring that, for all blade elements, the optimum design does not result in outlet velocities less than 0.26 of the inlet velocity at any flow rate in the design interval. This constraint is never active for the optimum designs.

Tangential Velocity in Outlet. The ratio of tangential to axial velocity at the outlet is kept below 1.1 for all streamtubes and for all flow rates. This limit is imposed to avoid vortex breakdown downstream of the rotor, a flow-state which cannot be captured by the aerodynamic model. The above criterion for vortex breakdown is based on Squire [10], where stability analysis was applied to three cases of uniform axial velocity with different spanwise distributions of tangential velocity. The analysis indicated that vortex breakdown occurs when the ratio of tangential to axial velocity is between 1.0 and 1.2, thus justifying the choice of 1.1 as the limit.

Stall Limit, $\Delta\alpha_{\text{stall}}$. At high angles of attack, the flow on the blades may stall. This results in large unsteady forces acting on the blades, followed by fatigue problems. Furthermore, a large increase in noise emission occurs under stalled conditions (Sharland [11]). Here, we define stall to occur when the lift coefficient reaches its maximum value and the corresponding angle of attack is denoted by α_{stall}. For all flow rates and for each blade element, the difference between α_{stall} and the actual angle of attack, α, is determined. Denoting the smallest of these differences by $\Delta\alpha_{\text{stall}}$, a flow well below stall is ensured by demanding that $\Delta\alpha_{\text{stall}} \geqslant 1$, thus keeping the angle of attack, for all flow rates and for all blade elements, at least one degree below stall.

2.4 Optimization Algorithm. The optimization problem proposed in Sections 2.1–2.3 defines a differentiable and nonlinear objective function to be solved with a set of nonlinear constraints. The algorithm chosen for the solution of the problem is the sequential quadratic algorithm by Han [12], extended by Powell [13].

The algorithm requires gradients of the objective function and constraints with respect to the design variables. Explicit differentiation of the aerodynamic model is very complicated and the gradients are evaluated approximately, using finite differences. The computational effort for each iteration in the optimization algorithm is thus proportional to the number of design variables, NDV.

3 Results and Discussion

The following proposed guidelines apply for an optimum design and will be further discussed later:

- The pressure rise decreases with increasing flow rate. Therefore, the pressure rise constraint applies at the highest flow rate in the design interval. Furthermore, this constraint is expected to be active for all optimum designs, since an excessive pressure rise results in increased tangential velocities which, in the present investigation of a rotor-only fan, is considered as loss.
- The angle of attack on the blade increases with decreasing flow rate. Thus, if active, the stall limit constraint applies at the lowest flow rate in the design interval.
- The loss in the downstream diffuser, as well as the tip clearance loss, increases with increasing hub radius. Thus, it is anticipated that the hub radii will be small for the optimum designs, thereby lowering the losses. However, for small hub radii, the blade speed is low at the inner part of the rotor and the axial throughflow velocity is small due to the large annulus area. Both of these conditions result in low relative velocities and it becomes difficult to exchange the required momentum at the inner part of the blade. This in turn results in lowered axial velocities at the hub and the constraint on the tangential velocity may become active.
- The optimizations are carried out for an interval of flow rates, and thus for an interval of axial throughflow velocities. For small hub radii, the low blade velocity, combined with the variations in axial velocity, results in large variations of the angle of attack on the blade elements. Although influenced by all operating conditions and limits, an essential parameter for an optimum design is a lift-to-drag ratio close to maximum for all blade elements. The large angle of attack interval at the inner region of the blade implies that, in some parts of the flow rate interval, this part of the blade operates at angles of attack far away from maximum lift-to-drag ratio. Furthermore, large variations in angles of attack implies that the stall limit constraint may become active.

Before the optimization was applied to a real case, initial investigations were carried out as described in Section 3.1. First, the effect of varying the number of Bézier vertices for the curves describing the spanwise distribution of chord, stagger, and camber was examined. Second, the effect of varying the number of calculation points in the design interval was examined. After these preliminary investigations, a series of optimizations aimed at finding the optimum efficiency for various design conditions was carried out. This is described in Sections 3.2 and 3.3.

3.1 Initial Investigations. As discussed in Section 2.4, the number of calls to the performance analysis model in each iteration increases approximately linearly with the number of design variables. Furthermore, the number of iterations in the optimization algorithm tends to increase with increasing number of design variables. It is thus extremely important to keep the number of vertices in the Bézier polygons, describing chord, stagger and camber, to a minimum without sacrificing the freedom of the design too much. A series of optimizations was carried out, varying the number of vertices in the Bézier polygons. Using $N_d = 19$ points in a design interval defined by $Q_c = 6\ \text{m}^3/\text{s}$ and $\Delta Q = 2\ \text{m}^3/\text{s}$, it was found that five vertices in the Bézier polygons resulted in an optimum efficiency determined within approxi-

mately 0.01 percent of the efficiency obtained with eight vertices. This accuracy is adequate and five vertices in the Bézier polygons are used in all of the following optimizations.

Another important factor affecting the computational effort during the optimizations is the number of points, N_d, chosen to divide the design interval when evaluating the integral in Eq. (1). A linear dependence exists between the number of points and the calculation time. Using the same optimization case as described above, but varying N_d, it was found that for $N_d \geq 13$, the optimum efficiency was essentially independent of N_d. Thus $N_d = 13$ points are used in all of the subsequent calculations of $\overline{\eta}$.

3.2 Dependence on Design Interval Width. In order to clarify the dependence of optimum efficiency, $\overline{\eta}_{\max}$, on the width of the design interval, a series of optimizations was carried out for various values of ΔQ. The optimizations were carried out with $B = 24$ blades and the center of the design interval was $Q_c = 6\ \mathrm{m}^3/\mathrm{s}$ for all cases. In Fig. 2, $\overline{\eta}_{\max}$ is shown as a function of ΔQ. Also included in the figure are vertical lines indicating when the constraints become active. At design interval widths of $\Delta Q = 1.4\ \mathrm{m}^3/\mathrm{s}$ and above, the constraint for the stall limit is active and for $\Delta Q = 1.8\ \mathrm{m}^3/\mathrm{s}$ and above, the constraint limiting the tangential velocity is active.

As expected, the optimum efficiency decreases with increasing width of the design interval. For small values of ΔQ, the angles of attack experienced by the blade elements are close to the angle of attack at maximum lift-to-drag ratio. However, increasing the width of the design interval, the range of angles of attack experienced by the blade elements increases and, at least for some parts of the design interval, the lift-to-drag ratio is far from maximum.

For $\Delta Q \geq 1.4\ \mathrm{m}^3/\mathrm{s}$, the stall constraint becomes active which means that the increasing angle of attack interval can only be expanded towards lower angles of attack for some of the blade elements, thus limiting the design further. In Fig. 2, this can be observed as a slightly more decreasing $\overline{\eta}_{\max}$. For $\Delta Q \geq 1.8\ \mathrm{m}^3/\mathrm{s}$, the tangential velocity constraint becomes active as well, which is seen as an even faster decrease of $\overline{\eta}_{\max}$. For ΔQ larger than the values shown in Fig. 2, it was not possible to obtain a feasible design. For the largest flow rate interval resulting in a solution, the geometry of the rotor is determined completely by the constraints and thus independent of the objective function used.

An important thing to note from Fig. 2 is that an axial fan which operates well in a design interval of e.g., $\Delta Q = 1.4\ \mathrm{m}^3/\mathrm{s}$ has a decrease in $\overline{\eta}_{\max}$ of only about two points compared to the case of $\Delta Q = 0\ \mathrm{m}^3/\mathrm{s}$. This indicates that axial fans which operate well under various conditions may be designed with the present method.

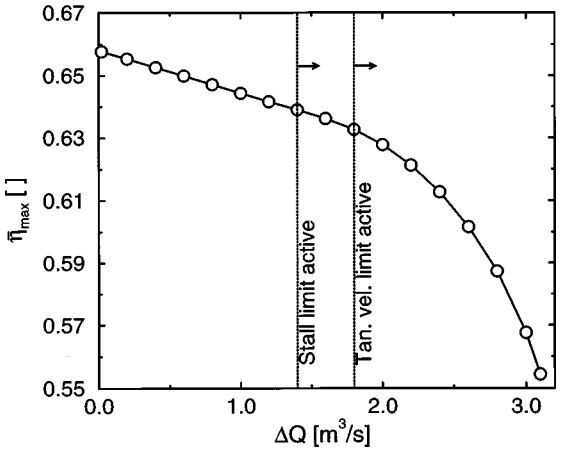

Fig. 2 Optimum efficiency as a function of design interval width, $Q_c = 6\ \mathrm{m}^3/\mathrm{s}$. The stall limit constraint is active for $\Delta Q \geq 1.4\ \mathrm{m}^3/\mathrm{s}$, and the tangential velocity limit constraint is active for $\Delta Q \geq 1.8\ \mathrm{m}^3/\mathrm{s}$.

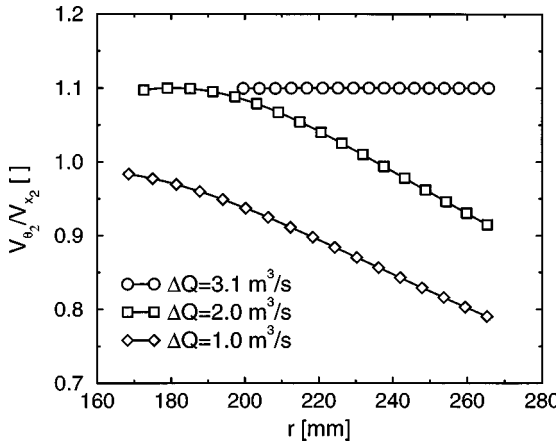

Fig. 3 Tangential to axial velocity ratio at fan outlet for the optimum designs for three different widths of the design interval. The curves are for the lowest flow rate in the design interval. The constraint on the tangential velocity was $V_{\theta_2}/V_{x_2} \leq 1.1$.

To further investigate the constraint on the tangential velocity, Fig. 3 shows the tangential to axial velocity ratio far downstream of the fan for three of the above design interval widths. All curves are for the lowest flow rate in the design interval ($Q = Q_c - \Delta Q/2$), at which the tangential to axial velocity ratio is maximum. It is seen that the tangential to axial velocity ratio constraint is not active for the case of $\Delta Q = 1.0\ \mathrm{m}^3/\mathrm{s}$. For $\Delta Q = 2.0\ \mathrm{m}^3/\mathrm{s}$ the constraint influences the inner part of the blade and for $\Delta Q = 3.1\ \mathrm{m}^3/\mathrm{s}$, the flow across the whole blade is determined by the constraint.

Figure 4 shows the optimum spanwise distributions of chord, stagger and camber, respectively, for the three design interval widths selected above. For $\Delta Q = 3.1\ \mathrm{m}^3/\mathrm{s}$, the case at which the tangential velocity constraint is active for all radii, the spanwise

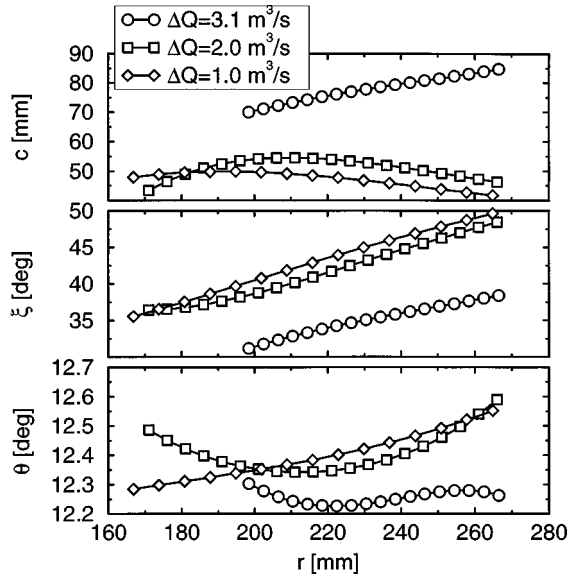

Fig. 4 Optimum spanwise distributions of chord (top), stagger angle (center), and camber angle (bottom) for three different widths of the design interval

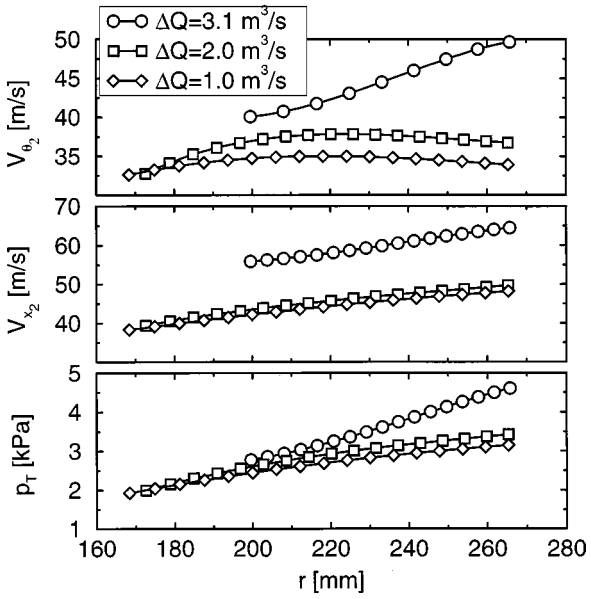

Fig. 5 Radial distributions of tangential velocity (top), axial velocity (center) and total pressure rise (bottom) for three different widths of the design interval. The curves are calculated at the flow rate of the design interval center ($Q_c = 6.0\ m^3/s$).

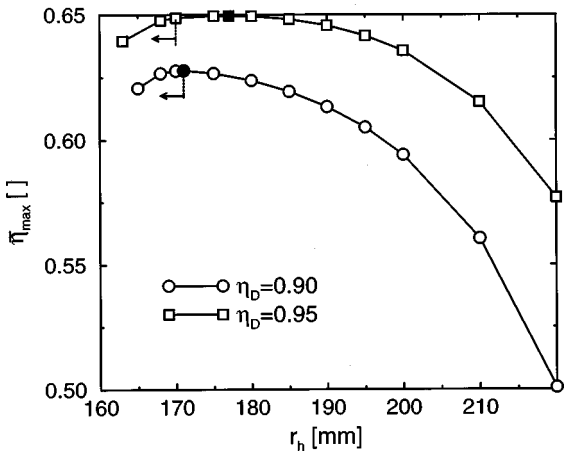

Fig. 6 Optimum efficiency as a function of hub radius. $Q_c = 6\ m^3/s$, $\Delta Q = 2\ m^3/s$. Filled symbols show the optimum hub radius, i.e., when the hub radius is included as a design variable. Arrows indicate when the tangential velocity limit constraint becomes active.

distributions are influenced by the constraint. This is most clearly seen on the chord distribution which increases nearly linearly from hub to tip. As noted above, this design interval is the largest at which a solution could be found and the design is determined by the constraints alone. For $\Delta Q = 2.0\ m^3/s$, the tangential velocity constraint is active at the inner part of the blade. This is reflected in the spanwise distributions with a significant increase in chord and an almost constant stagger angle at the inner part of the blade. Furthermore, the camber angle decreases at the inner part and increases at the outer part of the blade. Finally, for $\Delta Q = 1.0\ m^3/s$, where the constraints for the tangential velocity and for the stall limit both are inactive, the spanwise distributions exhibit a more regular behavior. Although a slight increase in chord is experienced at the inner part of the blade, the chord generally decreases toward the tip. The stagger angle and the camber angle increase all along the blade.

To further investigate the optimum designs, Fig. 5 depicts the spanwise distributions of tangential velocity, axial velocity, and total pressure rise, respectively, for the same three design interval widths as above. All curves are calculated at Q_c, the center of the design interval. For $\Delta Q = 3.1\ m^3/s$, the tangential velocity increases nearly linearly along the blade, with a relatively large gradient. This in turn results in a large variation in total pressure, increasing from the hub toward the tip. For $\Delta Q = 2.0\ m^3/s$, the geometry of the inner part of the blade is restricted due to the constraint on the tangential velocity. This is reflected in the tangential velocity distribution which increases significantly at the inner part of the blade after which it settles at a nearly constant value. For the spanwise distribution of total pressure rise, this is seen as a large increase at the inner part of the blade. Finally, for $\Delta Q = 1.0\ m^3/s$, the tangential velocity distribution increases slightly at the inner part of the blade, followed by a small decrease at the outer part of the blade. Generally, the tangential velocity is smaller than for the case with $\Delta Q = 2.0\ m^3/s$ which, for the distribution of total pressure rise, results in a smaller slope.

3.3 Dependence on Hub Radius. As discussed in the first part of Section 3, the losses in the downstream diffuser and from the tip clearance height increases with increasing hub radii. In the previous section, the hub radius was included as a design variable, thereby obtaining the value which results in the highest efficiency of the fan. In this section, the sensitivity of the efficiency on the hub radius is investigated by carrying out a series of optimizations for varying hub radius, r_h. The center of the design interval is $Q_c = 6\ m^3/s$ and the width of the design interval is $\Delta Q = 2.0\ m^3/s$. As described in the introduction to Section 3, the downstream loss in the diffuser is highly influenced by the hub radius and the investigation is carried out using two different diffuser efficiencies, $\eta_D = 0.90$ and $\eta_D = 0.95$.

In Fig. 6 the efficiency as a function of hub radius is shown for the two diffuser efficiencies. Also included in the figure are the hub radii resulting in the optimum efficiency, determined by optimizations, where the hub radius was included as a design variable. These are indicated by solid symbols. The constraint for the stall limit was active for all optimizations and the constraint for the tangential velocity limit was active for small hub radii as indicated by arrows in the figure.

In accordance with the introductory remarks of Section 3, the optimizations with the larger downstream loss ($\eta_D = 0.90$) has a rapid decrease in optimum efficiency with increasing hub radius, whereas the case with a smaller downstream loss has a slower decrease. Also, the optimum hub radius marked with solid symbols, is larger for the case with the smaller downstream loss.

For small hub radii it becomes difficult to obtain the required pressure rise, thus limiting the geometry of the blades. This in turn results in a decreased efficiency, even though the downstream losses become smaller. For smaller hub radii than the ones shown in Fig. 6, it was not possible to obtain a solution to the optimization problem.

If the hub radius is determined from factors other than maximum efficiency, e.g., size of electrical motor or the use of standard hub designs, Fig. 6 may be used to investigate the consequences of the performance of the fan on changing the hub radius. As an example, it is seen that for the case of $\eta_D = 0.95$, the hub radius can be increased with approximately 25 mm from the optimum value with a decrease in efficiency of about two points. For the case of $\eta_D = 0.90$, the same efficiency decrease occurs for an increase in hub radius of about 22 mm.

4 Conclusion

An arbitrary vortex flow model for rotor-only axial fans has been combined successfully with a standard method for numerical design optimization of constrained nonlinear problems.

Optimizations were carried out to maximize the efficiency in a flow rate interval. The pressure rise was constrained to be above a required value at the high flow rate. Furthermore, the angle of attack was constrained to stay below stall at the low flow rate. To avoid vortex breakdown, a constraint was introduced, limiting the ratio of tangential to axial velocity in the outlet.

The dependence of optimum efficiency on the design interval width was investigated. For small design intervals, the efficiency is only weakly dependent on the design interval. Thus, fans that operate well for a range of flow rates may be designed using the present numerical optimization method, with only a limited penalty on efficiency.

The optimum efficiency was found to be dependent on hub radius. For very low hub radii, it is difficult to satisfy the imposed constraints and for large hub radii, losses due to tip clearance and due to the downstream diffuser becomes large. From this investigation, the implications of prescribing a certain hub radius can be estimated.

Finally, it must be emphasized that the objective function, design variables and constraints investigated in the present work are merely examples. The design method is quite general and can easily be extended to include other constraints and other design variables, or even a change of objective function.

Acknowledgments

The work was partly supported by the Danish Energy Agency under contract no. 1253/96-0002.

Nomenclature

a, b = secondary drag coefficients
B = number of blades
c = chord length
F = objective function (figure of merit)
g_j = constraint no. j
NCON = no. of constraints
NDV = no. of design variables
N_d = no. of design interval divisions
p_T = integrated rotor pressure rise
Δp_D = downstream diffuser loss
P = mechanical shaft power
Q = flow rate
Q_c = flow rate at center of design interval
ΔQ = width of design interval
r_h, r_t = rotor hub and tip radii
s = interblade spacing, $s=2\pi r/B$
t = tip clearance height
α = angle of attack
α_{stall} = angle of attack at stall
$\Delta\alpha_{\text{stall}}$ = minimum of all $\alpha_{\text{stall}}-\alpha$ values
η = fan efficiency, $\eta=Q\cdot p_T/P$
$\overline{\eta}$ = mean value of fan efficiency in design interval
$\overline{\eta}_{\max}$ = optimum fan efficiency
η_D = downstream diffuser efficiency
Ω = angular velocity of rotor
Φ_n = design variable no. n
σ = solidity, $\sigma=c/s$
θ = camber angle
ξ = stagger angle

References

[1] Wright, T., 1996, ''Low Pressure Axial Fans,'' *Handbook of Fluid Dynamics and Fluid Machinery. - 3: Applications of Fluid Dynamics*, J. A. Schetz and A. E. Fuhs, eds., Wiley, Chichester, pp. 2340–2356.
[2] Wallis, R. A., 1961, *Axial Flow Fans. Design and Practice*, George Newnes Limited, London.
[3] Wallis, R. A., 1968, ''Optimisation of Axial Flow Fan Design,'' *Mechanical and Chemical Engineering Transactions, The Institution of Engineers, Australia*, **MC4**, No. 1, pp. 31–37.
[4] Dugao, Z., Jiang, Z., and Song, J., 1996, ''Optimization Design of an Axial Flow-Fan Used for Mining Local-Ventilation,'' Comput. Ind. Eng., **31**, No. 3, pp. 691–696.
[5] Bolton, A. N., 1990, ''Installation Effects in Fan Systems,'' *Proceedings of the Institution of Mechanical Engineers, Part A 204*, pp. 201–215.
[6] Sørensen, D. N., and Sørensen, J. N., 2000, ''Toward Improved Rotor-Only Axial Fans—Part I: A Numerically Efficient Aerodynamic Model for Arbitrary Vortex Flow,'' ASME J. Fluids Eng., **122**, No. 2, pp. 318–323.
[7] Kahane, A., 1948, ''Investigation of Axial-Flow Fan and Compressor Rotors Designed for Three-Dimensional Flow,'' Tech. Note 1652, NACA, Langley Memorial Aeronautical Laboratory, Langley Field, Va.
[8] Press, W. H., Teukolsky, S. A., Vetterling, W. T., and Flannery, B. P., 1992, *Numerical Recipes in FORTRAN: The Art of Scientific Computing*, 2nd ed., Cambridge University Press, p. 128.
[9] Emery, J. C., Herrig, L. J., Erwin, J. R., and Felix, A. R., 1958, ''Systematic Two-Dimensional Cascade Tests of NACA 65-Series Compressor Blades at Low Speeds,'' Report TR-1368, NACA, Langley Aeronautical Laboratory, Langley Field, Va.
[10] Squire, H. B., 1960, ''Analysis of the vortex breakdown phenomenon. Part I,'' Report 102, Imperial College of Science and Technology, Aeronautics Department.
[11] Sharland, I. J., 1964, ''Sources of Noise in Axial Flow Fans,'' J. Sound Vib., **1**, No. 3, pp. 302–322.
[12] Han, S. P., 1976, ''Superlinearly Convergent Variable Metric Algorithms for General Nonlinear Programming Problems,'' Math. Program., **11**, pp. 263–282.
[13] Powell, M. J. D., 1978, ''A Fast Algorithm for Nonlinearly Constrained Optimization Calculations,'' *Lecture Notes in Mathematics*, G. A. Watson, ed., Vol. 630, pp. 144–157.

Investigating Three-Dimensional and Rotational Effects on Wind Turbine Blades by Means of a Quasi-3D Navier-Stokes Solver

P. K. Chaviaropoulos
Dr., Head of the Research and Development Department,
CRES-Center for Renewable Energy Sources,
19th km Marathonos Ave.,
190 09 Pikermi Attiki, Greece

M. O. L. Hansen
Dr. Assistant Professor,
Department of Energy Engineering,
Fluid Mechanics Section,
Technical University of Denmark, bldg. 404,
DK-2800 Lyngby, Denmark

Three-dimensional and rotational viscous effects on wind turbine blades are investigated by means of a quasi-3D Navier-Stokes model. The governing equations of the model are derived from the 3-D primitive variable Navier-Stokes equations written in cylindrical coordinates in the rotating frame of reference. The latter are integrated along the radial direction and certain assumptions are made for the mean values of the radial derivatives. The validity of these assumptions is cross-checked through fully 3-D Navier-Stokes calculations. The resulting quasi-3D model suggests that three-dimensional and rotational effects be strongly related to the local chord by radii ratio and the twist angle. The equations of the model are numerically integrated by means of a pressure correction algorithm. Both laminar and turbulent flow simulations are performed. The former is used for identifying the physical mechanism associated with the 3-D and rotational effects, while the latter for establishing semiempirical correction laws for the load coefficients, based on 2-D airfoil data. Comparing calculated and measured power curves of a stall controlled wind turbine, it is shown that the suggested correction laws may improve significantly the accuracy of the predictions. [S0098-2202(00)02702-4]

Introduction

The state of the art aeroelastic codes used today for simulating horizontal axis wind turbines still rely on simple aerodynamic models based on the ''blade element momentum theory'' (BEM). It is recognized that the overall problem, including deformations of the elastic structure, stochastic inflow conditions, complicated geometry (as far as the nacelle and the tower are present) and massively separated flow in stall controlled machines, is highly complex and stiff. This prohibits the use of more elaborate flow solvers (Navier-Stokes solvers, for instance) which are systematically used today in other aerodynamic applications. Although quite simple, the BEM method yields surprisingly accurate predictions of the aerodynamic loads provided that ''proper'' lift and drag-incidence curves are used for the airfoils mounted on the rotor blade. The evident question is how these proper data are obtained. It is common experience that the use of the mostly available steady two-dimensional airfoil data may lead to serious discrepancies between measured and simulated power production and loads; especially for stall regulated wind turbines. The two main reasons responsible for this are (i) the inability of the steady airfoil data to respond to fast inflow transients (e.g., dynamic stall effects) and (ii) the absence of any correction with respect to the three-dimensionality of the flow due to the blade geometry and rotation. The systematic under-prediction of the blade loads in stalled conditions, when pure 2-D airfoil data are used, is mainly attributed to that second reason. Therefore, there is a strong need for expressing appropriate correction laws for airfoil data that would improve the reliability of the aeroelastic simulations.

Himmelskamp [1], who was the first to address the three-dimensional effects of rotation, found lift coefficients as high as 3 near the hub of a fan blade. Recent experiments carried out for wind turbine blades by Ronsten [2] and Bruining et al. [3] confirmed that the effective lift-coefficient was higher than expected, especially at the inboard sections of the blade. Numerical investigation of the three-dimensional and rotational effects on wind turbine blades is, today, limited to quasi-3D approaches, since fully 3D Navier-Stokes computations have just started to appear in the literature (see Hansen et al. [4] for instance). Such a quasi-3D approach, based on the viscous-inviscid interaction method, was introduced by Snel et al. [5,6]. Based on systematic use of their model, Snel et al. proposed a semi-empirical law for the correction of the 2-D lift curve, identifying the local chord to radii (c/r) ratio of the blade section as the main parameter of influence. This result has later been confirmed by Soerensen and Soerensen [7] and Shen and Soerensen [8], who performed airfoil computations applying a quasi-3D Navier-Stokes model, based on the streamfunction-vorticity formulation.

A quasi-3D model based on the primitive variables form of the incompressible Navier-Stokes equations is presented in this paper and applied for both laminar and turbulent flows. The incompressibility assumption is suitable for wind engineering applications where the Mach number is limited to a maximum of approximately 0.2. The model equations resemble the 2-D Navier-Stokes system except from an additional transport-diffusion equation for the radial momentum component and two source terms appearing into the continuity and the axial momentum equations. All the source terms are weighted with the c/r ratio indicating that the three-dimensional effects are stronger at the inner part of the blade where c/r becomes relatively large. In addition to the local chord to radii parameter the present model introduces a second parameter of importance, the local twist angle of the blade section. The resulting equations are numerically integrated by means of an unsteady incompressible Navier-Stokes solver of the ''pressure correction'' kind. The standard k-ω model of Wilcox [9], supported by wall-function-type boundary conditions, is used for turbulence closure.

The development of the quasi-3D model is discussed in the first part of the paper. A limited number of laminar flow simulations are discussed in the Results section, where particular emphasis is given in understanding the underlying physical mechanism which triggers the 3-D and the rotational effects. Semi-empirical correc-

Contributed by the Fluids Engineering Division for publication in the JOURNAL OF FLUIDS ENGINEERING. Manuscript received by the Fluids Engineering Division October 3, 1997; revised manuscript received February 22, 2000. Associate Technical Editor: C. H. Merkle.

tion laws based on systematic turbulent flow computations for the NACA 63-2-15 airfoil are proposed for the lift drag and pitching moment coefficients and to validate these corrections an example of a BEM power curve computation is finally shown.

The Quasi-3D Model

A simplified quasi-3D model has been devised in order to identify the influence of the three-dimensional and rotational effects on the blade section characteristics. The governing equations are derived using the following steps:

Step 1: The incompressible Navier-Stokes equations are written in conservative form in the cylindrical coordinate system, (Θ, z, r) (see Bird et al. [10]) which rotates with the blade with a constant rotational speed Ω (see Vavra [11]). Θ denotes the peripheral, z the axial and r the radial (blade spanwise) direction. The infinitesimal length in the peripheral direction is $ds=rd\Theta$. For simplicity the equations are presented here in their laminar form:

Continuity

$$\frac{\partial W_\Theta}{\partial \Theta}+\frac{\partial (rW_z)}{\partial z}+\frac{\partial}{\partial r}(rW_r)=0 \tag{1}$$

Momentum, Θ-Component

$$\frac{\partial W_\Theta}{\partial t}+\frac{\partial}{\partial \Theta}\left\{\frac{W_\Theta^2}{r}+\frac{\Phi}{r}-\nu\frac{\partial}{\partial \Theta}\left(\frac{W_\Theta}{r^2}\right)\right\}+\frac{\partial}{\partial z}\left\{W_zW_\Theta-\nu\frac{\partial W_\Theta}{\partial z}\right\}+\frac{\partial}{\partial r}\left\{W_rW_\Theta-\nu\left(\frac{1}{r}\frac{\partial (rW_\Theta)}{\partial r}\right)\right\}=\nu\frac{2}{r}\frac{\partial}{\partial \Theta}\left(\frac{W_r}{r}\right)-2W_r\left(\frac{W_\Theta}{r}+\Omega\right) \tag{2}$$

Momentum, z-Component

$$\frac{\partial W_z}{\partial t}+\frac{\partial}{\partial \Theta}\left\{\frac{W_\Theta}{r}W_z-\nu\frac{\partial}{\partial \Theta}\left(\frac{W_z}{r^2}\right)\right\}+\frac{\partial}{\partial z}\left\{W_z^2+\Theta-\nu\frac{\partial W_z}{\partial z}\right\}+\frac{\partial}{\partial r}\left\{W_rW_z-\nu\left(\frac{\partial W_z}{\partial r}\right)\right\}=\nu\frac{1}{r}\frac{\partial}{\partial r}\left(\frac{W_z}{r}\right) \tag{3}$$

Momentum, r-Component

$$\frac{\partial W_r}{\partial t}+\frac{\partial}{\partial \Theta}\left\{\frac{W_\Theta}{r}W_r-\nu\frac{\partial}{\partial \Theta}\left(\frac{W_r}{r^2}\right)\right\}+\frac{\partial}{\partial z}\left\{W_zW_r-\nu\frac{\partial W_r}{\partial z}\right\}+\frac{\partial}{\partial r}\left\{W_r^2+\frac{p}{\rho}-\nu\frac{1}{r}\frac{\partial (rW_r)}{\partial r}\right\}=-\nu\frac{2}{r^2}\frac{\partial W_\Theta}{\partial \Theta}-\frac{W_r^2}{r}+\frac{1}{r}(W_\Theta+\Omega r)^2 \tag{4}$$

$\mathbf{W}$ stands for the relative velocity vector, ρ for the fluid density, p is the static pressure, and ν the kinematic viscosity. It is recalled that $\mathbf{W}=\mathbf{V}-\mathbf{\Omega xr}$, where $\mathbf{V}$ is the velocity vector in the absolute frame. Φ is a pressure like term including the centrifugal effect

$$\Phi=\frac{p}{\rho}-\frac{1}{2}(\Omega r)^2 \tag{5}$$

Step 2: The equations are integrated along the radial direction and ''mean radial values,'' denoted with an overbar, are obtained. The mean value operator reads:

$$\overline{()}=\frac{1}{\Delta r}\int_r^{r+\Delta r}()\,dr \tag{6}$$

As a consequence,

$$\overline{\left(\frac{\partial ()}{\partial t}\right)}=\frac{\partial \overline{()}}{\partial t},\quad \overline{\left(\frac{\partial ()}{\partial \Theta}\right)}=\frac{\partial \overline{()}}{\partial \Theta},\quad \overline{\left(\frac{\partial ()}{\partial z}\right)}=\frac{\partial \overline{()}}{\partial z} \tag{7}$$

Step 3: The resulting system of equations is subjected to the following assumptions:

$$\overline{\left(\frac{\partial (W_\Theta/r)}{\partial r}\right)}=\overline{\left(\frac{\partial W_z}{\partial r}\right)}=\overline{\left(\frac{\partial W_r}{\partial r}\right)}=0,$$

$$\overline{\left(\frac{\partial^2 (W_\Theta/r)}{\partial r^2}\right)}=\overline{\left(\frac{\partial^2 W_z}{\partial r^2}\right)}=\overline{\left(\frac{\partial^2 W_r}{\partial r^2}\right)}=0,$$

$$\overline{\left(\frac{\partial (p_t/\rho)}{\partial r}\right)}=q\Rightarrow\overline{\left(\frac{\partial (p/\rho)}{\partial r}\right)}=q-\frac{1}{\bar r}(\overline{W_\Theta}+\Omega\bar r)^2,$$

$$\overline{ab}\approx\overline{a}\,\overline{b} \tag{8}$$

In other words, it is thus assumed that (i) the mean value of the radial derivatives (first and second) of the contravariant relative velocity components are small and can be neglected, (ii) the radial derivative of the total pressure (related to the specific work) is a section-depending constant, called q, and (iii) mean values of products can be approximated with products of mean values. Far from the airfoil the velocities are $W_\Theta=-\Omega r$, $W_z=$ constant and $W_r=0$, which directly satisfy the above quasi-3D assumptions. The validity of these assumptions in the viscous boundary layer close to the airfoil is discussed in the next section.

Step 4: The outcome of the analysis is the following set of equations including the modified continuity equation (9) and Eq. (10)–(12) accounting for the momentum balance in the (Θ, z, r) directions, respectively.

$$\nabla_{2D}\cdot\mathbf{W}_{2D}+\frac{\overline{W_r}}{\bar r}=0 \tag{9}$$

$$N_{2D}(\overline{W_\Theta})+\frac{\partial \overline{\Phi}}{\partial s}=-2\overline{W_r}\left(\frac{\overline{W_\Theta}}{\bar r}+\Omega\right)+\frac{2}{\mathrm{Re}\,\bar r}\frac{\partial \overline{W_r}}{\partial s} \tag{10}$$

$$N_{2D}(\overline{W_z})+\frac{\partial \overline{\Phi}}{\partial z}=0 \tag{11}$$

$$N_{2D}(\overline{W_r})=-q+\frac{2}{\bar r}(\overline{W_\Theta}+\Omega\bar r)^2-\frac{1}{\mathrm{Re}}\left[\frac{2}{\bar r}\frac{\partial \overline{W_\Theta}}{\partial s}+\frac{1}{\bar r^2}\overline{W_r}\right] \tag{12}$$

In the above system of equations subscript 2D denotes ''equivalent'' two-dimensional properties on the (Θ, z) plane and N stands for the Navier-Stokes scalar operator.

$$\mathbf{W}_{2D}\equiv[\overline{W_\Theta},\overline{W_z}],\quad \nabla_{2D}\equiv\left[\frac{1}{\bar r}\frac{\partial}{\partial \Theta},\frac{\partial}{\partial z}\right]\equiv\left[\frac{\partial}{\partial s},\frac{\partial}{\partial z}\right],$$

$$\overline{\Phi}=\frac{\overline{p}}{\rho}-\frac{1}{2}(\Omega\bar r)^2$$

$$N_{2D}=\frac{\partial}{\partial t}+\mathbf{W}_{2D}\cdot\nabla_{2D}-\frac{1}{\mathrm{Re}}\nabla_{2D}^2 \tag{13}$$

The presented set is nondimensional. Dimensionless variables are introduced as follows:

$$(r,z)\to(r,z)/c\Rightarrow\nabla_{2D}\to\nabla_{2D}\cdot c,\quad t\to t|\mathbf{W}_{2D}|_\infty/c$$

$$W\to|\mathbf{W}_{2D}|_\infty,\quad \Omega\to|\mathbf{W}_{2D}|_\infty/c,\quad \Phi\to\Phi/|\mathbf{W}_{2D}|_\infty^2 \tag{14}$$

where c stands for the chord of the local blade section, Re is the Reynolds number and ∞ denotes far-field conditions.

The initial conditions needed for the solution of the quasi-3D problem are provided under the assumption that the far-field flow is uniform at the absolute frame, having a nonzero axial velocity component ($V_z=W_z$) only. To compare quasi-3D against pure

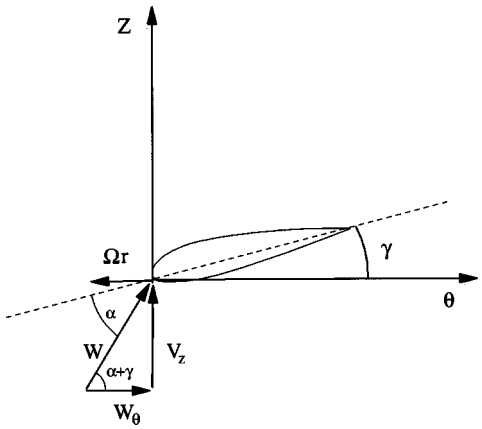

Fig. 1 Velocity triangle at the (z,Θ) plane

2-D results the quasi-3D initial conditions are formulated in the 2-D sense. Considering the flow around a blade section of twist angle γ, see Fig. 1, the following relations provide the far-field velocity conditions and the corresponding rotational speed Ω.

$$W_{\Theta\infty}=\cos(\gamma+\alpha),\quad W_{z\infty}=\sin(\gamma+\alpha),\quad \Omega=-\frac{1}{r}\cos(\alpha+\gamma) \tag{15}$$

Before concluding this section a brief discussion is held on the governing equations and their boundary conditions for better understanding the shortcomings and consequences of the proposed model. The following remarks are therefore made:

(i) Compared to the 2-D problem, the quasi-3D one includes an additional momentum equation, Eq. (12), for the radial velocity component, while two source terms involving this radial component are added into the continuity and the peripheral momentum equations. All the extra terms are weighted with the $1/r$ factor, or the c/r ratio in dimensional quantities. This implies that the quasi-3D effects become stronger as c/r increases (inner part of the blade), which is in full accordance with the experimental observations. The 3-D and rotational effects are strictly due to the Coriolis force and not to the centrifugal force. The effect of the latter is well-hidden in the pressure-like term Φ which replaces the static pressure in the governing equations. Clearly, Eqs. (9)–(12) degenerate to the 2-D Navier-Stokes equations when $c/r\rightarrow 0$ and $q=0$.

(ii) The influence of the twist angle is implicitly taken into account in the above analysis. Actually, γ along with α define the ''equivalent'' rotational speed Ω affecting the strength of the source terms appearing in the peripheral and radial momentum equations.

(iii) The main production term appearing in Eq. (12), i.e., the first R.H.S. term, is always positive leading to the generation of a radial velocity field of positive sign (hub to tip). The production is larger as c/r increases and W_Θ decreases. W_Θ takes small values within the wall shear layer, the thickness of which depends on the Reynolds number. Thus, a Reynolds number effect should be expected. When the flow is detached, radial velocity is generated in the separation bubble. The above remarks imply that even for large c/r ratios the solutions of the 2-D and the quasi-3D problem are rather identical at low angles of attack and high Reynolds numbers, where the flow remains fully attached and the boundary layer is thin, while larger differences, depending on the extent of the separation bubble, should be expected for detached flows.

(iv) The resulting quasi-3D model depends strongly on the assumptions made. It is perfectly understood that the fully 3-D flow around a rotating blade does not satisfy strictly any of the above assumptions in the vicinity of the blade as also shown with the full 3-D computation described below. It is also understood that the proposed simplification set is by no means unique. Regarding the approximations of the radial derivatives of the velocity vector, these apply on the contravariant components instead of the cylindrical components themselves, in an attempt to satisfy the far-field conditions at least. Regarding the pressure field, it is preferred to model the total pressure instead of the static pressure radial derivative since it is expected, by intuition, that the work distribution along the blade span should affect the 3-D character of the flow. In all applications that follow the ''work distribution'' parameter q is supposed to be zero. Positive q values are expected to reduce the 3-D and rotational effects.

The extension of the model for turbulent flow is straightforward. The main difference compared to the equations already presented is the introduction of the eddy viscosity in the diffusion term of the ''2-D'' Navier-Stokes operator N.

Validation of the Quasi-3D Assumptions

To investigate whether the quasi-3D assumptions are approximately valid in the viscous boundary layer close to the airfoil a full 3-D computation is performed on a single rotating blade enclosed in a tube between two cylinders as described in (Hansen et al. [12]). The blade is non-tapered, non-twisted and based on the NACA63-415 airfoil. The pitch setting is 0 degrees. The inner and outer radial boundaries are 1 and 20 chords from the rotational axis, respectively. Only the blade mid-section is investigated, i.e., 10 chords from the cylindrical boundaries. The inflow velocity V_z and the rotational speed Ω is specified to give a geometrical angle of attack of 15 degrees and a Reynolds number of 1.55×10^6 at the mid-span. The k-ω, SST turbulence model, see Menter [13], is used and the flow is assumed turbulent from the leading edge. At mid span the computation show a trailing edge separation starting at approximately 50 percent chord. In the separation bubble the radial velocity becomes quite high with a maximum value of 0.8 times the local rotational speed, Ωr, of the blade.

The present investigation is limited to the assumptions made for the first radial derivatives of the velocity components (first line of Eq. (8)). Due to quite high angles of attack in the inboard part of the blade the solution never becomes stationary, but at a certain time two residuals are computed denoted RES1 and RES2. RES1 is the residual for the continuity equation (1) and RES2 denotes the residual for the modified continuity equation (9), where the quasi-3D assumptions have been applied. Within a circle of a radius of 1 chord around the mid-section airfoil the maximum value of RES1 is 164 times bigger than the maximum absolute difference between RES1 and RES2 verifying the quasi-3D assumption for the radial derivative of the radial velocity component. To investigate the validity of the assumption on $\partial W_z/\partial r$ the following ratio, R_1, is calculated in all computational cells within the boundary layer, the denominator expressing some norm of the local W_z gradient.

$$R_1=\frac{|\partial W_z/\partial r|}{|\partial(W_z/r)/\partial\Theta|+|\partial W_z/\partial z|+|\partial W_z/\partial r|} \tag{16}$$

In a similar way the following ratio, R_2, is used regarding $\partial(W_\Theta/r)/\partial r$

$$R_2=\frac{|\partial(W_\Theta/r)/\partial r|}{|\partial(W_\Theta/r)/\partial r|+|\partial(W_\Theta/r)/\partial z|+|\partial(W_\Theta/r^2)/\partial\Theta|} \tag{17}$$

At mid-span the average values of R_1 and R_2 in the vicinity of the blade, i.e., in the viscous region, are 2.18×10^{-2} and 1.87×10^{-2}, respectively, suggesting that the quasi-3D assumptions are well satisfied in this case.

Brief Description of the Unsteady Quasi-3D Navier-Stokes Solver

The equations of the quasi-3D model (9)–(12) are numerically integrated by means of an unsteady, implicit, matrix-free, pressure correction algorithm. The matrix free pressure correction solver employs a conjugate gradient scheme, which is suitable for problems with nonsymmetric characteristic matrix. Spatial discretization is performed on C-type structured body fitted meshes employing second order accurate numerical schemes. For turbulent flow computation the standard k-ω (Wilcox [9]) is employed. The model is equipped with wall function-type boundary conditions for coarse grid computations. Transition may be either fixed or free. Details on the basic 2-D code can be found in Chaviaropoulos [14].

Results and Discussion

Having performed one full 3-D Navier-Stokes computation, which indicated that the quasi 3-D assumptions seem reasonable, numerical results are now presented for laminar as well as turbulent flows using the quasi 3-D method. The boundary conditions employed in both cases are of the isolated airfoil type (undisturbed flow conditions at the far-field boundary, periodicity effects on the blade-to-blade surface are not taken into account). The laminar flow results are mainly explored to identify the triggering mechanism of the 3-D and rotational effects. The turbulent flow results are used for expressing correction laws for the lift, drag and pitching moment coefficients of the NACA 63-2-15 airfoil. It is noted that the NACA 63-2-XX family is one of the favorites of the wind turbine blade manufacturers. Finally, a BEM computation is shown, where the empirical corrections have been used to correct pure 2-D airfoil data and it is seen that this improves the results considerably, especially at the high wind speed regime, where the blades are stalled.

Quasi-3D Computations for Laminar Flows

Quasi-3D results are presented for the NACA 0015 airfoil at a Reynolds number of 400 and at an angle of attack of 15 degrees. The choice of a rather low Reynolds number was intentional for producing a ''stable'' separation bubble to facilitate the investigation. Several parametric runs have been performed in terms of the c/r ratio [0, 0.1, 0.2, 0.3] and the twist angle [0, 10, 20 degrees]. A C-type 197×41 grid with 150 nodes on the airfoil has been used in all cases. The mean distance of the first grid-line from the airfoil is $5\times10^{-4}c$. With the exception of the $c/r=0$ case, which presented a little unsteadiness, all calculations resulted in a steady, converged, solution where the L2 residual norms of all equations dropped at least five orders of magnitude from the free-stream initialization. The calculated lift *Cl* and drag *Cd* coefficients (mean values in time, when needed) increase with c/r and decrease with the twist angle faster than linearly. For the $c/r=0.3$ and twist=0 degrees case the lift coefficient is nearly doubled compared to pure 2-D results ($c/r=0$).

The increase of lift and drag is better understood considering Fig. 2 where the pressure coefficient *Cp* and the skin friction *Cf* are plotted against x/c for the zero twist angle runs. It is seen that although the flow remains massively separated in all cases (actually the separation point location is not really affected by c/r) the suction side distribution of the pressure coefficient moves rapidly towards lower levels as c/r increases. The lift coefficient and the pressure drag, contributing to the total drag, are therefore increased. The significant drop of the pressure coefficient along the suction side can be interpreted as follows. Consider the contour plot detail of the W_{2D} magnitude (the in-plane component) shown in Figs. 3(a) and 3(b) corresponding to the $c/r=0$ and $c/r=0.3$ cases. It is evident that the volume of the separation bubble corresponding to $c/r=0.3$ is much reduced compared to the 2-D ($c/r=0$) result. At the same time a strong radial velocity component is developing within the separation bubble when the 3-D

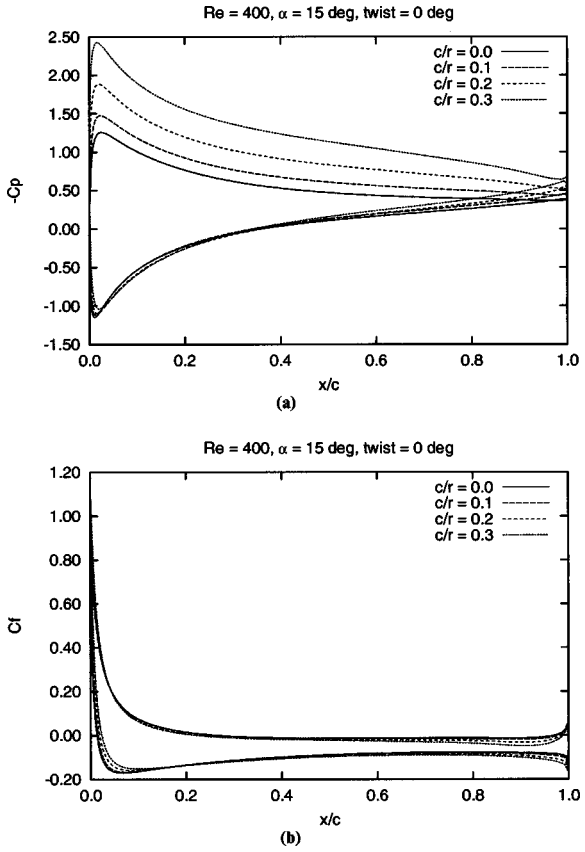

Fig. 2 Influence of the c/r ratio on (a) the pressure and (b) the skin friction coefficient of the NACA 0015 airfoil in laminar flow. Re=400, α=15 degrees, twist=0 degrees.

effect is present, see Fig. 4 for the contour plots of W_r. As already discussed earlier, the development of this strong radial velocity field is due to the production term of the radial momentum equation and this term becomes significant in the presence of a separation bubble. The continuity and the axial momentum bal-

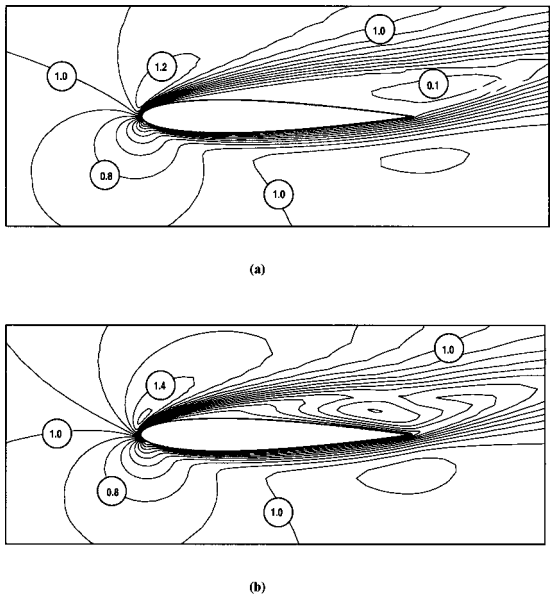

Fig. 3 Laminar flow around NACA 0015, Re=400, α=15 degrees, twist=0 degrees. Contour plots of the in-plane (W_{2D}) velocity magnitude, (a) 2-D flow, (b) c/r=0.3. Contour step =0.1.

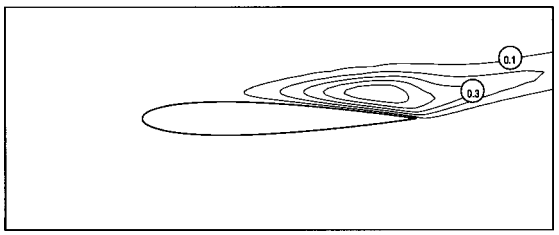

Fig. 4 Laminar flow around NACA 0015, Re=400, α=15 degrees, twist=0 degrees. Contour plot of the radial velocity component W_r. Contour step=0.1.

ance imply that mass is sucked out of the (Θ, z) plane to compensate for the developing radial component. Thus, the separation bubble is reduced, the flow is compressed along the suction side of the airfoil and the pressure level drops proportionally there.

Quasi-3D Computations for Turbulent Flows

Turbulent flow results are presented for the NACA 63-2-15 airfoil at Reynolds number 2 million, a rather characteristic number for a wind turbine blade section. All calculations have been performed using the k-ω model with wall functions, assuming fully turbulent flow conditions. A series of parametric runs has been performed in terms of the c/r ratio and the twist angle as presented in Table 1. It is seen that two sets of angles of attack have been used, called SET1 and SET2. SET1 is wider, including angles of attack from 5 to 29 degrees with steps of 1 degree, while SET2 includes selective values focusing on the stall–post-stall regime. A C-type 197×45 grid with 145 nodes on the airfoil has been used in all cases. The mean distance of the first grid-line from the airfoil is $2\times10^{-4}c$. For the $c/r=0$ case steady results, corresponding to converged solutions, have been obtained for angles of attack lower than 13 degrees. Convergence is assumed when the L2 residual norms of all equations are dropped four orders of magnitude starting from the potential flow initialization. A periodic variation of the load coefficients is obtained at higher angles of attack. The load coefficients presented below for those cases represent mean values in time. The amplitude of the periodic oscillations is, however, reduced as c/r increases. This is probably due to the reduction of the separation bubble volume, as explained earlier.

The calculated values of the lift *Cl*, drag *Cd* and pitching moment *Cm* coefficients, corresponding to the $c/r=0$ (viscous 2D) and the $c/r=0.3$ (viscous 3D) cases, are presented versus the angle of attack in Fig. 5 for the 0 degrees twist angle. The corresponding inviscid values are plotted in the same figure. Note that the ''inviscid'' label at the *Cd* plot corresponds to the minimum drag value of the 2-D runs for reasons which will be explained below. It is seen that quasi-3D lift curve lies between the corresponding inviscid and 2-D values while both the drag and pitching moment curves are well above the corresponding 2-D values. As expected, the differences between the 2-D and the quasi-3D curves are more pronounced at higher angles of attack. Looking for a semi-empirical correction law for the load coefficients we adopt the idea of Snel et al. [6] to express the 3-D correction of

Table 1 Parametric quasi-3D runs for the NACA 63-2-15 airfoil

	$c/r=0$	$c/r=0.1$	$c/r=0.2$	$c/r=0.3$
twist=0 deg	SET 1	SET 2	SET 2	SET 1
5 deg				SET 2
10 deg				SET 2
15 deg				SET 2
20 deg				SET 2

Set 1: α [5 To 29 deg, Step 1 deg] Re=2 mil., Fully Turbulent
Set 2: α[12, 15, 20, 25 deg] Re=2 mil., Fully Turbulent

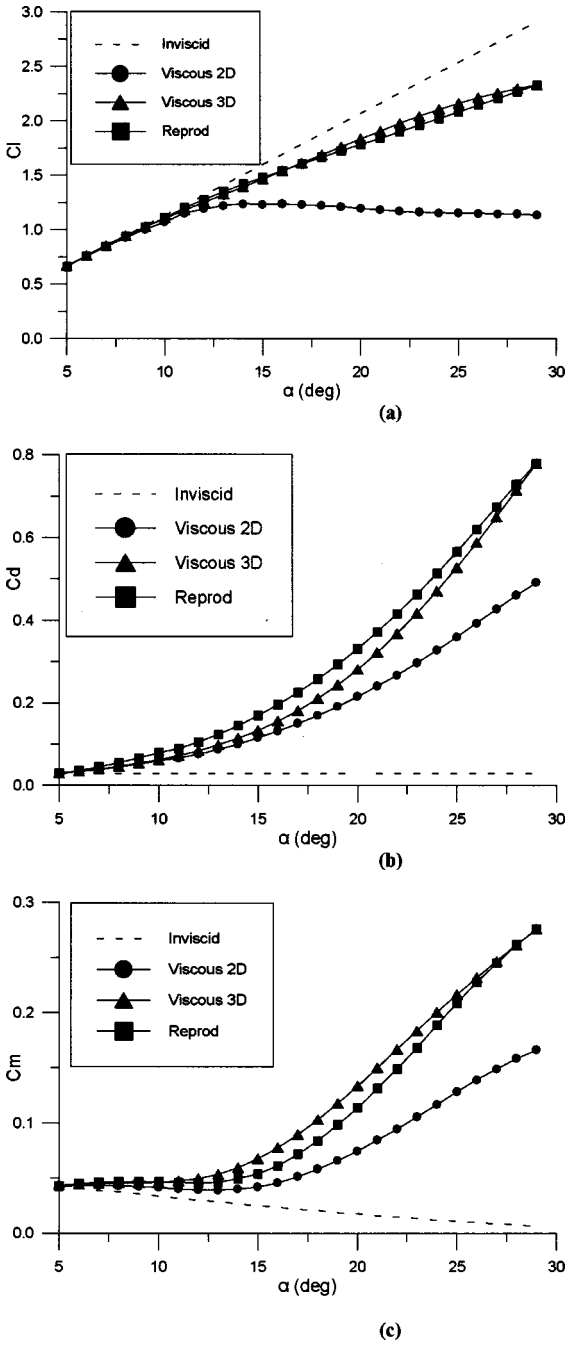

Fig. 5 2-D and quasi-3D load coefficients versus angle of attack, (*a*) *Cl*, (*b*) *Cd*, and (*c*) *Cm*. NACA 63-2-15, Re=2×10^6, fully turbulent flow, twist=0 degrees.

the lift coefficient as a fraction of the difference ΔC_l between the inviscid value $C_{l,\mathrm{INV}}$ and the corresponding 2-D value $C_{l,2\mathrm{D}}$. The obtained results for *Cd* and *Cm* suggest that a similar correction law can be used for the 3-D effect on the drag and pitching moment coefficients as well. In addition, the influence of the twist angle, not present in the analysis of Snel at al., could be introduced through the ΔC_l multiplier. In view of the above the following correction law is proposed:

$$C_{X,3\mathrm{D}}=C_{X,2\mathrm{D}}+a(c/r)^h\cos^n(\mathrm{twist})\Delta C_X;\quad X=l,d,m \qquad (18)$$

where

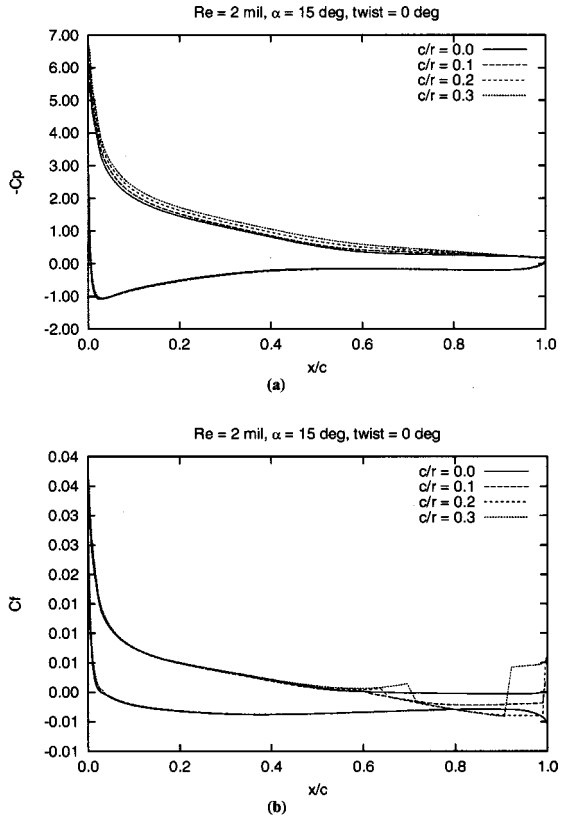

Fig. 6 Influence of the *c*/*r* ratio on (*a*) the pressure and (*b*) the skin friction coefficients. NACA 63-2-15, Re=2 mil, α=15 degrees, fully turbulent flow. Twist=0 degrees.

$$\Delta C_l = C_{l,\mathrm{INV}} - C_{l,\mathrm{2D}}$$
$$\Delta C_d = C_{d,\mathrm{2D}} - C_{d,\mathrm{2D\text{-}MIN}} \qquad (19)$$
$$\Delta C_m = C_{m,\mathrm{2D}} - C_{m,\mathrm{INV}}$$

The three constants of the model a, h, and n are calibrated using a best-fit procedure on the computational data base. This procedure resulted in the following numbers, $a=2.2$, $h=1$, $n=4$. For the NACA 44XX series Snel et al. [6] proposed the values $a=3$ and $h=2$, however as they state in their paper the ΔC_l multiplier is probably airfoil and Reynolds dependent. The lift, drag and pitching moment curves resulting from the above model are also shown in Fig. 5 under the label ''reproduced'' and, in general, compare well with the quasi-3D results.

The physical mechanism producing the airfoil overloading has already been discussed in the laminar results section. To illustrate the statement the calculated pressure and skin friction coefficients for different values of c/r and twist angles are presented versus x/c for 15 degrees angle of attack in Fig. 6. It is seen that no significant variations of *Cf* are encountered in the attached part of the flow while the location of the separation point is practically unaltered. Nevertheless, the pressure coefficient along the suction side of the airfoil drops to lower levels as c/r is increased, increasing the lift and the pressure drag contribution to the total drag.

Finally, to test the correction formulas (18) and (19) a BEM computation is performed on a Bonus 300 Combi stall regulated wind turbine. The rotor is comprised by three LM14.2 blades, the diameter is 31 m the pitch is zero and the rotational speed is 31 rpm. The LM14.2 blade is based on NACA63-4XX and NACA63-2XX airfoils. Measured 2-D lift and drag coefficients for the NACA63-415, NACA63-418, NACA63-421, NACA63-212, NACA63-215 and NACA63-218 airfoils are found in Abbott and Doenhoff [15]. In the absence of measured data beyond 20 degrees angle of attack an extrapolation procedure is employed which is standard in wind engineering practice. It is assumed that all the applied airfoils are equally loaded at high angles of attack and that their load coefficients are those presented in Table 2. The results of the BEM model are presented in Fig. 7, showing the computed power curve with and without corrections. It is seen that the power is underestimated compared to measurements when the uncorrected 2-D airfoil data are used. Using the suggested value $h=1$ helps to increase the power for high wind speeds while using $h=1.3$ excellent results are obtained. It must be emphasized that the BEM results depend on the airfoil data and thus also on the data assumed for the high angle of attack regime. It is very clear, however, that the suggested 3-D corrections improve considerably the results at high wind speeds where the flow is separated. At the low wind speed regime where the flow is attached no corrections are actually needed. The measured power curve is found in Petersen [16].

Table 2 Assumed airfoil data for high angles of attack

α	C_l	C_d
25	0.95	0.35
30	1.00	0.48
40	1.00	0.70
50	0.90	0.90
70	0.50	1.15
90	0.00	1.30

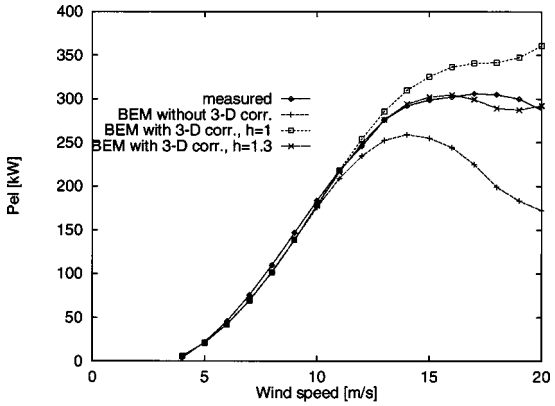

Fig. 7 Measured and computed electrical power for a Bonus 300 Combi wind turbine using ''pure'' 2-D airfoil data and using the same data corrected for 3-D rotational effects, Eqs. (18) and (19)

Conclusions

Navier-Stokes modeling is used to identify and quantify the influence of rotational and three-dimensional effects on the loading of wind turbine blades. A quasi-3D flow model is established and an existing 2-D incompressible Reynolds averaged solver has been suitably enriched with a simplified radial momentum equation and source terms to account for three-dimensional and rotational effects. The equations of the model are derived from the 3-D incompressible Navier-Stokes equations, expressed in the cylindrical coordinate system, taking mean radial values and making consistent assumptions for the mean values of the radial derivatives. The main aim of this effort is to provide insight to the physical mechanisms driving these effects and to express appropriate semi-empirical correction laws for the load coefficients of airfoils mounted on wind turbine blades.

Theoretical considerations and numerical experimentation imply that the two most important parameters that trigger three-

dimensional effects are the chord by radii ratio and the twist angle of the considered blade section. It also appears that these effects do not influence the aerodynamic performance in the attached flow regime significantly, while they play an important role at higher angles of attack where the flow is massively separated. Results presented for both laminar and turbulent flows indicate that when the flow separates the Coriolis force sucks mass from the separation bubble and redirects it to the radial direction, leading to a relative reduction of the volume of the separation bubble. The reduction of the bubble volume produces a pressure drop along the suction side of the airfoils increasing, thus, the blade loading.

Systematic turbulent flow computations have been performed for the NACA 63-2-15 airfoil, at a realistic Reynolds number for wind engineering applications, and semi-empirical correction laws are proposed for its load coefficients. Comparing calculated and measured power curves of a stall controlled wind turbine it is shown that the suggested correction laws may improve significantly the accuracy of the predictions.

Acknowledgments

The authors want to thank the XII Directorate of the European Commission and the Greek Secretariat of Research and Development for co-funding this work under the Joule contract JOR-CT95-0007.

Nomenclature

a, h, n = constants of the quasi-3D correction law
c = airfoil chord
Cl, Cd, Cm = lift, drag, and pitching moment coefficients
Cp, Cf = pressure and skin friction coefficient
N = Navier-Stokes operator
p = pressure
q = work distribution constant
$\mathbf{r}$ = position vector
Re = Reynolds number
s = length in the peripheral direction
t = time
$\mathbf{V}$ = velocity vector, absolute frame
$\mathbf{W}$ = velocity vector, relative frame
x, y = airfoil-fitted coordinates
z, r, Θ = cylindrical coordinates
α = angle of attack
γ = twist angle
ν = kinematic viscosity
ρ = fluid density
Φ = pressure-like term
Ω = rotational speed

Subscripts

2D = two-dimensional properties
3D = three-dimensional properties
INV = inviscid
MIN = minimum value
t = stagnation properties
z, r, Θ = cylindrical components
∞ = far-field properties

Superscripts

$-$ = mean radial value

References

[1] Himmelskamp, H., 1945, ''Profile Investigation on a Rotating Airscrew,'' Technical Report Ph.D. Dissertation, Gottingen, Germany.
[2] Ronsten, G., 1991, ''Static Pressure Measurements on a Rotating and a Non-Rotating 2.375 m Wind Turbine Blade—Comparison with 2-D Calculations,'' Proc. of the EWEC '91 Conference, Amsterdam, pp. 214–220.
[3] Bruining, A., Van Bussel, G. J. W., Corten, G. P., and Timmer, W. A., 1993, ''Pressure Distribution from a Wind Turbine Blade; Field Measurements Compared to 2-Dimensional Wind Tunnel Data,'' Technical report IW-93065R, Delft Univ. of Technology, Institute of Wind Energy.
[4] Hansen, M. O. L., Soerensen, J. N., Michelsen, J. A., and Soerensen, N. N, 1997, ''A Global Navier-Stokes Rotor Prediction Model,'' 35th AIAA Aerospace Sciences Meeting & Exhibit, Reno, AIAA paper 97-0970.
[5] Snel, H., Houwink, R., and Piers, W. J., 1992, ''Sectional Prediction of 3-D Effects for Separated Flow on Rotating Blades,'' Eighteenth European Rotorcraft Forum, Avignon, France,
[6] Snel, H., Houwink, R., Bosschers, J., Piers, W. J., and Bruining, A., 1993, ''Sectional Prediction of 3-D Effects for Stalled Flows on Rotating Blades and Comparison with Measurements,'' Proc. of the ECWEC '93 Conference, Travemunde, Germany, pp. 395–399.
[7] Soerensen, D. N., and Soerensen, J. N., 1995, ''Quasi 3-Dimensional Model for Rotating Airfoil'' 13th AIAA Applied Aerod Conf., San Diego, CA, AIAA 95-1916.
[8] Shen, W. Z., and Soerensen, J. N., 1999, ''Quasi-3D Navier-Stokes Model for Rotating Airfoil,'' J. Comput. Phys., **150**, pp. 518–548.
[9] Wilcox, D. C., 1993, *Turbulence Modelling for CFD*, DCW Industries Inc., La Canada, CA, ISBN 0-9636051-0-0.
[10] Bird, R. B., Steward, W. E., and Lightfoot, E. N., *Transport Phenomena*, Wiley, LCCCN: 60-11717, pp. 82–92.
[11] Vavra, M. H., 1974, *Aero-Thermodynamics and Flow in Turbomachines*, R. E. Krieger Publ. ISBN 0-88275-189-1, pp. 107–132.
[12] Hansen, M. O. L., Soerensen, N. N., Soerensen, J. N., and Michelsen, J. A., 1997, ''Extraction of Lift, Drag and Angle of Attack from Computed 3-D Viscous Flow around a Rotating Blade,'' European Wind Energy Conference, Dublin, pp. 499–502.
[13] Menter, F. R., 1993, ''Zonal Two Equation k-ω Turbulence Models for Aerodynamic Flows,'' AIAA paper 93-2906.
[14] Chaviaropoulos, P., 1994, ''A Matrix-Free Pressure Solver for the Incompressible Navier-Stokes Equations Application to 2-D Flows,'' Proceedings of ECCOMAS Conf., Stuttgart, Germany.
[15] Abbott, I. H., and Doenhoff, A. E., 1959, *Theory of Wing Sections*, Dover Publications,
[16] Petersen, H., 1995, ''Powerkurveanalyser for danske og udenlandske vindmoeller'' (in Danish), Energistyrelsen J. No. 1. 51171/95-0007.

Aerodynamic Torque of a Butterfly Valve—Influence of an Elbow on the Time-Mean and Instantaneous Aerodynamic Torque

F. Danbon
Ph.D Student

C. Solliec
Associate Professor
e-mail: camille.solliec@emn.fr

Ecole des Mines de Nantes,
Département Systèmes,
Energétiques et Environnement,
Division Dynamique,
des Fluides et Procédés,
4, rue A. Kastler,
B. P. 20 722,
F 44 307 Nantes, France

Many technological devices use butterfly valves to control the flow of the process or as safety unit. The principal advantages of this type of valve are their simplicity, their low cost, their speed of closing and the weak pressure drop which they produce when they are completely open. For installations of large size, the actuator of the valve can be very expensive; thus it is essential to know well the fluid forces and the resulting torque exerted on the valve. Consequently, the variation of the shaft torque of the butterfly valves according to the opening is of great interest to calculate the power of the actuator. Initially the flow around the valve is characterized by means of hot wire anemometry. It is noted that the disturbances induced by the elbow and/or the valve are felt until a distance from approximately 8 times the pipe diameter. A method of direct measurement by torquemeter and an indirect method by integration of the pressure forces on the faces of the valve give access to the time-mean and instantaneous torque on the valve shaft. Comparisons between the direct and indirect measurement of the torque are made before engaging the analysis of the results. Close to the full opening, the torque presents fluctuations harmful to suitable lifespan of the valve. Compared to the straight pipe case, the temporal and spectral analyses of the instantaneous torque prove that the elbow induces important fluctuations when the valve is completely open. Several tests carried out according to the valve/elbow spacing show that these effects disappear beyond a distance from 8 to 10 times the diameter of the pipe. [S0098-2202(00)02902-3]

1 Introduction

Butterfly valves are common industrial piping components, which are used for flow control or safety equipment in a variety of processes, (Eom [1], Silvester [2], and Morris et al. [3,4]). A butterfly valve consists of three basic components: the valve seat, the valve disk, and the supporting shaft. Because of its simple mechanical assembly, and the small flow resistance of the disk in the fully open position, butterfly valves provide a relatively high flow capacity. Moreover, they are compact and lightweight, low cost in comparison to the other devices of comparable size, and their simple rotational action means that they are easily combined with actuators. More recently, the fluid torque has received attention for on/off applications in which quick with high security closure is essential. An accurate knowledge of the fluid dynamic forces acting on the valve disk, including the time average and fluctuating aerodynamic torque, is required to design the actuator in this low tolerance application (Fig. 1).

Kurkjian and Pratt [5] indicate that the total shaft torque required to operate butterfly valves can be separated into four major components:

- The seating-friction torque results from the mechanical friction between the disk edge and the waterproof seat.
- The bearing torque results from the load of line pressure acting on the valve disk and transmitted by the valve shaft to the bearings.
- The hydrostatic torque is attributable to the hydrostatic pressure forces in terms of the height of a fluid and induced by the difference in head vertically across a horizontal line. This static torque occurs at intermediate positions of disk only when its axis is horizontal.
- The aero or hydrodynamic torque is the result of forces produced by the fluid.

For economical and convenient reasons, in most cases, the piping systems are very compact. Consequently, the valve is generally placed in critical spots near a bifurcation, an elbow, a tank or a centrifugal pump. As noted by Morris [6], many of these piping geometries have an influence on the operating characteristics, on the pressure drop and especially on the average and fluctuating torque.

The object of this research is to analyze the fluctuations of the

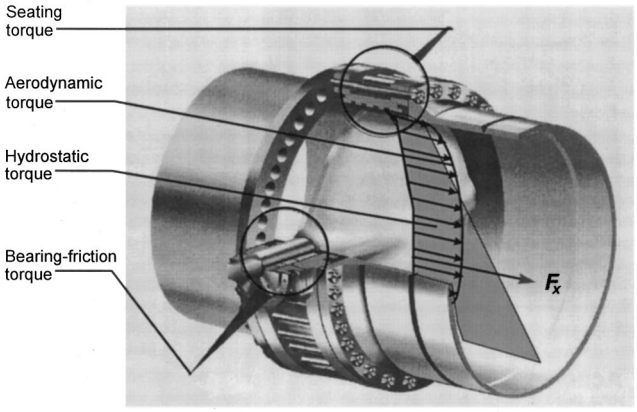

Fig. 1 Forces acting on a butterfly valve

Contributed by the Fluids Engineering Division for publication in the JOURNAL OF FLUIDS ENGINEERING. Manuscript received by the Fluids Engineering Division October 8, 1999; revised manuscript received February 16, 2000. Associate Technical Editor: D. R. Williams.

instantaneous torque according to the valve/elbow spacing, of the aperture of the valve and to make recommendations for the installation of this kind of flow control unit.

2 Experimental Facilities and Methodologies

2.1 Wind Tunnel Facility Description. Several experiments have been conducted to measure the torque characteristics of a three-dimensional butterfly valve, which is a 1/6 model of a commercially available valve. The tests were conducted in a modular air circuit driven by a 10,000 m^3/h centrifugal fan and a variable speed motor. The test pipe is 0.3 m in diameter. At the entry of the circuitry we can place either a straight pipe or a 90 deg elbow at variable distance from the valve.

A schematic view of the experimental facility is depicted in Fig. 2.

The valve disk angle α, can be continually set from the fully open position $\alpha=0$ deg to the closure $\alpha=90$ deg. The flow rate is measured with a Wilson crossflow meter placed at outlet of the fan to free itself from the disturbances induced by the valve or the elbow. The inlet duct Reynolds number, $\mathrm{Re}=V_d D/\nu$, varies through the range $5.0\times10^4<\mathrm{Re}<10^6$.

We have studied the influence of an elbow of curvature radius $R_C=2/3\ D$ located 1 to 8 diameters upstream the valve on the time average and on the fluctuating torque. As in most industrial plants the valve shaft is in the elbow plane.

2.2 Torque Measurement Methods. The shaft of the model is supported by ball bearings. Therefore, as soon as the valve is sufficiently opened, the bearing and seal torques are insignificant in comparison to the aerodynamic torque. As the axis of the valve is vertical, the hydrostatic torque is null. The aerodynamic torque is determined by two distinct methods: either it is measured directly with a torque transducer attached to the valve shaft, or it is calculated by integration of the instantaneous pressure forces acting on the two faces of the disk. The nondimensional torque coefficient $C_T(\alpha,t)$ is that one used by Solliec and Danbon [7]:

$$C_T(\alpha,t)=\frac{T(\alpha,t)}{\frac{1}{2}\rho\cdot V_d^2\cdot D^3} \tag{1}$$

For the statistical analysis of the torque coefficient, we will also use the rms of the torque which is defined in the following:

$$\sigma_c=\sqrt{\overline{(C_T(t)-\overline{C_T})^2}} \tag{2}$$

Direct Measurement. The first method used to measure the torque $T(\alpha,t)$ is based on a strain gauge torquemeter, which has a range from 0 to 12 Nm. The measurement principle is based on the torsion of a cantilever beam attached to the valve shaft at one end and held at the other one by a ball bearing. The socket extensions are instrumented with strain gauges wired into a Wheatstone bridge circuit which gives a voltage output proportional to the aerodynamic torque. The sensitivity of the torquemeter given by manufacturer is 2 mV/V. Thus, for 10 V full-scale output and an operating range supply of 0-12 Nm, the sensitivity is 0.6448 Nm/mV$\pm$0.0017 Nm/mV with 95 percent of confidence. We have checked the manufacturer calibration, by testing the torquemeter in pure torsion on a specific test bench. We find a sensitivity very close to that reported.

The extensometry principle requires that the beam of the torquemeter presents a finished stiffness. Taking into account the flow fluctuations, the low mechanical stiffness of the valve/torquemeter unit involves vibrations of the valve by aeromechanical coupling. Thus, only the time average torque is directly accessible by this method.

The correct measurement of the torque fluctuations with such an apparatus requires knowing the mechanical transfer function of the system and to extract it in the frequential field. The measurement of this transfer function is not easy. For such measurements, it is thus safer to use the indirect method.

Torque Measurements by Integration. The instantaneous parietal pressures forces acting on the valve disk are integrated to calculate the resulting torque $T(\alpha,t)$. The instantaneous pressures are obtained by means of a system of two piezoresistive multichannel transducers (range 2500 and 17,000 Pa, resolution 0.01 percent FS) distributed by the American company Pressure System Incorporated. Both surfaces of the valve are covered by 28 pressure taps.

Each piezoresistive pressure scanner has 32 channels which can be digitally addressed at the maximum rate of 20,000 readings/s with an electronic device. This pilot has been especially developed for synchronous fluctuating pressure measurements by Solliec and Mary [8]. The output voltage of each sensor is transmitted sequentially to the A/D card installed in a PC.

Pressure taps are connected to the scanner with identical vinyl tubes of 0.8 mm in diameter and 0.6 m in length which are brought outside the valve body through its shaft, Fig. 3. Static calibration done for each pressure channel shows that the electrical response of the transducer is proportional to the pressure. On each vinyl tube, a calibrated pneumatic restrictor creates a pressure drop to ensure the good frequency response and the antialiasing filtering of each pressure sensor up to 100 Hz, see also Solliec and Mary [8]. Thus, the maximum frequency response of all the 56 pressure lines is 100 Hz. The time lag between the A/D conversions is lower than 2 ms, the sampling rate is 200

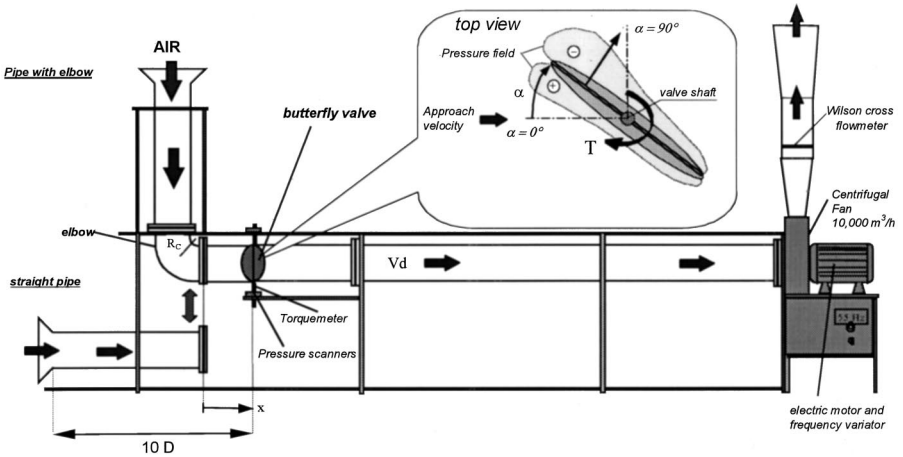

Fig. 2 Schematic view of the test bench and nomenclature

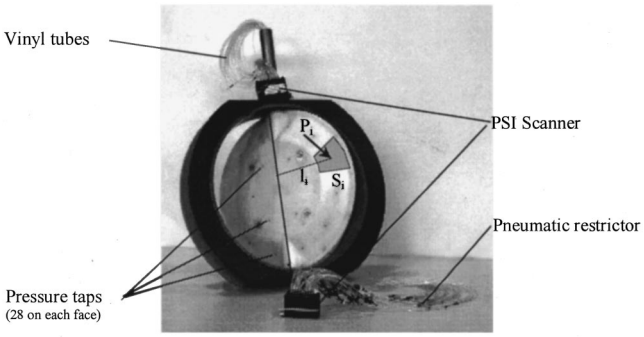

Fig. 3 Photography of the valve model (1/6) with its pressure taps and scanners

readings/s, with a sampling duration of 40 s. Figure 3 shows the valve model equipped with its pressure scanners.

The static pressure taps are distributed from the edges of the disk to the central part, to take into account the pressure distribution from the trailing and the leading edges, Fig. 4. The shape of the valve enabled us to install pressure taps very close to the valve disk edges. This pressure tap distribution is important because the higher pressures are obtained near the edges of the disk and hence strongly influence the torque calculation due to the important lever arm.

The torque $T(t)$ is calculated by finite elementary surface area integration, see Eq. (3) and Fig. 4.

$$T(t)=\sum_{i=1}^{56} P_i(t)\times S_i\times l_i \tag{3}$$

With this method the valve could be steadily locked on the test bench. Consequently, the model cannot rotate and there is no effect of the mechanical vibrations of the valve or of the test bench on the measurements quality. This method is then more suitable than the direct one to study the origin and the magnitude of the aerodynamic buffeting of the valve.

Note that with this indirect method the influences of viscous forces are neglected. Comparisons between the two methods have been done to verify the validity of this measurement method. Results will be presented in a later section.

3 Aerodynamic of the Butterfly Valve

3.1 Introduction. The flow around the three-dimensional butterfly valves has not been studied in depth. Except the numerical simulations carried out by Huang and Kim [9] only few publications cover this subject. Because of the strong three-dimensionality of the flow, the analysis of the flow characteristics are not easy, particularly when the valve is partially open or located in a critical spot.

We present in the following a relatively detailed aerodynamic analysis of the flow characteristics downstream of the valve when it is fully opened and closed with an angle of 30 deg. Several velocity profiles are carried out in two orthogonal median plans, at several coordinates x/D varying from 0 to 11 in presence or in absence of the elbow and with or without the valve. Each radial profile is made up of 27 measuring stations.

These results will be then discussed and compared with those obtained for the fluctuating aerodynamic torque. Taking into account the number of points of measurement necessary to process each configuration, only the critical valve/elbow spacing of one diameter ($x/D=1$) and the two openings, $\alpha=0$ and 30 deg are studied.

Velocity fields are investigated by a hot wire anemometer which is controlled by a Flowlite unit distributed by Dantec Measurement Technology. The sampling time is one minute with an A/D conversion rate of 600 Hz.

3.2 Velocity Fields in Presence of the Valve

Full Opening of the Disk. Before analyzing the flow around the valve and the efforts induced, a first series of measurement was carried out to check the quality of the flow in the test bench. Figure 5 represents the radial velocity profiles and the turbulence intensity at different cross sections in the straight pipe configuration. Measurements are taken without the valve from $x/D=0$ (future location of the elbow exit) to 11. The upstream pipe length starting from the future valve location (i.e., $x/D=1$) is of 11 diameters.

At $x/D=0$, the measured flow is quite similar to a fully developed turbulent flow. The turbulence intensity is relatively constant along the radius and remains lower than 5 percent.

In the case of the straight pipe, Fig. 6, we can observe that the flow downstream of the valve is disturbed little by the valve. The flow detaches very weakly since the wake is hardly thicker than the valve. The flow restored downstream the valve at a distance equal to approximately 4 times the diameter of the pipe.

Figures 7 and 8 represent the velocity and the turbulence intensity profiles in two orthogonal plans between $x/D=0$ up to 11 when a 90 deg elbow is added at $x/D=0$. The elbow induces strong distortions of the velocity and turbulence intensity profiles in both the vertical and horizontal plans. An area of flow detachment is observed in the inside of the elbow, starting from the inner radius. These disturbances are particularly important at the future valve location ($x/D=1$) and are extended until at least 8 to 10 D downstream this section in the two directions y and z. Thus, it is noted that the valve is located in a particularly critical spot with strong three-dimensional flow instabilities.

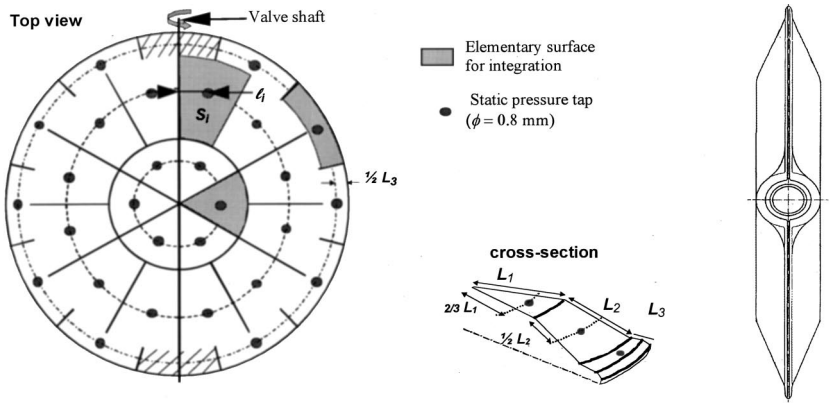

Fig. 4 Pressure taps location and cross section of the valve

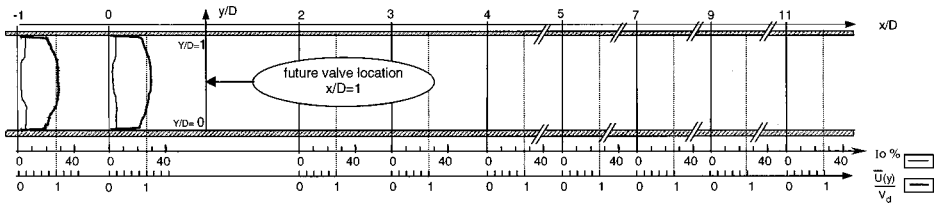

Fig. 5 Velocity and turbulence intensity in the median horizontal plane-straight pipe configuration (V_d=40 m/s, uncertainty in $U=\pm 2$ percent)

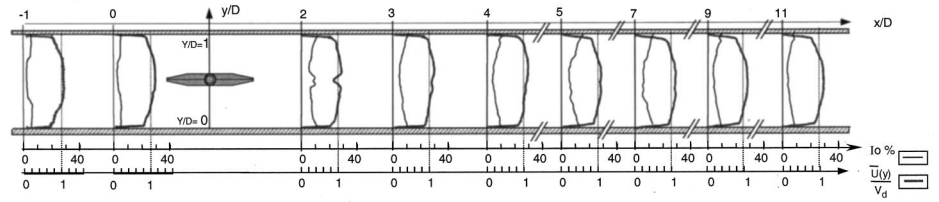

Fig. 6 Velocity and turbulence intensity profiles in the median horizontal plane-straight configuration (V_d=40 m/s, α=0 deg, uncertainty in $U=\pm 2$ percent and in $\alpha=\pm 1$ deg)

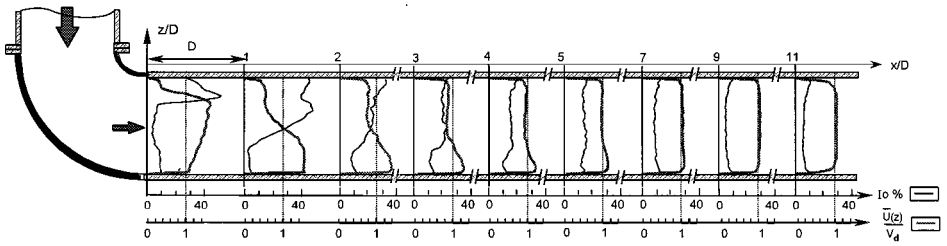

Fig. 7 Velocity and turbulence intensity profiles in the median vertical plane-elbow configuration (V_d=40 m/s, uncertainty in $U=\pm 2$ percent)

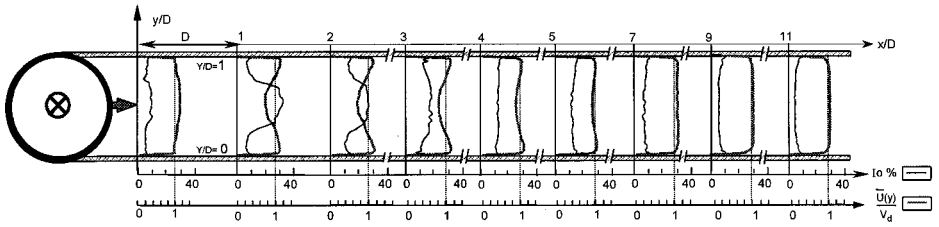

Fig. 8 Velocity and turbulence intensity profiles in the median horizontal plane-elbow configuration (V_d=40 m/s, uncertainty in $U=\pm 2$ percent)

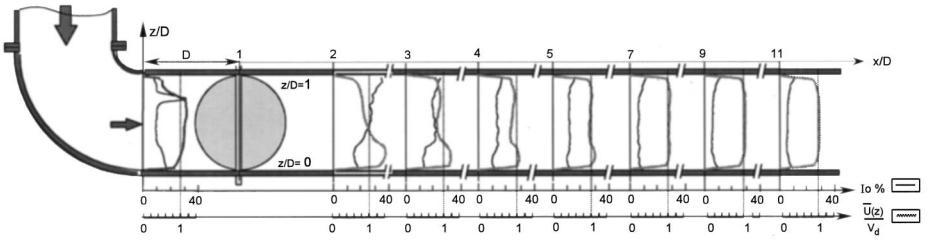

Fig. 9 Velocity and turbulence intensity profiles in the median vertical plane-elbow configuration (V_d=40 m/s, α=0 deg, uncertainty in $U=\pm 2$ percent and in $\alpha=\pm 1$ deg)

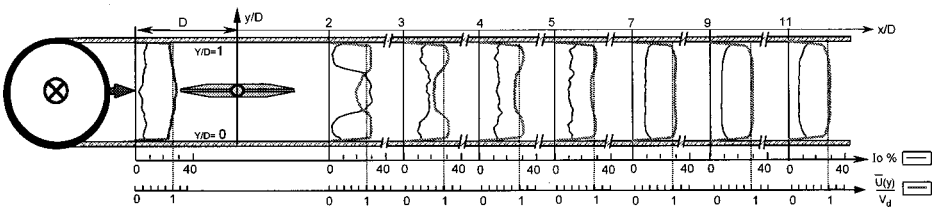

Fig. 10 Velocity and turbulence intensity profiles in the median horizontal plane-elbow configuration (V_d=40 m/s, α=0 deg, uncertainty in $U=\pm 2$ percent and in $\alpha=\pm 1$ deg)

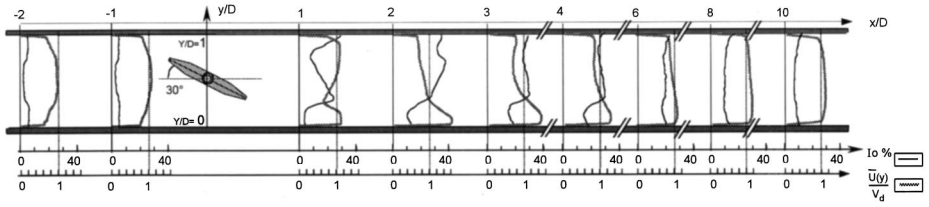

Fig. 11 Velocity and turbulence intensity profiles in the median horizontal plane-straight pipe configuration (V_d=40 m/s, α=30 deg, uncertainty in $U=\pm 2$ percent and in $\alpha=\pm 1$ deg)

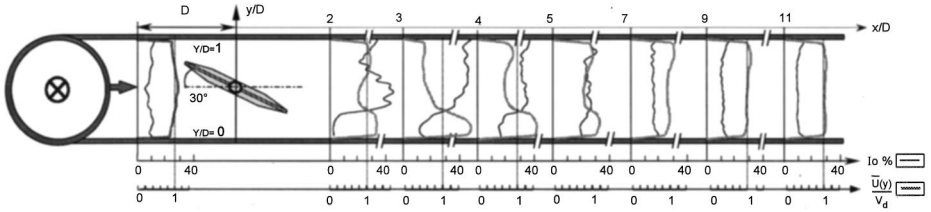

Fig. 12 Velocity and turbulence intensity profiles in the median horizontal plane-elbow configuration (V_d=40 m/s, α=30 deg, uncertainty in $U=\pm 2$ percent and in $\alpha=\pm 1$ deg)

When the valve is installed, comparison of Figs. 7 and 9 shows that the flow in the vertical plan remains very similar to that one without the valve.

In the median horizontal plan, Fig. 10, we do not observe any major disturbance created by the valve. The wake of the valve is completely drowned in the disturbances produced by the elbow.

Velocity field for the valve at 30 deg. When the valve is 30 deg opened, Fig. 11, the flow downstream the valve is extremely complex and strongly three-dimensional. The flow is disturbed up to a distance much more important than for the fully opened position. The length of re-establishment of regular flow is of approximately 10 times the diameter of the pipe. With this opening, the flow is much more disorganized than for the fully opened position of the valve until an important length downstream. The turbulence intensity reaches a maximum of 40 percent in the part of the wake corresponding to the downstream face of the profile. We also observe an important increase of the average velocity in the part of the wake located downstream the trailing edge of the profile.

When the elbow is added, Fig. 12, the downstream flow presents an important radial gradient of velocity and turbulence intensity. There is combination of the effects due to the elbow and those of the valve. However, the flow is also restored at 10 diameters downstream of the valve.

4 Torque of a Butterfly Valve Located in a Straight Pipe Section and Downstream of an Elbow

4.1 Time-Mean Torque. Except for the work of Morris and Dutton [10,11], who conducted an exhaustive experimental investigation on a butterfly valve downstream of a mitered elbow, no extensive study of fluid torque acting on butterfly valves located in an industrial piping system has been done. Like them, we focus our intention on the influence of a 90 deg elbow on the aerodynamic torque. We describe the influence of elbow on the time-mean and also on the instantaneous torque coefficient. In all cases the valve shaft is, as in most industrial plants, in the elbow plan. The valve is set up from one to eight diameters downstream of the elbow exit.

Preliminary tests have shown that the torque coefficient remains constant when the Reynolds number is higher than $6\ 10^5$, see Solliec and Danbon [7]. Thus respecting the similarity, the extrapolation of the results to large diameters, to others fluids or to different velocities is possible.

The time-mean torque $T(\alpha)$, normalized by the peak torque value $T_{\max}=T(30\,\text{deg})$, is plotted on Fig. 13 for the straight pipe

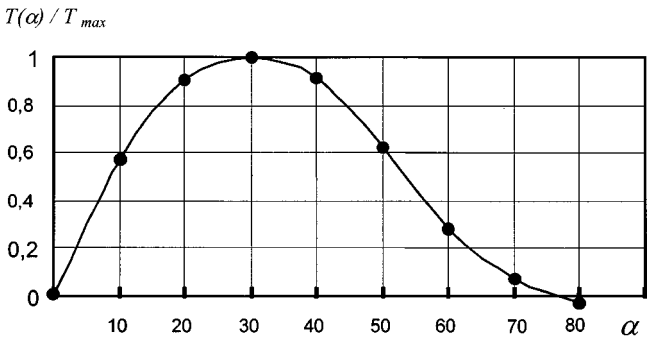

Fig. 13 Time-mean torque coefficient as a function of the valve disk angle (uncertainty in $T=\pm 2$ percent and in $\alpha=\pm 1$ deg)

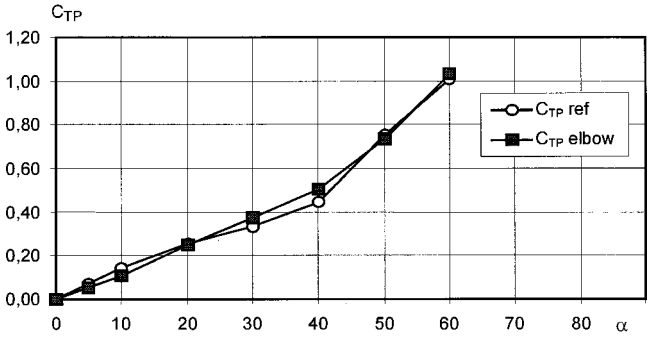

Fig. 14 Influence of the elbow on the time-mean torque coefficient C_{TP} at $x/D=1$ (uncertainties in $C_{TP}=\pm 2$ deg and in $\alpha=\pm 1$ deg)

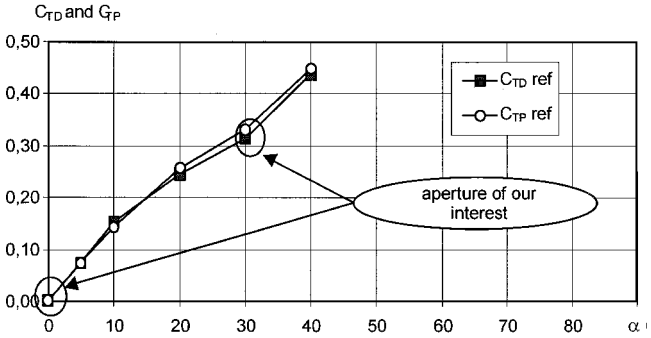

Fig. 15 Comparison between time-mean torque coefficients C_{TP} and C_{TD} for different opening angles in the straight pipe configuration (uncertainties in $C_T=2$ percent and in $\alpha=\pm 1$ deg)

case. The curve gives the evolution of the mean torque with the valve disk opening. For this valve design, the maximum torque occurs at 30 deg. Although the geometry of the valve is not the same one, this value of angle where the maximum appears is close to that obtained by other authors like Bryer and Walshe [12].

Figure 14 shows the effect of the elbow on the average torque. It appears that for both this position and this orientation of the valve, there is only a very little modification induced by the presence of the elbow.

The torque coefficient C_T is a linear function of the valve angle opening for angles lower than 40 deg. The very small flow rate obtained near the valve closure creates strong inaccuracy in the flow rate measurement, consequently we do not present any results for angles greater than 60 deg.

4.2 Comparison Between the Direct and Indirect Measurement Methods. As mentioned previously, only the indirect method of torque measurement gives easy access to the torque fluctuations. Before carrying on the experiments we have checked that this method of measurement gives the same results as that by torquemeter. Measurements are carried out on the same valve model equipped successively with the pressure scanners and with the torquemeter.

The mean torque coefficient C_{TP}, calculated by pressure integration, is compared to that C_{TD} directly measured with the torquemeter. Results, plotted in Fig. 15, show a relatively good consistence between the two methods.

The difference between the two measurement methods can be explained by the low number of pressure taps used to calculate the torque. In fact, the inner diameter of the valve shaft does not give enough places to thread more than 28 vinyl tubes in each shaft extremity. However, the discard between these two different approaches is of less than 5 percent.

According to these results, we can also conclude that for the two apertures $\alpha=0$ and 30 deg the viscous forces are negligible in comparison to the pressure forces. Thereafter all the results presented herein were obtained by the indirect method.

4.3 Fluctuating Torque

Time History of the Torque Coefficient. Figures 16 and 17 show the instantaneous torque coefficient fluctuations, at $\alpha=0$ and 30 deg in the straight pipe configuration and in presence of an elbow located at a variable distance varying from 1 to 8 diameters upstream from the valve.

The average value of the torque remains unchanged for all the distances x/D tested here. On the contrary, the torque fluctuations are strongly dependent on this distance.

We can also observe that near the open position, the torque coefficient changes randomly in sign. These fluctuations and the change of sign are induced by the nonsynchroneous pressure fluctuations on the two valve faces.

As reported by several authors, for example, Strzelecki et al. [13] the flow field downstream of an elbow is extremely complex. At low Reynolds number it exhibits Dean vortices, rotating counterclockwise eddies, and Görtler instabilities. Visualizations reported by this author also show a detached flow region beginning in the inside radius of the elbow and spreading up downstream. Figure 18 gives the schematic structure of these vortices in case of a flow at low Reynolds number.

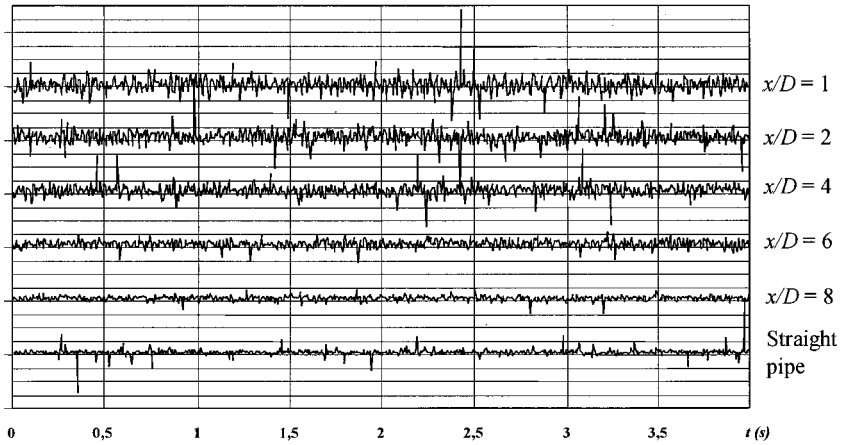

Fig. 16 Time history of the torque coefficient in presence of an elbow located at $x/D=1$ to 8 and in the straight pipe configuration, $\alpha=0$ deg

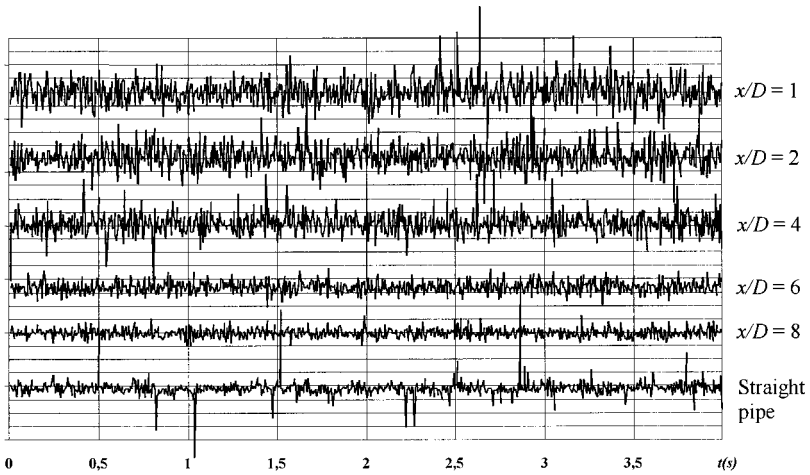

Fig. 17 Time history of the torque coefficient in presence of an elbow located at $x/D=1$ to 8 and in the straight pipe configuration, $\alpha=30$ deg

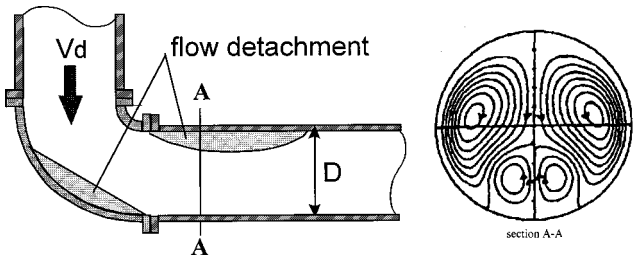

Fig. 18 Flow structure downstream of an elbow

These kinds of vortices are also present in turbulent flow but are not as well organized. If they are not well synchronized, they may produce nonsynchronous pressure fluctuations on both faces of the valve and its buffeting if its axis is in symmetry plane of the elbow.

Mechanical vibrations induced by the flow could produce a significant random load of the butterfly valve components. It could result in the valve shaft or body failure by mechanical stress or in mechanical resonance of the system.

Statistical Analysis of the Buffeting. As demonstrated before, the torque fluctuations are strongly conditioned by the distance x/D, see Fig. 19. Beyond $x/D=8$, the rms torque coefficients in the elbow configuration are at least two times less than those obtained at $x/D=1$. The disturbances induced by the elbow seem to disappear downstream $x/D=8$. This result is confirmed by the analysis of the velocity and of the turbulence intensity profiles downstream from the elbow (see Fig. 7). We also observe that the rms values for the straight pipe case are slightly greater than those obtained in presence of the elbow for $x/D=8$. This can be due to the too short entry length (11 D) in the straight pipe configuration. Even if the center pipe velocity gives the same flow rate for each case, the velocity distribution is not exactly the same in the straight pipe configuration as in the elbow case, see Fig. 5 ($x/D=-1$) and Fig. 8 ($x/D=7$).

Spectral Analysis. The buffeting analysis is also performed in the spectral domain. The power spectrum of the torque coefficient is shown in Fig. 20 as a function of x/D for $\alpha=0$ deg. No frequencies attributable to organized vortex shedding are visible in the straight pipe case; the power spectrum density is flat. When the elbow is added and when the spacing x/D decreases from 8 to 1, it appears gradually a frequency band where the energy of the signal is much more important.

When fully opened and installed near the elbow, the valve is continuously excited by the flow fluctuations. As the length x/D increases, the vortices are disorganized and less synchronized, thus the aerodynamic excitation disappears. Beyond $x/D=8$, we can consider that the disturbances produced by the elbow completely disappeared.

With 30 deg of incidence, Fig. 21, we also observe a strong increase of the signal energy for x/D ranging between 1 and 4. However, the frequency band where the energy is the most important is broader than previously. There is at the same time excitations of the valve by the vortices produced by the elbow and weakly by the flow detachments generated by the valve itself.

Beyond $x/D=6$, we can consider that only the flow detach-

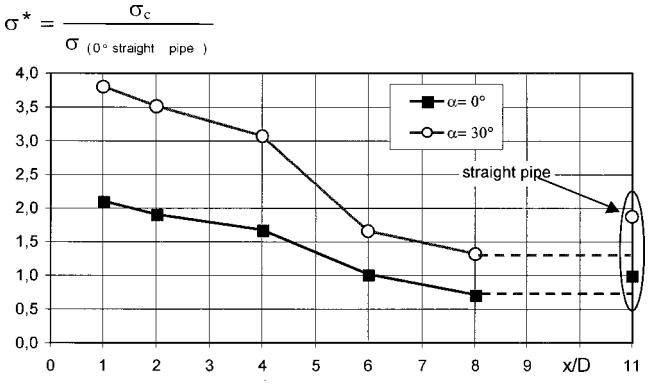

Fig. 19 Root mean square of the torque coefficient according to the spacing x/D and to the valve angle α

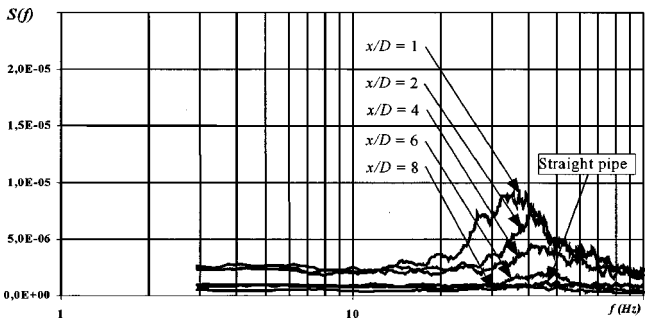

Fig. 20 Power spectrum of the torque for $\alpha=0$ deg at different distances x/D

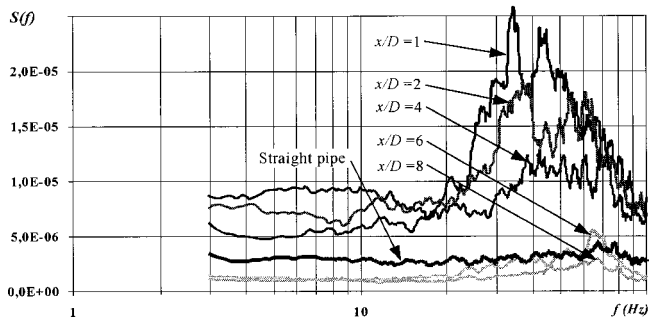

Fig. 21 Power spectrum of the torque for α=30 deg at different distances x/D

ments of the valve produce the turbulent excitation. We also notice an increase in the energy of the signal at a frequency close to 65 Hz.

Except for shut off and throttling control applications, this case of aperture is of less practical interest because this situation appears only briefly during the fully closed and the fully opened positions. Nonetheless, it is very important to ensure that the system does not enter in mechanical resonance during the opening and closing of the valve.

5 Conclusion

Measurements of torque on the axis of a butterfly valve were carried out on a scaled down model installed on a test bench representing actual installations. Configurations of piping of common use were tested to analyze the aerodynamic of the valve and the influence of the geometry on the time-mean and instantaneous torque.

Concerning the aerodynamic of the valve, we can conclude that the perturbations created by the valve itself on the downstream flow have completely disappeared for $x/D=10$. Thus the installation of a flowmeter for flow control application must be made beyond this distance.

Several results, giving the influence of the valve opening angle and of the upstream piping configuration on the magnitude of the torque, are reported and compared to each other. It is shown that the presence of an elbow set up upstream of the valve has no effect on the mean torque values. Using an indirect method for the torque measurement, we have compared the magnitude of the fluctuations of the torque coefficient in case of a valve located in a straight pipe section and in the vicinity of an elbow located upstream at a variable distance x/D.

The statistical and spectral analyses of the instantaneous torque show the influence of the elbow on the increase of the energy level of the fluctuations, and on the modification of the buffeting frequencies.

The turbulence generated by the elbow and combined with vortex shedding from the leading edges of the valve are responsible of important instantaneous torque fluctuations. The effects of the elbow are felt until a distance x/D close to 8, beyond this position only the flow detachments of the valve, which are less energetic, arise.

Finally, we recommend to install the valve at a minimum of 8 D downstream of the elbow. If not possible, it is also possible to close slightly the valve in order to obtain a torque of constant sign.

Acknowledgments

This work is supported by K. S. B-Amri society, Research & Development Department, Parc Rémora-33 170 Gradignan, France. The authors are very grateful to Dr. Pascal L'Hôte and P. Olivier who initiated and followed this research.

Nomenclature

C_T = torque coefficient [ ]
D = nominal pipe diameter [m]
f = frequency [hz]
I_0 = turbulence intensity [ ]
L_i = length [m]
l_i = elementary lever arm [m]
P_i = local pressure on the valve [Pa]
Rc = radius of curvature [m]
Re = pipe Reynolds number [ ]
S_i = elementary surface [m^2]
$S(f)$ = power spectrum [m^2/s]
T = aerodynamic valve shaft torque [Nm]
t = time [s]
U = local velocity in the pipe [m/s]
V_d = flow rate velocity [m/s]
x = distance of the valve from the elbow [m]
y = horizontal radial coordinate [m]
z = vertical radial coordinate [m]
ρ = air density (ρ=1.18 kg/m^3)
σ_c = rms of the torque coefficient [ ]
α = valve disk angle [°]
ϕ = pressure tap diameter [m]
ν = cinematic viscosity [m^2/s]

Subscript

D = relative to direct measurement
P = relative to indirect measurement
T = relative to torque
i = time sample or elementary surface indice
max = maximum value
ref = reference configuration (straight pipe)

References

[1] Eom, K., 1988, ''Performance of butterfly-valves as a flow controller,'' ASME J. Fluids Eng., **110**, pp. 16–19.
[2] Silvester, R. S., 1982, ''Torque induce by butterfly-valve carrying a compressible flow,'' Proc. Inst. Mech. Eng., **196**, pp. 229–237.
[3] Morris, M. J., Dutton, J. C., and Addy, A. L., 1987, ''Peak torque characteristics of butterfly-valves,'' *Proceedings of the Forum on Industrial Applications of Fluids Mechanics*, ASME, **54**, pp. 63–66.
[4] Morris, M. J., and Dutton, J. C., 1989, ''Aerodynamic torque characteristics on butterfly-valves in compressible flow,'' ASME J. Fluids Eng., **111**, pp. 392–399.
[5] Kurkjian, A., and Pratt, H. C, 1974, ''Follow these simple rules to get life from your large butterfly-valves,'' *Air Gas and Liquid Handling*, Power, McGraw-Hill Inc., New York, pp. 42-45. .
[6] Morris, M. J., 1987, ''An investigation of compressible flow through butterfly-valves,'' Ph.D. thesis, Department of Mechanical and Industrial Engineering, University of Illinois at Urbana-Champaign.
[7] Solliec, C., and Danbon, F., 1999, ''Aerodynamic torque acting on a butterfly valve. Comparison and choice of a torque coefficient,'' ASME J. Fluids Eng., **121**, No. 4, pp. 914–917.
[8] Solliec, C., and Mary, J., 1995, ''Simultaneous measurements of fluctuating pressures using piezoresistive multichannel transducers as applied to atmospheric wind tunnel tests,'' J. Wind Eng. Ind. Aerodyn., **56**, pp. 71–86.
[9] Huang, C., and Rhyn, H., Kim, 1996, ''Three-dimensional analysis of partially open butterfly-valve flows,'' ASME J. Fluids Eng., **118**, pp. 562–568.
[10] Morris, M. J., and Dutton, J. C., 1989, ''Compressible flow field characteristics of butterfly-valves,'' ASME J. Fluids Eng., **111**, pp. 399–407.
[11] Morris, M. J., and Dutton, J. C., 1991, ''An experimental investigation of butterfly-valve performance downstream of an elbow,'' ASME J. Fluids Eng., **113**, pp. 81–85.
[12] Bryer, D. W., and Walshe, D. E., 1969, ''Devices for reducing the fluid-dynamic torque on butterfly-valve discs,'' National Physical Laboratory Aerodynamics Division, Report 1298.
[13] Strzelecki, A., Abolivier, M., Prenel, J. P., and Gajan, P., 1997, ''Visualisation d'écoulements dans un coude par translation de nappe synchronisée,'' *Visualisation et traitement d'images en Mécanique des Fluides*, Proc. 7^e colloque National, Saint-Louis, pp. 239–243.

Evaluation of Blade Passage Analysis Using Coarse Grids

Steven M. Miner
Associate Professor,
Mechanical Engineering Department,
United States Naval Academy,
Annapolis, MD 21402

This paper presents the results of a study using coarse grids to analyze the flow in the impellers of an axial flow pump and a mixed flow pump. A commercial CFD code (FLOTRAN) is used to solve the 3-D Reynolds Averaged Navier Stokes equations in a rotating cylindrical coordinate system. The standard $k-\varepsilon$ turbulence model is used. The meshes for this study use 22,000 nodes and 40,000 nodes for the axial flow impeller, and 26,000 nodes for the mixed flow impeller. Both models are run on a SPARCstation 20. This is in contrast to typical analyses using in excess of 100,000 nodes. The smaller mesh size has advantages in the design environment. Stage design parameters for the axial flow impeller are, rotational speed 870 rpm, flow coefficient $\phi=0.13$, head coefficient $\psi=0.06$, and specific speed 2.97 (8101 US). For the mixed flow impeller the parameters are, rotational speed 890 rpm, flow coefficient $\phi=0.116$, head coefficient $\psi=0.094$, and specific speed 2.01 (5475 US). Evaluation of the models is based on a comparison of circumferentially averaged results to measured data for the same impeller. Comparisons to measured data include axial and tangential velocities, static pressure, and total pressure. A comparison between the coarse and fine meshes for the axial flow impeller is included. Results of this study show that the computational results closely match the shapes and magnitudes of the measured profiles, indicating that coarse CFD models can be used to accurately predict performance. [S0098-2202(00)02202-1]

Keywords: CFD, Axial, Mixed, Pump, Impeller

Introduction

Designers are continually being challenged to provide pumps that operate more efficiently, quietly, and reliably at lower cost. Key to building these machines is a better understanding of, and ability to predict their hydraulic and dynamic characteristics. Understanding and predicting these characteristics requires a detailed knowledge of the flow fields within the stationary and rotating passages of the pump. With the advent of more powerful computers, Computational Fluid Dynamics (CFD) is seeing more and more use in predicting the flow fields in both the stationary and rotating passages of turbomachines. Lakshminarayana [1] provides a review of the techniques that are currently being used, as well as, an assessment of the state of the art.

Most of the previous work in the area of axial flow machines has been for compressible flow, and was driven by the gas turbine industry. Adamczyk et al. [2], and Furukawa et al. [3] are typical examples. Examples of incompressible studies of axial flow machines are Yu et al. [4], Yang [5]. In both cases, compressible and incompressible flow, the solutions have been obtained using codes that are developed in house, using meshes that have in excess of 100,000 nodes, and are run on super computer platforms. The hardware and time requirements for models of this size are not suitable for use in day to day design applications.

The present work uses FLOTRAN to obtain solutions for the flow field and pressure field within the impellers of an axial and a mixed flow pump. The code is run on a Sun SPARCstation 20, and the model sizes are 20,000 to 40,000 nodes. The analysis of the axial flow impeller was done after the impeller was built and tested. The analysis was performed to assess the suitability of using coarse grids for predicting impeller performance.

The mixed flow impeller was analyzed during the design phase. The initial blade geometry was based on the results from a streamline curvature code. This initial geometry was then modeled using FLOTRAN. Results of the CFD code were used to generate plots of the circumferentially averaged velocity and pressure profiles at the impeller exit. Using these results the designer modified the blade, hub, and shroud shapes to improve the pump performance. The CFD model geometry was modified to reflect the new shapes and a new solution was generated. The process of modifying the geometry and generating a new solution required one day, new solutions were always generated using the previous solution as the starting point. The blade, hub, and shroud profiles were modified and reanalyzed a total of five times to produce the desired flow and pressure characteristics, the results presented for the mixed flow impeller are for the final geometry, which was built and tested. The ability to modify the model geometry and obtain results in one day made using CFD feasible in the design process.

Results presented here include circumferentially averaged velocity and pressure profiles downstream of the impeller. The computational results are compared to measured data for both impellers.

CFD Formulation

FLOTRAN is a finite element based code which solves the Reynolds Averaged Navier Stokes equations in primitive variable form. The equations are solved in conservative form using an equal-order velocity-pressure formulation, which is second order accurate. The advection terms are handled using a monotone-streamline upwind technique. The equal-order formulation and the upwind technique were developed by Rice and Schnipke [6,7]. The sequential solution of the pressure-velocity equations is based on the SIMPLER method of Patankar [8]. Turbulence is modeled using the two equation model of Launder and Spalding [9]. The near wall node is handled using the law of the wall and the log law of the wall depending on the value of y^+. For both geometries considered here the values of y^+ were less than 600. Discussion of the code and the boundary condition implementation can be found in the ANSYS theory manual [10].

Solution convergence is determined by monitoring the normalized rates of change for each dependent variable. The solution is considered converged when these rates of change have decreased by three to four orders of magnitude. Typically, the velocities and

Contributed by the Fluids Engineering Division for publication in the JOURNAL OF FLUIDS ENGINEERING. Manuscript received by the Fluids Engineering Division March 22, 1999; revised manuscript received February 10, 2000. Associate Technical Editor: D. P. Telionis.

turbulence quantities drop by four orders of magnitude and the pressure drops by three orders. In addition to the normalized rates of change, the mass balance for the model is checked, as well as, the locations and values of the minimum and maximum for each dependent variable. When all these are stable from one iteration to the next the solution is considered converged.

For the impeller analyses discussed in this paper the equations governing the turbulent incompressible flow are formulated in a rotating reference frame. The continuity and momentum equations become:

$$\nabla\cdot(\rho\mathbf{U})+\frac{\partial\rho}{\partial t}=0 \tag{1}$$

$$\frac{D(\rho\mathbf{U})}{Dt}+2\rho\boldsymbol{\omega}\times\mathbf{U}+\rho\boldsymbol{\omega}\times\boldsymbol{\omega}\times\mathbf{r}=\rho\mathbf{g}-\nabla P+\mu_e\nabla^2\mathbf{U} \tag{2}$$

where P is modified to account for effects due to rotation, and μ_e is the linear combination of the kinematic viscosity and the turbulent viscosity derived from the $k-\varepsilon$ model. These equations along with the appropriate boundary conditions are solved for the three components of velocity and the pressure. Boundary conditions used for this analysis include stationary and moving walls, specified inlet velocities, specified outlet pressure, and periodic boundaries.

Geometry

The geometry of the axial flow pump is described in detail by White et al. [11]. The pump is a two stage design with contra-rotating impellers. The analysis presented in this paper is for the first stage impeller. Design parameters for the stage are rotational speed 870 rpm, flow rate 0.32 m^3/s, and head rise 4.5 m. These result in the following nondimensional parameters, flow coefficient $\phi=0.13$, head coefficient $\psi=0.06$, and specific speed 2.97 (8101 US). Figure 1 shows a perspective view of the impeller. This particular impeller has the shroud attached to the blade tips, which eliminates the blade tip leakage flow. The hub radius varies from 0.064 m at the leading edge to 0.088 m at the trailing edge. The shroud radius is constant throughout at 0.15 m. The Reynold's number based on the blade tip speed is 3.8×10^6.

A perspective view of the mixed flow impeller is shown in Fig. 2. This design is a derivative of the axial flow pump described by White et al. [11], with the contra-rotating impellers being replaced with an impeller/stator combination for each stage. The impellers are still contra-rotating for the mixed flow design. The analysis presented in this paper is for the first stage impeller only. Design parameters for the stage are rotational speed 890 rpm, flow rate 0.28 m^3/s, and head rise 7.4 m. These result in the following nondimensional parameters, flow coefficient $\phi=0.116$, head coefficient $\psi=0.094$, and specific speed 2.01 (5475 US). As with the axial flow impeller, the mixed flow impeller has the shroud attached to the blade tips, which eliminates the blade tip leakage flow. The hub radius varies from 0.037 m at the leading edge to 0.107 m at the trailing edge. The shroud radius varies from 0.126 m at the leading edge to 0.149 m at the trailing edge. The Reynold's number based on the blade tip speed at the trailing edge is 3.9×10^6.

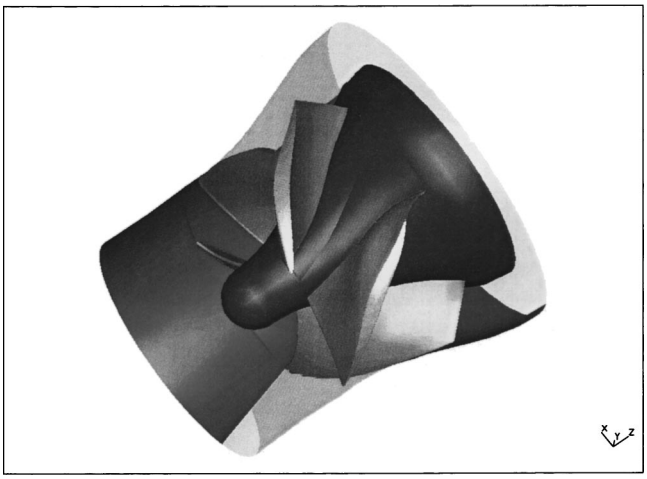

Fig. 2 Mixed flow impeller

Due to symmetry, only one of the blade passages for each impeller needs to be analyzed. Figure 3 illustrates this blade passage with the appropriate upstream and downstream extensions. This becomes the geometry that is modeled in the rotating reference frame. At the inlet to the domain the axial velocity is a constant based on the through flow for the pump. The absolute tangential velocity at the inlet is zero, which implies in the rotating frame the relative velocity is $-r\omega$, and the radial velocity is zero. The inlet to the solution domain is located approximately six chord lengths upstream of the blade leading edge. The only specification made at the outlet is that the static pressure in the absolute frame is uniform and set to zero. This absolute condition is converted into the appropriate relative pressure in the rotating frame. This condition is applied roughly eight chord lengths downstream of the blade trailing edge. Periodic boundaries are used upstream and downstream of the blade leading and trailing edges, respectively. For the rotating solid surfaces all of the velocity components are set to zero. This includes all the surfaces within the blade passage,

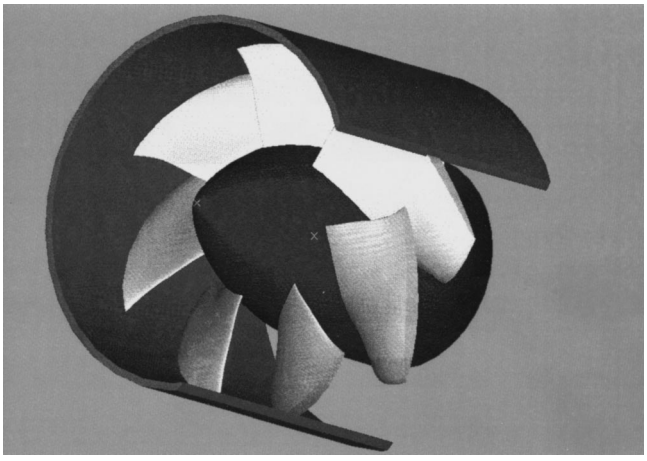

Fig. 1 Axial flow impeller

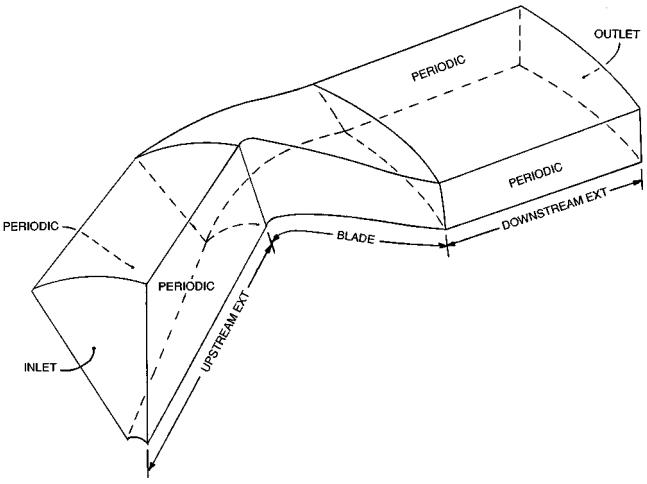

Fig. 3 Solution domain

the nose cone portion of the hub upstream of the blade leading edge, and a short section of the hub downstream of the trailing edge. The shroud surfaces upstream and downstream of the blade passage are stationary in the absolute reference frame. In the rotating frame they are treated as moving boundaries with the axial and radial components of velocity set to zero and the tangential component set equal to $-r_0\omega$ for the shroud, and $-r_i\omega$ for the hub.

Two meshes are used in the analysis for the axial flow impeller. One has 22,176 nodes, with 21 nodes blade to blade, 16 nodes hub to shroud, and 66 nodes inlet to outlet, of which 31 are in the blade passage. The other has 40,131 nodes, with 21 nodes blade to blade, 21 nodes hub to shroud, and 92 nodes inlet to outlet, of which 61 are in the blade passage. The second mesh was generated to check the sensitivity of the solution to the mesh density. For the mixed flow impeller the number of nodes is 26,299 nodes, with 17 nodes blade to blade, 17 nodes hub to shroud, and 91 nodes inlet to outlet, of which 31 are in the blade passage. The nodes are spaced more closely near the hub, shroud, and blade surfaces, as well as, near the leading and trailing edges.

The time required to generate the completed FEA models was approximately 8 hours. The solution for the axial flow impeller required 400 iterations and 58 hours of CPU time. In the case of the mixed flow impeller the solution for the initial geometry required 500 iterations and 85 hours of CPU time. Subsequent updates to the geometry and an updated solution could be obtained within 24 hours, 8 hours to modify the model and 15 hours to update the solution. Updated solutions were always started from the previous converged solution. Having a one day turn around time allows CFD analysis to be used in the design process.

Results

The results presented in this paper for the axial flow impeller include comparisons between measured and computed results upstream and downstream of the impeller. The upstream plane is 3 chord lengths upstream of the leading edge. The downstream plane is 0.2 chord lengths downstream of the trailing edge. Upstream comparisons are made for the axial and tangential components of velocity. Downstream comparisons include axial and tangential components of velocity, static pressure, and total pressure. Downstream comparisons are also shown for the 20,000 node model and the 40,000 node model. In the case of the mixed flow impeller, results include velocity and pressure profiles 0.35 chord lengths downstream of the impeller. For both impellers the data presented are circumferentially averaged. Velocity results are absolute and nondimensionalized by the blade tip velocity U_t, pressures are nondimensionalized by $\rho U_t^2/2$, and the radius is nondimensionalized by the shroud radius r_0. The measured data reported for the axial flow impeller is from White et al. [11]. The velocity and pressure traverse data was obtained using a three hole probe, total pressure was obtained by combining the velocity and static pressure results. The measured data for the mixed flow impeller was obtained using the same test rig and measurement techniques.

Figure 4 shows the comparisons for the axial flow pump at the upstream location. The computed axial velocity is within 10 percent of the measured result. The computed axial velocity profile is not as developed as the measured profile, which causes the computed profile to be flatter than the measured result. This indicates that the location of the inlet for the solution domain may need to be moved further upstream, or an alternative would be to use the fully developed turbulent profile as the inlet condition. The tangential profiles do not agree as well as the axial profiles. The difference between the measured and computed result is 2.5 percent of the tip speed, with the computed result lagging the measured. Some of this difference is due to solving the equations in the rotating reference frame, where the tangential velocity at the inlet is specified as a negative value. In addition, the absolute velocity is obtained by adding the rotational speed to the velocity

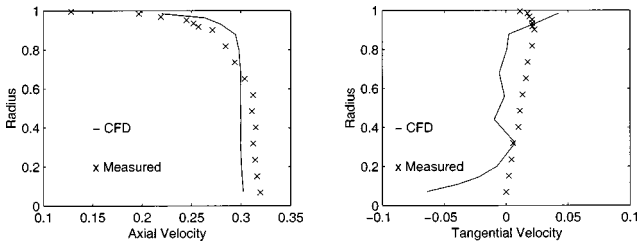

Fig. 4 Nondimensional results, upstream location

computed in the relative frame. Small errors in the relative velocity, on the order of 5 percent, would account for all the difference between the computed and measured results. Despite these differences the computed and measured results both show an increase in the tangential velocity from the center line to the outer radius. This preswirl is caused by the rotation of the impeller downstream.

Figure 5 gives the results of the downstream comparisons for the axial flow impeller. The axial velocities agree to within 2.5 percent from the hub to the shroud. The axial profile shows the flow shifted back toward the hub leaving a deficit at the shroud. The computed results for the tangential velocity show more uniform turning of the flow than the measured results. At the hub and the shroud the tangential velocities show good agreement, differences midspan are as large as 14 percent. However, the shape of the tangential velocity profile from hub to shroud is captured by the computed results. It should be noted that the measurements were made with the counter rotating impeller downstream of the measurement location. The counter rotation of the downstream impeller would tend to reduce the magnitude of the tangential velocity at the measurement location. However, the model does not reflect this influence. Both the shape and the magnitude of the static pressure profile are correctly predicted. The maximum error is less than 10 percent. The computed total pressure correctly predicts the shape of the measured profile. The differences in the magnitude are due to the differences that were seen in the tangential velocity profiles. The over-prediction seen in the tangential velocity manifests itself in the total pressure profile. Still, the maximum error in the magnitude is less than 13 percent.

Figure 6 gives the results of the mesh comparison. Neither plot shows significant difference between the coarse and fine meshes. This indicates that it might be possible to use an even coarser mesh. The advantage of using the coarsest mesh possible is that it reduces the model generation and solution times. This reduction in

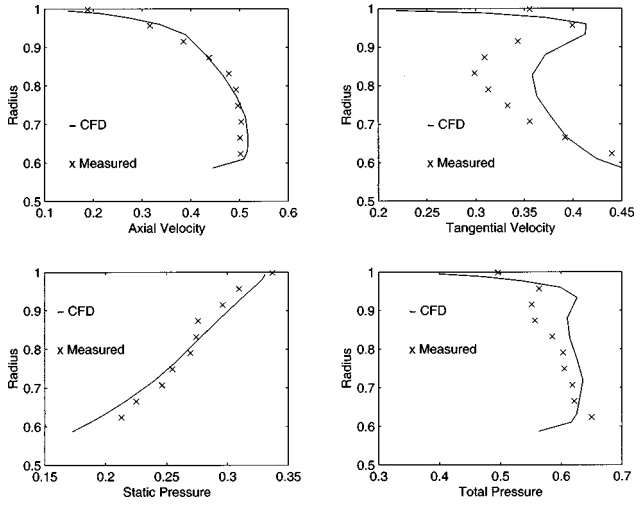

Fig. 5 Nondimensional results, downstream location

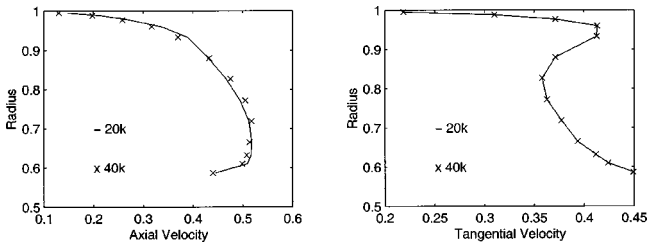

Fig. 6 Fine and coarse mesh comparison, downstream location

time makes it possible to use CFD in an iterative design process. By way of comparison, the solution for the coarse mesh required 400 iterations and 58 hours of CPU time, the fine mesh required 400 iterations and 111 hours of CPU time.

Figure 7 gives the results of the downstream comparisons for the mixed flow impeller. The axial velocities agree to within 12.5 percent from the hub to the shroud, with the largest difference occurring at the hub. The predicted results show a thicker boundary layer at the hub than the measured results. The measured results for the tangential velocity show more uniform turning of the flow than the predicted results. The largest differences occur at the shroud and are roughly 20 percent. A primary cause of the difference is the downstream boundary condition in the computation, which models the shroud as a surface that moves in the opposite direction of the impeller in the rotating frame. This moving surface extends to the exit of the solution domain and would tend to increase the relative tangential velocity, which would cause a decrease in the absolute tangential velocity in the vicinity of the shroud surface. However, in the actual pump there is a stator immediately downstream of the impeller which reduces the effect of the stationary shroud surface on the flow exiting the impeller. Away from the shroud surface the tangential velocities agree to within 8 percent. The maximum error in the static pressure profile is 16 percent and occurs at the shroud surface. Away form the shroud the error is less than 3 percent. The error at the shroud is primarily due to the moving surface boundary condition. The moving boundary causes the relative tangential velocity to be higher than expected, this higher velocity gives rise to a lower static pressure in this region. The agreement between the computed and measured total pressure profiles is not good. The differences at the shroud surface are caused by the disagreement in the tangential velocity at the shroud surface. At the hub surface the differences are due to the disagreement in the axial velocity at the hub surface. However, the difference in the average total pressure is less than 10 percent.

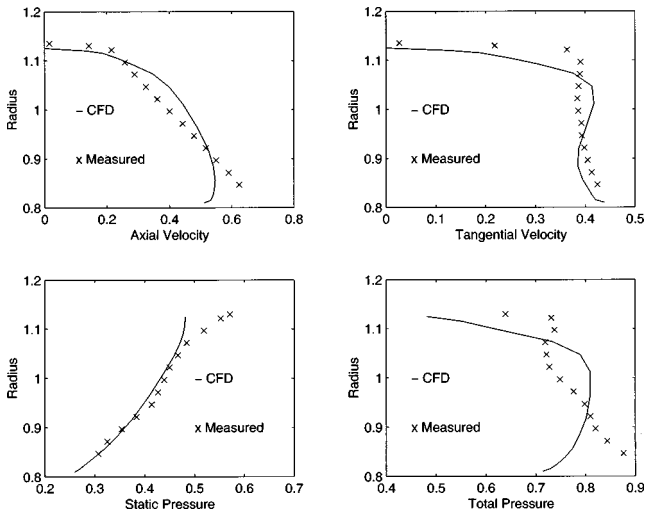

Fig. 7 Nondimensional results, downstream location

Conclusions

The following conclusions are based on the results of this study.

1 Results from the CFD code show good agreement with measured results for the axial and mixed flow pumps. Both the shape and magnitude of the velocity and pressure profiles were correctly predicted.

2 The largest errors were found in the predictions of the tangential velocity, and were due to the downstream boundary conditions used in the models.

3 Using small models, CFD can be used effectively in the design process. Turn around times of one day are possible using a work station.

Acknowledgements

This work was supported by the Naval Surface Warfare Center, Carderock Division, Annapolis Detachment, and the Naval Academy Research Council.

Nomenclature

$\mathbf{g}$ = gravitational vector
P = modified static pressure
$\mathbf{r}$ = radius vector
r_i = hub radius
r_0 = shroud radius
$\mathbf{U}$ = velocity vector
U_t = blade tip speed
μ_e = effective viscosity
ρ = density
ϕ = flow coefficient
ψ = head coefficient
$\boldsymbol{\omega}$ = angular velocity vector

References

[1] Lakshminarayana, B., 1991, ''An Assessment of Computational Fluid Dynamic Techniques in the Analysis and Design of Turbomachinery—The 1990 Freeman Scholar Lecture,'' ASME J. Fluids Eng., **113**, No. 3, pp. 315–352.
[2] Adamczyk, J. J., Celestina, M. L., Beach, T. A., and Barnett, M., 1989, ''Simulation of 3-D Viscous Flow within a Multi-Stage Turbine,'' ASME Paper 89-GT-152.
[3] Furukawa, M., Yamasaki, M., and Inoue, M., 1991, ''A Zonal Approach for Navier-Stokes Computations of Compressible Cascade Flow Fields Using a TVD Finite Volume Method,'' ASME J. Turbomach., **113**, No. 4, pp. 573–582.
[4] Yu, W. S., Lakshminarayana, B., and Thompson, D. E., 1995, ''Computation of Three-Dimensional Viscous Flow in High Reynolds Number Pump Guide Vane,'' *Numerical Simulations in Turbomachinery*, ASME, FED-Vol. 227, pp. 117–122.
[5] Yang, C. I., 1995, ''A Simulation of Viscous Incompressible Flow Through a Multiple-Blade-Row Turbomachinery with a High-Resolution Upwind Finite Differencing Scheme,'' *Numerical Simulations in Turbomachinery*, ASME, FED-Vol. 227, pp. 11–18.
[6] Rice, J. G., and Schnipke, R. J., 1985, ''Monotone Streamline Upwind Finite Element Method for Convection-Dominated Flows,'' Comput. Methods Appl. Mech. Eng., **48**, No. 3, pp. 313–327.
[7] Rice, J. G., and Schnipke, R. J., 1985, ''Equal-Order Velocity-Pressure Formulation That Does Not Exhibit Spurious Pressure Modes,'' Comput. Methods Appl. Mech. Eng., **58**, No. 2, pp. 135–149.
[8] Patankar, S. V., 1980, *Numerical Heat Transfer and Fluid Flow*, Hemisphere, New York, NY.
[9] Launder, B. E., and Spalding, D. B., 1974, ''The Numerical Computation of Turbulent Flows,'' Comput. Methods Appl. Mech. Eng., **3**, pp. 269–289.
[10] ANSYS, 1999, ''ANSYS 5.6 Theory Manual,'' Doc. No. 001242, ANSYS Inc., Canonsburg, PA.
[11] White, J. W., Purnell, J. G., and Stricker, J. G., 1993, ''In-Line Submersible Pump,'' *Proceedings of the 2nd ASME Pumping Machinery Symposium*, ASME, FED-Vol. 154, pp. 369–375.

J. López
Assistant Professor,
E.T.S. de Ingenieros Industriales,
Universidad Politécnica de Cartagena,
30203 Cartagena, Spain

J. Hernández
Professor,
E.T.S. de Ingenieros Industriales, UNED,
Ciudad Universitaria,
28040 Madrid, Spain

F. Faura
Associate Professor,
E.T.S. de Ingenieros Industriales,
Universidad Politécnica de Cartagena,
30203 Cartagena, Spain
e-mail: JHernandez@ind.uned.es

G. Trapaga
Principal Research Associate,
Department of Materials
Science and Engineering,
Massachusetts Institute of Technology,
Cambridge, MA 02139

Shot Sleeve Wave Dynamics in the Slow Phase of Die Casting Injection

An analysis is carried out on the wave formed during the slow phase of die casting injection processes. Viscous effects are assumed to be negligible and the problem is treated two-dimensionally using finite amplitude wave theory. Two commonly used types of plunger movements are considered, for which all the possible wave profiles are analyzed in depth as a function of the parameters which characterize the law of acceleration applied to the plunger, the initial shot sleeve filling fraction, and the geometrical characteristics of the problem. Different relationships between the relevant dimensionless parameters of the system are proposed, which make it possible to optimize the injection process, and so reduce the entrapment of air which leads to porosity. The validity of such relationships is analyzed in detail for different ranges of parameters. Some of the results obtained for the optimum acceleration are compared with those of other authors and experimental measurements. Finally, a law of plunger acceleration which would completely eliminate the air from the shot sleeve at the end of the slow phase of injection and minimizes the filling time is derived. [S0098-2202(00)02002-2]

Introduction

Die casting in horizontal cold chambers is currently the most common process for manufacturing near-net shape cast components, and allows very high production rates with close dimensional tolerance and a good surface finish. The most common defect in die casting is porosity, which limits the integrity of the casting, generally produces low quality casting and makes this type of process only adequate for parts that do not require heat treatment (or welding) to conform to the specified mechanical properties.

There are different mechanisms involved in porosity formation (Campbell [1]), although the most important one in die casting is generally the entrapment of air during the injection process. A die casting machine is shown schematically in Fig. 1. The molten metal is injected into a mold from a horizontal shot sleeve in which the metal is pushed by a plunger. The sleeve is partially filled with a volume of molten metal and the plunger then moves the length of the sleeve (plunger stroke), which is usually fixed. In the injection process, the initial air in the mold and in the shot sleeve may be trapped in the molten metal as small air bubbles that will cause porosity when the metal is solidified. To minimize air entrapment, the molten metal injection process usually consists of slow and fast shot phases (Fig. 1). In the slow shot phase, the plunger first forces the molten metal to rise and fill the upper section of the shot sleeve, and then moves at constant speed until the shot sleeve is completely filled with molten metal. During the plunger movement, a wave is formed. Experimental observations by Garber [2] show that a critical plunger speed exists to raise the wave to the ceiling of the shot sleeve without rolling. Other authors, including Karni [3], Tszeng and Chu [4], and Garber [2], proposed analytical expressions to obtain this critical speed. If the plunger reaches a speed higher than the critical one, the wave will reflect at the shot sleeve ceiling and the front might roll over, causing air entrapment. On the other hand, if the plunger speed does not reach the critical speed, the wave might reflect at the end wall of the chamber and trap air in front of the plunger.

To reach the critical speed, the plunger must be initially accelerated, and the evolution of the wave profile will obviously depend on the plunger acceleration law. Although there are different theoretical and experimental studies concerning the influence of plunger acceleration on the injection process, in practice little emphasis is given in planning the die casting process to controlling the acceleration of the plunger as it moves to reach its critical velocity. Some theoretical studies can be found in Thome et al. [5], Brevick et al. [6], and Tszeng and Chu [4]. Experimental studies like those of Karni [3] and Duran et al. [7] are confined to cases in which the plunger moves with a velocity which increases linearly with the distance travelled, resulting in an acceleration which grows exponentially with time. The reason for this choice is that in die casting machines the plunger speed profiles are typically programmed by specifying the plunger velocity as a function of plunger position. With this law of motion, Duran et al. [7] observed that, for a given shot sleeve geometry and initial filling fraction, there is an optimum acceleration which minimizes the volume of entrapped air. Tszeng and Chu [4] formulated a math-

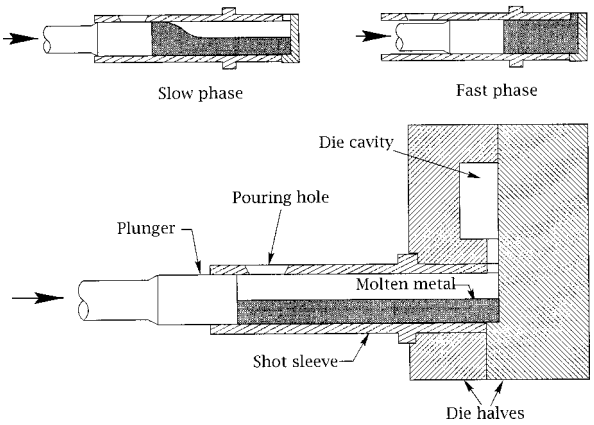

Fig. 1 Schematic sketch of a typical die casting machine

Contributed by the Fluids Engineering Division for publication in the JOURNAL OF FLUIDS ENGINEERING. Manuscript received by the Fluids Engineering Division October 13, 1998; revised manuscript received February 16, 2000. Associate Technical Editor: M. S. Cramer.

ematical model based on simple wave theory to study the transient wave formation in the shot sleeve for the same type of plunger motion and experimental conditions as used by Duran et al. [7]. They analyzed the profiles of the wave front and obtained an optimum plunger acceleration by imposing the condition that the wave begins to break up when the upper tip of the wave front has reached the end wall of the shot sleeve. They found that the predicted optimum acceleration compared very well with the experimental measurements made by Duran et al. [7]. However, Tszeng and Chu's study was limited to a relatively narrow range of experimental conditions, in which values for some critical parameters required to optimize the operating conditions were fixed a priori, as will be further discussed later. They determined the optimum acceleration parameters from an analysis based on the graphical representation of wave profiles and on the calculation of the least positive slope angle of the free surface over the whole wave front, but this was also limited to the particular operating conditions considered in Duran's paper.

The objective of the research described in this paper was to carry out a detailed and systematic study of the wave dynamics in the slow shot phase of the injection process, which allows the selection of optimum process variables (plunger speed and acceleration parameters, initial filling fraction and shot sleeve dimensions) that will minimize air entrapment. For this purpose, the flow of the molten metal in the shot sleeve is analyzed using simple wave theory. Some theoretical considerations are briefly presented in the next section. Two different acceleration laws are considered, and a detailed study of the possible wave profiles for a wide range of the relevant parameters is presented. The place and time of discontinuity formation in the wave are determined for different situations. Depending on the wave profile form, we discuss the selection of parameters which will reduce the amount of air trapped. To reduce the quantity of trapped air the wave must be prevented from breaking up inside the sleeve, and possible air entrapment effects due to wave reflection on the end wall of the sleeve should be avoided. Since the length of the slow phase should be kept to a minimum to achieve maximum production and to prevent the metal from solidifying during the injection process, it seems reasonable to impose the limiting condition that the front of the wave should begin to break up just at the end wall of the sleeve. The analysis will provide analytical relationships between the relevant parameters that will facilitate both the selection of optimum process variables and the determination of limiting operating conditions that should be avoided in any circumstance. The predictions obtained for optimal acceleration as a function of the initial filling fraction are compared with the results of Tszeng and Chu [4] and with the experimental results of Duran et al. [7]. Neither of the acceleration laws previously considered made it possible to choose the parameters which would give rise to a vertical wave profile at the exact time when it reaches the end wall of the sleeve (which would prevent any partial reflection of the wave and reduce to zero the amount of air at the moment of impact). For this reason, we attempted to deduce a law of acceleration which would satisfy the desired condition.

Theoretical Considerations

The problem is considered as two-dimensional, with the coordinate system represented in Fig. 2. The sleeve bottom is assumed flat (at $y=0$) and the free surface is defined by $y=h(x,t)$. We shall assume that viscous effects are negligible and that the typical value of $h(x,t)$ is much smaller than the typical horizontal length scale of the wave, so that the shallow-water approximation can be used. With this approximation, the vertical component of acceleration can be neglected when compared with gravitational acceleration, g, and therefore the pressure distribution can be considered as hydrostatic: $p=p_0+\rho g(h-y)$. If the horizontal velocity component, u, is initially independent of y, it can be deduced that

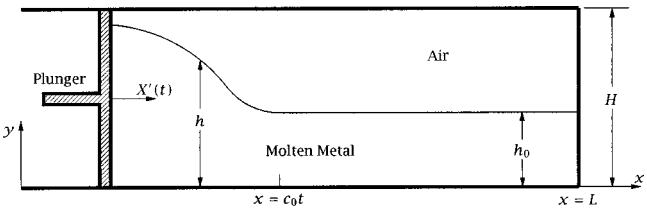

Fig. 2 Schematic representation of the problem and coordinate system

u becomes independent of y at any time. Introducing $c(x,t)=(gh)^{1/2}$, the governing equations can then be written as (Lamb [8])

$$\left[\frac{\partial}{\partial t}+(u+c)\frac{\partial}{\partial x}\right](u+2c)=0, \tag{1}$$

$$\left[\frac{\partial}{\partial t}+(u-c)\frac{\partial}{\partial x}\right](u-2c)=0. \tag{2}$$

Using the method of characteristics, these equations reduce to the statement that

$$u\pm 2c=\text{constant} \tag{3}$$

along characteristic lines defined by

$$\frac{dx}{dt}=u\pm c. \tag{4}$$

Let us suppose that the molten metal in the sleeve is initially at rest and has a uniform depth h_0, and that the plunger surface in contact with the metal begins to move at $t=0$ in the positive x-direction according to the law $x=X(t)$, with $X(0)=0$. According to Eq. (3), along any negative characteristic emanating from the undisturbed region in the xt-plane, where $u=0$ and $c=c_0=(gh_0)^{1/2}$, the following condition is satisfied:

$$c=\frac{u}{2}+c_0. \tag{5}$$

Since $u+2c$ is constant along each positive characteristic, it can be deduced from Eq. (5) that u is also constant along it. Then, integrating the positive characteristic of Eq. (4) and using Eq. (5) gives

$$x=(\tfrac{3}{2}u+c_0)t+f(u). \tag{6}$$

where $f(u)$ is a function of velocity that can be determined from boundary conditions. For a given time t_1, the plunger surface is located at $x=X(t_1)$ and the velocity along the positive characteristic through the point $(X(t_1),t_1)$ is therefore $u=X'(t_1)$. Introducing this condition into Eq. (6) gives

$$f(u)=X(t_1)-[\tfrac{3}{2}X'(t_1)+c_0]t_1, \tag{7}$$

so that the solution can be written, in parametric form, as

$$x=X(t_1)+[\tfrac{3}{2}X'(t_1)+c_0](t-t_1), \tag{8}$$

$$u=X'(t_1). \tag{9}$$

These equations determine the velocity and all other magnitudes as an implicit function of x and t. Using Eq. (5), we get

$$c=c_0+\frac{X'(t_1)}{2}, \tag{10}$$

from which the wave profile can be obtained at every instant.

A discontinuity will be formed in the wave if h and u become multivalued functions of x at $t \geqslant t_c$. The location, x_c, and time, t_c, of formation of the discontinuity are determined by the following simultaneous conditions:

$$\left.\frac{\partial x}{\partial t_1}\right)_t = 0, \tag{11}$$

$$\left.\frac{\partial^2 x}{\partial t_1^2}\right)_t = 0. \tag{12}$$

The second condition must be replaced by $t_1 = 0$ if the discontinuity is formed just at the foremost part of the simple wave (in this case, the first two crossing characteristics come from $t_1 = 0$ and $t_1 = 0^+$).

Given that the sleeve from which the injection is made is generally circular in cross section and that the flow is symmetrical with respect to the vertical plane of the sleeve, the results obtained with the hypothesis introduced in this section will only be applicable to this symmetrical plane. Despite this limitation, the analysis which follows will enable us to take into account the essential characteristics of the flow which will help determine the optimum variables for the process. A discussion on the shape of the free surface outside of the symmetry plane in circular cross section sleeves can be found in Tszeng and Chu [4].

Plunger Motion With Exponential Acceleration

Tszeng and Chu [4] and, before them, Duran et al. [7] in their experimental study considered the following law for the plunger motion:

$$x = X(t) = x_0 e^{\alpha t}, \tag{13}$$

where x_0 is the plunger position at $t = 0$ and $\alpha = X'(t)/x$ is the variation of the plunger velocity per unit of traveling distance, which is assumed to be constant. According to this law, the plunger would have a velocity

$$X'(t) = \alpha x_0 e^{\alpha t}, \tag{14}$$

and therefore $X'(0) = \alpha x_0$ at $t = 0$. Tszeng and Chu [4], however, did not give details on the type of plunger acceleration law assumed to move the plunger from rest to this initial velocity. In order to consider that the plunger begins to move from rest, we will assume the following law instead of that of Eq. (14) (α and β are positive constants):

$$X'(t) = \alpha\beta(e^{\alpha t} - 1), \tag{15}$$

which gives the same acceleration $X''(t) = \alpha^2\beta e^{\alpha t}$ as Eq. (14). Integrating Eq. (15), assuming that the initial location of the plunger surface is at $x = 0$, gives

$$X(t) = \beta(e^{\alpha t} - \alpha t - 1). \tag{16}$$

Substituting Eqs. (15) and (16) into Eq. (8), we obtain

$$x = \beta(e^{\alpha t_1} - \alpha t_1 - 1) + (\tfrac{3}{2}\alpha\beta e^{\alpha t_1} - \tfrac{3}{2}\alpha\beta + c_0)(t - t_1). \tag{17}$$

Place and Time of Formation of the Discontinuity

We now seek the place and time of formation of a discontinuity in the wave. From the condition expressed by Eq. (11) applied to Eq. (17), we obtain

$$t_c = t_1 + \frac{2c_0 + \alpha\beta(e^{\alpha t_1} - 1)}{3\alpha^2\beta e^{\alpha t_1}}, \tag{18}$$

and, from Eq. (12),

$$t_c = t_1 + \frac{4}{3\alpha}, \tag{19}$$

where t_c is the critical time at which h and u become multivalued functions of x. From Eqs. (18) and (19), we obtain

$$t_c = \frac{1}{\alpha}\left[\frac{4}{3} + \ln\left(\xi - \frac{1}{3}\right)\right], \tag{20}$$

where

$$\xi = \frac{2c_0}{3\alpha\beta} \tag{21}$$

is the inverse of a Froude number.

For $\xi = 4/3$, it is deduced from Eqs. (19) and (20) that $t_1 = 0$, and the discontinuity is thus formed at the instant

$$t_c = \frac{\xi}{\alpha} = \frac{4}{3\alpha}. \tag{22}$$

The place of formation of the discontinuity can be obtained by substituting t by t_c from Eq. (22) into Eq. (17) and making $t_1 = 0$, and obviously corresponds to the foremost part of the wave (perturbations along the characteristic that comes from $t_1 = 0$ propagate with velocity c_0),

$$x_c = c_0 t_c = \frac{4c_0}{3\alpha}. \tag{23}$$

For $\xi < \frac{4}{3}$, the condition of Eq. (12), that would lead to negative values of t_1, must be replaced by $t_1 = 0$, which is equivalent to imposing that $u = 0$ at the boundary of the molten metal at rest, so that the time of formation of the discontinuity can be determined from the condition $(\partial x/\partial t_1)_t = 0$ for $t_1 = 0$:

$$t_c = \frac{\xi}{\alpha}. \tag{24}$$

The location where the discontinuity is formed is again obtained from Eq. (17),

$$x_c = c_0 t_c = \tfrac{3}{2}\xi^2\beta. \tag{25}$$

The discontinuity is thus formed at the foremost part of the wave, where the second derivative of Eq. (12) need not vanish.

For $\xi > 4/3$, the discontinuity is formed at a time given by Eq. (20). This happens at an intermediate point between the plunger and the foremost part of the wave, that can be determined by introducing Eqs. (19) and (20) into Eq. (17):

$$x_c = \beta[5\xi - 4 - \ln(\xi - \tfrac{1}{3})]. \tag{26}$$

Since the plunger velocity is actually kept constant when the metal free surface reaches the shot sleeve ceiling, we will discuss later why Eqs. (20) and (26) may not be valid for some operating conditions, since the condition expressed by Eq. (12) cannot be used.

Minimum Initial Filling Fraction

As discussed in the Introduction, the wave produced by the plunger motion should increase the level of the molten metal just enough to fill the shot sleeve section completely. Once this level has been reached, the plunger should move at a constant speed. In the following, we will seek the minimum value of the initial filling fraction, $f = h_0/H$, that is required to avoid the breakup of the wave before the molten metal reaches the shot sleeve ceiling ($y = H$) at the plunger surface. This value of f can be determined from the condition that the wave height at the plunger surface becomes equal to H at an instant $t_H = t_c$. The plunger velocity at this instant, u_H, can be obtained from Eq. (5), making $u = u_H$ and $c = \sqrt{gH}$:

$$u_H = 2(\sqrt{gH} - \sqrt{gh_0}), \tag{27}$$

and t_H can be determined by substituting $u_H = X'(t)$ from Eq. (27) into Eq. (15):

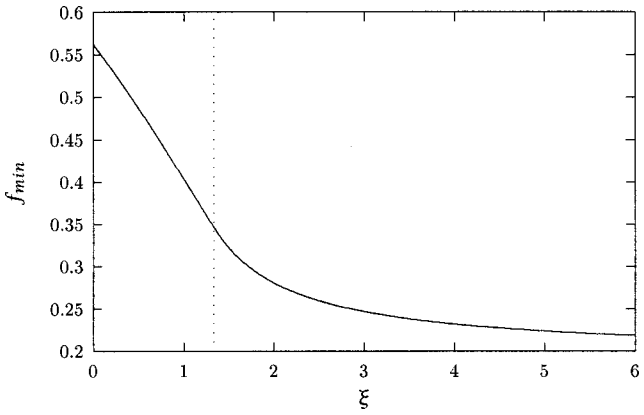

Fig. 3 Minimum initial filling fraction, f_{min}, as a function of ξ, for the motion law of Eq. (15)

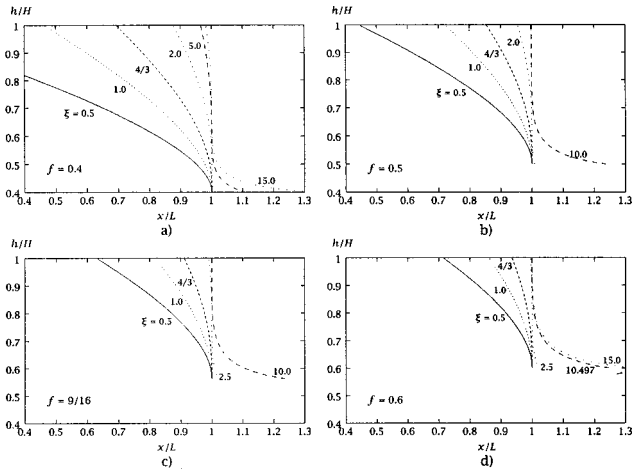

Fig. 4 Wave profiles at $t=t_c$, satisfying the condition $x_c=L$, for different values of the initial filling fraction and ξ, for the motion law of Eq. (15)

$$t_H=\frac{1}{\alpha}\ln\left[\frac{2(\sqrt{gH}-\sqrt{gh_0})}{\alpha\beta}+1\right]. \tag{28}$$

Equating this expression to Eqs. (20) and (24), we get

$$f_{\min}=\begin{cases}\left[\dfrac{3\xi}{3\xi+(\xi-\frac{1}{3})e^{4/3}-1}\right]^2, & \text{if } \xi>\frac{4}{3},\\ \left(\dfrac{3\xi}{3\xi+e^{\xi}-1}\right)^2, & \text{if } \xi\leqslant\frac{4}{3}.\end{cases} \tag{29}$$

This expression, represented in Fig. 3, gives the minimum initial filling fraction as a function of ξ. For $f<f_{\min}$, the wave cannot reach the sleeve ceiling before it breaks up.

It should be mentioned that Eq. (27), which gives the critical plunger speed, is identical to that obtained by Tszeng and Chu [4].

Optimum Acceleration Parameters

As already mentioned, the plunger motion into the sleeve should avoid the breakup of the wave during the filling process and possible air entrapment effects due to wave reflection on the end wall of the sleeve. Furthermore, as the filling time of the slow phase must be minimized for high production rates to be maintained and to avoid metal solidification during the filling process, the wave should begin to break up just at $x=x_c=L$.

If we impose the condition that the discontinuity is formed at the end wall of the sleeve, all the working conditions in which the discontinuity appears at any section located between the plunger and the foremost part of the wave would produce the reflection of the wave before it begins to breakup at $x=L$. As discussed previously, such conditions correspond to $\xi>4/3$. Since the plunger velocity is kept constant for $t>t_H$, the time of formation of the discontinuity will be given by Eq. (20) provided that $t_1\leqslant t_H$. Substituting t_1 obtained from Eqs. (19) and (20),

$$t_1=\frac{1}{\alpha}\ln\left(\xi-\frac{1}{3}\right), \tag{30}$$

and t_H from Eq. (28) into the condition $t_1\leqslant t_H$, gives

$$f\leqslant f^*=\left[\frac{9\xi}{4(3\xi-1)}\right]^2. \tag{31}$$

For $\xi\to\infty$, the maximum value of f given by Eq. (31) tends to $f^*=9/16$; for $\xi\to 4/3$, it tends to $f^*=1$. If we make $x_c=L$ in Eq. (26), we get

$$\frac{L}{\beta}=5\xi-4-\ln(\xi-\tfrac{1}{3}), \tag{32}$$

which yields, for a given L and h_0, the required relationship between α and β to make the wave begin to break up at the end wall of the sleeve when $\xi>4/3$ and the condition of Eq. (31) is satisfied.

For $\xi>4/3$ and $f>f^*$, the condition expressed by Eq. (12) must be replaced by $t_1=t_H$, with t_H given by Eq. (28). The condition that the discontinuity appears at the end wall of the sleeve can be imposed by making $x=L$ and $t=t_c$ in Eq. (8), and by substituting t_c-t_1 from Eq. (18) and $t_1=t_H$ from Eq. (28). By rearranging the resulting expression, we finally get

$$\frac{L}{\beta}=\frac{\frac{3}{2}\xi^2 f^{-1/2}(3f^{-1/2}-2)}{3\xi(f^{-1/2}-1)+1}+3\xi(f^{-1/2}-1)-\ln[3\xi(f^{-1/2}-1)+1], \tag{33}$$

which is the equivalent relationship to that of Eq. (32) for cases with $f>f^*$. In the limiting case of $f=f^*$, Eq. (33) reduces to Eq. (32). It should be noticed that Eqs. (32) and (33) have been obtained without taking into account that the foremost part of the wave begins to reflect on the end wall of the shot sleeve before the discontinuity can be formed at $x=L$.

For cases with $\xi\leqslant 4/3$, the expression equivalent to Eqs. (32) and (33) is obtained by making $x_c=L$ in Eq. (25):

$$\frac{L}{\beta}=\frac{3}{2}\xi^2. \tag{34}$$

Notice that, in this case, there is no reflection of the wave before the discontinuity is formed at $x=L$.

Figure 4 shows wave profiles at $t=t_c$ that satisfy the condition $x_c=L$, for different values of the initial filling fraction and ξ. According to the above, for values of $\xi>4/3$ the wave will begin to break up at some point between the foremost and topmost part of the wave. For filling fractions below 9/16, there is an ξ value below which the wave will not reach the ceiling of the shot sleeve before breaking up. For example, from Eq. (29) represented in Fig. 3, the limiting values of ξ are 1.025 and 0.420 for $f=0.4$ and $f=0.5$, respectively (Figs. 4(*a*) and 4(*b*)). In Fig. 4(*a*) it can be seen that for the represented values of $\xi=0.5$ and $\xi=1$, the molten metal does not reach the ceiling of the sleeve before the wave begins to break up. On the other hand, for filling fractions above 9/16 a limiting value of ξ exists, above which the discontinuity will appear in the topmost part of the front of the wave. For example, for $f=0.6$ a limiting value of $\xi=10.497$ (Fig. 4(*d*)) is obtained from Eq. (31). Notice that for very large values of ξ the wave will begin to reflect quite a long time before t_c.

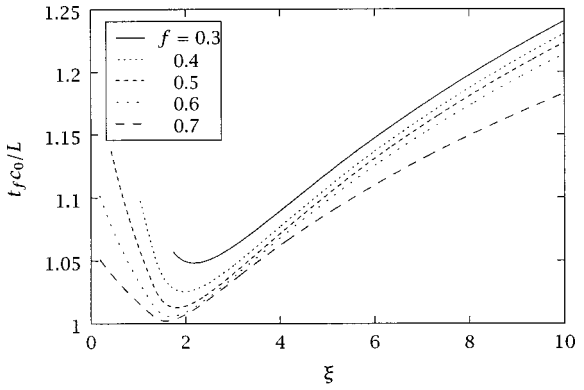

Fig. 5 Nondimensional filling time as a function of ξ for different values of f and the motion law of Eq. (15), for operating conditions satisfying $x_c = L$

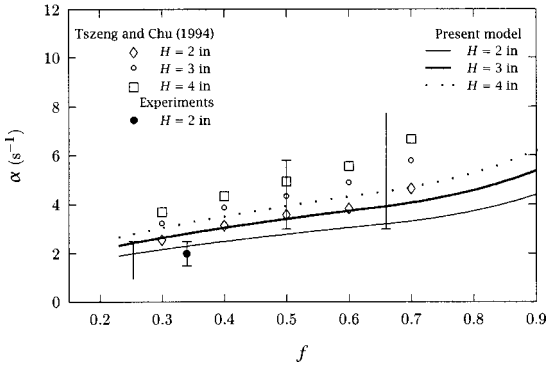

Fig. 6 Comparison of the optimum value of α predicted in this work and that obtained by Tszeng and Chu [4] for a plunger stroke $L = 18$ in., with experimental measurements by Duran et al. [7]

It is interesting to compare the filling times, t_f, corresponding to each of the wave profiles represented in Fig. 4. From mass conservation, the filling time can be expressed as the sum of t_H and the time remaining until the sleeve is completely filled once the molten metal has reached the sleeve ceiling:

$$t_f = t_H + \frac{L(1-f) - X(t_H)}{u_H}. \tag{35}$$

Substituting Eqs. (16), (27), and (28) into Eq. (35) gives

$$\frac{t_f}{L/c_0} = \frac{1}{L/\beta}\left\{\left[\frac{3}{2}\xi + \frac{1}{2(f^{-1/2}-1)}\right]\ln[3\xi(f^{-1/2}-1)+1] - \frac{3}{2}\xi\right\} + \frac{(1-f)}{2(f^{-1/2}-1)}. \tag{36}$$

Substituting L/β from Eqs. (32), (33), and (34), for its respective ranges of validity, into Eq. (36), the filling time, made nondimensional with L/c_0, is obtained as a function of ξ and f for the wave profiles shown in Fig. 4. It is worth remarking that L/c_0 is the time that the foremost part of the wave front takes to reach the end wall of the sleeve. The nondimensional filling time is represented in Fig. 5 as a function of ξ for different values of f, for values of ξ higher than the limit given by Eq. (29). It can be seen in this figure that, for a given value of f, the minimum filling time is obtained for values of ξ around 2, and tends to $\xi = 4/3$ in the limit $f \to 1$. Clearly, t_f must be shortened as much as possible in order to reduce the total injection time. On the other hand, if it is assumed that the volume of entrapped air is proportional to the volume of air within the shot sleeve at the instant when the foremost part of the wave reaches the end wall, it can be deduced from the wave profiles represented in Fig. 4 that the volume of entrapped air would be minimized for a certain value of ξ above 4/3, depending on f.

Taking all the above into account, it can be concluded that the optimal value of ξ will depend on f and be somewhat greater than 4/3. The exact determination of the influence of ξ on air entrapment effects, for the operating conditions represented in Fig. 4, for which $x_c = L$, will depend on a detailed analysis of the shot sleeve filling process after the foremost part of the wave reaches the end wall of the sleeve.

Comparison With Other Results and With Experiments

Figure 6 shows a comparison between the optimum acceleration parameter α predicted in this work and that obtained by Tszeng and Chu [4] for cases with a plunger stroke $L = 18$ in., shot sleeve diameters $H = 2$, 3, and 4 in. and initial filling percentages varying from 20 percent to 70 percent. The parameter β has been taken as equal to 1 in. in order to reproduce the law of plunger motion employed by Tszeng and Chu [4]. These authors obtained their results by analyzing the profiles taken by the front of the wave for different values of α at the moment when the top of the wave front has travelled a distance $L = 18$ in. from $x = 0$. The idea was to determine the highest possible acceleration that does not cause the slope in the wave front to be vertical. It can be seen that the present model predicts values of the optimum acceleration lower than those obtained by Tszeng and Chu [4], although the overall agreement between both is qualitatively good.

It can be observed that ξ is higher than 4/3 for all the conditions represented in Fig. 6, so that the optimum values of α have been determined either from Eq. (32) when $f \leqslant f^*$, or from Eq. (33) when $f > f^*$. Notice that Eq. (32) yields a value of $\xi = 4.695$, for which Eq. (31) gives $f^* = 0.652$. For this value of $\xi = 4.695$, Eq. (29) gives a minimum filling fraction of 0.226; for lower fractions, the wave will break up before the molten metal reaches the ceiling of the shot sleeve, which agrees with the results of Tszeng and Chu [4] for a filling fraction of 0.2. It is expected that plunger accelerations lower than those predicted by Eqs. (32) and (33) could produce not only longer filling times, but also an increase of air entrapment due to wave reflection effects.

Duran et al. [7] carried out a series of water analogue experiments for a circular shot sleeve of $L = 18$ in. and a diameter of 2 in., and measured the volume of entrapped air during the filling process for different plunger accelerations. Their experiments were carried out with the same type of plunger movement as used by Tszeng and Chu [4], except that Duran et al. [7] assumed the critical velocity u_H to be higher than that given by Eq. (27). The results of the measurements made by Duran et al. [7] are shown in Fig. 7. Notice that the initial filling fraction in this figure, f', is the volume fraction of the circular section. For $f' = 0.3$, they measured the minimum value of entrapped air for an acceleration parameter $\alpha = 2\ \mathrm{s}^{-1}$; from Fig. 7 it is deduced that the optimum must lie between 1.5 and 2.5 s^{-1}. For $f' = 0.2$, 0.5, and 0.7, the experimental measurements do not permit us to identify the minimum volume of air trapped in the range of the accelerations measured. Nevertheless, it can be deduced from these measurements that this minimum will probably be found for values of α below 2.5 s^{-1} when $f' = 0.2$ (the minimum measured in the range of experimental accelerations corresponds to $\alpha = 2\ \mathrm{s}^{-1}$), and above 3 s^{-1} when $f' = 0.7$. For $f' = 0.5$, the minimum amount of air trapped will probably correspond to a value of α between 3 and 5.8 s^{-1}. It can be seen, then, that the comparison of these experimental results with our results and those of Tszeng and Chu [4] is more justified when $f' = 0.3$, and less conclusive when $f' = 0.2$, 0.5, and 0.7, since it would be necessary to know the experimental measurements for a wider range of accelerations. Figure 6 shows the value of α corresponding to the minimum volume of trapped

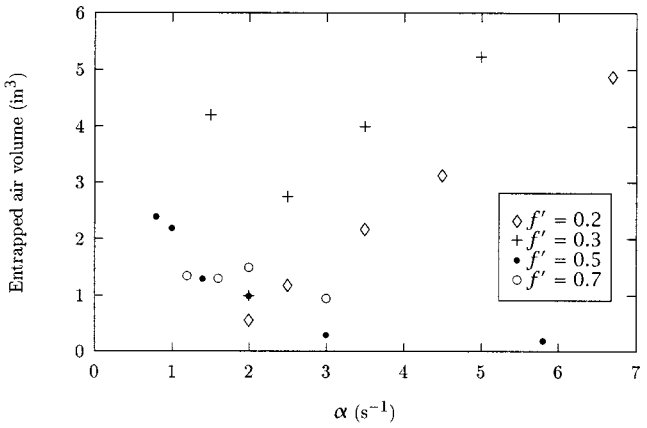

Fig. 7 Experimental measurements of entrapped air volume by Duran et al. [7]

air measured for $f'=0.3$, which corresponds to $f=0.340$ in the symmetry plane. Within the above limitations and uncertainties, there is very good agreement with the result obtained in our study. For $f'=0.2$, 0.5, and 0.7, which, respectively, correspond to $f=0.254$, 0.5, and 0.660 in the symmetry plane, the ranges of the possible values of the optimum α, according to the experiments, are indicated in Fig. 6 by vertical lines. A good agreement is also found between predictions and experiments for $f'=0.2$. When $f'=0.5$ or 0.7, the experimental measurements seem to indicate that the values of the optimal acceleration parameter α are probably nearer to those predicted by Tszeng and Chu [4].

It is important to emphasize that when the value of β is fixed, as it was in this section, it is not possible to independently select an optimum value of ξ. However, it will generally be possible to vary β and so there will be greater flexibility in the choice of process variables. In this respect, the lack of generality involved in the treatment used by previous investigators has clearly been excelled in the current work, as shown in the analysis presented in previous sections.

Plunger Motion With Time-Power Acceleration Law

We will now consider the case of the plunger moving from rest with a velocity

$$X'(t)=\gamma t^n, \tag{37}$$

with γ and n being positive constants. This type of law of movement is typical of casting machines in which the velocity of the plunger is specified as a function of time. Integrating Eq. (37) and assuming that the initial location of the plunger surface is at $x=0$ gives

$$X(t)=\frac{\gamma}{n+1}t^{n+1}. \tag{38}$$

An analysis of this case for the analogous one-dimensional flow of gas in a semi-infinite cylindrical pipe terminating in a plunger was presented by Landau and Lifshitz [9]. When $n<1$, it can easily be shown that, for a given time, $h(x)$ is multivalued for any $t>0$, so that a discontinuity is formed at the plunger surface at $t=0$. (It should be noticed that, for $n<1$, the plunger moves with an infinite acceleration at $t=0$.)

Substituting Eqs. (37) and (38) into Eq. (8), and from the conditions expressed by Eqs. (11) and (12), we get

$$t_c=\left(\frac{2c_0}{3\gamma}\right)^{1/n}\left[\frac{3n+1}{3(n-1)}\right]^{(n-1)/n} \tag{39}$$

and

$$t_1=\left(\frac{2c_0}{\gamma}\,\frac{n-1}{3n+1}\right)^{1/n}. \tag{40}$$

The minimum value of the initial filling fraction is determined, as in the previous section, from the condition that the wave height at the plunger surface becomes equal to H at an instant $t_H=t_c$. Substituting $u_H=X'(t)$ from Eq. (27) into Eq. (37) gives

$$t_H=\left[\frac{2c_0}{\gamma}(f^{-1/2}-1)\right]^{1/n}, \tag{41}$$

and equating this expression to Eq. (39), we get

$$f_{\min}=\frac{1}{\left[\dfrac{1}{3^n}\left(\dfrac{3n+1}{n-1}\right)^{n-1}+1\right]^2}. \tag{42}$$

This expression, represented in Fig. 8, can be compared with that corresponding to the exponential law, given in Eq. (29).

For $n>1$ the discontinuity is formed at some intermediate location between the foremost part of the wave and the plunger surface, so that it is not possible for the wave to begin to break-up at the end wall of the sleeve before its foremost part reflects against it. As in the previous section, since the plunger velocity is kept constant for $t>t_H$, the time of formation of the discontinuity will be given by Eq. (39) provided that $t_1\leqslant t_H$. Substituting t_1 from Eq. (40) and t_H from Eq. (41) into the condition $t_1\leqslant t_H$ gives

$$f\leqslant f^*=\left(\frac{3n+1}{4n}\right)^2. \tag{43}$$

The maximum value of f given by Eq. (43) tends to $f^*=9/16$ for $n\to\infty$ and to $f^*=1$ for $n\to 1$. Making $x=L$ and $t=t_c$, and introducing t_1 from Eq. (40) and t_c from Eq. (39) into Eq. (8), we get

$$\frac{L\gamma^{1/n}}{c_0^{(n+1)/n}}=\frac{5n^2+\dfrac{1}{3}(2n-1)}{(n+1)(n-1)^2}\left(2\,\frac{n-1}{3n+1}\right)^{(n+1)/n}, \tag{44}$$

which yields, for a given L and h_0, the required relationship between n and γ to make the wave begin to break up at the end wall of the sleeve when $n>1$ and the condition of Eq. (43) is satisfied. The equivalent relationship to that of Eq. (33), corresponding to $f>f^*$, which can also be obtained in this case by replacing the condition of Eq. (12) by $t_1=t_H$, is

$$\frac{L\gamma^{1/n}}{c_0^{(n+1)/n}}=\frac{1}{n+1}\left[2(f^{-1/2}-1)\right]^{(n+1)/n}+\frac{2f^{-1/2}(3f^{-1/2}-2)}{3n}[2(f^{-1/2}-1)]^{(1-n)/n}. \tag{45}$$

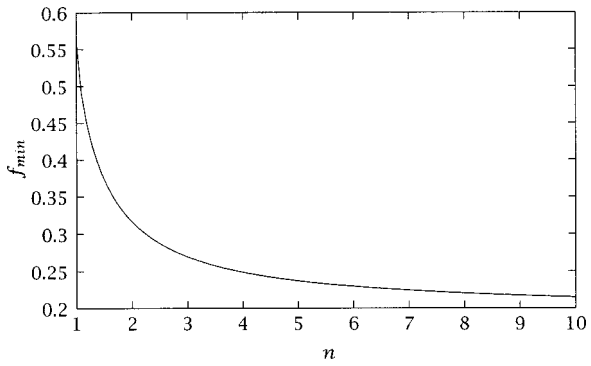

Fig. 8 Minimum initial filling fraction, f_{min}, as a function of n, for the motion law of Eq. (37)

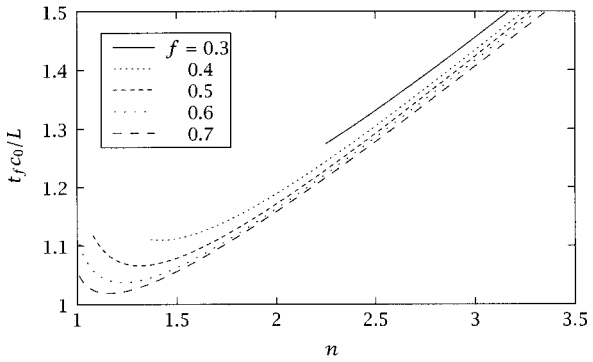

Fig. 9 Nondimensional filling time as a function of *n* for different values of *f* and the motion law of Eq. (37), for operating conditions satisfying $x_c = L$

For $n=1$, Eq. (40) gives $t_1=0$, so that the discontinuity is formed at the foremost part of the wave front at the instant

$$t_c=\frac{2c_0}{3\gamma}. \tag{46}$$

The place of formation of the discontinuity can be obtained by substituting t_c from Eq. (46) into Eq. (8) with $t_1=0$, and is obviously

$$x_c=c_0t_c=\frac{2c_0^2}{3\gamma}. \tag{47}$$

Introducing the condition that $x_c=L$, from Eq. (47) we get the equivalent relationship to those of Eqs. (44) and (45)

$$\frac{L\gamma}{c_0^2}=\frac{2}{3}, \tag{48}$$

which gives the required acceleration that makes the wave begin to break up at the end wall of the sleeve.

The shot sleeve filling time can be obtained by substituting Eqs. (38), (27), and (41) into Eq. (35):

$$\frac{t_f}{L/c_0}=\frac{c_0^{(n+1)/n}}{L\gamma^{1/n}}\frac{n}{n+1}[2(f^{-1/2}-1)]^{1/n}+\frac{1-f}{2(f^{-1/2}-1)}. \tag{49}$$

For operating conditions satisfying $x_c=L$, the filling time can be obtained by substituting $L\gamma^{1/n}/c_0^{(n+1)/n}$ from Eqs. (44), (45), and (48), for its respective ranges of validity, into Eq. (49). This filling time, made nondimensional with L/c_0, is represented in Fig. 9 as a function of n for different values of f, for values of n higher than the limit given by Eq. (42). It can be observed that the minimum filling time is obtained for a value of n which increases as f decreases.

By comparing Figs. 5 and 9 we can conclude that the law of exponential acceleration requires shorter filling times and is normally preferable to the time-power law.

Determination of an Optimum Acceleration Law

It has already been demonstrated that neither acceleration law considered makes it possible to eliminate air from the shot sleeve before the wave begins to break up or reflect off the end wall of the sleeve. An optimum acceleration law can be obtained from Eq. (8) if we assume that the wave profile is vertical at $x=L$. This assumption ensures that there is no breakup or reflection of the wave during the filling process, and that the volume of air within the shot sleeve, at the instant of formation of the discontinuity, is equal to zero.

Substituting t by t_c and x by x_c into Eq. (8) gives

$$\frac{3}{2}X'(t_1)+\frac{X(t_1)}{t_c-t_1}=\frac{x_c}{t_c-t_1}-c_0, \tag{50}$$

which indicates that all the positive characteristics from points $(X(t_1),t_1)$ cross at the critical point (x_c,t_c). With the condition that $X(t)=0$ at $t=0$, the solution of Eq. (50), giving the location of the plunger surface as a function of time, is

$$X(t)=3x_c\left[1-\left(1-\frac{t}{t_c}\right)^{2/3}\right]-2c_0t. \tag{51}$$

If we now introduce the condition that the discontinuity is formed just at $x_c=L$, so that $t_c=L/c_0$, Eq. (51) becomes

$$X(t)=3L\left[1-\left(1-\frac{c_0t}{L}\right)^{2/3}\right]-2c_0t. \tag{52}$$

The corresponding velocity and acceleration laws are then

$$X'(t)=2c_0\left[\left(1-\frac{c_0t}{L}\right)^{-1/3}-1\right], \tag{53}$$

$$X''(t)=\frac{2c_0^2}{3L}\left(1-\frac{c_0t}{L}\right)^{-4/3}. \tag{54}$$

It can easily be deduced that the molten metal reaches the shot sleeve ceiling at a time

$$t_H=\frac{L}{c_0}(1-f^{3/2}), \tag{55}$$

so that t_H tends to t_c as $f\to 0$. For $t>t_H$ the plunger velocity should be kept constant.

Introducing Eqs. (52) and (53) into Eqs. (8) and (9), the wave profile can be obtained as a function of time for a given h_0 and L

$$\frac{x}{L}=1+\left[2-3\left(\frac{h}{h_0}\right)^{1/2}\right]\left[1-\frac{(gh_0)^{1/2}}{L}t\right]. \tag{56}$$

The evolution of the wave profile is presented in Fig. 10 for different values of the initial filling fraction. It can be observed that the wave profile will be vertical at $t/t_c=1$, so that all the initial air volume will be forced out without being entrapped. Moreover, with this motion law the duration of the slow shot phase is minimized by making the filling time equal to $t_c=L/c_0$, which obviously decreases as the initial filling fraction increases. Despite the partial experimental validation of the model, presented above, for the particular case of an exponential acceleration law, the assessment of the new plunger acceleration

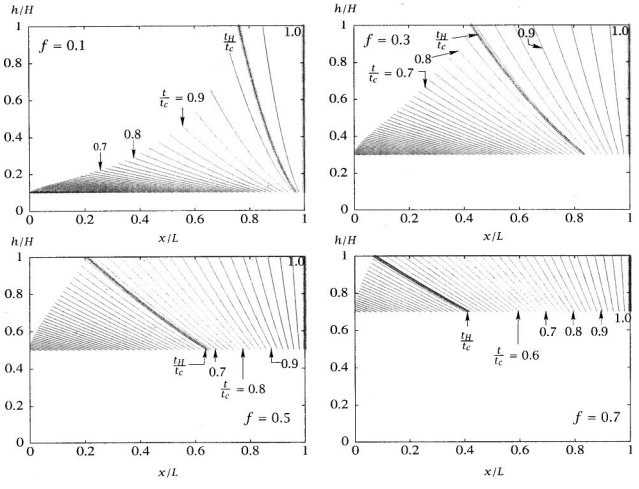

Fig. 10 Evolution of the wave profile with t/t_c for different values of the initial filling fraction and the optimum plunger acceleration law of Eq. (54)

law would require a comparison of the analytical predictions with experimental results, which are not available in the literature at present. This, however, will be the subject of a future publication.

Although viscosity and nonhydrostatic effects might have some influence on the flow in the shot sleeve under certain circumstances, the proposed optimum acceleration law, obtained neglecting these effects, and the analysis of wave motion presented in this work, can be of significant help in the selection of optimum process variables. A numerical investigation, whose results will be published elsewhere, is currently being carried out in order to analyze the influence of viscosity and nonhydrostatic effects on wave evolution. The possible effects of wave reflection against the end wall of the shot sleeve and of the interaction between the wave and the sleeve ceiling for $t \geqslant t_H$ are being analyzed in detail. For wide ranges of conditions, predictions of the present analysis show an overall good agreement with preliminary numerical results (Hernández et al. [10]).

Conclusions

A study of the wave evolution in the slow shot phase of die casting injection processes is presented. An analysis of the possible wave profiles has been carried out for different acceleration laws and wide ranges of the relevant parameters, for which the place and time of formation of a discontinuity in the wave are determined. We obtained nondimensional relationships between the parameters characterizing the acceleration law applied to the plunger, the initial filling fraction and the geometrical characteristics of the shot sleeve. These relationships make it possible to select the variables of the process in such a way that air entrapment is minimized, thus reducing the porosity of the manufactured pieces, and injection time is kept as small as possible. Parameter ranges which should be avoided have been determined.

For the time-exponential acceleration law we have deduced that the optimum value of parameter ξ depends on the initial filling fraction and must be somewhat greater than 4/3. It is expected that the optimum value of ξ will increase with decreasing values of f. A detailed analysis of processes caused by the reflection of the wave against the end wall of the shot sleeve and its interaction with the sleeve ceiling would be necessary for a more precise determination of this optimum value. We have found that a minimum initial filling fraction is required to avoid the break-up of the wave before the molten metal reaches the shot sleeve ceiling, which is a decreasing function of ξ with a maximum of 9/16 in the limit $\xi \to 0$ (infinite Froude number) and $f_{\min}=0.195$ when $\xi \to \infty$. Similar results have been obtained for the time-power acceleration law. We have found that the exponential law produces steeper wave profiles and so requires shorter filling times, what makes the time-exponential law generally preferable to the time-power law, particularly for low values of the initial filling fraction.

We compared the predictions obtained for the optimal acceleration parameter α as a function of initial filling fraction with the results of Tszeng and Chu [4], obtaining an acceptable qualitative agreement, despite our slightly lower values. The results were also compared with those obtained experimentally by Duran et al. [7], again with good agreement despite the uncertainties involved in the comparison.

We observed that neither of the acceleration laws considered makes it possible to obtain a set of factors which totally removes air from inside the shot sleeve at the moment when the wave reaches the end wall. To eliminate these limitations, we have analytically deduced an acceleration law which makes it possible to obtain a vertical profile of the wave when it reaches the end wall of the shot sleeve for any value of the initial shot sleeve filling fraction, and additionally minimizes the filling time of the slow phase.

Acknowledgments

The authors gratefully acknowledge the support of the Spanish Comisión Interministerial de Ciencia y Tecnología (CICYT) under grants TAP97-0489 and PB98-0007.

Nomenclature

c = wave speed relative to the fluid for a depth h
c_0 = wave speed relative to the fluid for a depth h_0
f = initial filling fraction, h_0/H
$f_{\min}$ = minimum initial filling fraction
f' = initial filling fraction for a circular shot sleeve
f^* = value of f defined in Eqs. (31) and (43)
g = gravitational acceleration
h = height of the free surface
h_0 = initial depth of molten metal
H = height of the shot sleeve
L = length of the shot sleeve
n = parameter in Eq. (37)
p = pressure
t = time
t_c = time of formation of the discontinuity
t_f = filling time of the shot sleeve
t_H = time at which the molten metal reaches the sleeve ceiling
t_1 = time in Eqs. (8) and (9)
u = horizontal velocity component of molten metal
u_H = plunger velocity when the molten metal reaches the sleeve ceiling
x = horizontal coordinate
x_c = location of formation of the discontinuity
y = vertical coordinate
α,β = parameters of the exponential law of Eq. (15)
ξ = dimensionless parameter defined in Eq. (21)
γ = parameter of the time-power law of Eq. (37)
ρ = density

References

[1] Campbell, J., 1991, *Castings*, Butterworth-Heinemann, Oxford.
[2] Garber, L. W., 1982, ''Theoretical Analysis and Experimental Observation of Air Entrapment During Cold Chamber Filling,'' Die Cast. Eng., **26**, May–June pp. 14–22.
[3] Karni, Y., 1991, ''Selection of Process Variables for Die Casting,'' Ph.D. thesis, The Ohio State University, Ohio, USA.
[4] Tszeng, T. C., and Chu, Y. L., 1994, ''A Study of Wave Formation in Shot Sleeve of a Die Casting Machine,'' ASME J. Eng. Ind., **116**, No. 2, pp. 175–182.
[5] Thome, M. C., and Brevick, J. R., 1993, ''Modeling Fluid Flow in Horizontal Cold Chamber Die Casting Shot Sleeves,'' AFS Trans., **101**, pp. 343–348.
[6] Brevick, J. R., Armentrout, D. J., and Chu, Y., 1994, ''Minimization of Entrained Gas Porosity in Aluminum Horizontal Cold Chamber Die Casting,'' Trans. NAMRI/SME, **22**, pp. 41–46.
[7] Duran, M., Karni, Y., Brevick, J., Chu, Y., and Altan, T., 1991, ''Minimization of Air Entrapment in the Shot Sleeve of a Die Casting Machine to Reduce Porosity,'' Technical Report ERC/NSM-C-91-31, The Ohio State University.
[8] Lamb, H., 1945, *Hydrodynamics*, Dover, New York.
[9] Landau, L. D., and Lifshitz, E. M., 1959, *Fluid Mechanics*, Pergamon Press, Oxford.
[10] Hernández, J., López, J., Gómez P., and Faura, F., 1999, ''Influence of Non-Hydrostatic and Viscous Effects on Shot Sleeve Wave Dynamics in Die Casting Injection,'' *ASME/JSME Fluids Engineering Conference. Forum on Advances in Free Surface and Interface Fluids Dynamics*, FED-Vol. 248, San Francisco, CA.

Turbulent Boundary Layers on Surfaces Covered With Filamentous Algae

Michael P. Schultz
Department of Mechanical Engineering,
United States Naval Academy,
Annapolis, MD 21402

Turbulent boundary layer measurements have been made on surfaces covered with filamentous marine algae. These experiments were conducted in a closed return water tunnel using a two-component, laser Doppler velocimeter (LDV). The mean velocity profiles and parameters, as well as the axial and wall-normal turbulence intensities and Reynolds shear stress, are compared with flows over smooth and sandgrain rough walls. Significant increases in the skin friction coefficient for the algae-covered surfaces were measured. The boundary layer and integral thickness length scales were also increased. The results indicate that profiles of the turbulence quantities for the smooth and sandgrain rough walls collapse when friction velocity and boundary layer thickness are used as normalizing parameters. The algae-covered surfaces, however, exhibited a significant increase in the wall-normal turbulence intensity and the Reynolds shear stress, with only a modest increase in the axial turbulence intensity. The peak in the Reynolds shear stress profiles for the algae surfaces corresponded to the maximum extent of outward movement of the algae filaments. [S0098-2202(00)01902-7]

Introduction

Biofouling is the colonization of a surface exposed in the aquatic environment by microorganisms, plants, and animals. On marine vehicles, biofouling leads to increased surface roughness and frictional drag. In the past, calcareous or ''hard'' fouling organisms such as barnacles were the most problematic to ship operators. At present, the duty cycles of modern merchant ships, marked by short periods in port and in larvae-rich coastal areas, favor the settlement and growth of algae (Callow [1]). The most common macroalgae found on copper-based antifouling paints is the filamentous green alga *Enteromorpha*. Its dominance results from its nearly global distribution, high reproductive potential, and ability to withstand large variations in environmental conditions (Callow [2]). Since filamentous algae can form a significant presence on the hulls of marine vehicles, their effect on skin friction and turbulent boundary layer structure is of practical interest.

A substantial body of research has been devoted to studying the effects of marine fouling on frictional resistance. A review of much of this work was given in Schultz [3]. Atmospheric boundary layer investigations over plant canopies are analogous in many respects, and a review of this work is given in Raupach and Thom [4] and Raupach et al. [5]. Several studies have looked at the effect of flexible vegetation on turbulent shear flows and, therefore, are of particular relevance to the present investigation. Kouwen and Unny [6] studied turbulent open channel flow over plastic strips. The primary contribution of their work was the formulation of a dimensionless, stiffness parameter that related the density and amount of bending stress of the roughness to the wall shear stress. The stiffness parameter proposed by Kouwen and Unny was as follows:

$$\frac{1}{k_0}\left(\frac{mEI}{\rho U_\tau^2}\right)^{1/4} \tag{1}$$

Lewkowicz and Das [7] used uniformly distributed nylon tufts attached to a rough flat plate to model a turbulent boundary layer flow over a filamentous algae layer. Both mean and turbulence quantities were measured. They found that the model algae layer caused significant increases in the physical growth of the boundary layer, the wall shear stress, and the turbulent normal and shear stresses. The roughness function, ΔU^+, for their model algae film collapsed well to Eq. (2) for $40 \leqslant k^+ \leqslant 800$.

$$\Delta U^+ = \frac{0.89}{\kappa}\ln(k^+) + 1.055 \tag{2}$$

Ikeda et al. [8] used both laser Doppler velocimetry (LDV) and particle image velocimetry (PIV) to study the organized, three-dimensional vortical motions above flexible aquatic plants. The plants were modeled using nylon filaments. They noted that the mean axial velocity profile had an inflection point below the top of the roughness layer. The turbulent normal and shear stresses were found to be largest near the top of the roughness layer. The wavy motion often associated with flow over filamentous surfaces (e.g., the waves in a field of grain) was shown to be induced by the movement of elliptical vortices generated intermittently above the vegetation layer.

Schultz and Swain [9] investigated the effect of natural, algal biofilms on turbulent boundary layers. The roughness layers tested were composed mainly of diatom slimes and blue-green algae, with only one specimen having a significant coverage of filamentous macroalgae. The results showed an increase in C_f of 33 percent to 187 percent on the fouled specimens. The biofilms tested showed varying effect on the turbulent normal and shear stresses when those quantities were normalized with the friction velocity. It was concluded that a large part of the variability in the results was due to the heterogeneity of the biofilms that were tested.

The aim of the present experimental investigation was to better understand the structure of turbulent boundary layers that develop over natural, filamentous marine algae layers. To accomplish this, boundary layer measurements were made on test surfaces colonized by algae. The experiments were conducted in water tunnel using a two-component LDV. The mean velocity profiles and bulk flow parameters as well as the turbulent normal and shear stresses are compared with flows over smooth and sandgrain rough walls.

Experimental Facilities and Method

The experimental work was carried out at the Harbor Branch Oceanographic Institution (HBOI) closed return, closed jet water

Contributed by the Fluids Engineering Division for publication in the JOURNAL OF FLUIDS ENGINEERING. Manuscript received by the Fluids Engineering Division October 20, 1999; revised manuscript received February 8, 2000. Associate Technical Editor: J. K. Eaton.

tunnel (Gangadharan et al. [10]). The tunnel is 2.44 m in height, 8.53 m in length, and 1.22 m in width, and the test section is 0.61 m by 0.61 m and is 2.54 m in length. Flow management devices include turning vanes placed in the tunnel corners and a polycarbonate honeycomb flow straightener in the entrance to the contraction section. The resulting freestream turbulence intensity in the test section is ~1.3 percent.

The test matrix consisted of five specimens. One smooth surface and specimens covered with #240 grit and #36 grit sandpaper served as controls. The remaining two specimens were allowed to foul with the filamentous green alga, *Enteromorpha spp.* over a period of about 30 days. In order to look at boundary layer development over the algae layer, velocity profiles were taken at five downstream positions. These were taken at 1.15 m, 1.30 m, 1.45 m, 1.60 m, and 1.75 m downstream of the leading edge of the test fixture and at a nominal freestream velocity of 1.6 ms^{-1}.

The algae used in the present study were grown at the HBOI Aquaculture facility. Water from the Indian River Lagoon was continuously pumped through a sand filtration system and into grow-out tanks. During the experiments, the salinity of the water in the tanks ranged from 25 ppt to 40 ppt. The water temperature ranged from 25°C to 35°C. Test specimens were fabricated from cast acrylic sheet and were exposed for ~30 days. Each specimen measured 558 mm in width, 1168 mm in length, and 12.7 mm in thickness. Still digital photographs and video clips of the algae layer under flow were taken. Image analysis allowed the mean thickness of the layer to be estimated. This was accomplished by digitizing the side profile of the algae layer and measuring its height above the acrylic substrate. The roughness height of the sandgrain rough specimens was measured using a BMT stylus-type hull roughness analyzer. The stylus was 1.6 mm in diameter and the profile length was 50 mm. The maximum peak to valley height was measured 100 times and averaged to estimate the roughness height for the surface. The accuracy of the device is ±0.01 mm or ±5 percent, whichever is greater. A description of the test surfaces with their roughness heights is given in Table 1.

The test specimens were inserted into a flat plate test fixture mounted horizontally in the tunnel. The plate was 0.58 m in width, 2.06 m in length, and 54 mm thick. It was constructed of polyvinylchloride (PVC) and stainless steel and was mounted horizontally in the tunnel's test section. The leading edge of the test fixture was shaped to mimic the forward portion of a NACA 0012-64 airfoil. The forward most 280 mm of it was covered with #36 grit sandpaper to hasten development of a turbulent boundary layer. The use of a strip of roughness to artificially thicken a boundary layer was proposed by Klebanoff and Diehl [11]. The forward edge of the specimen was located 710 mm from the leading edge of the plate.

Velocity measurements were made using a TSI two-component, fiber-optic LDV system. The LDV used a four beam arrangement and was operated in backscatter mode. The probe volume diameter was ~90 μm, and its length was ~1.3 mm. The viscous length (ν/U_τ) varied from a minimum of 9 μm for the algae covered surface to a maximum of 18 μm for the smooth wall. The diameter of the probe volume, therefore, ranged from 10 viscous lengths for the algae covered surface to 5 viscous lengths for the smooth wall. The LDV probe was mounted on an AMPRO System 1618, three-axis traverse unit. The traverse allowed the position of the probe to be maintained to ± 5 μm in all directions. In order to facilitate two-component, near wall measurements, the probe was tilted downwards at an angle of 4 deg to the horizontal and was rotated 45 deg about its axis. Using this setup, measurements were made as close as 50 μm to the wall. Velocity measurements were conducted in coincidence mode with 30,000 random samples per location. Doppler bursts for the two channels were required to fall within a 40 μs coincidence window or the sample was rejected.

In this study, two methods were used to determine the skin friction coefficient, C_f, for each of the test specimens. For the smooth surface, C_f was found using the Clauser chart method with the log-law constants $\kappa=0.41$ and $B=5.0$. The total stress method, as presented in Ligrani and Moffat [12], was used to verify these results. For the rough walls, C_f and ε were obtained using the modified Clauser chart procedure given by Perry and Li [13]. Again, the total stress method was used to verify the C_f values obtained using the modified Clauser chart. The roughness functions for the rough wall profiles were obtained using the law of the wall (Eq. (3)) with the previously obtained values of U_τ and ε.

$$U^+=\frac{1}{\kappa}\ln(y+\varepsilon)^+ + B - \Delta U^+ \tag{3}$$

The boundary layer thickness and Coles' wake parameter for all of the profiles was then found by using a nonlinear least squares algorithm to fit the experimental data from the overlap region out to ~0.9δ to Coles' law of the wake in universal defect form (Eq. (4)).

$$\frac{U_e-U}{U_\tau}=-\frac{1}{\kappa}\ln\left[\frac{(y+\varepsilon)}{\delta}\right]+\frac{2\Pi}{\kappa}\left[\cos^2\left(\frac{\pi}{2}\frac{(y+\varepsilon)}{\delta}\right)\right] \tag{4}$$

Uncertainty Estimates

Precision uncertainty estimates for the velocity measurements were made using repeatability tests. Ten replicate profiles were taken on both a smooth and a rough plate. The standard error for each of the measurement quantities was then calculated for both samples. In order to estimate the 95 percent confidence limits for a statistic calculated from a single profile, the standard error was multiplied by the two-tailed t value ($t=2.262$) for 9 degrees of freedom and $\alpha=0.05$, as given by Coleman and Steele [14]. The resulting precision uncertainties in the mean velocities were ±0.7 percent in the outer region of the boundary layer and ±1.5 percent in the near-wall region. For $\overline{u'^2}$ and $\overline{v'^2}$, the precision was ±1.4

Table 1 Description of test surfaces

Specimen	k (mm)	St. Dev. (mm)	% Roughness Coverage	Description
Smooth	NA	NA	NA	Cast acrylic surface
#240 grit sandpaper	0.07	0.03	100	#240 grit commercial wet/dry sandpaper
#36 grit sandpaper	0.93	0.11	100	#36 grit commercial wet/dry sandpaper
Algae #1	6.4	1.3	50	filamentous, green algae (*Enteromorpha spp.*) with underlying diatomaceous slime film; individual algae filaments up to 71 mm in length
Algae #2	3.8	0.4	35	filamentous, green algae (*Enteromorpha spp.*) with underlying diatomaceous slime film; individual algae filaments up to 58 mm in length

percent in the outer region and ±2.7 percent in the near-wall region. The precision uncertainty in $\overline{u'v'}$ was ±5 percent.

LDV measurements are also susceptible to a variety of bias errors including fringe bias, validation bias, velocity bias, and velocity gradient bias. Fringe bias is due to the fact that scattering particles passing through the measurement volume at large angles may not be measured since several fringe crossing are needed to validate a measurement. In this experiment, the fringe bias was considered insignificant, as the beams were shifted well above the burst frequency representative of twice the freestream velocity (Edwards [15]). Validation bias results from filtering too close to the signal frequency and any processor biases. In general these are difficult to estimate and vary from system to system. No corrections were made to account for validation bias. Velocity bias results from the greater likelihood of high velocity particles moving through the measurement volume during a given sampling period. The present measurements were burst transit time weighted (Buchhave et al. [16]) to correct for velocity bias. Velocity gradient bias is due to variation in velocity across the measurement volume. The correction scheme of Durst et al. [17] was used to correct u'. The corrections to the mean velocity and the other turbulence quantities were quite small and therefore neglected. An additional bias error in the v' measurements of ~2 percent was caused by introduction of the w' component due to inclination of the LDV probe.

The uncertainties in C_f for the smooth walls using the Clauser chart and the total stress method were ±5 percent and ±7 percent, respectively. The uncertainties in C_f for the rough walls using the modified Clauser chart and the total stress method were ±10 percent and ±13 percent, respectively. The increased uncertainty for the rough walls resulted mainly from the extra two degrees of freedom (ε and ΔU^+) in the analysis. The uncertainties in δ, δ^*, and θ were ±8 percent, ±5 percent, and ±6 percent, respectively.

Results and Discussion

The bulk flow parameters for the five test specimens are given in Table 2. The displacement, momentum, and boundary layer thickness for the algae-covered surfaces were all significantly increased with respect to the smooth wall values. The average increases in δ^*, θ, and δ for algae #1 were 81 percent, 57 percent, and 18 percent, respectively. For algae #2, the increases in δ^*, θ, and δ were 83 percent, 58 percent, and 19 percent above the smooth wall values. Results from Lewkowicz and Das [7], on a simulated filamentous algae layer, showed that it increased the boundary layer thickness by 25 percent to 30 percent above that of a background roughness.

In the present study, increases in the mean values of δ^*, θ, and δ were also noted on the sandgrain rough surfaces, although not to as great an extent. Only slight increases in the integral length scales and boundary layer thickness, all of which fell within the uncertainty of the measurements, were noted on the 240-grit surface. Average increases in δ^* and θ of 53 percent and 34 percent, respectively, were found on the 36-grit surface. The boundary layer thickness was also increased slightly on this surface, but the increase was not significant given the uncertainty in the measurement.

Figure 1 presents C_f versus Re_θ for all the test surfaces using the Clauser chart methods. The results of Coles [18] are also shown for comparison. It is of note that good agreement between the Clauser chart (or modified Clauser chart) and the total stress method was seen for most of the profiles. The mean absolute difference in C_f from the two methods was 3 percent for the smooth surface, 4 percent for the sandgrain rough surfaces, and 6 percent for the algae-covered surfaces. The skin friction coefficients for algae #1 averaged 125 percent higher than the smooth wall values, while algae #2 averaged 110 percent higher. The increase in C_f for 36-grit sand roughness averaged 84 percent. The skin friction coefficients for the 240-grit sand roughness were

Table 2 Boundary layer parameters

Specimen	x (m)	U_e (ms^{-1})	Re_θ	δ (mm)	δ* (mm)	θ (mm)	H
Smooth	1.15	1.50	4020	28	3.7	2.8	1.35
	1.30	1.53	4400	31	4.0	3.0	1.33
	1.45	1.46	4700	33	4.4	3.4	1.31
	1.60	1.50	5250	36	4.8	3.7	1.32
	1.75	1.53	5570	38	5.0	3.8	1.29
240-grit	1.15	1.56	4870	29	4.2	3.1	1.35
	1.30	1.55	5150	32	4.4	3.3	1.35
	1.45	1.53	5410	33	4.6	3.5	1.34
	1.60	1.56	5730	36	4.8.	3.6	1.33
	1.75	1.56	6130	39	4.9	3.8	1.28
36-grit	1.15	1.60	6510	30	5.5	3.7	1.50
	1.30	1.61	6890	33	6.0	3.9	1.55
	1.45	1.59	8130	35	6.7	4.6	1.48
	1.60	1.60	8850	39	7.4	4.9	1.53
	1.75	1.61	9390	42	7.8	5.3	1.48
Algae #1	1.15	1.61	6400	30	5.4	3.5	1.53
	1.30	1.64	8270	34	7.0	4.5	1.56
	1.45	1.67	9910	40	8.4	5.3	1.58
	1.60	1.66	11700	45	9.2	6.3	1.47
	1.75	1.70	13020	49	10.1	6.8	1.49
Algae #2	1.15	1.56	7270	30	6.1	4.0	1.53
	1.30	1.54	8850	36	7.5	4.9	1.55
	1.45	1.56	9680	40	8.1	5.3	1.54
	1.60	1.59	11070	44	9.0	5.9	1.53
	1.75	1.53	11380	48	9.4	6.3	1.49

9 percent higher than the smooth wall, but this is not a significant difference given the experimental uncertainty. It should be noted that the present smooth wall C_f results averaged 3 percent higher than those of Coles [18].

Figures 2 and 3 show the mean velocity profiles for algae #1 and #2 as they develop downstream. Included for comparison is Eq. (5), the smooth wall log-law using the Stanford Conference values for the slope and intercept (Coles [19]).

$$U^+ = 5.62 \log y^+ + 5.0 \tag{5}$$

One feature of interest in these graphs is the roughness function. The results of Schultz and Swain [9] showed erratic streamwise variation in ΔU^+ for turbulent boundary layers developing over slime films. The authors attributed this to the heterogeneous

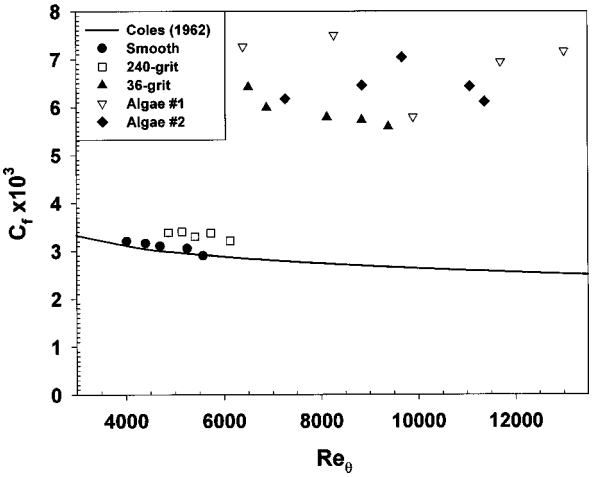

Fig. 1 Skin friction coefficient versus momentum thickness Reynolds number for the five test specimens (uncertainties in C_f: ±5 percent for the smooth specimen; ±10 percent for fouled profiles)

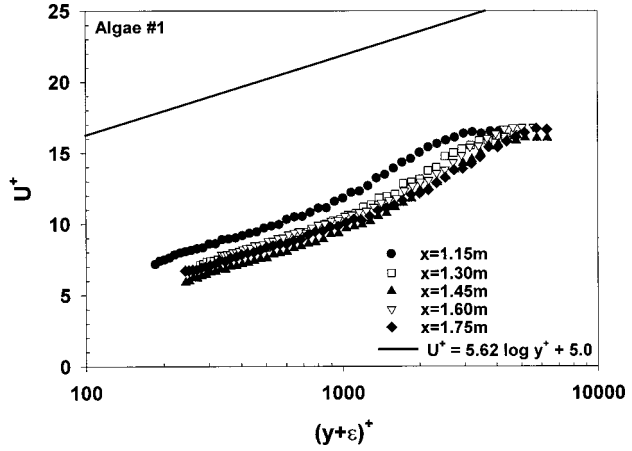

Fig. 2 Mean velocity profiles for algae #1 (uncertainty in U^+ ±7 percent)

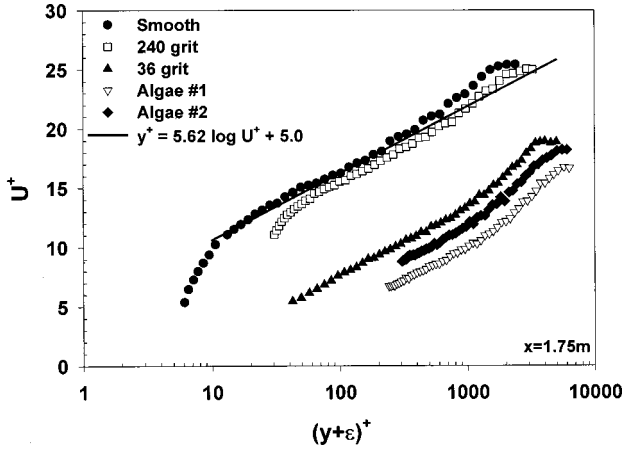

Fig. 4 Mean velocity profiles for the five test specimens @ $x = 1.75$ m (uncertainty in U^+: ±4 percent for the smooth surface; ±7 percent for the rough surfaces)

nature of the biofilms that were tested. The present results were taken on fairly uniform, filamentous algae layers, and the erratic behavior of the roughness function is notably absent. Figure 4 shows the mean velocity profiles for all five test specimens at $x = 1.75$ m. The figure illustrates that the roughness functions for the two algae-covered plates were larger than for the sandgrain rough surfaces.

The roughness functions for the rough test surfaces are presented in Fig. 5. Also included are the roughness functions for uniform sand roughness as given by Colebrook and White [20], Schlichting [21], and Bandyopadhyay [22]. It was not the primary aim of the present investigation to develop relationships that correlate some physical measure of algae to their roughness function. To attempt this would require measurements over a much larger U_τ range than were taken in this study. It is interesting, however, to see how the present results compare those of standard roughness types. The scatter in the values of ΔU^+ versus k^+ was larger for the algae-covered specimens than for the sandgrain rough specimens. This is likely due to nonuniformities in the thickness and composition of the algae surface. The results of Schultz and Swain [9] on highly heterogeneous slime roughness showed significantly more scatter than the present results.

Profiles of the turbulent normal stresses, $\overline{u'^2}/U_\tau^2$ and $\overline{v'^2}/U_\tau^2$, and the turbulent shear stress, $\overline{-u'v'}/U_\tau^2$, for algae #1 are presented in Figs. 6, 7, and 8, respectively. The graphs are shown to illustrate the downstream development in the turbulence quantities

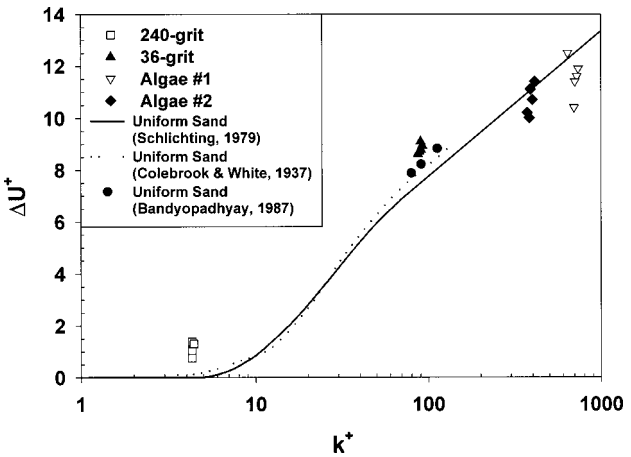

Fig. 5 Roughness functions for the test specimens (uncertainty in ΔU^+ ±13 percent)

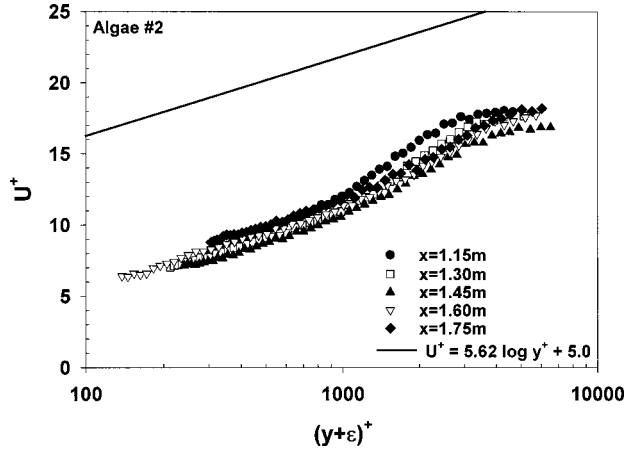

Fig. 3 Mean velocity profiles for algae #2 (uncertainty in U^+ ±7 percent)

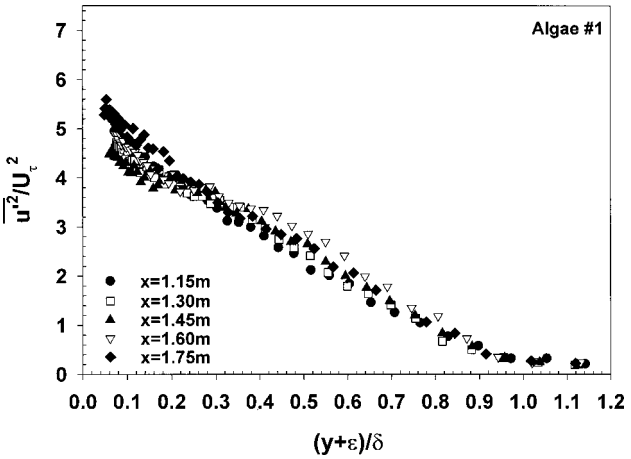

Fig. 6 Turbulent normal stress $\overline{u'^2}/U_\tau^2$ for algae #1 (uncertainty in $\overline{u'^2}/U_\tau^2$ ±10 percent)

over the filamentous algae layer. Similar results were also obtained for algae #2. Although there is some scatter, the results indicate that the turbulence profiles over these algae layers reach a nearly self-similar state.

The profiles of the turbulent normal stress, $\overline{u'^2}/U_\tau^2$, for all the

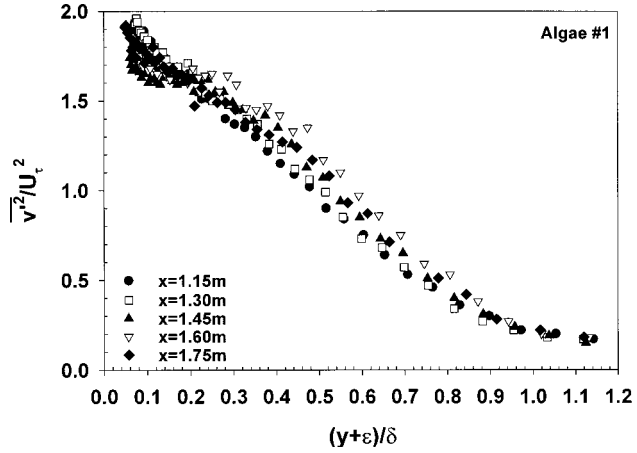

Fig. 7 Turbulent normal stress $\overline{v'^2}/U_\tau^2$ for algae #1 (uncertainty in $\overline{v'^2}/U_\tau^2$ ±10 percent)

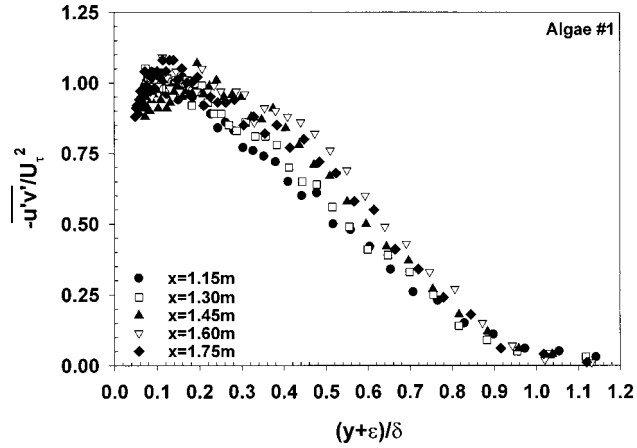

Fig. 8 Turbulent shear stress $-\overline{u'v'}/U_\tau^2$ for algae #1 (uncertainty in $-\overline{u'v'}/U_\tau^2$ ±11 percent)

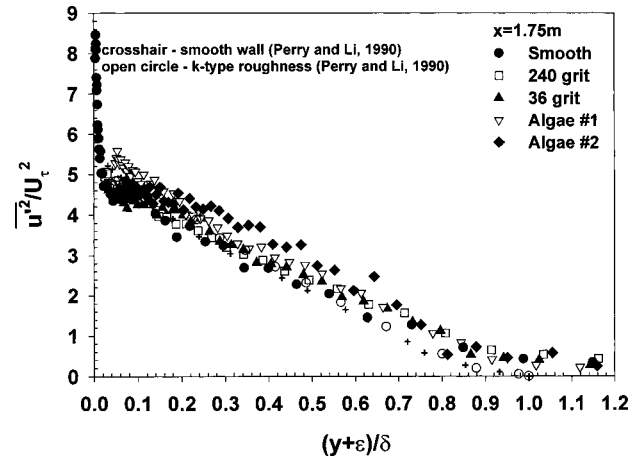

Fig. 9 Turbulent normal stress $\overline{u'^2}/U_\tau^2$ for all the test surfaces @ $x=1.75$ m (uncertainty in $\overline{u'^2}/U_\tau^2$: ±6 percent for the smooth surface; ±10 percent for the rough surfaces)

test surfaces at $x=1.75$ m are shown in Fig. 9. Also included in the graph are the data of Perry and Li [13] for a smooth wall and a *k*-type, mesh roughness. Reasonable agreement between the present results and those of Perry and Li is seen. The exceptions are the algae covered surfaces. Algae #1 showed a modest increase in $\overline{u'^2}/U_\tau^2$ near the roughness layer, and algae #2 exhibited an increase in $\overline{u'^2}/U_\tau^2$ over a larger region of the boundary layer. The present experimental results also agree qualitatively with those of Krogstad et al. [23] who found only a modest change in $\overline{u'^2}/U_\tau^2$ for a mesh-type roughness compared to a smooth wall boundary layer.

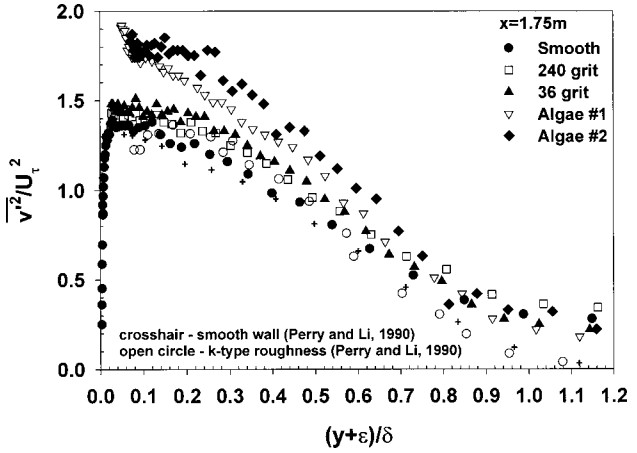

Fig. 10 Turbulent normal stress $\overline{v'^2}/U_\tau^2$ for all the test surfaces @ $x=1.75$ m (uncertainty in $\overline{v'^2}/U_\tau^2$: ±6 percent for the smooth surface; ±10 percent for the rough surfaces)

Profiles of the turbulent normal stress, $\overline{v'^2}/U_\tau^2$, for all the test surfaces at $x=1.75$ m are shown in Fig. 10. The results of Perry and Li [13] are included for comparison. Agreement among the present smooth and sandgrain rough results and those of Perry and Li was seen. Both algae-covered surfaces showed significant increases in $\overline{v'^2}/U_\tau^2$ over both the smooth and sandgrain rough surfaces. The increase amounted to ~ 30 percent near the roughness layer and was observed well out into the outer region of the boundary layer. Image analysis of the video clips of the algae under flow indicates that the maximum extent of outward movement of the filaments during turbulent bursts was $\sim 0.18\delta$ and $\sim 0.15\delta$ for algae #1 and #2, respectively, at $x=1.75$ m. The region of significantly increased $\overline{v'^2}/U_\tau^2$ extends to >2.5 times the maximum extent of outward movement of the filaments. It is of note that Krogstad et al. [23] also observed a significant increase in $\overline{v'^2}/U_\tau^2$ for fully-rough boundary layer flow over mesh roughness. Krogstad and Antonia [24] concluded that the major effect

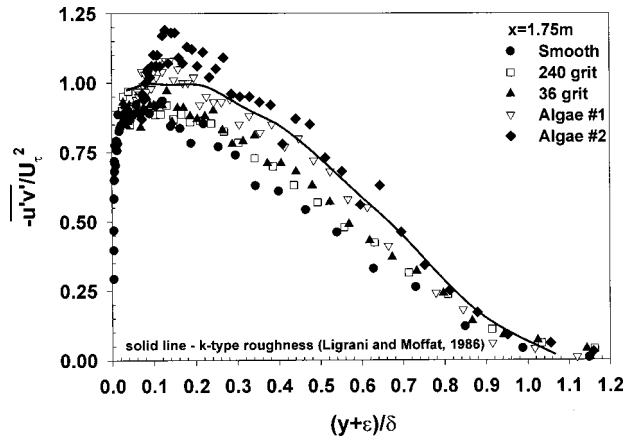

Fig. 11 Turbulent shear stress $-\overline{u'v'}/U_\tau^2$ for all the test surfaces @ $x=1.75$ m (uncertainty in $-\overline{u'v'}/U_\tau^2$: ±7 percent for the smooth surface; ±11 percent for the rough surfaces)

of this roughness was to tilt the large-scale structures towards the wall-normal direction, leading to a higher degree of isotropy and higher values of v'. This was not observed in the present results over the sandgrain roughness but was apparent in the flows over the algae-covered surfaces. The results of Schultz and Swain [9] indicated increases in both $\overline{u'^2}/U_\tau^2$ and $\overline{v'^2}/U_\tau^2$ for boundary layers over biofilms, although there was large degree of variability in their results.

Profiles of the turbulent shear stress, $\overline{-u'v'}/U_\tau^2$, for the test surfaces at $x=1.75$ m are shown in Fig. 11. The results of Ligrani and Moffat [12] for a fully-rough boundary layer on a uniform spheres rough surface are also included. Fairly good collapse of the smooth and sandgrain rough surfaces to single curve was observed. These profiles fell somewhat below the results of Ligrani and Moffat. This may have been due to Reynolds number effects. The results of Ligrani and Moffat are for a fully-rough boundary layer at $\mathrm{Re}_\theta=18{,}700$. The present values of Re_θ were significantly less ($\mathrm{Re}_\theta \leqslant 9{,}300$). It is interesting to note that Krogstad et al. [23] observed a moderate increase in the Reynolds shear stress for flows over a mesh *k*-type roughness. This was attributed to both an increase in the magnitude of the burst and sweep events and the frequency of these events. In the present study, a significant increase was observed in the Reynolds shear stress for the algae-covered surfaces in the log-law region. The increase was more variable for $\overline{-u'v'}/U_\tau^2$ than for $\overline{v'^2}/U_\tau^2$. Algae #1 had an increase of ~17 percent in $\overline{-u'v'}/U_\tau^2$ at 0.1δ as compared to the smooth and sandgrain rough walls. There was an increase of ~30 percent for algae #2 in the same region. A greater degree of scatter was seen in the algae profiles, and this can be attributed to the dynamic nature of the algae surface while under flow. It is of note that the peak in $\overline{-u'v'}/U_\tau^2$ corresponds approximately to the maximum extent of outward movement of the algae filaments.

In a recent study on a smooth wall and two rough walls (rods and mesh) with the same roughness function, Krogstad and Antonia [25] found that $\overline{u'^2}/U_\tau^2$ was largely unaffected by the nature of the surface except near the wall. However, they found significant differences in profiles of $\overline{v'^2}/U_\tau^2$ and $\overline{-u'v'}/U_\tau^2$ that extended well into the outer region of the boundary layer. It is interesting to note that the present algae results showed similar trends for all of these turbulence quantities.

Conclusion

Comparisons of turbulent boundary layers developing over filamentous marine algae with smooth and sandgrain rough surfaces have been made. A significant increase in C_f was measured for the algae-covered surfaces as compared with the smooth wall results. The increase averaged 125 percent and 110 percent for the two algae specimens tested. A significant increase was also noted in δ^*, θ, and δ for these surfaces. The present results show that the profiles of $\overline{u'^2}/U_\tau^2$, $\overline{v'^2}/U_\tau^2$, and $\overline{-u'v'}/U_\tau^2$ for boundary layers over the smooth and sandgrain rough walls collapse within experimental uncertainty. The algae-covered surfaces exhibited only a modest increase in $\overline{u'^2}/U_\tau^2$. More sizeable increase in $\overline{v'^2}/U_\tau^2$ and $\overline{-u'v'}/U_\tau^2$ were observed in the log-law region of the boundary layer. The region of increased $\overline{v'^2}/U_\tau^2$ extended well into the outer region (>2.5 times the maximum extent of outward movement of the algae filaments). The peak in the $\overline{-u'v'}/U_\tau^2$ profiles corresponded with the maximum extent of outward movement of the algae filaments. The present profiles of the turbulence quantities indicate that boundary layers over fairly uniform filamentous algae may become nearly self-similar. The roughness functions for these algae layers behave like *k*-type roughness, scaling to some degree on their mean height while under flow. Scatter in the roughness functions of these surfaces indicates that further research is needed to better correlate the physical measures of the algae layer with their roughness function.

Acknowledgments

I would like to thank the Division of Bioengineering and Environmental Systems at the National Science Foundation (grant BES9713110) and Prof. S. N. Gangadharan of Embry-Riddle Aeronautical University for supporting this research. Harbor Branch Foundation is also acknowledged for supporting the project with a postdoctoral fellowship for the author. Thanks go to B. Kovach at the Center for Corrosion and Biofouling Control at Florida Institute of Technology for measuring the surface profiles of the sandgrain rough surfaces. I also gratefully acknowledge Prof. P. Bradshaw, Prof. K. Flack, and Prof. C. Subramanian for reviewing drafts of this manuscript and providing many useful suggestions.

Nomenclature

B = log-law intercept
C_f = skin friction coefficient $=(\tau_0)/(1/2\rho U_e^2)$
E = elastic or Young's modulus
H = shape factor $=\delta^*/\theta$
I = moment of inertia of cross section of algae filament
k = roughness height
k_0 = undeflected roughness height
m = roughness density parameter
Re_θ = momentum thickness Reynolds number $=\theta U_e/\nu$
t = *t*-statistic
U, V = mean velocity in the x and y direction
U_e = freestream velocity
ΔU^+ = roughness function
u, v = instantaneous velocity in the x and y direction
u', v' = fluctuating velocity component in the x and y direction
U_τ = friction velocity $=\sqrt{\tau_0/\rho}$
x = streamwise distance from plate leading edge
y = normal distance from the boundary
α = statistical significance level
δ = boundary layer thickness
δ^* = displacement thickness
ε = wall datum error
κ = von Karman constant (=0.41)
ν = kinematic viscosity of the fluid
θ = momentum thickness
ρ = density of the fluid
τ_0 = wall shear stress

Superscript

$+$ = inner variable (normalized with U_τ or ν/U_τ)

References

[1] Callow, M. E., 1996, ''Ship Fouling: The Problem and Methods of Control,'' Biodeter. Abstracts, **10**, No. 4, pp. 411–421.
[2] Callow, M. E., 1986, ''Fouling Algae from 'In-Service' Ships,'' Botanica Marina, **24**, pp. 443–503.
[3] Schultz, M. P., 1998, ''The Effect of Biofilms on Turbulent Boundary Layer Structure,'' Florida Institute of Technology, Ph.D. Dissertation, May.
[4] Raupach, M. R., and Thom, A. S., 1981, ''Turbulence in and above Plant Canopies,'' Annu. Rev. Fluid Mech., **13**, pp. 97–129.
[5] Raupach, M. R., Antonia, R. A., and Rajagopalan, S., 1991, ''Rough-Wall Turbulent Boundary Layers,'' Appl. Mech. Rev., **44**, No. 1, pp. 1–25.
[6] Kouwen, N., and Unny, T. E., 1973, ''Flexible Roughness in Open Channels,'' ASCE J. Hydraul. Div., **99**, No. HY5, May, pp. 713–728.
[7] Lewkowicz, A. K., and Das, D. K., 1986, ''Turbulent Boundary Layers on Rough Surfaces With and Without a Pliable Overlayer: A Simulation of Marine Fouling,'' Int. Shipbuild. Prog., **33**, pp. 174–186.
[8] Ikeda, S., and Kanazawa, M., 1996, ''Three-Dimensional Organized Vortices above Water Plants,'' ASCE J. Hydrau. Eng., **122**, No. 11, pp. 625–633.
[9] Schultz, M. P., and Swain, G. W., 1999, ''The Effect of Biofilms on Turbulent Boundary Layers,'' ASME J. Fluids Eng., **121**, pp. 44–51.
[10] Gangadharan, S., Wimberly, C. R., Clark, A., and Collino, B., 1996, ''Design, Construction and Operation of a Cost Effective Water Tunnel at Harbor Branch Oceanographic Institution,'' Paper presented at SNAME Southeast Section Meeting, Oct. 11, Fort Pierce, FL.
[11] Klebanoff, P. S., and Diehl, F. W., 1951, ''Some Features of Artifically Thickened Fully Developed Turbulent Boundary Layers with Zero Pressure Gradient,'' NACA TN 2475.

[12] Ligrani, P. M., and Moffat, R. J., 1986, ''Structure of Transitionally Rough and Fully Rough Turbulent Boundary Layers,'' J. Fluid Mech., **162**, pp. 69–98.
[13] Perry, A. E., and Li, J. D., 1990, ''Experimental Support for the Attached-Eddy Hypothesis in Zero-Pressure Gradient Turbulent Boundary Layers,'' J. Fluid Mech., **218**, pp. 405–438.
[14] Coleman, H. W., and Steele, W. G., 1995, ''Engineering Application of Experimental Uncertainty Analysis,'' AIAA J., **33**, No. 10, pp. 1888–1896.
[15] Edwards, R. V., 1987, ''Report of the Special Panel on Statistical Particle Bias Problems in Laser Anemometry,'' ASME J. Fluids Eng., **109**, pp. 89–93.
[16] Buchhave, P., George, W. K., and Lumley, J. L., 1979, ''The Measurement of Turbulence with the Laser-Doppler Anemometer,'' Annu. Rev. Fluid Mech., **11**, pp. 443–503.
[17] Durst, F., Fischer, M., Jovanovic, J., and Kikura, H., 1998, ''Methods to Set Up and Investigate Low Reynolds Number, Fully Developed Turbulent Plane Channel Flows,'' ASME J. Fluids Eng., **120**, pp. 496–503.
[18] Coles, D., 1962, ''The Turbulent Boundary Layer in a Compressible Fluid,'' The Rand Corp., Rep. R-403-PR.
[19] Coles, D. 1969, ''The Young Person's Guide to the Data,'' Computation of Turbulent Boundary Layers–1968 AFOSR-IFP Stanford Conference, Vol. 2, D.E. Coles and E.A. Hirst, eds., Thermosciences Division, Stanford University, pp. 1–45.
[20] Colebrook, C. F., and White, C. M., 1937, ''Experiments with Fluid Motion in Roughened Pipes,'' Proc. R. Soc. London, Ser. A **161**, pp. 367–381.
[21] Schlichting, H., 1979, *Boundary-Layer Theory*, Seventh Edition, McGraw-Hill.
[22] Bandyopadhyay, P. R., 1987, ''Rough-Wall Turbulent Boundary Layers in the Transition Regime,'' J. Fluid Mech., **180**, pp. 231–266.
[23] Krogstad, P. A., Antonia, R. A., and Browne, L. W. B., 1992, ''Comparison Between Rough- and Smooth-Wall Turbulent Boundary Layers,'' J. Fluid Mech., **245**, pp. 599–617.
[24] Krogstad, P. A., and Antonia, R. A., 1994, ''Structure of Turbulent Boundary Layers on Smooth and Rough Walls,'' J. Fluid Mech., **277**, pp. 1–21.
[25] Krogstad, P. A., and Antonia, R. A., 1999, ''Surface Roughness Effects in Turbulent Boundary Layers,'' Exp. Fluids, **27**, pp. 450–460.

High Pressure Annular Two-Phase Flow in a Narrow Duct: Part I—Local Measurements in the Droplet Field

Thomas A. Trabold
Project Manager,
Xerox Corporation,
Rochester, NY 14580

Ranganathan Kumar
Senior Engineer
Lockheed Martin Corporation,
Schenectady, NY 12301

Detailed measurements have been made in a high pressure, adiabatic (boiled at the inlet) annular flow in a narrow, high aspect ratio duct using a gamma densitometer, hot-film anemometer and high-speed video photography. Measurements of void fraction, droplet frequency, velocity, drop size, and interfacial area concentration have been made to support the three-field computational capability. An important aspect of this testing is the use of a modeling fluid (R-134a) in a vertical duct which permits visual access in annular flow. This modeling fluid accurately simulates the low liquid-to-vapor density ratio of steam-water flows at high pressures. These measurements have been taken in a narrow duct of hydraulic diameter 4.85 mm, and a cross-section aspect ratio of 22.5. However, the flow displays profiles of various shapes not only in the narrow dimension, but also in the width dimension. In particular, the shape of the void profiles depends on the entrained droplet flux from the edges in the vapor core. The average diameter from these profiles compare well with the models developed in the literature. Interfacial area concentration for these low density ratio flows is higher than the highest concentration reported for air-water flows. Video records show that along with the bow-shaped waves, three-dimensional λ-shaped waves appear in annular flows for high flow rates.
[S0098-2202(00)00902-0]

Introduction

The inception of wall-heated two-phase annular flow occurs through a complex flow regime transition. The annular flow regime consists of a liquid film on the wall and a vapor core with droplets formed from the shearing of the roll waves. Hewitt and Hall-Taylor [1] discussed the physical mechanisms that occur in annular flow and the physical models that describe these mechanisms. In order to delineate the heat transfer effects, researchers have performed adiabatic tests in two immiscible fluids such as air and water. In fact, most of the correlations and models in annular flow such as interfacial shear, entrainment/deposition and droplet motion have been validated using air-water experiments. However, to date, the integrated effects of these physical mechanisms in annular flow have not been captured and compared with local measurements of void fraction and droplet velocity.

While the flow pattern in air-water annular flows is qualitatively similar to that of heated annular flow in that the liquid film stays on the wall, enclosing a vapor core, there could be significant differences in the local variables measured due to density ratio effects. Development of mechanistic models for multidimensional computer codes for predicting two-phase flows in many heated systems relies on local measurements of variables in high pressure flows. Since it is difficult to measure local quantities in steam-water flows at high pressure, this paper concentrates on annular flow measurements in a refrigerant fluid, R-134a, with the same density ratio as steam-water at high pressures.

Most of the measurements available in the literature have been made for circular tubes. In rectangular geometries, for some flow conditions, the collection of liquid at the edges allows the liquid film to have different thicknesses and the roll waves to have different amplitudes. Consequently, the droplet disintegration mechanism in noncircular geometries is nonisotropic and three-dimensional. There is a need to generate such data in the literature for the development of entrainment and drop size models for noncircular geometries.

The objectives of this paper are to: 1) extend the existing data base in annular flows to high pressure adiabatic boiling flows (high vapor-to-liquid density ratios); and 2) provide detailed local measurements of void fraction, droplet frequency, droplet velocity, drop diameter and interfacial area density using hot film anemometry for a wide range of flow rates and two system pressures. Some of these measurements are used for comparison with the numerical results presented in Part II of the current paper (Kumar and Trabold [2]). This study expands upon previous work (Trabold et al. [3]) by considering two system pressures of 2.4 MPa and 1.4 MPa, and profiles across the wide test section dimension, which sheds light on the three-dimensionality of the flow in thin, high aspect ratio, vertical ducts.

It is important to emphasize that the two-phase flow system considered in this study involves fluid physical properties for which very few detailed local data exist. At 1.4 and 2.4 MPa, R-134a has a liquid-to-vapor density ratio of 16.2 and 7.3, respectively, compared to a ratio of about 850 for atmospheric pressure air-water. Similarly, the surface tension of R-134a is 0.0048 and 0.0021 N/m at 1.4 and 2.4 MPa, respectively, compared with 0.072 for water at atmospheric conditions. As is demonstrated throughout the discussion that follows, these physical properties have significant effects on two-phase flow dynamics.

Experimental Apparatus and Measurement Systems

The experimental investigation was performed to assist in developing and validating individual closure models, as well as to qualify the integrated prediction capability of the three-field approach in annular flow provided in Part II of this paper.

Test Section. The test section (Fig. 1) was designed to be flat and narrow for easy optical access and to separate out edge ef-

Contributed by the Fluids Engineering Division for publication in the JOURNAL OF FLUIDS ENGINEERING. Manuscript received by the Fluids Engineering Division December 4, 1998; revised manuscript received January 25, 2000. Associate Technical Editor: M. Sommerfeld.

fects. The test section has a length of 1.2 m, a cross-section aspect ratio of 22.5, and a hydraulic diameter of 4.85 mm. Optical access to the flow is provided by eight quartz windows, each 38.1 mm thick by 76.2 mm wide by 0.28 m long. The center 57.2 mm of the windows comprises the transverse (Y) dimension of the flow duct. The working fluid used in this study is refrigerant R-134a (1,1,1,2-tetrafluoroethane) which, aside from its practical importance, is of scientific interest because of its very low liquid-to-vapor density ratio and low surface tension (i.e., 7.3 and 0.0021 N/m, respectively, at 2.4 MPa). An instrument scanning mechanism positions most of the instrumentation about the test section at any vertical, streamwise location and permits scans in a horizontal plane transverse to the test section. Two-phase annular flow was created using heaters located upstream of the test section inlet. The absence of wall vapor generation makes it easier to evaluate momentum exchange models without considering heat transfer effects.

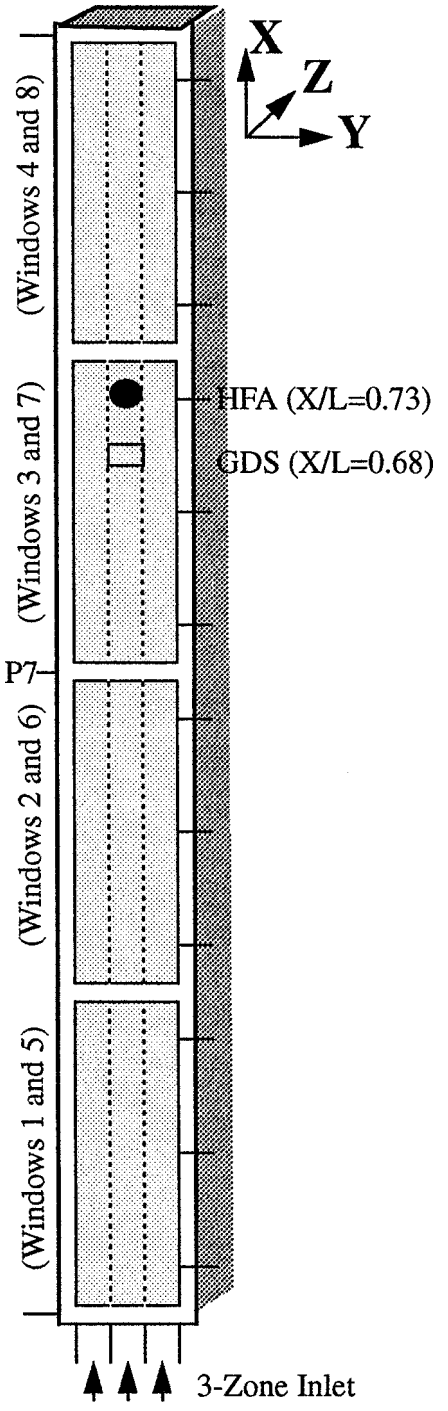

Fig. 1 Front view of the R-134a test section and measurement locations

Gamma Densitometer. A gamma densitometer system (GDS) is used to set the desired cross-section average void fraction in the test section, and also to compare the average of local void fractions obtained using the hot-film anemometer (HFA), described below. The GDS consists of a shielded 9 curie Cesium-137 source located on one side of the test section, and a Sodium Iodide (NaI) gamma detector on the other side. The gamma densitometer provides a direct density measurement of a two-phase mixture in the path of a gamma beam using the gamma beam intensities through the empty and two-phase-fluid-filled test section. The void fraction, α, at any given position through the test section is calculated from

$$\alpha = \frac{(\rho_l - \rho)}{(\rho_l - \rho_g)}. \tag{1}$$

The liquid and vapor phase densities, ρ_l and ρ_g are determined from a database for R-134a saturation properties at the measured test section exit temperature.

The gamma beam width can be changed by rotating the source collimator. The wide beam, when directed through the edge of the test section, interrogates the entire cross-section of the fluid and yields a measurement of the cross-sectional average void fraction. This measurement is first compared to the predicted average void fraction prior to comparisons of other variables. Void fraction data scans are also obtained in the narrow dimension (Y) using the narrow beam directed through the test section edge. These line-averaged measurements are used to compare integrated model predictions in Part II of this paper by Kumar and Trabold [2]. Two minute counting times were used for both wide and narrow beam edge measurements. The total uncertainty, based on a root-sum-square combination of precision (random) and systematic (bias) components at 95 percent confidence ($\pm 2\sigma$), was determined for each type of GDS measurement. The wide beam edge measurement was obtained twice and averaged for a total uncertainty of ± 0.017 in void fraction. For each narrow beam edge measurement, the total uncertainty is ± 0.032.

Hot-Film Anemometer. A constant temperature hot-film anemometer (HFA) has been used previously to measure void fraction in refrigerant fluids R-113 and R-134a (Trabold et al. [4,5]). This earlier work was extended to velocity and droplet size measurements in annular flow by Trabold et al. [3].

Void Fraction. In the current setup, a dual-sensor probe was installed at $X = 88.4$ cm ($182\, D_h$) in the center of the width dimension of the quartz window. This HFA probe consists of two active sensing elements which are separated in the streamwise dimension by some known distance. The sensors were made of platinum with 25 μm diameter and 254 μm active length. As described in detail in the earlier publications, a combined slope and level thresholding method originally proposed by Carvalho and Bergles [6] was used to analyze the HFA output voltage signals for determination of local vapor volume fraction. These measurements have been confirmed in bubbly, slug and annular flows through comparison between the integrated averages of local HFA data and line-average GDS measurements.

Droplet Velocity. The use of two sensors permits acquisition of interfacial velocity measurements based on the cross-correlation between two output voltage signals. The maximum in the cross-correlation function corresponds to the most probable time required for a gas-liquid interface to travel between the HFA sensors, from which the mean interfacial velocity is calculated.

The upstream sensor measures the void fraction and the droplet frequency, and the twin-sensor arrangement affords measurement of the droplet velocity.

Droplet Diameter. In addition to the local void fraction, a measurement of local liquid droplet frequency is also obtained by counting the number of positive voltage pulses per known measurement time (Trabold et al. [3]). Using the void fraction and frequency measurements from the upstream sensor, and velocity measurement from the dual sensor, the spherical equivalent droplet diameter can be calculated as

$$d_d = 1.5 \frac{V_d \alpha_d}{f_d}. \tag{2}$$

Droplet size measurements were limited to test runs for which a 50 kHz digitization rate of the voltage signal was used. Droplet size calculations are not reported for narrow dimension positions (Z in Fig. 1) where the presence of the wall and liquid film would influence the random motion of the dispersed liquid field. Since the probe position must be greater than one droplet diameter from the wall, drop diameter measurements are presented in Results and Discussion for $Z/t > 0.2$.

Interfacial Area Concentration. The interfacial area concentration (a_i) is of central importance in modeling the thermal-hydraulic behavior of two-phase flows. This parameter corresponds to the surface area between gas and liquid phases per volume of two-phase mixture, and as such has units of inverse length. For separated flows, such as the annular flows studied in the present work, quantification of a_i is complicated by the fact that two distinct fluid structures (interfacial waves and dispersed liquid droplets) contribute to the total interfacial area. The following discussion outlines how the parameters measured in the present set of experiments makes quantification of the droplet contribution to interfacial area possible, based on a set of simplifying assumptions.

Measurements of average interfacial area concentration in annular two-phase flow are quite limited and local annular flow data in rectangular geometries are nonexistent. Kataoka and Ishii [7] characterized the average interfacial area concentration in annular flow by combining contributions from interfacial waves and dispersed droplets:

$$\overline{a_i} = \frac{4 C_{an}}{D_h} \sqrt{\frac{\overline{\alpha}}{1-\overline{\alpha}_d}} + \frac{\overline{\alpha}}{1-\overline{\alpha}_d} \left(\frac{6 \overline{\alpha}_d}{d_{sm}} \right) \tag{3}$$

where C_{an} is a wave roughness parameter, $\overline{\alpha}_d$ is the average volume fraction of the dispersed droplet field and d_{sm} is the Sauter mean droplet diameter. If this expression is applied locally in the region of the flow where only the vapor core and droplets are present, the interfacial area density reduces to

$$a_i = \frac{6 \alpha_d}{d_{sm}} = \frac{4 f_d}{V_d}. \tag{4}$$

For small droplets, the Sauter mean and volume equivalent diameters are approximately the same. This relation has been used for interfacial area concentration measurements in bubbly flows, based on the assumptions of spherical bubbles and bubble velocity that is constant and possesses one component of flow direction only (Galaup [8], Kataoka and Serizawa [9], Cartellier and Achard [10]). The expression given in Eq. 4 was derived by Galaup [8] from purely geometrical considerations for bubbles in continuous liquid, and is valid for nondeformable and convex interfaces with no statistical correlation between bubble velocity and interface orientation. Equation 4 depends upon neither the dispersed phase size distribution nor the shape. Galaup [8] derived Eq. 4 for measurements of bubbles in air-water flows, where the characteristic size of the bubbles far exceeded the effective size of the measurement device. In the present experiments, there are conditions under which very small droplets (i.e., size of the same order as the 25 μm diameter HFA sensor) were measured and hence it is not reasonable to consider the droplets to be nondeformable. It is to be expected therefore that the largest error associated with the application of Eq. 4 will be for very small droplets, generally for average void fractions in excess of 90 percent. The behavior of liquid droplets upon interaction with the HFA sensor remains an open issue. Although in the process of deformation a droplet would lose some of its momentum, the generally close agreement between HFA and nonintrusive LDV velocity measurements (Trabold et al. [3]) suggests that the presence of the sensor has little effect on droplet motion.

Table 1 Uncertainty bands for measurements with hot-film anemometer

void fraction	• repeatability based on pooled standard deviation • biases: threshold voltage, small droplets, test section position, sampling time	±0.025
droplet frequency	• same as void fraction • also, droplet impaction bias	-79 to +90 Hz at w = 106 kg/hr -321 to +652 Hz at w = 532 kg/hr
droplet velocity	• repeatability • biases: velocity sampling, droplet size, cross-correlation, sensor spacing, test section position	-7.5% to +7.0% (near wall) -7.0% to +6.4% (far wall)

Measurement Uncertainty. The measurement uncertainty for all reported HFA data was calculated based on the root-sum-square uncertainty interval for 95 percent confidence:

$$U = \pm [B^2 + (t_{95} S_{\overline{x}})^2]^{1/2} \tag{5}$$

where B is the bias limit (systematic error) and $t_{95} S_{\overline{x}}$ is the precision limit (random error). The error sources considered, and the uncertainty bands associated with local HFA measurement, are summarized in Table 1. The measurement of droplet frequency is complicated by the analysis of variable amplitude voltage signals originating from droplets of different sizes, or glancing impactions of droplets on the HFA sensor. Therefore, some of the droplets striking the sensor may not produce measurable voltage peaks, thereby biasing the frequency measurement. Because of the somewhat greater uncertainty in the frequency data, the measurements of droplet diameter and interfacial area concentration, which are inferred from frequency and other measurements, also have a relatively large uncertainty.

Flow Visualization. A high speed video (HSV) system operated at 250 frames per second was used to obtain images of the annular flow through the quartz window. Backlighting was used with a strobe light source illuminating a white diffuser. These images were used to study the behavior of the disturbance waves that appeared as dark rings, and measure their frequency and velocity for different flow conditions. At high pressure and high flows, the liquid phase is comprised of a very dense field of small and large bubbles, and their interfaces scatter the incident light resulting in undistinguishable images. Hence, use of the HSV system was generally limited to lower mass flow rates.

Results and Discussion

Detailed local measurements were obtained in annular flow of R-134a through a thin, vertical duct with an aspect ratio of 22.5. The two system pressures investigated were 1.4 and 2.4 MPa, which provided comparable density ratios as found in many practical pressurized steam-water applications. The measurements made using a dual-sensor hot-film anemometer included local void fraction, droplet frequency and velocity. The hydraulic diameter of the test section is 4.85 mm, and the wall-bounded liquid film thickness for most cases extended to less than 0.5 mm from the wall. The closest measurement point to the wall for the current measurements is 0.15 mm. Although these dimensions are small compared to the 57.2 mm width (Y) dimension of the flow duct,

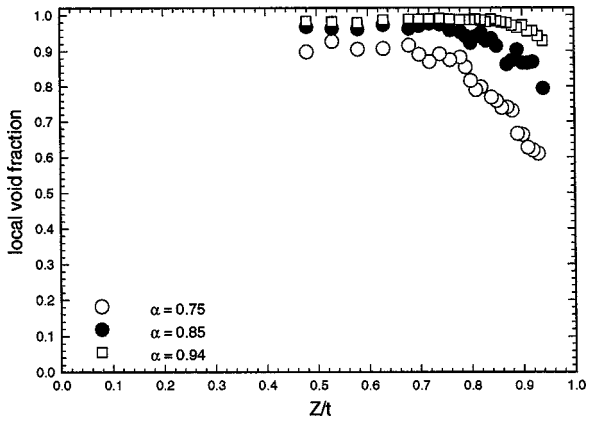

Fig. 2 Local *Z*-dimension void fraction distributions for $w = 106$ kg/hr and $P = 2.4$ MPa

void profiles in the narrow (Z) dimension provide insight to the dominating flow regime transition, droplet entrainment and dryout mechanisms. Another area of modeling interest is the magnitude of drop size and interfacial area density, both of which have been inferred from the local measurements and compared with available air-water data.

One of the most significant findings from the present R-134a experimental program is that the basic structure of the phase distribution across the narrow (Z) dimension is strongly dependent upon the mass flow rate, and is for many conditions significantly different from most previously published data. Local HFA Z-dimension void fraction profiles are shown in Fig. 2 for $w = 106$ kg/hr and $P = 2.4$ MPa, with the cross-sectional average void fraction varied by adjusting the power applied to heaters upstream of the test section inlet. Because of the flow symmetry, the measurements were only obtained to about duct centerline ($Z/t = 0.5$). At $\bar{\alpha} = 0.75$, the void profile is approximately parabolic as the flow undergoes transition from churn-turbulent to annular flow. As the average void fraction is increased from 0.75 to 0.85 and then to 0.92, the wall-bounded film thickness reduces, and the near-wall void fraction gradient decreases as the flatness in the profiles extends closer to the wall. The maximum local void fraction in each case increases as the average void fraction is increased as expected, but stays below 1.0 due to the presence of droplets shearing off the disturbance waves in the liquid film. The shapes of these profiles are generally consistent with most of the data published for low pressure flows, for example the air-water experiments of Jones and Zuber [11] conducted in a 0.51 by 6.35 cm rectangular duct.

Figure 3 shows the local void fraction profiles for a higher flow rate ($w = 532$ kg/hr) at two different pressures. For these experimental test runs, the HFA hardware was modified to afford traversing of the probe beyond the duct centerline, in order to confirm the flow symmetry. These two sets of profiles are compared with one another for the same average void fraction (as indicated in the lower left corner of each figure), and each profile is compared with the line-average void fraction measured using the gamma densitometer, as indicated in each figure by a horizontal dashed line. Considering first the measurements for 1.4 MPa in Fig. 3(a), as the void fraction is increased from $\bar{\alpha} = 0.7$ to 0.95, the flow appears to proceed through several distinct transitions in the two-phase flow structure. Although the $\bar{\alpha} = 0.70$ profile has the ''classic'' parabolic shape, similar to the $\bar{\alpha} = 0.75$ data illustrated in Fig. 2, the local data for an average void fraction of 0.80 show a distinct local maximum at $Z/t = 0.8$, with an approximately 6 percent void fraction decrease between this location and the duct centerline. As the average void fraction is increased to 0.95, the void fraction profile becomes ''inverted,'' with maximum void fraction near the wall and minimum void fraction at the duct centerline.

Now turning our attention to Fig. 3(b) for 2.4 MPa, the profiles are dramatically different from those for the lower pressure in Fig. 3(a) and those for the same pressure and lower flow rate in Fig. 2. These void profiles in Fig. 3(b) change shape from a center-peaked distribution for $\bar{\alpha} = 0.5$ during transition (not shown) to a near-wall maxima as the void fraction is increased to 0.71. This behavior results from the thinning of the liquid film with increasing mass flow, and the void inversion in the middle of the test section is mainly due to the large flux of entrained droplets from the edges. The thinning of the film was also observed on the high-speed video record. As the void fraction is increased to 0.8 and then 0.88 (highest void achievable for this pressure and flow rate), the inversion decreases slightly. The plots show that the magnitude of void fraction measured by HFA is significantly higher compared to the GDS cross-section average indicated by the dashed line in each figure. This suggests the presence of a thick liquid film near the two transverse (Y) edges. At $\bar{\alpha} = 0.88$, the void profile in the vapor core is approximately flat and two-dimensional, as the liquid film is depleted around the perimeter of the cross-section. As discussed previously by Trabold et al. [3], the distinct void fraction inversions measured for $w = 532$ kg/hr are related to the droplet entrainment mechanism. The production of dispersed droplets by shearing of the waves in the liquid film is ultimately dependent upon the liquid-to-gas density ratio, which for R-134a is 16.2 and 7.3 for $P = 1.4$ and 2.4 MPa, respectively, and the very low surface tension of 0.0048 and 0.0021 N/m at the same conditions. In the vast majority of experimental investigations for which local measurements are available, such as air-water and similar low pressure systems, this density ratio is on the order of 100 to 1000, and the surface tension is on the order of 0.01 to 0.1 N/m.

To understand the characteristics of the liquid film and the disturbance waves and other wave patterns in the annular flow field, high speed video pictures of the flow were viewed from the flat side of the test section through the quartz windows. Although the thickness of the liquid films, which are on the order of 0.15 mm to 0.5 mm for these flows, could not be directly measured, the types of wave surfaces, their velocity and frequency could be determined. At low void fractions ($\bar{\alpha} \sim 0.75$), as was noted in the center-peaked parabolic void profiles, the overall flow is still undergoing late stages of transition into the annular regime, although it is locally annular near the center. At higher void fraction ($\bar{\alpha} = 0.94$), sequential video pictures (one frame image is shown in Fig. 4) show that the waves appear as dark rough patches. The wave velocity is expected to be lower near the edges and maximum near the center, and hence the waves are clearly bow-shaped. The successive disturbance waves were counted, and the distance between two waves was measured over a period of time to obtain wave velocity and frequency. For a flow rate of 106 kg/hr, the wave frequency increases from 16 Hz to 34 Hz as the void fraction is increased from 0.71 to 0.94. As the flow rate is increased to 266 kg/hr, the wave frequencies for void fractions 0.71 and 0.82 are 50 Hz and 66 Hz, respectively. Thus, in general, the wave trends observed in high pressure refrigerant flows are similar to those of air-water flows, namely, the wave frequency increases with both gas flows (through increasing void fraction) and liquid flow rates (Hall-Taylor et al. [12], Hall-Taylor and Nedderman [13]). However, the superficial gas velocity for these cases is on the order of 1 to 2 m/sec. Compared to Okada et al.'s [14] wave frequency versus superficial gas velocity plot, the frequency in the current high gas density flows is significantly higher, consistent with Gill et al.'s [15] measurements in high gas density flows.

The average wave velocity measured from the video pictures for $\bar{\alpha} = 0.94$ is 0.57 m/s. For a neutrally stable film, using a simple force balance at the interface between the liquid film and the vapor core, the wave velocity can be obtained as

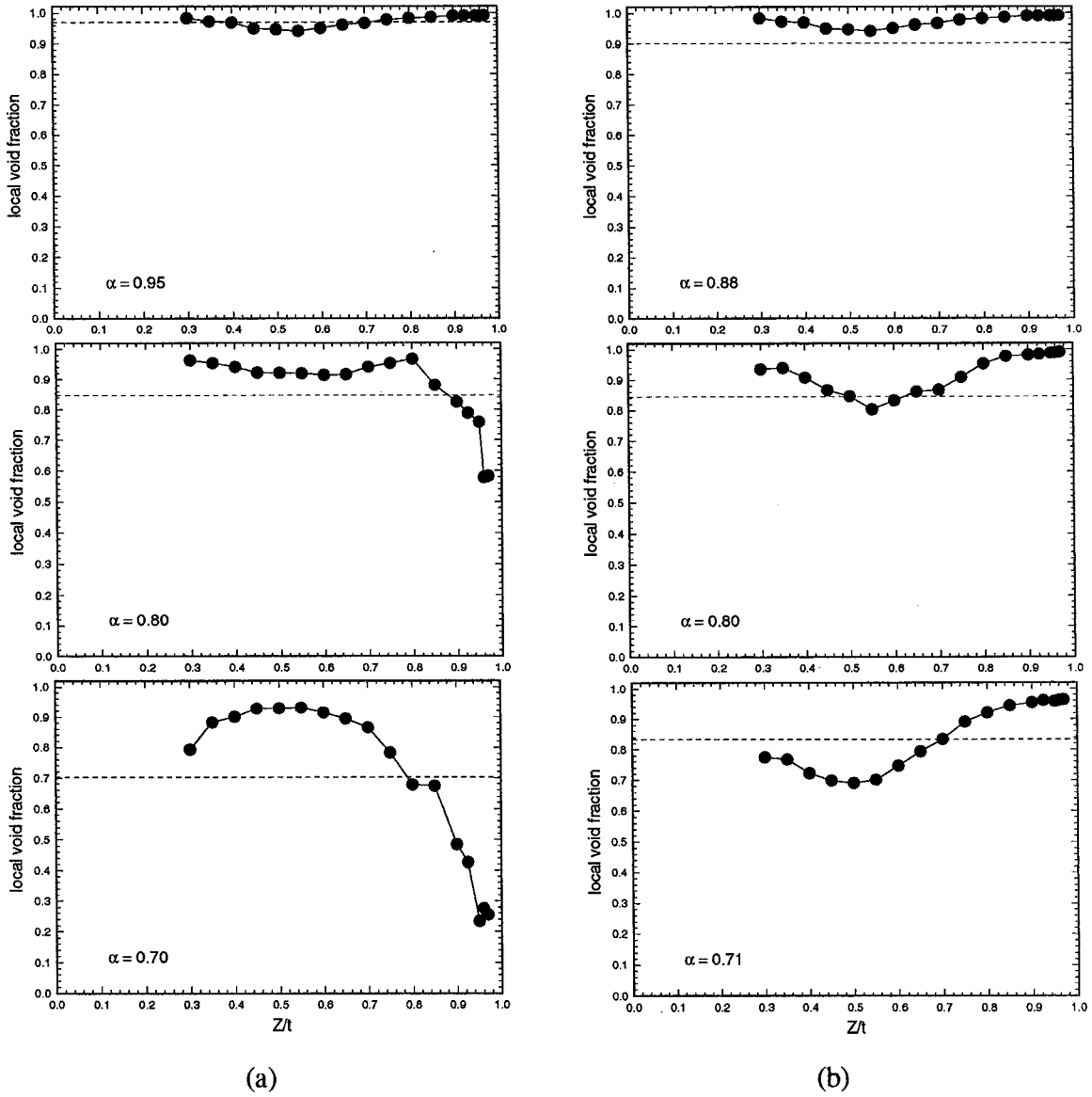

Fig. 3 Local HFA *Z*-dimension void fraction profiles for $w=532$ kg/hr (*a*) *P P*=1.4 MPa; (*b*) *P*=2.4 MPa. Dashed line is the cross-section average void fraction using the gamma densitometer.

$$u_w=\frac{\sqrt{\frac{\rho_g}{\rho_1}}u_g+u_1}{1+\sqrt{\frac{\rho_g}{\rho_1}}}. \tag{6}$$

The average values of vapor velocity, u_g, and liquid velocity, u_1, can be calculated using the one-dimensional relationship in terms of measured quality and mass flux as

$$u_g=\frac{x}{\alpha}\frac{G}{\rho_g};\quad u_1=\frac{(1-x)}{(1-\alpha)}\frac{G}{\rho_1}. \tag{7}$$

A similar expression was also obtained by Gottmann et al. [16]. The wave velocity calculated using Eqs. (6) and (7) is 0.62 m/s which compares well with the wave velocity measured from video footage.

The visualized waves are not always clearly defined in the video images. When the liquid film at the transverse (*Y*) edges is thick, as in the case of 266 and 532 kg/hr in the void fraction range of 0.85, several waves emerging from one edge are observed to only extend to the middle of the test section. These half waves are initially relatively slow but then occasionally coalesce with half waves originating from the other edge, and then travel much faster as full bow-shaped waves. These disturbance waves may approach a slow moving half wave upstream and form a λ-shaped wave. The λ-shaped waves then propagate through the film. Although this unique phenomenon has not been reported previously, it is not unlike the circumferential ring waves observed recently in air-water flows in tubes (Ohba et al. [17], Okada et al. [14]), but much more distinguished and three-dimensional because of the high aspect ratio of the duct.

To develop an understanding of the effect of this observed liquid film wave behavior on the dispersed droplet field, as well as to assess the degree of three-dimensionality of the flow, a dual-sensor hot-film probe was installed between the third and fourth window elevations (i.e., between Windows 3 and 7 and Windows 4 and 8; see Fig. 1). This probe scanned across the *Y* dimension at the test section center plane (i.e., $Z/t=0.5$). In Fig. 5, local *Y*-dimension velocity data are presented for $P=1.4$ MPa and 2.4 MPa at $w=532$ kg/hr, the same conditions for which *Z*-dimension

Fig. 4 Photographs of waves in annular flow

void fraction data are provided in Fig. 3. The transverse velocity profiles for these two pressures exhibit a dip near the transverse test section center. This is a result of the disturbance waves that originate near the edges of the test section merging in the center and deposit a higher concentration of larger, presumably slower moving, liquid droplets. This hypothesis is strengthened by the void profiles that display a decrease in void fraction for many of the runs near the test section center, which is consistent with the video images in Fig. 4 indicating dark regions of slower moving fluid in the center.

One of the most important parameters that governs the transport process in the annular vapor core is droplet entrainment. The ratio of the liquid phase in the film to that in droplet form varies according to the fluid flow rates and the density ratio. Although no direct measurement of the entrained fraction of droplets is available for refrigerant flows in non-circular ducts, the amount of entrainment affects the void fraction distribution which can be compared with models as discussed in Part II of this paper. Among the different types of generation of droplets associated with entrainment (Hewitt and Hall-Taylor [1]), roll wave shearing and liquid bridge disintegration mechanisms are considered most responsible in the current flow situation. Since roll waves are present both on the flat side of the walls as well as the edges, and even if the mechanism of entrainment is the same for each, the rates may be different. Since the wave patterns from the videos and the void fraction profiles suggested that the edge film is considerably thicker, it is possible that liquid bridges may exist for some flow conditions, which would disintegrate contributing to large size droplets.

The characteristics of the dispersed droplet field in the narrow (Z) dimension are captured in Figs. 6 and 7 which illustrate local void fraction, droplet velocity, droplet frequency, droplet diameter and interfacial area density. The void fraction and velocity data have been qualified previously based upon comparisons to simultaneous gamma densitometer and laser Doppler velocimetry (LDV) measurements.

In Fig. 6, the effect of cross-sectional average void fraction on the Z-dimension parameter distributions is illustrated for $w = 532$ kg/hr and $P = 1.4$ MPa. The void fraction data (Fig. 6(a)) were presented previously in Fig. 3(a), but are included here for completeness. Despite the inversion in the local void fraction data, resulting in a local minimum at the duct centerline, the velocity (Fig. 6(b)) increases monotonically from the measurement position nearest the wall. For the lower void fraction condition ($\bar{\alpha} = 0.80$), there is a definite change in the profile from the near-wall region ($0.9 < Z/t < 1.0$) to the central core region ($Z/t < 0.85$). For this experimental condition, it appears that the HFA probe is being traversed through the wall-bounded liquid film, into the interfacial waves, and finally into the dispersed droplet field. No such velocity trend is observed for $\bar{\alpha} = 0.95$, as the liquid film is very thin, and the HFA probe is exposed only to dispersed droplets in continuous vapor.

The local frequency measurements presented in Fig. 6(c) show that there is an approximately 75 percent increase in f_d upon increasing the average void fraction from 0.80 to 0.95. The lower void fraction data display nearly constant frequency across the vapor core, while a slight maximum exists in the profile for $\bar{\alpha} = 0.95$. As given previously in Eq. (2), the local droplet diameter can be calculated from measurements of void fraction, velocity and frequency, and these data are plotted in Fig. 6(d). From the inversion in the void fraction scans (Fig. 6(a)), it is evident that the liquid volume fraction ($\alpha_d = 1 - \alpha$) is greatest at the duct centerline. Because the gradients in velocity and frequency are small, this volume fraction peak also leads to a peak in the local droplet diameter near the centerline. As expected, there is a significant decrease in the magnitude of the diameters as the cross-sectional average void fraction is increased from 0.80 to 0.95. As given by Eq. (4), the local interfacial area concentration in the vapor core can be calculated from measurements of velocity and frequency. The data scans for two average void fraction at $P = 1.4$ MPa and $w = 532$ kg/hr are shown in Fig. 6(e). Because the velocity and frequency increase in similar proportions upon increasing the void fraction from 0.80 to 0.95, the net result is that the local a_i values are nearly equivalent. Also, the profiles are approximately flat over the range $0.3 < Z/t < 0.8$.

Figure 7 shows the effect of mass flow rate on the local Z-dimension parameter distributions for a fixed system pressure of 2.4 MPa and cross-sectional average void fraction of 0.94. Because of the very high average vapor volume fraction, the liquid film is quite thin and the void fraction profiles (Fig. 7(a)) are nearly flat as the probe is traversed through the dispersed droplet field. In Fig. 7(b) it is seen that the local velocity increases by a factor of approximately five, which is in line with the increase in the mass flow rate from 106 to 532 kg/hr. The droplet frequency data in Fig. 7(c) illustrate the more than ten-fold increase in droplet frequency at the higher flow rate, as well as the significant gradient in frequency between near-wall and centerline measurement locations for $w = 532$ kg/hr. The data in Fig. 7(d) show a definite decrease in droplet diameter for the higher flow rate. Unlike the trend shown in Fig. 6(e), the interfacial area concentration is strongly dependent on mass flow rate, and apparently increases toward the duct centerline. Interfacial area concentration results are discussed further later.

Various drop size models have been discussed by Azzopardi [18]. Trabold et al. [3] presented drop size measurements for high pressure flows. Their measurements did not include lower pressure (still significantly higher than atmospheric pressure) cases. The objective of the current presentation of the reanalyzed droplet data is to test the available models in the literature and implement the most suitable model in the three-field code to obtain integrated predictions (Kumar and Trabold, Part II [2]). Two models under consideration are Ueda's [19,20] based on his R-113 refrigerant

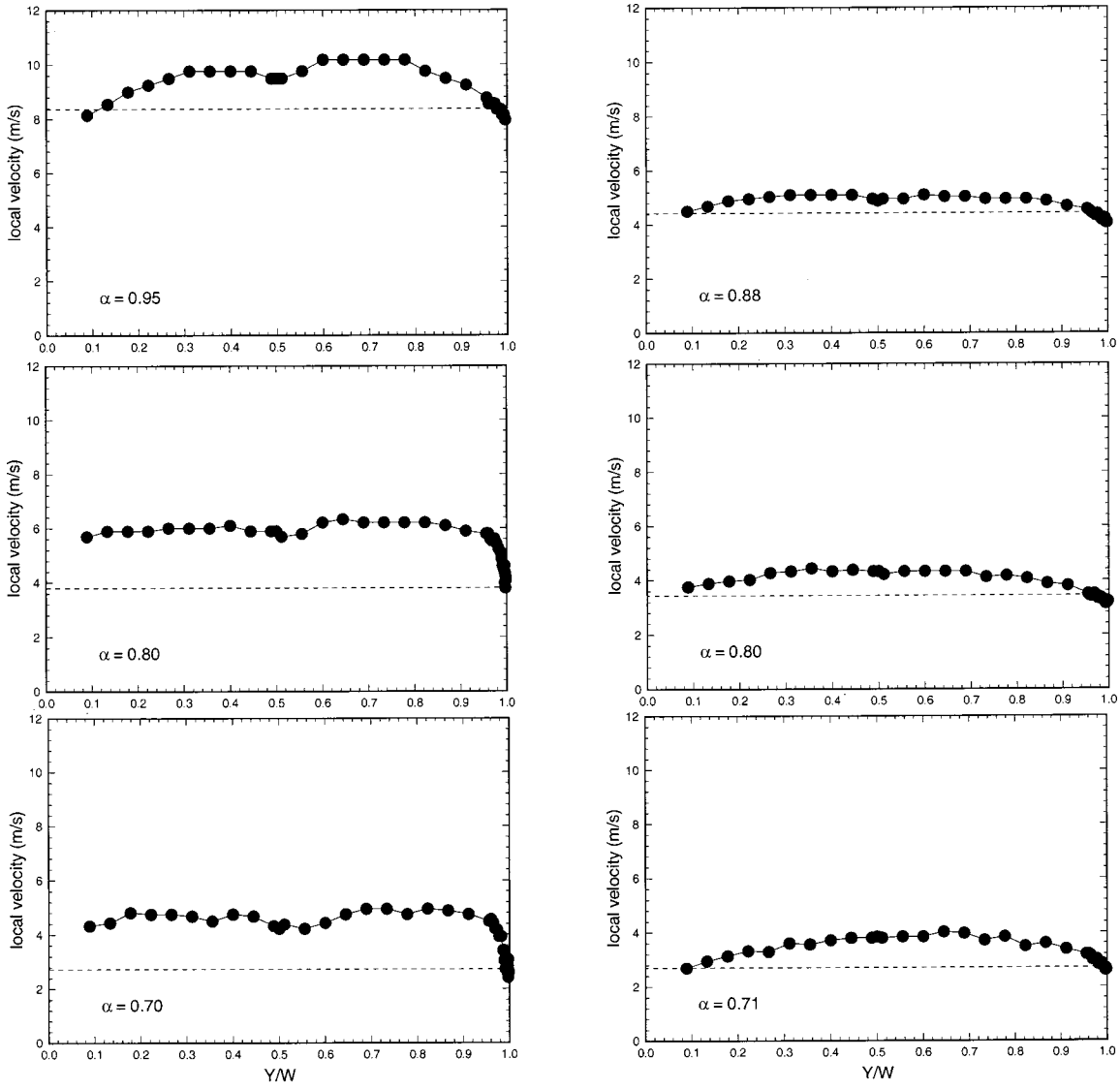

Fig. 5 Local *Y*-dimension velocity profiles for $w=532$ kg/hr (*a*) $P=1.4$ MPa; (*b*) $P=2.4$ MPa. Dashed line is the mixture velocity

data, and a more mechanistically based model by Kocamustafaogullari et al. [21]. By introducing the vapor-to-liquid density ratio, a correlation was derived to describe data for a variety of fluids, including R-113, water and aqueous glycerol solutions:

$$\frac{d_m}{D_h}=5.8\times10^{-3}\left[\frac{\sigma}{\mu_g U_g}\left(\frac{\rho_g}{\rho_1}\right)^{1.25}\right]^{0.34}=5.8\times10^{-3}R^{0.34} \quad (8)$$

where d_m is the volume weighted droplet diameter.

A comparison of the mean R-134a droplet diameter measurements (averaged from the presented profiles) and the correlation of Ueda [19] is illustrated in Fig. 8. The parameter R was calculated using R-134a physical properties at saturation pressures of 1.4 and 2.4 MPa. Included in Fig. 8 are the air-water data of Wicks and Dukler [22], which were also obtained in a rectangular duct. It is evident that the Ueda droplet size relation underpredicts much of the R-134a data, as well as most of the data of Wicks and Dukler.

The second model considered is by Kocamustafaogullari et al. [21] who developed an expression for the Sauter mean droplet diameter, by considering the maximum stable droplet size in the turbulent vapor core:

$$\frac{d_{sm}}{D_h}=0.65C_w^{-4/15}\mathrm{We}_m^{-3/5}\left(\frac{\mathrm{Re}_g^4}{\mathrm{Re}_1}\right)^{1/15}\left[\left(\frac{\rho_g}{\rho_1}\right)\left(\frac{\mu_g}{\mu_1}\right)\right]^{4/15}\left(\frac{\Delta\rho}{\rho_1}\right)^{-3/5}$$
$$=0.65K \quad (9)$$

where:

$$C_w=\frac{1}{35.34N\mu^{0.8}} \quad \text{for } N\mu\leqslant\frac{1}{15} \quad (10)$$

$$N\mu=\text{viscosity number}=\frac{\mu_f}{\left[\rho_f\sigma\left(\frac{\sigma}{g\Delta\rho}\right)^{1/2}\right]^{1/2}} \quad (11)$$

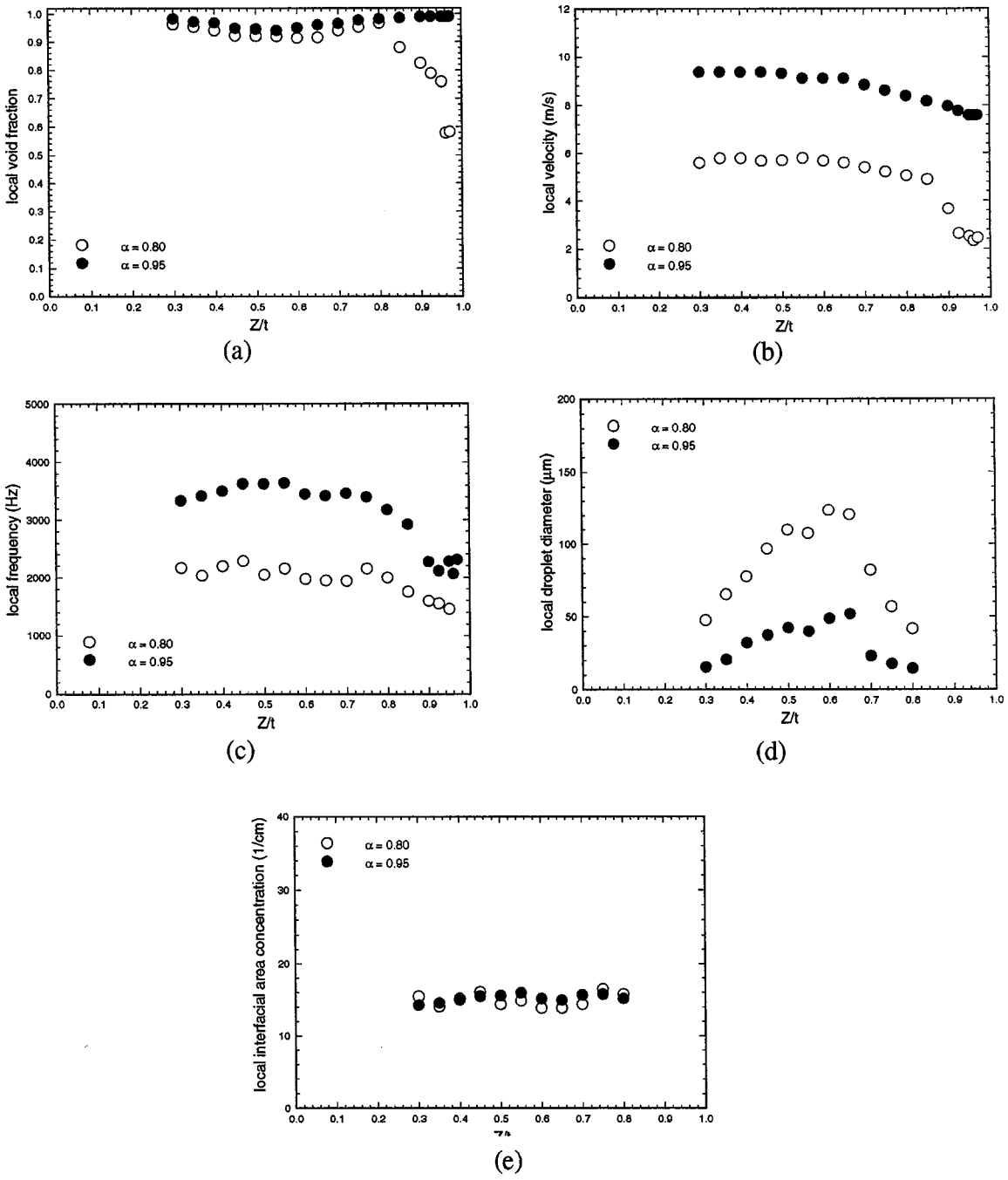

Fig. 6 Local *Z*-dimension parameter distributions for $w=532$ kg/hr and $P=1.4$ MPa; (*a*) void fraction; (*b*) velocity; (*c*) frequency; (*d*) droplet diameter; (*e*) interfacial area concentration.

$$\mathrm{We}_m = \text{modified Weber number} = \frac{\rho_g D_h \langle j_g \rangle^2}{\sigma} \qquad (12)$$

and the gas Reynolds number (Re_g) and liquid Reynolds number (Re_l), are based on the phasic superficial velocities. In Fig. 9, the mean R-134a droplet diameter data obtained at $P=1.4$ and 2.4 MPa are compared with the relation of Kocamustafaogullari et al. (Eq. (10)) and the rectangular duct data of Wicks and Dukler [22]. It should be noted that the factor $(\Delta\rho/\rho_1)^{-3/5}$ appears on the right-hand side of Eq. (9) based on the original derivation for fluids having small density ratios. For high pressure (2.4 MPa), this factor increases droplet diameter by more than 9 percent. The data plotted in Fig. 9 show some scatter about the line representing Eq. (9), but this relation reasonably describes the overall trend in the data. This is significant because of the wide variety of fluid physical properties, gas and liquid flow rates and duct geometries investigated, and the various measurement techniques employed. Perhaps the most encouraging aspect of this data comparison is that the liquid-to-gas density ratio varied from 7.3 for R-134a to 3700 in the helium-water experiments of Jepson et al. [23].

Now, more attention is paid to interfacial area concentration profiles illustrated in Figs. 6(*e*) and 7(*e*). Once again, this calculation is limited to regions of the flow for which the hot film results showed close agreement with simultaneous LDV measurements (Trabold et al. [3]). The local interfacial area concentration falls within a fairly narrow range along the narrow *Z*-dimension. This result is not surprising since most droplet frequency and droplet velocity profiles were flat in the vapor core. The local

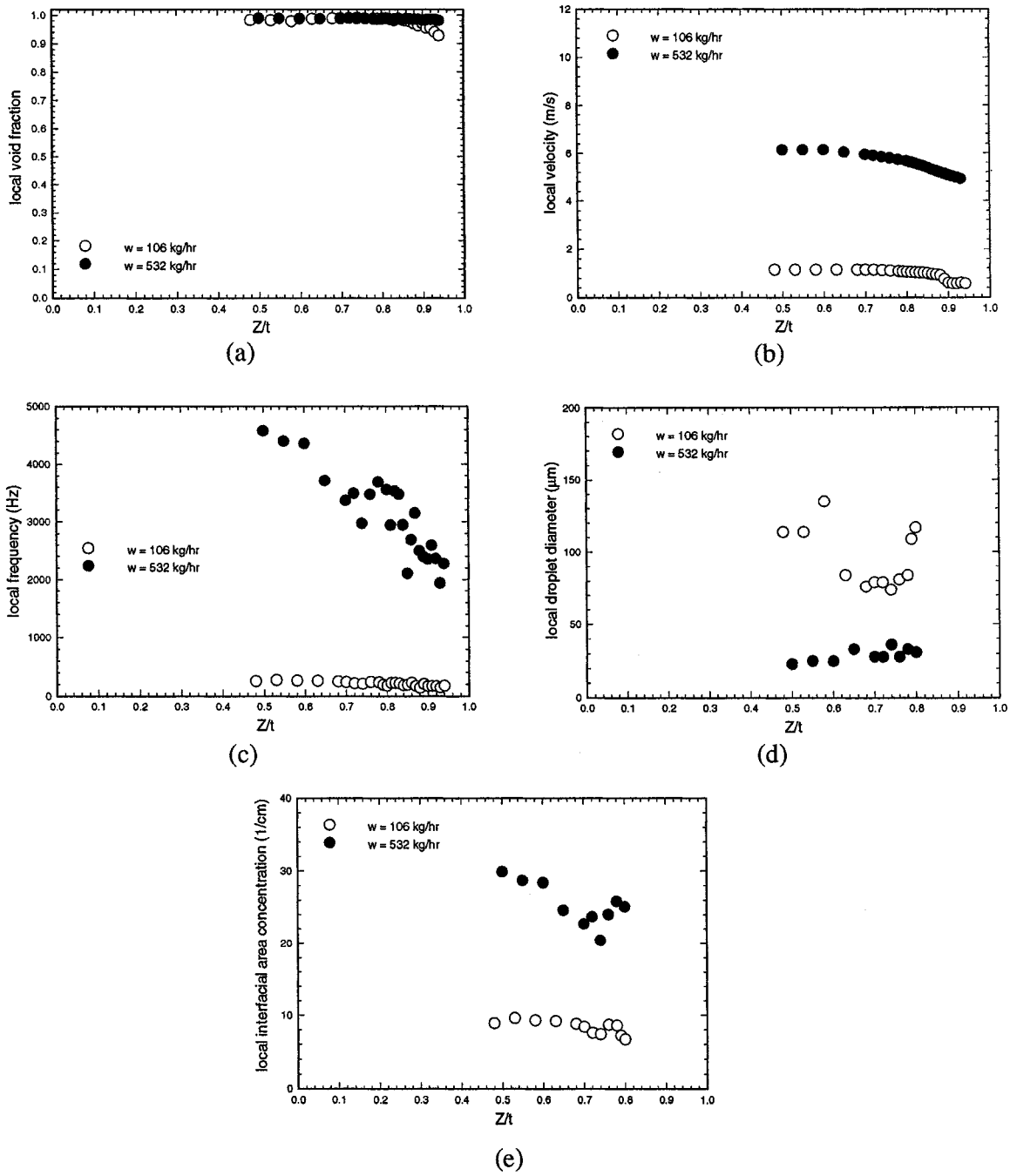

Fig. 7 Local *Z*-dimension parameter distributions for α=0.94 and *P*=2.4 MPa; (*a*) void fraction; (*b*) velocity; (*c*) frequency; (*d*) droplet diameter; (*e*) interfacial area concentration.

measurements acquired for each experiment were spatially averaged, and the results are presented in Fig. 10 to demonstrate the variation with average void fraction. Several points can be made from this figure. For the same void fraction and system pressure, as the mass flow rate is increased, the interfacial area concentration increases. For the same flow rate of 532 kg/hr, as the pressure is increased from 1.4 MPa to 2.4 MPa, the interfacial concentration increases. The distribution of interfacial area with void fraction is relatively flat within the experimental uncertainty.

As documented by Ishii and Mishima [24], most data available for interfacial area concentration, a_i, correspond to air-water flows in circular pipes. The largest average interfacial area concentration reported in such flows is 25 cm^{-1} measured at a gas superficial velocity of 37 m/s (Wales [25]). For many of the test conditions covered in the present study, the average a_i significantly exceeds this value even though the maximum gas superficial velocity was only 7.2 m/s.

The wide variations between the present R-134a experiments and those available in air-water may be related to two key parameters: the fraction of entrained liquid and the mean liquid droplet size. For a given quality, the entrainment fraction corresponds to the mass fraction of the liquid phase that is contained in the dispersed droplet field. Liquid in the form of dispersed droplets would contribute more to the interfacial area than if flowing as part of the liquid film. A large value of entrainment fraction would, of course, correspond to a large average droplet volume fraction, α_d. For a representative pipe diameter of 1 cm and volume mean droplet diameter of 500 μm, Ishii and Mishima devel-

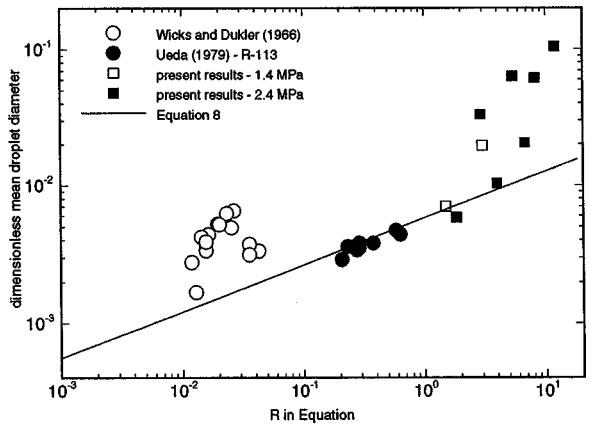

Fig. 8 Comparison of droplet diameter data to relation of Ueda [19]

oped a plot of the characteristic interfacial area concentrations for variations in both average void fraction, $\bar{\alpha}$, and average droplet volume fraction, α_{fd}. For many of the present experiments, both the local void fraction profiles and high-speed video records suggest the presence of a thin liquid film. Therefore, much of the liquid phase is contained within the liquid droplets, thereby increasing the value of α_{fd} and the expected range of average interfacial area concentrations.

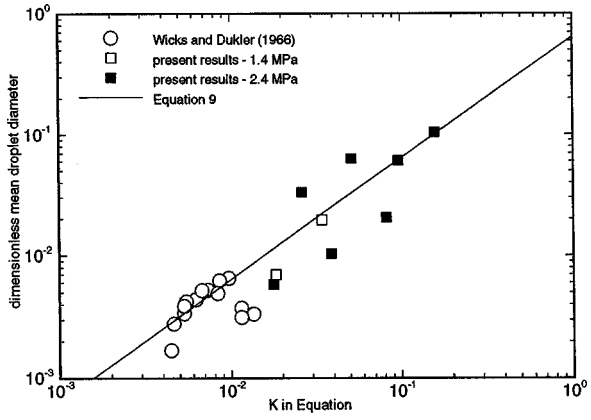

Fig. 9 Comparison of droplet diameter data to relation of Kocamustafaogullari et al. [21]

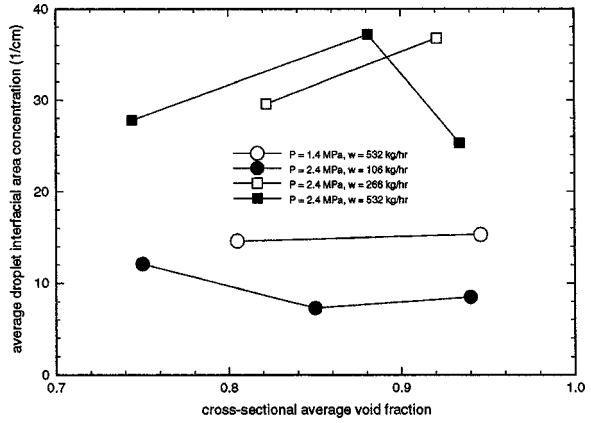

Fig. 10 Relationship between average void fraction and interfacial area concentration for $P=1.4$ and 2.4 MPa

For a given volume of liquid, the interfacial area is greater for a larger number of small droplets. Therefore, an inverse functionality exists between a_i and the droplet diameter, as described by Eq. (4). The ratio of expected droplet size in an air-water flow through a 1 cm diameter pipe to that in TF-116 can be estimated by invoking the correlation of Ueda [20]. For a given gas superficial velocity, Eq. (8) yields

$$\frac{d_{R-134a}}{d_{\text{air-water}}} = \frac{\left\{ D_h \left[\frac{\sigma}{\mu_g} \left(\frac{\rho_g}{\rho_1} \right)^{1.25} \right]^{0.34} \right\}_{R-134a}}{\left\{ D_h \left[\frac{\sigma}{\mu_g} \left(\frac{\rho_g}{\rho_1} \right)^{1.25} \right]^{0.34} \right\}_{\text{air-water}}}. \tag{13}$$

Substitution of the appropriate physical property and hydraulic diameter information yields a diameter ratio of 1.1 for R-134a at 2.4 MPa and 1.25 at 1.4 MPa. Hence, the expected droplet size for R-134a is of the same order of magnitude as a typical air-water flow for which interfacial area concentration data are reported. It may therefore be concluded that the higher interfacial area concentration in the refrigerant flow is primarily a result of a larger entrainment fraction.

Conclusions

Detailed local measurements of void fraction, droplet frequency, velocity, mean drop size, and interfacial area concentration have been obtained using a hot-film anemometer in annular flow through a vertical duct. These measurements improve the current understanding of physical mechanisms, as well as extend the existing data base in low liquid-to-vapor density ratio flows. The line-averaged void fraction and the droplet velocity measurements have been primarily obtained to validate the integrated effects of the models in Part II of this work. By making measurements in both coordinates of the cross-section, it has been shown that even in vertical flows for an aspect ratio of 22.5, the flow can be three-dimensional with a large flux of entrained droplets from the edges. These droplets lead to an inversion in the void fraction, which is predominant for void fraction less than 0.9 for almost all flow rates. The flow is three-dimensional for void fractions much less than 0.9 and high flow rates. Corresponding to the void profiles, the droplet diameter profiles increase or decrease toward the center of the duct depending on the average void fraction and the flow rate. The average droplet diameter agrees well for both system pressures with the model proposed by Kocamustafaogullari et al. [21] when the lower liquid-to-vapor vapor density ratio is taken into account. Interfacial area concentration increases with flow rate and pressure, and is found to be significantly higher compared to similar measurements made in air-water flows. This appears to be due to a larger entrainment fraction in the low density ratio refrigerant flows.

The wave patterns have been analyzed using high speed photography, and the wave velocity measured by wave counting matches reasonably well with one-dimensional models for neutrally stable film. Disturbance waves are bow-shaped when two-dimensional as is usually observed in circular tubes, and λ-shaped when three-dimensional. These limited measurements suggest that the wave frequency increases with both gas flows (through increasing void fraction) and liquid flow rates as reported by Hall-Taylor et al. [12] and Hall-Taylor and Nedderman [13] in air-water flows, and with gas density as reported by Gill et al. [15].

Acknowledgments

The authors gratefully acknowledge Messrs. W. O. Morris and L. Jandzio for their efforts in the operation of the test facility, Mr. D. M. Considine for his efforts in flow visualization, and Dr. G. J. Kirouac for his direction of the experimental program.

Nomenclature

a_i = interfacial area concentration
B = measurement bias
D_h = duct hydraulic diameter
d_m = volume mean droplet diameter
d_{sm} = sauter mean droplet diameter
f_d = droplet frequency
G = mass flux
j = superficial velocity
L = test section length
P = pressure
Re = Reynolds number
$S_{\bar{x}}$ = precision index
t = duct thickness
t_{95} = student's t for 95 percent confidence
u = mean phasic velocity
U = measurement uncertainty
V = HFA output voltage
V_d = droplet velocity
W = duct width
We_m = modified Weber number
w = mass flow rate
x = quality
X = streamwise (length) dimension
Y = transverse (width) dimension
Z = spacing (thickness) dimension
$\alpha,\bar{\alpha}$ = void fraction
$\Delta\rho$ = density difference
μ = dynamic viscosity
ρ = density
σ = surface tension
τ_m = time associated with maximum cross-correlation factor

Subscripts

d = droplet field
g = gas phase
l = liquid phase
w = wave

References

[1] Hewitt, G. F., and Hall-Taylor, N. S., 1970, *Annular Two-Phase Flow*, Pergamon Press.
[2] Kumar, R., and Trabold, T. A., 2000, ''High Pressure Annular Two-Phase Flow in a Narrow Duct: Part II—Three Field Modeling,'' ASME J. Fluids Eng., **122**, pp. 375–384.
[3] Trabold, T. A., Kumar, R., and Vassallo, P. F., 1999, ''Experimental Study of Dispersed Droplets in High Pressure Annular Flows,'' ASME J. Heat Transfer, **121**, pp. 924–933.
[4] Trabold, T. A., Moore, W. E., Morris, W. O., Symolon, P. D., Vassallo, P. F., and Kirouac, G. J., 1994, ''Two Phase Flow of Freon in a Vertical Rectangular Duct. Part II: Local Void Fraction and Bubble Size Measurements,'' *Experimental and Computational Aspects of Validation of Multiphase Flow CFD Codes*, I. Celik et al., (ed.), ASME, FED-Vol. 180, pp. 67–76.
[5] Trabold, T. A., Moore, W. E., and Morris, W. O., 1997, ''Hot-Film Anemometer Measurements in Adiabatic Two-Phase Refrigerant Flow through a Vertical Duct,'' ASME Fluids Engineering Division Summer Meeting, Vancouver, B.C., Paper FEDSM97-3518.
[6] Carvalho, R., and Bergles, A. E., 1992, ''The Pool Nucleate Boiling and Critical Heat Flux of Vertically Oriented, Small Heaters Boiling on One Side,'' Rensselaer Polytechnic Institute, Heat Transfer Laboratory Report HTL-12, August.
[7] Kataoka, I., and Ishii, M., 1982, ''Mechanism and Correlation of Droplet Entrainment and Deposition in Annular Two-Phase Flow,'' Argonne National Laboratory Report ANL-82-44.
[8] Galaup, J. P., 1976, ''Contribution to the Study of Methods for Measuring Two-Phase Flow,'' Center D'Etudes Nucleaires de Grenoble, Report No. 136.
[9] Kataoka, I., and Serizawa, A., 1990, ''Interfacial Area Concentration in Bubbly Flow,'' Nucl. Eng. Des., **120**, pp. 163–180.
[10] Cartellier, A., and Achard, J. L., 1991, ''Local Phase Detection Probes in Fluid/Fluid Two-Phase Flows,'' Rev. Sci. Instrum., **62**, pp. 279–303.
[11] Jones, O. C., and Zuber, N., 1978, ''Use of a Cylindrical Hot-Film Anemometer for Measurement of Two-Phase Void and Volume Flux Profiles in a Narrow Rectangular Channel,'' Heat Transfer Res. Appl. AIChE Symposium Series, Vol. 74, No. 174, pp. 191–204.
[12] Hall-Taylor, N. S., Hewitt, G. F., and Lacey, P. M. C., 1963, ''The Motion and Frequency of Large Disturbance Waves in Annular Two-Phase Flow of Air-Water Mixtures,'' Chem. Eng. Sci., **18**, pp. 537–552.
[13] Hall-Taylor, N. S., and Nedderman, R. M., 1968, ''The Coalescence of Disturbance Waves in Annular Two-Phase Flow,'' Chem. Eng. Sci., **23**, pp. 551–564.
[14] Okada, O., Fujimatsu, T., Fujita, H., and Nakajima, Y., 1995, ''Measurement of Droplet Size Distribution in an Annular Mist Flow in a Vertical Pipe by Immersion Liquid Method,'' Proc. 2nd Int. Conf. on Multiphase Flow, Paper IP2, pp. 11–18.
[15] Gill, L. E., Hewitt, G. F., and Roberts, D. N., 1969, ''Studies of the Behavior of Disturbance Waves in a Long Vertical Tube,'' UKAEA Report AERE R6012.
[16] Gottmann, M., Oishi, T., Sridhar, K. R., and Kumar, R., 1998, ''Interface Shape and Wave Velocities of Air-Water Flows in a Vertical Duct,'' Proc. ASME HTD-Vol. 361-5, IMECE, Anaheim.
[17] Ohba, K., Nakamura, and Naimi, F. 1995, ''A New Kind of Interfacial Wave on Liquid Film in Vertically Upward Air-Water Two-phase Annular Flow,'' Proc. 2nd Int. Conf. on Multiphase Flow, Paper IP1, pp. 27–33.
[18] Azzopardi, B. J., 1997, ''Drops in Annular Two-Phase Flow,'' Int. J. Multiphase Flow, **23**, Suppl., pp. 1–53.
[19] Ueda, T., 1979, ''Entrainment Rate and Size of Entrained Droplets in Annular Two-Phase Flow,'' Bull. JSME, **22**, pp. 1258–1265.
[20] Ueda, T., 1981, ''On the Droplets Entrained in Two-Phase Annular and Mist Flows,'' *Two-Phase Flow Dynamics*, A. E. Bergles and S. Ishigai, eds., Hemisphere, pp. 75–93.
[21] Kocamustafaogullari, G., Smits, S. R., and Razi, J., 1994, ''Maximum and Mean Droplet Sizes in Annular Two-Phase Flow,'' Int. J. Heat Mass Transf., **37**, pp. 955–965.
[22] Wicks, M., and Dukler, A. E., 1966, ''In Situ Measurements of Drop Size Distribution in Two-Phase Flow—A New Method for Electrically Conducting Liquids,'' *Proc. of the 3rd Int. Heat Transfer Conf.*, **5**, pp. 39–49.
[23] Jepson, D. M., Azzopardi, B. J., and Whalley, P. B., 1989, ''The Effect of Gas Properties on Drops in Annular Flow,'' Int. J. Multiphase Flow, **15**, pp. 327–339.
[24] Ishii, M., and Mishima, K., 1981, ''Study of Two-Fluid Model and Interfacial Area,'' Argonne National Laboratory Report ANL-80-111.
[25] Wales, C. E., 1966, ''Physical and Chemical Absorption in Two-Phase Annular and Dispersed Horizontal Flow,'' AIChE J., **12**, pp. 1166–1171.

High Pressure Annular Two-Phase Flow in a Narrow Duct: Part II—Three-Field Modeling

Ranganathan Kumar
Senior Engineer,
Lockheed Martin Corporation,
Schenectady, NY 12301

Thomas A. Trabold
Project Manager,
Xerox Corporation,
Rochester, NY 14580

This paper outlines the development of a three-field modeling approach in annular flow and the predictive capability of an analysis code. Models have been developed here or adapted from the literature for the thin film near the wall as well as the droplets in the vapor core, and have been locally applied in a fully developed, two-phase adiabatic boiling annular flow in a duct heated at the inlet at high pressure. Numerical results have been obtained using these models that are required for the closure of the continuity and momentum equations. The two-dimensional predictions are compared with local void fraction and droplet velocity (using a hot film anemometer), and average void fraction (using gamma densitometry) for a refrigerant fluid flowing in a narrow vertical duct with a cross-section aspect ratio of 22.5. Predicted results match the experimental data well for high void fraction annular flows, validating the overall modeling approach.
[S0098-2202(00)01002-6]

Introduction

Annular flow research is the most challenging among all the flow regimes in two-phase flows because liquid exists as both continuous film and droplets. This regime is also the most important because it is usually a precursor to wall dryout. Annular flow usually occurs through a transition from the slug/churn turbulent flow regimes at high void fractions. It presents a complicated pattern of liquid phase in the form of a base film, disturbance waves and droplets, separated by a vapor core. The interface between the thin liquid film and the vapor core is characterized by a wavy motion. There are generally two types of waves: the high amplitude, low wavelength disturbance or roll waves, and the low amplitude, high wavelength ripple waves, which act to both increase the interfacial shear stress and introduce droplets into the gas core. There can also be gas entrainment in the liquid film. Hall-Taylor et al. [1] and Hewitt and Hall-Taylor [2] discuss the physical mechanisms that occur in annular flow and the physical models that describe these mechanisms.

The random motion of the waves presents some special problems in annular flow modeling and measurements that are not present in bubbly flows. These waves affect the interfacial shear stress, droplet motion, deposition, and entrainment rates. These complexities have been individually modeled by various authors. Numerous papers have appeared in the literature that attribute the increase in interfacial shear in annular flow to the wave motion. Progress in modeling interfacial shear can be traced from a simple correlation between the film thickness and the interfacial friction factor (Wallis [3]) to a law-of-the-wall approach (Hewitt and Govan [4]) to introducing wave and turbulence characteristics (Kang and Kim [5]). Similarly, a number of papers have dealt with the droplet motion in the turbulent vapor core, and in particular, the drop size and entrainment and deposition of droplets (Cousins and Hewitt [6], Kataoka et al. [7], Ueda [8], and Azzopardi and Teixeira [9]).

These papers and many others contributed significantly to two-phase annular flow modeling and experimental data base. These models capture the features of the vapor core separated by a convoluted interface, and together they contribute to the appropriate distribution and motion of the droplets in the vapor core. However, such an integrated effect of these physical mechanisms has not been numerically modeled in annular flows to date.

The current paper discusses the methodology and solutions to ensemble-averaged transport equations that describe the two-phase annular flow. An averaging process (Drew [10]) is used to derive a system of governing equations to describe the macroscopic flow phenomenon. As done in capturing the turbulence characteristics, the averaging process usually filters out the details of the flow fields; and, therefore, additional closure equations or models need to be introduced. In the traditional two fluid approach, the liquid and vapor phases are treated separately with a set of governing equations attributed to each phase. By contrast, a four-field approach as presented by Siebert et al. [11] is used to subdivide the flow further into fields rather than phases. These idealized fields are: dispersed vapor field (dv), continuous liquid (cl), dispersed liquid (dl), and continuous vapor (cv). Within each continuous field, a dispersed field of the opposite phase can exist.

This paper has three specific objectives. 1) An ensemble averaging approach is used in a three-field framework and applied in a two-dimensional analysis code. Since the flow is annular and no heating is applied on the wall, dispersed vapor (dv) field is not created, and in effect, only three fields are used in the current flow situation. 2) Mechanistically based models are developed or currently available models are adapted from the literature for closure of the governing equations. Specifically, interfield (entrainment and deposition) models, interphase (interfacial shear) models, and other force models are locally applied to appropriately separate the liquid film from the vapor core, and to capture the physics of the droplet motion. 3) Predictions are compared with measurements obtained using hot film anemometry and gamma densitometry for different flow rates and two system pressures in a refrigerant fluid, R-134a (SUVA), at elevated temperature and pressure conditions. Emphasis is placed on the analysis of vapor fraction in the continuous vapor field and velocity in the dispersed liquid field. Shortcomings of modeling are discussed.

Governing Equations

Drew [10] described a fundamental interpretation of time and space averages by defining the ensemble average based on the probability of a process occurring among a set of processes. To ensemble average the governing set of equations, a phase indicator function, X_k, is introduced as:

Contributed by the Fluids Engineering Division for publication in the JOURNAL OF FLUIDS ENGINEERING. Manuscript received by the Fluids Engineering Division December 4, 1998; revised manuscript received January 25, 2000. Associate Technical Editor: M. Sommerfeld.

$$X_k(x,t)=\begin{cases}1 & \text{if phase } k \text{ at } x,t\\ 0 & \text{otherwise}\end{cases} \tag{1}$$

The average of the phase indicator function, X_k, is the volume fraction of phase k, α_k, and the normal derivative of this phase indicator function is the interfacial area density. All the remaining variables are weighted averages as

$$\overline{\rho_k}=\frac{\overline{\rho_k X_k}}{\overline{X_k}}=\frac{\overline{\rho_k X_k}}{\alpha_k}, \tag{2}$$

and

$$\overline{f_k}=\frac{\overline{f_k X_k \rho_k}}{\alpha_k \overline{\rho_k}}. \tag{3}$$

To perform the ensemble averaging process, the conservation equations and interface jump conditions are each multiplied by the phase indicator function, X_k, and then the equation is averaged using Eqs. (2) and (3). The final forms of the ensemble-averaged phasic governing equations can be written for any number of fields present in the flow. The predictive capability in the annular flow regime with no wall heating can be improved by an optimum number of three idealized fields: continuous liquid (cl), continuous vapor (cv) and dispersed liquid (dl). The dl-field is contained within the cv-field, and the cl-field is separated from the cv-field. The transfer of mass between fields (cl-dl and dl-cl) occurs through the hydrodynamic mechanisms of liquid bridge breakup, entrainment and deposition. This redistribution of mass among the different fields provides the predictive capability to handle flow regime transitions as continuous events rather than as discrete events. The governing equations for the three fields are given in the following Cartesian tensor form.

Conservation of phasic mass

$$\frac{\partial}{\partial t}(\alpha_i\rho_i)+\nabla\cdot(\alpha_i\rho_i\mathbf{v}_i)=\sum_{j\neq i}(\Gamma_{ji}-\Gamma_{ij}) \tag{4}$$

Conservation of phasic momentum

$$\begin{aligned}\frac{\partial}{\partial t}(\alpha_i\rho_i\mathbf{v}_i)+\nabla\cdot(\alpha_i\rho_i\mathbf{v}_i\mathbf{v}_i)&\\ =-\alpha_i\nabla p_i-\boldsymbol{\tau}_i\cdot\nabla\alpha_i+\nabla\cdot\alpha_i(\boldsymbol{\tau}_i+\boldsymbol{\tau}_i^{\mathrm{Re}})&\\ +\mathbf{M}_i+\sum_{j\neq i}[D_{ij}(\mathbf{v}_j-\mathbf{v}_i)+\Gamma_{ji}\mathbf{v}_i-\Gamma_{ij}\mathbf{v}_i]&\end{aligned} \tag{5}$$

Volume fraction constraint

$$\sum_i \alpha_i=1;\quad 0\leqslant\alpha_i\leqslant 1 \tag{6}$$

Here, subscript i denotes the field under consideration (i=cl, dl, cv). In the presence of three fields, there are only two admissible interfaces: cv-cl, and cv-dl. The dv-cl interface is not admitted or discussed in this paper. A double subscript denotes a quantity transferred from the field indicated by the first index (donor phase) to the field indicated by the second index (receptor phase). Γ represents the interfacial mass transfer rate between fields due to entrainment and deposition. $D_{ij}(\mathbf{v}_j-\mathbf{v}_i)$ represents the interfacial drag force between fields, and $\mathbf{M}_i$ represents nondrag interfacial forces between fields.

The phases are coupled via interfacial transfer terms (underlined in Eqs. (4) and (5)), and jump conditions are used to relate the transfer of mass, momentum, and energy across the interface. The continuity jump condition requires zero mass accumulation on the interface. The momentum jump condition dictates that the net force acting on the interface is balanced by surface tension effects. In drag-like terms, the velocity difference across the interface is equal to the difference between the phasic velocities; but in mass transfer terms, the mass is assumed to depart the donor phase at the donor phase velocity and arrive in the receptor phase with that same velocity.

***k-ε* Transport Equations.** The form of the k-ε transport equations used here is a simple extension of the steady-state single phase model to two-phase flows. These transport equations are used only for the continuous liquid (cl) and continuous vapor (cv) fields. The production terms are refined in the wall node for annular flows as will be described in the modeling section. The dissipation of kinetic energy, ε, is calculated from the transport equation for turbulent dissipation.

Kinetic Energy Equation

$$\nabla\cdot(\rho_i\alpha_i\mathbf{v}_i k_i)=\nabla\cdot\left\{\alpha_i\left(\mu_i+\frac{\mu_i^T}{\sigma_k}\right)\nabla k_i\right\}+P_i-\rho_i\alpha_i\varepsilon_i \tag{7}$$

where

$$P_i=\alpha_i\mu_{\mathrm{eff}}\nabla u_k\cdot(\nabla u_k+\nabla u_k^T). \tag{8}$$

Kinetic Energy Dissipation Equation

$$\nabla\cdot(\rho_i\alpha_i\mathbf{v}_i\varepsilon_i)=\nabla\cdot\left\{\alpha_i\left(\mu_i+\frac{\mu_i^T}{\sigma_\varepsilon}\right)\nabla\varepsilon_i\right\}+C_1\frac{\varepsilon_i}{k_i}P_i-C_2\rho_i\alpha_i\frac{\varepsilon_i^2}{k_i} \tag{9}$$

Boundary Conditions

At the inlet to the duct, the following values are set for each of the four fields: 2 velocity components, density, volume fraction, k and ε. Since the quality is measured from the experiments, the inlet cv-volume fraction is set based on the quality and vapor-liquid density ratio. If a phase is not present at the inlet ($\alpha_i=0$), then its inlet conditions do not affect the results, and reasonable values corresponding to zero-slip, saturated conditions are typically given. A pressure boundary condition is specified across the exit plane of the duct. No slip boundary conditions are used on the walls of the duct. Setting the system pressure and fluid type completes the flow specification.

In the three-field (cl, cv, and dl) formulation used, thirteen transport equations (one continuity and two momentum equations per field; k and ε equations in the two continuous fields) and one algebraic equation (volume fraction constraint) are solved. This equals the number of unknowns (u, v, and α in each of the three fields, one pressure common to all fields, and k and ε in the cl- and cv-fields). Details of the numerical schemes are available in Siebert et al. [11].

Numerical Procedure

The system of governing differential equations is discretized using a finite volume formulation in which first order hybrid upwinding is used for the convection terms. The discretized equations are solved using the SIMPLEC algorithm (Patankar [12]). Pressure velocity coupling is enforced using the algorithm developed by Rhie and Chow [13]. The phase-coupling algorithm originally developed by Spalding [14] for a nonstaggered grid in the commercial code, CFDS-FLOW3D (AEA [15]), was substantially modified to incorporate a multi-field flow scheme (Siebert and Antal [16]). Several different grid spacings were examined (for example, 37×16, 37×24, and 37×32) and the numerical results presented are generated with nonuniformly spaced grids (37×16) using the Cray C90 computer. This grid was found to be adequate for the experimental conditions reported. Solution convergence was measured by examining the mass, momentum and energy residuals in the continuous liquid field. Additional measures of convergence included global mass and energy balances (typically $<10^{-5}$).

Discussion of Models

Since the equations are ensemble-averaged, physical information is lost. This information is recovered in the equations through closure conditions/models. These models represent field-to-field and field-to-wall interactions, and are underlined in Eqs. (4) and (5). The models that are categorized as drag and nondrag models are either developed here or adapted from the literature. The one-dimensional models obtained from the literature are modified to apply locally on a two-dimensional basis. The annular flow models discussed in this section are divided into two categories: 1) thin film, and 2) droplet models. The thin film contains the cl-cv interface, and are further divided into wall and interfacial models. The vapor core contains the droplets, and hence the cv-dl interface.

Thin Film Models.

Wall Lateral Force. In a three-field prediction (i.e., without the dv-field), the formation and maintenance of annular flow is determined by the forces which act on the wavy interfaces. Specifically, an aerodynamic force, called the wall lateral force, which restores the quasi-equilibrium condition on the cl-cv interface due to a Bernoulli type pressure force. Woodmansee and Hanratty [17] assumed that atomization is governed by a Kelvin-Helmholtz mechanism and that the destabilizing force is the pressure variation over the wave. This force is taken to be proportional to the product of the density and the square of the relative velocity between the phases. Antal et al. [18] developed a bubbly flow lateral force to move the bubbles toward the center of the duct. This model was modified by Kumar and Edwards [19] using a length scale that is proportional to the hydraulic diameter instead of the bubble diameter.

The form of the annular flow wall lateral force is written as

$$\mathbf{M}^w = \frac{2\alpha_{\mathrm{cv}}\rho_1 v_R^2}{D_h}\left(\left(C_{w2}\frac{D_h}{2y_{\mathrm{wall}_1}}\right)^a + (-C_{w1})^a\right)^{1/a} - \left(\left(C_{w2}\frac{D_h}{2y_{\mathrm{wall}_2}}\right)^a + (-C_{w1})^a\right)^{1/a} \tag{10}$$

where a is a smoothing parameter, y_{wall1} is the distance to the nearer wall, and y_{wall2} is the distance to the farther wall. The smoothing function is used to remove a discontinuity in the wall force. For this analysis, following an optimization study on the coefficients, values of -1.7×10^{-5} and 2×10^{-5} are used for C_{w1} and C_{w2}.

Wall Shear. It is assumed that the continuous liquid is in contact with the wall in annular flow, and flows as single-phase Couette flow along the wall. Therefore, the wall shear is applied only to the cl-field and not to the dl- or cv-fields. Wall shear stress is related to the turbulent kinetic energy by

$$\tau_w = C_\mu^{0.5}\rho_l k_{p,\mathrm{cl}}. \tag{11}$$

Using the definition of friction velocity and the relationship in Eq. (11), the scaled variable, y^+, can be redefined as

$$y^+ = \frac{\rho_l(y_c)C_\mu^{0.25}k_{p,\mathrm{cl}}^{0.5}}{\mu_l} \tag{12}$$

where y_c is half the thickness of the film, given by the product of the cl-volume fraction and the nodal distance, y_p. Now, the wall shear stress can be written as

$$\tau_w = T_m u_{p,\mathrm{cl}}, \quad \text{where} \tag{13}$$

$$T_m = \frac{\rho_l C_\mu^{0.25}k_{p,\mathrm{cl}}^{0.5}}{u_p^+}. \tag{14}$$

The nondimensional velocity, u_p^+, uses a law-of-the-wall formulation which is recast as

$$u_p^+ = \frac{1}{\kappa}\ln(Ey^+) \tag{15}$$

where E and κ are new constants to be determined for two-phase flows. Equations (13), (14), and (15) provide the wall shear stress at every wall node in the streamwise direction in terms of the neighboring node p perpendicular to the wall. C_μ in Eq. (14) takes a constant value of 0.09. The constants E and κ in Eq. (15) are the single-phase values, 9.0 and 0.4, respectively.

Interfacial Shear. Interfacial shear models have been developed in the literature for annular flow based on the extensions of single-phase flow approaches to account for the wavy interface and entrainment. By considering that the waves on the interface act as roughness elements, a two-phase friction factor similar to the pipe friction factor for single-phase flow has been developed. The liquid film is treated as a rough surface and can be expressed in terms of an equivalent sand roughness. Gill et al. [20] calculated the equivalent sand roughness and showed that the interfacial shear increased with increasing film thickness.

Wallis [3] showed that at atmospheric pressure for air-water flows, a wavy annular film is equivalent to a sand roughness of four times the film thickness over the range $0.001<k_s/D<0.03$, where k_s is the grain size of the equivalent sand roughness. He stated that the interfacial shear stress depends on the difference between the gas velocity and some characteristic interface velocity. For gas velocity much larger than liquid velocity, he proposed an interfacial shear model as:

$$\tau_i = f_i\,\tfrac{1}{2}\rho_g u_g^2 \tag{16}$$

where

$$f_i = f_{sp}\left(1+300\frac{\delta}{d_h}\right), \tag{17}$$

δ is the film thickness, and f_{sp} is the single-phase friction factor taken to be 0.005. The quantity in parentheses in Eq. (17) is the two-phase correction factor, which is merely a simplification of the shift in the logarithmic laws proposed in the literature (Dobran [21], Hewitt [22], and Kumar and Edwards [19]).

cl-cv Interfacial Area Density and Mean Description of the Wave Structure. In order to model the cv-cl interfacial area density, some assumptions about the interface must be made. For this analysis, the continuous liquid is assumed to flow as a film along the wall. The wall is assumed to be completely wetted ($\alpha_{\mathrm{cl}}=1.0$ at the wall), and the cl-volume fraction decreases rapidly in the first few nodes away from the wall. In the actual flow situation, the steepness of the transition from the wall ($\alpha_{\mathrm{cl}}=1$ to the core $\alpha_{\mathrm{cl}}\sim0$) is determined by the film thickness and wave characteristics of the interface. These wave characteristics, in turn, are determined by the flow rates, heat fluxes, and momentum forces acting on the interface. The smooth transition in α_{cl} may be interpreted as the effect of a wavy interface on the mean void distribution, although the details of the wave structure are not captured by this model.

The derivation of the interfacial area density is developed within the cell model averaging framework (Drew [10]). Using a phase indicator function as given in Eq. (1) and Reynolds rules of averaging, the interfacial area density is calculated from the gradient normal to the wall in the cl void fraction, or

$$A'''_{\mathrm{cl\text{-}cv}} = \nabla\alpha\cdot\hat{n} \tag{18}$$

where $\hat{n}$ is a vector normal to the wall.

Droplet Models.

Droplet Entrainment. The total entrainment rate is modeled as the sum of two separate physical phenomena: the entrainment of droplets from the roll wave shearing and the break-up of continuous liquid bridges, as follows.

$$\Gamma_{\text{cl-dl}}=\Gamma^{f}_{\text{cl-dl}}+\Gamma^{b}_{\text{cl-dl}}. \tag{19}$$

It is assumed that these two types of entrainment are separable and occur in different regions of the flow. The film entrainment model of Kataoka and Ishii [23] was adapted to multidimensional predictions by extending the original averaged one-dimensional models to two dimensions. It is assumed that the entrainment mass flux given by the Kataoka and Ishii [23] correlation is the same for a film in a small thickness/width duct whose surface area and thickness is the same as that in the cylindrical geometry. It is further assumed that the correlation can be ''localized'' by replacing the cross section-averaged quantities in the dimensionless numbers with local values. The entrainment rate, $\Gamma^{f}_{\text{cl-dl}}$, is given by the following set of equations.

$$\frac{G_E D_h}{\mu_{\text{cl}}}=6.6\times 10^{-7}\text{Re}_1^{0.74}\text{Re}_{\text{cl}}^{0.185}\text{We}^{0.925}\left(\frac{\mu_g}{\mu_f}\right)^{0.26}, \tag{20}$$

where

$$\text{Re}_1=\frac{\rho_1(\alpha_{\text{dl}}u_{\text{dl}}+\alpha_{\text{cl}}u_{\text{cl}})D_h}{\mu_1}, \tag{21}$$

$$\text{Re}_{\text{cl}}=\frac{\rho_1\alpha_{\text{cl}}u_{\text{cl}}D_h}{\mu_1}, \tag{22}$$

and

$$\text{We}=\frac{\rho_v(\alpha_{\text{cv}}u_{\text{cv}})^2D_h}{\sigma}\left(\frac{\rho_1-\rho_g}{\rho_g}\right)^{1/3}. \tag{23}$$

Since the droplets are entrained from the cl-cv interface, the local mass flux is calculated and applied through the local cl-cv interfacial area density, as

$$\Gamma^{f}_{\text{cl-dl}}=G_E A'''_{\text{cl-cv}}. \tag{24}$$

The droplets are also formed in the transition regime where the liquid bridges break up. The fragmentation is caused by flow instabilities and surface tension. These droplets have varying size. A triangular relationship based on the concept of a critical Weber number, breakup time and velocity history by Pilch and Erdman [24] is used in this model. When the breakup occurs, the droplet velocity is assumed to be equal to the mean velocity of the cl-field from which it was created. The mass transfer rate due to breakup is given by the following set of equations.

$$\Gamma^{b}_{\text{cl-dl}}=C_1\overline{\alpha_{\text{cv}}}\rho_l f\alpha_{\text{cl}}, \tag{25}$$

where

$$f=Fu_{\text{cv}}\sqrt{\rho_v/\rho_l}/D_0, \tag{26}$$

$$D_0=2\sqrt{\frac{\sigma}{g(\rho_l-\rho_g)}}, \tag{27}$$

and

$$F=0.07(\text{We}^{0.5}-5.0). \tag{28}$$

Eq. (28) is a simplified correlation developed here from Pilch and Erdman's [24] measurements for different Weber number ranges. Pilch and Erdman [24] proposed their correlation for the breakup of isolated liquid drops that are suddenly exposed to a high-velocity field. Weber number, We, in Eq. (28) is given by

$$\text{We}=D_0\rho_v u_{\text{cv}}^2/\sigma \tag{29}$$

In the current flow situation, as can be noted in Eq. (25), liquid breakup of the cl-field occurs only when the cv-field is present, i.e., in the presence of an interface. Therefore, it may be viewed that the cl-field present in the node along with the cv-field is a large drop which is about to break up.

Droplet Deposition. The deposition model is a simple, flux based model that approximates the mass flow rate of droplets into the continuous liquid film as

$$\Gamma_{\text{dl-cl}}=\rho_l u_{\text{dl}}A'''. \tag{30}$$

The droplet velocity is given by the speed at which dl is carried normal to the plane of deposition.

Drop Size. Several correlations for mean drop size are available in the literature (Tatterson et al. [25], Ueda [8], and Kocamustafaogullari et al. [26]). Ueda's [8] model has been chosen for its simplicity, ease of local implementation (no global physical parameters), and because their experiments were conducted for fluids having a relatively low surface tension and high vapor-to-liquid density ratio. Comparisons of Ueda's correlation with the measured average drop size are presented in Part I of this paper (Trabold and Kumar [27]). The correlation is given by

$$d_D=5.8\times 10^{-3}D_h\left[\frac{\sigma}{\mu_v u_{\text{cv}}}\left(\frac{\rho_g}{\rho_l}\right)^{1.25}\right]^{0.34}. \tag{31}$$

The hot-film anemometer probe may not measure all droplets which strike the sensor, and hence bias the size measurement toward larger droplets. Therefore, it is assumed that the measured droplet size may be better represented by the volume weighted diameter. The few data points from the current experiments which are well predicted by the Ueda relation as given by Trabold and Kumar [27] also correspond to a majority of the modeling conditions, namely, $\overline{\alpha}>0.9$.

Droplet Drag. This model, initially proposed by Ishii and Zuber [28], was developed for the viscous and the distorted particle regime from similarity criteria derived between single and multiple particle behavior and the definition of a mixture viscosity, as

$$C_D=\max\left(\begin{array}{ll}\dfrac{24}{\text{Re}_D}(1.0+0.1\text{Re}_D^{3/4}) & \\ \dfrac{2}{3}d_D\left[\dfrac{g\Delta\rho}{\sigma}\right]^{1/2} & \left[\dfrac{1+17.67(1-\alpha_{\text{dl}})^{18/7}}{18.67(1-\alpha_{\text{dl}})^3}\right]^2\end{array}\right), \tag{32}$$

where

$$\text{Re}_D=\frac{\rho_g|v_r|d_D(1-\alpha_D)^{2.5}}{\mu_g} \tag{33}$$

The factor, $(1-\alpha_D)^{2.5}$, modifies the viscosity and thus accounts for the increased drag on a nonspherical droplet. This factor also accounts for the effect of the interaction of multiple droplets on each other.

Droplet Lift. A nondrag force which plays a role in the annular vapor core is the lift force which appears as a source term in the momentum equation. The constitutive relationship given in Eq. (34) models the force generated as an inviscid fluid with constant strain and rotation flows past a sphere. This force captures the influence of the continuous field velocity gradient on the dispersed field, thereby impacting the transverse distribution of the dispersed phase. It is based on the derivation for a bubbly lift force using a non-inertial reference frame which rotates at a rate equal to the far field fluid rotation (Drew and Lahey [29]). Potential flow theory is used to construct the inviscid flow field around the sphere and the force is calculated by integrating the interfacial pressure over the sphere's surface. In the droplet field, the fields are switched, and the lift force is given by

$$M^{L}_{\text{cv}}=-M^{L}_{\text{dl}}=C_L\rho_{\text{cv}}\alpha_{\text{dl}}\mathbf{v}_R\times(\nabla\times\mathbf{v}_{\text{cv}}), \tag{34}$$

where

$$\mathbf{v}_R=\mathbf{v}_{\text{cv}}-\mathbf{v}_{\text{dl}}. \tag{35}$$

The lift coefficient, C_L, for a single bubble is 0.5 for inviscid flows, but may be much lower for highly viscous flows (Eichhorn and Small [30]). In this study, C_L is taken to be 0.2.

Turbulent Dispersion of Droplets. A turbulent dispersion model for bubbles was developed by de Bertodano [31] by making an analogy of thermal diffusion of air molecules in the atmosphere. A thought experiment was made for a bounded turbulent bubbly mixture whose dispersion is similar to that of air molecules, except that the motion of the bubbles is produced by the turbulent energy of the liquid phase instead of the thermal energy

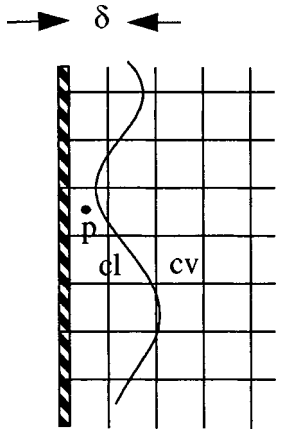

Fig. 1 Schematic of the computational grid across the interface

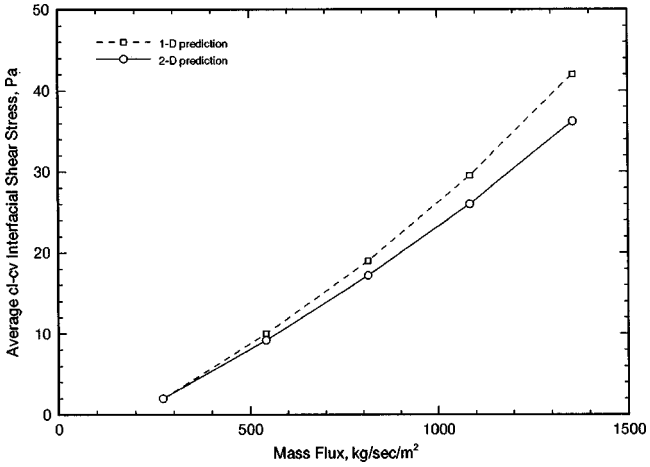

Fig. 2 Comparison of average interfacial shear stress between one-dimensional and two-dimensional analysis

Table 1 Flow conditions used for model validation

Case no.	System pressure MPa	Flow rate kg/hr	Average void fraction	Inlet quality	Density ratio ρ_1/ρ_g
1	1.4	532	.80	.24	16.2
2	1.4	532	.95	.48	16.2
3	1.4	1064	.95	.42	16.2
4	2.4	106	.94	.92	7.3
5	2.4	106	.90	.79	7.3
6	2.4	266	.92	.66	7.3
7	2.4	532	.94	.70	7.3
8	2.4	1064	.90	.49	7.3

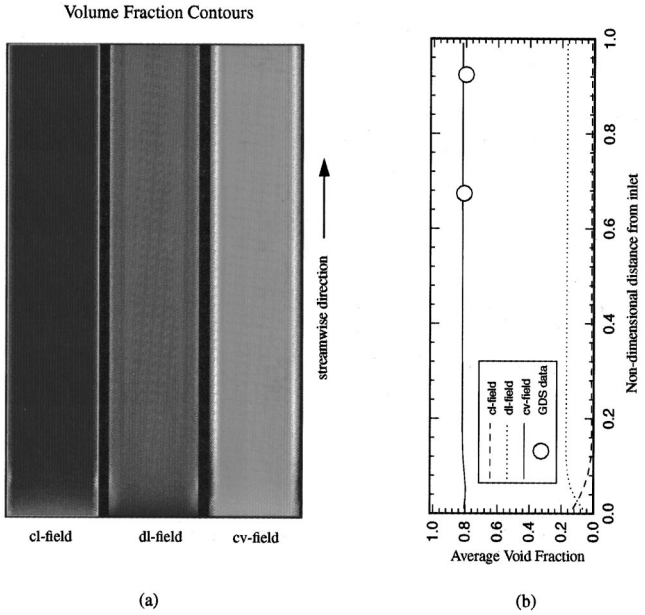

Fig. 3 (*a*) Contour plots of volume fraction in each field; (*b*) corresponding average volume fraction profiles along the streamwise direction and comparison with GDS data

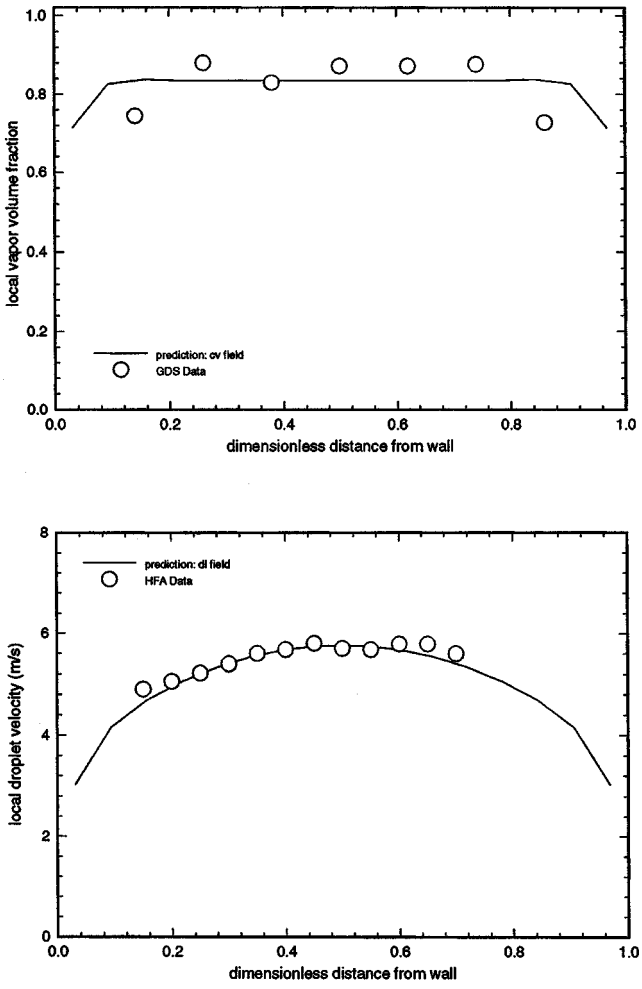

Fig. 4 Comparison of model predictions with experiments. Case 1: $P=1.4$ MPa; $w=532$ kg/hr; $\bar{\alpha}=0.8$.

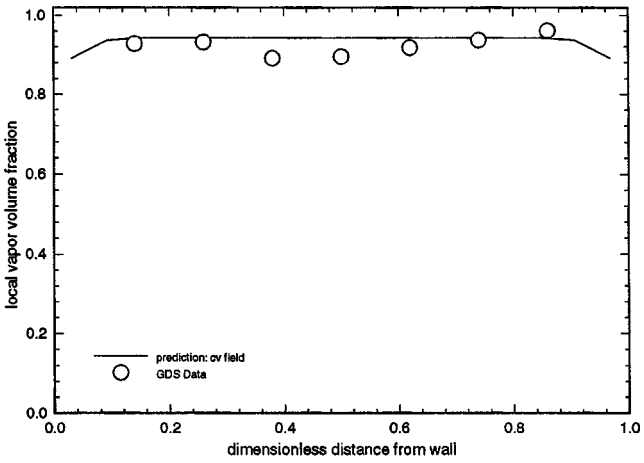

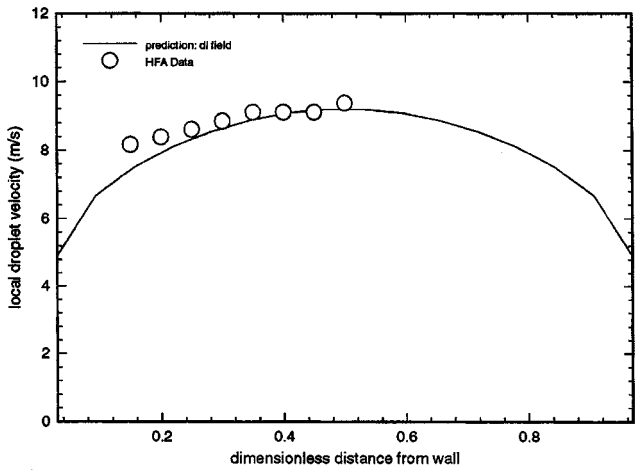

Fig. 5 Comparison of model predictions with experiments. Case 2: $P=1.4$ MPa; $w=532$ kg/hr; $\bar{\alpha}=0.95$.

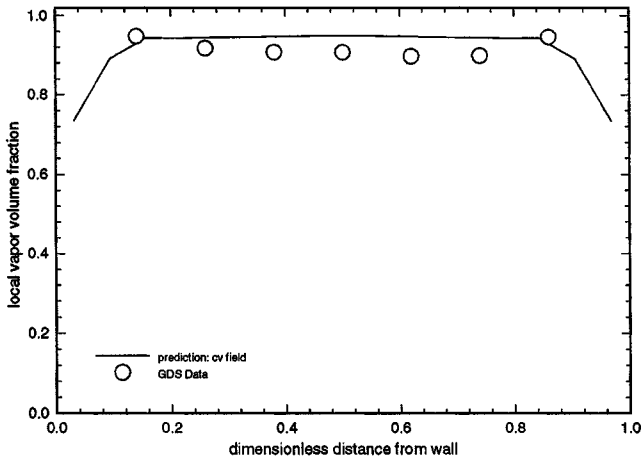

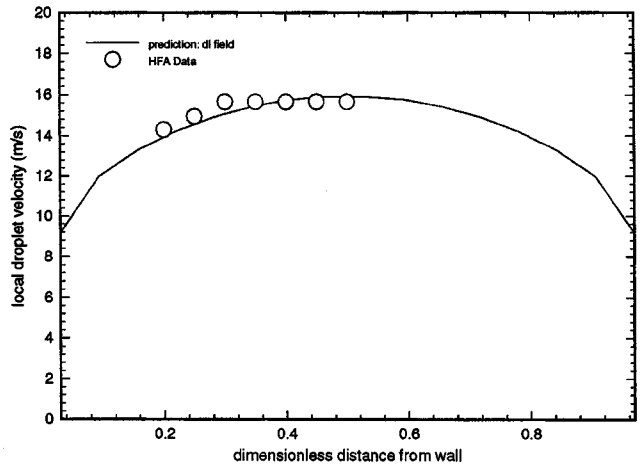

Fig. 6 Comparison of model predictions with experiments. Case 3: $P=1.4$ MPa; $w=1064$ kg/hr; $\bar{\alpha}=0.95$.

of the air molecules. In annular flow, the dispersion model is adapted for liquid droplets in a vapor medium, and is given by

$$T_{\mathrm{dl}}^{d}=-0.1\rho_v k_{\mathrm{cv}}\nabla \ln \alpha_{\mathrm{dl}}. \tag{36}$$

Since this model involves a gradient of void fraction, it is possible to construct it from the cross-correlation term of fluctuating void fraction and fluctuating velocity.

cv-dl Interfacial Area Density. The droplet interface is assumed to arise around a spherically shaped dispersed field (dl) whose diameter is locally defined (see the ''Drop Size'' section). Based on the spherical equivalent drop size, the interfacial area density is given by

$$A'''_{\mathrm{cv\text{-}dl}}=\frac{6\alpha_{\mathrm{dl}}}{d_D}. \tag{37}$$

Results and Analysis

The models described in the previous section have been implemented into the three-field, two-dimensional solver, and the results are compared with adiabatic annular flow data obtained in refrigerant (R-134A) flows in a vertical duct with a cross-section aspect ratio of 22.5 in Part I of this paper (Trabold and Kumar [27]). First, the local application of the interfacial models are discussed and one-dimensional results are compared with the current two-dimensional results, followed by the comparison of integrated predictions.

Local Application of the cl-cv Interfacial Models.

Interfacial Shear. For proper adaptation of one-dimensional models in the literature in a two-dimensional analysis code, appropriate model coefficients must be determined. For example, interfacial shear given by Eqs. (16) and (17) was originally formulated for flow in a circular tube where the interfacial area is the equivalent of that for a film of thickness δ on the walls. The continuous liquid layer extends from the wall to the wave troughs, and the disturbed wavy layer of thickness from the crests to the troughs of the waves. Due to this distortion of the interface by the waves of small and large amplitudes (sketch shown in Fig. 1), it is difficult to define δ. Further, it is inappropriate to use such a parameter in a local formulation. When interfacial shear is applied on a local basis, it must be modified to account for the effect of averaging on the model. This is done by determining the local interfacial shear at every node by replacing δ with y in Eq. (17), and applying it to a local interfacial area. This ensures that when the local interfacial area density is zero, the interfacial shear is also zero. Thus the interfacial area density, in effect, eliminates the need for a film thickness model in a multi-dimensional formulation.

The magnitude of the interfacial shear depends on the local relative velocity; therefore, in Eq. (16), u_g is replaced by $(u_{\mathrm{cv}}-u_{\mathrm{cl}})$ as was originally intended by Wallis [3]. Since, this local velocity difference is much smaller than the difference in the average velocities, an empirical coefficient of 1.34 was obtained by

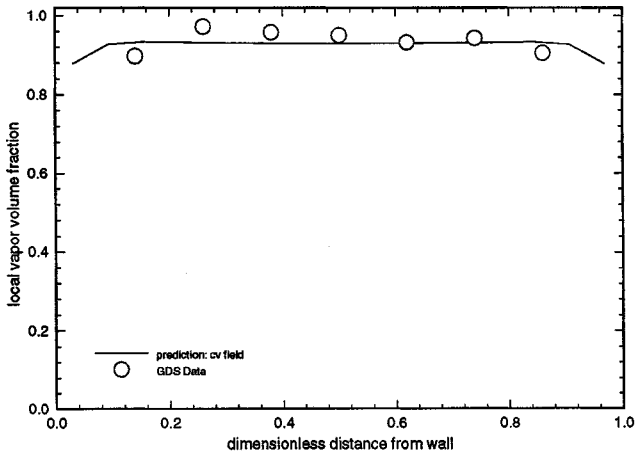

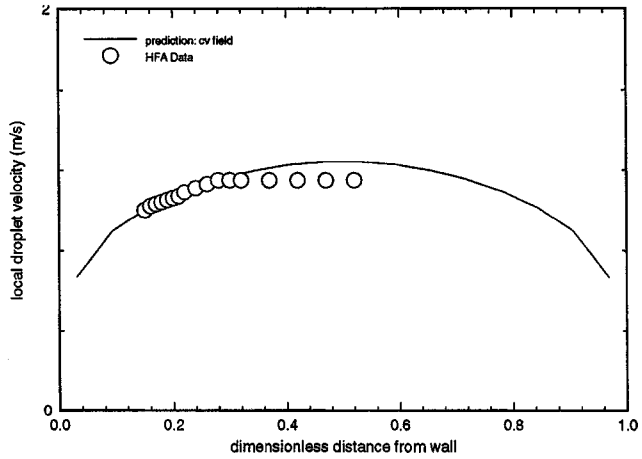

Fig. 7 Comparison of model predictions with experiments. Case 4: $P=2.4$ MPa; $w=106$ kg/hr; $\bar{\alpha}=0.94$.

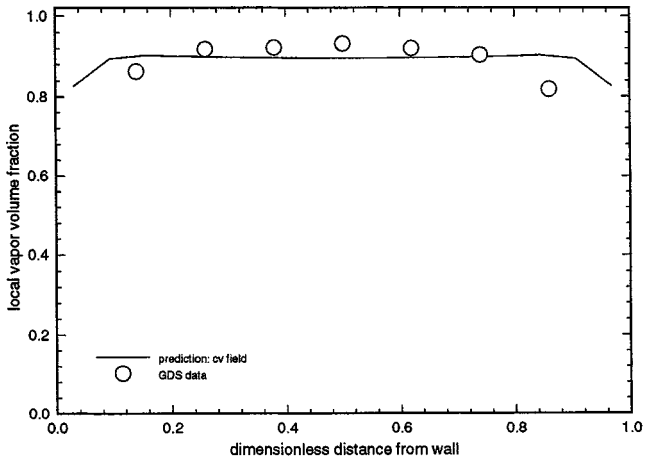

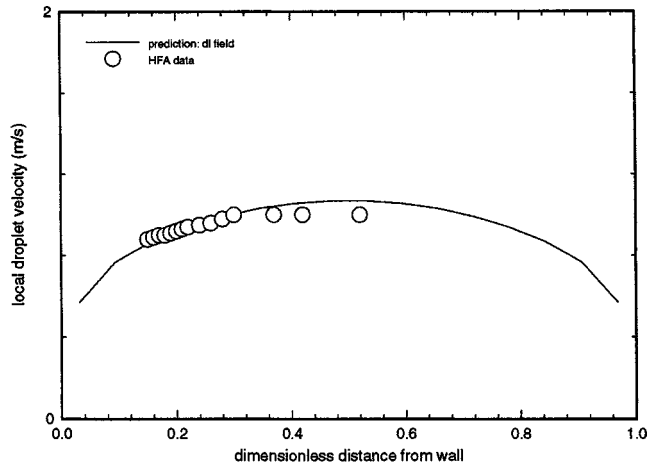

Fig. 8 Comparison of model predictions with experiments. Case 5: $P=2.4$ MPa; $w=106$ kg/hr; $\bar{\alpha}=0.90$.

matching the void fraction data. Using this parameter, two-dimensional predictions were obtained for different mass flux and a void fraction of 90 percent. The interfacial shear was then averaged across the test section and compared with the equivalent one-dimensional interfacial shear as shown in Fig. 2. It can be seen from this figure that the distribution coefficient captures the effects of averaging adequately at low flows. At the highest mass flux, the two-dimensional prediction is about 15 percent lower than to its one-dimensional counterpart. This means that the coefficient is probably dependent on a global parameter such as Reynolds number.

Entrainment/Deposition. The entrained flux and deposition flux of droplets are linked in that they must be the same in equilibrium. This was ensured in the current analysis. The entrainment rate was also calculated for a one-dimensional homogeneous flow for some of the flow conditions given in Table 1. This entrainment rate was compared favorably with the current two-dimensional analysis. Unlike air-water annular flows where the entrained fraction is typically less than 0.3, for high pressure refrigerant flows, these values range between 0 and 1. Surface tension plays a major role in determining the entrained flux. For SUVA, the surface tension is lower, thus increasing the entrainment rate. In two-dimensional flow, the entrainment rate is expected to differ across the narrow thickness dimension with the maximum occurring at the interface. This is once again captured by means of the interfacial area density which peaks at the interface. When the two-dimensional entrained flux is averaged across the thickness, it should yield the one-dimensional value, as was the case in the current analysis. Although no measured entrainment rate in SUVA is available, the forces are balanced to allow good integrated predictions as seen in the next section.

Integrated Model Predictions and Comparisons. In this section, an integrated model prediction is performed to test the current models. Averaged void fraction data and droplet velocity were obtained using a gamma densitometer and a hot film anemometer, respectively.

The contour plots in Fig. 3(*a*) show the axial development of the phasic volume fractions in the test section. The three color contour plots show the volume fraction in a x-y slice plane for the continuous liquid, dispersed liquid, and continuous liquid fields, respectively. Figure 3(*b*) shows the axial variation of the transverse average volume fraction for each field. The flow is induced by setting an inlet cv-volume fraction based on the inlet quality measured from the experiments, x_i, using the relationship,

$$\alpha_{\mathrm{cv}}=\frac{1}{1+\dfrac{\rho_y}{\rho_1}\left(\dfrac{1-x_i}{x_i}\right)}. \tag{38}$$

The annular flow structure forms very rapidly, and a thin liquid film develops at the walls and reaches a fully developed condition within the first few hydraulic diameters in the streamwise direction. Film entrainment dominates in the annular region, with the local entrainment rate, $\Gamma^f_{\mathrm{cl\text{-}dl}}$, peaking at the location of the film

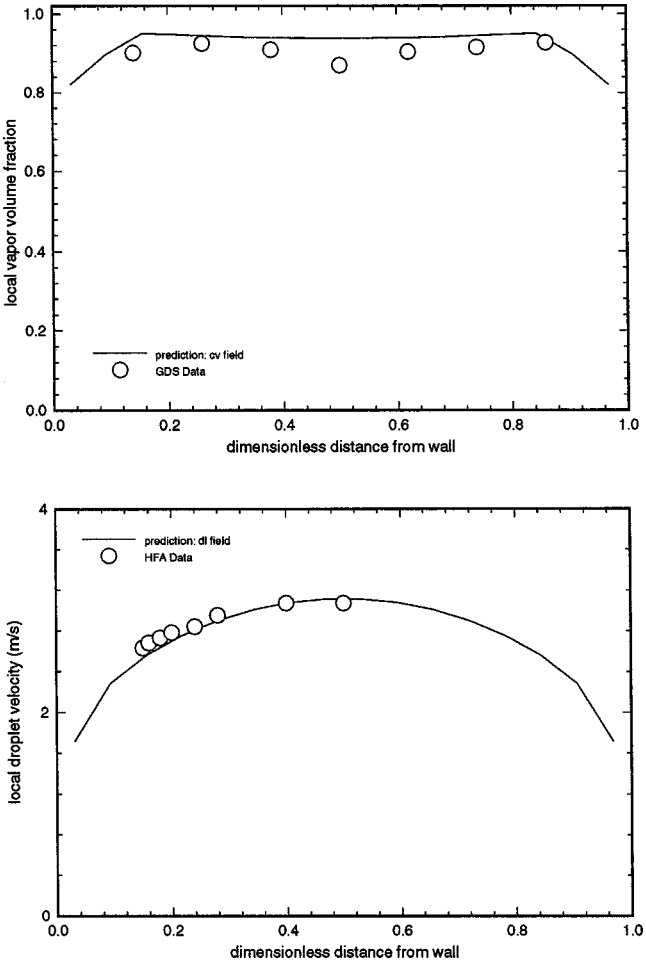

Fig. 9 Comparison of model predictions with experiments. Case 6: $P=2.4$ MPa; $w=266$ kg/hr; $\bar{\alpha}=0.92$.

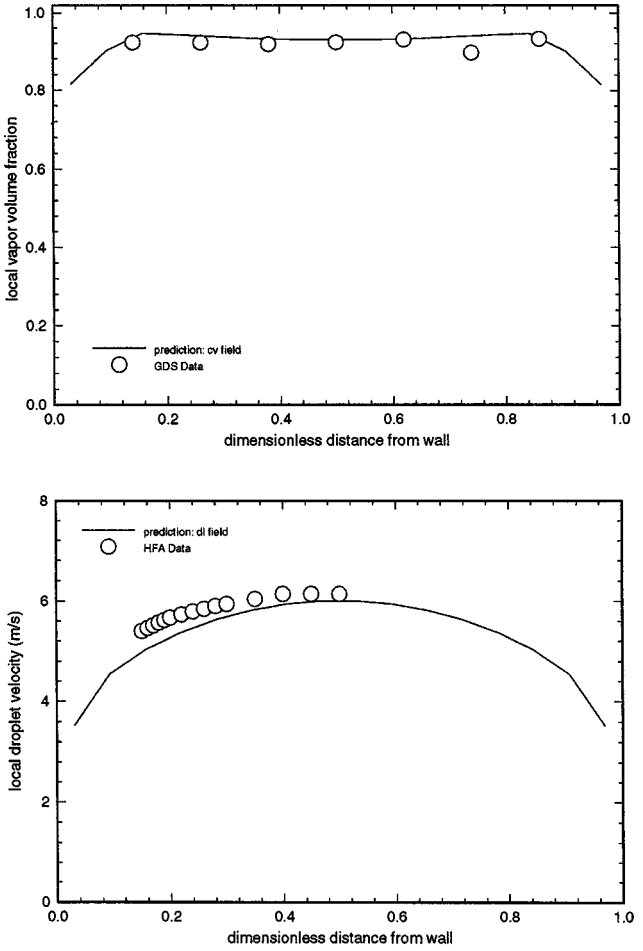

Fig. 10 Comparison of model predictions with experiments. Case 7: $P=2.4$ MPa; $w=532$ kg/hr; $\bar{\alpha}=0.94$.

interface. The shift of mass from cl to dl due to bridge break-up, $\Gamma^{b}_{\text{cl-dl}}$, dominates near the inlet where the flow enters as a mixture of continuous liquid and continuous vapor. Here, bridges of liquid between the vapor pockets are fragmented into dispersed liquid. After the flow develops, the cross-section average void fraction prediction is compared with experimentally measured void fraction at two different downstream locations (Fig. 3(*b*)). This cross-check was done for every run and the comparisons were found to be good.

In Figs. 4–11, local comparisons of droplet velocity and the void fraction are made for 8 cases at two system pressures, different flow rates and void fractions at or above 80 percent. These flow conditions are provided in Table 1, with the first three cases run at 1.4 MPa and the next five at 2.4 MPa. For all these cases, the modeling coefficients provided in the previous section remained the same. High void fraction flows are chosen such that the flow is predominantly two-dimensional for valid comparison with analysis. In general, the local predictions of void fraction and droplet velocity are remarkably good, validating the overall modeling approach taken. Specific observations of general model behavior, deviations and discrepancies in Figures 4 to 11 are discussed below.

In Fig. 4, for 1.4 MPa, the liquid film on the wall is thick at $\alpha=0.8$, and the flow is locally annular is the vapor core. The void profile maintains a center-peaked distribution as the flow appears to undergo late stages of transition. A mixture of continuous vapor slugs separated by liquid bridges flow together in a continuous liquid field. The fully annular void prediction is flatter due to fairly uniformly distributed liquid droplets in the vapor core. The droplet volume fraction prediction for this case is 18 percent. The model does not discriminate between the droplets and liquid ligaments as it considers them as one distributed liquid (dl) field, and therefore, it is not surprising that for this case which is not purely annular, there is a very high dl-volume fraction in the vapor core.

As the average void fraction is increased to 95 percent at 1.4 MPa (Figs. 5 and 6), the gas core velocity increases and tears the liquid droplets from the surface of the thin film. The liquid film becomes thinner, and a noticeable wall-peaked distribution in void fraction occurs. The dip in void fraction at the centerline is probably due to the migration of droplets from the edges of the test section where high amplitude roll waves are formed. Since the film is thicker near the edges than at the flat walls, the fragmentation of the edge films gives rise to much bigger droplet diameters. This three-dimensionality in the flow field due to a finite aspect ratio of 22.5 is not captured by the current two-dimensional predictions. For these high flows, the drop size measurement profiles display an increasing trend towards the centerline from the wall (Trabold and Kumar [27]). The drop size model provided in the previous section is based on the premise that the drop size is controlled by the interaction between the dl and the cv fields. Therefore, the droplets entrained near the liquid film, as predicted by the model, tend to be larger in size compared to those in the main vapor core where the droplets are subjected to turbulent break up. Thus, the current model cannot predict the increasing trend in the drop size measurements. The predicted drop size pro-

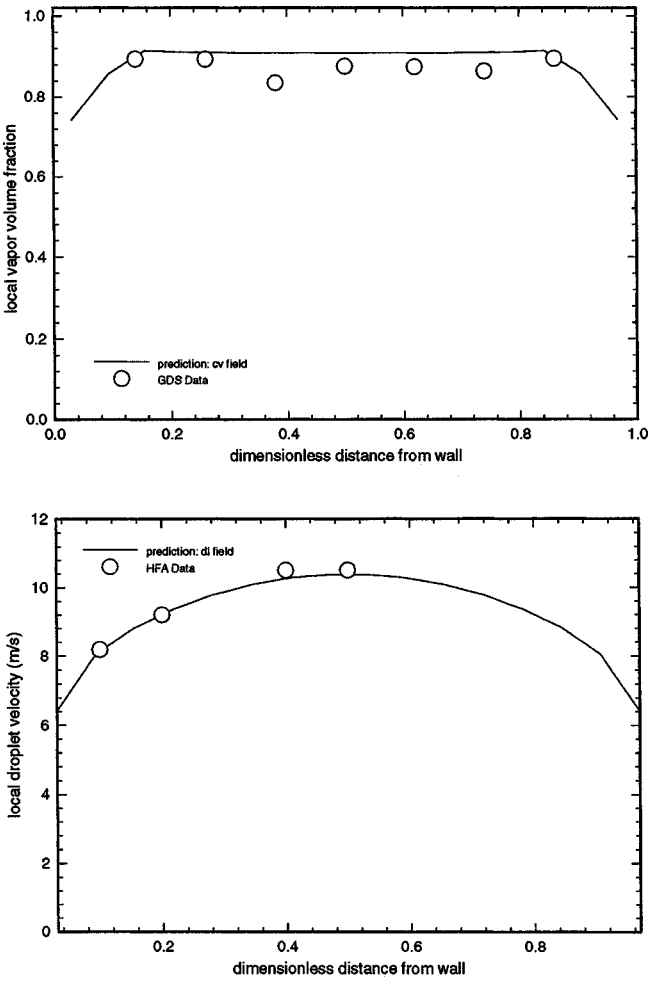

Fig. 11 Comparison of model predictions with experiments. Case 8: $P=2.4$ MPa; $w=1064$ kg/hr; $\bar{\alpha}=0.90$.

files (not shown here) always have a decreasing trend, but the average predicted value was found to be close to the average experimental value.

The entrainment rate as given by the droplet entrainment model is enhanced at the higher pressure of 2.4 MPa for which the gas density is higher and the surface tension is lower. In general, at very high void fractions ($\alpha>0.9$), the liquid film is relatively thin around the perimeter of the duct. The droplets emanating from the edge films are similar in size compared to other entrained droplets, and the two-dimensional approximation is reasonable for numerical analysis. Three-dimensional formulation is necessary to predict lower void fraction annular flows. Since the liquid-to-gas density ratio for 2.4 MPa is 7.3 (closely simulating steam-water conditions at very high pressures) which is nearly half of that for 1.4 MPa, the droplet velocities for 2.4 MPa are lower than their lower pressure counterparts (Figs. 7–11). These velocities range from ~1 m/s to ~10 m/s, and are closer to the corresponding mixture velocities for these flows. Droplet velocities reported in the literature for annular flows are in two-phase annular flows with very low vapor-to-liquid density ratios (as in air-water), and are an order of magnitude higher than the current velocities.

Summary and Conclusions

A three-field model capable of predicting both local and global annular flow characteristics has been developed. Locally based droplet and film models have been either developed here or adapted from the literature for closure of the governing equations. Interfield (liquid-liquid) models, interphase (liquid-vapor) models and other force models are locally applied to appropriately separate the liquid film from the vapor core, and to capture the physics of the droplet motion. This paper provides substantial information on the individual and integrated effects of these models in annular flow, and compares the predictions with the average and local void fraction and droplet velocities in a refrigerant fluid (R-134a) using hot film anemometry and gamma densitometry.

The proposed set of models appears to adequately predict local distribution of the variables in purely annular flows. However, the model set needs to be strengthened for the prediction of slug-to-annular transition flows at void fractions in the range of 70 percent to 85 percent. In this regard, including a fourth dispersed vapor field to account for the trapping of bubbles in the liquid film, and a three-dimensional analysis may be necessary. As a consequence of the interfacial waves breaking at the tips, droplet deposition and droplet entrainment processes have a significant impact on the interfacial shear stress. The current models for drop size and entrainment/deposition need to be reevaluated and their effect on the current interfacial shear model tested. Additional data on the interfacial wave frequency, velocity and area concentration obtained in Part I of this paper (Trabold and Kumar [27]) should be used to develop mechanistic interfacial shear model that can be locally applied.

Acknowledgments

The authors are grateful to Dr. D.P. Edwards for his initial model development efforts and many fruitful discussions, and to Mr. B.W. Siebert and Dr. R.F. Kunz for their efforts in code development.

Nomenclature

A''' = interfacial area density, 1/m
d_D = droplet diameter, m
D_h = hydraulic diameter, m
f = liquid bridge breakup frequency
f_i = interfacial friction factor
f_{sp} = single-phase friction factor
G = mass flux, kg/hr/m^2
k = kinetic energy
k_s = wall roughness, m
M_i = nondrag force in i-field
p = pressure, Pa
P = turbulence production term
Re = Reynolds number
t = duct thickness, m
u = axial velocity, m/s
u^* = friction velocity, m/s
u_R = relative velocity, m/s
$\mathbf{v}$ = velocity vector
w = mass rate of flow, kg/hr
We = Weber number
x_i = inlet quality
y, Y = thickness dimension, m

Symbols

α = void fraction
δ = liquid film thickness
μ = dynamic viscosity
ν = kinematic viscosity
ρ = density
τ_w = shear stress
$\boldsymbol{\tau}_i$ = shear stress tensor in i-field
$\boldsymbol{\tau}_i^{\mathrm{Re}}$ = Reynolds stress tensor in i-field
$\Delta\rho$ = change in density from vapor to liquid phase
Γ_{ij} = interfacial mass transfer rate from field i to j
ε = turbulent energy dissipation

Subscripts and superscripts

cv = continuous vapor field
cl = continuous liquid field
dl = dispersed liquid field
g = gas
f,l = liquid

References

[1] Hall-Taylor, N. S., Hewitt, G. F., and Lacey, P. M. C., 1963, ''The Motion and Frequency of Large Disturbance Waves in Annular Two-Phase Flow of Air-Water Mixtures,'' Chem. Eng. Sci., **18**, pp. 537–552.

[2] Hewitt, G. F., and Hall-Taylor, N. S., 1970, *Annular Two-Phase Flow*, Pergamon Press.

[3] Wallis, G. B., 1969, *One-Dimensional Two-Phase Flow*, McGraw-Hill, New York.

[4] Hewitt, G. F., and Govan, A. H., 1990, ''Phenomena and Prediction in Annular Two-Phase Flow,'' ASME FED-Vol. 99, Advances in Gas-Liquid Flows, J. H. Kim et al., eds.

[5] Kang, H. C., and Kim, M. H., 1993, ''The Relation Between the Interfacial Shear Stress and the Wave Motion in a Stratified Flow,'' Int. J. Multiphase Flow, **19**, No. 2, pp. 35–49.

[6] Cousins, L. B., and Hewitt, G. F., 1968, ''Liquid Phase Mass Transfer in Annular Two-Phase Flow: Droplet Deposition and Liquid Entrainment,'' UKAEA Report AERE-R5657.

[7] Kataoka, I., Ishii, M., and Mishima, K., 1983, ''Generation and Size Distribution of Droplet in Annular Two-Phase Flow,'' ASME J. Fluids Eng., **105**, pp. 230–238.

[8] Ueda, T., 1979, ''Entrainment Rate and Size of Entrained Droplets in Annular Two-Phase Flow,'' Bull. JSME, **22**, pp. 1258–1265.

[9] Azzopardi, B. J., and Teixeira, J. C. F., 1994, ''Detailed Measurements of Vertical Annular Two-Phase Flow—Part I: Drop Velocities and Sizes,'' ASME J. Fluids Eng., **116**, pp. 792–795.

[10] Drew, D. A., 1992, ''Analytical modeling of multiphase flows,'' *Boiling Heat Transfer*, R. T. Lahey, ed., Elsevier, pp. 31–84.

[11] Siebert, B. W., Maneri, C. G., Kunz, R. F., and Edwards, D. P., 1995, ''A Four-Field Model and CFD Implementation for Multi-Dimensional, Heated Two-Phase Flows,'' *Proc. of the 2nd Int. Conf. on Multiphase Flow*, Kyoto, Japan.

[12] Patankar, S. V., 1980, *Numerical Heat Transfer and Fluid Flow*, Hemisphere Publishing, NY.

[13] Rhie, C. M., and Chow, W. L., 1983, ''Numerical Study of the Turbulent Flow Past an Airfoil with Trailing Edge Separation,'' AIAA J., **21**, No. 11, pp. 1525–1532.

[14] Spalding, D. B., 1980, ''Mathematical Methods in Nuclear Reactor Thermal-Hydraulics,'' *Proceeding of ANS Meeting on Nuclear Reactor Thermal-Hydraulics*, R. T. Lahey, ed., pp. 1979–2023.

[15] FLOW3D, 1992, ''Release 3.2 User's Manual Computational Fluid Dynamics Services,'' *AEA Industrial Technology*, Harwell Laboratory, Oxford, UK.

[16] Siebert, B. W., and Antal, S. P., 1993, ''An IPSA-Based Two-Fluid Algorithm for Boiling Multi-Phase Flows,'' *First CFDS Int. User Conf.*, Oxford, UK.

[17] Woodmansee, D. E., and Hanratty, T. J., 1969, ''Mechanism for the Removal of Droplets from a Liquid Surface by a Parallel Air Flow,'' Chem. Eng. Sci., **24**, pp. 299–307.

[18] Antal, S. P., Lahey, Jr., R. T., and Flaherty, J. E., 1991, ''Analysis of Phase Distribution in Fully Developed Laminar Bubbly Two-Phase Flow,'' Int. J. Multiphase Flow, **17**, No. 5, p. 635.

[19] Kumar, R., and Edwards, D. P., 1996, ''Interfacial Shear Modeling in Two-Phase Annular Flow,'' Proc. ASME Heat Transfer Division, Int. Mech. Eng. Congress and Exposition, Atlanta, GA, HTD-Vol. 334, pp. 381–389.

[20] Gill, L. E., Hewitt, G. F., Hitchon, J. W., and Lacey, P. M. C., 1963, ''Sampling Probe Studies of the Gas Core in Annular Two-Phase Flow-I: The Effect of Length on Phase and Velocity Distribution,'' Chem. Eng. Sci., **18**, pp. 525–535.

[21] Dobran, F., 1983, ''Hydrodynamic and Heat Transfer Analysis of Two-Phase Annular Flow with a New Liquid Film Model of Turbulence,'' Int. J. Heat Mass Transf., **26**, No. 8, pp. 1159–1171.

[22] Hewitt, G. F., 1991, ''Annular Flow Phenomena,'' *Proc. Japan Soc. Multiphase Flow on Waves and Turbulence in Multiphase Flow, and its Application*, Sept., pp. 126–154.

[23] Kataoka, I., and Ishii, M., 1983, ''Entrainment and Deposition Rates of Droplets in Annular Two-Phase Flow,'' ASME-JSME Thermal Engineering Joint Conference, Vol. 1, pp. 69–80.

[24] Pilch, M., and Erdman, C. A., 1987, ''Use of Breakup Time Data and Velocity History Data to Predict the Maximum Size of Stable Fragments for Acceleration-Induced Breakup of a Liquid Drop,'' Int. J. Multiphase Flow, **13**, No. 6, pp. 741–757.

[25] Tatterson, D. C., Dallman, J. C., and Hanratty, T. J., 1977, ''Drop Sizes in Annular Gas-Liquid Flows,'' AIChE. J., **22**, pp. 68–76.

[26] Kocamustafaogullari, G., Smits, S. R., and Razi, J., 1994, ''Maximum and Mean Droplet Sizes in Annular Two-Phase Flow,'' Int. J. Heat Mass Transf., **37**, pp. 955–965.

[27] Trabold, T. A., and Kumar, R., 2000, ''High Pressure Annular Two-Phase Flow in a Narrow Duct: Part I—Local Measurements in the Droplet Field,'' ASME J. Fluids Eng., **122**, pp. 364–374.

[28] Ishii, M., and Zuber, N., 1979, ''Drag Coefficient and Relative Velocity in Bubbly, Droplet or Particulate Flow,'' AIChE. J., **25**, pp. 843–855.

[29] Drew, D. A., and Lahey, R. T., 1987, ''The Virtual Mass and Lift Force on a Sphere in Rotating and Straining Inviscid Flow,'' Int. J. Multiphase Flow, **13**, No. 1, pp. 113–121.

[30] Eichhorn, R., and Small, S., 1964, ''Experiments on the Lift and Drag of Spheres Suspended in a Poiseuille Flow,'' J. Fluid Mech., **20**, No. 3, p. 513.

[31] Lopez de Bertodano, M., 1992, ''Turbulent Bubbly Two Phase Flow in a Triangular Duct,'' Ph.D. thesis, Rensselaer Polytechnic Institute, Troy, NY, 1992.

A Study of Near-Field Entrainment in Gas Jets and Sprays Under Diesel Conditions

Scott Post
Research Assistant

Venkatraman Iyer
Research Assistant

John Abraham
Associate Professor

School of Mechanical Engineering
Purdue University,
West Lafayette, IN 17906

This paper presents a computational study of entrainment characteristics in the near-field of gas jets under atmospheric and Diesel conditions and sprays under Diesel conditions. Computed flowfield information is used to estimate the rate of mass entrainment in the jet and derive the entrainment rate constant. The value of the entrainment rate constant is compared to experimental results in the literature. It is found that the computed values of the constant in the near-field are less than the values in the self-similar region of the jet with the values increasing monotonically from the orifice to the self-similar region. These results are consistent with experimental results. In the case of sprays, it is found that it is difficult to arrive at firm conclusions because the results are sensitive to several parameters that are not well known and to the numerics. The computed results for sprays are also discussed relative to measurements in sprays quoted in the literature.
[S0098-2202(00)00802-6]

Introduction

Understanding the structure of transient jets is of importance in the context of understanding Diesel combustion processes. In the Diesel engine, the transient spray jet has a dominant influence on the flow field in that the injected momentum flow rate controls the rate of mixing of the fuel and air. Models for sprays have been developed and are widely employed by researchers and engine designers (Bracco [1], Reitz [2], O'Rourke and Amsden [3], Andrews [4]). However, these models have limitations related to inadequate understanding of the physics of atomization and drop dynamics, the modeling of collisions and coalescence, and numerics (Abraham [5], Iyer and Abraham [6,7], Aneja and Abraham, [8,9]). In fact, in many cases the limitations may lead to inaccurate trends. It has also been shown recently that computed gas jets may reproduce the structure of measured Diesel sprays in terms of penetration and spread with adequate accuracy (Iyer and Abraham [6,7]). However, prior to employing it for studies in Diesel engines, it is important to compare the details of computed and measured gas jets so that the adequacy of the models may be assessed. In particular, the near-field behavior of jets is of importance in Diesel engines where, in some cases, the distance from the injector orifice to the wall may be in the near-field region. In the case of a gas jet, the near field is defined as that part of the jet where it has not achieved self-similar profiles.

Much work has been done on determining the entrainment and velocity profiles in free gas jets under steady-state conditions. In a now classic work, Ricou and Spalding [10] measured the mass entrainment rate in gas jets as a function of axial distance and the ratio of injected density to the ambient gas density by employing a porous cylinder and estimating the mass flux into the cylinder as a function of axial distance. Using physical arguments, they obtained the following expression, which relates the normalized entrained mass flux at any axial distance to the normalized axial distance:

$$\frac{\dot{m}(x)-\dot{m}_i}{\dot{m}_i}=K\left(\frac{x}{d}\right)\left(\frac{\rho_a}{\rho_i}\right)^{1/2} \tag{1}$$

where K is referred to as the entrainment constant, and $d_e = d(\rho_i/\rho_a)^{1/2}$ is an effective orifice diameter. From their experimental results, they found a value of 0.32 for K in the far-field. This and other works are reviewed by Abraham [11] who found that the measured entrainment constant, as reported in the literature, varied in the range of 0.2 to 0.457 in the far field. These results may depend on several parameters, including the type of nozzle used and the velocity profile at the orifice and the measurement technique employed. Studies of near-field entrainment rate constant in gas jets are fewer.

Crow and Champagne [12] used hot-wire anemometry to measure the steady-state velocity in the near-field of a free gas jet. Their work includes measurements of the centerline velocity of the jet and radial velocity profiles in the near field. They showed that the entrainment in the near field is less than in the far field. Hill [13] used an adaptation of Ricou and Spalding's [10] technique to measure local entrainment rates in steady jets. He found that the entrainment is less in the near field than the far field, and that the value of the entrainment constant increases with axial distance in the near field. He suggested that the near field is about 13 diameters long. Wall et al. [14] also employed an apparatus like that of Ricou and Spalding [10] and found that entrainment constant increases as a function of axial distance in the near field. In a related work, Liepmann and Gharib [15] made Particle Image Velocimetry (PIV) measurements in the near field of water jets at low Reynolds numbers to determine the entrainment constant and found that the entrainment constant increases with axial distance in the near field. All of the above measurements are in steady jets. Andriani et al. [16] present a comparative study of gas jets and Diesel sprays in the near field. They employed Laser Doppler Velocimetry (LDV) to take measurements of the radial velocity profiles of the flowfield up to 200 diameters from the orifice. They found that the entrainment constant increases from the orifice as a function of axial distance for both gas jets and sprays. Andriani et al. [16] also made some measurements in the developing, or transient, part of the jet. A transient jet consists of an unsteady head vortex region that is followed by a quasi-steady region that behaves much like a steady jet. As time increases the length of the steady region increases.

In the case of sprays, we will focus our attention on sprays under Diesel conditions only. This implies that the sprays are atomizing and vaporizing. It also implies that the sprays are unsteady. Only under these conditions can sprays be compared to gas jets (Iyer and Abraham [6]). Measurements of entrainment characteristics in sprays are far fewer than in gas jets. To our

Contributed by the Fluids Engineering Division for publication in the JOURNAL OF FLUIDS ENGINEERING. Manuscript received by the Fluids Engineering Division January 21, 1999; revised manuscript received December 20, 1999. Associate Technical Editor: C. L. Merkle.

Table 1 Summary of entrainment measurements in Diesel sprays

Author	Year	Fuel	Ambient	Injection velocity (m/s)	Orifice size (mm)	Ambient pressure (bar)	Ambient temp. (K)	Meas. method	Entrainment constant	x/d_e range
Cho et al. [17]	1990	Diesel fuel	Air	237	0.29	10.8 to 99.1	300	Tracer	0.32	25 to 150
Ha et al. [18]	1984	Diesel fuel	CO_2	~150	0.32	13.5	300	Hot-wire	0.27	30 to 300
Andriani et al. [16]	1996	Diesel fuel	Air	255	0.25	1.0 to 7.0	300 to 473	LDV	0.04 to 0.24	8 to 200

knowledge, there are no direct measurements of entrainment velocities or determination of the entrainment rate constant in sprays when both the injection and ambient conditions correspond to those in Diesel engines. Table 1 presents a summary of three experiments in the literature where the entrainment constant has been derived or measured in sprays. For these cases, the injection conditions correspond approximately to those of Diesel engine sprays, but the ambient conditions do not. Cho et al. [17] used velocities estimated from the movement of tracer particles to calculate the volume entrained by sprays from $x/d_e=25$ to $x/d_e=150$. Ha et al. [18] used hot-wire anemometry to measure the entrainment velocities from $x/d_e=30$ to $x/d_e=300$. Andriani et al. [15] is the only work that presents measurements of the entrainment constant as a function of axial distance in the near field in sprays at relatively higher pressure. Their measurements are over a length from $x/d_e=8-200$. It is interesting to observe that the measured entrainment constant in the far field approaches that of the gas jets. This is not surprising since these atomizing sprays behave like incompressible gas jets in the far field (Bracco [19]). The measured results also seem to indicate that, in the near field, the values of the entrainment constant would depend on several parameters. In general, these parameters are those that relate to the rate of transfer of momentum from the liquid phase to the ambient. Hence, smaller drop sizes result in higher values of K. Increased rates of vaporization result in higher values of K. The nature of atomization in the near field would also affect the measured values of K. For example, it is possible to reason that the presence or absence of an intact liquid core may affect the values of K. As a result of these dependencies on K, measured values show significant variation in terms of numerical values ranging from minimum values of $K=0.05$ from some cases to $K=0.24$ for other cases (Andriani et al. [16]). For the conditions for which measurements are presented, Andriani et al. [16] show a lower entrainment rate constant for the spray relative to the gas jet.

The Contribution of This Work

A multidimensional model that employs the k-ε model for turbulence, is used to compute near-field entrainment in gas jets and sprays. The computed results are compared for the first time with measurements reported in the literature in the near field. It is shown that the entrainment constant increases with axial distance in the near field, in agreement with the measured results. The far-field measured values of the entrainment constant are also reproduced within 10 percent. Sensitivity to the assumed initial velocity profile is discussed. Computations of near-field entrainment in sprays and comparisons with measurements reported in the literature are also presented. The computed entrainment rate constant is shown to be lower in the spray than in the gas jets. However, in the spray, inadequate understanding of the physics and numerical resolution issues make it somewhat more challenging to draw definitive conclusions. In most practical applications, such as Diesel engines, the multidimensional modeling of the flowfield employs the k-ε model of turbulence (Magi [20], Amsden [21], Abraham [5]).

This work is also an assessment of the adequacy of the k-ε model in being able to reproduce measured entrainment rate constants in gas jets and sprays in such models for Diesel engines. This work is also a contribution in comparing the entrainment constants in gas jets and sprays.

Methods for Estimating the Entrainment Constant

There are two methods typically employed for calculating entrainment in gas jets and sprays. The first involves calculating the axial mass flow rate, $\dot{m}(x)$, across any plane perpendicular to the jet axis. The entrainment constant may then be calculated from

$$K=\left(\frac{d\dot{m}(x)}{dx}\right)\left(\frac{d}{\dot{m}_i}\right)\left(\frac{\rho_i}{\rho_a}\right)^{1/2} \tag{2}$$

A second method involves analyzing the inward radial flow of entrained gas into the jet through a cylindrical control surface of radius r. The axial entrained mass flux $\dot{m}_e(x)$, which is equal to $\dot{m}(x)-\dot{m}_i(x)$, can be calculated at any axial location x, using the following equation:

$$\dot{m}_e(x)=\int_0^x \rho_a(x,r)v(x,r)2\pi r\ dx \tag{3}$$

This assumes that r is selected such that $\rho_a v r$ remains constant as r increases. Then the entrainment constant at any axial location may be estimated from (1), recognizing that $dm/dx=dm_e/dx$, as:

$$K=\frac{d\dot{m}_e(x)}{dx}\cdot\frac{d}{\dot{m}_i}\cdot\left(\frac{\rho_i}{\rho_a}\right)^{1/2} \tag{4}$$

where $d\dot{m}_e(x)/dx=2\pi r\rho_a v$. If the density is constant in the flowfield, as it is in the gas jet computations in this work, we may employ the volume flux, $\dot{Q}(x)$, instead of the mass flux, $\dot{m}_e(x)$.

The Multidimensional Model

The Physical Model. The model employed in this work is an axisymmetric version of a more general model for computing flows, sprays, and combustion in internal combustion engines (Magi [20]). The model solves the two-phase flow of liquid droplets in gas. The gas phase is treated in an Eulerian fashion. The general ensemble averaged conservation equations of mass, momentum, energy and species for unsteady compressible flows are solved with sub-models for turbulence and heat and momentum fluxes at the walls. Turbulence is modeled using the k-ε model with wall functions for the heat and momentum fluxes at the wall (Launder and Spalding [22]). The liquid phase (spray droplets) is treated in a Lagrangian frame of reference. The droplets are tracked in space and time. The liquid and the gas momentum are coupled through the drag and pressure forces. Atomization is modeled by a line source of drops (Chatwani and Bracco [23]). The initial angle of the spray, the size of the injected drops and the steady intact core length are derived from Taylor's theory of the rate of growth of perturbations on planar liquid surfaces induced by gases flowing over it. The resulting expressions can be found

in Chatwani and Bracco [23] and Magi [20]. Collision and coalescence are modeled using the approach of O'Rourke and Bracco [24]. The collision frequency between drops is calculated based on the number density of drops and relative velocity between the drops. The outcome of a collision can either be coalescence or separation. The criterion for drop separation after collision is that the rotational energy of the coalesced drop pair exceeds the surface energy required to reform the original drops from the coalesced pair. This depends on the Weber number, the ratio of inertial to surface tension forces of the drops. The probability of coalescence is inversely proportional to the Weber number. Drop dispersion due to turbulence is modeled using the eddy-lifetime approach of Gosman and Ioannides [25]. The secondary drop break-up model of Reitz and Diwakar [26] is used to compute the drop sizes when the drops further break up after atomization due to surface instabilities produced by the Kelvin-Helmholtz instability mechanism. The vaporization rate is modeled by solving the quasi-steady equation for mass and energy conservation for individual droplets (O'Rourke and Bracco [24], Abraham and Magi [27], Abraham and Givler, [28]).

Numerics. The gas-phase equations are solved by means of a strongly implicit finite volume method (Magi [20]). A discretized pressure equation is obtained by combining the discretized momentum and continuity equations. The pressure equation is solved by Stone's iterative method. The pressure, momentum, and energy equations are iterated till convergence is obtained for the pressure and temperature. The solution for the k-ε equations are obtained explicitly after the momentum, pressure and energy are solved. The convective terms in the conservation equations are discretized by first-order upwind scheme and the diffusive terms are discretized using second-order central differences. The time derivative is discretized by first-order backward difference. It should be noted that the equations solved are the unsteady compressible ensemble-averaged Navier-Stokes equations. For the liquid phase, a collection of drops having identical properties are grouped into a computational parcel and each parcel is tracked using the Lagrangian conservation equations with sub-models for collisions and coalescence, secondary break-up, turbulent dispersion, and vaporization. The formation of drops and the initial drop sizes are computed using the atomization model discussed before.

Boundary Conditions

1 Inflow: The jet issues out of an orifice with a flat velocity profile which is steady with time. A triangular inlet velocity profile is also used to assess the effect of the velocity profile.

2 Wall boundary conditions: Impermeable walls are placed on the wall adjacent to the orifice and at the outer periphery of the jet. The normal velocity is zero at the walls and the fluxes of momentum and energy are computed using the wall functions.

3 Downstream boundary condition: The downstream boundary of the jet is considered to be open. This is achieved by specifying the pressure at the downstream boundary to be the initial chamber pressure, which is uniform across the chamber.

Computational Domain and Conditions

A schematic of the computational domain used for the gas jet computations is shown in Fig. 1. The grid is stretched both axially and radially to provide high resolution in the near field near the orifice where the velocity gradients are highest. We will present results below to show grid sensitivity. The initial conditions for the computations are given in Table 2. In all cases with gas jet injection, the temperature and density of the injected gas are set to be the same as that of the ambient. Initial values of k and ε are chosen to provide an ambient diffusivity that will be much smaller than the diffusivity generated in the jet shear layer (Abraham [11,5]). With this small initial value of diffusivity, the choice of initial k and ε would not significantly influence the computed results, provided adequate resolution is employed (Abraham [5], Abraham and Magi [27]).

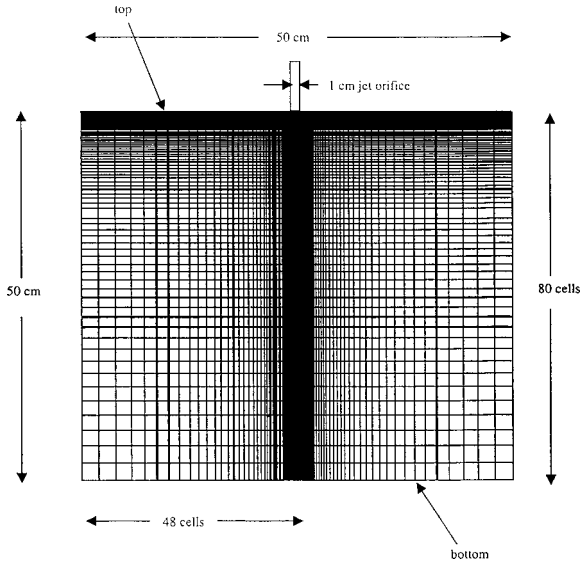

Fig. 1 The computational domain and grid used for gas jet computations

Table 2 Initial conditions

Initial conditions	Atmospheric jet	Jet under diesel engine conditions
Injection velocity (m/s)	15	476
Orifice diameter (cm)	1.0	0.1246
Ambient pressure (bar)	1.0	85.4
Ambient temperature (K)	300	992
Ambient density (kg/m^3)	1.16	30.0
Reynolds number	10,000	422,000
Mach number at injector	0.04	0.74

Results and Discussion

Single-Phase Computations at Low Reynolds Number (Atmospheric Conditions). The first set of results that we present will be to show that the subsequent results are independent of the numerics, the ambient turbulence parameters and the walls in the computational domain. In this first set, we will present results from five computations, which we will refer to as Cases GA-GE. These computations are carried out for the atmospheric jet. Case GA uses a computational grid with a resolution of 80 (axial)$\times$48 (radial) cells, as shown in Fig. 1. Case GB employs a grid of 120$\times$72 cells. In Cases GA and GB there are 16 cells in the orifice. Cases GA and GB compare two resolutions. In Case GC, there are 12 cells in the orifice radius, with a total of 80$\times$48 cells. Cases GA and GC compare two resolutions in the orifice. Computations are reported for Case GD with different initial ambient turbulence values but with other conditions remaining the same as those of Case GA. The two sets of turbulence values employed are listed in Table 3. We also studied the effect of the size of the

Table 3 Initial ambient k-ε values

Initial conditions	Cases GA-GC, GE	Case GD
k (m^2/s^2)	1.48×10^{-2}	1.48×10^{-3}
ε (m^2/s^3)	1.98×10^{-1}	1.98×10^{-2}
Diffusivity (m^2/s)	1.0×10^{-4}	1.0×10^{-5}

domain on our computed results. In Case GE the orifice to cylinder wall distance is increased to 50 cm from the 25 cm of Case GA. The resolution in the inner part of the domain, from the centerline to a radius $r=25$ cm, is kept the same as in Case GA, while 12 extra cells are added in the outer domain with a uniform width that is equal to the largest cell in the domain of Case GA, which is about 2 cm. Typical computational times on a HP C-200 workstation are about 1.5 days for Case GA and about 3.5 days for Case GB. Employing higher resolution, or going to three-dimensional computations while maintaining the same resolution, is very challenging. Conditions for Cases GA–GE are shown in Table 4.

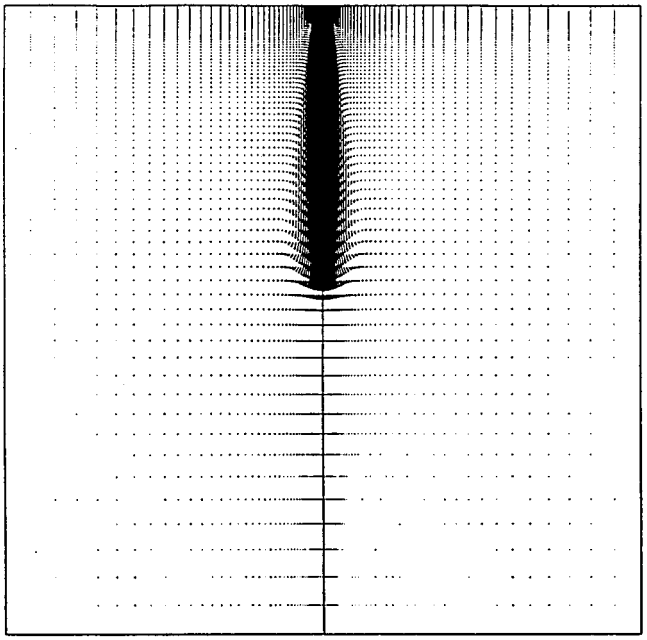

a) GA

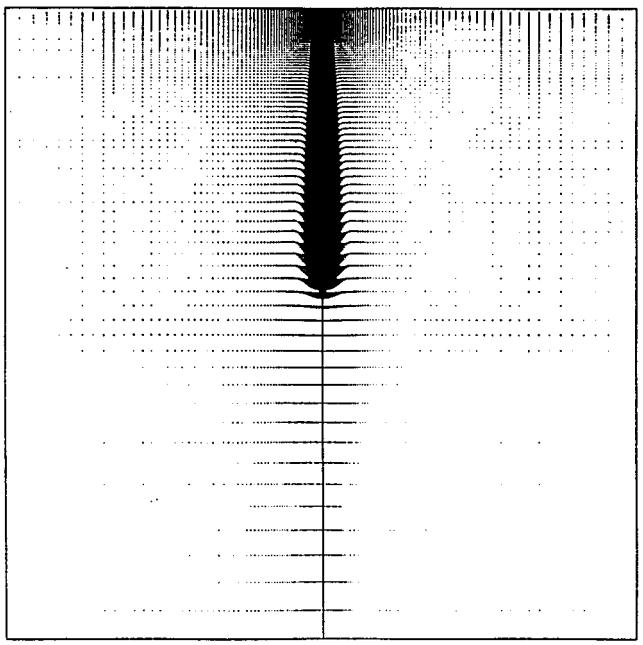

b) GB

Fig. 2 Velocity vector plots at 50 ms after start of injection for two gas jet computations. (*a*) Case GA; (*b*) Case GB.

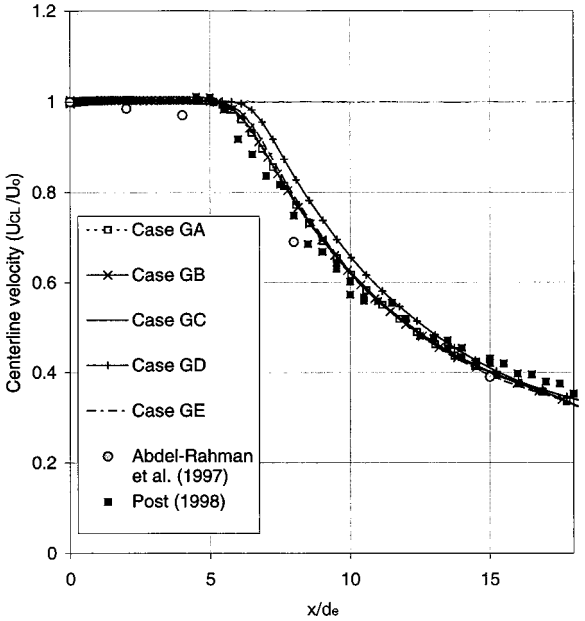

Fig. 3 Jet centerline velocity at 50 ms after start of injection in the steady region of an atmospheric jet. Computations are compared with two sets of experimentally measured values.

Figure 2 shows computed velocity vectors at 50 ms after the start of injection (ASI) for Cases GA and GB. These qualitative pictures do not show noticeable differences. Hence, we will examine quantitative results. Figure 3 shows the nondimensional centerline velocity variation with nondimensional axial distance for all the five cases above. It may be seen that these values are within 3 percent of each other in the steady part of the jet shown from the origin to $x/d_e=18$. Figure 3 also shows two sets of experimental data of centerline velocity as a function of axial distance (Abdel-Rahman et al. [29], Post [30]). The computed results agree with the experimental values within 12 percent. It is interesting to observe that the computations appear to reproduce the potential core length with adequate accuracy. It is about six diameters. Figure 4 shows the variation of the half-width, $y_{1/2}$, of the jet as a function of axial distance for the five cases. It may be seen that they are all with 10 percent of each other. In the expression $y_{1/2}=C\,x$, the value of the constant C that may be derived from the figure is about 0.10. This value is somewhat larger than the measured values quoted in the literature but in much closer agreement with the experimental values than those of earlier references (Pope [31], Hanjalic and Launder [32], Kuo and Bracco [33], Wood and Chen [34], and Wilcox [35]). This may be in part due to inadequate resolution but also due to the additional terms in the full set of equations that we are solving as opposed to the boundary layer equations in the references above. The adequate agreement of results from the different cases appears to indicate that our selection of numerical parameters and initial ambient turbulence parameters is such that the results are sufficiently insensitive to grid resolution, including the number of cells in the orifice, and ambient turbulence to give us the *correct trends*. It is impractical for us to employ much higher resolution. Our computations solve the compressible and unsteady equations of fluid flow. These are the equations that are solved in multidimensional engine models. In fact, the resolution employed here is much higher than those that are practical under engine conditions. The size of the computational domain is sufficiently large that the results are not influenced by the walls (Abraham et al. [36]). Further discussion of results will be with respect to computations that are adequately grid-independent, and independent of wall influences and the choice of initial turbulence parameters.

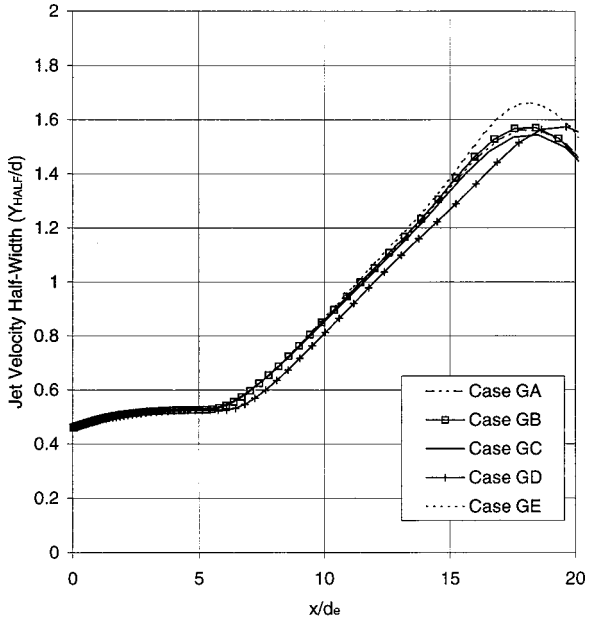

Fig. 4 Jet velocity half-width at 50 ms after start of injection in atmospheric jet

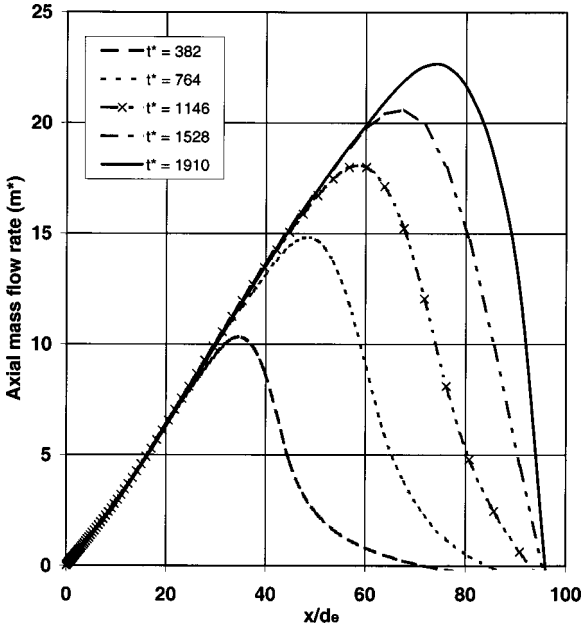

Fig. 6 Axial mass flow rate at different times after start of injection for gas jet under Diesel conditions

Single-Phase Computations at High Reynolds Number (Diesel Conditions). It is known that in the self-similar region of steady jets the axial mass flow rate increases linearly with axial distance (Ricou and Spalding [10]). Figure 5 shows the computed nondimensional axial mass flow rate as a function of nondimensional axial distance for the atmospheric jet. The nondimensional mass flow rate is defined as $m^*=(\dot{m}(x)-\dot{m}_i)/\dot{m}_i$. We have plotted the results at different nondimensional times after start of injection. The nondimensional time is defined as $t^*=t/(d(\rho_i/\rho_a)^{1/2}/U_i)$. It may be seen that in the steady part of the jet, and beyond the first ten diameters, the mass flow rate increases linearly with the axial distance. Figure 6 shows the same results for a gas jet under conditions comparable to what is found in a Diesel engine. Comparing the results for the atmospheric and the Diesel jet at values corresponding to the same nondimensional time and axial distance, it may be seen that the results for the jets are about the same. This is expected since the jets are in the fully turbulent regime. For example, at $t^*=382$ and $x^*=25$, $m^*\approx 8$, in both the atmospheric jet and in the Diesel jet. The axial mass flow rate may be employed to calculate the entrainment rate constant, K, using Eq. (2). An alternative method to calculate K is to employ Eq. (4). Figure 7 shows the computed values of K using both methods for the atmospheric and Diesel jets, plotted as a function of the nondimensional axial distance. The two methods give about the same result except in the very near field ($x/d_e<4$). These differences in the very near field may arise from the assumption

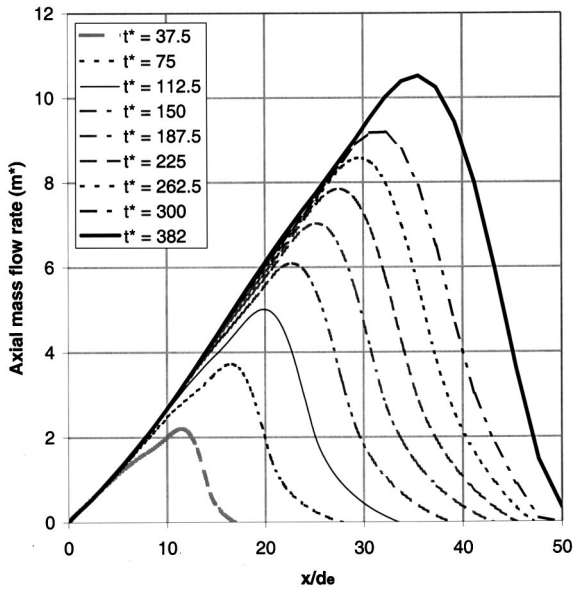

Fig. 5 Axial mass flow rate at different times after start of injection for gas jet under atmospheric conditions

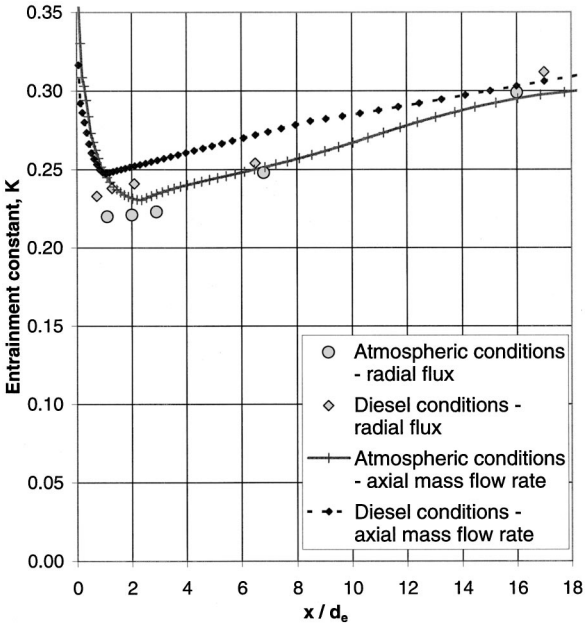

Fig. 7 Computed nondimensional entrainment constant in the near field of steady gas jets using the axial flux and radial flux methods to compute entrainment

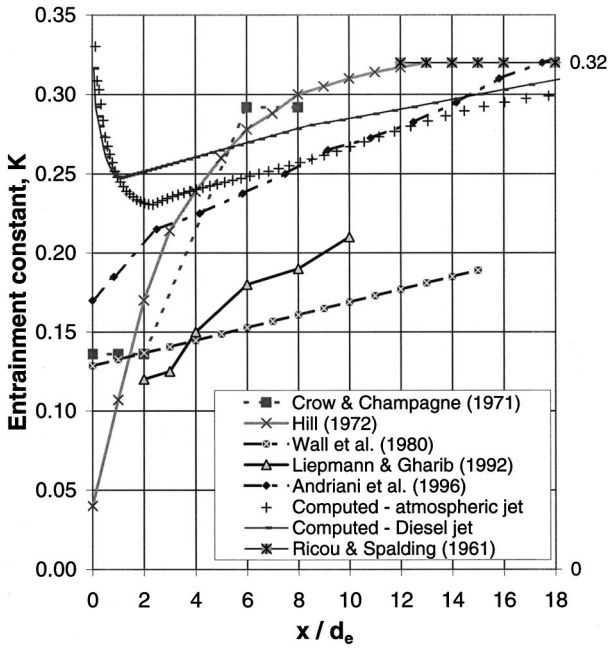

Fig. 8 A comparison of computed entrainment constant in the near-field of steady gas jets with measured results from literature

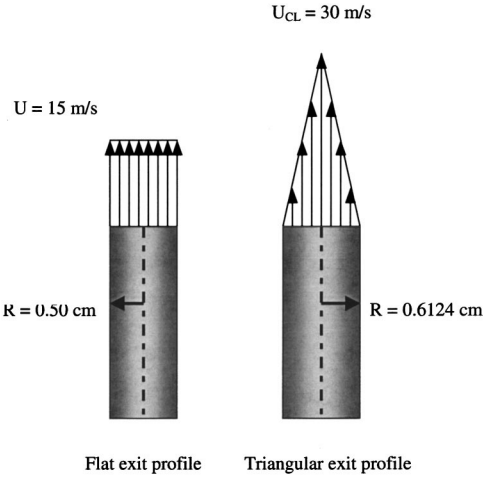

Fig. 9 Inlet velocity profiles used in gas jet computations

about the jet exit velocity profile, as will be shown later. Figure 8 shows the computed values of K and several sets of experimental results including the value of 0.32 due to Ricou and Spalding [10] in the self-similar region. There appears to be a consistent trend in the measurements and computations of an increase in K with axial distance in the near field. The computed values are greater than the measured values of Wall et al. [14] and Liepmann and Gharib [15], but are close to the values of Andriani et al. [16]. The measurements of Hill [13] follow a somewhat different trend than the others with a rather rapid increase initially followed by a slower rise to a steady value of about 0.32 in the self-similar region. The computed results appear to approach the value of 0.32 in the self-similar region.

It is possible that the very near-field results for $x/d_e<4$ are sensitive to the assumptions about the orifice exit velocity profile. We have assumed a top-hat profile in the results presented above. This may be unrealistic since the effects of boundary layers in the injector may result in a decrease in velocity as the walls are approached. To assess the effect of the assumed orifice velocity profile on the results, we also considered a triangular velocity profile, in which the velocity approaches zero at the orifice wall. Figure 9 shows the top-hat and triangular profiles. In selecting the triangular velocity profile, we imposed the constraint that the mass and momentum flow rates for the jets with the two profiles are identical. When these constraints are imposed and a triangular profile is assumed, a maximum orifice exit centerline velocity of 30 m/s and an orifice radius of 0.6124 cm is obtained, relative to the uniform velocity of 15 m/s and orifice radius of 0.5 cm for the top-hat profile.

Figures 10 and 11 show the computed variation of centerline velocity with axial distance and the entrainment constant with axial distance respectively for the two orifice exit velocity profiles. It may be seen that the centerline velocity profiles for the cases are practically identical beyond the potential core. It is also seen that for $x/d_e<10$, the triangular profile results in a lower value of K. This may be expected as the shear layer would grow slower at the interface of the jet surface as it exits from the orifice with a velocity at the periphery of zero. This would result in a slower generation of turbulence, and hence lower entrainment. Hence, the assumption about the velocity profile has a noticeable effect on the very near-field results. It is also possible that when the injection velocity is high, there may be significant Mach number effects when Ma>0.3. However, since the centerline velocity quickly decays, Mach number effects should not be significant far from the orifice. Furthermore, since the Reynolds numbers at the orifice for all the jets considered here are at least 10,000, the jets can be considered fully turbulent throughout their entire flow field and all the velocities should scale with the injection velocity, so that the results are independent of Reynolds number.

In the context of Diesel engines, our interest is more in transient jets than in steady jets. It would be interesting to compare the entrainment constant $K(t)$ in the transient jet with values in the steady jet. Figure 12 shows the variation with time and axial distance of computed values of the entrainment constant, in the transient jet, normalized by its value at the same axial location in the steady jet. The steady values used here are those from Fig. 7 obtained by employing Eq. (4). The transient values are also ob-

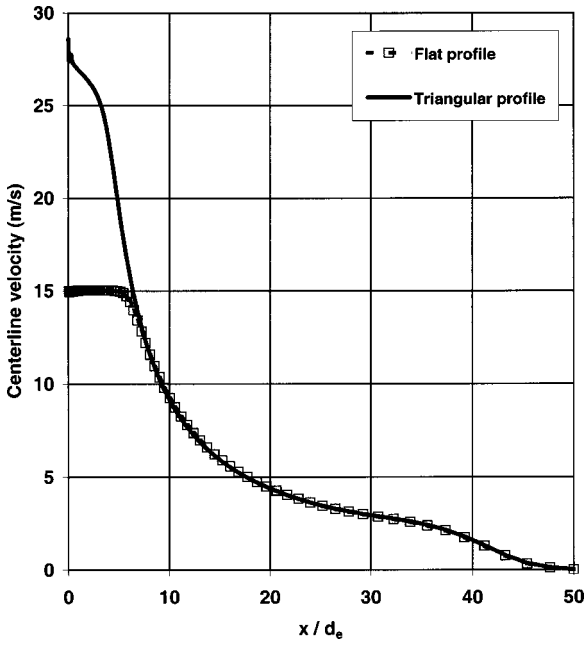

Fig. 10 Computed centerline velocity in gas jet Case GA at 200 ms after start of injection with flat and triangular orifice exit velocity profiles

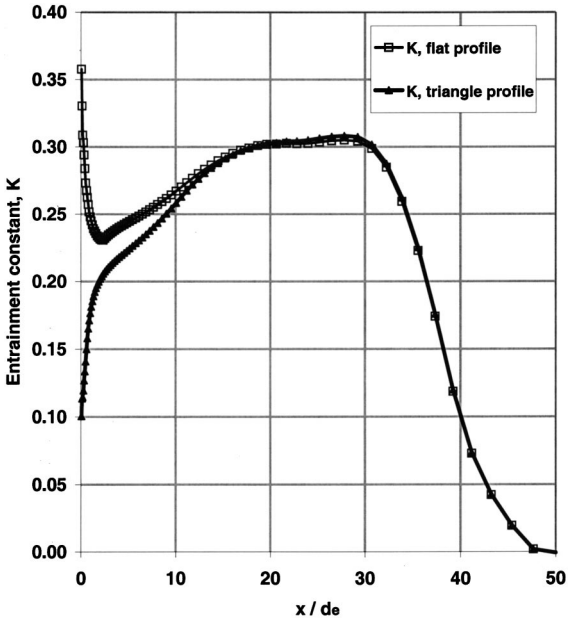

Fig. 11 Computed entrainment constant in gas jet Case GA at 200 ms after start of injection with flat and triangular orifice exit velocity profiles

tained using Eq. (4). It is interesting to observe that the normalized entrainment constant, $K(t)/K_{\text{steady}}$, is less than 1 in the transient jet. It is difficult to interpret these results definitively and conclude that the lower values of the entrainment rate constant imply lower entrainment in the transient jet. The results, however, indicate that the steady values of K that we obtained earlier may not be representative of transient Diesel injection. It appears reasonable to deduce that the transient jet induces less of the ambient fluid into motion relative to the steady jet. Measurements reported in the literature also indicate that the entrainment rate increases during the transient phase of fuel injection till a steady value is reached (Cossali et al. [37], Kozma and Farrell [38]). In principle, it would be the transient values of entrained mass that would be of most interest to engine designers. Consider some typical numbers relevant to an engine running at a speed of 1500 rpm. The duration of injection is about 2 ms and the duration of combustion is about 6 ms. Consider an average injection velocity of 300 m/s, orifice diameter of 0.2 mm, injected fluid density of 800 kg/m^3 and ambient density of 20 kg/m^3, in a cylinder with a bore of 10 cm. Then a time period of 1 ms, which corresponds to about 10 crank angle degrees in the engine, after the start of injection, would correspond to about $t^*=225$ on the figure. At this time, $K^*\approx 1$ till about $x/d_e=10$ but drops to $K^*\approx 0.9$ at $x/d_e\approx 20$ and then rises before dropping to 0 at x/d_e of about 27. It is also interesting to observe that at larger values of t^* after start of injection, a greater part of the overall jet has values of K^* close to 1. This is possibly because the head vortex occupies a smaller part of the jet structure.

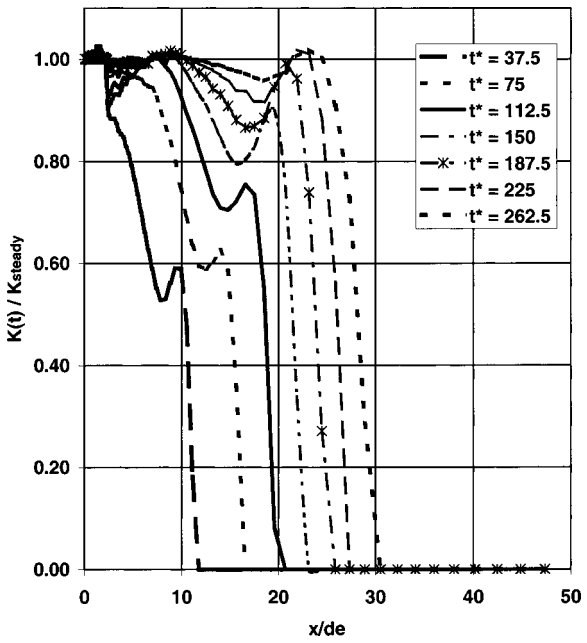

Fig. 12 Normalized entrainment constant in transient jet at different times after start of injection

Spray Computations at High Reynolds Number. Our motivation for the work in gas jets under Diesel conditions has arisen from our findings that the penetration rates and spread angles of gas jets appear to agree with those of measured sprays under such conditions (Iyer and Abraham [6,7]). However, computed near-field entrainment characteristics of sprays have not been compared with computed or measured gas jets nor with measured results in sprays in the past. We will present below the results of computed and measured entrainment characteristics in sprays. The measurements that we have employed are those of Andriani et al. [16]. In the experiment, Diesel fuel was injected into a closed cylindrical chamber of 206 mm diameter equipped with four quartz windows and designed to withstand higher air temperatures and pressures than normal. A single-hole Bosch injector with 0.25 mm orifice diameter was used for the spray experiments. The nozzle opening pressure was fixed at 21.4 MPa and the injection duration was 3.3 ms. The velocity of the air was measured by a dual beam LDV system, comprising a 5-W Ar^+ laser and a 40-MHz Bragg cell for frequency shifting and directional sensitivity. The entrainment was determined by measuring the air velocity normal to a cylindrical control surface enclosing the jet. Figure 13 shows a schematic indicating the nozzle, spray and a cylindrical control surface through which the entrained mass enters. The cylinder can be subdivided into many rings as shown in Fig. 13. The radial air mass flow rate through any ring may be estimated using Eq. (4). The radius of the cylindrical control surface was chosen as 10 mm. The comparisons are made with one set of spray experiment for which the conditions are given in Table 5. This condition was

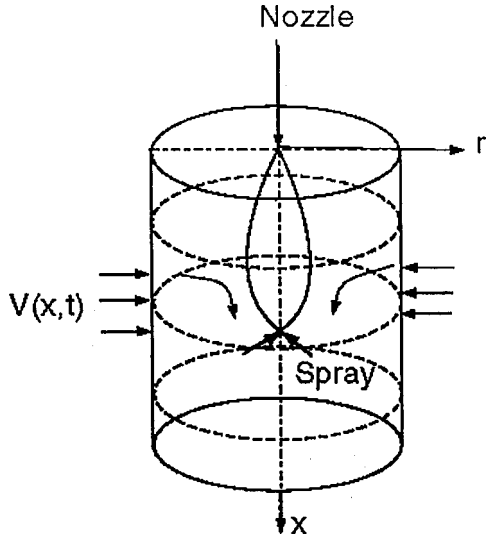

Fig. 13 Schematic of the cylindrical control surface that defines the measure locations

Table 4 Conditions for gas jet computations

Case	Grid resolution	Number of cells in orifice radius	Initial ambient diffusivity (m^2/s)	Centerline to cylinder wall distance
GA	80×48	8	1.0×10^{-4}	0.25 m
GB	120×72	8	1.0×10^{-4}	0.25 m
GC	80×48	12	1.0×10^{-4}	0.25 m
GD	80×48	8	1.0×10^{-5}	0.25 m
GE	80×60	8	1.0×10^{-4}	0.50 m

selected as it represents the highest ambient pressure and temperature conditions in the chamber. Notice that even for this case, the pressure and temperature are lower than in a Diesel engine. We have not made an extensive set of comparisons with measured results here as such measurements are not available under Diesel conditions. But, the comparisons presented below will illustrate the challenges with spray computations. We have discussed these challenges in prior work (Abraham [5], Iyer and Abraham [6], Aneja and Abraham [9]), but not from the point of view of entrainment.

The computations are carried out in an axisymmetric chamber with the same diameter as employed in the measurements. Injection and ambient conditions are also identical to the extent possible. These are listed in Table 5. The injection velocity was calculated to be 255 m/s using the expression below assuming a coefficient of discharge, C_d of about 0.6. Initial unsteadiness of the injection rate in the experiments could affect the initial transient, but should not affect the steady spray results.

$$U_i = C_d \sqrt{\frac{2\Delta P}{\rho_i}} \tag{5}$$

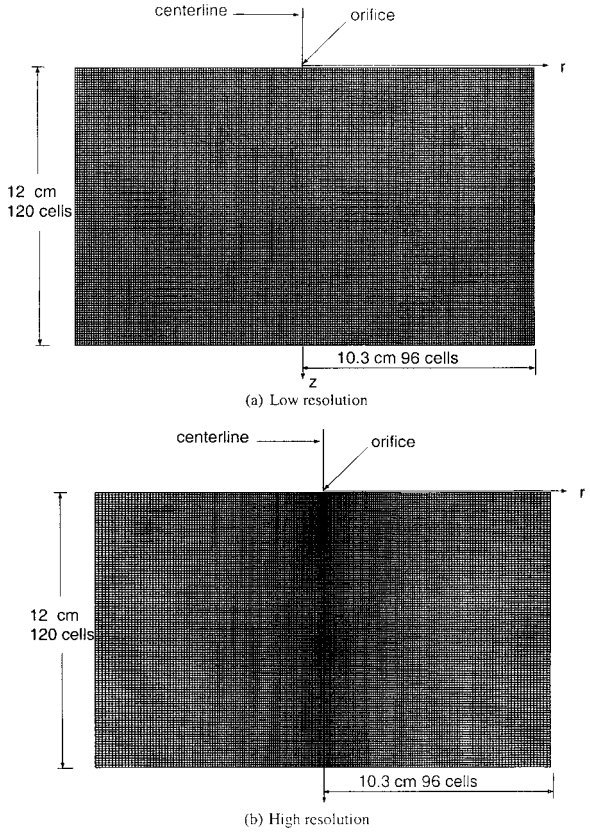

Fig. 14 Computations grid for spray computations

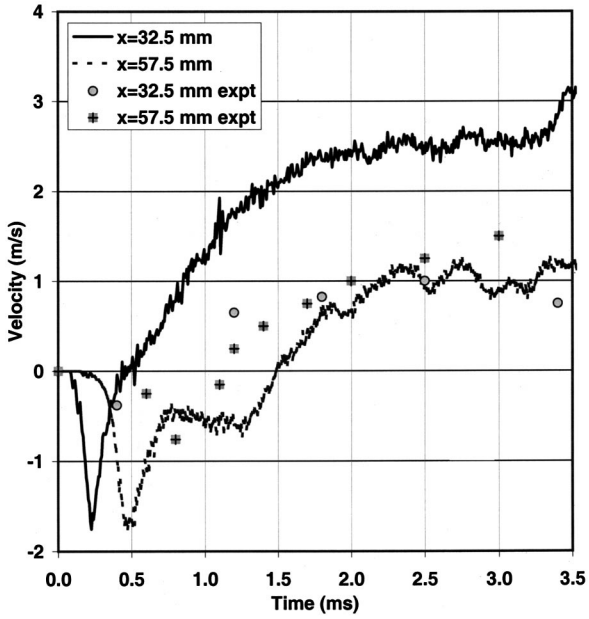

Fig. 15 Variation of entrainment velocity with time in spray at two different axial locations for Case SA

Figures 14(*a*) and 14(*b*) show two numerical grids that we have employed. The low-resolution grid is a uniform grid with cell size of 1 mm in the radial and 1 mm in the axial direction. The high-resolution grid is a nonuniform grid with higher resolution near the jet centerline and the finest cell size of 0.6 mm in the radial and 1 mm in the axial direction. As discussed in prior work, employing even higher resolution near the orifice of the spray jet poses a difficulty because the spray models are formulated under the assumption that the gas void fraction in any computational cell is close to one (Abraham [5], Iyer and Abraham [6], and MacInnes and Bracco [39]). However, it has also been shown that it may be necessary to employ grids that resolve the injector orifice in the computation of transient jets to obtain results that are adequately independent of the resolution. This presents a quandary. When inadequate resolution is employed, transient results are sensitive to the initial values of turbulence parameters in the two-equation k-ε model (Abraham [9]). More recent studies have shown that the collisions and coalescence submodels also do not give converged results (Aneja and Abraham [9]).

In the measurements, the entrainment rate constant was determined using Eq. (4), which we have referred to as the radial flux method. Figure 15 shows the variation with time after start of injection of computed and measured velocities at a radial distance of 10 mm at two axial planes, 32.5 mm and 57.5 mm from the injector orifice. The computed velocities follow the trend of the measured velocities. However, the *computed* steady-state velocities at the axial distance of 32.5 mm is greater than the measured ones indicating a greater entrainment and thereby a greater entrainment rate constant. It may be seen that at 32.5 mm and 57.5 mm from the orifice, the *measured* steady values of radial velocities are about the same, indicating that K may have reached a steady value here at these axial distances from the orifice. Figure 16 shows the computed and measured entrainment constant in the spray as a function of nondimensional axial distance. Computed cases SA–SF are summarized in Table 6. The computed entrainment constant for the lower resolution, Case SA, and higher resolution, Case SB, are shown. In addition, computed results of the entrainment constant for two sets of initial ambient k-ε values shown in Table 7, Cases SA and SC, and with and without collisions and coalescence, Cases SA and SD, are also shown. It may be seen that in all cases the computed values of K in the near field

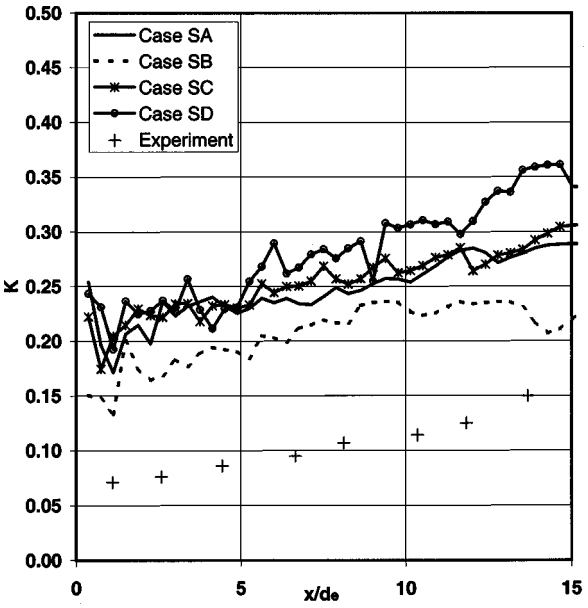

Fig. 16 A comparison of measured and computed entrainment constant in steady sprays

are greater than the measured ones. The computed values of K show the general trend of increasing from near the orifice to the far field. Curve SB, in comparison to Curve SA, shows that the results are sensitive to the numerical resolution. For the change in resolution considered here, the value of K changes by about 25 percent at $x/d_e = 15$. These results imply that if it were possible to employ even higher resolution, the computed results may come closer to the measured ones. This would then have the further implication that though computed gas jet penetration and spread angles may agree adequately with measured spray results (Iyer and Abraham [6]), near-field entrainment characteristics of gas jets and sprays may be different with the spray entraining less than the gas jet in the near field. This may be seen by comparing the entrainment constants for the gas jets on Fig. 7 with values on

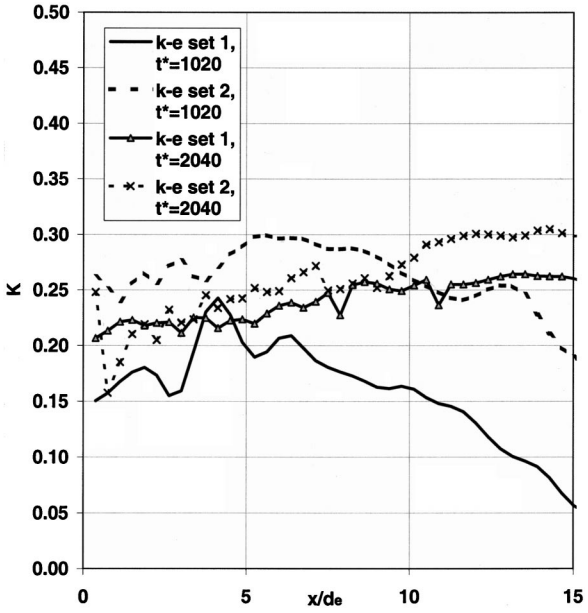

Fig. 17 A comparison of the effects of different initial k-ε values on computed entrainment constant in sprays. Cases SA and SC shown at two different times ASI.

Table 5 Conditions in the spray experiment

Ambient pressure	0.6 MPa
Temperature	298 K
Ambient density	7.02 kg/m^3
Density ratio (ρ_a/ρ_i)	0.00853
Injection pressure	70 MPa
Radius of cylinder	10.3 cm
Height of cylinder	12.0 cm
Initial gas temperature	298 K
Initial gas pressure	6.0 atm
Orifice diameter	0.25 mm
Injection velocity	255 m/s
Injection duration	3.3 ms

Fig. 16 for Case SB. Curves SA and SC show that the steady value of the entrainment constant is not very sensitive to the initial values of k and ε in the ambient. This is consistent with prior findings (Abraham [5]). *This conclusion only holds for steady jets.* The transient results are expected to be sensitive to the ambient values of k and ε (Abraham [5]). Figure 17 shows the computed values of the entrainment rate constant at $t^* = 1020$ and $t^* = 2040$ when the two sets of k-ε values given in Table 7 are used. These results are in the transient jet. It is seen that the results are noticeably different for the two cases for the two sets of k-ε values. It has been shown that the drastic differences in results arise from inadequate grid resolution near the orifice during the transient. Results for Cases SA and SD on Fig. 16 show that the submodel for collisions and coalescence of drops has a noticeable effect with the entrainment constant being larger in the absence of collisions and coalescence. These results are consistent with the findings of Aneja and Abraham [9] that the submodels for collisions and coalescence of drops lead to the formation of drops larger than the injected ones. In fact, they showed that the models do not give converged results with larger drops resulting from increased spatial resolution in the presence of collisions and coalescence. Such larger drops would be less effective in transferring the injected momentum to the ambient air and, hence, the entrainment constant would decrease. This is also, at least, part of the explanation for the reduced entrainment constant for Case SB relative to Case SA above.

We have assessed the effect of vaporization and the effect of the size of injected drops, in the absence of vaporization, on the computed entrainment rate constant. Figure 18 shows the computed entrainment rate constant for Case SA of Fig. 16, and for two additional cases, SE and SF. In Case SE, the ambient temperature is increased from 298 to 900 K but the ambient density is not changed. The drops vaporize as a result of the increased temperature. In Case SF, the initial Sauter mean radius (SMR) of the injected drops is increased by a factor of 10 from about 2.6 μm to

Table 6 Conditions for spray computations

Case	Grid resolution	k-ε set used (Table 7)	Injected drop size (μm)	Ambient temperature (K)	Collisions used?
SA	Low	1	2.6	298	Yes
SB	High	1	2.6	298	Yes
SC	Low	2	2.6	298	Yes
SD	Low	1	2.6	298	No
SE	Low	1	2.6	900	Yes
SF	Low	1	26.0	298	Yes

Table 7 Initial ambient k-ε values used

Set	k (m^2/s^2)	ε (m^2/s^3)	l_{sc} (m)	τ_t (s)	ν_t (m^2/s)
1	1.48×10^{0}	1.98×10^{3}	1.5×10^{-4}	7.5×10^{-4}	1.0×10^{-4}
2	1.48×10^{-2}	1.98×10^{-1}	1.5×10^{-3}	7.5×10^{-2}	1.0×10^{-4}

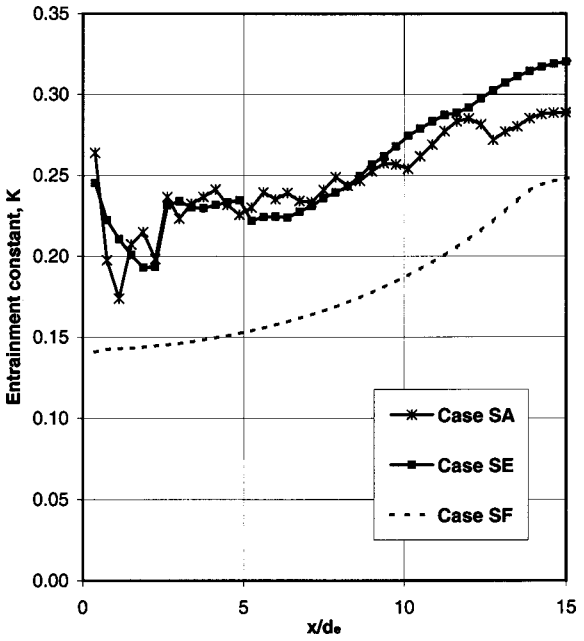

Fig. 18 Computed entrainment constant for sprays at 3 ms ASI showing effects of ambient temperature and initial drop size on computed entrainment

26 μm. It may be seen that the increased vaporization rate increases the entrainment constant in this case. At an axial distance of $x/d_e=15$, K increases by about 10 percent. A possible explanation for the relatively small increase is that drops of size 2.6 μm in SMR in the nonvaporizing case are already rather small and hence transfer their momentum to the ambient rapidly. In the case of the increased initial drop sizes, it may be seen that the entrainment rate constant decreases by 12–25 percent in the range of axial distances considered. This is as expected. Larger drops are less effective in transferring their momentum to the ambient.

Summary and Conclusions

A multidimensional model for flows and sprays in Diesel engines is employed to study the entrainment characteristics of gas jets and sprays. Turbulence is represented by the k-ε model. It is shown that the model reproduces, consistent with measurements, the increase in entrainment rate constant with axial distance in the near field till a constant value is reached in the self-similar region. The constant value that is reproduced in the self-similar region is within 10% of measured values of 0.32. In the case of sprays, consistent with experimental results, the model reproduces a lower entrainment rate constant in the near field than in the gas jets. However, the measured values are not reproduced quantitatively with adequate accuracy. The results of this work combined with other results presented in the literature for sprays indicate that the quantitative differences may arise from several factors including the effects of numerics and inadequacy of spray submodels that are commonly used for Diesel sprays. None of the Lagrangian drop models currently available give resolution independent results when the spatial distribution of the drops is highly nonuniform. In general, the experimental results appear to indicate lower values of entrainment rate constant in sprays when drop sizes are larger and/or vaporization rate is slower. In the far field, the entrainment rate constant approaches the value of gas jets consistent with the assumption that the spray behaves like an incompressible gas jet in the far field. Additional work needs to be done in the case of sprays to clarify these processes and, more importantly, to address the serious limitations of the models.

Acknowledgments

The authors acknowledge the support of Cummins Engine Company, Detroit Diesel Corporation, and Navistar Corporation for this work.

Nomenclature

D = diffusivity, m^2/s
d = orifice diameter, m
J = momentum flow rate, kg-m/s^2
k = turbulent kinetic energy, m^2/s^2
K = entrainment constant
l_{sc} = turbulent length scale, m
$\dot{m}$ = mass flow rate, kg/s
p = pressure, Pa
Q = volume flow rate, m^3/s
r = radial distance, m
t = time, s
T = temperature, K
U,u = axial velocity, m/s
V,v = radial velocity, m/s
X,x = axial distance, m
y = radial distance, m
ε = rate of dissipation of turbulence kinetic energy, m^2/s^3
μ = gas viscosity, kg/m-s
ρ = gas density, kg/m^3
τ_t = turbulent time scale, s
ν_1 = turbulent viscosity, m^2/s

Subscripts

a = ambient
e = entrained, effective
i = injection
p,e = partial entrained

Superscripts

$*$ = nondimensional

References

[1] Bracco, F., 1985, ''Structure of High-Speed Full-Cone Sprays,'' *Recent Advances in the Aerospace Sciences*, C. Casci, ed., Plenum Publishing Corporation, pp. 189–212.
[2] Reitz, R., 1987, ''Modeling Atomization Processes in High-Pressure Vaporizing Sprays,'' Atom. Spray Technol., **31**, pp. 309–337.
[3] O'Rourke, P., and Amsden, A., 1987, ''The TAB Method for Numerical Calculation of Spray Droplet Breakup,'' Society of Automotive Engineers Paper SAE 872089.
[4] Andrews, M., 1993, ''The Large-Scale Fragmentation of the Intact Liquid Core of a Spray Jet,'' Atomization Sprays, **3**, pp. 29–54.
[5] Abraham, J., 1997, ''What is Adequate Resolution in the Numerical Computations of Transient Jets?'' SAE Trans., **106**, pp. 141–151.
[6] Iyer, V., and Abraham, J., 1997, ''Penetration and Dispersion of Transient Gas Jets and Sprays,'' Combust. Sci. Technol., **130**, pp. 315–334.
[7] Iyer, V., and Abraham, J., 1998, ''The Computed Structure of a Combusting Transient Jet Under Diesel Conditions,'' SAE Trans., **107**, pp. 1669–1693.
[8] Aneja, R., and Abraham, J., 1998, ''Comparisons of Computed and Measured Results of Combustion in a Diesel Engine,'' Society of Automotive Engineers Paper SAE 980786.
[9] Aneja, R., and Abraham, J., 1998, ''How Far Does the Liquid Penetrate in a Diesel Engine: Computed Results vs. Measurements?'' Combust. Sci. Technol., **138**, pp. 233–256.
[10] Ricou, F., and Spalding, D., 1961, ''Measurements of Entrainment by Axisymmetrical Turbulent Jets,'' J. Fluid Mech., **11**, pp. 21–32.
[11] Abraham, J., 1996, ''Entrainment Characteristics of Transient Gas Jets,'' Numer. Heat Transfer, Part A, **30**, pp. 347–364.
[12] Crow, S., and Champagne, F., 1971, ''Orderly Structure in Jet Turbulence,'' J. Fluid Mech., **48**, pp. 547–591.
[13] Hill, B., 1972, ''Measurement of Local Entrainment Rate in the Initial Region of Axisymmetric Turbulent Air Jets,'' J. Fluid Mech., **51**, pp. 773–779.
[14] Wall, T., Nguyen, H., Subramanian, V., Mai-Viet, T., and Howley, P., 1980, ''Direct Measurements of the Entrainment by Single and Double Concentric Jets in the Regions of Transition and Flow Establishment,'' Trans. Inst. Chem. Eng., **58**, pp. 237–241.
[15] Liepmann, D., and Gharib, M., 1992, ''The Role of Streamwise Vorticity in the Near-Field Entrainment of Round Jets,'' J. Fluid Mech., **245**, pp. 643–668.
[16] Andriani, R., Coghe, A., and Cossali, G., 1996, ''Near-Field Entrainment in Unsteady Gas Jets and Diesel Sprays: A Comparative Study,'' *Twenty-Sixth*

Symposium (International) on Combustion, The Combustion Institute, Pittsburgh, pp. 2549–2556.
[17] Cho, I., Fujimoto, H., Kuniyoshi, H., Ha, J., Tanabe, H., and Sato, G., 1990, ''Similarity Law of Entrainment into Diesel Spray and Steady Spray,'' Society of Automotive Engineers Paper SAE 900447.
[18] Ha, J., Iida, N., Sato, G., Hayashi, A., and Tanabe, H., 1984, ''Experimental Investigation of the Entrainment into Diesel Spray,'' Society of Automotive Engineers Paper SAE 84107.
[19] Bracco, F., 1985, ''Modeling of Engine Sprays,'' SAE Trans., **94**, pp. 144–167.
[20] Magi, V., 1987, ''A New 3-D Code for Flows, Sprays, and Combustion in Reciprocating and Rotary Engines,'' *Mechanical and Aerospace Engineering Report*, No. 1793, Princeton University.
[21] Amsden, A., 1993, ''KIVA-3: A KIVA Program with Block-Structured Mesh for Complex Geometries,'' Los Alamos Laboratory Report No. LA-12503-MS, Los Alamos, New Mexico.
[22] Launder, B. E., and Spalding, D. B., 1974, ''The Numerical Computations of Turbulent Flows,'' Comput. Methods Appl. Mech. Eng., **3**, pp. 269–289.
[23] Chatwani, A., and Bracco, F., 1985, ''Computation of Dense Spray Jets,'' *ICLASS 85*, Paper 1B/1/1, Proceedings published by the Institute of Energy, London.
[24] O'Rourke, P., and Bracco, F., 1980, ''Modeling of Drop Interactions in Thick Sprays and a Comparison with Experiments,'' *Proceedings of the Institution of Mechanical Engineers*, Vol. 9, pp. 101–106.
[25] Gosman, A., and Ioannides, E., 1981, ''Aspects of Computer Simulation of Liquid-Fueled Combustors,'' American Institute of Aeronautics and Astronautics Paper AIAA 810323.
[26] Reitz, R., and Diwaker, R., 1987, ''Structure of High-Pressure Fuel Sprays,'' Society of Automotive Engineers Paper SAE 870598.
[27] Abraham, J., and Magi, V., 1998, ''A Model for Multicomponent Droplet Vaporization in Sprays,'' SAE Trans., **107**, pp. 603–613.
[28] Abraham, J., and Givler, S., 1999, ''Conditions in Which Vaporizing Fuel Drops Reach a Critical State in a Diesel Engine,'' Society of Automotive Engineers Paper SAE 1999-01-0511.
[29] Abdel-Rahman, A., Chakroun, W., and Al-Fahed, S., 1997, ''LDA Measurements in the Turbulent Round Jet,'' Mech. Res. Commun., **24**, pp. 277–288.
[30] Post, S., 1998, ''A Computational and Experimental Study of Near-Field Entrainment in Steady Gas Jets,'' M.S.M.E. thesis, Purdue University.
[31] Pope, S. B., 1978, ''An Explanation of the Turbulent Round-Jet/Plane-Jet Anomaly,'' AIAA J., **16**, pp. 279–281.
[32] Hanjalic, K., and Launder, B., 1980, ''Sensitizing the Dissipation Equation to Irrotational Strains,'' ASME J. Fluids Eng., **102**, pp. 34–40.
[33] Kuo, T.-W., and Bracco, F. V., 1982, ''On the Scaling of Impulsively Started Incompressible Turbulent Round Jets,'' ASME J. Turbomach., **104**, pp. 191–197.
[34] Wood, P. E., and Chen, C. P., 1985, ''Turbulence Model Predictions of the Radial Jet—A Comparison of k-ε Models,'' Can. J. Chem. Eng., **63**, pp. 177–182.
[35] Wilcox, D. C., 1994, Turbulence Modeling for CFD, DCW Industries, Inc., La Canada, California.
[36] Abraham, J., Khan, A., and Magi, V., 1999, ''Jet-Jet and Jet-Wall Interactions in a Diesel Engine,'' Society of Automotive Engineers Paper SAE 1999-01-0513.
[37] Cossali, G., Gerla, A., Coghe, A., and Brunello, G., 1996, ''Effect of Gas Density and Temperature on Air Entrainment in a Transient Diesel Spray,'' Society of Automotive Engineers Paper SAE 960862.
[38] Kozma, J., and Farrell, P., 1997, ''Air Entrainment in a High Pressure Diesel Spray,'' Society of Automotive Engineers Paper SAE 971620.
[39] MacInnes, J., and Bracco, F., 1992, ''Comparisons of Deterministic and Stochastic Computations of Drop Collisions in Dense Sprays,'' *Numerical Approaches to Combustion Modeling, Progress in Astronautics and Aeronautics*, E. S. Oran and J. P. Boris, eds., AIAA, Washington D.C., Vol. 135, pp. 615–642.

Prediction of the Circumferential Film Thickness Distribution in Horizontal Annular Gas-Liquid Flow

Evan T. Hurlburt
Postdoctoral Research Associate,
Department of Chemical Engineering,
University of Illinois Urbana-Champaign,
291 Roger Adams Lab, Box C-3,
600 South Mathews Avenue,
Urbana, IL 61801

Ty A. Newell
Associate Professor of Mechanical Engineering,
Department of Mechanical
and Industrial Engineering,
University of Illinois Urbana-Champaign,
1206 W. Green St.,
Urbana, IL 61801

This paper develops a liquid film symmetry correlation and a liquid film thickness distribution model for horizontal annular gas-liquid pipe flows. The symmetry correlation builds on the work of Williams et al. (1996) (Droplet Flux Distributions and Entrainment in Horizontal Gas-Liquid Flows,'' Int. J. Multiphase Flow, Vol. 22, pp. 1–18). A new correlating parameter is presented. The liquid film thickness model is based on the work of Laurinat et al. (1985) (Film Thickness Distribution for Gas-Liquid Annular Flow in a Horizontal Pipe,'' PhysicoChem. Hydrodynam., Vol. 6, pp. 179–195). The circumferential momentum equation is simplified to a balance between the normal Reynolds stress in the film's circumferential direction and the circumferential component of the weight of the film. A model for the normal Reynolds stress in the circumferential direction is proposed. The symmetry correlation is used to close the model equations. The model is valid for films with disturbance waves, and is shown to be applicable to air-water flows over a range of conditions from low velocity asymmetric to high velocity symmetric annular flows. [S0098-2202(00)02102-7]

Keywords: Two-Phase Flow, Annular Flow, Horizontal Gas-Liquid Flow, Liquid Film Thickness Distribution

1 Introduction

The circumferential film thickness distribution in horizontal annular air-water flows has been measured over a range of tube diameters by several researchers (Dallman [1], Fukano and Ousaka [2], Laurinat [3], Paras and Karabelas [4], Williams [5]). From these studies we can see how the local time averaged film thickness is influenced by the flow conditions. Two general observations from these experiments are: 1) the film thickness is small relative to the tube radius—typical local film thickness values are between one tenth and one thousandth of the tube radius; 2) the film is asymmetric—it is thicker on the bottom of the tube than on the top.

A model to predict the film thickness was developed by Laurinat et al. [6]. The model includes momentum balances in the axial, radial, and circumferential directions and a mass balance which accounts for the redistribution of mass due to atomization and deposition of droplets. This work has been the starting point for subsequent modeling efforts (e.g., Fukano and Ousaka [2], Lin et al. [7]).

Laurinat set the value of flow condition dependent constants in his model to bring the film thickness predictions in agreement with the experimental film thickness data. This allowed evaluation of the relative significance of each of the terms in the momentum balance on the film thickness distribution. For the flow conditions considered, the normal stress gradient due to liquid phase velocity fluctuations in the circumferential direction was found to be the dominant factor controlling the distribution. The interfacial shear acting on the liquid surface due to secondary flow in the gas core was found to be of significance only near the top of the tube. Atomization and deposition resulted in some film redistribution, but the effects were relatively small.

Lin et al. [7] took circumferential film thickness measurements and compared them to predictions from Laurinat's model. The data were taken at low superficial gas velocities in the stratified-annular region of the annular flow regime. At these velocities they concluded the interfacial shear due to secondary gas flows plays an important role in distributing the liquid film.

Fukano and Ousaka [2] modified Laurinat's model to more directly include the effects of the waves on the liquid surface. This was done using a model for the normal stress in the liquid that is a function of the static pressure gradient in the gas. The static pressure gradient is due to waves on the liquid surface. The result is a continual flow of liquid up the tube walls in regions with disturbance waves and a downward draining flow in the flatter regions before and after the waves. Experimental evidence of this mechanism has been observed by Sutharshan et al. [8]. Interfacial shear due to secondary flows was assumed to be negligible in Fukano and Ousaka's model.

In this paper, a symmetry correlation is presented and used with a modified form of Laurinat's model to develop a set of equations that predict the circumferential film thickness distribution in annular flows. Experimental data are used to develop a functional relationship between the film thickness and the wave induced normal Reynolds stress. By combining the information from the symmetry correlation with the film model, the value of a parameter in the normal Reynolds stress relation can be estimated. The only input parameters needed in the model are the gas and liquid superficial velocities, U_{SG} and U_{SL}, and the entrained liquid fraction, E.

2 Theory

(a) Liquid Film Circumferential Symmetry. Dallman [1] took time averaged circumferential film thickness measurements in a 2.31 cm diameter horizontal tube over a range of air and water mass flow rates in the annular flow regime. Data from four of these flow conditions are shown in Fig. 1 and Fig. 2. The four curves in these graphs cover the range of symmetry conditions seen in annular flow. At low air mass flow rates the distribution is

Contributed by the Fluids Engineering Division for publication in the JOURNAL OF FLUIDS ENGINEERING. Manuscript received by the Fluids Engineering Division January 30, 1999; revised manuscript received February 16, 2000. Associate Technical Editor: P. E. Raad.

highly asymmetric with the majority of the liquid flowing along the bottom of the tube. As the air mass flow rate increases (for a given water mass flow rate) symmetry increases. At very high air mass flow rates the film becomes nearly symmetric.

Symmetry has been quantified by Williams et al. [9] using the parameter, $A_L/(h_0 d)$. Here, A_L is the cross-sectional area of the film, $A_L = \int_0^{\pi} (d-2h) h d\overline{x}$, h is the local film thickness, h_0 is the film thickness at the bottom, d is the tube diameter, and $\overline{x}$ is the angle from the bottom of the tube. As the flow becomes more symmetric, $A_L/(h_0 d)$ approaches its maximum value, $\pi(1 - 2m/d)$, where m is the average film thickness. It approaches its minimum value, $(4/3)(h_0/d)^{0.5}$, when the flow is stratified.

In the present work the symmetry parameter is defined as the average film thickness divided by the film thickness at the bottom of the tube, h_{avg}/h_0, where h_{avg} is given by

$$h_{avg} = \frac{1}{\pi} \int_0^{\pi} h d\overline{x}. \tag{1}$$

The parameter h_{avg}/h_0 approaches its maximum value, 1, at high velocities as the flow becomes more symmetric. It approaches its minimum value, $(4/(3\pi))(h_0/d)^{0.5}$, at low velocities where the flow is stratified. Values of h_{avg}/h_0 are shown with the distributions in Fig. 1 and Fig. 2.

Williams correlated symmetry with the Froude number, $\mathrm{Fr} = U_{SG}/(gd)^{0.5}$. This incorporates the effect of the gas mass flow rate on symmetry through the superficial gas velocity. It does not, however, account for the increase in asymmetry that occurs as the liquid mass flow rate increases for a given gas velocity.

In order to include the liquid mass flow rate dependence, correlation of the symmetry data was attempted using other nondimensional groups. The best correlation was found using $(\dot{m}_G/\dot{m}_L)^{0.5}\mathrm{Fr}$. This parameter is the square root of the ratio of the gas phase power to the power required to pump the liquid at its mass flow rate from the bottom of the tube to the top of the tube, $(\dot{m}_G U_{SG}^2/\dot{m}_L g d)^{0.5}$. A plot of h_{avg}/h_0 versus $(\dot{m}_G/\dot{m}_L)^{0.5}\mathrm{Fr}$ using Laurinat's data is shown in Fig. 3.

Figure 4 shows h_{avg}/h_0 versus $(\dot{m}_G/\dot{m}_L)^{0.5}\mathrm{Fr}$ over a range of tube diameters and L/d's from a variety of different studies (Dallman [1], Fukano and Ousaka [2], Hurlburt and Newell [10], Jayanti et al. [11], Laurinat [3], Paras and Karabelas [4], Williams [5]). The larger data set has more scatter, but the general trend seen in Fig. 3 remains. (The data sets showing a more rapid transition toward symmetric annular flow (Hurlburt and Newell [10] and Jayanti et al. [11]) are at the lowest L/d's. These flows may not be ''fully developed'' which is argued by Whalley [12] to require an L/d of about 400.)

A curve fit to the data for typical values of h_0 is shown in Fig. 4, and is given by

$$\frac{h_{avg}}{h_0} = \frac{4}{3\pi}\left(\frac{h_0}{d}\right)^{0.5} + 0.9\left[1 - \exp\left(-\frac{(\dot{m}_G/\dot{m}_L)^{0.5}\mathrm{Fr}}{90}\right)\right], \tag{2}$$

where

$$\mathrm{Fr} = U_{SG}/(gd)^{0.5}. \tag{3}$$

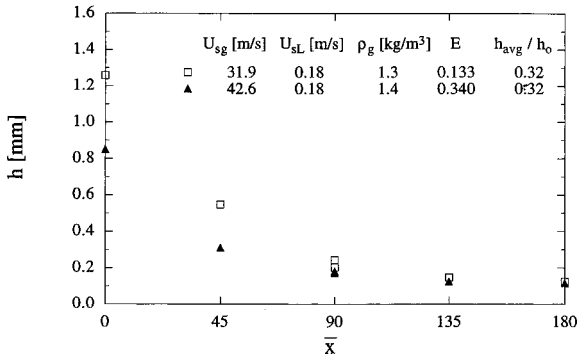

Fig. 1 Film thickness measurements versus angle. Air-water data from Dallman [1] in a 2.31 cm diameter horizontal tube at an L/d of 600.

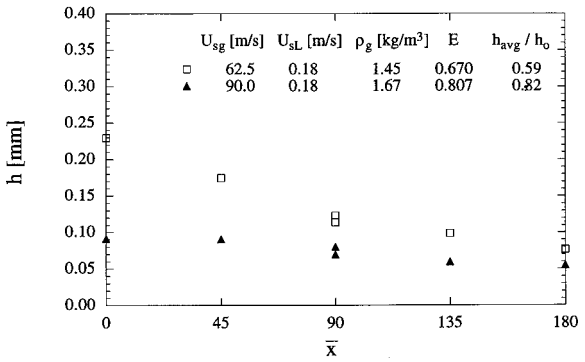

Fig. 2 Film thickness measurements versus angle. Air-water data from Dallman [1] in a 2.31 cm diameter horizontal tube at an L/d of 600.

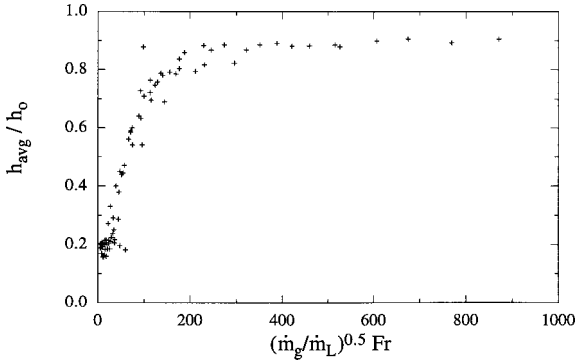

Fig. 3 Symmetry parameter versus $(\dot{m}_g/\dot{m}_L)^{0.5}$Fr. Air-water data from Laurinat [3] in a 5.08 cm diameter horizontal tube at an L/d of 300.

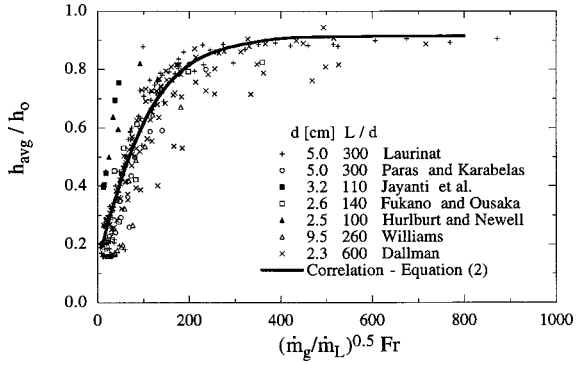

Fig. 4 Symmetry parameter versus $(\dot{m}_g/\dot{m}_L)^{0.5}$Fr. Air-water data from several studies.

(b) Prediction of the Circumferential Film Thickness Distribution. The momentum balance equations developed in Laurinat et al. [6] are used to predict the film thickness. The following is a list of the assumptions used in this model:

1 The liquid film thickness is small relative to the tube radius. This allows the use of Cartesian instead of cylindrical coordinates.
2 The liquid phase is turbulent resulting in forces due to gradients in the fluctuating velocities.
3 The film height is not varying significantly with time. (The equations use time averaged quantities and predict the time averaged behavior.)
4 The influence of the waves on the transfer of momentum from the gas phase to the liquid phase in the axial direction can be accounted for indirectly through an interfacial axial shear.
5 The tube diameter is large enough that surface tension forces can be ignored.
6 A constant pressure is imposed by the gas phase on the surface of the liquid phase.
7 The turbulent stresses, τ_{xx} and τ_{xz}, can be modeled as independent of radial position.

An implicit assumption is that gas entering the liquid, traveling through, and exiting the liquid as bubbles can be ignored. This process was observed by Hewitt et al. [13].

The circumferential momentum balance is used to determine the film thickness. The radial momentum balance is used to eliminate the pressure gradient in the circumferential direction. The forces responsible for holding the liquid against the radial component of the film's weight are not considered.

Momentum Equations

Laurinat developed the time-averaged momentum equations for fully-developed flow. The coordinate system is Cartesian with x as the circumferential direction, y as the radial direction, and z as the axial direction.
The axial momentum equation is

$$\frac{\partial \tau_{yz}}{\partial y}+\frac{1}{a}\frac{\partial \tau_{xz}}{\partial \bar{x}}=0. \tag{4}$$

The circumferential momentum equation is

$$-\frac{1}{a}\frac{\partial p}{\partial \bar{x}}+\frac{\partial \tau_{yx}}{\partial y}+\frac{1}{a}\frac{\partial \tau_{xx}}{\partial \bar{x}}-\rho_L g\sin\bar{x}=0. \tag{5}$$

The radial momentum equation is

$$-\frac{\partial p}{\partial y}-\rho_L g\cos\bar{x}=0. \tag{6}$$

Here τ_{xx} and τ_{xz} are Reynolds stresses due to circumferential and axial velocity fluctuations, u' and w', (with $\tau_{xx}=-\rho_L\overline{u'^2}$ and $\tau_{xz}=-\rho_L\overline{u'w'}$), τ_{yz} is the axial shear stress, τ_{yx} is the circumferential shear stress, p is the liquid pressure, ρ_L is the liquid density, a is the tube radius, and $\bar{x}$ is the circumferential distance from the bottom of the tube in radians ($\bar{x}=x/a$).

Integration of (6) from any point, y, to the gas-liquid interface gives

$$-p|_h+p|_y-\rho_L g(h-y)\cos\bar{x}=0. \tag{7}$$

If we ignore surface tension effects, the interface pressure, $p|_h$, can be assumed equal to the gas phase pressure, p_0. If the gas phase pressure does not vary circumferentially, the radial momentum balance can be differentiated to solve for the static pressure gradient in the circumferential direction,

$$\frac{\partial p}{\partial \bar{x}}-\rho_L g\cos\bar{x}\frac{dh}{d\bar{x}}=0. \tag{8}$$

Substitution of (8) into (5) gives

$$\frac{\partial \tau_{yx}}{\partial y}+\frac{1}{a}\frac{\partial \tau_{xx}}{\partial \bar{x}}-\rho_L g\sin\bar{x}-\frac{\rho_L g}{a}\cos\bar{x}\frac{dh}{d\bar{x}}=0. \tag{9}$$

The stress terms in (4) and (9) are nondimensionalized using the shear for single-phase flow in a smooth tube,

$$\tau_s=0.023\,\mathrm{Re}_G^{-0.2}\rho_G U_{SG}^2. \tag{10}$$

Here Re_G is the gas Reynolds number, $\mathrm{Re}_G=\rho_G U_{SG} d/\mu_G$, and ρ_G, is the density of the gas. Length terms are nondimensionalized using the friction velocity, $\sqrt{\tau_s/\rho_L}$, and the kinematic viscosity of the liquid, ν_L.

The nondimensional momentum balance equations describing the liquid film flow are

$$\frac{\partial \tau_{yz}^+}{\partial y^+}+\frac{1}{a^+}\frac{\partial \tau_{xz}^+}{\partial \bar{x}}=0, \tag{11}$$

and

$$\frac{\partial \tau_{yx}^+}{\partial y^+}+\frac{1}{a^+}\frac{\partial \tau_{xx}^+}{\partial \bar{x}}-\frac{1}{a^+\mathrm{Fr}_{\tau_s}}\sin\bar{x}-\frac{1}{a^{+2}\mathrm{Fr}_{\tau_s}}\cos\bar{x}\frac{dh^+}{d\bar{x}}=0, \tag{12}$$

where

$$\mathrm{Fr}_{\tau_s}=\frac{\tau_s}{\rho_L g a}, \tag{13}$$

and

$$h^+=\frac{h}{\nu_L}\left(\frac{\tau_s}{\rho_L}\right)^{0.5}. \tag{14}$$

Simplification of the Momentum Equations. In this section further simplifications to the momentum equations are made. The simplifications are based on Laurinat's findings of the relative influence of the terms in the momentum balance on the film thickness distribution. For the conditions considered these findings include:

1 The effect of atomization and deposition on the circumferential distribution of the film is relatively small.
2 Interfacial circumferential shear due to secondary flows in the gas is significant only near the top of the tube. (This is supported by recent measurements taken by Dykhno et al. [14] in a 9.53 cm horizontal pipeline. The secondary flow was found to be circulating in a downward direction for conditions in which a film is present on the wall.)
3 The static pressure gradient due to the circumferential film thickness gradient is small relative to the normal stress.
4 The dispersion term, $1/a^+\partial\tau_{xz}^+/\partial\bar{x}$, appears to be small relative to the axial shear.

The first simplification to the equations uses the result that the interfacial shear and atomization and deposition have only a small effect on the time averaged film distribution. When this is true, the local circumferential liquid film velocity, u, is zero (the time averaged upflow and downflow are the same). The radial stress gradient, $\partial\tau_{yx}^+/\partial y^+$, can then be eliminated from (12) and the circumferential momentum balance becomes

$$\frac{\partial \tau_{xx}^+}{\partial \bar{x}}-\frac{1}{\mathrm{Fr}_{\tau_s}}\sin\bar{x}-\frac{1}{a^+\mathrm{Fr}_{\tau_s}}\cos\bar{x}\frac{dh^+}{d\bar{x}}=0. \tag{15}$$

The second simplification uses the finding that the static pressure gradient is small relative to the normal stress. (In air-water flows, this term is only of significance near the bottom when the film thickness is greater than about 2 mm.) Equation (15) then becomes

$$\frac{\partial \tau_{xx}^{+}}{\partial \bar{x}} - \frac{1}{\mathrm{Fr}_{\tau_s}} \sin \bar{x} = 0. \tag{16}$$

In this form, the circumferential component of the weight of the film is balanced only by the circumferential normal stress gradient, i.e., by the variation of the wave induced circumferential velocity fluctuations.

The final simplification to the momentum equations uses the result that the dispersion term, $1/a^{+}\partial \tau_{xz}^{+}/\partial \bar{x}$, is small. The axial momentum balance (11) then becomes

$$\frac{\partial \tau_{yz}^{+}}{\partial y^{+}} = 0. \tag{17}$$

This implies that the axial shear is constant in the radial direction. We will refer to this radially constant axial shear as the interfacial axial shear, τ_i^{+}, where $\tau_{yz}^{+} = \tau_{yz}^{+}|_h = \tau_i^{+}$.

Liquid Film τ_{xx}^{+} Relation. To implement (16), a relation for the normal Reynolds stress, τ_{xx}^{+}, is needed. In this section, an equation relating τ_{xx}^{+} to the liquid film thickness is proposed. Detailed circumferential film thickness measurements taken by Dallman [1] are used in developing the relation.

If we assume τ_{xx}^{+} is a function only of h^{+}, Eq. (16) can be rewritten as

$$d\tau_{xx}^{+}/dh^{+} = \sin(\bar{x})/[\mathrm{Fr}_{\tau_s}(dh^{+}/d\bar{x})]. \tag{18}$$

The derivative, $dh^{+}/d\bar{x}$, can be calculated from film thickness data taken around the perimeter of the tube. With $dh^{+}/d\bar{x}$ and the known flow conditions, $\sin(\bar{x})/[\mathrm{Fr}_{\tau_s}(dh^{+}/d\bar{x})]$ can be used as an estimate of $d\tau_{xx}^{+}/dh^{+}$. A plot of $-\sin(\bar{x})/[\mathrm{Fr}_{\tau_s}(dh^{+}/d\bar{x})]$ versus h^{+} is shown in Fig. 5 for data taken by Dallman in a 2.31 cm diameter tube.

Figure 5 offers insight into the functional dependence between τ_{xx}^{+} and h^{+}. The derivative of τ_{xx}^{+} initially decreases rapidly and then decreases relatively slowly for large h^{+}. A function whose derivative captures this behavior is,

$$\tau_{xx}^{+} = -\tau_{xx,\max}^{+}\left[1 - \exp\left(-\frac{h^{+}-6}{18}\right)\right]. \quad (h^{+} > 6) \tag{19}$$

The stress described by τ_{xx}^{+} is the result of circumferential velocity fluctuations induced by waves. Asali and Hanratty [15] found that wave activity dramatically decreased at a liquid film Reynolds number below 370 (approximately $h^{+} = 6$). In order to incorporate this observation the value of τ_{xx}^{+} is assumed to approach zero at $h^{+} = 6$. The maximum normal stress, $\tau_{xx,\max}^{+}$, depends on the gas and liquid mass flow rates.

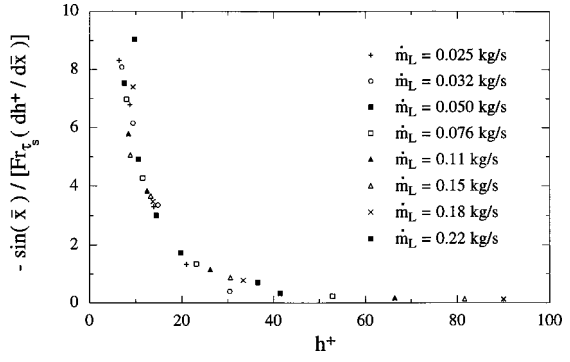

Fig. 5 Estimate of $d\tau_{xx}^{+}/dh^{+}$ versus h^{+} using (18) and circumferential film thickness measurements. Data from Dallman [1] in a 2.31 cm diameter horizontal tube at $U_{SG} = 30$ m/s.

The film thickness data used to generate Fig. 5 were all taken at $U_{SG} = 30$ m/s. At this velocity, the entrained liquid fraction is low. This minimizes the effect of droplet atomization and deposition on $dh^{+}/d\bar{x}$. Similar results are seen at higher velocities, but with more scatter in the derivative near the top of the pipe.

Circumferential Film Thickness Solution. Using (19) for τ_{xx}^{+}, (16) becomes

$$-\frac{\tau_{xx,\max}^{+}}{18}\exp\left(-\frac{h^{+}-6}{18}\right)\frac{dh^{+}}{d\bar{x}} - \frac{1}{\mathrm{Fr}_{\tau_s}}\sin\bar{x} = 0. \tag{20}$$

This differential equation can be solved analytically for h^{+}. The solution, which depends on the nondimensional film thickness at the bottom of the tube, h_0^{+}, is

$$\frac{h^{+}-6}{h_0^{+}-6} = \frac{\ln[\alpha - \beta(\cos\bar{x} - 1)]}{\ln\alpha}, \tag{21}$$

where

$$\alpha = \exp\left(-\frac{h_0^{+}-6}{18}\right), \tag{22}$$

$$\beta = \frac{1}{\tau_{xx,\max}^{+}\mathrm{Fr}_{\tau_s}}, \tag{23}$$

and

$$h_0^{+} = \frac{h_0}{\nu_L}\left(\frac{\tau_s}{\rho_L}\right)^{0.5}. \tag{24}$$

Note that at large Fr_{τ_s}, h^{+} approaches h_0^{+} and the film approaches a symmetric condition.

To evaluate (21), $\tau_{xx,\max}^{+}$ and h_0^{+} must be determined. The symmetry correlation, (2), eliminates $\tau_{xx,\max}^{+}$ as an unknown. Prediction of h_0^{+} requires an interfacial axial shear relation, a relation for the average axial velocity of the liquid film, mass conservation, and an entrainment model which predicts the fraction of the total liquid mass flowing as droplets suspended in the gas core. Relations for the interfacial axial shear and the average axial velocity of the liquid film are developed in the following sections. An entrainment model is not developed in this paper.

τ_i Model. The term τ_i is the local shear on the liquid interface in the axial direction. Is has been studied experimentally via pressure drop and liquid film mass flow rate measurements by Asali and Hanratty [15] for vertical air-water flows. The correlation from this study shows interfacial shear to be a strong function of the film thickness,

$$\frac{\tau_i}{\tau_s} - 1 = 0.45\,\mathrm{Re}_G^{-0.2}(\phi h_i^{+} - 4), \tag{25}$$

where

$$\phi = \frac{\mu_L}{\mu_G}\left(\frac{\rho_G}{\rho_L}\right)^{0.5}, \tag{26}$$

$$h_i^{+} = \frac{h u_i^{*}}{\nu_L}, \tag{27}$$

and

$$u_i^{*} = \left(\frac{\tau_i}{\rho_L}\right)^{0.5}. \tag{28}$$

Asali's interfacial shear correlation is based on vertical annular flow data. In this paper we assume the correlation to be applicable in predicting the local axial shear based on the local film thickness in horizontal flow.

Asali's interfacial shear correlation is developed from data in which the product ϕh_i^+ is less than 100. In this region $\tau_i/\tau_s - 1$ shows the linear increase with non-dimensional film thickness seen in Eq. (25). For films with ϕh_i^+ greater than 100, the data in Asali and Hanratty [15] show a less rapid rate of increase of $\tau_i/\tau_s - 1$ with film thickness. An equation that approximates the behavior of $\tau_i/\tau_s - 1$ for both $\phi h_i^+ < 100$ and $\phi h_i^+ > 100$ is given by

$$\frac{\tau_i}{\tau_s} - 1 = 10\left[1 - \exp\left(-\frac{\phi h_i^+}{250}\right)\right]. \tag{29}$$

Axial Velocity. The liquid film average velocity can be estimated from the experimental correlations of Asali and Hanratty [15] and Henstock and Hanratty [16]. Asali correlated film thickness with liquid film Reynolds number in the ripple regime ($\mathrm{Re}_{LF} < 370$),

$$h_i^+ = 0.34\,\mathrm{Re}_{LF}^{0.6} \tag{30}$$

where

$$\mathrm{Re}_{LF} = \frac{4\dot{m}_{LF}}{\pi d \mu_L}. \tag{31}$$

Here $\dot{m}_{LF}$ is the liquid film mass flow rate. Henstock correlated film thickness with Re_{LF} in the disturbance wave regime ($\mathrm{Re}_{LF} > 370$),

$$h_i^+ = 0.0379\,\mathrm{Re}_{LF}^{0.9}. \tag{32}$$

When the film thickness is small relative to the tube diameter, Re_{LF} can be written

$$\mathrm{Re}_{LF} = \frac{4 h w_{\mathrm{avg}}}{\nu_L}. \tag{33}$$

Using (33) in (30) and solving for w_{avg}, a relation for the average liquid velocity in the ripple regime is found,

$$\frac{w_{\mathrm{avg}}}{u_i^*} = 1.5(h_i^+)^{0.666}. \tag{34}$$

Using (33) in (32) and solving for w_{avg}, a relation for the average liquid velocity in the disturbance wave regime is found,

$$\frac{w_{\mathrm{avg}}}{u_i^*} = 9.5(h_i^+)^{0.111}. \tag{35}$$

These relations can be combined into a single relation covering both regimes.

$$\frac{w_{\mathrm{avg}}}{u_i^*} = [(1.5(h_i^+)^{0.111})^{-2} + (9.5(h_i^+)^{0.111})^{-2}]^{0.5} \tag{36}$$

Mass Conservation. The entrainment, E, is the ratio of the liquid mass flow rate suspended in the gas core, $\dot{m}_{LE}$, to the total liquid mass flow rate.

$$E = \dot{m}_{LE}/\dot{m}_L \tag{37}$$

When the entrainment is known the liquid film mass flow rate can be calculated from

$$\dot{m}_{LF} = \dot{m}_L - \dot{m}_{LE}. \tag{38}$$

The local film thickness and local average axial velocity are related to the mass flow rate in the liquid film by the integral

$$\dot{m}_{LF} = 2a\rho_L \int_0^{\pi} h w_{\mathrm{avg}} d\bar{x}. \tag{39}$$

Film Thickness Prediction. The model equations and their range of validity are summarized below. The equations can be solved for a given superficial gas and superficial liquid velocity ($U_{SG} = \dot{m}_G/\rho_G \pi d^2/4$, $U_{SL} = \dot{m}_L/\rho_L \pi d^2/4$), and a known value of the entrainment.

Film Thickness Model Summary

Film thickness distribution: (21) with parameters given by (10), (13), (14), (22), (23), and (24)

Symmetry correlation: (2) with h_{avg} given by (1) and Fr given by (3)

Interfacial axial shear correlation: (29) with parameters given by (26), (27), and (28)

Liquid film mass flow rate: (37), (38), and (39) with w_{avg} given by (36)

Model Range of Validity

Minimum film thickness: $h^+ = 6$

Maximum film thickness at the bottom: $h_0 \sim 2$ mm

Diameter range: $d \sim 1$ to 5 cm

Figure 6 and Fig. 7 show model predictions compared to film thickness measurements taken by Dallman [1] for the conditions in Fig. 1 and Fig. 2. The entrained liquid fractions used are from experiments by Dallman [1]. Values of $\tau^+_{xx,\max}$ for each curve are shown in the figures.

Figure 8 shows model predictions compared to film thickness measurements taken by Laurinat [3] in a 5.08 cm tube. The entrained liquid fraction is from experiments by Laurinat [3]. Model predictions from Laurinat et al. [6] are also presented for comparison.

Figure 9 shows model predictions compared to film thickness measurements taken by Fukano and Ousaka [2] in a 2.60 cm tube.

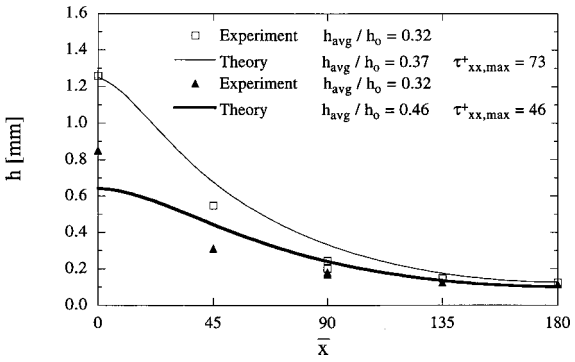

Fig. 6 Model predictions compared to experimental data. Experimental air-water data from Dallman [1] in a 2.31 cm diameter horizontal tube at an *L/d* of 600. Flow conditions shown in Fig. 1.

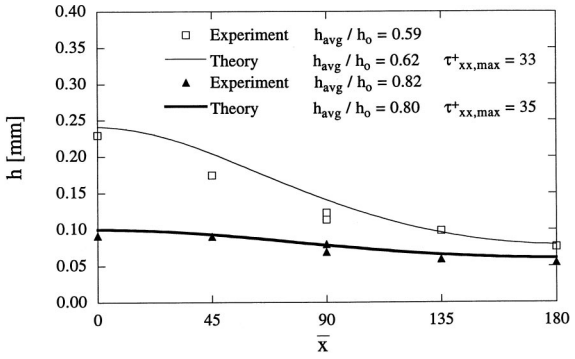

Fig. 7 Model predictions compared to experimental data. Experimental air-water data from Dallman [1] in a 2.31 cm diameter horizontal tube at an *L/d* of 600. Flow conditions shown in Fig. 2.

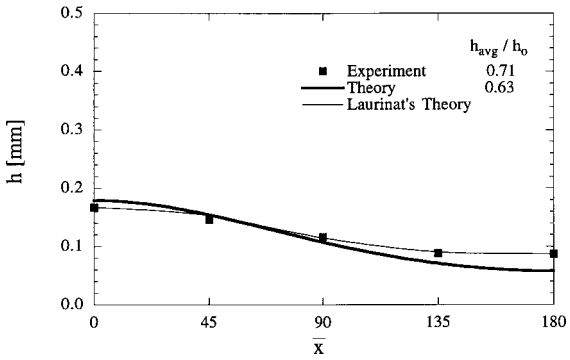

Fig. 8 Model predictions compared to Laurinat's model and experimental data. Air-water data from Laurinat [3] in a 5.08 cm diameter horizontal tube. $U_{SG}=56.8$ m/s, $U_{SL}=0.075$ m/s, $\rho_G=2.04$ kg/m^3, and $E=0.782$.

(The entrainment is not available and was estimated to be 0.6.) Model predictions from Fukano and Ousaka [2] are also presented for comparison.

Figure 10 shows model predictions compared to film thickness measurements taken by Paras and Karabelas [4] in a 5.08 cm tube. (The entrainment is not available and was estimated to be 0.5.) Model predictions made using both the symmetry value from (2) and the symmetry value from the experimental data are shown for comparison.

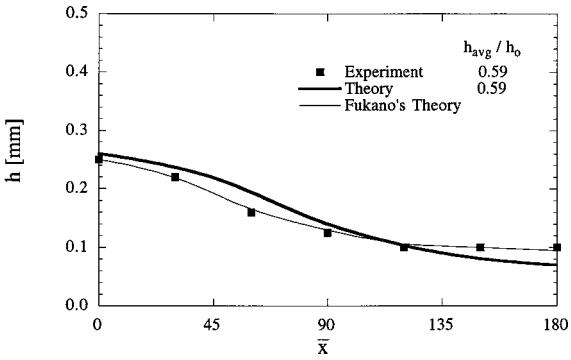

Fig. 9 Model predictions compared to Fukano's model and experimental data. Air-water data from Fukana and Ousaka [2] in a 2.60 cm diameter horizontal tube. $U_{SG}=48.7$ m/s, $U_{SL}=0.10$ m/s, $\rho_G=1.6$ kg/m^3. Entrainment is estimated at 0.6.

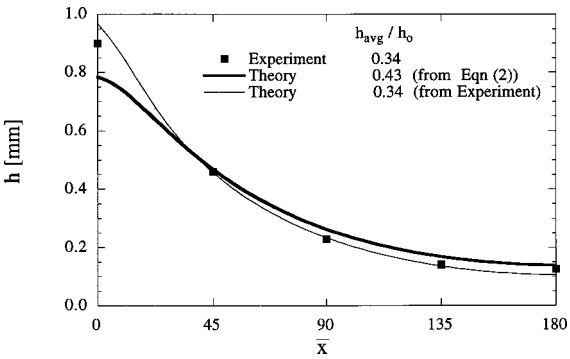

Fig. 10 Model predictions compared to experimental data. Air-water data from Paras and Karabelas [4] in a 5.08 cm diameter horizontal tube. $U_{SG}=46.8$ m/s, $U_{SL}=0.20$ m/s, $\rho_G=2.31$ kg/m^3. Entrainment is estimated at 0.5.

3 Discussion

As seen in Figs. 6–10, the simplified model presented in this work is capable of estimating the film thickness of both symmetric and asymmetric annular flows over a wide range of film thicknesses. The redistribution of the film by entrained droplet deposition and the interfacial shear in the circumferential direction do not appear to play a significant role in estimating the film thickness for the range of velocities and pipe diameters considered. Inclusion of these terms does result in some gains in accuracy as seen in the comparison to Laurinat's predictions in Fig. 8. The disadvantage to this approach is that it requires the specification of flow condition dependent model parameters that are not readily available.

A contribution of this paper is the use of experimental film thickness data to develop a relation for the circumferential normal stress, τ_{xx}^{+}. When introduced in the momentum balance this relation results in a simple analytical expression that successfully predicts the film thickness distribution. This normal stress relation differs from the relations used both by Laurinat and by Fukano and Ousaka [2]. The comparison between the models in Fig. 8 and Fig. 9 suggests that while based on somewhat different relations, the three approaches can give similar results. It is not clear, however, whether the Laurinat or the Fukano and Ousaka models give results which are similar to the present model when the film thickness at the bottom is of the order of 1 mm. No predictions for highly asymmetric conditions are given in these works.

The model's circumferential normal stress is assumed to be a function of the local film thickness. This stress is the result of wave induced velocity fluctuations. The film thickness dependence of the stress is likely due to the film thickness dependence of the waves. Wave height has been observed to be a strong function of film thickness. Hurlburt and Newell [10] took instantaneous film thickness measurements in a 2.5 cm diameter tube and found the standard deviation of the film thickness to be proportional to and of similar order to the average film thickness.

The sensitivity of the model to the symmetry correlation is seen in Fig. 6 and Fig. 10. The deviation of the model from the measured values is in part due to the inaccurate estimate of the symmetry parameter for these conditions.

Use of the model in tubes of diameter less than 1 cm has not been attempted. It is likely that in small tubes surface tension effects would need to be considered when estimating the symmetry and when solving the momentum balance equations.

The model applies only over the range of annular flow conditions in which disturbance waves cover the entire cross section. This is the majority of the annular flow regime in tubes of diameter less than 5 cm. In larger diameter tubes, the greater circumferential distance involved can result in the film thickness reaching a value of $h^{+}=6$ at some point up the tube wall. If a film is present above this point, it is believed to be the result of the deposition of entrained droplets. A local entrainment model would need to be added for the model to be used in these circumstances.

The symmetry correlation was developed using data in which annular flow was observed. The model could be extended to low gas velocity flow conditions in which only a partial annulus occurs. This would require consideration of partial annulus symmetry data. The height on the tube at which the film thickness goes to zero could be estimated by the height at which the film thickness prediction decreases to $h^{+}=6$.

Acknowledgments

The authors appreciate the support of the Air Conditioning and Refrigeration Center at the University of Illinois at Urbana-Champaign under project 45. We also appreciate Professor Hanratty's sharing of his experience, insight, and enthusiasm.

Nomenclature

μ_G = gas viscosity
μ_L = liquid viscosity
ϕ = property ratio group
ν_L = liquid kinematic viscosity
ρ_G = gas density
ρ_L = liquid density
τ_i = axial interfacial shear stress
τ_s = smooth tube wall shear stress
τ_{xx} = liquid Reynolds stress
$\tau_{xx,\max}$ = maximum value of the circumferential liquid Reynolds stress
τ_{xz} = liquid Reynolds stress
τ_{yx} = interfacial shear in the circumferential direction
τ_{yz} = axial shear stress
a = tube radius
A_L = cross-sectional area of the liquid film
d = tube diameter
E = entrainment
Fr = Froude number, $\mathrm{Fr}=U_{SG}/(gd)^{0.5}$
Fr_{τ_s} = Froude number, $\mathrm{Fr}_{\tau_s}=\tau_s/\rho_L g a$
g = gravitational constant
h = liquid film thickness
h^+ = nondimensional liquid film thickness based on smooth tube shear
h_{avg} = circumferential average liquid film thickness
h_i^+ = nondimensional film thickness based on interfacial shear stress
h_0 = liquid film thickness at the bottom of the tube
L = tube length
m = average film thickness
$\dot{m}_G$ = vapor mass flow rate
$\dot{m}_L$ = total liquid mass flow rate
$\dot{m}_{LE}$ = entrained liquid mass flow rate
$\dot{m}_{LF}$ = liquid film mass flow rate
p = liquid pressure
p_0 = gas phase pressure
Re_G = gas Reynolds number, $\mathrm{Re}_G=\rho_G U_{SG} d/\mu_G$
Re_{LF} = liquid film Reynolds number, $\mathrm{Re}_{LF}=2\dot{m}_{LF}/\pi a \mu_L$
u = liquid film circumferential velocity
u' = liquid film circumferential velocity fluctuation
u_i^* = liquid friction velocity based on interfacial shear stress, $u_i^*=(\tau_i/\rho_L)^{0.5}$
U_{SG} = superficial gas velocity
U_{SL} = superficial liquid velocity
w = liquid film axial velocity
w' = liquid film axial velocity fluctuation
w_{avg} = average axial liquid film velocity
x = circumferential distance from the bottom of the tube
$\overline{x}$ = angle from the bottom of the tube, $\overline{x}=x/a$
y = radial distance
z = axial distance

References

[1] Dallman, J. C., 1978, ''Investigation of separated flow model in annular-gas liquid two-phase flows,'' Ph.D. thesis, University of Illinois, Urbana.
[2] Fukano, T., and Ousaka, A., 1989, ''Prediction of the circumferential distribution of film thickness in horizontal and near-horizontal gas-liquid annular flows,'' Int. J. Multiphase Flow, **15**, pp. 403–419.
[3] Laurinat, J. E., 1982, ''Studies of the effect of pipe size on horizontal annular two-phase flows,'' Ph.D. thesis, University of Illinois, Urbana, IL.
[4] Paras, S. V., and Karabelas, A. J., 1991, ''Properties of the liquid layer in horizontal annular flow,'' Int. J. Multiphase Flow, **17**, pp. 439–454.
[5] Williams, L. R., 1990, ''Effect of pipe diameter on horizontal annular two-phase flow,'' Ph.D. thesis, University of Illinois, Urbana.
[6] Laurinat, J. E., Hanratty, T. J., and Jepson, W. P., 1985, ''Film thickness distribution for gas-liquid annular flow in a horizontal pipe,'' PhysicoChem. Hydrodynam., **6**, pp. 179–195.
[7] Lin, T. F., Jones, O. C., Lahey, R. T., Block, R. C., and Murase, M., 1985, ''Film thickness measurements and modelling in horizontal annular flows,'' PhysicoChem. Hydrodynam., **6**, pp. 197–206.
[8] Sutharshan, B., Kawaji, M., and Ousaka, A., 1995, ''Measurement of circumferential and axial liquid film velocities in horizontal annular flow,'' Int. J. Multiphase Flow, **21**, pp. 193–206.
[9] Williams, L. R., Dykhno, L. A., and Hanratty, T. J., 1996, ''Droplet flux distributions and entrainment in horizontal gas-liquid flows,'' Int. J. Multiphase Flow, **22**, pp. 1–18.
[10] Hurlburt, E. T., and Newell, T. A., 1996, ''Optical measurement of liquid film thickness and wave velocity in liquid film flows,'' Exp. Fluids, **21**, pp. 357–362.
[11] Jayanti, S., Hewitt, G. F., and White, S. P., 1990, ''Time-dependent behavior of the liquid film in horizontal annular flow,'' Int. J. Multiphase Flow, **16**, pp. 1097–1116.
[12] Whalley, P. B., 1987, *Boiling, Condensation, and Gas-Liquid Flow*, Clarendon Press, Oxford.
[13] Hewitt, G. F., Jayanti, S., and Hope, C. B., 1990, ''Structure of thin liquid films in gas-liquid horizontal flow,'' Int. J. Multiphase Flow, **16**, pp. 951–957.
[14] Dykhno, L. A., Williams, L. R., and Hanratty, T. J., 1994, ''Maps of mean gas velocity for stratified flows with and without atomization,'' Int. J. Multiphase Flow, **20**, pp. 691–702.
[15] Asali, J. C., Hanratty, T. J., and Andreussi, P., 1985, ''Interfacial drag and film height for vertical annular flow,'' AIChE J., **31**, pp. 895–902.
[16] Henstock, W. H., and Hanratty, T. J., 1976, ''The interfacial drag and the height of the wall layer in annular flows,'' AIChE J., **22**, pp. 990–1000.

Turbulent Three-Dimensional Air Flow and Trace Gas Distribution in an Inhalation Test Chamber

P. W. Longest, Jr.
Graduate Student

C. Kleinstreuer
Professor

Department of Mechanical
and Aerospace Engineering,
North Carolina State University,
Raleigh, NC 27695-7910

J. S. Kinsey
Environmental Engineer,
U. S. Environmental Protection Agency,
National Health and Environmental Effects
Research Laboratory,
Research Triangle Park, NC 27711

Steady incompressible turbulent air flow and transient carbon monoxide transport in an empty Rochester-style human exposure chamber have been numerically simulated and compared with experimental data sets. The system consisted of an inlet duct with a continuous carbon monoxide point source, 45- and 90-degree bends, a round diffuser, a round-to-square transition, a rectangular diffuser, the test chamber, a perforated floor, and again transition pieces from the chamber to an outlet duct. Such a configuration induced highly nonuniform vortical flow patterns in the chamber test area where a pollutant concentration is required to be constant at breathing level for safe and accurate inhalation studies. Presented are validated momentum and mass transfer results for this large-scale system with the main goals of determining the development of tracer gas (CO) distributions in the chamber and analyzing the contributions to CO-mixing. Numerical simulations were conducted employing a k-ϵ model and the latest available RNG k-ϵ model for air and CO-mixing. Both models predict similar velocity fields and are in good agreement with measured steady and transient CO-concentrations. It was found that secondary flows in the inlet section and strong vortical flow in the chamber with perforated flooring contributed to effective mixing of the trace gas at breathing levels. Specifically, in the height range of 1.4 m$<h<$2.0 m above the chamber floor, predicted CO-concentrations rapidly reached a near constant value which agrees well with experimental results. This work can be extended to analyze trace gas mixing as well as aerosol dispersion in occupied test chambers with or without flow redirection devices installed in the upstream section. A complementary application is particle transport and deposition in clean rooms of the electronic, pharmaceutical, and health care industries.
[S0098-2202(00)01702-8]

Introduction

In order to conduct realistic, large-scale, health impact assessments of air pollutants, e.g., trace gases or aerosols, safe, controllable and accurate test environments are required. Such conditions must be analyzed for human inhalation test chambers. The U.S. Environmental Protection Agency (EPA) Human Studies Facility (HSF) is equipped with seven so-called Rochester style chambers for human exposure studies.

The chamber of interest, HSF Chamber 3, has a test floor area of 5.2 m^2 with an 8.5 m total height ($x^*=20.9$) and is used for gas pollutant exposures (cf. Fig. 1). Far upstream of the chamber the pollutant, here carbon monoxide gas, is injected at the fan inlet of a conditioning system, i.e., filtration, temperature and humidity control. The air and pollutant exit the conditioning system at a maximum flow rate of 0.3209 m^3/s with a positive pressure head as highly turbulent flow ($Re_d=84{,}300$) for the 0.3048 m (0.75 d) diameter duct. The fluid mixture then navigates an inlet duct configuration passing through a 90-degree bend of $d=0.4064$ m and descends 1.52 m ($x^*=3.74$), with a Reynolds number of $Re_d=63{,}200$, prior to entering a series of diffusers. The flow is expanded through a 10-degree half-angle round diffuser, a 25-degree half-angle round-to-square transition, and finally a 37-degree half-angle square-to-square diffuser which ends with a cross section equivalent to that of the chamber. The test section, which has an approximately square cross section, is 3.2 m ($x^*=7.87$) high as measured from the last diffuser to the perforated floor. If the velocity were uniform in the test area, the Reynolds number based on hydraulic diameter would be $Re_d=11{,}300$, where $D_h=2.27$ m (5.59 d). The floor of the chamber consists of 21-percent open-area-plates through which the flow penetrates and is then exhausted, by means of a negative pressure, through a square-tapered duct at the chamber exit.

The driving force for air circulation in the chamber is normally a positive pressure in the inlet duct and a negative pressure at the exit. The negative pressure is supplied by exhaust fans far downstream of the chamber. The positive and negative pressures are balanced, i.e., controlled via an air-balance control system, to produce a pressure of approximately -24.9 Pa gage ($p^*=-3.51$) in the chamber test section. The body of the chamber is operated at a negative pressure in order to prevent pollutant escape upon accidental opening to the outside environment. The system is considered to be isothermal and of planar symmetry, i.e., symmetric about a mid-plane slice.

Motivation. It is expected that the chamber geometry, with its curved inlet configuration in conjunction with the perforated floor, creates a highly vortical flow field which predominantly rotates in the vertical plane. For gaseous pollutants, such a flow field should produce a uniform CO distribution with time assuming a near-constant input. In an actual inhalation study, however, areas of diminished CO-concentration will be generated and must be quickly restored to steady state. Based on the needs for a near-uniform trace gas environment and zero up-flow to avoid foreign particle entrainment, geometric modifications of the upstream chamber components to create alternative chamber flow fields are being considered. Thus, as a first step, air flow field validation and an understanding of pollutant transport mechanisms in the chamber are necessary and can be used at a later point as a powerful design tool for predicting the effects of certain modifications, i.e., flow redirection devices, chamber occupancy, breathing patterns, etc. In this study, numerical simulation of the Rochester chamber was implemented and validated based on experimental gaseous mixing results.

Contributed by the Fluids Engineering Division for publication in the JOURNAL OF FLUIDS ENGINEERING. This paper was presented in part at the ASME Fluids Engineering Division Summer Meeting, Washington, DC, June 1998. Manuscript received by the Fluids Engineering Division April 15, 1998; revised manuscript received February 9, 2000. Associate Technical Editor: D. P. Telionis.

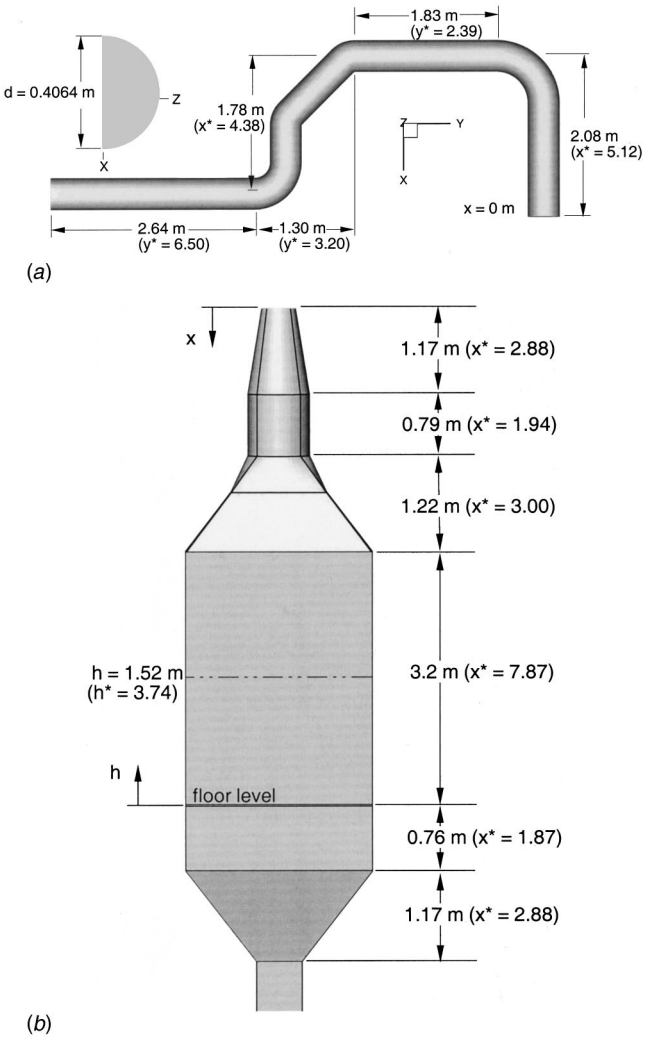

Fig. 1 Geometry of in-plane chamber system: (*a*) inlet pipe and (*b*) Rochester-style human exposure chamber with inlet and outlet components

Literature Review. Experimental and numerical simulations of the gas flow field in Rochester chambers were not found in the open literature. Closely related topics in which extensive work has been completed include dilution ventilation and turbulence modeling for single system components. Dilution ventilation is the mixing of volumes of fresh air into a contaminated work space to control exposures of potentially hazardous gases and aerosols (Committee on Industrial Ventilation [1]). Given a simple room containing a well-mixed contaminant, with a small inlet and outlet, dilution ventilation theory predicts the concentration will decay exponentially as a function of the degree of mixing (Burgess et al. [2]). Since the degree of mixing is extremely case-specific, this method is of no value in determining detailed pollutant concentrations in the Rochester chamber. Another tool commonly used by industrial hygienists is residence time distribution (RTD) as discussed by Nabar [3]. This method can conveniently be implemented with trace gas experimentation by introducing a pulse of a contaminant and measuring the rate at which the gas exits (Nauman and Buffham [4]).

Turbulence Model. Selection of an appropriate turbulence model for numerical simulation of the Rochester chamber geometry required consideration of computational cost, anticipated flow phenomena, and the variables of primary interest. Determined in this study are the specific mixing characteristics of the Rochester chamber as well as the general flow features. To maintain a reasonable computational cost for the simulation of this considerably large geometry, two-equation turbulence models are implemented. Of such models, the standard k-ϵ and a recent RNG k-ϵ are considered in order to determine their merits for such applications. However, it is widely held that k-ϵ models, particularly with pressure independent wall functions, don't work well for adverse pressure gradients and flow separation (Wilcox [5]). Asymptotically consistent models are often used in such cases (cf. Jones and Launder [6]), but these models require increased near wall grid resolution, driving the computational cost out of reasonable bounds for the complex geometry of the Rochester chamber. Anticipated flow features include a primary rotating eddy due to the curved inlet configuration as well as points of flow separation and reattachment. It is speculated that, due to the rotating vortical-flow, separation points will be limited to the sharp expansions in the chamber geometry. Reattachment is then the more difficult feature for the model to capture. Comparison to benchmark backward facing step studies was, therefore, the criterion for selecting the appropriate version of the k-ϵ model.

One of the most recent forms of the k-ϵ model is based on renormalization group theory (RNG) and was developed by Yakhot and Orszag [7] and Yakhot et al. [8]. The latest available revision of the RNG k-ϵ model (Yakhot et al. [8]) is reported to both produce excellent results for the backward facing step problem and to be less sensitive to the details of near-wall treatment (Speziale and Thangam [9]). The RNG k-ϵ model may then be well suited to predict turbulent mixing and general velocity field features in the Rochester chamber.

Theory

The mean flow is governed by the incompressible Reynolds-averaged continuity and Navier-Stokes equations with the assumption of an eddy viscosity (cf. Kleinstreuer [10]).

$$\frac{\partial U_i}{\partial x_i} = 0 \tag{1}$$

and

$$U_j \frac{\partial U_i}{\partial x_j} = B - \frac{1}{\rho}\frac{\partial P}{\partial x_i} + \frac{\partial}{\partial x_j}\left[(\nu + \nu_T)\left(\frac{\partial U_i}{\partial x_j} + \frac{\partial U_j}{\partial x_i}\right)\right] \tag{2}$$

where

$$\nu_T = C_\mu \frac{k^2}{\epsilon} \tag{3a}$$

with

$$k = \tfrac{1}{2}\overline{u_i' u_i'} \tag{3b}$$

and

$$\epsilon = \nu \overline{\frac{\partial u_i'}{\partial x_j}\frac{\partial u_i'}{\partial x_j}} \tag{3c}$$

For the current analysis of the Rochester chamber, the RNG k-ϵ model with a standard two-layer wall function will be evaluated. To ensure that the mixing rate and general velocity fields are relatively insensitive to k and ϵ approximations, particularly near wall boundaries, the k-ϵ model will be used for comparison. For such models, calculation of the turbulence kinetic energy and dissipation rate requires two additional partial differential equations

$$\frac{\partial k}{\partial t} + U_j \frac{\partial k}{\partial x_j} = \tau_{ij}\frac{\partial U_i}{\partial x_j} - \epsilon + \frac{\partial}{\partial x_j}\left[\left(\nu + \frac{\nu_T}{\sigma_k}\right)\frac{\partial k}{\partial x_j}\right] \tag{4}$$

and

$$\frac{\partial \epsilon}{\partial t} + U_j \frac{\partial \epsilon}{\partial x_j} = C_{\epsilon 1}\frac{\epsilon}{k}\tau_{ij}\frac{\partial U_i}{\partial x_j} - C_{\epsilon 2}\frac{\epsilon^2}{k} + \frac{\partial}{\partial x_j}\left[\left(\nu + \frac{\nu_T}{\sigma_\epsilon}\right)\frac{\partial \epsilon}{\partial x_j}\right] \tag{5}$$

In total, there are five coefficients to be specified: C_μ, $C_{\epsilon 1}$, $C_{\epsilon 2}$, σ_k, and σ_ϵ. In the k-ϵ model, these coefficients are constants and obtained from benchmark experiments for equilibrium turbulent boundary layers and isotropic turbulence as follows (cf. Wilcox [5])

$$C_\mu = 0.09 \tag{6a}$$

$$C_{\epsilon 1} = 1.44 \tag{6b}$$

$$C_{\epsilon 2} = 1.92 \tag{6c}$$

$$\sigma_k = 1.0 \tag{6d}$$

and

$$\sigma_\epsilon = 1.3 \tag{6e}$$

For the RNG k-ϵ model, the coefficients were calculated explicitly with corrections to the constants in the dissipation rate equation made by Yakhot et al. [8] resulting in

$$C_\mu = 0.085 \tag{7a}$$

$$C_{\epsilon 1} = 1.42 - \frac{\eta(1-\eta/\eta_\infty)}{1+\beta\eta^3} \tag{7b}$$

$$C_{\epsilon 2} = 1.68 \tag{7c}$$

$$\sigma_k = 0.7179 \tag{7d}$$

and

$$\sigma_\epsilon = 0.7179 \tag{7e}$$

where

$$\eta = Sk/\epsilon \tag{8a}$$

$$\eta_\infty = 4.38 \tag{8b}$$

$$\beta = 0.015 \tag{8c}$$

and

$$S = (2\overline{S}_{ij}\overline{S}_{ij})^{1/2} \tag{8d}$$

and $\overline{S}_{ij}$ is the mean rate of strain tensor.

The Reynolds-averaged mass transport equation (cf. Kleinstreuer [10]) can be written in the form

$$\frac{\partial(\rho Y_A)}{\partial t} + \frac{\partial(\rho U_j Y_A)}{\partial x_j} = \frac{\partial}{\partial x_j}\left[\left(\frac{\mu}{\mathrm{Sc}} + \frac{\mu_T}{\mathrm{Sc}_t}\right)\frac{\partial Y_A}{\partial x_j}\right] \tag{9}$$

where Schmidt number for the binary diffusion of air and carbon monoxide is $\mathrm{Sc}=0.8315$ and the turbulent Schmidt number (Sc_t) is on the order of one.

For the inlet boundary condition, the duct configuration was modeled four bends upstream of the chamber inlet (cf. Fig. 1(*a*)) assuming steady, incompressible, three-dimensional (3-D), planar-symmetric, isotropic turbulent flow and smooth walls. The mid-plane symmetry assumption is conservative because out-of-plane inlet bends create extra swirl and hence a higher degree of inlet mixing of the pollutant(s). A fully developed profile representing a flow rate of 0.3209 m^3/s with a homogeneous kinetic turbulence energy, k, of 1.225×10^{-2} m^2/s^2 ($T=3.670\times10^{-2}$) and a turbulence dissipation rate, ϵ, of 1.112×10^{2} m^2/s^3 ($\epsilon^*=1.667$) was incorporated (Comer et al. [11]). The inlet effective viscosity was obtained by extrapolating from downstream conditions rather than computing it from the approximate inlet k and ϵ values. The model included the tapered outlet of the chamber leading to a square cross section of 0.584 m (1.44 d) width (cf. Fig. 1(*b*)) which was then extended far downstream such that the flow would be fully developed at the exit. The outflow boundary condition was taken to be -26.5 Pa ($p^*=-3.74$) based on pressure measurements in a downstream section of uniform flow and numerically only implies a zero normal gradient be imposed on the velocity.

Prior experimental flow visualization indicated that the perforated floor or grate of the chamber, in terms of its pressure drop, has a significant affect on the flow field. An empirical correlation by Idelchik [12] was used to develop a body force term for the x-momentum equation applicable to the floor control volumes, i.e.,

$$B_x = -C_x u_x^2 \tag{10}$$

where B_x is the body force, $C_x=70.3$ m^{-1} is an empirical constant based on the perforated plate geometry, and u_x is the normal or approach velocity for each control volume in [m/s]. To restrict lateral motion in the floor cells, a similar technique was employed by adjusting C_y and C_z until the respective velocity components were sufficiently damped.

Solution Method

The computational fluid dynamics package CFX 4.2 (AEA Technology, Bethel Park, PA) was used for numerical simulation. CFX 4.2 is a control-volume-based solver and employs a structured, multiblock, body-fitted coordinate discretization scheme. In order to reduce the required computer resources, the simulation was split into two parts, the first being a solution of the inlet duct configuration. User supplied Fortran was implemented to apply the duct exit profiles as the inlet boundary conditions for the chamber. Simulations consisted of first determining the steady-state velocity field, governed by Eqs. (1)–(8) and then solving the turbulent transport equation (9) for transient CO-concentration in the multicomponent flow, i.e., species are mixed on the molecular level.

All turbulent flow equations were discretized in space to be second-order accurate using centered differencing or a similar modified scheme for the advection terms. Evaluation of the resultant coupled nonlinear equations was performed iteratively using a Picard linearization and applying an algebraic multigrid technique. The outer iteration procedure was stopped when the global mass residual had been reduced from its original value by four orders of magnitude. To ensure that a converged solution had been reached, the residual reduction condition was increased to 10^{-5} and results were compared. The stricter convergence criterion was slowly reached with small oscillations and produced a negligible effect on both velocity and turbulence quantities. Momentum residuals were also monitored and found to be on the order of the required accuracy at convergence. The computational time required for the full flow field solution of the chamber was approximately 36 hours on a SUN Ultra 60 workstation (300 Mhz, 512 MB RAM).

The transient solution of the turbulent transport equation (9) required both spatial and temporal discretization. Considering the goal of time accurate concentration tracking, a second-order accurate ''time-centered'' Crank-Nicholson approach was used for temporal discretization. Investigation revealed that the spatial discretization scheme employed for the mass fraction advection term should also be second-order accurate to avoid numerical diffusion. Solution of the turbulent transport Eq. (9) was continued until the global mass fraction residual had been reduced by six orders of magnitude.

To ensure grid convergence, the computational domain size and configuration was adjusted until an acceptable level of grid independence was achieved. Assuming planar symmetry, grids consisting of 80,000, 120,000, and 160,000 cells were tested. Little variation in the parameters of interest, i.e., CO-concentration and the general velocity field, was noticed between the two highest grid density solutions (maximum relative error 2.8 percent). Solutions will be presented for the 120,000 control volume mesh. Likewise, the appropriate size for the inlet duct configuration was found to be 100,000 cells. The inlet grid configuration, for the

duct and upper-chamber section, was of the butterfly blocking design with an axial slice consisting of 598 control volume centers. Three additional blocks were added to the symmetric geometry beginning at the third diffuser to allow for 1320 control volume centers at a slice taken in the chamber test area. For both the inlet configuration and the chamber geometry, the distance to the first control volume center from the boundary ranged $10<y^+<80$, where y^+ is the dimensionless sublayer scaled distance.

Experimental Methods

CO Measurements. A series of tracer gas measurements was performed of the pollutant distribution in Chamber 3 for both transient response to a step CO input and for steady-state conditions. In these tests, 99.6 percent carbon monoxide was injected at two constant rates into the suction side of the chamber supply fan using a system consisting of a compressed gas cylinder, pressure regulator, and mass flow controller. A low CO mass flow rate ($\dot{m}_L = 6.63\times10^{-3}$ kg/min) was implemented for steady-state measurements and, in a separate experiment, a higher concentration step input ($\dot{m}_H = 1.13\times10^{-2}$ kg/min) was used to monitor CO-concentration rise as conditions reached a quasi-steady state. The mass flow controller was calibrated prior to testing using a NIST-traceable flow standard (DryCal Model DC-1).

For all tests conducted, the concentration of CO was monitored using a TECO Model 48C continuous analyzer. To determine the quasi-steady CO-distribution, measurements were conducted at two heights in the breathing zone and nine sampling locations across the chamber cross section. In addition, a multi-point calibration was performed on the Model 48°C prior to testing, using a NIST-traceable calibration gas standard. The results of the tracer gas tests are summarized in Table 1 based on 30-second average concentrations obtained from the analyzer at each grid location.

To evaluate transient mixing characteristics of the chamber, a

Table 1 Summary statistics for CO tracer gas tests

Summary Statistic[a]	h = 1.52 m Measurement Height[b]	h = 0.91 m Measurement Height[b]
No. of Data Points[c]	16	16
Concentration Range (ppmv)[d]	32.72 to 34.87	32.49 to 34.73
Mean Concentration (ppmv)[d]	33.90	33.73
Standard Deviation	0.7181	0.7742
Range of Percent Difference from Mean Concentration	-2.861 to 3.481	-2.965 to 3.676

[a] Conducted over a 3 x 3 measurement grid within the interior chamber cross section.
[b] Location of sampling line inlet above the perforated floor.
[c] Number of 30-sec averages per grid location. 30-sec averages calculated by electronic data logger from individual 10-sec readings supplied by continuous analyzer. Some initial data points discarded in calculation of averages, etc. to compensate for disturbances created when enter/leaving the chamber.
[d] ppmv ≙ parts per million by volume

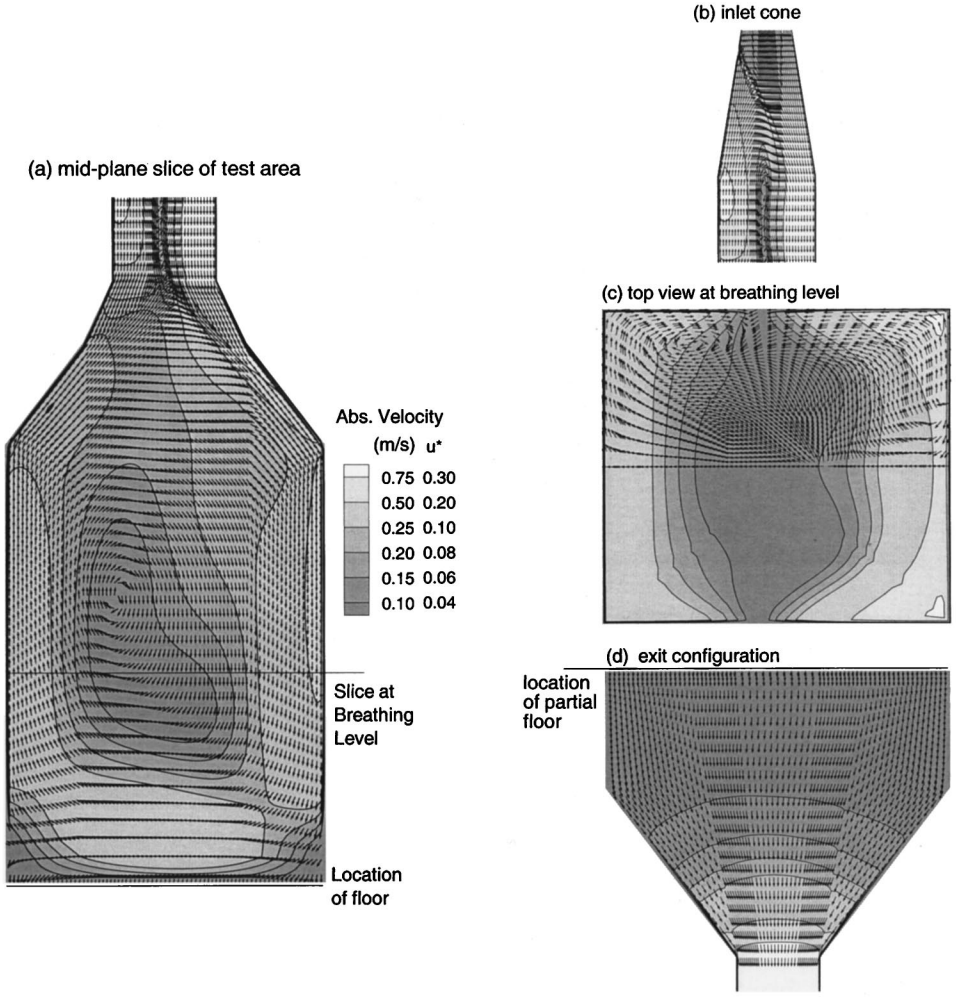

Fig. 2 Cross-sectional views of flow velocity vectors overlaid with absolute velocity magnitude contours: (*a*) mid-plane slice of test area; (*b*) mid-plane slice of inlet cone; (*c*) top view of breathing level; and (*d*) mid-plane slice of flow exit configuration

step CO input concentration was introduced upstream at an initial time. CO-concentration was monitored in the outlet duct configuration at a location sufficiently removed such that the flow was fully developed and well mixed. Quasi-steady CO-concentration occurred approximately 370 seconds ($t^*=6.63$) after the initial upstream input (cf. Fig. 6). The reference time scale used in computing $t^*=t/\tau$, is the time for a fluid element beginning at the upstream inlet and traveling along the centerline at the local mean velocity to reach the outlet monitoring point.

Results and Discussion

Flow Model Validation. An extensive model validation study was carried out for key components and flow features of the Rochester chamber (cf. Longest and Kleinstreuer [13]). Turbulent flow through a 90-degree bend was simulated and successfully compared with experimental data of Enayet et al. [14] for $\mathrm{Re}_d=43{,}000$. Using the latest available RNG k-ϵ turbulence model, the correct reattachment length for turbulent flow over a backward facing step was achieved within 4.5 percent at $\mathrm{Re}_d=44{,}000$, based on the inlet channel height, when compared to the measurements of Eaton and Johnston [15] (cf. Speziale and Thangam [9]). Speziale and Thangam [9] reported similar results with the use of the same RNG k-ϵ model.

Generally, there are very strong physical arguments and a number of comparisons to experimental data that warn against the use of k-ϵ variety models in situations of adverse pressure gradients. It was our experience, however, for a select number of test cases, that the RNG k-ϵ model performed acceptably well (superior to the k-ϵ) for mild to moderate adverse pressure gradients as found in the chamber geometry. Specifically, the RNG k-ϵ turbulence model predicted well the measured separation point in a plane one-sided 10-degree half-angle diffuser at $\mathrm{Re}_d=10{,}000$ (Obi et al. [16]; cf. Durbin [17]); skin friction factor, axial pressure, and centerline velocity in a 3-D conical diffuser with inlet $\mathrm{Re}_d=82{,}000$ (Fraser [18]); as well as smooth separation in a 3-D conical diffuser with inlet $\mathrm{Re}_d=125{,}000$ (McDonald and Fox [19]). The surprisingly good agreements between simulation results and experimental data sets for key geometric components of the system, at similar Reynolds numbers, instilled sufficient confidence to employ the RNG k-ϵ model as a predictor of turbulent air flow in the human inhalation test chamber.

Air Flow Results. The RNG k-ϵ model was implemented to numerically simulate the turbulent airflow characteristics of Chamber 3. Based on CFD modeling, it was found that the upstream bends deliver a highly skewed inlet velocity profile which enters the top diffuser (cf. Fig. 2(b)). The three-step expansion from the round inlet duct to the nearly square chamber generates, in conjunction with the perforated floor, strong vortical flow fields in the test chamber. A single large recirculating zone is formed in the vertical plane as the flow descends the wall in line with the outside of the 90-degree bend, strikes the floor and partially traverses the opposite wall (cf. Fig. 2(a)). As a result, there is a region of low velocity magnitude, i.e., less than 0.1 m/s ($u^*<0.04$), in the center of the chamber. The vertical recirculating zone extends well into the first conical diffuser (cf. Fig. 2(b)), leading to enhanced mixing of the trace gas. The floor grate represents a flow resistance that redirects and reduces velocity gradients in the air flow field, part of which then accelerates in the outlet nozzle to the exit duct (cf. Fig. 2(d)).

Most important, the skewed inlet velocity field and partial floor produce significant vortical flows in the chamber as indicated in Fig. 2(c). Particularly at breathing level, $h\approx 1.52$ m, ($h^*=3.74$) the secondary flow pattern emanates from the mid-plane and traverses the walls where downstream and upstream flow is highest, i.e., the walls along which the vertical eddy rotates. The highest trace gas concentrations are expected along these walls, therefore the secondary flow serves to enhance mass transfer to all areas of the chamber. The k-ϵ model with two-layer wall functions was also implemented to test the sensitivity of the velocity field with respect to k-ϵ approximations. The resulting velocity field was found to be nearly identical to the RNG k-ϵ results with respect to primary and secondary flows.

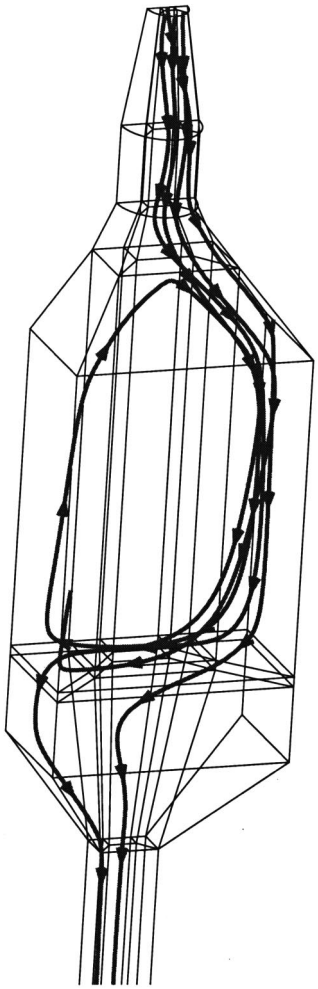

Fig. 3 Paths of stream traces in chamber

The 3-D flow effects are clearly visible in Fig. 3 which depicts stream traces introduced at different inlet positions. The skewed velocity inlet profile and subsequent recirculating in the inlet region force the main stream to enter the chamber off center along the side of a wall which, in conjunction with the flow resistance of the floor, sets up a major recirculating zone. The stream trace paths highlight these two primary chamber flow patterns. Thus, depending on the release position, stream traces are either quickly transported out of the chamber through the floor or circulate indefinitely due to the strong vortical flow. Secondary flow contributes to the stream trace trajectory by dispersing the paths in a direction normal to the plane of symmetry.

Local distributions of the turbulence level and nondimensional dissipation rate as generated by the RNG k-ϵ model are shown in Fig. 4. Starting with the inlet to the round-to-round diffuser and ending at floor level, Fig. 4 depicts the mid-plane turbulence quantities T and ϵ^* across the chamber at four locations. The skewed turbulent flow field leaving the 90-degree bend and entering the round-to-round diffuser is characterized by asymmetric T and ϵ^* profiles with high values for $T\sim\overline{(u_i')}$ near the maximum mean velocity and with high values for $\epsilon^*\sim\overline{(\partial u_i'/\partial x_k)^2}$ at the walls (cf. Fig. 4(a)). At the inlet to the square-to-square (third) diffuser, the turbulence quantities are of similar asymmetric distribution with the highest values occurring at the location of peak

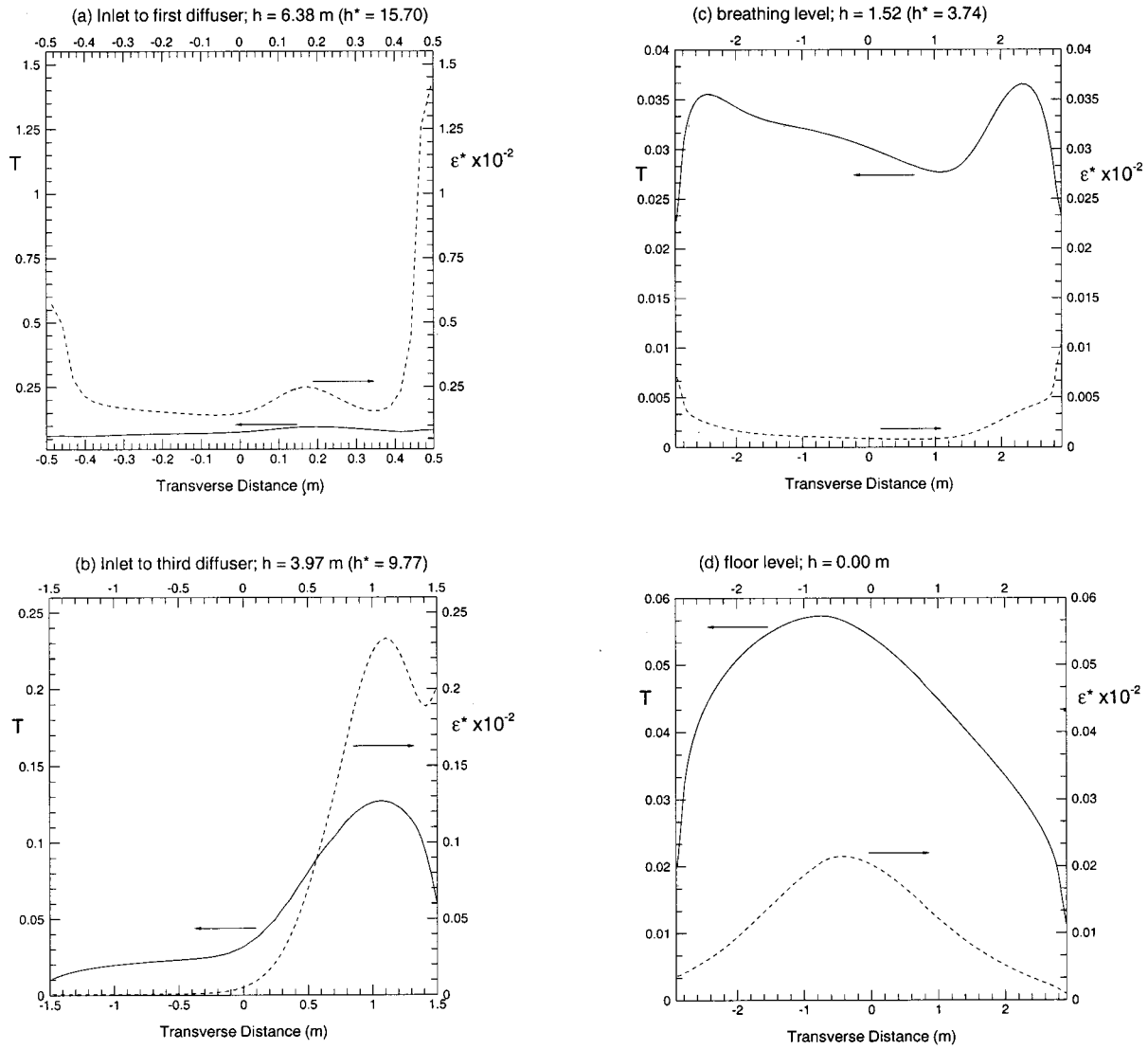

Fig. 4 Local distribution of mid-plane turbulence level and nondimensional dissipation rate at various downstream locations: (*a*) inlet to first diffuser, $h=6.38$ m ($h^*=15.70$); (*b*) inlet to third diffuser, $h=3.97$ m ($h^*=9.77$); (*c*) breathing level, $h=1.52$ m ($h^*=3.74$); (*d*) floor level, $h=0.00$ m

downstream velocity (cf. Fig. 4(*b*)). Approximately 1.5 meters above the floor (cf. Fig. 4(*c*)), both profiles are almost symmetric with characteristic maxima for T near the chamber walls, reflecting the turbulent flow field in the chamber (cf. Fig. 2), and the highest values for ϵ^* at the chamber walls. The presence of the floor destroys the profile symmetry with a single new maximum value for T at the location of high upflow. It is noted that the turbulence level in the chamber test section (cf. Figs. 4(*c*) and 4(*d*)) is several orders of magnitude lower than in the inlet duct configuration (cf. Figs. 4(*a*) and 4(*b*)). The turbulence dissipation also rapidly declines in the x-direction resulting in a linear reduction of eddy viscosity which directly correlates to the contribution of turbulent mixing. Solving the inlet duct configuration separately from the chamber geometry helped to alleviate the stiffness and possible accuracy troubles in the solution of the linearized k-ϵ equations introduced by large changes in turbulence quantities.

Area-averaged turbulent energy levels and nondimensional dissipation rates in the stream-wise direction are shown in Figs. 5(*a*) and 5(*b*) for both the RNG k-ϵ and k-ϵ solutions. Inside the chamber test area, the T and ϵ^* functions are lowest with near-constant values. Inside the second diffuser, i.e., during the round-to-square transition, both averaged turbulence functions drop dramatically to the low, near-constant levels found in the chamber with slight increases occurring in the system's exit duct. The highest values for T and ϵ^* are found in the system's inlet components due to the narrow pathways, high velocities, and significant changes in flow geometry. Both models predict similar turbulence quantities for this geometry, especially inside the chamber test area. The effect of upstream variation in turbulence quantities on mixing characteristics is to be determined.

Trace Gas Results. The CO-trace gas experiments revealed a more rapid than expected progression to steady state as well as a nearly constant CO-concentration at the average breathing level across the chamber. Considering a CO point source before the fourth upstream bend, numerical results matched the transient and steady state measurements and helped to explain the experimental observations. Figure 6 illustrates the case of a CO-mass fraction introduced upstream at time $t=0$ and measured in the outlet section as conditions progress to steady state. For the numerical simulation, a characteristic travel time was estimated to account for the variation in upstream injection positions. The turbulent Schmidt number was slightly adjusted resulting in good agreement between measured CO-concentration and numerical results

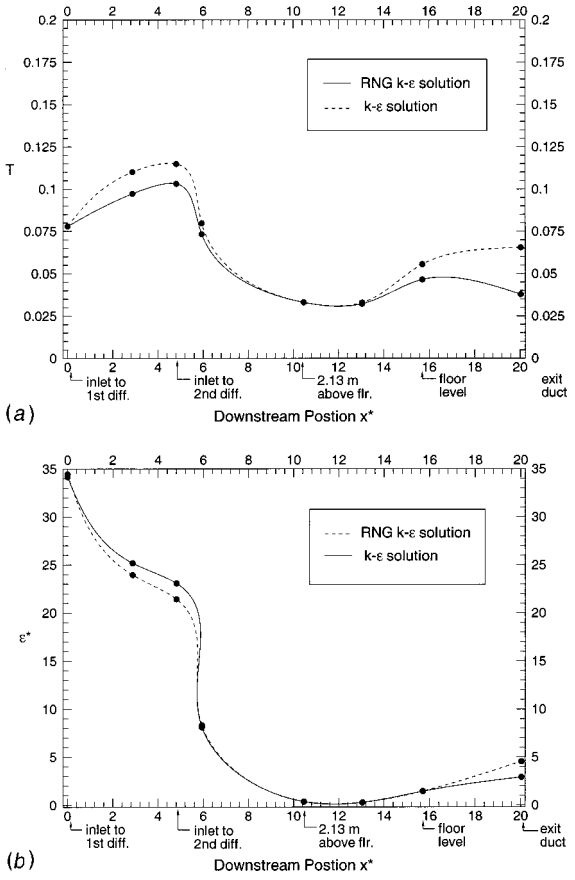

Fig. 5 Area averaged turbulence quantities from RNG k-ϵ and k-ϵ solutions: (*a*) turbulence level and (*b*) nondimensional dissipation rate in chamber

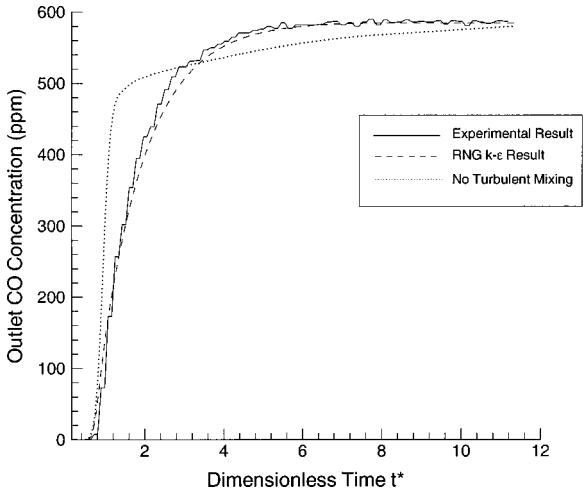

Fig. 6 Measured and predicted transient CO-concentration at the outlet for an upstream step-input

(cf. Fig. 6). The time required to reach the steady-state value of 584 ppm in the outlet section was predicted by the model to be 430 seconds ($t^*=7.70$), compared to the measured value of 370 seconds ($t^*=6.63$). From Fig. 5 it was evident that the k-ϵ model approximated higher k and lower ϵ values in the inlet section which would indicate a higher degree of mixing (cf. Eqs. (3*a*) and (5)). The transient outlet concentration (cf. Fig. 6), however, was found to be insensitive to this discrepancy, and both k-ϵ models produced curves that were nearly identical. Successive mid-plane contours of CO-concentration variation in time are illustrated in Fig. 7 and reveal that, numerically, a period of 430 seconds is required for the CO-concentration in the chamber test section to reach a constant value.

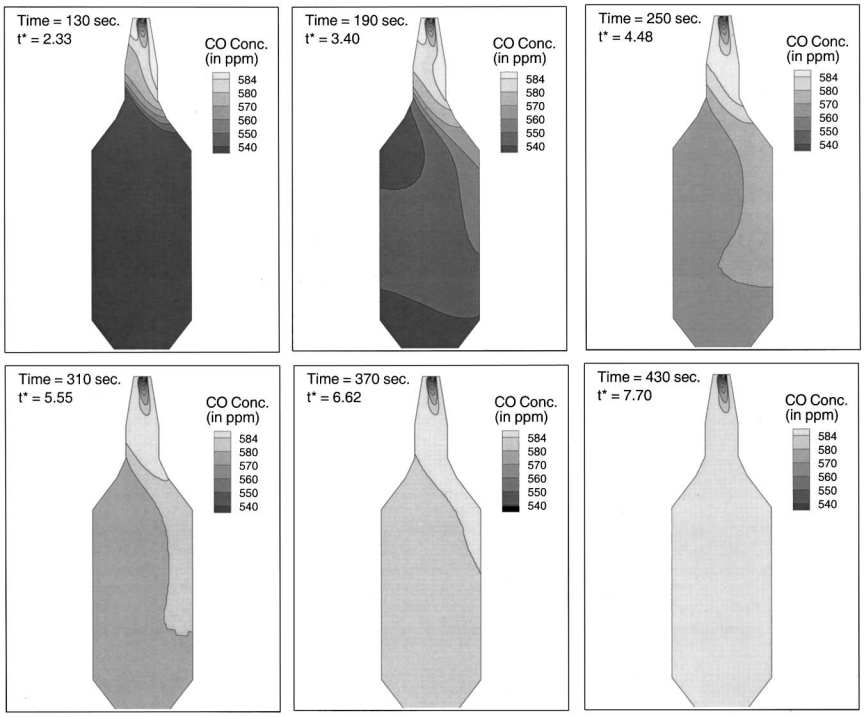

Fig. 7 Mid-plane contours over time of CO-concentration for an upstream step-input

Table 2 Comparison of measured versus predicted CO-concentration at breathing level for sampling points given in Fig. 8

Sampling Point	Measured CO Concentration (ppmv)[a]	Predicted CO Concentration (ppmv)[a]	Percent Difference From Measured Value
1	34.18	34.30	-0.35
2	34.29	34.25	0.12
3	34.79[c]	34.39[c]	1.16
4	34.30	34.32	0.01[b]
5	33.16	34.30	-3.38
6	33.00[d]	34.22[d]	-3.63

[a] ppmv ≙ parts per million by volume
[b] Set Point ≙ reference concentration
[c] highest concentration
[d] lowest concentration

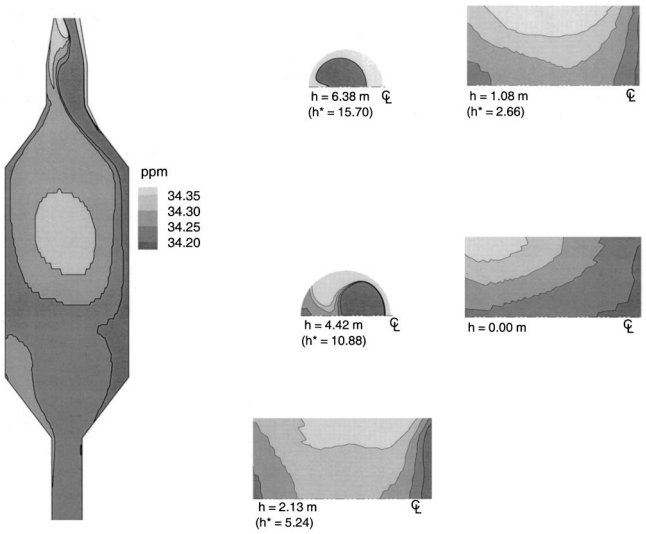

Fig. 9 Quasi-steady contours of CO-concentration for an injection point upstream of the fourth inlet bend; consecutive horizontal plane slice positions measured upward from the partial floor

For quasi-steady-state conditions, theoretical CFD predictions matched the five measurement points at breathing level, i.e., $h = 1.52$ m ($h^* = 3.74$), within ± 3.63 percent (cf. Table 2). Figure 8 depicts the cross section of the chamber with near-uniform CO-concentration contours in the lower half and the horizontal air velocity field in the upper half. Clearly, measurable secondary flow assists in the even distribution of the trace gas. For quasi-steady conditions, mid-plane and cross-sectional views of CO-concentration contours are depicted in Fig. 9. CO-concentration enters the chamber with a 25 percent variation between high and low values. The inlet diffusers therefore provide a high degree of mixing resulting in the near constant concentrations observed in Figs. 8 and 9.

The importance of skewed versus uniform velocity inlet profile, and hence the degree of upstream mixing has been documented by Longest and Kleinstreuer [13]. In addition, parametric sensitivity analyses revealed that trace gas convection, especially due to the partial floor enhanced cross-flows and large eddies, is the major mixing mechanism. Specifically, the two primary vortical flow field patterns are the single eddy circulation in the vertical plane and horizontal eddies spiraling down the quadrants of the chamber (cf. Figs. 2(*a*) and 2(*c*)). On first observation, the large vertical eddy would seem to impede the goal of well-mixed flow and is the cause of the somewhat linear contours of CO-concentration in horizontal planes observed in Figs. 8 and 9. The vertical eddy does, however, extend well into the first inlet diffuser, the effect of which is dilution of the incoming concentrations and enhanced mixing (cf. Figs. 9 and 2(*a*)). Equally important to well-mixed flow is the effect of the secondary flow pattern. Viewing consecutive horizontal planar contours of CO-concentration (cf. Fig. 9), it becomes evident that the secondary velocity pattern serves to drive mass transfer by means of convection producing a rapidly increasing constant concentration environment. Turbulent diffusion has approximately a ten percent mixing effect, mainly smoothing out local variations in CO-concentrations.

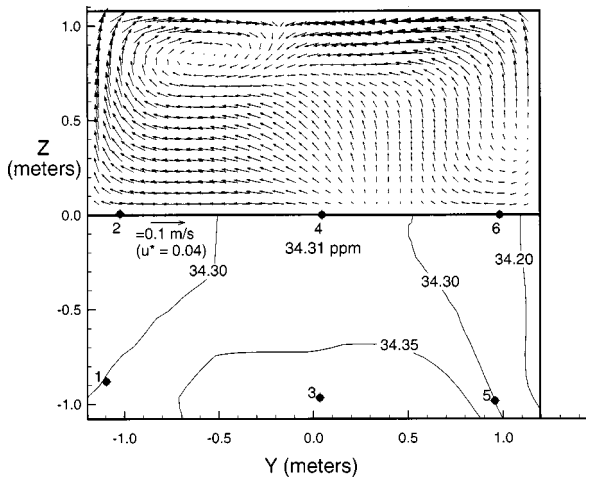

Fig. 8 Horizontal plane view taken $h = 1.52$ m ($h^* = 3.74$) above the chamber floor of secondary velocity vectors (upper half) and quasi-steady contours of CO-concentration measured in ppmv (lower half)

Conclusions

In order to visualize the flow characteristics in an empty Rochester style inhalation chamber and determine steady-state and transient pollutant concentrations, numerical simulations were employed with a user-enhanced commercially available CFD program. A computational model of the Rochester inhalation chamber was validated by comparing turbulent flow simulations of the system's components with previously conducted experimental benchmark studies at similar Reynolds numbers. Upon validation, the components were assembled to create a model of the Rochester chamber that was proven to be mesh independent. The assumptions of steady turbulent flow in a 3-D planar symmetric model were chosen in conjunction with appropriate boundary conditions to generate a realistic flow field. This study makes available a validated numerical model at a reasonable computational cost for the investigation of similar cases. Furthermore, for the geometry and flow patterns considered, results were relatively insensitive to the type of k-ϵ model selected.

Trace gas experiments, conducted concurrently with the numerical simulations, revealed a rapid progression to steady state and a basically constant pollutant concentration at breathing level for the chamber of interest. Numerical simulation was then implemented to first validate and then explain the mechanism behind the steady near-equal concentration contours. It was concluded that the secondary velocity components, which are highly prevalent in the chamber due to the partial floor and the existence of a skewed inlet profile, convect the trace gas to all areas of the chamber and thereby create a near-uniform pollutant environment at average breathing levels, i.e., $1.4 < h < 2.0$ m ($3.4 < h^* < 4.9$), for steady-state operation. Without such secondary velocity compo-

nents, pollutant concentrations would be quite nonuniform. Turbulence quantities k and ϵ, which are proportional to T and ϵ^*, are relatively high in the inlet sections of the chamber contributing to mixing. Upon flow deceleration, k and ϵ decrease significantly to the order of 0.01 resulting in the observed ten percent mixing due to turbulence diffusion. An additional parameter contributing to the uniform concentration in the chamber is the variation of trace gas concentrations at the inlet of the chamber. Concentrations in the chamber will be well mixed to a degree as specified first by the inlet conditions, including the upstream location of the trace gas injection point, and then by the mixing capacity of the chamber. It is noted that the significant secondary velocity components present in the flow field serve to cause a beneficial reduction in start-up time, i.e., time to reach steady state.

Finally, it is noted that a highly vortical flow field, such as that generated in Chamber 3, is generally not desirable from an exposure point of view. Recirculating of air near the chamber floor may transport extraneous aerosols and gases into the breathing zone which can adversely affect the results of controlled pollutant exposure studies. These issues, as well as depletion of pollutant by different breathing patterns of human subjects, are currently under investigation (cf. Comer et al. [11], Kleinstreuer and Hyun [20]). The present results are, however, a basis for future numerical studies of inhalation test chambers and also for clean rooms which are of importance to the electronic, pharmaceutical and health care industries.

Acknowledgments

Financial support from the U.S. EPA (HSD, Chapel Hill, NC) and the use of CFX software from AEA Technology (Bethel Park, PA) are gratefully acknowledged.

Disclaimer

Although the research described in this article has been supported by the U.S. Environmental Protection Agency, it has not been subjected to Agency review and therefore does not necessarily reflect the views of the Agency, and no official endorsement should be inferred. Mention of tradenames or commercial products does not constitute endorsement or recommendation for use.

Nomenclature

B = body force, N/kg
C_μ, $C_{\epsilon 1}$, $C_{\epsilon 2}$, = turbulence constants for the k-ϵ models
D_{AB} = binary diffusion of species A in B, m^2/s
D_h = hydraulic diameter, m
d = inlet duct diameter (0.4064 m)
h = height above chamber floor, m
h^* = nondimensional height above chamber floor, $h^*=h/d$
k = turbulent kinetic energy, m^2/s^2 (at inlet $k_r = 0.01225$ m^2/s^2)
$\dot{m}$ = mass flow rate of CO
p = pressure, Pa gage
p^* = nondimensional pressure, $p^*=p/\rho V^2$
Q = volumetric flow rate, m^3/s
Re_d = Reynolds number based on diameter, $u_i D_h/\nu$
Sc = Schmidt number, ν/D_{AB}
Sc_t = turbulent Schmidt number
$\overline{S_{ij}}$ = mean rate of strain tensor
T = turbulence level, $T=1/V^*(2/3k_r)^{1/2}$
t^* = nondimensional time, $t^*=t/\tau$
u_i = velocity components in Cartesian coordinates, m/s
u^* = nondimensional velocity magnitude component, $|u_i|/V$
U_i = local time-mean velocity
u_i' = fluctuating velocity component, m/s
$\overline{u_i' u_j' \rho}$ = components of Reynolds stress tensor, N/m^2
u_τ = friction velocity, $\sqrt{\tau_w/\rho}$
V = mean inlet velocity (2.47 m/s)
Y_A = mass fraction of species A to the total mass
y^+ = dimensionless sublayer scaled distance, $u_\tau y/\nu$
x, y, z = Cartesian coordinates
x^*, y^*, z^* = nondimensional dimension (x/d, y/d, z/d)
ϵ = turbulence dissipation rate, m^2/s^3
ϵ^* = nondimensional turbulence dissipation rate, $0.5^* d^* \epsilon/k^{3/2}$
η, η_∞, β = additional turbulence model constants
ν = kinematic viscosity, m^2/s
ν_T = eddy viscosity, m^2/s
ρ = density, kg/m^3
σ_k, σ_ϵ = turbulence constants for the k-ϵ models
τ = time for a fluid particle to traverse the geometry (55.85 s)
τ_w = wall shear stress

References

[1] Committee on Industrial Ventilation, 1992, *Industrial Ventilation: A Manual of Recommended Practice*, 21st ed., American Conference of Governmental Industrial Hygienists, Cincinnati, OH.
[2] Burgess, W. A., and Ellenbecker, M. J., and Treitman, R. D., 1989, *Ventilation for Control of the Work Environment*, Wiley, New York.
[3] Nabar, R., 1994, ''Residence Time Distributions and Computational Fluid Dynamics to Characterize Dilution Ventilation in a Confined Space Model,'' Ph.D. Dissertation, University of Michigan.
[4] Nauman, E. B., and Buffham, B. A., 1983, *Mixing in Continuous Flow Systems*, Wiley, New York.
[5] Wilcox, D. C. 1998, *Turbulence Modeling for CFD*, DCW Industries, California.
[6] Jones, W. P., and Launder, B. E., 1972, ''The Prediction of Laminarization with a Two-Equation Model of Turbulence,'' Int. J. Heat Mass Transf., **15**, pp. 301–314.
[7] Yakhot, V., and Orszag, S. A., 1986, ''Renormalization Group Analysis of Turbulence. I. Basic Theory,'' J. Sci. Comput., **1**, pp. 3–51.
[8] Yakhot, V., Orszag, S. A., Thangam, S., Gatski, T. B., and Speziale, C. G., 1992, ''Development of Turbulence Models for Shear Flows by a Double Expansion Technique,'' Phys. Fluids, **A.4**, No. 7, pp. 1510–1520.
[9] Speziale, C. G., and Thangam, S., 1992, ''Analysis of an RNG Based Turbulence Model for Separated Flows,'' Int. J. Eng. Sci., **30**, No. 10, pp. 1379–1388.
[10] Kleinstreuer, C., 1997, *Engineering Fluid Dynamics—An Interdisciplinary Systems Approach*, Cambridge University, New York.
[11] Comer, J. K., Kleinstreuer, C., Longest, P. W., Kim, C. S., and Kinsey, J. S., 1998, ''Computational Aerosol Transport and Deposition Analyses for Human Exposure Chambers and Model Respiratory Airways,'' *Proceedings of FEDSM'98, Paper No. 4811*, Washington, DC.
[12] Idelchik, I. E., 1994, *Handbook of Hydraulic Resistance*, 3rd ed., CRC Press, Boca Raton, FL.
[13] Longest, P. W., and Kleinstreuer, C., 1997, *Phase I Report: Simulation and Analysis of Turbulent Three Dimensional Air Flow and Mass Transfer in Rochester Chamber Three*, Research Report for the U.S. EPA. MAE Department, N. C. State Univ., Raleigh, NC.
[14] Enayet, M. M., Gibson, M. M., Taylor, A. M. K. P., and Yianneskis, M., 1982, ''Laser-Doppler Measurements of Laminar and Turbulent Flow in a Pipe Bend,'' Int. J. Heat Mass Transf., **3**, pp. 213–219.
[15] Eaton, J., and Johnston, J. P., 1980, Technical Report MD-39. Stanford University.
[16] Obi, S. Ohimuzi, H., Aoki, K., and Masuda, S., 1993, ''Experimental and Computational Study of Turbulent Separating Flow in an Asymmetric Plane Diffuser,'' 9th Symposium on Turbulent Shear Flow, Kyoto, Japan, pp. P305-1–P305-4.
[17] Durbin, P. A., 1994, ''Separated Flow Computations with the κ-ϵ-v^2 Model,'' AIAA J., **33**, pp. 659–664.
[18] Fraser, H., 1958, ''The Turbulent Boundary Layer in a Conical Diffuser,'' J. Hydraul. Div., Am. Soc. Div. Eng., **1684**, pp. 1–17.
[19] McDonald, A. T., and Fox, R. W., 1966, ''An Experimental Investigation of Incompressible Flow in Conical Diffusers,'' Int. J. Mech. Sci., **8**, pp. 125–139.
[20] Kleinstreuer, C., and Hyun, S., 1999, *Task III Report: Comparison of Potential Flow Redirection Devices and Summary of Modeling Results*, Research Report for the U.S. EPA. MAE Department, N. C. State Univ., Raleigh, NC.

Hironori Horiguchi[1]
Graduate Student and JSPS Research Fellow,
Osaka University, Graduate School of
Engineering Science,
1-3 Machikaneyama,
Toyonaka, Osaka, 560-8531 Japan
e-mail: horiguti@me.es.osaka-u.ac.jp

Satoshi Watanabe
Lecturer,
Kyushu University, Graduate School of
Engineering,
6-10-1 Hakozaki,
Fukuoka, 812-8581 Japan
e-mail: fmnabe@mech.kyushu-u.ac.jp

Yoshinobu Tsujimoto
Professor,
Osaka University, Graduate School of
Engineering Science,
1-3 Machikaneyama,
Toyonaka, Osaka, 560-8531 Japan
e-mail: tujimoto@me.es.osaka-u.ac.jp

Theoretical Analysis of Cavitation in Inducers With Unequal Blades With Alternate Leading Edge Cutback: Part I—Analytical Methods and the Results for Smaller Amount of Cutback

With the idea of reducing the region of rotating cavitation by cutting back the leading edge of blade alternately and enhancing the stability of alternate blade cavitation, an analysis of steady cavitation and its stability were made for unequal blade cascade. The cavities on longer uncut blades are generally longer but they become shorter in a certain range of inlet cavitation number. This peculiar behavior is explained by an interaction effect of a local flow near cavity closure with the leading edge of the opposing blades. It is also shown that the region with stable cavities can be extended and the onset region of rotating cavitation can be diminished by cutting back the leading edge of blade alternately. In Part II, the effect of the amount of cutback is discussed.
[S0098-2202(00)00402-8]

Introduction

Various kinds of cavitation related instabilities such as rotating cavitation (Kamijo et al. [1] and Tsujimoto et al. [2]), cavitation surge and alternate blade cavitation (de Bernardi et al. [3]) have been important problems for developing reliable turbopump inducers for rocket engines. For a four-bladed inducer, de Bernardi et al. [3]) have shown that the alternate blade cavitation, the rotating cavitation and the asymmetric fixed cavitation occurs successively prior to the head break down. In three-bladed inducers, the alternate blade cavitation does not occur and the rotating cavitation is said to occur at higher inlet pressure than in four-bladed inducers. While the rotating cavitation can cause supersynchronous shaft vibration, the alternate blade cavitation is substantially harmless to rotor vibration because the fluid force on each blade is balanced. This is one of the reasons for which the four-bladed inducer is adopted for ARIANE-5 engine.

In the present study, we examine theoretically whether or not the region of rotating cavitation can be reduced by enhancing alternate blade cavitation by cutting back the leading edge of blade alternately. From this point of view, an analysis of steady cavitation and its stability, and also the analysis of rotating cavitation were made for unequal blade cascades. In Part I, the analytical method is presented and the results are shown for the case of small amount of cutback. The effects of the amount of cutback are discussed in Part II.

Fundamental Flow Fields

We consider a cascade of flat plates with the chord length C_n, the spacing h, and the stagger angle β as shown in Fig. 1. More specifically, we examine a cascade obtained by cutting back the leading edge by Le_n from an equal blade cascade with the solidity C/h. We assume an upstream flow of magnitude U and the angle of attack α. The complex conjugate velocity fluctuation at upstream infinity is denoted by $\tilde{N}e^{i\beta}e^{j\omega t}$, where $\tilde{N}$ is the amplitude of axial velocity fluctuation, i and j denote the imaginary units in space and time, respectively, and $\omega=\omega_R+j\omega_I$ is the complex frequency with its real part ω_R signifying the frequency and the imaginary part ω_I the decay rate. We define the index of blades by taking account of the periodicity of blade row for the inducer with blade number Z_N: the blade located on x-axis is given the index zero, and the index increases in positive direction of y-axis and the index of Z_Nth blade returns to zero. We consider the case of partial cavitation with cavity length l_n on the nth blade. In the present study, the leading edge of blades is cut back alternately by Le and this is the only difference from the analysis of alternate blade cavitation (Horiguchi et al. [4]).

The velocity disturbances due to the blades and cavities are represented by source distributions q_n on the cavity region, vortex distributions γ_{1n} and γ_{2n} on the blade, and trailing vortices γ_{tn} on the wake surface of the blades. The singularities are distributed on the blades and their downstream extension assuming that the flow disturbance is small. Then the complex conjugate velocity can be represented as follows.

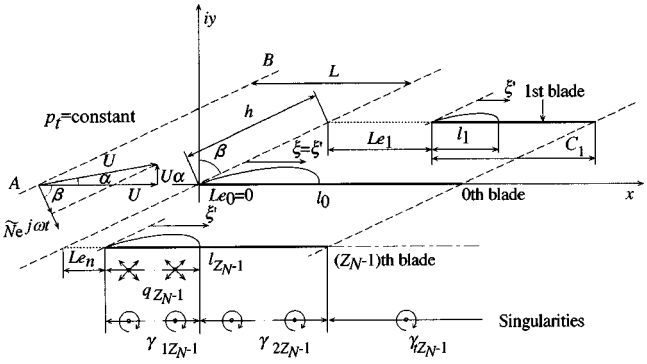

Fig. 1 Cascade with leading edge cutback

[1]Currently Research Associate at Tokushima University, Faculty of Engineering, 2-1 Minamijosanjima, Tokushima 770-8506, Japan.

Contributed by the Fluids Engineering Division for publication in the JOURNAL OF FLUIDS ENGINEERING. Manuscript received by the Fluids Engineering Division June 7, 1999; revised manuscript received February 1, 2000. Associate Technical Editor: J. Katz.

$$w(z,t)=u-i\nu$$
$$=U\mathrm{e}^{-i\alpha}+\tilde{N}\mathrm{e}^{i\beta}\mathrm{e}^{j\omega t}+\frac{1}{2\pi}\sum_{n=0}^{Z_N-1}\left\{\left[\int_0^1[q_n(s_1)+i\gamma_{1n}(s_1)]\times[f_n(z,l_ns_1)-f_n(-L,l_ns_1)]l_nds_1+i\int_1^2\gamma_{2n}(s_2)[f_n\{z,(C_n-l_n)s_2+(2l_n-C_n)\}-f_n\{-L,(C_n-l_n)s_2+(2l_n-C_n)\}](C_n-l_n)ds_2+i\int_{C_n}^{\infty}\gamma_{tn}(\xi)[f_n(z,\xi)-f_n(-L,\xi)]d\xi\right\}\right. \quad (1)$$

$$f_n(z,\xi)=\frac{\pi}{Z_Nh}\mathrm{e}^{-i(\pi/2-\beta)}\times\cot\left\{\frac{\pi}{Z_Nh}(z-\xi-Le_n)\mathrm{e}^{-i(\pi/2-\beta)}-\frac{n}{Z_N}\pi\right\} \quad (2)$$

where the coordinate ξ signifies the distance downstream from the leading edge along the blade. It has been assumed that the magnitude of the singularities is the same on the blades with the same index. Here, the parameters s_1 and s_2 have been introduced to take account of the variable cavity length l_n:

$$\xi=l_ns_1 \quad (0<\xi<l_n,\ 0<s_1<1,\ n=0,1,\ldots,Z_N-1) \quad (3)$$

$$\xi=(C_n-l_n)s_2+(2l_n-C_n) \quad (l_n<\xi<C_n,\ 1<s_2<2,\ n=0,1,\ldots,Z_N-1) \quad (4)$$

All the singularities are specified on these coordinates s_1 and s_2 moving in accord with the variable cavity length l_n. In the present analysis, with large value of L ($L=1000$C in the present calculation), $f(-L,\xi)$ is approximated by $-\pi\mathrm{e}^{i\beta}/h$.

The strength of the singularities and the cavity length are separated into steady and unsteady components:

$$\begin{aligned}q_n(s_1)&=q_{sn}(s_1)+\tilde{q}_n(s_1)\mathrm{e}^{j\omega t}\\ \gamma_{1n}&=\gamma_{1n}(s_1)+\tilde{\gamma}_{1n}(s_1)\mathrm{e}^{j\omega t}\\ \gamma_{2n}&=\gamma_{2n}(s_1)+\tilde{\gamma}_{2n}(s_1)\mathrm{e}^{j\omega t}\\ \gamma_{tn}&=\tilde{\gamma}_{tn}(\xi)\mathrm{e}^{j\omega t}\\ l_n&=l_{sn}+l_n\mathrm{e}^{j\omega t}\\ (n&=0,1,\ldots,Z_N-1)\end{aligned} \quad (5)$$

Substituting the expressions of Eq. (5) into Eq. (3), we divide the velocity into the uniform steady velocity $(U,U\alpha)$, the steady disturbance (u_s,ν_s), and the unsteady disturbance $(\tilde{u},\tilde{\nu})$ as follows.

$$\begin{aligned}u&=U+u_s+\tilde{u}\mathrm{e}^{j\omega t}\\ \nu&=U\alpha+\nu_s+\tilde{\nu}\mathrm{e}^{j\omega t}\end{aligned} \quad (6)$$

Here, it has been assumed that $\alpha\ll1$, $U\gg|u_s|$, $|\nu_s|\gg|\tilde{u}|$, $|\tilde{\nu}|$, and linearizations are made based on these assumptions throughout the present study.

Boundary and Complementary Conditions

Boundary conditions are applied on the coordinates s_1 and s_2 moving in accord with the variable cavity length l_n.

Boundary Condition on Cavity Surface. It is assumed that the pressure on the cavity surface $(z=nh\mathrm{e}^{i(\pi/2-\beta)}+l_ns_1+Le_n+0i,\ 0<s_1<1)$ is constant and equal to the vapor pressure p_ν. By applying the linearized momentum equation on the cavity surface, we obtain

$$\frac{\partial u}{\partial t}+\frac{U}{l_{sn}}\frac{\partial u}{\partial s_1}=-\frac{1}{\rho}\frac{1}{l_{sn}}\frac{\partial p}{\partial s_1}=0 \quad (7)$$

which results in the velocity $(U+u_{cn})$ on the cavity surface with

$$u_{cn}(s_1)=u_{cs}+\tilde{u}_{cn}\mathrm{e}^{-j(\omega l_{sn}/U)s_1}\mathrm{e}^{j\omega t} \quad (8)$$

If we use the expressions of Eqs. (3) and (8), we can express the boundary condition on cavity surface as follows.

$$\mathrm{Real}\ \{w(nh\mathrm{e}^{i(\pi/2-\beta)}+l_ns_1+Le_n+0i)\}=U+u_{cs}+\tilde{u}_{cn}\mathrm{e}^{-j\omega l_{sn}/Us_1}\mathrm{e}^{j\omega t},\ (0<s_1<1) \quad (9)$$

Here, we assume that the 2-D flow around the cascade is connected to a space with constant total (=static) pressure p_t along AB at a distance $L+Le_n$ upstream from the leading edge of blade. From Bernoulli's equation applied between the space and the duct inlet AB, we obtain

$$p_{-Ls}=p_t-\frac{\rho}{2}U^2 \quad (10)$$

$$\tilde{p}_{-L}=-\rho U\tilde{N}\cos\theta \quad (11)$$

where p_{-Ls} and $\tilde{p}_{-L}$ are the steady and unsteady static pressure at $\xi=-L-Le_n$, respectively. By applying the unsteady Bernoulli's equation between the points $z=nh\mathrm{e}^{i(\pi/2-\beta)}-L$ on AB and the leading edge of cavity $(z=nh\mathrm{e}^{i(\pi/2-\beta)}+Le_n)$, we can relate the velocity on the cavity surface with the pressure at $z=nh\mathrm{e}^{i(\pi/2-\beta)}+Le_n$.

$$u_{cs}=\frac{p_{-Ls}-p_\nu}{\rho U}=\frac{\sigma U}{2} \quad (12)$$

$$\frac{\partial[\mathrm{Real}\{W(nh\mathrm{e}^{i(\pi/2-\beta)}-L)-W(nh\mathrm{e}^{i(\pi/2-\beta)}+Le_n)\}]}{\partial t}+U\tilde{u}_{cn}-U\tilde{N}\cos\beta=\frac{\tilde{p}_{-L}}{\rho} \quad (13)$$

where p_ν and $\sigma=2(p_{-Ls}-p_\nu)/\rho U^2$ are the vapor pressure and the cavitation number, respectively. Equations (12) and (13) with (11) give the tangential velocity on the cavity surface to be used in Eq. (9).

Boundary Condition on Wetted Surface. The vertical components of velocity on wetted surface $\{(z=nh\mathrm{e}^{i(\pi/2-\beta)}+l_ns_1+Le_n-0i,\ 0<s_1<1)$ and $(z=nh\mathrm{e}^{i(\pi/2-\beta)}+(C_n-l_n)s_2+(2l_n-C_n)+Le_n\pm0i,\ 1<s_2<2)\}$ should be 0. These conditions can be represented by

$$\mathrm{Imag}[w(nh\mathrm{e}^{i(\pi/2-\beta)}+l_ns_1+Le_n-0i)]=0 \quad (0<s_1<1) \quad (14)$$

$$\mathrm{Imag}[w\{nh\mathrm{e}^{i(\pi/2-\beta)}+(C_n-l_n)s_2+(2l_n-C_n)+Le_n\pm0i\}]=0 \quad (1<s_2<2) \quad (15)$$

Cavity Closure Condition. The cavity thickness η_n should satisfy the following kinematic condition.

$$\frac{\partial\eta_n}{\partial t}+\frac{1}{l_n}\left(U-s_1\frac{dl_n}{dt}\right)\frac{\partial\eta_n}{\partial s_1}=\nu(nh\mathrm{e}^{i(\pi/2-\beta)}+l_ns_1+Le_n+0i)=q_n(s_1) \quad (16)$$

The cavity thickness is separated into steady and unsteady components as follows.

$$\eta_n(s_1)=\eta_{sn}(s_1)+\tilde{\eta}_n(s_1)\mathrm{e}^{j\omega t} \quad (17)$$

Equation (16) is separated into steady and unsteady components after linearization. By integrating these equations, we obtain

$$\eta_n(s_1)=\frac{l_{sn}}{U}\int_0^{s_1} q_n(s_1')ds_1' \tag{18}$$

$$\tilde{\eta}_n(s_1)=\frac{l_{sn}}{U}\int_0^{s_1}\tilde{q}_n(s_1')\mathrm{e}^{-j(\omega l_{sn}/U)(s_1-s_1')}ds_1' + \frac{\tilde{l}_n}{U}\int_0^{s_1}\left(1+j\frac{\omega l_{sn}}{U}s_1'\right)q_{sn}(s_1')\mathrm{e}^{-j(\omega l_{sn}/U)(s_1-s_1')}ds_1' \tag{19}$$

The cavity closure conditions are

$$\eta_{sn}(1)=\tilde{\eta}_n(1)=0 \tag{20}$$

Kutta's Condition. We assume that the pressure difference across the blade is vanishing at the trailing edge. If we apply the momentum equation on the pressure and suction sides of a blade and making subtraction of these equations after linearization, this condition can be expressed as follows.

$$\frac{d}{dt}\left[\int_0^1\gamma_{1n}(s_1)l_n ds_1+\int_1^2\gamma_{2n}(s_2)(C_n-l_n)ds_2\right]+U\gamma_{2n}(2)=0 \tag{21}$$

Equation (23) is equivalent to Kelvin's circulation conservation law signifying that the vortex wake of strength γ_{2n} (2) is shed from the trailing edge on the mean velocity U, correspondingly to the change in blade circulation.

If we assume that the trailing free vorticity $\gamma_{tn}(\xi)$ is transported on the free stream, it can be represented by γ_{2n} (2) as follows.

$$\tilde{\gamma}_{tn}=\tilde{\gamma}_{2n}(2)\mathrm{e}^{-j(\omega l_{sn}/U)(\xi-C_n)/l_{sn}} \tag{22}$$

Downstream Condition. We consider the case when the downstream duct length is infinite. Then the downstream flow rate fluctuation would be suppressed owing to the infinite inertia effect. Then we obtain the following relation.

$$\tilde{N}+\frac{1}{Z_N h}\sum_{n=0}^{Z_N-1}\left\{\int_0^1\tilde{q}_n(s_1)l_n ds_1\right\}=0 \tag{23}$$

Analytical Method

The unknowns are the steady and unsteady parts of singularity distributions $q_n(s_1)$, $\gamma_{1n}(s_1)$, $\gamma_{2n}(s_2)$, the cavity length l_n, the cavity surface velocity u_c, and the magnitude of inlet velocity fluctuation. These are determined from the steady and unsteady parts of Eqs. (8)–(15), (18)–(21) and (23). Here, we introduce the following functions for the steady components of singularities.

$$\begin{aligned} C_{qn}(s_1)&=q_{sn}(s_1)/U\alpha \\ C_{\gamma_{1n}}(s_1)&=\gamma_{1sn}(s_1)/U\alpha \\ C_{\gamma_{2n}}(s_2)&=\gamma_{2sn}(s_2)/U\alpha \end{aligned} \tag{24}$$

We consider the strengths of singularities at discrete points $s_1=S_{1k}$, $s_2=S_{2k}$ as unknowns. The locations of the discrete points S_{1k} and S_{2k} are defined as follows so that they distribute densely near leading and trailing edges of the cavity and the blade,

$$S_{1k}=\frac{1}{2}\left\{1-\cos\left(\frac{k-1}{N_C-1}\pi\right)\right\}\quad(0<S_{1k}<1,\ k=1\sim N_C) \tag{25}$$

$$S_{2k}=1+\frac{1}{2}\left\{1-\cos\left(\frac{k-1}{N_B-1}\pi\right)\right\}\quad(1<S_{2k}<2,\ k=1\sim N_B) \tag{26}$$

where N_C and N_B are the numbers of discrete points in coordinates s_1 and s_2, respectively. The strength of singularities is basically assumed to be linear between these discrete points. However, near the leading and trailing edge of cavity, the singular behavior of linearized cavitating flow obtained by Geurst [5] is taken into account. The strength distributions are assumed to be $q_n(s_1)\sim s_1^{(-1/4)}$ and $\gamma_{1n}(s_1)\sim s_1^{(-1/4)}$ near the leading edge of cavity and blade, $q_n(s_1)\sim(1-s_1)^{(-1/2)}$ and $\gamma_{2n}(s_2)\sim(s_2-1)^{(-1/2)}$ near the trailing edge of cavity. The boundary conditions are applied at the midway between these discrete points.

The values of the functions given by Eq. (24) at $s_1=S_{1k}$ ($k=1\sim N_C$), $s_2=S_{2k}$ ($k=1\sim N_B$) are considered to be unknowns. By evaluating the integrals in Eq. (3) using these values, we can express the boundary conditions and complimentary conditions as follows. For steady component,

$$[A_s(l_{sn})]\begin{Bmatrix} C_{q_n}(S_{11}) \\ \vdots \\ C_{\gamma_{1n}}(S_{11}) \\ \vdots \\ C_{\gamma_{2n}}(S_{21}) \\ \vdots \\ \sigma/2\alpha \end{Bmatrix}=\{B_s\} \tag{27}$$

and for unsteady component,

$$[A_u(l_{sn},\omega)]\begin{Bmatrix} \tilde{q}_n(S_{11}) \\ \vdots \\ \tilde{\gamma}_{1n}(S_{11}) \\ \vdots \\ \tilde{\gamma}_{2n}(S_{21}) \\ \vdots \\ \tilde{u}_{cn} \\ \vdots \\ \alpha l_n \\ \vdots \\ \tilde{N} \end{Bmatrix}=\{0\} \tag{28}$$

where $A_s(l_{sn})$, $A_u(l_{sn},\omega)$ are coefficient matrices, B_s is a constant vector. The steady flow can be determined from Eq. (27), which shows that the steady cavity lengths l_{sn} are functions of $\sigma/2\alpha$. Equation (28) is a set of linear homogeneous equations. For the cases with externally forced disturbances such as inlet pressure or flow rate fluctuations, we would have nonzero vector on the right-hand side representing the forced disturbances. For the present cases without any external disturbances, the determinant of the coefficient matrix $A_u(l_{sn},\omega)$ should satisfy

$$|A_u(l_{sn},\omega)|=0 \tag{29}$$

so that we have nontrivial solutions. This equation gives the complex frequency $\omega=\omega_R+j\omega_I$ as functions of steady cavity length l_{sn}. This indicates that the cavitation number σ and the incidence angle α can affect the stability through the form of $\sigma/2\alpha$.

In the present study, we carry out two kinds of stability analysis, one of which is to determine the statical stability of steady cavitation and the other is an analysis of rotating cavitation. In the statical stability analysis, we examine the stability of the cavitation in inducers with even number of blades with alternate blade leading edge cutback, by putting $Z_N=2$. This assumes that the phase of the disturbance is the same for all longer or shorter blades ($\theta_{0,2}=\theta_{1,3}=0°$). The reason for this assumption will be explained later. The phase difference of the disturbances on longer and shorter blades are set free and determined from the calculation. The duct length L is set to be $1000C$. We define the following normalized complex frequency based on the circumferential wave length $Z_N h$ ($Z_N=2$) of the disturbance.

$$k=k_R+jk_I=\frac{\dfrac{\omega}{2\pi}Z_N h}{U_T}\quad(Z_N=2) \tag{30}$$

where k_R represents the normalized frequency and k_I the normalized decaying rate.

In the analysis of rotating cavitation, we consider only the rotating cavitation mode with 1 cell in four-bladed inducer with equal and unequal length blades. We assume that the upstream velocity fluctuation $\tilde{N}e^{i\beta}e^{j\omega t}$ equals to 0 to have only the circumferentially propagating mode. This assumption is equivalent to the assumption that the inlet duct length L is infinite. We further assume that the phase of disturbance differs by 180 deg on adjacent longer or shorter blades ($\theta_{0,2}=\theta_{1,3}=180$ deg) to simulate the rotating cavitation with 1 cell in four-bladed inducer. The phase difference of the disturbances on the adjacent (longer and shorter) blades is set free and determined from the calculation. In the analysis for the rotating cavitation, we define the following normalized frequency with circumferential wave length $Z_N h$ ($Z_N=4$).

$$k=k_R+jk_I=\frac{\dfrac{\omega}{2\pi}Z_N h}{U_T} \quad (Z_N=4) \tag{31}$$

Here, k_R represents the ratio of propagation velocity of disturbance to the peripheral speed U_T of cascade in a frame moving with the cascade. To judge the direction of the propagation, we use the phase difference $\theta_{0,1}(=\theta_{2,3})$ of cavity length fluctuation on the 1st (3rd) blade (shorter) to the 0th (2nd) blade (longer). When k_R has positive (negative) value, the disturbance propagates in the same (opposite) direction of cascade when $0<\theta_{0,1}<\pi$ and opposite (same) direction when $-\pi<\theta_{0,1}<0$. The propagation velocity ratio k_R^*, the ratio of propagation velocity of disturbance to the moving speed of cascade in a stationary frame, can be determined as follows.

$$\begin{aligned} k_R^*&=1+k_R \quad (0<\theta_{0,1}<\pi) \\ k_R^*&=1-k_R \quad (-\pi<\theta_{0,1}<0) \end{aligned} \tag{32}$$

In the present study, we use k_R given by Eq. (30) in the analysis of statical stability and k_R and k_R^* given by Eqs. (31) and (32) in the analysis of rotating cavitation.

The steady cavity length obtained with $N_C=N_B=37$ agrees with that with $N_C=N_B=100$ to second or third places of decimals. Thus, $N_C=N_B=37$ is considered to be sufficient for the discussions in the present paper.

Results and Discussions

Steady Cavitation. Figure 2 shows the development of steady cavity length in the equal blade cascade ($Le/h=0.0$) with $C/h=2.0$ and $\beta=80$ deg, and in a cascade with alternate blade leading edge cutback with $Le/h=0.2$ on the equal blade cascade. Alternate blade cavitation starts to occur in equal blade cascade when the cavity length develops to $l_s/h=0.65$. The development of cavity in the cascade with $Le/h=0.2$ is closely related to the development of alternate blade cavitation in equal blade cascade. The shape of the cavity corresponding to (a)–(g) in Fig. 2 is shown in Fig. 3.

First, we consider the case with decreasing $\sigma/2\alpha$ from larger value of $\sigma/2\alpha$. When the value of $\sigma/2\alpha$ is sufficiently large (such as (a) and (b) in Fig. 2), the length of the cavity on longer blade is longer than that of the cavity on shorter blade as shown in Figs. 3 (a) and (b). As $\sigma/2\alpha$ decreases, the cavities on both blades develop. When the length of the cavity on shorter blade approaches 65 percent of the distance $L1$ shown in Fig. 2, the cavity on longer blade starts to diminish quickly and the cavity on shorter blade develops quickly ((c) and (d) in Figs. 2 and 3). This behavior, which is also found in experiments, can be explained by the interaction of the flow toward the blade suction surface observed near the cavity closure, with the leading edge of opposing blade. Detailed discussions will be made in Part II including the cases with larger amount of cutback.

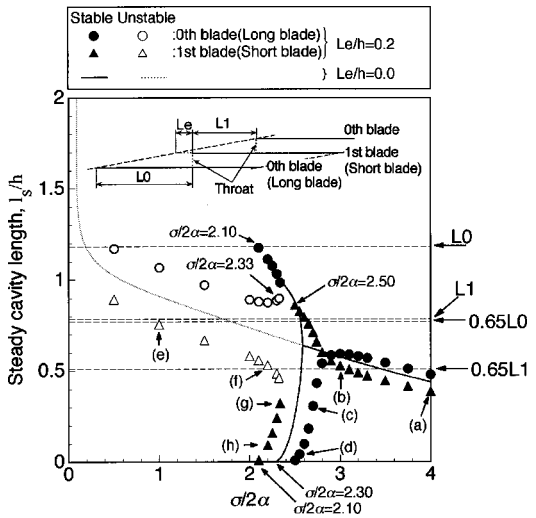

Fig. 2 Steady cavity length and its stability for the cascades with the amount of leading edge cutback, $Le/h=0.0$ and 0.2, from the original cascade with ($C/h=2.0$, $\beta=80$ deg)

Second, we consider the case of increasing $\sigma/2\alpha$ from smaller value of $\sigma/2\alpha$. In the region of sufficiently small $\sigma/2\alpha$ (such as (e) in Fig. 2), the lengths of cavities on longer and shorter blades are both longer than 65 percent of $L0$ and $L1$, respectively (Figs. 3 (e)). As the value of $\sigma/2\alpha$ increases, the lengths of both cavities decrease. When the length of the cavity on shorter blade becomes shorter than 65 percent of $L1$, the cavity rapidly diminishes until the length of the cavity becomes almost 0, whereas the cavity on longer blade develops quickly, as shown in (g) and (h) of Figs. 2 and 3. Here, we should note that, in this region of $\sigma/2\alpha$, two couples of solutions are obtained. The set of solutions with larger cavity length difference is herein called ''alternate blade cavitation'' to distinguish it from other set of solution corresponding to equal length cavitation. For the transition between these two modes, the disturbances on the longer blades and shorter blades should have the same phase, respectively, and the phase difference on longer and shorter blades should be 180 deg. This is the reason for the assumption on the phase for the statical stability analysis of steady solution.

We should note that the curves from larger and smaller values of $\sigma/2\alpha$ are not continuous and there exists a region of $\sigma/2\alpha$ without steady solution. The peculiar behavior of steady cavity

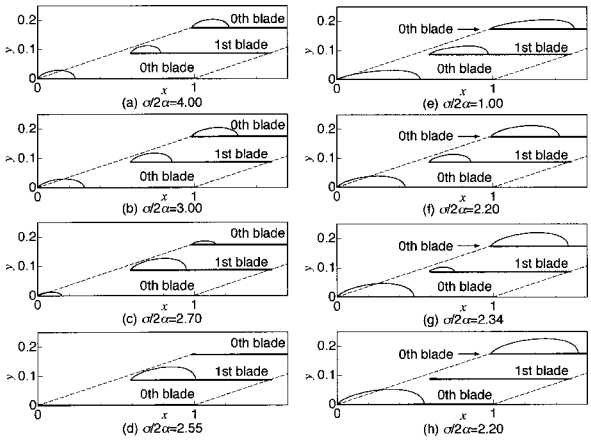

Fig. 3 Steady cavity shape for the cascade with $C/h=2.0$, $\beta=80$ deg and $Le/h=0.2$ for $\alpha=4$ deg (the conditions for each case are shown by (a)–(h) in Fig. 2)

development is found also in experiment. Detailed discussion is made in Part II as to the mechanism of the steady cavity developments including the cases with larger amount of cutback and experiments.

Statical Stability of Steady Solutions. Figures 4 (*a*) and (*b*) show the frequency of amplifying modes and the phase difference $\theta_{0,1}$ of cavity length fluctuation on the 1st (shorter) blade relative to the 0th (longer) blade, respectively, for the steady cavitation shown by the solid lines in the upper figure corresponding to equal length cavitation. Mode I represents the unstable divergence type mode with $k_R=0$, $\theta_{0,1}=180$ deg, indicating that the cavitation will shift to the alternate blade cavitation with exponential time dependence. Mode I appears only in the region of $\sigma/2\alpha \leqq 2.33$. Thus the solutions corresponding to equal length cavitation is statically unstable in the region of $\sigma/2\alpha \leqq 2.33$ and stable in the other region of $\sigma/2\alpha$ (strictly speaking, we need to examine all possible modes to verify the stability. Here, the stability is examined only for the disturbance with the same phase on the blades with odd or even number of index). The phase differences $\theta_{0,1}$ of Modes II–V change largely as shown in Fig. 4 (*b*). Mode II may be called surge because $\theta_{0,1}$ is small. Judging from the frequency, Modes III–V correspond to those of high frequency oscillations, which appeared in equal blade cascade (Horiguchi et al. [3]).

Figures 5 (*a*) and (*b*) show the frequency of amplifying modes and the phase difference $\theta_{0,1}$ of cavity length fluctuation, respectively, for the cavitation corresponding to alternate blade cavitation. No divergence type modes with $k_R=0$ are found. Thus the cavitation corresponding to alternate blade cavitation is considered to be statically stable.

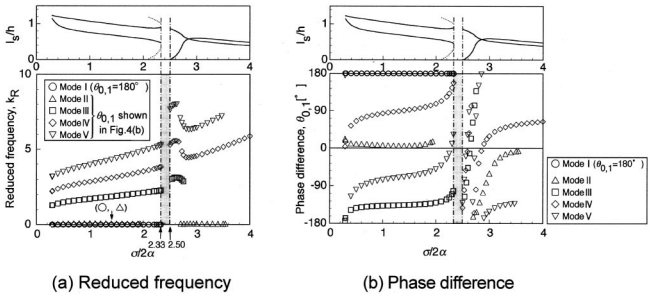

(a) Reduced frequency (b) Phase difference

Fig. 4 Results of statical stability analysis of steady cavitation for the cascade with the alternate leading edge cutting with $Le/h=0.2$. The original cascade is with $C/h=2.0$ and $\beta=80$ deg. It is assumed that $\theta_{0,2}=\theta_{1,3}=0$ deg and unstable modes are plotted for the steady cavitation corresponding to equal length cavitation shown by the solid lines in the upper part of each figure. (*a*) Reduced frequency, (*b*) phase difference.

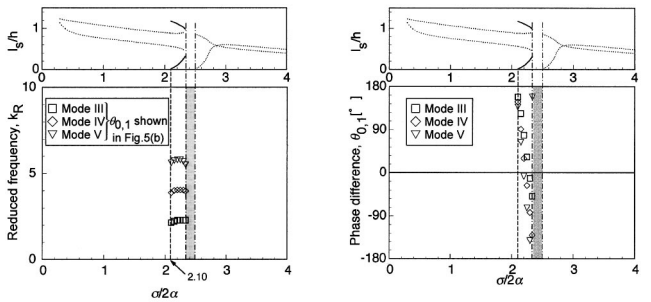

(a) Reduced frequency (b) Phase difference

Fig. 5 The same as Fig. 4, for the steady cavitation corresponding to alternate blade cavitation. (*a*) Reduced frequency, (*b*) phase difference.

Comparison With the Result of the Equal Blade Cascade. Returning to Fig. 2, the lengths of stable and unstable cavities are expressed by solid and dotted lines, respectively, for the cascade with equal length blades. The alternate blade cavitation starts to develop when the length of cavity reaches about 65 percent of the pitch. When the lengths of longer and shorter cavities of alternate blade cavitation approaches h and 0, respectively, the stable alternate blade cavitation disappears (at $\sigma/2\alpha=2.30$) and there exists no stable solution for smaller values of $\sigma/2\alpha$.

In Fig. 2, the lengths of the cavities of stable and unstable cavitations for unequal blade cascade are also shown by ●, ▲ and ○, △, respectively. The minimum values of $\sigma/2\alpha$ for the stable cavitation for this case is 2.10, which is smaller than 2.30 for equal blade cascade. This fact suggests that the stable region can be enlarged by cutting back the leading edge alternately. However, no steady cavitation exists in the region of $2.33<\sigma/2\alpha<2.50$ where we may have some kind of unsteady cavitation.

Rotating Cavitation. Figure 6 shows the result of the analysis for the rotating cavitation in the equal blade cascade. The phase $\theta_{0,1}$ of cavity length fluctuation on the 1st blade relative to that on the 0th blade is obtained to be 90 deg for Modes I–III. Mode I and Mode II represent the forward ($k_R^*>1$) and backward ($k_R^*<1$) rotating cavitation, respectively. Mode III represents higher order forward rotating cavitation. These modes are also found in the analysis by Watanabe et al. [6]. Focusing only on the conventional rotating cavitation, Mode I, the maximum value of $\sigma/2\alpha$ with rotating cavitation is 2.34.

Figure 7 shows the result of rotating cavitation analysis for the alternate blade cavitation in equal blade cascade, in which the longer cavity is assumed to occur on 0th (2nd) blade. Herein, we used normalized frequency k_R instead of the propagation velocity ratio k_R^*, because the phase difference $\theta_{0,1}$ changes largely and it is difficult to determine the propagating direction. Judging from the frequency, the mode obtained here corresponds to Mode III in the equal length cavitation.

Figures 8 (*a*) and (*b*) show the frequency and the phase difference $\theta_{0,1}$ of unstable mode, respectively, for the cavitation corresponding to equal length cavitation. In Fig. 8 (*b*), the frequency is shown in terms of the propagation velocity k_R^*. The value of k_R^* of Mode I is a little larger than unity. Mode I corresponds to the conventional forward rotating cavitation observed in experiments.

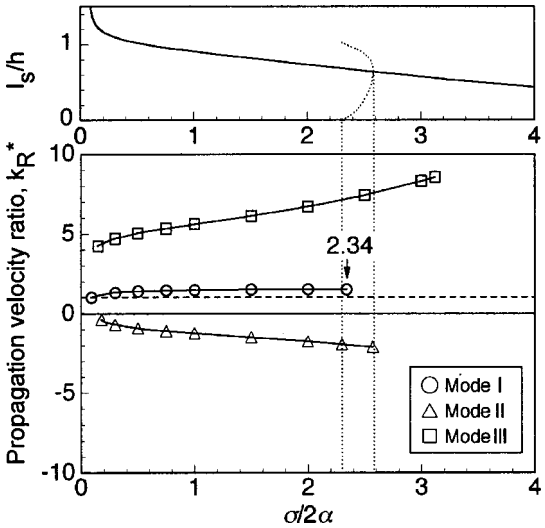

Fig. 6 Results of stability analysis for rotating cavitation for the equal blade cascade with $C/h=2.0$ and $\beta=80$ deg. It is assumed that $\theta_{0,2}=\theta_{1,3}=180$ deg and unstable modes are plotted for the equal length cavitation shown by the solid lines in the upper part of each figure.

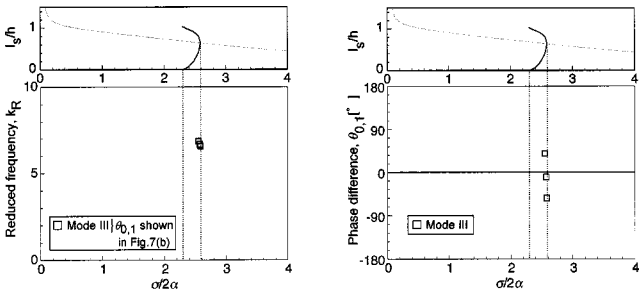

(a) Reduced frequency (b) Phase difference

Fig. 7 The same as Fig. 6, for the alternate blade cavitation. (*a*) Reduced frequency, (*b*) phase difference.

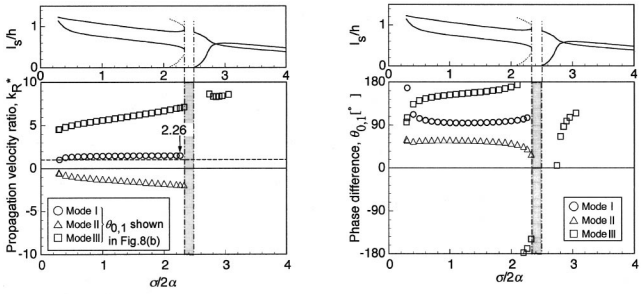

(a) Propagation velocity ratio (b) Phase difference

Fig. 8 Results of stability analysis for rotating cavitation for the cascade with the alternate leading edge cutting with $Le/h=0.2$. The original cascade is with $C/h=2.0$ and $\beta=80$ deg. It is assumed that $\theta_{0,2}=\theta_{1,3}=180$ deg and unstable modes are plotted for the steady cavitation corresponding to equal length cavitation shown by the solid lines in the upper part of each figure. (*a*) Propagation velocity ratio, (*b*) phase difference.

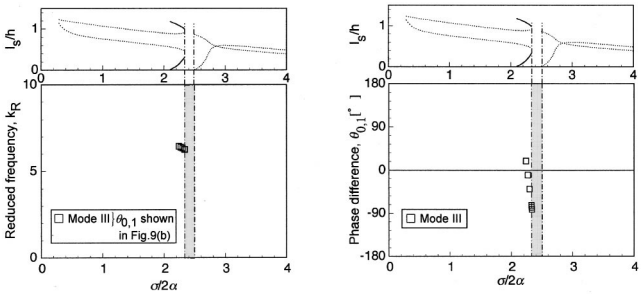

(a) Reduced frequency (b) Phase difference

Fig. 9 The same as Fig. 8, for the steady cavitation corresponding to alternate blade cavitation. (*a*) Reduced frequency, (*b*) phase difference.

Thus the rotating cavitation can also occur in unequal blade cascade. The maximum value of $\sigma/2\alpha$ for rotating cavitation (Mode I) is 2.26, which is a little smaller than the value for the equal blade cascade, $\sigma/2\alpha=2.34$. This indicates that the onset region of rotating cavitation can be reduced by the inequality of blade. Judging from the frequency, Modes II and III correspond to Modes II and III in the equal blade cascade, respectively. The phase differences $\theta_{0,1}$ in Modes II and III are significantly different from 90 deg for the equal blade cascade, showing that the propagation process of those modes are different from that in equal blade cascade. The results for the alternate blade cavitation branch is shown in Fig. 9. The frequency is represented by k_R. Only one mode corresponding to Mode III in Fig. 8 is obtained.

Conclusions

1 Normally the cavities on longer blades are longer than those on shorter blades. However, there exists a region of where longer blades have shorter cavities. This peculiar behavior is related with the development of alternate blade cavitation in equal blade cascade.

2 The alternate cutback of the leading edge can enlarge the region of stable cavitation and suppress the rotating cavitation to some content. However, there appears a region of $\sigma/2\alpha$ where there exists no steady cavitation.

3 Various modes of unstable cavitation occur in the region with smaller values of $\sigma/2\alpha$ than that where the alternate blade cavitation occurs. It suggests that the cavitation is basically unstable in such a region.

Acknowledgment

This study was partly supported by the Grant-in-Aid for Scientific Research from the Ministry of Education, Science, Sports and Culture.

Nomenclature

A_s = coefficient matrix for steady component
A_u = coefficient matrix for unsteady component
B_s = constant vector
C = chord length
$C_q, C_{\gamma 1}, C_{\gamma 2}$ = normalized strengths of steady components of singularities
f = a function used in equation of complex velocity
h = blade pitch
i = imaginary unit in space, $i^2=-1$
j = imaginary unit in time, $j^2=-1$
k = complex propagation velocity ratio in a frame moving with a cascade, $k_R+jk_I=((\omega/2\pi)Z_N h)/U_T$
k_R = propagation velocity ratio in a frame moving with a cascade
k_I = decay ratio
k_R^* = propagation velocity ratio in a stationary frame
L = distance between the leading edge of blade and the space with constant total pressure, 1000C
$L0, L1$ = distance between the leading edges of adjacent blades, see Fig. 2
Le = amount of cutback of leading edge
l = cavity length
N = amplitude of upstream axial velocity fluctuation
N_C, N_B = number of discrete points fixed on coordinate s
n = blade index
p_{-L} = pressure at $\xi=-L-Le_n$
p_t = total pressure
p_v = vapor pressure
q = strength of source
S = location of discrete point on coordinate s
s = a coordinate stretching in accord with variable cavity length
t = time
U = upstream mean velocity
U_T = peripheral velocity (moving speed) of cascade, $U\sin(\alpha+\beta)$
u, v = flow velocity in x- and y-direction
W = complex velocity potential
w = complex conjugate velocity, $u-iv$
Z_N = number of blade

z = complex coordinate, $x+iy$
α = angle of attack
β = stagger
γ = strength of vortex
η = cavity thickness
$\theta_{m,n}$ = phase of disturbances on nth blade relative to mth blade
ξ = distance downstream from the leading edge along blade
ρ = density
σ = cavitation number, $(p_{-Ls}-p_v)/\frac{1}{2}\rho U^2$
ω = complex angular frequency, $\omega_R+j\omega_I$
ω_R = angular frequency
ω_I = decay ratio

Superscript

$\sim$ = unsteady component

Subscript

1,2 = index of cavitating and noncavitating region in terms of coordinate s
c = cavity surface
k = index of discrete point
n = blade index
s = steady component
t = trailing free vortex

References

[1] Kamijo, K., Shimura, T., and Watanabe, M., 1977, ''An Experimental Investigation of Cavitating Inducer Instability,'' ASME Paper 77–Wa/FW–14.

[2] Tsujimoto, Y., Kamijo, K., and Yoshida, Y., 1993, ''A Theoretical Analysis of Rotating Cavitation in Inducers,'' ASME J. Fluids Eng., **115**, No. 1, pp. 135–141.

[3] de Bernardi, J., Joussellin, F., and Von Kaenel, A., 1993, ''Experimental Analysis of Instabilities Related to Cavitation in a Turbopump Inducer,'' Proceedings, 1st International Symposium on Pump Noise and Vibrations, Clamart, France, pp. 1–9.

[4] Horiguchi, H., Watanabe, S., Tsujimoto, Y., and Aoki, M., 2000, ''A Theoretical Analysis of Alternate Blade Cavitation in Inducers,'' ASME J. Fluids Eng., **122**, Mar., pp. 156–163.

[5] Geurst, J. A., 1959, ''Linearized Theory for Partially Cavitated Hydrofoils,'' Int. Shipbuilding Progress, **6**, No. 60, pp. 369–384.

[6] Watanabe, S., Kotaro, S., Tsujimoto, Y., and Kamijo, K., 1998, ''Linear Analysis of Rotating Cavitation by a Singularity Method,'' (in Japanese) Trans. Jpn. Soc. Mech. Eng., Ser. B, **64**, pp. 1675–1682.

Hironori Horiguchi[1]
Graduate Student and JSPS Research Fellow,
Osaka University,
Graduate School of Engineering Science,
1-3 Machikaneyama,
Toyonaka, Osaka, 560-8531 Japan
e-mail: horiguti@me.es.osaka-u.ac.jp

Satoshi Watanabe
Lecturer,
Kyushu University,
Graduate School of Engineering,
6-10-1 Hakozaki,
Fukuoka, 812-8581 Japan
e-mail: fmnabe@mech.kyushu-u.ac.jp

Yoshinobu Tsujimoto
Professor,
Osaka University,
Graduate School of Engineering Science,
1-3 Machikaneyama,
Toyonaka, Osaka, 560-8531 Japan
e-mail: tujimoto@me.es.osaka-u.ac.jp

Theoretical Analysis of Cavitation in Inducers With Unequal Blades With Alternate Leading Edge Cutback: Part II—Effects of the Amount of Cutback

In Part I, it was found that the alternate blade cutback of the leading edge causes a peculiar behavior in the development of steady cavitation. A stability analysis showed that the alternate blade cutback can reduce the onset region of rotating cavitation by enhancing the stability of alternate blade cavitation. In this report, we examine the effects of the amount of cutback. It was found that the development of steady cavity is significantly different depending on the amount of cutback. Those steady cavity developments are explained by the interaction of local flow near the cavity closure with the leading edge of the opposing blade just in the same way as for the development of alternate blade cavitation. It is also shown that the range of cavitation number with stable cavitation can be increased by increasing the amount of cutback. [S0098-2202(00)00502-2]

Introduction

In Part I (Horiguchi et al. [1]), with the idea of reducing the onset region of rotating cavitation by enhancing the stability of alternate blade cavitation by cutting back the leading edge alternately, we carried out steady and stability analyses of cavitation in the cascades with equal and unequal length blades. It was found that, by cutting the blade by 20 percent of spacing from the leading edge alternately, we can increase the stable region of cavitation and diminish the onset region of rotating cavitation in terms of $\sigma/2\alpha$, where σ and α are the cavitation number and the angle of attack respectively.

In the present report, we examine the effects of the amount of leading edge cutback. We carry out the analyses of cavitation in the cascade with the various amount of leading edge cutback in the same way as the first report. The results are shown for the cascade with $Le/h=0.2$, 0.4, 0.6 and 0.8 where Le and h are the amount of cutback and the spacing, respectively. It is shown that the amount of cutback has a substantial effect on the development of steady cavitation. Discussions are made as to the effects of the amount of leading edge cutback on the steady cavitation, its stability and rotating cavitation.

Steady Cavitation

Figure 1 shows the development of steady cavitation in the cascades with various amount of cutback Le/h from the original equal blade cascade with the solidity $C/h=2.0$ and stagger $\beta=80$ deg. The cavity length on longer blades is shown by ○ and ●, and that on shorter blades △ and ▲. Open and closed symbols show statically unstable and stable cavities determined from the stability analysis discussed later. Figure 1 also shows the results for the equal blade cascades with ($C/h=2.0$ and $\beta=80$ deg) and ($C/h=1.0$ and $\beta=80$ deg). The alternate blade cavitation is also shown. Note that the steady cavity development for smaller amount of cutback with $Le/h=0.2$ and 0.4 is closely related with the alternate blade cavitation.

The Cases With Smaller Amount of Cutback ($Le/h=0.2$ and 0.4). The development of steady cavitation can be sorted into two types depending on the amount of cutback. With a smaller amount of cutback, $Le/h=0.2$ and 0.4 shown in Fig. 1(*a*) and (*b*) respectively, there appears a region of $\sigma/2\alpha$ in which the cavity on shorter blade is the longer than that on the longer blade. Such region cannot be found for a larger amount of cutback, $Le/h=0.6$ and 0.8 as shown in (*c*) and (*d*) of Fig. 1.

The peculiar behavior in the steady cavity development can be explained by an interaction of a local flow near the cavity closure with the leading edge of the opposing blade, which also explains the development of alternate blade cavitation (Horiguchi et al. [2]). Figure 2 shows the flow around the cavity in the cascade with ($C/h=2.0$, $\beta=80$ deg). Near the cavity closure point, we find a region in which the velocity vector is inclined toward the blade on which the cavity exists. This region starts to interact with the leading edge of adjacent blade when the cavity length grows to about 65 percent of the blade spacing. In this region, the angle of attack to the adjacent blade is smaller. Under the interaction, the cavity on the adjacent blade becomes smaller with smaller angle of attack to the blade. If the cavity on one blade becomes longer than 0.65 h, the cavity on adjacent blade will become shorter as shown in Fig. 2(*c*). This is the mechanism for the alternate blade cavitation which occurs at $l_s/h_0 \fallingdotseq 0.65$.

The development of steady cavity for $Le/h=0.2$ and $Le/h=0.4$ (Fig. 1(*a*) and (*b*)) is examined with the above interaction effects in mind. The distances $L0$ and $L1$ are defined in the figure and 0.65 $L0$ and 0.65 $L1$ are indicated.

For $\sigma/2\alpha>3.5$, the cavities on shorter/longer blades are shorter than 0.65 $L1$/0.65 $L0$ respectively, showing that they are both not under the interaction with the leading edges of opposing blades. If we reduce the value of $\sigma/2\alpha$, the cavity on the shorter blade starts to interact with the leading edge of the longer blade with its length exceeding 0.65 $L1$. This causes the cavity on the longer blade to get shorter and in turn the cavity on the shorter blade gets longer. For $\sigma/2\alpha<1.5$, the cavities on the shorter/longer blades are longer

[1]Currently Research Associate at Tokushima University, Faculty of Engineering, 2-1 Minamijosanjima, Tokushima 770-8506, Japan.

Contributed by the Fluids Engineering Division for publication in the JOURNAL OF FLUIDS ENGINEERING. Manuscript received by the Fluids Engineering Division June 7, 1999; revised manuscript received February 1, 2000. Associate Technical Editor: J. Katz.

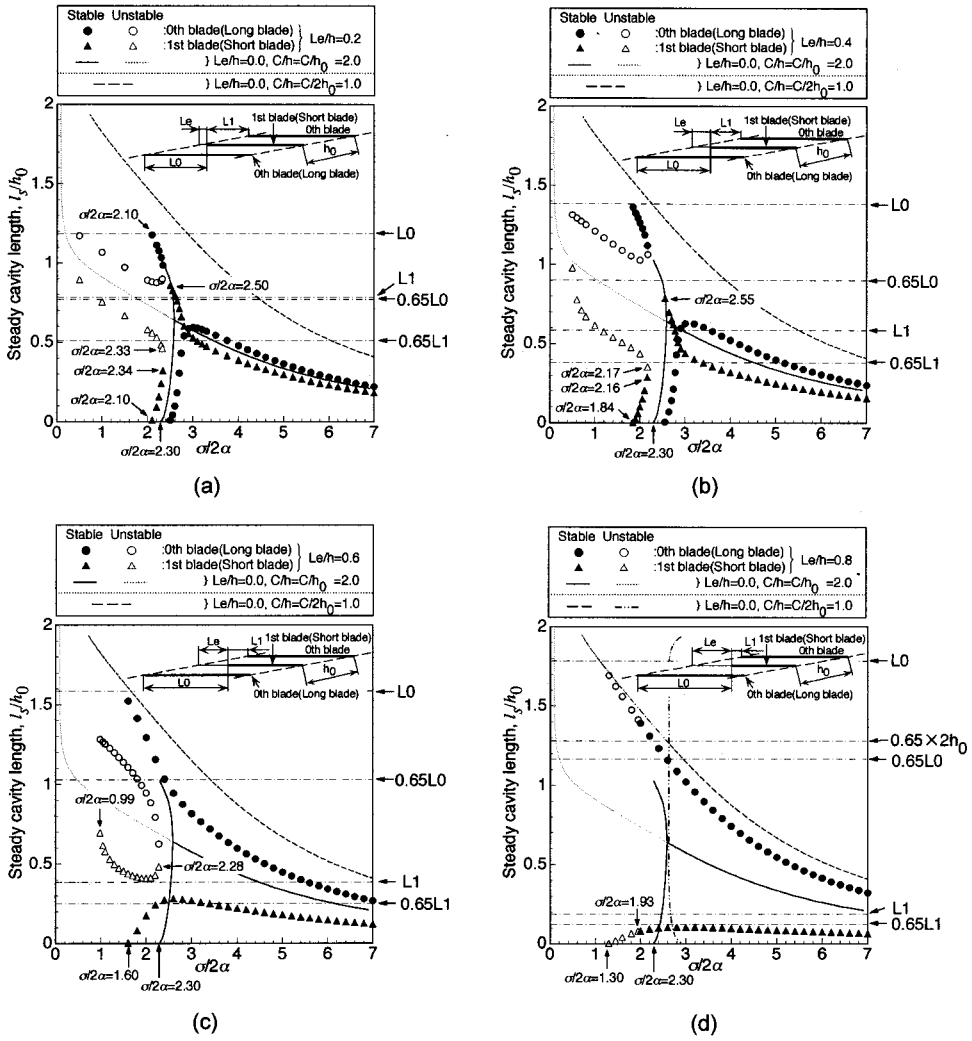

Fig. 1 Steady cavity length and its stability for the cascade with $C/h=2.0$, $\beta=80$ deg, $Le/h=0.2$, 0.4, 0.6 and 0.8. (*a*) $Le/h=0.2$, (*b*) $Le/h=0.4$, (*c*) $Le/h=0.6$, (*d*) $Le/h=0.8$

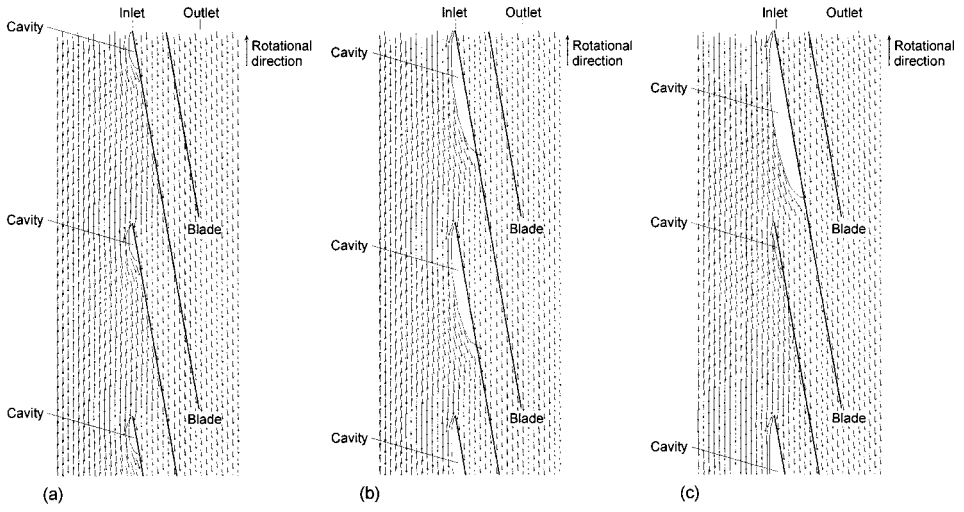

Fig. 2 Steady cavity shape and velocity in a cascade with equal blades, $C/h=2.0$ and $\beta=80$ deg for $\alpha=4$ deg. (*a*) Equal length cavitation ($\sigma/2\alpha=7.0$ $l_s/h=0.202$), (*b*) equal length cavitation ($\sigma/2\alpha=2.58$, $l_s/h=0.640$), (*c*) alternate blade cavitation ($\sigma/2\alpha=2.58$, $l_s/h=0.249$ and 0.882).

than 0.65 $L1$/0.65 $L0$, respectively, showing that they are both under the interaction with the leading edges of the opposing blades. If we increase the value of $\sigma/2\alpha$, the cavity on the shorter blade gets out from the interaction condition with its length becoming smaller than 0.65 $L1$, with the cavity on the longer blade under the interaction. This causes the quick decrease of the cavity length on the shorter blade and in turn the quick increase of that on the longer blade. The cavity length curves curl back and there appears a region of $\sigma/2\alpha$ in which two sets of solution exists. The stability analysis in a later section shows that the set of solution with larger difference of cavity lengths is statically stable.

The above discussion shows, for the cases with smaller amount of cutback, that the cavity length on shorter blades plays an important role in the development of steady cavity. This is because the cavity on the shorter blade gets into/out of the interaction more easily with $L1$ smaller than $L0$.

The Cases With Larger Amount of Cutback (Le/h=0.6 and 0.8). We should note first, as we increase the amount of cutback, Le/h, that the cavity length on the longer blades approaches that in equal blade cascade with halved solidity ($C/h=1.0$) of the original ($C/h=2.0$). The cavity length on shorter blades approaches zero. For $Le/h=0.8$, as we reduce $\sigma/2\alpha$, the cavity length on the longer blade exceeds 0.65 $L0$ while the cavity length on the shorter blade is kept less than 0.65 $L1$. The cavity length on the shorter blade starts to decrease when the cavity length on the longer blade exceeds 0.65 $L0$. For $Le/h=0.6$, general behavior of the cavitation solution extending from larger value of $\sigma/2\alpha$ is the same as for $Le/h=0.8$, except that the cavity length on the shorter blade exceeds 0.65$L1$. Unlike the cases with $Le/h=0.2$ and 0.4, the cavity on the shorter blade with $l_s > 0.65\,L1$ does not cause the shortening of the longer cavity. Probably this is because the shorter blade cavity is too small to affect the longer blade cavity. Shorter blade cavity decreases in its size once the longer blade cavity length exceeds 0.65 $L0$. For $Le/h=0.6$, there exists a solution extending from smaller value of $\sigma/2\alpha$. The shorter blade cavity length is always larger than $L1$ and starts to increase when the longer blade cavity length becomes smaller than 0.65 $L0$. However, this branch of solution is found to be statically unstable in the stability analysis presented in a later section.

The above discussion shows that the cavity development for the cases with larger amount of cutback depends largely on the size of the cavity on longer blades.

Thus, it was shown that all of the strange behavior of steady cavitation development shown in Fig. 1 can be explained by the interaction of local flow near cavity closure with the leading edge of the adjacent blade.

Experimental Results. To confirm the validity of the present analysis, a series of experiments are being carried out at Osaka University by cutting back the leading edges of a four bladed inducer. Details of the experiment will be reported in the paper (Yoshida et al. [3]). Figure 3(*a*) shows the length of cavities at the tip, with the amount of cutback 15 deg corresponding to $Le/h=0.159$ at the tip at $\phi=0.06$ (design flow coefficient=0.078). A hysteresis was observed: the results obtained with decreasing σ are shown. We find a region with shorter cavity on the longer blade, corresponding to (*a*) and (*b*) of Fig. 1. Figure 3(*b*) show the results with the amount of cutback 50 deg, corresponding to $Le/h=0.530$ at the tip, at $\phi=0.06$. The cavity development pattern is quite similar to those in (*c*) and (*d*) in Fig. 1. Although we may need to modify the value ''0.65'' to a larger value for the case of Fig. 3(*a*), the experimental results agree qualitatively with the predictions in Fig. 1.

The performance was not affected by the cutback significantly since both inlet and outlet blade angles were not changed by the cutback.

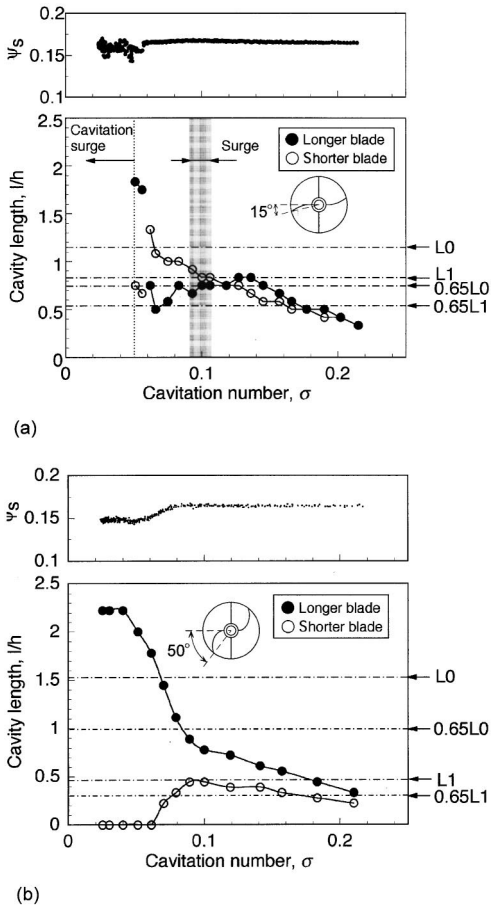

Fig. 3 Experimental cavity length at the tip of inducer at ψ_s =0.165 (ϕ=0.060), with σ decreased. (*a*) The amount of cutback 15 deg at the tip of inducer, corresponding to Le/h =0.159, (*b*) the amount of cutback 50 deg at the tip of inducer, corresponding to Le/h=0.530.

Stability Analyses

Statical Stability of Steady Solutions. The statical stability analysis is made by assuming that the disturbances have the same phase on the groups of blades with larger and smaller chord length. This allows the transition between two modes of steady cavitation shown in Fig. 1(*a*) $2.10<\sigma/2\alpha<2.33$, (*b*) $1.84<\sigma/2\alpha<2.16$ and (*c*) $1.60<\sigma/2\alpha<2.28$, with larger and smaller difference of the cavity lengths on longer and shorter blades. The complex frequency ω is normalized by

$$k=k_R+jk_I=\frac{\dfrac{\omega}{2\pi}Z_N h}{U_T} \quad (Z_N=2) \tag{1}$$

where k_R and k_I are reduced frequency and the damping rate, respectively. Figures 4, 5, and 6 show the reduced frequency k_R and the phase of the disturbance on 1st (shorter) blade relative to that on 0th (longer) blade of amplifying modes with $k_I<0$, for the cases with $Le/h=0.4$, 0.6 and 0.8, respectively (the results for $Le/h=0.2$ are shown in Figs. 4 and 5 of Part I). The steady solution examined is shown by the solid lines in the upper part of each figure. We focus on the divergence mode, Mode I with $k_R=0$. The existence of this mode shows the exponential increase of the disturbance and that the steady solution with this mode is statically unstable. The phase difference $\theta_{0,1}$ between longer and shorter blade is either 0 or 180 deg for Mode I. $\theta_{0,1}=180$ deg shows the disturbance transitioning to another set of steady solu-

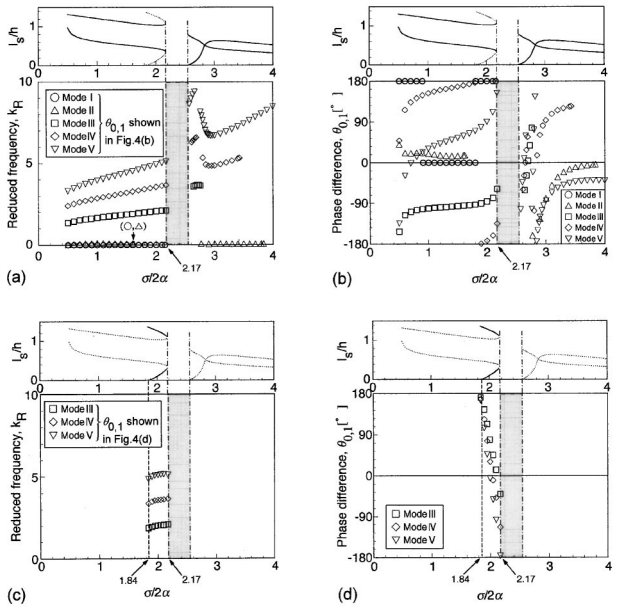

Fig. 4 Results of statical stability analysis of steady cavitation for the cascade with the alternate leading edge cutting with $Le/h=0.4$. The original cascade is with $C/h=2.0$ and $\beta=80$ deg. It is assumed that $\theta_{0,2}=\theta_{1,3}=0$ deg and unstable modes are plotted for the steady cavitation shown by the solid lines in the upper part of each figure. (*a*) Reduced frequency for the steady cavitation corresponding to equal length cavitation, (*b*) phase difference for the steady cavitation corresponding to equal length cavitation, (*c*) reduced frequency for the steady cavitation corresponding to alternate blade cavitation, (*d*) phase difference for the steady cavitation corresponding to alternate blade cavitation.

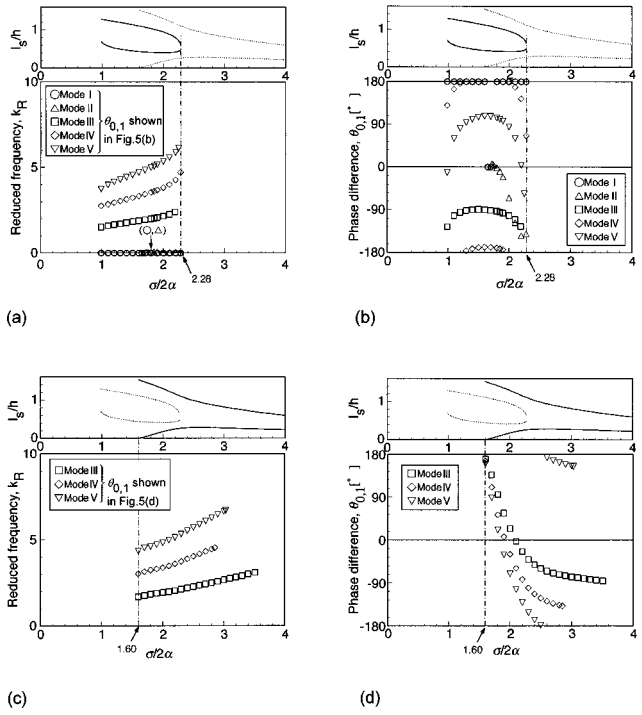

Fig. 5 The same as in Fig. 4, for $Le/h=0.6$. $\theta_{0,2}=\theta_{1,3}=0$ deg. (*a*) Reduced frequency for the steady cavitation with smaller difference in cavity length, (*b*) phase difference for the steady cavitation with smaller difference in cavity length, (*c*) reduced frequency for the steady cavitation with larger difference in cavity length, (*d*) phase difference for the steady cavitation with larger difference in cavity length.

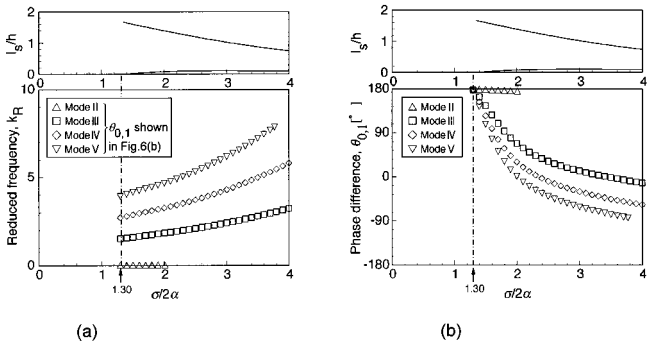

Fig. 6 The same as in Fig. 4, for $Le/h=0.8$. $\theta_{0,2}=\theta_{1,3}=0$ deg. (*a*) Reduced frequency, (*b*) phase difference.

tion. Mode I is not found for the case of $Le/h=0.8$ shown in Fig. 6. However, another type of divergence mode is found in Fig. 9. This will be discussed in the following section.

Various types of oscillating modes are also found. They are numbered Modes II–V. Judging from their frequency, the modes with the same number in Figs. 4–6 and also in Figs. 4 and 5 in Part I correspond with each other.

The statical stability of steady solution based on the existence of the divergence mode is shown in Fig. 1. The minimum value of $\sigma/2\alpha$ with stable solution decreases from 2.10 for $Le/h=0.0$ to 1.60 for $Le/h=0.6$ and then increases to 1.93 for $Le/h=0.8$. This shows that there exists an optimum amount of cutback to maxi-

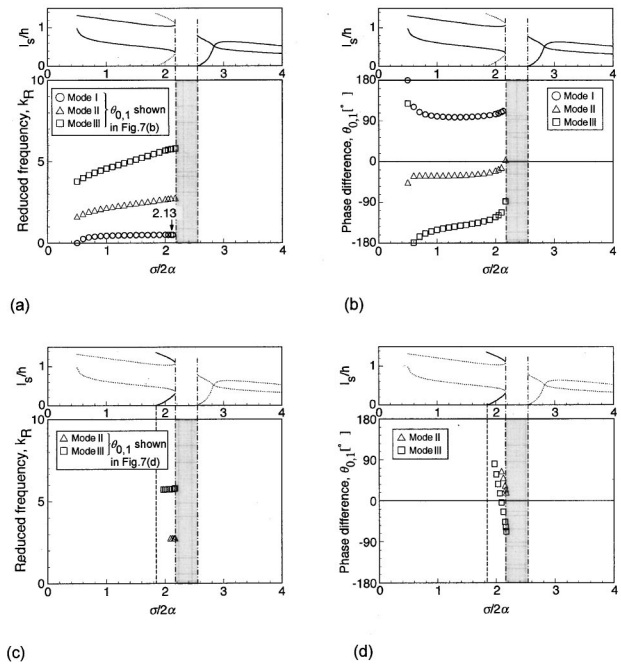

Fig. 7 Results of stability analysis of steady cavitation for the cascade with the alternate leading edge cutting with $Le/h=0.4$. The original cascade is with $C/h=2.0$ and $\beta=80$ deg. It is assumed that $\theta_{0,2}=\theta_{1,3}=180$ deg and unstable modes are plotted for the steady cavitation shown by the solid lines in the upper part of each figure. (*a*) Reduced frequency for the steady cavitation corresponding to equal length cavitation, (*b*) phase difference for the steady cavitation corresponding to equal length cavitation, (*c*) reduced frequency for the steady cavitation corresponding to alternate blade cavitation, (*d*) phase difference for the steady cavitation corresponding to alternate blade cavitation.

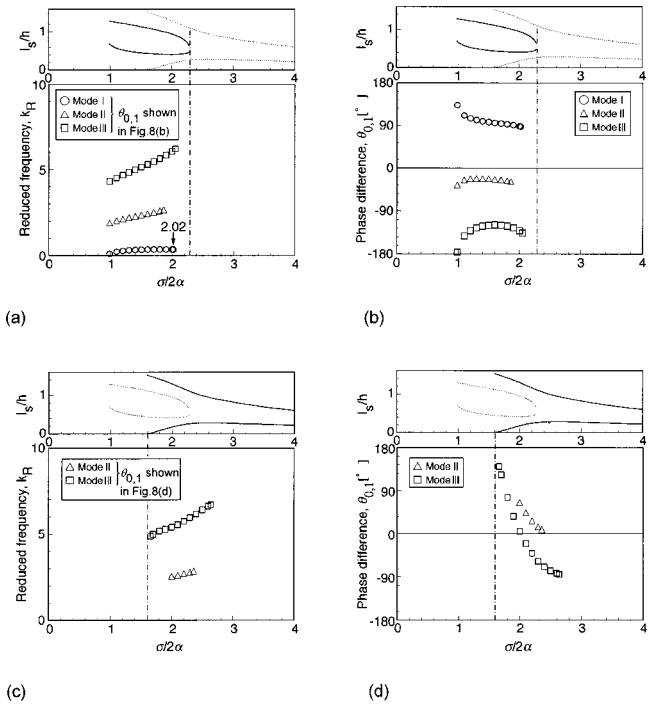

Fig. 8 The same as in Fig. 7, for $Le/h=0.6$. $\theta_{0,2}=\theta_{1,3}=180$ deg. (*a*) Reduced frequency for the steady cavitation with smaller difference in cavity length, (*b*) phase difference for the steady cavitation with smaller difference in cavity length, (*c*) reduced frequency for the steady cavitation with larger difference in cavity length, (*d*) phase difference for the steady cavitation with larger difference in cavity length.

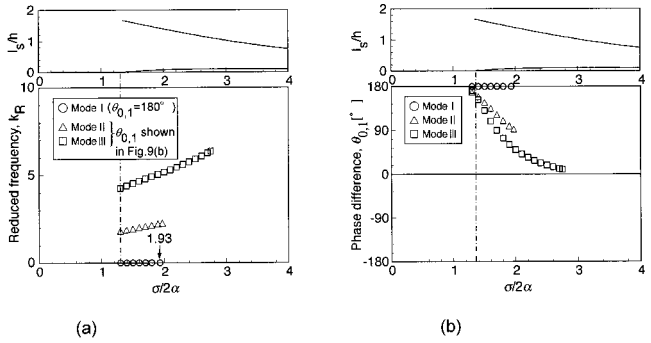

Fig. 9 The same as in Fig. 7, for $Le/h=0.8$. $\theta_{0,2}=\theta_{1,3}=180$ deg (*a*) Reduced frequency, (*b*) phase difference.

mize the stable region. However, we should note that a region of $\sigma/2\alpha$ without steady cavitation appears with intermediate amount of cutback ($Le/h=0.4$).

Rotating Cavitation. The stability analysis for rotating cavitation was made by assuming that the phase of disturbance differs by 180 deg on adjacent longer or shorter blades ($\theta_{0,2}=\theta_{1,3}=180$ deg) to simulate the rotating cavitation with 1 cell in four bladed inducer. The following normalized frequency is used

$$k=k_R+jk_I=\frac{\dfrac{\omega}{2\pi}Z_N h}{U_T} \quad (Z_N=4) \tag{2}$$

where k_R represents the ratio of propagation velocity to the peripheral speed U_T of the cascade in a frame moving with the cascade. The direction of propagation is determined from the value of $\theta_{0,1}$ ($=\theta_{2,3}$) obtained.

The results of rotating cavitation analysis are shown in Figs. 7, 8, and 9 for the cases with $Le/h=0.4$, 0.6 and 0.8, respectively. The results for $Le/h=0.0$ and 0.2 are shown in Figs. 6, 7 and Figs. 8, 9, respectively, of Part I. The frequency is shown as the relative propagation velocity.

Mode I represents conventional forward propagation rotating cavitation since $\theta_{0,1}$ is close to 90 deg, except for the case of $Le/h=0.8$ shown in Fig. 9. The propagation velocity ratio observed in stationary frame is given by $k_R{}^*=1+k_R$. The rotational speed k_R and $k_R{}^*$ of this mode decreases as the increase of Le/h. The maximum value of $\sigma/2\alpha$ with this mode decreases as the increase of Le/h, showing the stabilizing effect of leading edge cutback. For $Le/h=0.8$, the frequency k_R of Mode I is zero showing that the steady cavitation is statically unstable. For this mode, $\theta_{0,1}=\theta_{0,2}=180$ deg and $\theta_{0,3}=0$ deg. This suggests the transition to another type of ''alternate blade cavitation'' in which the cavities on two adjacent blades become longer and the next two shorter, corresponding to the alternate blade cavitation in a cascade with halved solidity of the original.

Judging from the frequency, Modes II and III correspond to backward rotating cavitation and forward rotating cavitation in equal blade cascades. However, the phase difference $\theta_{0,1}$ of these modes is quite different from the values for equal blade cascades, -90 and 90 deg, respectively. For these cases it would be more appropriate to consider that the cavity is ''oscillating'' rather than ''propagating.''

Conclusions

The results of the present study are summarized as follows.

1 The development of steady cavity is quite different depending on the amount of leading edge cutback. For smaller amount of cutting, the cavity on shorter blade plays an important role for the development, while that on longer blade is important for larger amount of cutting. The development is explained by the interaction of the flow near the cavity trailing edge with the leading edge of the opposing blade.

2 The stability of steady cavitation was examined. The minimum value of $\sigma/2\alpha$ with stable cavitation decreases as the increase of the amount of cutting. However, a region of $\sigma/2\alpha$ without steady cavitation solution appears with moderate amount of cutting.

3 The region of conventional rotating cavitation onset and its rotational frequency decreases as the increase of the amount of cutting.

4 With a larger amount of cutting ($Le/h=0.8$), the steady cavity on longer blade approaches that in equal blade cascade with halved solidity. The steady cavity becomes unstable in a mode shifting to an alternate blade cavitation in a cascade with halved solidity.

Acknowledgments

This study was partly supported by the Grant-in-Aid for Scientific Research from the Ministry of Education, Science, Sports and Culture. The experimental work was supported also by SEP, the division de SNECMA. The authors appreciate the arrangements by Dr. P. Geai and Dr. P. Morel.

Nomenclature

C = chord length
h = pitch
h_0 = pitch of the cascade with the solidity 2.0

k = complex propagation velocity ratio in a frame moving with a cascade, $k_R + jk_I = \frac{\frac{\omega}{2\pi} Z_N h}{U_T}$

k_R = propagation velocity ratio in a frame moving with a cascade

k_I = decay ratio

$L0,L1$ = distance between the leading edges of adjacent blades, see Fig. 1

Le = amount of cutback of leading edge

l = cavity length

p_{in} = inlet static pressure

p_{-L} = pressure at $x=-L-Le_n$

p_{out} = outlet static pressure

p_v = vapor pressure

U = upstream mean velocity

U_T = peripheral velocity (moving speed) of cascade, $U\sin(\alpha+\beta)$

Z_N = number of blade

α = angle of attack

β = stagger

$\theta_{m,n}$ = phase of disturbances on nth blade relative to mth blade

σ = cavitation number, $(p_{-Ls}-p_v)/(\frac{1}{2}\rho U^2)$

ω = complex angular frequency, $\omega_R + j\omega_I$

ω_R = angular frequency

ω_I = decay ratio

ψ_s = static pressure coefficient, $(p_{\text{out}}-p_{\text{in}})/(\rho U_T^2)$

Superscript

$\sim$ = unsteady component

Subscript

n = blade index

s = steady component

References

[1] Horiguchi, H., Watanabe, S., Tsujimoto, Y., and Aoki, M., 2000, ''Theoretical Analysis of Cavitation in Inducers with Unequal Blades with Alternate Leading Edge Cutback: Part I—Analytical Methods and the Results for Smaller Amount of Cutback,'' ASME J. Fluids Eng., **122**, June, pp. 412–418.

[2] Horiguchi, H., Watanabe, S., Tsujimoto, Y., and Aoki, M., 1999, ''A Theoretical Analysis of Alternate Blade Cavitation in Inducers,'' ASME J. Fluids Eng., **122**, 156–163.

[3] Yoshida, Y., Tsujimoto, Y., Kataoka, D., Horiguchi, H., and Wahl, F., 2000, ''Effect of Alternate Leading Edge Cutback on Unsteady Cavitation in 4-Bladed Inducers,'' *Proc., ASME 2000 Fluids Engineering Division Summer Meeting*, FEDSM 2000-11034.

Stability Analysis of One-Dimensional Steady Cavitating Nozzle Flows With Bubble Size Distribution

Yi-Chun Wang
Assistant Professor,
Department of Mechanical Engineering,
National Cheng Kung University,
Tainan 701, Taiwan

A continuum bubbly mixture model coupled to the Rayleigh-Plesset equation for the bubble dynamics is employed to study one-dimensional steady bubbly cavitating flows through a converging-diverging nozzle. A distribution of nuclei sizes is specified upstream of the nozzle, and the upstream cavitation number and nozzle contraction are chosen so that cavitation occurs in the flow. The computational results show very strong interactions between cavitating bubbles and the flow. The bubble size distribution may have significant effects on the flow; it is shown that it reduces the level of fluctuations and therefore reduces the ''cavitation loss'' compared to a monodisperse distribution. Another interesting interaction effect is that flashing instability occurs as the flow reaches a critical state downstream of the nozzle. A stability analysis is proposed to predict the critical flow variables. Excellent agreement is obtained between the analytical and numerical results for flows of both equal bubble size and multiple bubble sizes. [S0098-2202(00)00702-1]

Introduction

As cavitation occurs in a bubbly flow, the growth and violent collapse of bubbles may affect the flow field in a significant way. The extent of influence increases with the increase in the density of cavitation events. Consequently, a whole new set of phenomena may be manifest due to the strong interactions between cavitating bubbles and the flow. A recent example of this interaction is demonstrated in the work of Wang and Brennen [1]. They used a continuum bubbly mixture model coupled to the Rayleigh-Plesset equation in order to connect the local fluid pressure with the local bubble size. They investigated the quasi one-dimensional steady flows through a converging-diverging nozzle. Their results show that nonlinear bubble dynamics strongly affect the mean flow even for very small bubble populations. The phenomenon of flashing instability was demonstrated in their solutions; the flow became quasi-statically unstable and flashed to vapor if the radius of the cavitating bubble was greater than a critical value, R_c. Using a simple equilibrium analysis in a straight duct, Wang and Brennen showed that $R_c \approx R_s(\sigma/2\alpha_s)^{1/3}$, where σ is the cavitation number, α_s is the upstream void fraction, and R_s is the radius of upstream nuclei which were assumed monodisperse. The above expression for R_c resulted in over-estimates of 5 percent and 14 percent in the critical fluid velocity and in the critical void fraction, respectively, compared with their numerical solutions.

In this paper, we begin by performing a numerical computation to investigate the effect of an upstream nuclei distribution on steady cavitating nozzle flows. It is well acknowledged that the size distribution of the freestream microbubbles can significantly affect cavitation (see, for example, Ceccio and Brennen [2], Tanger et al. [3], Gindroz et al. [4]). One of the purposes of the present work is to determine the effect of bubble size distribution on the mean flow. The bubbly flow model employed here is the same as Wang and Brennen [1] except for the inclusion of effects of multiple bubble sizes. For steady flows, the system of field equations is in the form of an initial value problem. The presence of bubbles of multiple sizes results in a large number of coupled ordinary differential equations. Theoretically, if the nuclei have a continuous size spectrum, an infinite dimensional system is formed. In the present work we only consider a finite number of bubble sizes. Results obtained show that steady-state flow solutions can only exist for very small bubble populations. For a fixed cavitation number and degree of decompression, the flow flashes to vapor as the upstream void fraction is increased beyond a specific value. This is similar to the previous results of Wang and Brennen [1] except that the domain of upstream void fraction for which steady-state solution exists is about three times larger than for the case of monodisperse bubbles.

In order to predict the critical values of flow variables at which the flashing instability occurs, a method of stability analysis is proposed. Excellent agreement is obtained between the analytical and the numerical results for flows of both equal bubble size and multiple bubble sizes.

Model Equations for Steady Nozzle Flows With Nuclei Size Distribution

Referring to Fig. 1, a bubbly mixture, composed of an incompressible liquid and a large number of dispersed microbubbles, flows through a converging-diverging nozzle of length L and cross section A. The flow direction is in the positive x direction and the inlet of the nozzle is located at $x=0$. The flow is treated as quasi one-dimensional, that is, the local size distribution of the upstream nuclei is assumed to be uniform over the cross section of the duct and the cross-sectional area of the nozzle is sufficiently gradual. Boundary layer effects and possible separation downstream of the contraction are not considered. However, viscous and other energy dissipation effects are included in the bubble dynamics. A consideration of the boundary layer would, for example, be needed in order to compute the drag on the nozzle, but we are primarily interested here in the interaction of bubbles with the primary core of inviscid flow. We also note that under certain circumstances separation could be expected to occur in the diverging part of the nozzle; we assume here a perfect recovery (aside from dissipation associated with the bubble dynamics). Practically, the present cross-sectional area of the nozzle, $A(x)$, can be viewed as an effective area of the inviscid core.

The upstream nuclei size distribution is represented by a number density distribution function, $\chi(R_s)$. Therefore, the number of

Contributed by the Fluids Engineering Division for publication in the JOURNAL OF FLUIDS ENGINEERING. Manuscript received by the Fluids Engineering Division April 12, 1999; revised manuscript received December 20, 1999. Associate Technical Editor: J. K. Eaton.

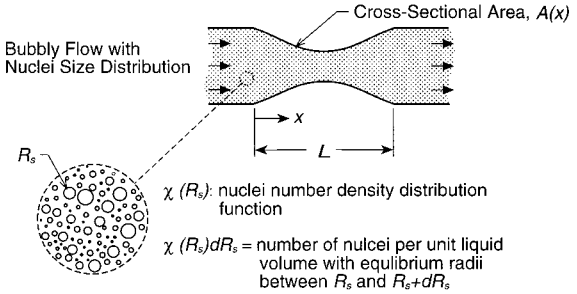

Fig. 1 Notation for bubbly liquid flow in a converging-diverging nozzle

bubbles per unit liquid volume with equilibrium size between R_s and R_s+dR_s is $\chi(R_s)dR_s$ and the local gas void fraction is given by

$$\alpha(x)=\frac{\int_{R_{s\,\mathrm{MIN}}}^{R_{s\,\mathrm{MAX}}}\tau(x;R_s)\chi(R_s)dR_s}{1+\int_{R_{s\,\mathrm{MIN}}}^{R_{s\,\mathrm{MAX}}}\tau(x;R_s)\chi(R_s)dR_s} \tag{1}$$

where $R_{s\,\mathrm{MIN}}$ and $R_{s\,\mathrm{MAX}}$ are the minimum and maximum radii of upstream nuclei and $\tau(x;R_s)$ is the volume of the individual bubble with upstream equilibrium radius of R_s. Several researchers have measured the number density distribution functions of freestream nuclei in different water tunnels (see, for example, Peterson et al. [5], Gates and Bacon [6], Katz [7] and in the ocean (O'Hern et al. [8]). The sizes of nuclei typically range from 10 μm to 200 μm with a distribution approximately fit by

$$\chi(R_s)=N/R_s^4 \tag{2}$$

The value of N is related to the degree of air content and can be obtained here by matching the prescribed value of the upstream void fraction, α_s, by substituting (2) into (1):

$$N=\frac{3\alpha_s}{4\pi(1-\alpha_s)\ln(R_{s\,\mathrm{MAX}}/R_{s\,\mathrm{MIN}})} \tag{3}$$

The equations of motion for analyzing the dispersed bubbly flow shown in Fig. 1 are based on van Wijngaarden's continuum bubbly mixture model (van Wijngaarden [9], see also, Biesheuvel and van Wijngaarden [10]). The principal assumptions of the model and their justification are briefly described here; the original references should be consulted for more detailed discussion of the derivation.

The bubbles are assumed to be spherical and have dimensions much smaller than the characteristic length of the fluid motion. Furthermore, bubbles do not break up under the influence of a viscous drag or a pressure gradient. In the present problem, these assumptions are justified as long as the size parameter R/L is small, the translational motion of bubbles relative to the liquid can be neglected, and surface tension is sufficiently large to keep the bubbles approximately spherical. For a bubbly flow in a converging-diverging nozzle, the relative velocity between phases increases along the converging section and subsequently decreases, as shown by the experiments of Muir and Eichhorn [11]. van Wijngaarden [9] explained this phenomenon by the behavior of Kelvin impulse. Qualitative estimation of the magnitude of the relative motion can be made using R/L (see Brennen [12], Section 5.11, for details). In the present simulation, the maximum value of the size parameter in the converging section of the nozzle is less than 0.1. Consequently, the relative motion is in a quasi-static regime and is negligible. Physically, this corresponds to a situation that the available time for a bubble to adjust its velocity in an accelerating flow is much larger than the typical time required for it to reach its terminal velocity.

Another major assumption of the bubbly mixture model is that the volume concentration of the bubbles is low. This assumption enables one to include the effects of bubble volume change on the flow using a bubble dynamic model, such as the Rayleigh-Plesset equation (see, for example, Biesheuvel and van Wijngaarden [10], Zhang and Prosperetti [13], for a mathematically rigorous derivation). The condition of low void fraction is also related to the assumptions that the bubbles retain their spherical shape and do not coalesce. Ishii and Mishima [14] showed that, for void fraction greater than 0.3, spherical bubbles must distort, agglomeration begins to occur after bubbles begin to touch and, finally, bubble fusion leads to a transition of the bubbly flow to a bubbly-slug regime. Results of the present computation show that this limit of void fraction is still met as the flow downstream of the nozzle becomes neutrally unstable.

These assumptions lead to the continuity and momentum equations of the one-dimensional steady bubbly duct flow with a constant mass flow rate:

$$(1-\alpha)uA=(1-\alpha_s)=\text{constant} \tag{4}$$

$$u\frac{du}{dx}=-\frac{1}{2(1-\alpha)}\frac{dC_P}{dx} \tag{5}$$

For convenience, we have defined the normalized cross-sectional area of the nozzle as $A(x)=A^*/A_s^*$. All quantities with superscript * represent dimensional values and the subscript s denotes the upstream quantities. All other variables are nondimensionalized by the minimum upstream bubble radius, $R_{s\,\mathrm{MIN}}^*$, the upstream flow velocity, u_s^*, and the liquid density, ρ_L^*. The local void fraction, $\alpha(x)$, is related to the local bubble radius, $R(x)$, by Eq. (1), $u(x)$ is the fluid velocity, $C_P(x)=(p^*(x)-p_s^*)/1/2\rho_L^*u_s^{*2}$ is the fluid pressure coefficient, $p^*(x)$ is the fluid pressure and p_s^* is the upstream pressure. Note that the nondimensional mixture density has been approximated by $\rho\approx(1-\alpha)$ in (4) and (5) since the liquid density is very much larger than the vapor density. Finally, the Rayleigh-Plesset equation Plesset and Prosperetti [15]) relates the local fluid pressure coefficient, $C_P(x)$, and the local bubble radius, $R(x;R_s)$:

$$R\left(u^2\frac{d^2R}{dx^2}+u\frac{du}{dx}\frac{dR}{dx}\right)+\frac{3u^2}{2}\left(\frac{dR}{dx}\right)^2+\frac{4}{\mathrm{Re}}\frac{u}{R}\frac{dR}{dx}+\frac{2}{\mathrm{We}\,R_s}\left[\frac{R_s}{R}-\left(\frac{R_s}{R}\right)^{3k}\right]+\frac{\sigma}{2}\left[1-\left(\frac{R_s}{R}\right)^{3k}\right]+\frac{1}{2}C_P=0 \tag{6}$$

where $\mathrm{We}=\rho_L^*u_s^{*2}R_{s\,\mathrm{MIN}}^*/S^*$ is the Weber number, S^* is the surface tension, $\sigma=(p_s^*-p_V^*)/1/2\rho_L^*u_s^{*2}$ is the cavitation number and p_V^* is the partial pressure of vapor inside the bubble. The partial pressure of noncondensable gas does not appear explicitly in (6) because the upstream equilibrium condition has been employed to eliminate this quantity. Equation (6) neglects the mass transfer between phases and assumes that the noncondensable gas inside the bubbles behaves polytropically with an index k ($k=1$ for constant bubble temperature and $k=\gamma$, the ratio of specific heats of the gas, for adiabatic bubbles). Note that the term containing the Reynolds number, $\mathrm{Re}=\rho_L^*u_s^*R_{s\,\mathrm{MIN}}^*/\mu_E^*$, accounts for dissipation effects caused by relative radial motion between the bubbles and the fluid. Here we have used an effective viscosity, μ_E^* (a function of equilibrium bubble radius, R_s), to incorporate the various bubble-damping mechanisms, namely acoustic, thermal, and viscous damping, described by Chapman and Plesset [16]. This assumption appears to be valid in the limit of low frequency bubble oscillations, where the combined effect of the

various damping mechanisms is to decrease the number and magnitude of rebounds after an initial collapse (Colonius et al. [17]). In the present steady flow, low frequency corresponds to a gradual throat contraction compared to a characteristic wavelength of the bubble oscillations.

Equations (4), (5) and (6) represent a coupled system which incorporates the interactive effects that the cavitating bubbles have on themselves and on the pressure and velocity of the fluid flow. Specifically, response (volumetric change) of the bubbles to the pressure in the surrounding liquid (as represented by (6)) results in a global accelerating velocity field (through (4)). Associated with this velocity field is a pressure gradient (Eq. (5)), which in turn determines the pressure encountered by each individual bubble in the mixture. Equation (6) neglects the local pressure perturbations experienced by one bubble due to the growth or collapse of a neighbor. d'Agostino and Brennen [18] showed that such local effects can usually be neglected compared to the global effects of bubble/flow interactions.

It must be emphasized that Eq. (6) is actually a system of ordinary differential equations in which $R(x;R_s)$ is the radius of bubbles with equilibrium size, R_s, and $R_s \in [R_{s\,\mathrm{MIN}}, R_{s\,\mathrm{MAX}}]$. Therefore, if the liquid contains a continuous spectrum of nuclei size distribution, the above governing equations form an infinite dimensional system. Numerically we can only deal with finite number of sizes. In the present computation, $n=100$ intervals are used to discretize the range of $[R_{s\,\mathrm{MIN}}, R_{s\,\mathrm{MAX}}]$. (Parenthetically it is found that the numerical solutions for a larger n (say, $n=200$) are very close to the present results, which suggests convergence to the continuous case if n is large enough.)

The cross-sectional area of nozzle, $A(x)$, is given by

$$A(x)=\begin{cases}\left\{1-\frac{1}{2}C_{P\,\mathrm{MIN}}\left[1-\cos\left(\frac{2\pi x}{L}\right)\right]\right\}^{-1/2}; & 0\leqslant x\leqslant L\\ 1; \quad x<0 \text{ and } x>L\end{cases} \tag{7}$$

which was used by Wang and Brennen [1] and will produce a simple sinusoidal decompression in the case of pure liquid flow with the minimum pressure coefficient, $C_{P\,\mathrm{MIN}}$, located at the nozzle throat.

In the present model the only energy dissipation is from bubble-damping. Multiplying Eq. (6) by $8\pi u R^2 dR/dx$ and integrating over the nuclei size spectrum, one can obtain the energy equation of the flow:

$$\frac{de}{dx}=-32\pi u\int_{R_{s\,\mathrm{MIN}}}^{R_{s\,\mathrm{MAX}}}\frac{R}{\mathrm{Re}}\left(\frac{dR}{dx}\right)^2\chi\,dR_s \tag{8}$$

in which

$$e=u^2+\frac{C_P}{\rho}+4\pi\int_{R_{s\,\mathrm{MIN}}}^{R_{s\,\mathrm{MAX}}}\left\{R^3\left(u\frac{dR}{dx}\right)^2+\frac{\sigma R^3}{3}\left[1+\frac{1}{k-1}\left(\frac{R_s}{R}\right)^{3k}\right]+\frac{2R^2}{\mathrm{We}}\left[1+\frac{2}{3(k-1)}\left(\frac{R_s}{R}\right)^{3k-1}\right]\right\}\chi\,dR_s \tag{9}$$

is the normalized energy density of the fluid. It is clear that e decreases along the flow direction due to effects of bubble-damping.

Numerical Results

Equations (1)–(9) are integrated using a fourth-order Runge-Kutta scheme with adaptive stepsize control. The stepsize is set as one initially and is automatically adjusted over the integration progress to ensure the maximum fractional change of bubble radius in the flow not exceeding 5 percent in each step. This is essential for marching through a violent bubble collapse. The minimum bubble radius at the final stage of collapse can be several orders of magnitude smaller than the equilibrium radius, but, is prevented from reaching zero due to the gas content in the bubbles.

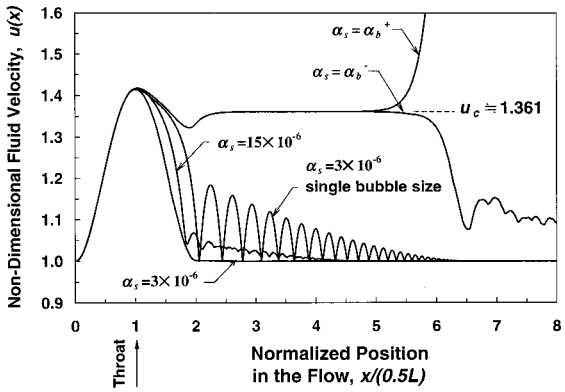

Fig. 2 The fluid velocity distribution as a function of the normalized position in the flow for four different upstream void fractions. Equilibrium sizes of the upstream nuclei are in the range of $[R^*_{s\,\mathrm{MIN}}, R^*_{s\,\mathrm{MAX}}]=[10,200]\ \mu$m and $R^*_s=10\ \mu$m for the case of single bubble size. Labels of $\alpha_s=\alpha_b^-$ and $\alpha_s=\alpha_b^+$ correspond to α_s just below and above the value of $\alpha_b \approx 17.86\times10^{-6}$. The various parameters are $L=900$, $\sigma=0.85$, $C_{P\,\mathrm{MIN}}=-1.0$. The critical fluid velocity which activates the flashing instability is labeled as u_c.

The following upstream flow conditions are chosen for illustration: a fluid, composed water at 20°C ($\rho^*_L=1000\,\mathrm{kg/m^3}$, $S^*=0.073\,\mathrm{N/m}$) and air bubbles ($k=1.4$) of equilibrium radii between 10 and 200 μm, flows with $u^*_s=10\,\mathrm{m/s}$ through a nozzle with profile given by Eq. (7); the nondimensional length of the nozzle is $L=900$. The minimum pressure coefficient, $C_{P\,\mathrm{MIN}}$, for the pure liquid flow is chosen as -1. The upstream cavitation number, σ, is set at 0.85, smaller than $-C_{P\,\mathrm{MIN}}$ so that cavitation will occur in the flow. Values of the effective liquid viscosity, μ^*_E, for bubbles with different equilibrium sizes were obtained using the data taken from Chapman and Plesset [16] to incorporate the various bubble-damping mechanisms. As a result, the Reynolds number in the system of the Rayleigh-Plesset equations ranges between 2.2 and 16.6. The Weber number has the value of 13.84. Four different upstream void fractions, α_s, are used in the computation and the results are shown in Figs. 2–5. Results of single bubble size ($R^*_s=10\ \mu$m) are also included for comparison.

As explored by Wang and Brennen [1], stable solutions can only exist for a limited range of the upstream void fraction, α_s. As α_s increases to a specific value, α_b, the flow downstream of the nozzle reaches a critical state (represented by a subscript c) and flashing instability occurs. The flow quickly flashes to vapor

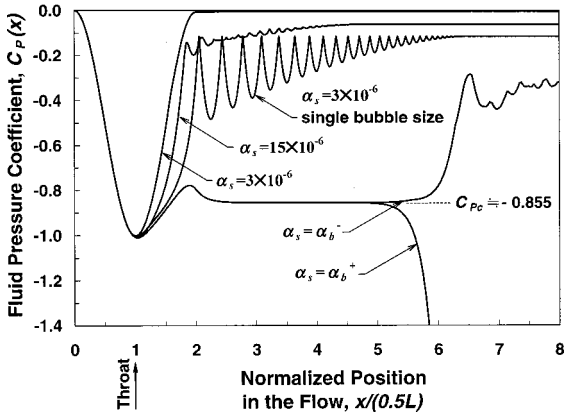

Fig. 3 The fluid pressure coefficient corresponding to Fig. 2

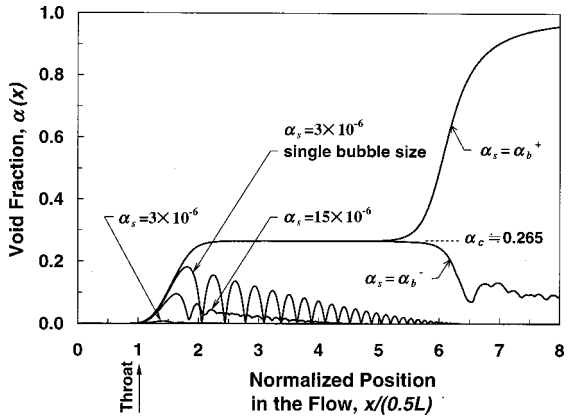

Fig. 4 The void fraction distribution corresponding to Fig. 2

due to the Bernoulli effect. In this circumstance, the growth of bubbles increases the fluid velocity through mass conservation of the flow. The velocity increase then causes the pressure to decrease according to momentum equation. The decrease of the pressure is fed back to the Rayleigh-Plesset equation and results in further bubble growth. It should be noted that, mathematically, this implies no steady-state flow solution exists since the present flow model is only valid for small void fractions. Unsteady calculations must be exercised for further investigation.

It is clear that the downstream fluctuation, which has a very large amplitude for the case of single bubble size, is greatly reduced by the size distribution effects. Unlike monodisperse bubbles, bubbles of different sizes have different downstream oscillating periods. (This periodicity is the ''ringing'' phenomenon described by Wang and Brennen, [1].) In other words, they do not oscillate in phase. These out-of-phase oscillations significantly suppress the global fluctuation in the flow. This multiple size effect has two important consequences: (1) much larger upstream void fraction is allowed before flashing occurs. (In the present computation $\alpha_b \approx 17.86\times10^{-6}$ is about three times larger than that of single bubble size.) (2) the fluid pressure (as shown in Fig. 3) returns to a larger value downstream and therefore represents a smaller ''cavitation loss.'' The second consequence is more clear by integrating Eq. (8) to obtain the distribution of fluid energy density along the flow, as shown in Fig. 5. The stepwise cavitation loss in each collapse and rebound of bubbles can be seen very clearly in the case of single bubble size.

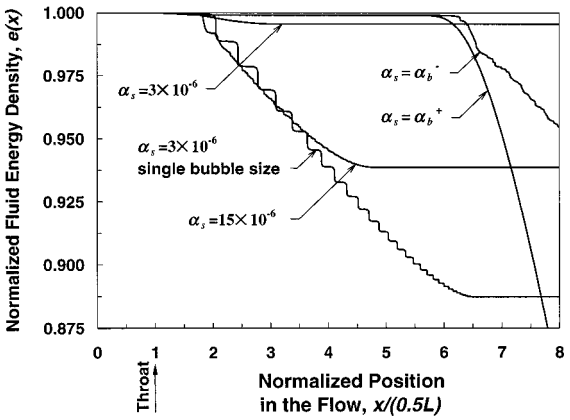

Fig. 5 The fluid energy density distribution corresponding to Fig. 2

Stability Analysis

In this section, an analytical model is proposed to predict the critical state of flow at which flashing instability occurs. Consider now a bubbly flow with single size of nuclei. Substituting Eq. (4) into (5) and integrating along x we obtain

$$C_P(x) = -2(1-\alpha_s)\left[\frac{f(x)}{A^2(x)} - 1 + \int_0^x \frac{A'(x)}{A^3(x)} f(x)dx\right] \quad (10)$$

where $A' = dA/dx$ and $f(x) = (1-\alpha_s)/(1-\alpha(x))$ is the reciprocal of the normalized mixture density. The local bubble void fraction, $\alpha(x)$, is related to the bubble radius, $R(x)$, by

$$(1-\alpha)^{-1} = 1 + \alpha_s R^3/(1-\alpha_s) \quad (11)$$

Now let $x = x_c$ be a position at which the the flow is in a neutrally unstable state. As shown in Wang and Brennen [1], x_c is located downstream of the nozzle (theoretically, $x_c \to \infty$) and all derivatives of R vanish at x_c. Substituting Eq. (10) into the Rayleigh-Plesset equation and doing simple algebra, we obtain an equation for the critical bubble radius, R_c, corresponding to $x = x_c$:

$$\frac{2}{\mathrm{We}}(R_c^{-1} - R_c^{-3k}) + \frac{\sigma}{2}(1 - R_c^{-3k}) - \alpha_s(1-\alpha_s)(R_c^3 - 1) - (1-\alpha_s)\int_0^L \frac{A'(x)}{A^3(x)} f(x)dx = 0 \quad (12)$$

in which $x_c > L$ and $A(x_c) = 1$ have been taken. Note that the expression of R_c obtained by Wang and Brennen [1] comes directly from Eq. (12) after dropping the last term and all of the higher order terms (since $R_c \gg 1$). The integration term in Eq. (12) shows that the critical bubble radius depends on the flow in the nozzle which, however, is unknown. The key point in the present method is to approximate $f(x)$ in a reasonable way.

It is found from the numerical solutions that no matter what configuration the nozzle has, as the flashing instability starts, the function, $f(x)$, for $0 \leqslant x \leqslant x_c$, can be approximated very well by an error function:

$$f(x) = (f_m - 1)\,\mathrm{erf}\left[\frac{\sqrt{\pi} f'(x_m)}{s(f_m - 1)}(x - x_m)\right] + f_m \quad (13)$$

where, as shown in Fig. 6, $f_m = (1+f_c)/2$, is the average of $f(0) = 1$ and f_c, the critical value of f at x_c, x_m is the position corresponding to f_m, and f'_m is the slope at x_m which has an expression of

$$f'_m = (1-\alpha_s)\frac{d}{dx}\left[1 + \frac{\alpha_s R^3}{1-\alpha_s}\right]\Bigg|_{x=x_m} = 3\alpha_s R_m^2 R'_m \quad (14)$$

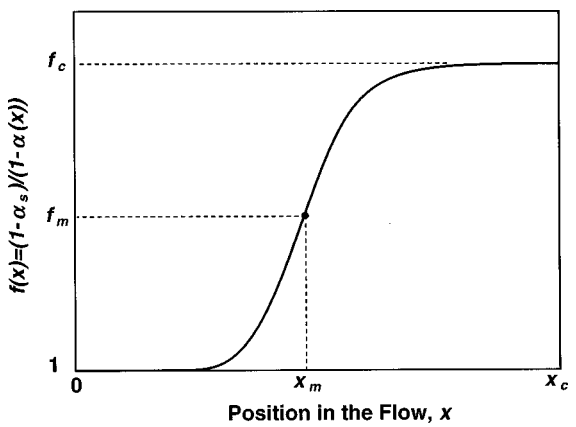

Fig. 6 Schematic of $f(x) = (1-\alpha_s)/(1-\alpha(x))$, for $0 \leqslant x \leqslant x_c$

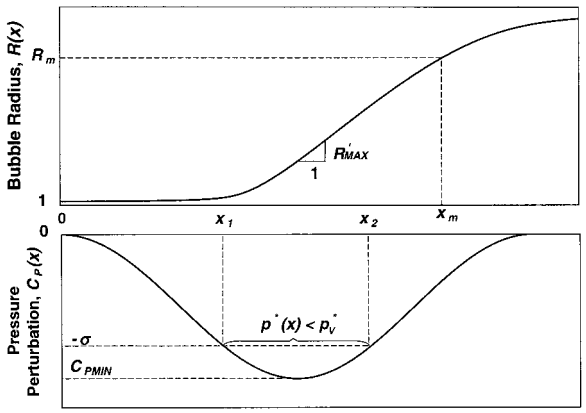

Fig. 7 Schematic of bubble growth through a low-pressure region

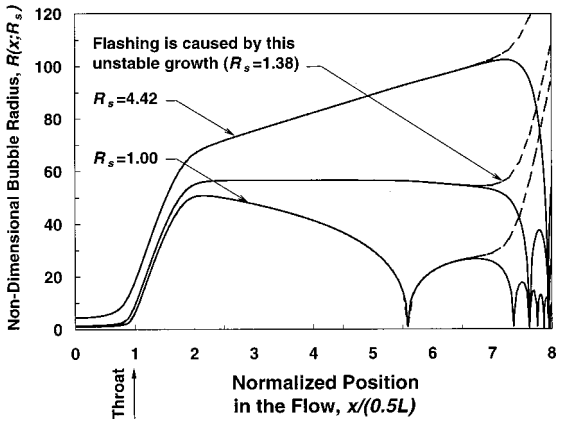

Fig. 8 Stable and unstable radius distributions for bubbles of three selected equilibrium sizes. Same parameters as Fig. 2 with $\alpha_s=\alpha_b^-$ (solid line) and $\alpha_s=\alpha_b^+$ (dashed line).

in which R_m and R'_m are the bubble radius and the bubble growth rate at x_m, respectively. The relation between f_m and R_c can be easily found using Eq. (11):

$$f_m=\frac{1}{2}\left(1+\frac{1-\alpha_s}{1-\alpha_c}\right)\approx 1+0.5\alpha_s R_c^3 \tag{15}$$

and this also leads to $R_m\approx 0.5^{1/3}R_c$. The bubble growth rate, R'_m, can be estimated as follows. Referring to Fig. 7, consider the typical growth of a cavitation bubble through a low-pressure region. As the bubble passes the position x_1, at which the pressure coefficient is equal to $-\sigma$, it experiences a pressure lower than the vapor pressure, p_V^*, and, therefore, starts to cavitate. The bubble grows explosively and quickly reaches an asymptotic growth rate, R'_{MAX}, which is given approximately by

$$R'_{\mathrm{MAX}}=[(-C_{P\,\mathrm{MIN}}-\sigma)/3]^{1/2}/u_{\mathrm{MAX}} \tag{16}$$

where u_{MAX} is the corresponding flow velocity to R'_{MAX} and the value of $-C_{P\,\mathrm{MIN}}-\sigma$ represents the intensity of tension to the bubble. Equation (16) is obtained simply by integrating (after dropping the viscous term) the Rayleigh-Plesset equation with C_P replaced by $C_{P\,\mathrm{MIN}}$ and u_{MAX} is to be taken as the throat velocity in the pure liquid flow. After passing x_2, the recovering pressure is higher than the vapor pressure and causes the decrease in dR/dx. Eventually the bubble growth rate goes to zero and the maximum bubble size occurs. To estimate R'_m, it is now assumed that the bubble growth rate decreases linearly from R'_{MAX} to 0 for $x_2<x<x_c$, i.e.,

$$R'_m=R'_{\mathrm{MAX}}\left(1-\frac{x_m-x_2}{x_c-x_2}\right) \tag{17}$$

Finally, Eq. (12) can be written as

$$\alpha_s(1-\alpha_s)\left\{1+0.5\int_0^L \mathrm{erf}\left[\frac{\sqrt{3\pi(-C_{P\,\mathrm{MIN}}-\sigma)}(x_c-x_m)}{2^{2/3}u_{\mathrm{MAX}}R_c(x_c-x_2)}\right.\right.$$
$$\left.\left.\times(x-x_m)\right]\frac{A'(x)}{A^3(x)}\,dx\right\}R_c^4-\frac{\sigma}{2}R_c-\frac{2}{\mathrm{We}}=0 \tag{18}$$

in which all higher order terms have been neglected. The critical bubble radius, R_c, can be calculated by iterating the nonlinear equation (18). A Levenberg-Marquardt method (see, for example, Dennis and Schnabel [19]) is used to determine R_c and x_m simultaneously subjected the convergence condition, $f(x_c)=1+\alpha_s R_c^3$, with x_c as large as possible.

To test the veracity of the analytical model we compare the critical flow variables found from Eq. (18) with the numerical results of Wang and Brennen [1] (from which $u_c=1.341$, $\alpha_c=0.254$, and $R_c=48.220$.) After substituting their basic parameters ($C_{P\,\mathrm{MIN}}=-1.0$, $\sigma=0.8$, $L=500$, $\alpha_s\approx 3\times 10^{-6}$, We$=137$) into Eq. (18), the critical bubble radius is found as $R_c=48.110$ (with $x_m=1.63(L/2)$ and $x_c=2.85(L/2)$) from which $u_c=1.339$ and $\alpha_c=0.253$ are obtained. The difference between the prediction and the numerical results is within 0.4 percent. This good agreement serves to validate the prediction criterion.

For the case of multiple bubble sizes, Eq. (10) still holds. The function, $f(x)$, now has the form of

$$f(x)=\frac{1-\alpha_s}{1-\alpha(x)}=(1-\alpha_s)\left[1+\frac{4\pi}{3}\int_{R_{S\,\mathrm{MIN}}}^{R_{S\,\mathrm{MAX}}}R^3(x;R_s)\chi(R_s)\,dR_s\right] \tag{19}$$

It is found in the present work that, as the flow becomes neutrally unstable, the bubble size distribution has very minor effects on the flow. A reason for this can be seen in Fig. 8 in which the bubble radius distribution for nuclei of three selected sizes is shown. It is clear that the flashing process is triggered by bubbles of a specific size and is thus very similar to the flow of single bubble size. This is further illustrated in Fig. 9 which shows distribution of $f(x)$ obtained from the analytic expression (Eq. (13)) and three numerical solutions, one of multiple bubble sizes and two of single size ($R_s^*=10\,\mu$m and 200 μm, respectively). The difference is minor.

Therefore, we can now predict the critical flow variables for the present example of multiple bubble sizes using the single size

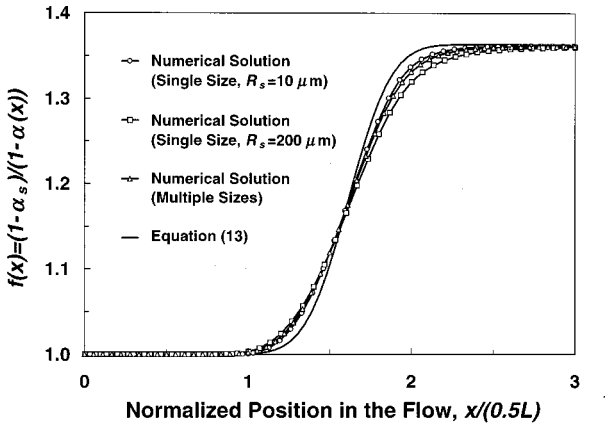

Fig. 9 Comparison of three numerically calculated $f(x)$ and that given by Eq. (13). Same parameters as Fig. 2.

model. Following the procedures described above, results of $u_c = 1.363$, $C_{Pc} = -0.856$, $\alpha_c = 0.267$ (with $x_m = 1.62(L/2)$ and $x_c = 2.50(L/2)$) are obtained. The prediction is also accurate (within 0.8 percent) in comparison with the numerical results (shown in Figs. 2–4).

Concluding Remarks

Numerical solutions for one-dimensional steady cavitating nozzle flows with bubble size distribution have been presented. It is shown that, for a fixed cavitation number and throat pressure coefficient, stable solutions can only exist for a limited range of the upstream void fraction. Very strong interactions between cavitating bubbles and the flow are found. The interaction effects are revealed in two aspects: (1) For quasi-statically stable flows, the growth and collapse of cavitation bubbles produce mean flow fluctuation downstream of the nozzle. However, the fluctuation is greatly suppressed by the presence of multiple bubble sizes and, therefore, results in a reduction of cavitation loss; (2) flashing instability occurs downstream of the nozzle as the flow reaches a critical state. In this circumstance, the effects of bubble size distribution are minor and the flow becomes unstable due to the unbound growth of bubbles of a specific size.

An analytical model based on the characteristics of growth of a cavitation bubble is proposed to predict the critical flow variables. Excellent agreement is obtained between the analytic and computational results for flows of both equal bubble size and multiple bubble sizes. It remains to be determined whether the flashing instability leads to the unsteady, oscillatory cavitating flows which are observed in practice.

Acknowledgments

The author is grateful to Professor T. Colonius for his useful comments. This research was supported by the National Science Council, Taiwan, R.O.C., under grant number NSC 87-2212-E-006-059.

Nomenclature

A = normalized cross-sectional area of nozzle
C_P = fluid pressure coefficient
$C_{P\,MIN}$ = minimum pressure coefficient for pure liquid flow
L = dimensionless length of the nozzle
N = proportional constant in the expression of nuclei number density distribution function
R = nondimensional bubble radius
Re = Reynolds number, $\rho_L^* u_s^* R_{s\,\mathrm{MIN}}^* / \mu_E^*$
R_s = nondimensional upstream bubble radius
R'_{MAX} = asymptotic bubble growth rate
$R_{s\,\mathrm{MAX}}^*$ = maximum upstream bubble radius
$R_{s\,\mathrm{MIN}}^*$ = minimum upstream bubble radius
S^* = surface tension of the liquid
We = Weber number, $\rho_L^* u_s^{*2} R_{s\,\mathrm{MIN}}^* / S^*$
e = normalized fluid energy density
f = reciprocal of the normalized volumetric fraction of the liquid phase
k = polytropic index for the gas inside the bubbles
p^* = fluid pressure
p_s^* = upstream pressure
p_V^* = vapor pressure
u = nondimensional fluid velocity
u_{MAX} = nondimensional fluid velocity corresponding to R'_{MAX}
u_s^* = upstream fluid velocity
x = dimensionless coordinate
α = void fraction of the bubbly fluid
α_b = upstream void fraction at which flashing instability occurs
χ = nuclei number density distribution function
γ = ratio of specific heats of the gas inside the bubbles
μ_E^* = effective dynamic viscosity of the liquid
ρ = dimensionless fluid density
ρ_L^* = density of the liquid
σ = cavitation number, $(p_s^* - p_V^*)/\frac{1}{2}\rho_L^* u_s^{*2}$
τ = nondimensional bubble volume

Subscripts

c = critical variables as flashing instability occurs
s = upstream quantity

Superscripts

$*$ = dimensional quantity
$'$ = derivative with respect to x

References

[1] Wang, Y.-C., and Brennen, C. E., 1998, ''One-Dimensional Bubbly Cavitating Flows Through a Converging-Diverging Nozzle,'' ASME J. Fluids Eng., **120**, pp. 166–170.
[2] Ceccio, S. L., and Brennen, C. E., 1991, ''Observations of the Dynamics and Acoustics of Travelling Bubble Cavitation,'' J. Fluid Mech., **233**, pp. 633–660.
[3] Tanger, H., Streckwall, H., Weitendorf, E.-A., and Mills, L., 1992, ''Recent Investigations of the Free Air Content and its Influence on Cavitation and Propeller-Excited Pressure Fluctuations,'' *Proceedings of the International Symposium on Propulsors and Cavitation*, Hamburg.
[4] Gindroz, B., Henry, P., and Avellan, F., 1992, ''Francis Cavitation Tests with Nuclei Injection: A New Test Procedure,'' *Proceedings of the 16th IAHR*, Sao Paulo.
[5] Peterson, F. B., Danel, F., Keller, A. P., and Lecoffre, Y., 1975, ''Comparative Measurements of Bubble and Particulate Spectra by Three Optical Methods,'' *Proceedings of the 14th International Towing Tank Conference*, Vol. 2, Ottawa, Canada, pp. 27–52.
[6] Gates, E. M., and Bacon, J., 1978, ''Determination of Cavitation Nuclei Distribution by Holography,'' J. Ship Res., **22**, No. 1, pp. 29–31.
[7] Katz, J., 1978, ''Determination of Solid Nuclei and Bubble Distributions in Water by Holography,'' Report No. 183-3, Division of Engineering and Applied Science, California Institute of Technology, Pasadena, CA.
[8] O'Hern, T. J., Katz, J., and Acosta, A. J., 1985, ''Holographic Measurements of Cavitation Nuclei in the Sea,'' *Proceedings of ASME Cavitation and Multiphase Flow Forum*, pp. 39–42.
[9] van Wijngaarden, L., 1972, ''One-Dimensional Flow of Liquids Containing Small Gas Bubbles,'' Annu. Rev. Fluid Mech., **4**, pp. 369–396.
[10] Biesheuvel, A., and van Wijngaarden, L., 1984, ''Two-Phase Flow Equations for a Dilute Dispersion of Gas Bubbles in Liquid,'' J. Fluid Mech., **148**, pp. 301–318.
[11] Muir, J. F., and Eichhorn, R., 1963, ''Compressible Flow of an Air-Water Mixture through a Vertical Two-Dimensional Converging-Diverging Nozzle,'' *Proceedings of the 1963 Heat Transfer and Fluid Mechanics Institute*, Stanford University Press, pp. 183–204.
[12] Brennen, C. E., 1995, *Cavitation and Bubble Dynamics*, Oxford University Press, New York.
[13] Zhang, D. Z., and Prosperetti, A., 1994, ''Ensemble Phase-Averaged Equations for Bubbly Flows,'' Phys. Fluids, **6**, No. 9, pp. 2956–2970.
[14] Ishii, M., and Mishima, K., 1983, ''Flow Regime Transition Criteria Consistent with a Two-Fluid Model for Vertical Two-Phase Flow,'' Reports NUREG/CR-3338 & ANL-83-42.
[15] Plesset, M. S., and Prosperetti, A., 1977, ''Bubble Dynamics and Cavitation,'' Annu. Rev. Fluid Mech., **9**, pp. 145–185.
[16] Chapman, R. B., and Plesset, M. S., 1971, ''Thermal Effects in the Free Oscillation of Gas Bubbles,'' ASME J. Basic Eng., **93**, pp. 373–376.
[17] Colonius, T., Brennen, C. E., and d'Auria, F., 1998, ''Computation of Shock Waves in Cavitating Flows,'' *ASME 3rd International Symposium on Numerical Methods for Multiphase Flow*, FEDSM98-5027.
[18] d'Agostino, L., and Brennen, C. E., 1988, ''Linearized Dynamics of Two-Dimensional Bubbly and Cavitating Flows over Slender Surfaces,'' J. Fluid Mech., **192**, pp. 485–509.
[19] Dennis, J. E., and Schnabel, R. B., 1983, *Numerical Methods for Unconstrained Optimization and Nonlinear Equations*, Prentice-Hall, Englewood Cliffs, NJ.

Journal of Fluids Engineering

Technical Briefs

An Experimental Investigation of the Effect of Freestream Turbulence on the Wake of a Separated Low-Pressure Turbine Blade at Low Reynolds Numbers

C. G. Murawaski
Research Engineer, Propulsion Directorate, AFRL/PRTT, Bldg 18, 1950 Fifth Street, WPAFB, OH 45433-7251

K. Vafai
Professor, Ohio State University, Department of Mechanical Engineering, 206 W. 18th Avenue, Columbus, OH 43210-1107; Fellow ASME

An experimental study was conducted in a two-dimensional linear cascade, focusing on the suction surface of a low pressure turbine blade. Flow Reynolds numbers, based on exit velocity and suction length, have been varied from 50,000 to 300,000. The freestream turbulence intensity was varied from 1.1 to 8.1 percent. Separation was observed at all test Reynolds numbers. Increasing the flow Reynolds number, without changing freestream turbulence, resulted in a rearward movement of the onset of separation and shrinkage of the separation zone. Increasing the freestream turbulence intensity, without changing Reynolds number, resulted in shrinkage of the separation region on the suction surface. The influences on the blade's wake from altering freestream turbulence and Reynolds number are also documented. It is shown that width of the wake and velocity defect rise with a decrease in either turbulence level or chord Reynolds number.
[S0098-2202(00)00202-9]

Introduction

For low-pressure turbines at low Reynolds numbers, the laminar boundary layer in the aft portion of the suction surface can be susceptible to large unsteady flow separation. This results in a degradation of overall turbine engine performance (Sharma et al. [1]). For this reason, low-pressure turbine aerodynamics has received an increased level of attention recently. Research conducted by Baughn et al. [2], Qui and Simon [3], and Bons et al. [4] have shown that profile losses increase as the Reynolds number decrease due to flow separation on the suction surface.

An experimental study was conducted in a two-dimensional linear cascade with low-pressure turbine blades. Flow Reynolds numbers, based on exit velocity and suction surface length, were varied from 50,000 to 200,000. Freestream turbulence was varied from 1.1 to 8.1 percent. Parts of the results in this report were presented in Murawski et al. [5]. The results are revisited and updated, focusing on Reynolds number and turbulence level effects on a low-pressure turbine airfoil and documenting the effect of these influences on the airfoil wake.

Experimental Apparatus. Figure 1 shows a schematic of the test apparatus. A centrifugal blower, controlled by a variable speed motor controller, pulls air through the apparatus. The inlet freestream turbulence intensity can be elevated by a passive turbulence grid located 1.45 m upstream of the cascade row. The grid is a wooden square mesh of 13 mm square bars with a 25.4 mm center-to-center spacing.

The cascade contains four low-pressure turbine blades with an axial chord length of 10.36 cm and a span-to-chord length aspect ratio of 1.1. The suction surface length is 15.24 cm. The pitch-to-chord ratio (solidity) is 0.88 and the flow is turned through 95 deg.

Instantaneous local velocities were acquired using a single element, hot-film probe. Mean upstream velocity and total pressure measurements were acquired with a pitot-static probe. Surface static pressures were measured using static pressure ports located at midspan on the surface of one blade.

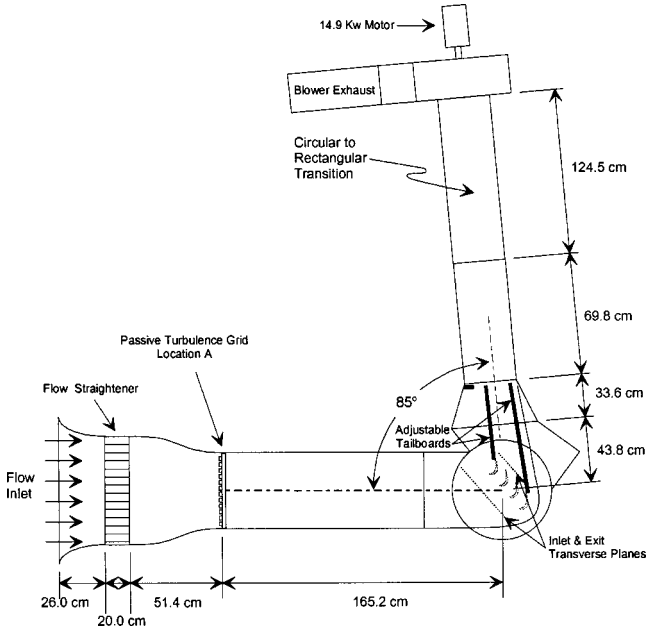

Fig. 1 Test apparatus schematic

Contributed by the Fluids Engineering Division of THE AMERICAN SOCIETY OF MECHANICAL ENGINEERS. Manuscript received by the Fluids Engineering Division March 3, 1999; revised manuscript received December 20, 1999. Associate Technical Editor: P. E. Raad.

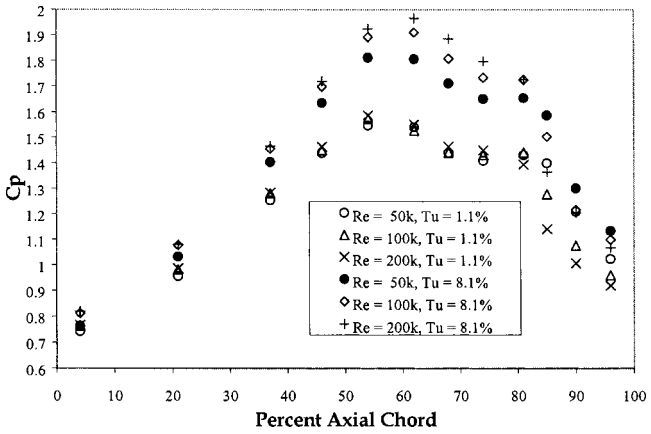

Fig. 2 Surface static pressure survey

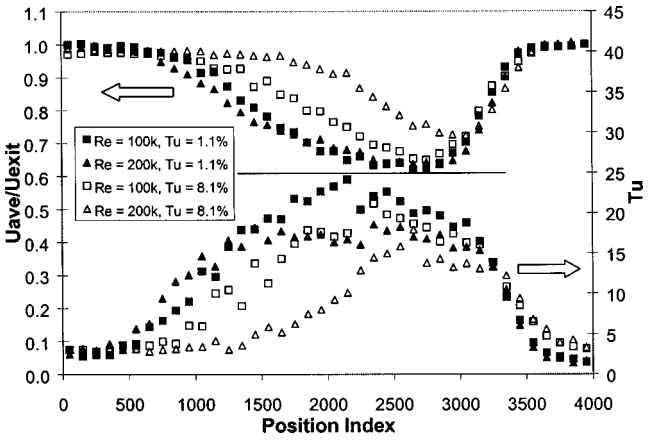

Fig. 4 Wake velocity survey for the average velocity and turbulence intensity

The experimental uncertainties were established using the method of Kline and McClintock [6]. The uncertainty of the velocity measurements from the pressure transducers and the single wire, hot-film probe was less than 2 percent. The maximum uncertainty in the pressure coefficient measurement was less than 4 percent.

Results

Inlet Profile. An inlet profile survey was performed by measuring velocities using a single hot-film probe located one blade chord upstream of the leading edges at mid-tunnel height. Without a turbulence generation grid, the inlet flow turbulence intensity was 1.1 percent. The passive turbulence grid created an inlet freestream turbulence level of 8.1 percent. The inlet axial flow velocity was uniform to within 7.5 percent with and without the turbulence grid.

Surface Static Pressure Results. Surface static pressure surveys for the suction surface of the turbine blade with freestream turbulence levels of 1.1 percent and 8.1 percent are presented in Fig. 2 in terms of a pressure coefficient defined by:

$$C_p = \frac{(P_{T\,\mathrm{in}} - P_{Si})}{\frac{1}{2}\rho U_{\mathrm{exit}}^2} \tag{1}$$

Along the suction side surface, from 0 to 50 percent of axial chord, the boundary layer remains attached for all Reynolds numbers. Over the last 50 percent of the suction side surface the boundary layer is affected by changes in Reynolds number and freestream turbulence intensity.

The pressure coefficient profiles of Fig. 2 contain a terrace (flat zone) in this region. Gaster [7] explained that the terrace is created by the initial portion of the separation bubble composed of a laminar shear layer and a dead air region. The shear layer then begins to interact with the separation bubble. A region of turbulent mixing occurs which may result in boundary layer reattachment. At the end of the dead air zone the magnitude of the velocity will increase near the wall. The initiation of transition appears as a region on the pressure coefficient curve that quickly falls off after the flat zone.

A separation zone is present in the pressure coefficient profiles for all Reynolds numbers. Increasing the Reynolds number results in a smaller terrace, which indicates a reduced size of the separation zone. Increasing both Reynolds number and freestream turbulence results in a smaller separation zone. The exact location of separation, transition, and reattachment are not precisely ascertained from surface static pressure surveys. However, the trends of Fig. 2 are consistent with and add value to the observations in the following sections.

Wakes. Changes in the size, length, and location of the separation zones on the turbine blade influence the size and strength of the wake. Each point on Fig. 3 represents a local instantaneous velocity recorded while a hot film probe was traversed parallel to and 2.54 cm behind the plane of the trailing edges of the cascade

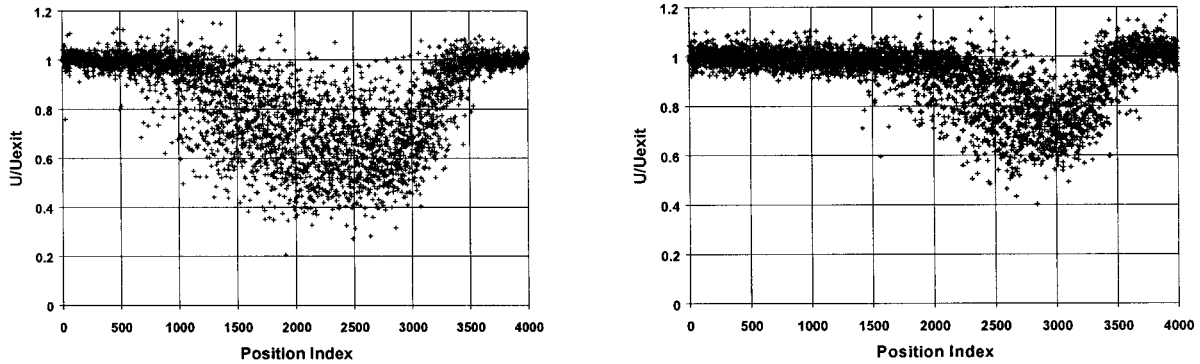

(a) Re =100k, Tu = 1.1%

(b) Re = 200k, Tu = 8.8%

Fig. 3 Instantaneous velocity wake survey: (*a*) Re=100 k,Tu=1.1 percent, (*b*) Re=200 k,Tu=8.1 percent,

turbine blade. Figure 3 shows that the wake dramatically decreases in size when the Reynolds number is increased from 100,000 to 200,000 and the freestream turbulence increases from 1.1 percent to 8.1 percent.

Figure 4 provides spatial averages of the instantaneous velocity surveys in the wake of the turbine blade wake. Spatial averages of velocity and turbulence intensity were calculated by averaging every 100 data points. The largest velocity defect and largest spatial turbulence intensity occurs when the freestream turbulence is 1.1 percent. At the lower Reynolds numbers, the thicker boundary layer, caused by flow separation at the rear of the suction surface, creates a larger local pressure drop, and more mixing occurs in the shear layer between the detached boundary layer and the freestream. This creates a larger wake and thus increased profile loss from the blade. As the Reynolds number is increased, with a freestream turbulence level of 1.1 percent, the level of fluctuation is diminished, while the width of the wake is almost constant.

Increasing the freestream turbulence level to 8.1 percent has a profound effect on the separation region on the suction side of the turbine blades in this cascade configuration. In each case, when the Reynolds number was kept constant and the freestream turbulence level was increased, the magnitude of the velocity deficit and the width of the wake decreased. The increase in freestream turbulence level diminishes the size of the separation region resulting in lower profile losses. In Fig. 4, when the freestream turbulence is held constant at 8.1 percent and the Reynolds number is increased, the velocity deficit and wake width decrease because the size of the separation zone is decreasing.

Conclusions

The effect of Reynolds number and freestream turbulence intensity on a low-pressure turbine cascade blade has been investigated in this work. The condition of the blade's boundary layer was the leading factor in the level of losses recorded in the wake. The losses from the blade decreased as the Reynolds number and freestream turbulence were increased.

At low levels of freestream turbulence, increasing the Reynolds number reduced the velocity deficit in the wakes, but did not reduce the width of the wake, resulting in only a minimal reduction of the profile losses.

For cases of freestream turbulence intensity of 8.1 percent, as Reynolds number increased, the suction side boundary layer changed dramatically. With increasing Reynolds number, the separation zone became smaller, reducing the velocity defect and decreasing the wake width, resulting in a substantial reduction in the blade's profile losses.

Acknowledgments

The assistance of Dr. Richard Rivir and Dr. Rolf Sondergaard of the Air Force Research Laboratory Propulsion Directorate is acknowledged. Professor Terrence Simon of the University of Minnesota and Dr. Ralph Volino of the U.S. Naval Academy provided technical support. The authors are grateful to Dr. Paul King of the Air Force Institute of Technology for use of the linear cascade.

Nomenclature

- Cp = local pressure coefficient
- P_{Si} = static pressure along the blade surface
- $P_{T\,\mathrm{in}}$ = total pressure at inlet to blade set
- Tu = freestream turbulence intensity ($u'_{\mathrm{rms}}/\overline{u}_{\mathrm{local}}$)
- U_{exit} = velocity at the exit of the blade set
- $\overline{u'}_{\mathrm{rms}}$ = root mean square of the fluctuating component of streamwise velocity
- $\overline{u}_{\mathrm{local}}$ = local mean streamwise velocity
- ρ = density

References

[1] Sharma, O. P., Ni, R. H., and Tanrikut, S., 1994, ''Unsteady Flows in Turbines-Impact on Design Procedure,'' AGARD-LS-195, Paper No. 5.

[2] Baughn, J. W., Butler, R. J., Byerley, A. R., and Rivir, R. B., 1995, ''An Experimental Investigation of Heat Transfer, Transition and Separation on Turbine Blades at Low Reynolds Number and High Turbulence Intensity,'' ASME Paper No. 95-WA/HT-25.

[3] Qiu, S., and Simon, T. W., 1997, ''An Experimental Investigation of Transition as Applied to Low Pressure Turbine Suction Surface Flows,'' ASME Paper No. 97-GT-455.

[4] Bons, J. P., Sondergaard, R., and Rivir, R. B., 1999, ''Control of Low-Pressure Turbine Separation Using Vortex Generator Jets,'' AIAA Paper No. 99-0367.

[5] Murawski, C. G., Sondergaard, R., Rivir, R. B., Vafai, K., Simon, T. W., and Volino, R. J., 1997, ''Experimental Study of the Unsteady Aerodynamics in a Linear Cascade with Low Reynolds Number Low Pressure Turbine Blades,'' ASME Paper No. 97-GT-95.

[6] Kline, S. J., and McClintock, F. A., 1953, ''Describing Uncertainties in Single-Sample Experiments,'' Mechanical Engineering, **75**, pp. 3–8.

[7] Gaster, M., 1966, ''The Structure and Behavior of Laminar Separation Bubbles,'' AGARD-CP-4, pp. 819–854.

Experimental Investigation of Flow Through an Asymmetric Plane Diffuser

(Data Bank Contribution)[1]

Carl U. Buice
Director of Application, Genemachines,
San Carlos, CA 94070

John K. Eaton
Department of Mechanical Engineering, Stanford University, Stanford, CA 94305
e-mail: eaton@vk.stanford.edu

[S0098-2202(00)00302-3]

Introduction

This data bank contribution provides measurements for a two-dimensional diffuser flow which includes separation and reattachment forming a separation bubble on one wall of the diffuser. Separated flows are difficult to predict because the separating and reattaching boundary layers are highly out of equilibrium. Advanced simulation techniques including large eddy simulation and detached eddy simulation are being developed to compute separated flows. Such simulations require realistic, time-dependent inflow conditions. These are most easily generated if the inlet flow is simple. For this reason, Obi et al. [1] made measurements in a nominally two-dimensional separated diffuser flow with fully developed channel flow inlet conditions. The test case is widely used, but there are questions about the two dimensionality of the flow.

The objective of the present work was to repeat the Obi et al. experiment using a larger aspect ratio apparatus and paying extra attention to the treatment of the endwall boundary layers. In addition, the straight tailpipe section of the diffuser was extended to allow a more extensive examination of the boundary layer down-

[1]Data have been deposited to the JFE Data Bank. To access the file for this paper, see instructions on p. 463 of this issue.

Contributed by the Fluids Engineering Division of THE AMERICAN SOCIETY OF MECHANICAL ENGINEERS. Manuscript received by the Fluids Engineering Division July 7, 1999; revised manuscript received January 25, 2000. Associate Technical Editor: D. P. Telionis.

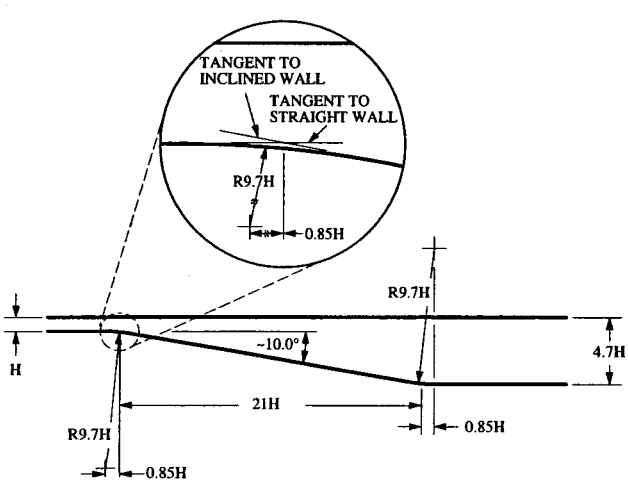

Fig. 1 Detailed drawing of test section geometry

stream of reattachment. This is an especially useful case for the study of recovering flows because the flow has a known end state of fully developed channel flow.

Experimental Apparatus and Techniques

The experiments were conducted in the blower-driven wind tunnel of Anderson and Eaton [2] modified with an additional contraction to a two-dimensional, plane-wall channel flow with a channel height H of 15 mm and a width of 610 mm. The high aspect ratio (41:1) inlet channel is 1.65 m long providing ample length to obtain fully developed turbulent channel flow at the inlet of the diffuser test section. The diffuser geometry shown in Fig. 1 replicates the geometry of Obi et al. [1]. There is an asymmetric expansion with an area ratio of 4.7 over a distance of 21 H giving a diffuser angle of 10 degrees. The rectangular tailpipe section (70.5 mm×610 mm) extends 56 H downstream of the diffuser before the flow exits to the room through a grid.

Even with the large aspect ratio, special care was required to obtain a two-dimensional flow. The endwall boundary layers were removed by adding thin splitter plates 4.7 H from each end wall starting 6 H upstream of the diffuser and extending to the end of the tunnel. A row of small holes was drilled through the splitter plates 3 H downstream of the diffuser inlet to thin the new end-wall boundary layer. Suction in the end-wall sections was adjusted to obtain two-dimensional flow everywhere in the test section. Buice and Eaton [3] document numerous tests of the two-dimensionality including measurements of the spanwise uniformity of the mean velocity and skin friction, and calculated balances of mass and momentum. The tests show that the flow is two dimensional to within the measurement resolution.

Multiple probe systems were used to provide the best accuracy in each region of the flow and to provide redundant measurements where possible. Wall static pressure was measured using 0.64 mm diameter taps connected to a Celesco P7D pressure transducer (+/−0.1 psid range). Overall uncertainty was less that 0.001 in. of water.

Mean velocity and turbulent stresses were measured using hot-wire anemometry in regions where the streamwise turbulence intensity was less than 30 percent. Details of the probes and techniques are given in Buice and Eaton [3]. The techniques were similar to those reported in Anderson and Eaton [1]. Single-wire measurements had mean velocity uncertainty of 2 percent and streamwise turbulence intensity uncertainty of 4 percent, except near the wall in the upstream channel as discussed below. Cross-wire uncertainty was 5 percent for the wall-normal Reynolds stress, and 10 percent for the shear stress, $u'v'$. Redundant measurements of the mean velocity and streamwise normal stress agreed with the single-wire results within the uncertainty estimates.

A single component pulsed wire anemometer was used for velocity measurements in the highly turbulent separated shear layer and in the recirculation zone. The mean velocity uncertainty was estimated to be 2 percent for velocities ranging from 5 to 12 m/s and around 5 percent for lower velocities. The uncertainty in the measurement of u' was less than 5 percent in regions of high

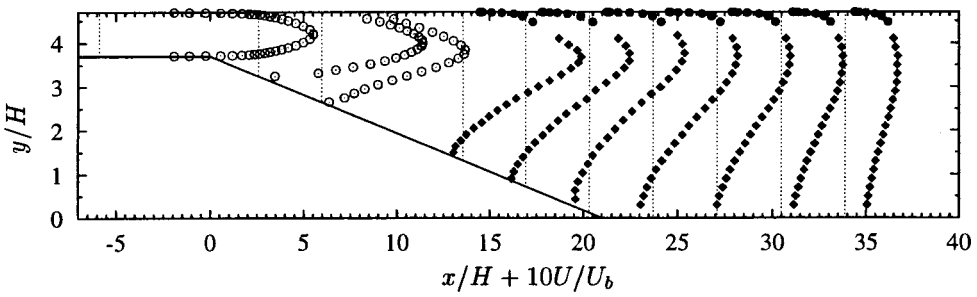

Fig. 2 Mean velocity profiles, U/U_b: ○, single wire boundary layer probe; ◇, pulsed wire probe; ●, single wire wall probe

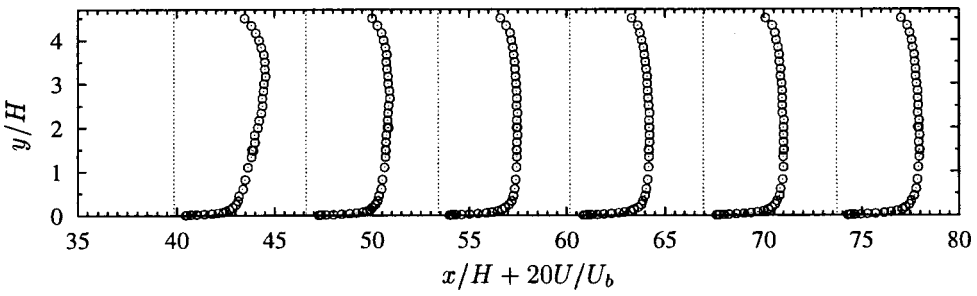

Fig. 3 Mean velocity profiles, U/U_b: ○, single wire boundary layer probe

turbulence intensity ($u'/U > 0.05$). In regions of lower turbulence intensity, the pulsed-wire turbulence measurements are unreliable, and we present only hotwire results.

A special wall mounted pulsed-wire called the pulsed-wall probe (Westphal et al. [4]) was used to measure near-wall velocity profiles in the recirculation region, and to infer the wall shear stress by moving the measurement location very close to the wall. With the wire drawn into the nearest position ($y = 0.15$ mm) the probe was calibrated directly for skin friction using fully developed channel flow as a reference. The uncertainty in the skin friction measurements was estimated to be a constant 0.02 N/m^2.

Data Reported in the Archive

All data in the archive are presented in a coordinate system in which the x-axis is parallel to the upstream channel, and has its origin at the intersection of the two lines tangent to the inlet channel wall and the inclined wall. The y axis is normal to the x axis and thus to the undeflected wall of the diffuser. The origin of the y axis is on the lower wall of the tailpipe so all y values are positive. All distances are normalized by the height of the inlet channel, H. Velocities are normalized by the bulk average velocity in the upstream channel, U_b. The upstream channel centerline velocity is $1.14U_b$. The tunnel was operated at $U_b = 20$ m/s giving an inlet channel Reynolds number, U_bH/ν of 20,000.

In comparing to the present data set, it is important that computations of the flow begin some distance upstream of the diffuser inlet since the streamlines begin to curve upstream of $x = 0$, causing local acceleration and distortion of the velocity profile. For this reason, the inlet conditions are specified at $x/H = -5.1$ where pressure measurements indicate a constant pressure gradient characteristic of fully developed channel flow. The present mean velocity and turbulence profiles are in excellent agreement with the data of Hussain and Reynolds [5], measured at a channel height Reynolds number of 21,300. The only exception are the turbulence intensity measurements for $y/H < 0.025$ where the present measurements are 10 to 20 percent lower. This is due to the inadequate spatial resolution of the single-wire probe which was 0.6 mm (45 wall units) long. The mean velocity and turbulence data indicate that the inlet flow has the characteristics of fully developed channel flow, and that any well-qualified channel-flow simulation can be used to provide inlet conditions for the diffuser simulation.

Figures 2 and 3 show the mean velocity profiles, illustrating the distribution of profile locations and the general development of the flow. Streamwise turbulence intensity, wall normal stress, and the Reynolds shear stress were all measured at the same profile locations. Note that the wall normal stress and Reynolds shear stress profiles do not extend into the separated flow region, where the cross wire would have a very large uncertainty. In addition to these profiles, measurements of the static pressure and the skin friction along the entire length of both test section walls are included in the data set. This includes measurements in the separated flow region where the pulsed-wall probe supplied measurements of the reverse-flow skin friction.

There are two aspects of this data set that offer a particular challenge to model developers. First, is the smooth wall separation and reattachment that make this case more challenging than the backward-facing step and similar abruptly separated flows. Also, of great interest is the recovering channel flow in the tailpipe. The profile near the wall recovers until it is virtually identical to the upstream channel. On the other hand, the velocity is more uniform than developed channel flow in the central region due to the strong turbulent mixing produced by eddies remaining from the separated flow. Thus, the turbulence is far from equilibrium with the mean flow, and offers a good test for length scale transport equations. The thermal diffusivity in this region is also far out of equilibrium, as shown by Buice and Eaton [6].

References

[1] Obi, S., Aoki, K., and Masuda, S., 1993, ''Experimental and Computational Study of Separating Flow in an Asymmetric Planar Diffuser,'' *9th Symposium on Turbulent Shear Flows*, Kyoto, Japan, pp. 305-1–305-4.

[2] Anderson, S. D., and Eaton, J. K., 1989, ''Reynolds Stress Development in Pressure-Driven Three-Dimensional Turbulent Boundary Layers,'' J. Fluid Mech., **202**, pp. 263–294.

[3] Buice, C. U., and Eaton, J. K., 1997, ''Experimental Investigation of Flow Through an Asymmetric Planar Diffuser,'' Report TSD-107, Department of Mechanical Engineering, Stanford University, Stanford, CA.

[4] Westphal, R. V., Eaton, J. K., and Johnston, J. P., 1981, ''A New Probe for Measurement of Velocity and Wall Shear Stress in Unsteady, Reversing Flow,'' ASME J. Fluids Eng., **103**, pp. 478–482.

[5] Hussain, A. K. M. F., and Reynolds, W. C., 1970, ''The Mechanics of a Perturbation Wave in Turbulent Shear Flow,'' Report FM-6, Department of Mechanical Engineering, Stanford University, Stanford, CA.

[6] Buice, C. U., and Eaton, J. K., 1999, ''Turbulent Heat Transport in a Perturbed Channel Flow,'' ASME J. Heat Transfer, **199**, pp. 322–325.

Couette Flow Profiles for Two Nonclassical Taylor-Couette Cells

Michael C. Wendl
Postdoctoral Research Associate, School of Medicine, Washington University, Saint Louis, MO 63108

Ramesh K. Agarwal
Bloomfield Distinguished Professor and Executive Director, National Institute for Aviation Research, Wichita, KS 67260

Exact solutions for the Couette profile in two nonclassical Taylor-Couette cells are reported. The profiles take the form of eigenfunction expansions, whose convergence rates can be significantly accelerated using a representative convergence acceleration algorithm. Results are thus suitable as initial conditions for high resolution numerical simulations of transition phenomena in these configurations. [S0098-2202(00)02602-X]

1 Introduction

Laminar flow transition modes are frequently studied using a Taylor-Couette cell, which consists of a cylindrical stator and rotor with fixed endwalls to confine the fluid. Numerical investigations typically use either Taylor's velocity profile (Taylor [1]) or the linear ''thin gap'' profile (Panton [2]) as an initial condition, perturbing it appropriately to examine the disturbance behavior (Criminale et al. [3], Hua et al. [4], Kedia et al. [5]). Both of these profiles are one-dimensional, neglecting spanwise variations such as end effects from the stator walls. While suitable for the theoretical case of infinite span, they are inappropriate for a number of practical situations, e.g., for cells whose span and gap dimensions are of the same order and for the so-called ''nonclassical'' cells whose gap dimension varies along the span (Wiener et al. [6]). Both of these types of cells generally exhibit significant spanwise dependencies. Moreover, variation in nonclassical cells can extend to the boundary, for example when the rotor radius is not constant.

The focus of this note is on deriving Couette flow profiles for two specific nonclassical configurations of current interest, a coni-

Contributed by the Fluids Engineering Division of THE AMERICAN SOCIETY OF MECHANICAL ENGINEERS. Manuscript received by the Fluids Engineering Division July 8, 1999; revised manuscript received February 7, 2000. Associate Technical Editor: M. R. Hajj.

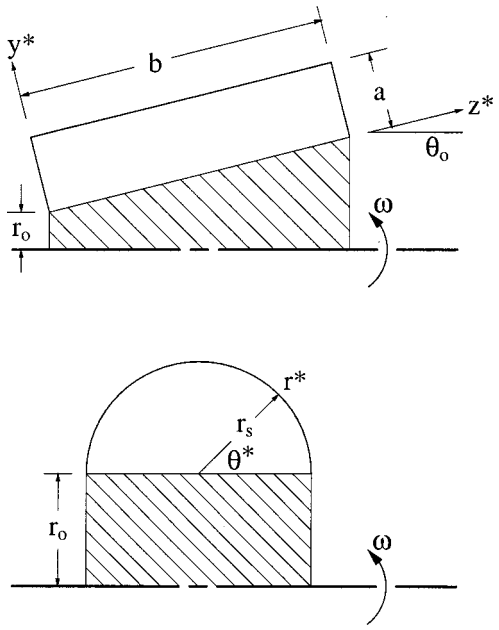

Fig. 1 Schematic of the conical cell (top) and the spanwise convex stator cell (bottom). Cross-hatched areas represent the rotor and the remaining line segments denote the stator. Cells are symmetric about the center line and the star notation indicates dimensional coordinates.

cal cell and a cell whose stator is convex along its span. Conical cells (Fig. 1(top)) have been used to examine supercritical flow modes, both experimentally (Wimmer [7–9]) and numerically (Abboud [10]), but transition modes have not yet been extensively studied. Results for convex stator geometries are currently limited to the idealized model of small convexity and infinite span (Eagles and Eames [11]). Although the standard Taylor profile can be conveniently adapted to this case, it is not an experimentally relevant configuration because of the assumption of infinite span. Therefore, the case of a semi-circular cross section is addressed (Fig. 1(bottom)) in this paper. This geometry exhibits both a finite span and significant convexity relative to the span. Exact solutions for the Couette profile for these two configurations do not appear in the literature (Carslaw and Jaeger [12], Berker [13], Wang [14]). The present approach employs, an integral transform method (Ölçer [15]) to obtain exact solutions as expansions in characteristic eigenfunctions. Convergence properties of these expansions, which determine their suitability for use in a numerical solver, are evaluated by applying a representative convergence acceleration algorithm (Brezinski [16], Singh and Singh [17]).

2 Analytical Solutions

Wimmer's experimental results on nonclassical cells (Wimmer [9]) suggest that the Couette mode cannot be physically sustained when curvature effects are significant. The fundamental flow mode is fully three-dimensional under such conditions. Consequently, geometries are presently restricted to small curvature effects; the gap dimension is assumed small compared to the rotor radius and the taper is also assumed small. As a result, curvature terms vanish and the Navier-Stokes equations reduce to Laplace's equation for the dimensionless azimuthal velocity component u (Wang [14]),

$$\nabla^2 u = 0. \tag{1}$$

For the conical cell model (Fig. 1(a)), gap width and cell span are a and b, respectively, the cone angle is $0 \leqslant \theta_0 \leqslant \pi/2$, the reference radius is $r_0 > 0$, and the Laplacian operator ∇^2 in Cartesian (x,y) coordinates is $\partial^2/\partial y^2 + \partial^2/\partial z^2$. Dimensional analysis yields three geometric parameters: the aspect ratio $\phi = b/a$, the radius ratio $R = r_0/a$, and the taper factor $T = b \sin\theta_0/r_0$, which is taken as a measure of taper effects. Wimmer's restriction [9] dictates that R^{-1} and T should be small. Using a and $a\omega$ as length and velocity scales, respectively (where ω is the rotor's rotation rate), the nondimensional boundary conditions are

$$u = 0 \quad at \quad z = 0, \; z = \phi, \quad and \quad y = 1, \tag{2a}$$

and

$$u = R + z \sin\theta_0 \quad at \quad y = 0. \tag{2b}$$

An appropriate integral transform pair is given by

$$\overline{u}(y,\beta_m) = \int_0^{\phi} Z(\beta_m, z') u(y,z') dz' \tag{3a}$$

and

$$u(y,z) = \sum_{m=1}^{\infty} \frac{Z(\beta_m, z)\overline{u}(y,\beta_m)}{\int_0^{\phi} Z^2(\beta_m, z') dz'}. \tag{3b}$$

The overbar notation represents a transform in the z coordinate direction, β_m are the corresponding eigenvalues, and $Z(\beta_m, z)$ are the corresponding eigenfunctions. All eigen-related quantities can be obtained from standard tables (Özişik [18]).

Applying transform (3a) to Eqs. (1), (2a), and (2b) yields the auxiliary equation $\overline{u}'' - \beta_m^2 \overline{u} = 0$, and two auxiliary boundary conditions $\overline{u} = 0$ at $y = 1$ and $\overline{u} = \phi R([1-(-1)^m] - T[-1]^m)/m\pi$ at $y = 0$. A Sturm-Liouville equation and integration by parts have been used to evaluate various terms. The solution of this system is

$$\overline{u} = \frac{\phi R([1-(-1)^m] - T[-1]^m)\sinh m\pi(1-y)/\phi}{m\pi \sinh m\pi/\phi}. \tag{4}$$

Inverse transform (3b) is applied to Eq. (4) to obtain the physical profile in (y,z) space. After eliminating all noncontributing modes, the final result is found to be

$$u(y,z) = \frac{2R}{\pi} \sum_{m=1}^{\infty} \left(\frac{2 \sinh \dfrac{(2m-1)\pi(1-y)}{\phi} \sin \dfrac{(2m-1)\pi z}{\phi}}{(2m-1)\sinh \dfrac{(2m-1)\pi}{\phi}} - \frac{T[-1]^m \sinh \dfrac{m\pi(1-y)}{\phi} \sin \dfrac{m\pi z}{\phi}}{m \sinh \dfrac{m\pi}{\phi}} \right). \tag{5}$$

It is readily apparent that for vanishing taper, $T \to 0$, Berker's two-dimensional thin-gap solution (Berker [13]) for the classical case is recovered.

The convex stator configuration in Fig. 1(bottom) is characterized by R, which is the radius of the rotor r_0, divided by the radius of the stator's cross section r_s. Since the endwalls are effectively formed by the stator itself, there is no separate characterization of the aspect ratio. Moreover, r_s describes the convexity which is a fixed ratio of 1:2 relative to the span of $2r_s$. The curvature restriction again suggests that R must be large. The Laplacian operator in Eq. (1) is now expressed in cylindrical (r,θ) coordinates as $(1/r)\partial/\partial r(r\partial/\partial r) + (1/r^2)\partial^2/\partial\theta^2$. After nondimensionalization, boundary conditions can be expressed as

$$u = R \quad at \quad \theta = 0 \quad and \quad \theta = \pi, \tag{6a}$$

and

$$u = 0 \quad at \quad r = 1. \tag{6b}$$

An appropriate integral transform pair is given by

$$\overline{u}(r,m)=\int_0^{\pi}\Theta(m,\theta')u(r,\theta')d\theta' \tag{7a}$$

and

$$u(r,\theta)=\sum_{m=1}^{\infty}\frac{\Theta(m,\theta)\overline{u}(r,m)}{\int_0^{\pi}\Theta^2(m,\theta')d\theta'}, \tag{7b}$$

where eigenvalues and eigenfunctions are denoted respectively by m and $\Theta(m,\theta)$. Because the domain of θ is $0\leqslant\theta\leqslant\pi$, this configuration is a special case in which the θ eigenvalues are integers, as indicated by Eq. (7*b*).

Transformation using Eq. (7*a*) yields $\overline{u}''+\overline{u}'/r-(m/r)^2\overline{u}+mR(1-\cos m\pi)/r^2=0$, a nonhomogeneous equation of the Euler-Cauchy type, and the boundary condition $\overline{u}=0$ at $r=1$. An auxiliary boundary condition $\overline{u}=$*finite* at $r=0$ is also available. By substituting $\overline{u}(r,m)=\overline{\psi}(r,m)+R(1-\cos m\pi)/m$, the homogeneous form of the equation for $\overline{\psi}$ is obtained and is solved with standard methods. The auxiliary solution is then obtained as

$$\overline{u}=\frac{R[(-1)^m-1](r^m-1)}{m}. \tag{8}$$

Inverting Eq. (8) using Eq. (7*b*), the physical solution in (r,θ) space is found after simplification to be

$$u(r,\theta)=R\left(1-\frac{4}{\pi}\sum_{m=1}^{\infty}\frac{r^{2m-1}\sin(2m-1)\theta}{(2m-1)}\right). \tag{9}$$

3 Numerical Evaluation of Series

Use of Eqs. (5) and (9) as initial profiles for numerical computations requires evaluating these expressions for each finite-volume in a computational grid. Processing effort increases not only with grid resolution, but is also dramatically affected in regions where convergence slows considerably. Brezinski's three step acceleration algorithm (Brezinski [16], Singh and Singh [17]) is applied to determine whether the number of terms required for convergence in such regions can be reduced to a manageable level. Taking S_m as the partial sum of m terms such that $S_m\rightarrow S$ as $m\rightarrow\infty$, where S is the complete summation, the two preliminary steps in the algorithm are $\Gamma_1^m=S_m$ and $\Gamma_2^m=(\Gamma_1^{m+1}-\Gamma_1^m)^{-1}$. Progressive estimates of S are given by the third step

$$\Gamma_3^m=\Gamma_1^{m+1}+\frac{(\Gamma_1^{m+2}-\Gamma_1^{m+1})(\Gamma_2^{m+2}-\Gamma_2^{m+1})}{\Gamma_2^{m+2}-2\Gamma_2^{m+1}+\Gamma_2^m}. \tag{10}$$

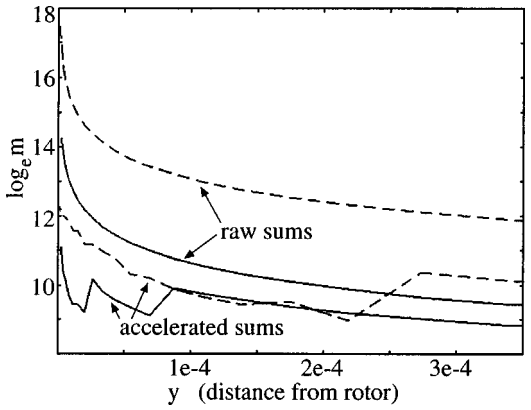

Fig. 2 Convergence properties of raw and accelerated series at $z=\phi/2$ in the conical cell; $\phi=1$, ——; $\phi=12.75$, — — —. The abscissa and ordinate show nondimensional distance from the rotor and $\log_e$ of the number of terms required for convergence, respectively.

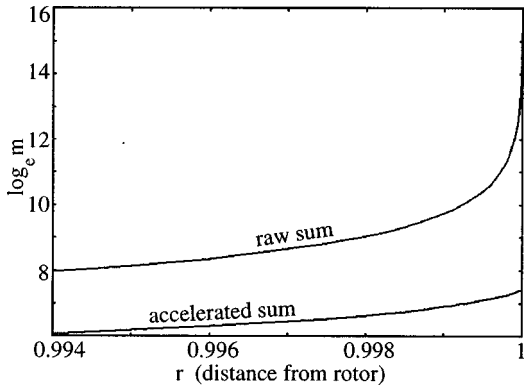

Fig. 3 Convergence properties of raw and accelerated series at $\theta=\pi/2$ in the convex stator cell. Axes are the same as for Fig. 2.

Convergence properties are examined for each cell at the center of their spans, i.e., at $z=\phi/2$ for the conical cell and $\theta=\pi/2$ for the convex cell. At the boundaries, the nondimensional grid size is taken to be of order $\delta=10^{-6}$ and is allowed to stretch at the rate of 25 percent toward the interior of the cross section. Convergence is considered achieved when double-precision accuracy has been attained.

Convergence properties of Eq. (5) are independent of R since it appears outside the summation. Moreover, T does not affect convergence for values in the range of physical interest, i.e., $0.01\leqslant T\leqslant 0.1$. The cell aspect ratio is thus the only important parameter. Two values are examined, $\phi=1$ for a square cross section and $\phi=12.75$, which corresponds to Wimmer's experimental configuration [9]. Convergence for both cases requires about 10^1 terms in the series near the stator and approximately 10^3 and 10^4 terms, respectively, for $\phi=1$ and $\phi=12.75$ at $y\sim 0.001$. These results can be considered acceptable for a coarse grid whose smallest volume is $\sim 10^{-3}$. However, for finer grids convergence slows considerably nearer to the rotor. Figure 2 shows results for $y<0.0003$; Brezinski's algorithm yields significant acceleration in this region. At $y\sim 10^{-6}$, the raw series for $\phi=1$, which requires approximately 10^6 terms for convergence, is accelerated by a factor of about 30. For $\phi=12.75$, the raw series requires on the order of 10^7 terms, while the accelerated series converges about 180 times faster.

Like the conical cell, convergence in much of the convex stator cross section ($r<0.99$) is reasonably good, requiring approximately 10^1 to 10^3 terms. However, convergence degrades rapidly for the remaining 1 percent of the cell near the stator (Fig. 3), requiring 10^7 terms for $r\sim 1-10^{-6}$. In this case, the Brezinski algorithm results in an acceleration factor of 10^4. The better performance for this configuration is due to the fact that Eq. (9) is monotonic, whereas Eq. (5) has alternating terms.

4 Conclusion

Exact series solutions for Couette flow profiles in two nonclassical geometries of current experimental interest are reported. Convergence of these series is shown to be improved significantly using a representative convergence acceleration algorithm. These results can therefore be effectively used as initial conditions for high-resolution numerical studies of flow transition in these cells.

References

[1] Taylor, G. I., 1923, ''Stability of a Viscous Liquid Contained Between Two Rotating Cylinders,'' Philos. Trans. R. Soc. London, Ser. A, **223**, pp. 289–343.
[2] Panton, R. L., 1984, *Incompressible Flow*, Wiley, New York.
[3] Criminale, W. O., Jackson, T. L., Lasseigne, D. G., and Joslin, R. D., 1997,

''Perturbation Dynamics in Viscous Channel Flows,'' J. Fluid Mech., **339**, pp. 55–77.
[4] Hua, B. L., Gentil, S. L., and Orlandi, P., 1997, ''First Transitions in Circular Couette Flow with Axial Stratification,'' Phys. Fluids, **9**, pp. 365–375.
[5] Kedia, R., Hunt, M. L., and Colonius, T., 1998, ''Numerical Simulations of Heat Transfer in Taylor-Couette Flow,'' ASME J. Heat Transfer, **120**, pp. 65–71.
[6] Wiener, R. J., Snyder, G. L., Prange, M. P., Frediani, D., and Diaz, P. R., 1997, ''Period-Doubling Cascade to Chaotic Phase Dynamics in Taylor Vortex Flow with Hourglass Geometry,'' Phys. Rev. E, **55**, pp. 5489–5497.
[7] Wimmer, M., 1985, ''Einfluß der Geometrie auf Taylor-Wirbel,'' Z. Angew. Math. Mech., **65**, pp. T255–T256.
[8] Wimmer, M., 1988, ''Viscous Flows and Instabilities Near Rotating Bodies,'' Prog. Aerosp. Sci., **25**, pp. 43–103.
[9] Wimmer, M., 1995, ''An Experimental Investigation of Taylor Vortex Flow Between Conical Cylinders,'' J. Fluid Mech., **292**, pp. 205–227.
[10] Abboud, M., 1988, ''Ein Beitrag zur theoretischen Untersuchung von Taylor-Wirbeln im Spalt zwischen Zylinder/Kegel-Konfigurationen,'' Z. Angew. Math. Mech., **68**, pp. T275–T277.
[11] Eagles, P. M., and Eames, K., 1983, ''Taylor Vortices Between Almost Cylindrical Boundaries,'' J. Eng. Math., **17**, pp. 263–280.
[12] Carslaw, H. S., and Jaeger, J. C., 1959, *Conduction of Heat in Solids*, Clarendon Press, Oxford.
[13] Berker, R., 1963, ''Intégration des équations du mouvement d'un fluide visqueux incompressible,'' *Handbuch der Physik*, (Flügge, S.), VIII/2, Berlin, Springer-Verlag.
[14] Wang, C. Y., 1991, ''Exact Solutions of the Steady-State Navier-Stokes Equations,'' Annu. Rev. Fluid Mech., **23**, pp. 159–177.
[15] Ölçer, N. Y., 1964, ''On the Theory of Conductive Heat Transfer in Finite Regions,'' Int. J. Heat Mass Transf., **7**, pp. 307–314.
[16] Brezinski, C., 1982, ''Some New Convergence Acceleration Methods,'' Math. Comput., **39**, pp. 133–145.
[17] Singh, S., and Singh, R., 1993, ''Use of Linear and Nonlinear Algorithms in the Acceleration of Doubly Infinite Green's Function Series,'' IEE-Proc. H, **140**, pp. 452–454.
[18] Özişik, M. N., 1980, *Heat Conduction*, Wiley, New York.

A Method for Validating Two-Dimensional Flow Configurations in Particle Streak Velocimetry

Y. M. Gbamelé
PhD Student

P. Desevaux
Assistant Professor

J.-P. Prenel
Professor

Institut de Génie Energétique, Université de Franche-Comté, 2, avenue Jean Moulin, F-90000, Belfort, France

A polychromatic flow visualization technique for Particle Streak Velocimetry (PSV) is described. The method uses several adjoining laser light sheets of different wavelengths with a homogeneous power density distribution. This method allows us to make sure of the 2-D and 3-D nature of flows and to improve the frames quality processed in PSV. The feasibility study of this qualitative technique is established on a hydrodynamic flow.
[S0098-2202(00)02402-0]

Contributed by the Fluids Engineering Division of THE AMERICAN SOCIETY OF MECHANICAL ENGINEERS. Manuscript received by the Fluids Engineering Division April 28, 1999; revised manuscript received February 16, 2000. Associate Technical Editor: S. Banerjee.

1 Introduction

The methods of velocity measurement by PIV, PTV, PSV have made progress these last years (Grant [1]). Large efforts have focused on the application of these techniques to the study of three-dimensional flow (Hinsch [2]). Unfortunately, the methods proposed are often heavy and complex to implement. So, before using such techniques, it is better to confirm the 2-D or 3-D nature of flows. We present here a qualitative technique based on the polychromatic laser tomography (Prenel et al. [3]) to dispel this ambiguity. The images obtained by this technique allow us to make sure of the 2-D or 3-D nature and can be directly processed in PSV to extract the velocity fields.

2 Optical Device

The optical setup (Fig. 1) used to realize three polychromatic laser sheets is taken from the device designed by Prenel et al. [4]. The light source is an argon-krypton laser (Spectra-Physics Laser Stabilite 2017) emitting in all lines with a power of about 4 W. The objective is to obtain parallel sheets with a homogeneous power density distribution and adjustable thickness and width (Prenel and Thiery [5]). This requires two fast horizontal and vertical simultaneous sweepings of the laser beam. So, the device is made up of a first telescope (T_1) which focuses the polychromatic beam at the entrance of an Acousto-Optical Deflector (AOD: AA.DTS.X-250, optical range 360–1100 nm). The AOD induces a horizontal sweeping of the beam. The triangular shape of the driving signal guarantees the homogeneity of the power density distribution along the sheet thickness and the amplitude controls its size. The telescope (T_2) focuses the beam in the zone of visualization. The Prism with Direct Vision (PDV) disperses the light and the three intense lines (red 647.1 nm, green 514.5 nm, and blue 488 nm) are carried back on three mirrors (M_1, M_2, and M_3). These mirrors restore the beams parallel and three prisms (P_1, P_2, and P_3) enable the space between the polychromatic beams to be adjusted.

The scanning mirror (SM) produces a vertical deviation of the

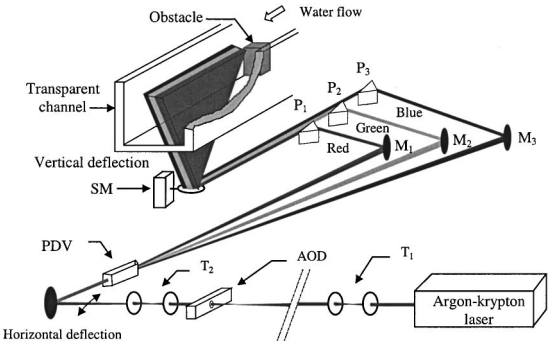

Fig. 1 Optical device

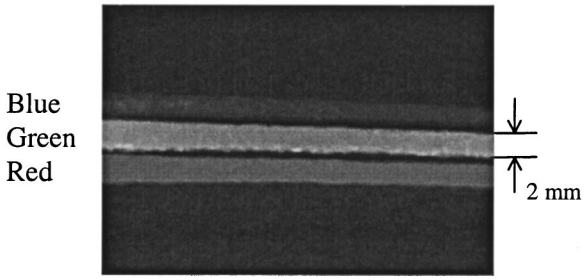

Fig. 2 Laser sheets dimensions

beams and guarantees the power density homogeneity along the sheets width. The scanning mirror amplitude sets the sheets width dimension.

For a long working distance and a weak sweeping angle, the polychromatic sheets become real parallelepipeds of light with a nearly homogeneous power density.

Figure 2 is a top view photography of the three adjoining laser light sheets. The sheets thickness (equal to 2 mm in the present picture) is the same for the three laser sheets and may be adjusted to values from 0.5 mm to 10 mm.

3 Practicability Experiment

The practicability of the method is established on a hydrodynamic flow generated in a transparent channel with a rectangular section (10 cm×4 cm). An obstacle (i.e., a 3 cm×1.5 cm vertical plate) is placed in the hydrodynamic channel (as shown in Fig. 3) in order to disturb the flow and to create 3-D effects. During the tests, the water flows out with an average velocity between 0.05 and 0.25 ms^{-1} corresponding to Reynolds numbers (relative to the hydraulic diameter of the water channel) varying from 3000 to 15,000. The water seeding is performed by means of rilsan spherical particles (Elf Atochem, weak size dispersion around 30 μm, volumic mass of 1.06 g/cm^3). The three light sheets illuminate three parallel planes along the principal flow direction. The flow is observed perpendicularly to the laser sheets by using a 3-CCD color video camera (Sony XC-003P). The images are digitized and stored as 715×535 pixels by an imaging technologies frame buffer board (MiroVideo). The observation field is limited to a rectangular area of 35 mm×25 mm. The three zones of the hydrodynamic channel, which are investigated during this feasibility study, are indicated in Fig. 3.

Figure 4 shows flow visualizations obtained by using the present technique. The exposure time used in the images presented is 1/25 s. When a particle moves in the studied zone, the luminous dash marking its trajectory during the acquisition time presents a uniform contrast due to the homogeneous power distribution within the light volumes. Consequently, the dynamic behavior of the particle can easily be quantified. It can be noticed that a single particle is about 6–7 pixels large. Moreover, the particle streak will be made up of one or several colors according to its displacement.

In 2-D flows parallel to the three sheets, the particles scatter in only one color (i.e., red, green, or blue color). These conditions are those of the initial flow upstream of the obstacle (zone 1) where the flow is expected to be strictly 2-D. This is confirmed by the flow visualization presented in Fig. 4(a) which reveals the presence of particle streaks made up of one color only. This picture shows that the flow remains strictly parallel to the plane illuminated by the laser light sheets. Such conditions are ideal for a classical study by PSV and the 2-D velocity field may be directly determined from such an image.

The photography displayed in Fig. 4(b) is related to the zone 3 located at a long distance (about 40 cm) behind the obstacle. We cannot a priori be sure of the 2-D or 3-D configuration of the flow in this region of the hydrodynamic channel. The flow visualizations performed by the present method clear up the ambiguity relating to the flow pattern and indicate the weak 3-D nature of the flow in this zone. Indeed, we can note the presence of few bicolor or tricolor streaks revealing the 3-D trajectories of some tracers. If these polychromatic streaks are in a small number, the flow may be studied in PSV as a 2-D flow. An image processing procedure may be applied to remove these few polychromatic streaks before extracting the 2-D velocity field.

For highly 3-D flows, the majority of the particle streaks will be made up of 2 or 3 colors. This is illustrated in Fig. 4(c) by the flow visualization performed in the immediate wake of the obstacle (zone 2).

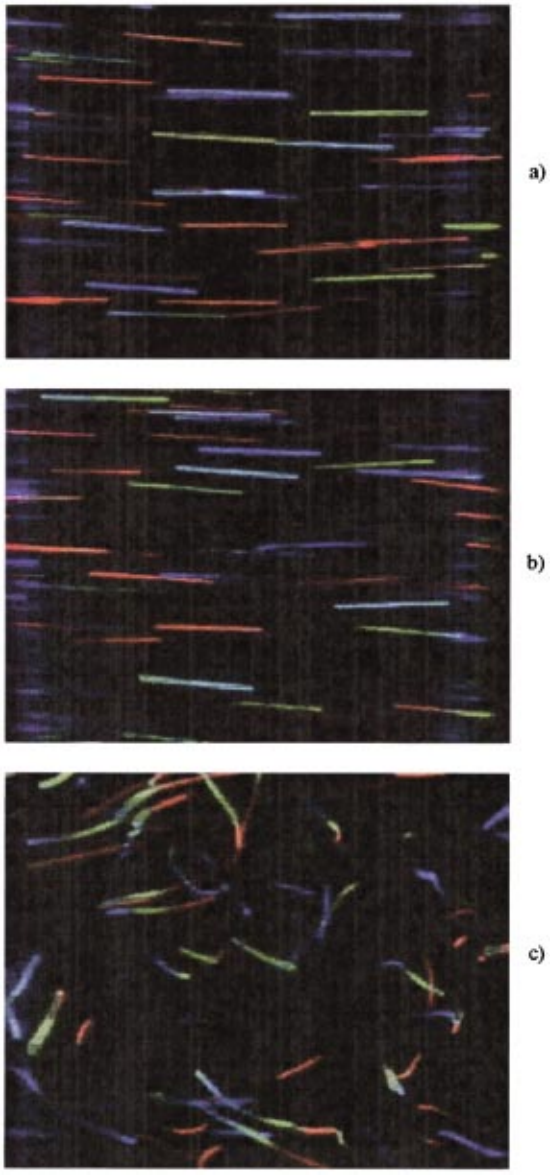

Fig. 4 (*a*) Strictly 2-D flow; (*b*) weakly 3-D flow; (*c*) highly 3-D flow

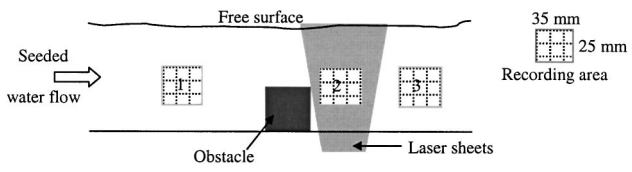

Fig. 3 Location of the investigated zones (side view of the hydrodynamic channel)

4 Concluding Remarks

A number of conclusions are offered relative to the flow visualization method developed in this paper:

1 The use of polychromatic laser tomography is a simple and efficient way for validating 2-D flow configurations.

2 For weakly 3-D flows, an image processing procedure may be applied to remove polychromatic streaks before extracting the two-dimensional velocity vectors.

3 The present method is illustrated by its application to a hydrodynamic-channel flow but may be extended to gas flows.

4 Limitations of the method depend mainly on the viewing system characteristics: the depth of field of the viewing system limits the laser sheets thickness, the camera sensitivity is not the same for all the wavelengths and consequently an adjustment of the wave lines intensities of the argon-krypton laser is required, and the exposure time of the viewing system must be long enough with respect to the flow velocity so that tracers having possibly 3-D trajectories may cross the three laser sheets in the thickness direction.

5 For very low velocity flows, the thickness of the laser sheets has to be reduced to its minimum value (0.5 mm with the present optical device) in order to enhance the sensitivity of the system to detect possible 3-D effects.

References

[1] Grant, I., 1997, ''Particle Image Velocimetry: A Review,'' Proc. Inst. Mech. Eng., Part C: J. Mech. Eng. Sci., **211**, pp. 55–76.

[2] Hinsch, K. D., 1995, ''Three-Dimensional Particle Velocimetry,'' Meas. Sci. Technol., **6**, pp. 742–753.

[3] Prenel, J. P., Porcar, R., Polidori, G., Texier, A., and Coutanceau, M., 1992, ''Wavelength Coding Laser Tomography for Flow Visualizations,'' Opt. Commun., **91**, pp. 29–33.

[4] Prenel, J. P., Thiery, L., and Marconot, B., 1997, ''Visualisation par volumes de lumière polychromatique à densité puissance homogène,'' *Proceedings du 7éme Colloque National de Visualisation et de Traitement d'Images en Mécanique des Fluides*, Saint-Louis, France, pp. 35–40.

[5] Prenel, J. P., and Thiery, L., 1997, ''Theoretical Study and Realization of Laser Light Sheets With a 3D Homogeneous Power Density and Controlled Geometrical Parameters,'' *Proceedings of the 1st Pacific Symposium on Flow Visualization and Image Processing*, Honolulu, Hawaii, pp. 537–541.

Analysis and Validation of One-Dimensional Models for Gaseous Flows in Micro-Channels

Hongwei Sun
Research Associate

Mohammad Faghri
Professor

Department of Mechanical Engineering and Applied Mechanics, University of Rhode Island, Kingston, RI 02881

The paper presents three one-dimensional models to simulate gaseous flows in micro-channels. These include no-slip flow, simple fully-developed, and locally fully-developed models. It is shown that the locally fully-developed model provides a more accurate prediction when both rarefaction and gas acceleration need to be considered in micro-flows. Furthermore, the effects of rarefaction and gas acceleration on the locally dimensionless pressure ratio are specified on the basis of the three models. The validation of these models is accomplished by comparison with the experimental results. [S0098-2202(00)02502-5]

Contributed by the Fluids Engineering Division of THE AMERICAN SOCIETY OF MECHANICAL ENGINEERS. Manuscript received by the Fluids Engineering Division December 9, 1998; revised manuscript received February 14, 2000. Associate Technical Editor: M. S. Cramer.

Introduction

For gaseous flows in micro-channels, the effect of rarefaction cannot be negligible because Knudsen numbers (ratio of mean free path to characteristic length) are usually greater than 0.01. Arkilic et al. [1,2] developed an analytical model based on the Navier-Stokes equation with the slip boundary condition to predict isothermal helium flows through a parallel plate channel and validated the model with the experimental results with pressure ratios up to 2.5. Shih et al. [3] validated this model by comparing the model results of mass flow rate and pressure distribution for nitrogen and helium flows through micro-channels with their experimental results. Direct Simulation Monte Carlo (DSMC) investigation by Piekos and Breuer [4] showed a discrepancy for pressure distribution when compared with the slip-flow model for a pressure ratio of 4.2. Sun et al. [5] investigated effects of velocity slip and temperature jump on the momentum and heat transport in micro-channels based on locally fully-developed assumption which was used by van den Berg [6] to analyze the compressible isothermal flows in capillaries.

The motivation of this work is to include the acceleration term in the conservation of momentum for a one-dimensional compressible flow model and to find out the relationship among the available one-dimensional models. Furthermore, the effects of rarefaction and gas acceleration on pressure distribution and mass flow rate are related to Re, Ma, and Kn based on the dimensional analysis for the simple fully-developed model and the locally fully-developed model.

One-Dimensional Models

For a laminar, constant-viscosity, fluid flow in a parallel plate channel, the conservation of axial momentum for an infinitesimal control volume with length dx can be expressed as:

$$-2hdP-2\overline{\tau}_w dx=d\left[\int_{-h}^{h}\rho u^2 dy\right] \tag{1}$$

where h is the half-depth of the channel and $\overline{\tau_w}$ refers to the average shear stress at the wall. DSMC simulation for gaseous flows in micro-channels shows that the maximum ratio of $v(x,y)/u(x,y)$ is less than one percent. Therefore, P can be assumed to be only a function of x.

Locally Fully-Developed Flow Model. High-pressure drops over relatively short lengths are common in gaseous flows through micro-channels. As a result, density and velocity continually change along the flow axis, and the flow cannot become fully developed. Therefore, a locally fully-developed model is introduced. In this model, the parabolic velocity profile and the wall shear stress are obtained from the fully developed condition and are locally applied at any cross-section along the micro-channel. In other words, the velocity profile u and the average wall shear stress $\overline{\tau_w}$ in Eq. (1) can be obtained from the Navier-Stokes equation with the slip boundary condition for fully developed flows as follows (Shih et al. [3]):

$$u(y)=\frac{h^2}{2\mu}\left(-\frac{dp}{dx}\right)\left[1.0+4\,\frac{2-\sigma_\gamma}{\sigma_\gamma}\mathrm{Kn}-\left(\frac{y}{h}\right)^2\right] \tag{2}$$

$$\overline{\tau}_w=-\mu\left.\frac{du}{dy}\right|_{y=h}=\frac{3}{4}\,\frac{\mathrm{Re}\,\mu^2}{\rho h^2\left(1+6\,\dfrac{2-\sigma_\gamma}{\sigma_\gamma}\mathrm{Kn}\right)} \tag{3}$$

where $\mathrm{Re}=\rho\overline{u}(4h)/\mu$, $\mathrm{Kn}=\lambda/(2h)$ and σ_γ represents the tangential momentum accommodation coefficient (TMAC) which depends on the gas species, surface characteristics and is usually close to unity.

By substituting Eqs. (2) and (3) into Eq. (1) and integrating along the x-direction using the ideal gas law and the continuity equation, an expression for the axial pressure distribution P can be obtained as follows:

$$\left(\frac{P}{P_{in}}\right)^2 - 1.0 + 12\,\mathrm{Kn}_{in}\left(\frac{P}{P_{in}} - 1.0\right) + 2\,\mathrm{Re}^2\,\alpha\beta\left[6\,\mathrm{Kn}_{in}\left(\frac{P_{in}}{P} - 1.0\right) - Ln\left(\frac{P}{P_{in}}\right)\right] = -24\,\mathrm{Re}\,\beta\frac{x}{h} \tag{4}$$

where β and α are given by:

$$\beta = \frac{\mu^2 RT}{(4hP_{in})^2}$$

$$\alpha = \frac{9}{4}\frac{\frac{8}{15} + \frac{16}{3}\overline{\mathrm{Kn}} + 16\,\overline{\mathrm{Kn}^2}}{(1 + 6\,\overline{\mathrm{Kn}})^2} \tag{5}$$

$\overline{\mathrm{Kn}}$ is the average Knudsen number along the channel. From Eq. (4), the corresponding mass flow rate can be obtained as follows:

$$G = \frac{h^3 w}{3RTL\mu}P_{out}^2\left[(P^*)^2 - 1.0 + 12\,\mathrm{Kn}_{out}(P^* - 1.0) - 2\left(\frac{\rho\overline{u}}{P_{out}}\right)^2 RT\alpha[6\,\mathrm{Kn}_{in}(P^* - 1.0) + Ln(P^*)]\right] \tag{6}$$

To the author's knowledge, Eqs. (4) and (6) for P and G are presented for the first time here.

Simple Fully-Developed Model. By neglecting the axial momentum change in Eq. (1) and using Eq. (3), the axial pressure distribution and mass flow rate can be obtained as follows:

$$\left(\frac{P}{P_{in}}\right)^2 - 1.0 + 12\,\mathrm{Kn}_{in}\left(\frac{P}{P_{in}} - 1.0\right) = -24\,\mathrm{Re}\,\beta\frac{x}{h} \tag{7}$$

$$G = \frac{Wh^3}{3RTL\mu}P_{out}^2[(P^*)^2 - 1.0 + 12\,\mathrm{Kn}_{out}(P^* - 1.0)] \tag{8}$$

Equations (7) and (8) are similar to the slip-flow model developed by Arkilic et al. [2] and Shih et al. [3] and are referred to as ''simple fully-developed model'' in this paper. The simple fully-developed model can predict the increase in mass flow rate due to gas rarefaction in flows through micro-channels.

Continuum Flow Model. By setting Knudsen numbers in Eqs. (7) and (8) to zero, the axial pressure distribution and the mass flow rate for the continuum flows can be obtained as:

$$\left(\frac{P}{P_{in}}\right)^2 - 1.0 = -24\,\mathrm{Re}\,\beta\frac{x}{h} \tag{9}$$

$$G = \frac{Wh^3}{3RTL\mu}P_{out}^2[(P^*)^2 - 1.0] \tag{10}$$

Comparison of Eqs. (8) and (10) shows that slip-flow causes an increase in mass flow rate for a given inlet and outlet pressures. However, according to Eq. (6), an increase in mass flow rate is reduced by gas acceleration for high pressure flow conditions. The following analysis reveals that the effect of the gas acceleration can be related to Mach number (Ma) in micro-flows when an isothermal assumption is valid.

Discussion and Validation

Pressure Distribution. Rarefaction and compressibility effects on gaseous flows in micro-channels have been studied by Beskok et al. [7] using numerical simulation for two-dimensional flows with a second-order slip boundary condition. However, for the first time in this paper, the relationships between the local pressure variation and the parameters Kn, Re, and Ma are shown based on the dimensional analysis for one-dimensional models.

For compressible no-slip flows, the axial $\mathbf{p}^2$ gradient can be obtained by differentiating Eq. (9) with respect to x as:

$$\left(\frac{dP^2}{dx}\right)_{\text{continuum}} = -\frac{3}{2}\frac{\mathrm{Re}\,\mu^2 RT}{h^3} \tag{11}$$

From the Eqs. (7) and (4), the corresponding relationships based on the simple fully-developed model and the locally fully-developed model can be obtained as:

$$\left(\frac{dp^2}{dx}\right)_{\text{simple}} = -\frac{3}{2}\frac{\mathrm{Re}\,\mu^2 RT}{h^3(1 + 6\,\mathrm{Kn})} \tag{12}$$

$$\left(\frac{dp^2}{dx}\right)_{\text{local}} = -\frac{3}{2}\frac{\mathrm{Re}\,\mu^2 RT}{h^3(1 + 6\,\mathrm{Kn})(1 - \mathrm{Re}^2\,\mathrm{Kn}^2/2\pi)} \tag{13}$$

where the following definition of Knudsen number is used:

$$\mathrm{Kn} = \frac{\mu\sqrt{\pi RT}}{2\sqrt{2}hp} \tag{14}$$

The subscript **continuum** refers to the compressible no-slip flow model and subscripts **slip** and **local** represent the simple fully-developed flow and the locally fully-developed flow model, respectively.

From Eqs. (11) and (12), it is clear that rarefaction reduces the pressure drop and friction factor. The reduction is quantified by the term $(1 + 6\,\mathrm{Kn})$. However, the negative effect is contributed by the gas acceleration term $(1 - \mathrm{Re}^2\,\mathrm{Kn}^2/2\pi)$ in Eq. (13). This conclusion—compressibility negating rarefaction—was also reached by Beskok et al. [7] based on his numerical simulation.

The Knudsen number can be expressed as a function of Mach number and Reynolds number (Eckert and Drake [8]) as:

$$\mathrm{Kn} = \frac{\lambda}{2h} = \sqrt{\gamma\pi/2}\,\frac{2\,\mathrm{Ma}}{\mathrm{Re}} \tag{15}$$

By using Eq. (15), the term $(1 - \mathrm{Re}^2\,\mathrm{Kn}^2/2\pi)$ in Eq. (13) can be replaced by $(1 - \gamma\,\mathrm{Ma}^2)$ to evaluate the gas acceleration. It is clear that rarefaction and acceleration have opposite effects on pressure variation and the terms $(1 + 6\,\mathrm{Kn})$ and $(1 - \gamma\,\mathrm{Ma}^2)$ represent the effects of slip flow and gas acceleration, respectively.

Mass Flow Rate. Comparison of mass flow rate versus pressure ratios between the three models and the experiment by Arkilic [1] is shown in Fig. 1. The experiment was conducted in a $52.25\,\mu\mathrm{m} \times 1.33\,\mu\mathrm{m} \times 7500\,\mu\mathrm{m}$ micro-channel using nitrogen as the working fluid. It was found that rarefaction has an important

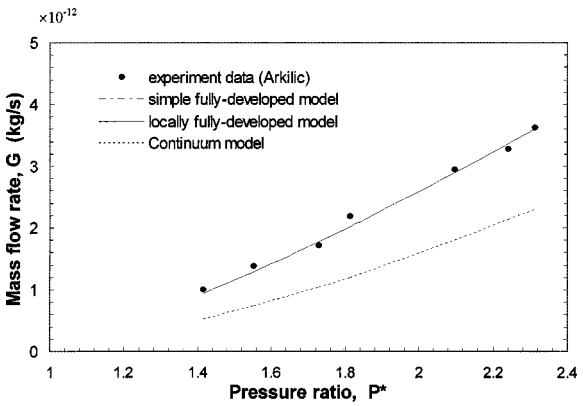

Fig. 1 Comparison of experimental results of Arkilic with the simple fully-developed model, the locally fully-developed model, and the continuum flow model

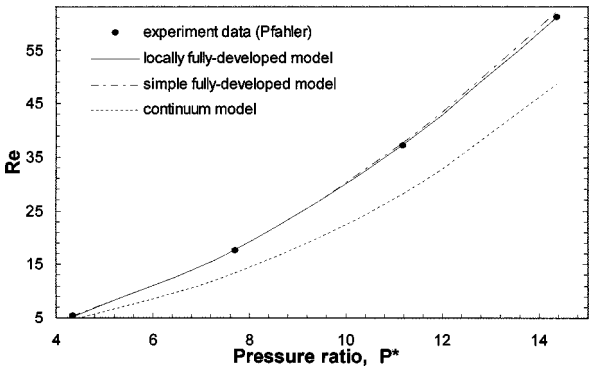

Fig. 2 Comparison of the experimental results by Pfahler [9] with the prediction from the three models

Table 1 Comparison between the terms $(1+6\,\mathrm{Kn})$ and $(1-\gamma\,\mathrm{Ma}^2)$ at the outlet for Pfahler's [9] experiment

P^*	$1+6$ Kn	$1-\gamma\,\mathrm{Ma}^2$
4.3	1.084	0.999
7.6	1.084	0.992
12.1	1.084	0.954
14.1	1.084	0.906
21.0	1.084	0.578

effect on mass flow rate in the microchannel as was also reported by other researchers. There exists a 17 percent deviation between the results from the continuum flow model and the experiment at the pressure ratio of 2.6 when the Knudsen numbers are 0.062 and 0.165 at the inlet and outlet, respectively. The deviation increases with the increase in pressure ratios. The simple fully-developed model and the local fully-developed model are both in good agreement with the experimental results for pressure ratios below 3.0. Simulation for higher-pressure ratios shows that the deviation between the two models is below 1.0 percent for a pressure ratio of 14.0. The term $\gamma\,\mathrm{Ma}^2$, which represents the effect of gas acceleration, has a magnitude of 10^{-6} at a pressure ratio of 2.6 and 10^{-4} for a pressure ratio of 14.0 and is still four orders of magnitudes smaller than the term 6 Kn which represents the effect of rarefaction.

Experimental data reported by Pfahler [9] was also employed to check the three models. In this experiment, nitrogen was driven through a $98.73\,\mu\mathrm{m}\times 4.65\,\mu\mathrm{m}\times 10{,}900\,\mu\mathrm{m}$ micro-channel and Reynolds number ranges from 5 to 60 with the fixed outlet Knudsen number of 0.014. Simulation results based on the continuum flow, simple fully-developed flow and local fully-developed flow models are presented in Fig. 2. It can be seen that the locally fully-developed model and the simple fully-developed model accurately predict the mass flow rate when P^* is smaller than 7.6. The deviation appears for higher values of P^*. The corresponding variations of the terms $(1+6\,\mathrm{Kn})$ and $(1-\gamma\,\mathrm{Ma}^2)$ are shown in Table 1. When $(1-\gamma\,\mathrm{Ma}^2)$ varies from 0.999 to 0.906 (P^* increase from 4.3 to 14.1), the deviation between the simple fully-developed and locally fully-developed flow models increases from 0.5 percent to 3 percent and become higher with increasing P^* based on the value of the term $(1-\gamma\,\mathrm{Ma}^2)$. Further experimental data for higher-pressure ratios is needed to check the accuracy of the locally fully-developed model in micro-flows.

Nomenclature

G = mass flow rate, $\rho\bar{u}W(2h)$
h = half-depth of the channel
Kn = Knudsen number, $\lambda/2h$
L = channel length
Ma = Mach number
P = pressure
P^* = inlet to outlet pressure ratio, $P_{\mathrm{in}}/P_{\mathrm{out}}$
R = gas constant
Re = Reynolds number, $\rho\bar{u}(4h)/\mu$
T = temperature
u = velocity in x-direction
$\bar{u}$ = average velocity in x-direction
v = velocity in y-direction
W = channel width
x,y = Cartesian coordinates
α,β = constants, Eq. (5)
γ = specific heat ratio
λ = mean free path
μ = viscosity
ρ = density
τ = shear stress
σ_γ = tangential momentum accommodation coefficient

Subscripts

continuum = compressible no-slip flow
in = inlet
local = locally fully-developed model
out = outlet
simple = simple fully-developed model
w = wall

References

[1] Arkilic E. B., Breuer K. S., and Schmidt M. A., 1994, ''Gaseous Flow in Micro-Channels,'' *Applications of Microfabrication to Fluid Mechanics*, ASME, FED-Vol. 197, pp. 57–66.
[2] Arkilic, E. B., Schmidt, M. A., and Breuer, K. S., 1997, ''Gaseous Slip Flow in Long Microchannels,'' J. Microelectromech. Syst., IEEE, **6**, pp. 167–178.
[3] Shih, J. C., Ho, C., Liu, J., and Tai, Y., 1996, ''Monatomic and Polyatomic Gas Flow Through Uniform Microchannels,'' Microelectromechanical Systems (MEMS), ASME, DSC-59, pp. 197–203.
[4] Piekos, E. S., and Breuer, K. S., 1996, ''Numerical Modeling of Micromechanical Devices Using the Direct Simulation Monte Carlo Method,'' ASME J. Fluids Eng., **118**, pp. 464–469.
[5] Sun, H., Gu, W., and Liu, W., 1998, ''Effects of Slip-flow and Temperature-jump on Momentum and Heat Transport in Micro-channels,'' J. Eng. Thermophys., **19**, No. 1, pp. 94–97.
[6] van den Berg, H. R., ten Seldam, C. A., and van der Gulik, P. S., 1993, ''Compressible Laminar Flow in a Capillary,'' J. Fluid Mech., **246**, pp. 1–20.
[7] Beskok, A., Karniadakis, G. E., Trimmer, W., 1996, ''Rarefaction and Compressibility Effects in Gas Microflows,'' ASME J. Fluids Eng., **118**, pp. 448–456.
[8] Eckert, E. R. G., and Drake R. M., 1972, *Analysis of Heat and Mass Transfer*, McGraw-Hill, New York.
[9] Pfahler J., Harley J., Bau H. H., and Zemel J., 1990, ''Liquid and Gas Transport in Small Channels,'' ASME, DSC-19, pp. 149–157.